Math-for-industry
Education & Research Hub

ISSN2188-1200

International Project Research-Workshop (I)

Forum “Math for Industry” 2025
- Challenge of Mathematics for Industry in the AI era -

Editors: Soon-Sun Kwon, Minjung Gim, Jae-Hun Jung

九州大学マス・フォア・インダストリ研究所

MI Lecture Note Vol.104 : Kyushu University

International Project Research-Workshop (I)

Forum “Math for Industry” 2025
- Challenge of Mathematics for Industry in the AI era -

Editors Soon-Sun Kwon, Minjung Gim, Jae-Hun Jung

About MI Lecture Note Series

The Math-for-Industry (MI) Lecture Note Series is the successor to the COE Lecture Notes, which were published for the 21st COE Program "Development of Dynamic Mathematics with High Functionality," sponsored by Japan's Ministry of Education, Culture, Sports, Science and Technology (MEXT) from 2003 to 2007. The MI Lecture Note Series has published the notes of lectures organized under the following two programs: "Training Program for Ph.D. and New Master's Degree in Mathematics as Required by Industry," adopted as a Support Program for Improving Graduate School Education by MEXT from 2007 to 2009; and "Education-and-Research Hub for Mathematics-for-Industry," adopted as a Global COE Program by MEXT from 2008 to 2012.

In accordance with the establishment of the Institute of Mathematics for Industry (IMI) in April 2011 and the authorization of IMI's Joint Research Center for Advanced and Fundamental Mathematics-for-Industry as a MEXT Joint Usage / Research Center in April 2013, hereafter the MI Lecture Notes Series will publish lecture notes and proceedings by worldwide researchers of MI to contribute to the development of MI.

October 2022
Kenji Kajiwara
Director, Institute of Mathematics for Industry

International Project Research-Workshop (I)
Forum "Math for Industry" 2025
- Challenge of Mathematics for Industry in the AI era -

MI Lecture Note Vol.104, Institute of Mathematics for Industry, Kyushu University
ISSN 2188-1200
Date of issue: January 5, 2026
Editors: Soon-Sun Kwon, Minjung Gim, Jae-Hun Jung
Publisher:
Institute of Mathematics for Industry, Kyushu University
Graduate School of Mathematics, Kyushu University
Motooka 744, Nishi-ku, Fukuoka, 819-0395, JAPAN
Tel +81-(0)92-802-4402, Fax +81-(0)92-802-4405
URL https://www.imi.kyushu-u.ac.jp/

Preface

In August 2025, the *Forum "Math-for-Industry" 2025 (FMfI 2025)* was held at the POSCO Center in Seoul, Republic of Korea, jointly organized by the **Institute of Mathematics for Industry (IMI)**, Kyushu University, and the **Department of Mathematics, Ajou University**, with support from the **Asia–Pacific Consortium of Mathematics for Industry (APCMfI)**, the **National Institute for Mathematical Sciences (NIMS)**, and other partner institutions in the Asia–Pacific region.

FMfI 2025 continued the tradition of the Math-for-Industry series, whose mission is to foster collaboration between academic mathematicians and industrial practitioners. Under the theme *"Mathematics for Innovation and Sustainability,"* this forum provided a platform to discuss how advanced mathematical theory and data-driven methodologies can contribute to sustainable technologies, intelligent manufacturing, climate solutions, and AI-powered industrial design.

The three-day program featured invited and contributed talks, focused sessions, and a round-table discussion on future directions of industrial mathematics in the era of artificial intelligence and global sustainability. Researchers and engineers from universities, research institutes, and companies across Japan, Korea, Australia, Malaysia, and other countries shared case studies demonstrating how mathematical modeling, optimization, and statistical computation can create tangible social and economic value.

This volume (or website) contains summaries of the lectures and presentations delivered during the forum. The Organizing Committee expresses sincere appreciation to all speakers, participants, and sponsoring organizations for their contributions to the success of FMfI 2025. We also thank the APCMfI Council and IMI Joint Usage Research Program for their continuous support in promoting international collaboration through mathematics for industry.

We hope that the discussions and outcomes of FMfI 2025 will further strengthen the link between mathematics and society and inspire new cooperative research toward sustainable industrial development.

November 2025.

Editors

Soon-Sun Kwon (Ajou University)

Minjung Gim (NIMS)

Jae-Hun Jung (POSTECH)


Forum "Math for Industry" 2025
- Challenge of Mathematics for Industry in the AI era -
18(Mon) – 20(Wed) August 2025
APCMfI and IAB Meetings and Free Activities on 17(Sun) Aug.
POSCO Center (Seoul, Korea)
Organizing Committee Co-chairs
• Soon-Sun Kwon (Ajou University)
• Minjung Gim (NIMS)
• Jae-Hun Jung (POSTECH)
Program Committee
• Shizuo Kaji (Kyushu University), Chair
• Osamu Saeki (Kyushu University)
• Kenji Kajiwara (Kyushu University)
• Arifah Bahar (Universiti Teknologi Malaysia)
• Philip Broadbridge (La Trobe University)
• Xiaoping Lu (University of Wollongong)
• Won-Yong Shin (Yonsei University)
• Masayo Hirose (Kyushu University)
• Keunsu Kim (Kyushu University)
• Minseok Choi (POSTECH)
AJOU Center for Mathematics·Statistics Indstry
ICIM
POSTECH MINDS
NRF
Institute of Mathematics for Industry
Asia Pacific Consortium of Mathematics for Industry

Program

August 18th

09:30 ~ 10:30 Plenary Talk

- **Jong-Chul Ye** (KAIST) "Guiding Diffusion and Flow Models for Image, Video and 4D"

10:45 ~ 11:45 Session 1

- **Kenji Fukumizu** (The Institute of Statistical Mathematics) "Pairwise Optimal Transports for Training All-to-All Flow-Based Condition Transfer Model "
- **Yeachan Park** (Sejong University) "Do Language Models Understand Math?"

14:00 ~ 15:00 Session 2

- **Takaharu Yaguchi** (Kobe university) "An Extension of SympNets for Learning of Multiple Hamilton Systems"
- **Kyunghoon Kim** (Core.Today) "Formal Thinking in the Age of AI: Why Mathematical Reasoning Matters More Than Ever"

15:15 ~ 16:15 Session 3

- **Yuichi Goto** (Kyushu University) "ANOVATS: A subsampling-based test for differences among short time series in marine studies"
- **Min-Woo Chae** (POSTECH) "Online Bernstein-von Mises theorem"

16:45 ~ 17:45 Session 4

- **Zaitul Marlizawati Zainuddin** (Universiti Teknologi Malaysia) "MultiObjective Optimization of Location-Routing Decisions in Biomass Supply Chains"
- **Ling Guo** (Shanghai Normal University) "Uncertainty Quantification in Scientific Machine Learning via the Information Bottleneck Principle "

August 19th

09:00 ~ 10:00 Session 5

- **Pierluigi Cesana** (IMI, Kyushu University) "Integrating AI and Human Expertise for the Design and Control of Smart Materials"
- **Tao Zhou** (Chinese Academy of Sciences) "Efficient deep learning methods for very high dimentional parabolic and HJB equations"

10:15 ~ 11:15 Session 6

- **Jae-Min Yoo** (KAIST) “Mining Interconnected Data: Robust, Generalizable, and Interpretable Methods”
- **Eun-Ho Koo** (Chonnam National University) “Efficient Node Classification on Simplicial Interaction via Augmented Maximal Clique Selection”

14:00 ~ 15:00 Session 7

- **Emi Tanaka** (Australian National University) “Growing success with statistics in plant breeding”
- **Ryoya Fukasaku** (IMI, Kyushu University) “Algebraic Approach for Statistical Models”

14:00 ~ 15:00 Round Table

- **Arifah Bahar**, **Emi Tanaka**, **Busayamas Pimpunchat**

15:30 ~ 17:30 Poster Session

August 20th

10:00 ~ 11:00 Session 8

- **Nguyen Dinh Hoa** (IMI, Kyushu University) “From Natural Intelligence To Artificial Intelligence”
- **Hongqiao Wang** (Central South University) “Accelerated Bayesian Optimal Experimental Design via Conditional Density Estimation and Informative Data”

11:00 ~ 11:30 Session 9

- **Hairong Yuan** (East China Normal University) “Some advances on mathematics of hypersonic flows”
- **Jae-Ryong Kweon** (POSTECH) “Pohang Earthquake, Thermalelastics among Rock Matrix zones and Mathematical Modelling”

13:00 ~ 14:00 Session 10

- **Ji-Su Hong** (The Miracle Soft) “Industrial AI Innovation: Mathematical Challenges and Applications”
- **Yong-Hoon Lee** (Mokpo University) “Integrating LIBS and Machine Learning for Practical Industrial Applications in Alloy Identification and Analysis”

14:15 ~ 15:15 Keynote

- **Hyun-Min Kim** (Pusan National University) “Mathematics in the Age of Intelligent Machines: From Ancient Logic to Industrial Innovation”


- Challenge of Mathematics for Industry in the AI era -
Forum "Math for Industry" 2025
18 (Mon) - 20 (Wed) August 2025, POSCO Center (Seoul, Korea)
posco

Table of Contents

Forum “Math for Industry” 2025

- Challenge of Mathematics for Industry in the AI era -

August 18 - 20, 2025, Seoul (POSCO Center), Republic of Korea

Guiding Diffusion and Flow Models for Image, Video and 4D

Jong-Chul Ye

KAIST

The recent emergence of diffusion models has driven substantial progress in image and video processing by establishing these models as powerful generative priors. However, challenges persist such as extension to 3D, video, and 4D problems. Meanwhile, flow models—though related—possess distinct characteristics from diffusion models, and their application in this domain remains relatively underexplored. In this talk, we present strategies to address these challenges, highlighting our recent work on solving video inverse problems using 2D diffusion models, video interpolation, 4D video generation, and FlowDPS—our state-of-the-art inverse solver based on flow models. Comprehensive experimental results demonstrate the effectiveness of diffusion and flow-based approaches.

Forum "Math for Industry" 2025

- Challenge of Mathematics for Industry in the AI era -

Guiding Diffusion and Flow Models for Image, Video and 4D

August 18, 2025

Jong Chul Ye
Professor
Graduate School of AI
KAIST, Korea

KAIST AI
Kim Jaechul Graduate School

❑ Quantum Mechanics : Diffusion Models

Striking Similarity

$$\mathrm{d}X(t) = b_f(X(t), t)\mathrm{d}t + \sigma \mathrm{d}W_f(t)\,.$$

- Path of quantum particle
- Path of image (signal) diffusion

$$\frac{\partial}{\partial t}\rho(x,t) + \frac{\partial}{\partial x}[v(x,t)\rho(x,t)] = 0$$

- Probability density wave
- Probability density function

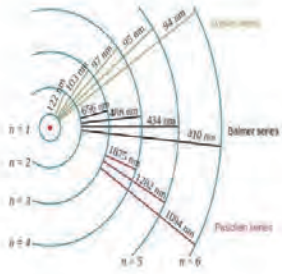

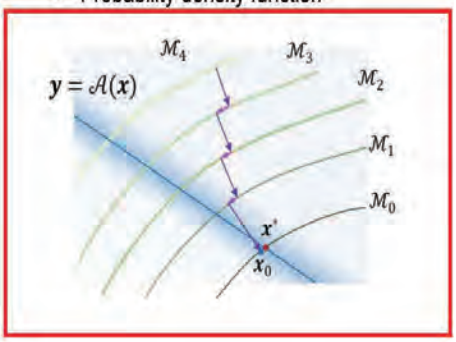

Understanding diffusion geometry→

Easy and correct way of guiding diffusion models

❑ Denoising Diffusion Probabilistic Models (DDPM)

Ho et al. NeurIPS 2020

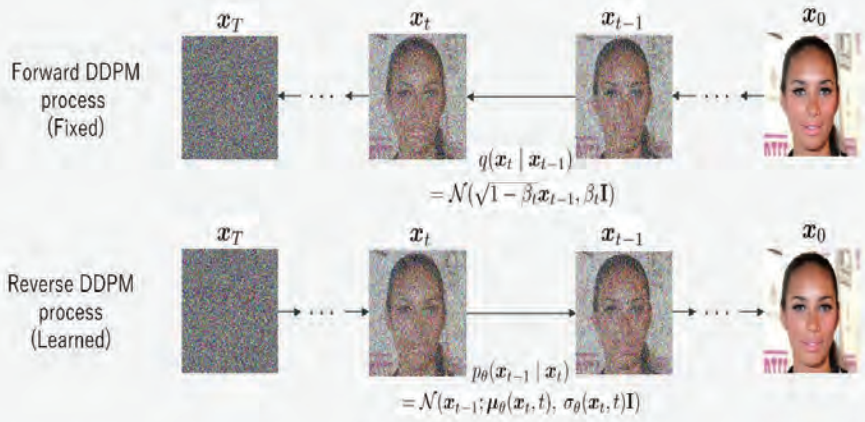

Discrete set of noise variances during forward diffusion

$$\beta_0, \cdots, \beta_T$$

❑ Self-Supervised Pretraining in Diffusion Models

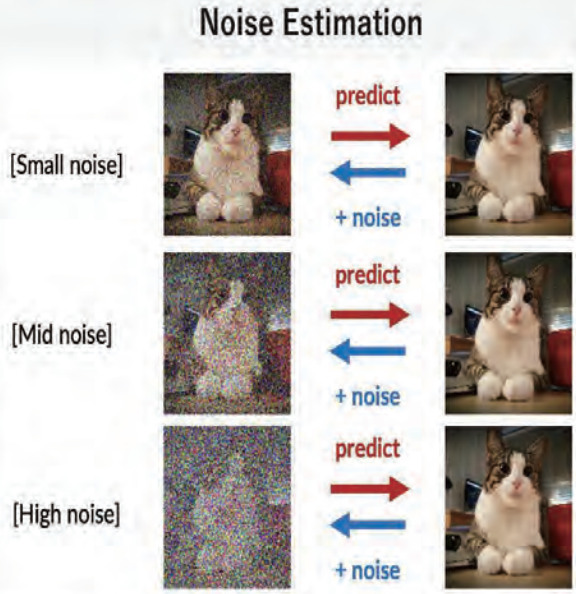

Figure Courtesy of Jiaming Song, Chung, Ye's ISBI 23 tutorial

❑ Self-Supervised Pretraining + Downstream

Algorithm 1 Training

1: **repeat**
2: $\mathbf{x}_0 \sim q(\mathbf{x}_0)$
3: $t \sim \text{Uniform}(\{1, \dots, T\})$
4: $\epsilon \sim \mathcal{N}(\mathbf{0}, \mathbf{I})$
5: Take gradient descent step on
$$\nabla_\theta \left\| \epsilon - \epsilon_\theta(\sqrt{\bar{\alpha}_t}\mathbf{x}_0 + \sqrt{1-\bar{\alpha}_t}\epsilon, t) \right\|^2$$
6: **until** converged

Algorithm 2 Sampling

1: $\mathbf{x}_T \sim \mathcal{N}(\mathbf{0}, \mathbf{I})$
2: **for** $t = T, \dots, 1$ **do**
3: $\mathbf{z} \sim \mathcal{N}(\mathbf{0}, \mathbf{I})$
4: $\mathbf{x}_{t-1} = \frac{1}{\sqrt{\alpha_t}}\left(\mathbf{x}_t - \frac{1-\alpha_t}{\sqrt{1-\bar{\alpha}_t}}\epsilon_\theta(\mathbf{x}_t, t)\right) + \sigma_t \mathbf{z}$
5: **end for**
6: **return** $\mathbf{x}_0$

"Variance Preserving (VP)" parameterization

Why diffusion models?

❑ Geometry of GANs

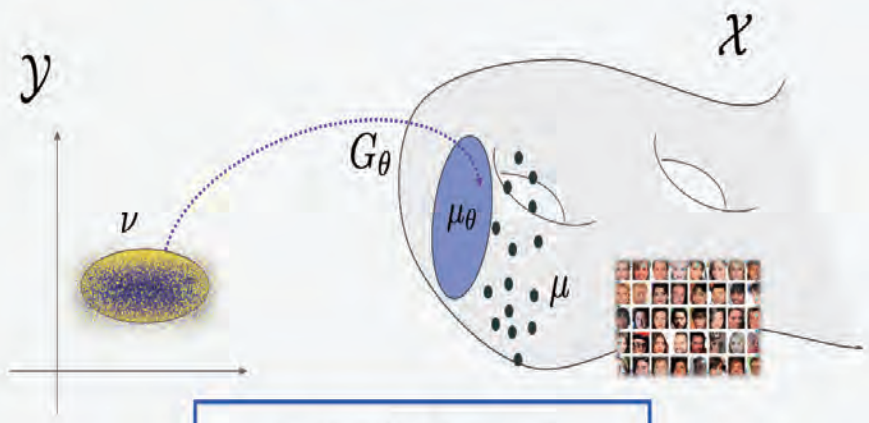

$$\min_\theta \operatorname{dist}(\mu_\theta, \mu)$$

subject to $\mu_\theta = G_{\theta\#}\nu$

❑ GAN mode collapsing

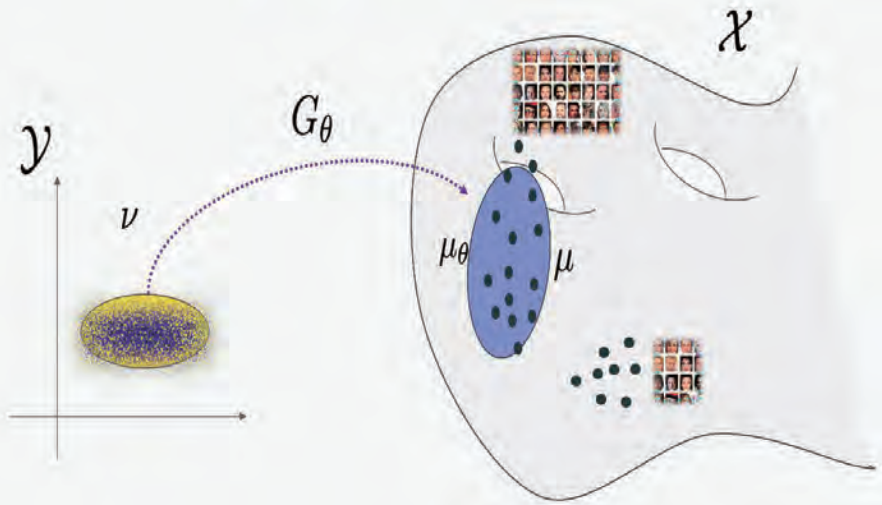

Multiple modes

❑ GAN overfitting

DiffusionCLIP: Kim et al. CVPR 2022

❑ Geometry of 1D Diffusion

Forward sampling: pixel-wise iid noise addition

$$\boldsymbol{x}_{t-1} = \boldsymbol{x}_t + \sigma_t \boldsymbol{\epsilon}_t$$

$$p(\boldsymbol{x}_{t-1}) = p(\boldsymbol{x}_t) * p(\sigma_t \boldsymbol{\epsilon}_t)$$

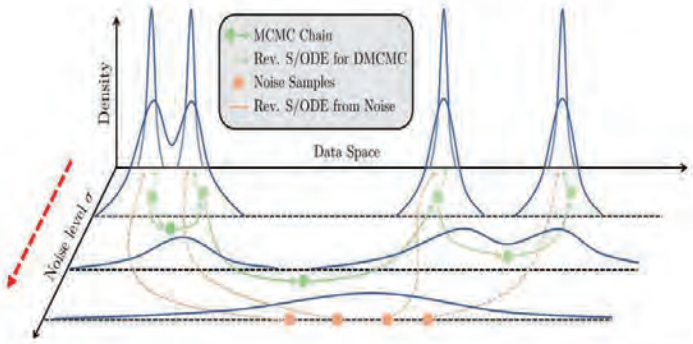

Kim et al, ICML 2023

❑ Recall: Scale Space Representation of Image

Scale-space theory is a framework for multi scale signal representation

$$L(\cdot,\cdot;t) = g(\cdot,\cdot;t) * f(\cdot,\cdot), \qquad g(x,y;t) = \frac{1}{2\pi t} e^{-(x^2+y^2)/2t}$$

Scale-space representation $L(x, y; t)$ at scale $t = 0$, corresponding to the original image f

Scale-space representation $L(x, y; t)$ at scale $t = 1$

Scale-space representation $L(x, y; t)$ at scale $t = 4$

Scale-space representation $L(x, y; t)$ at scale $t = 16$

❑ High dimensional geometry of diffusion

Chung et al, NeurIPS 2022

$RV: X = (X_1, X_2, \ldots, X_n), X_i \sim \mathcal{N}(0, \sigma^2)$

The Gaussian Shell Theorem

$\frac{||X||^2}{n} = \frac{X_1^2 + X_2^2 + \cdots + X_n^n}{n} \to \sigma^2$ (Law of Large number)

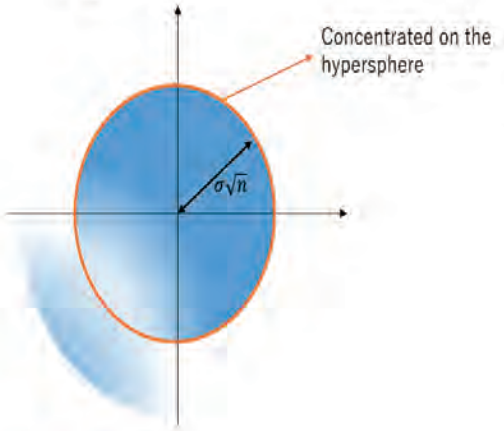

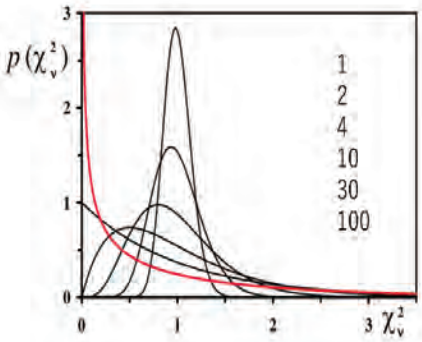

❑ High dimensional geometry of diffusion

Chung et al, NeurIPS 2022

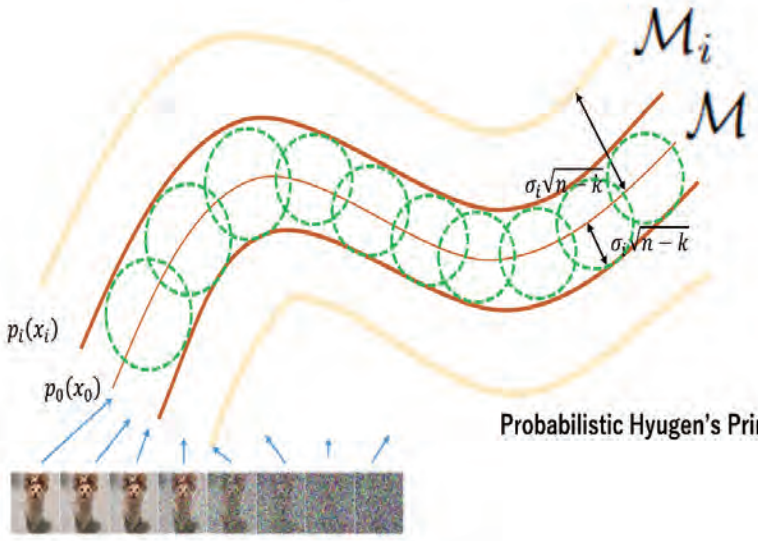

Probabilistic Hyugen's Principle?

❑ High dimensional geometry of diffusion

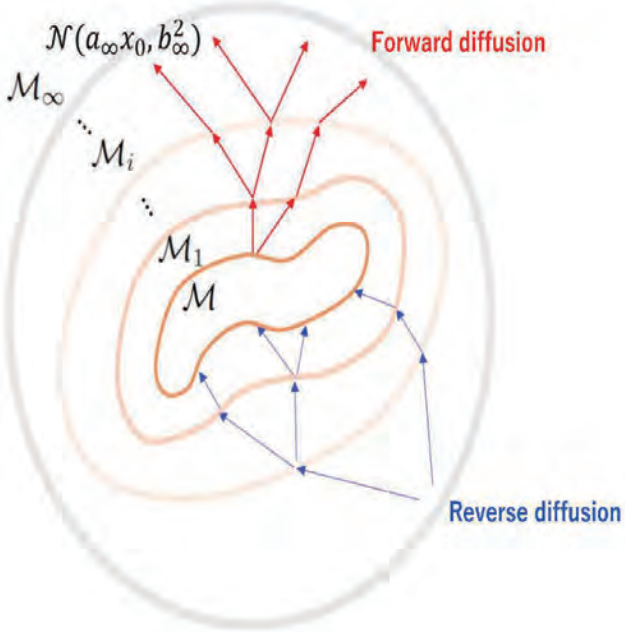

❑ Diffusion: scale space representation of distribution/PDF

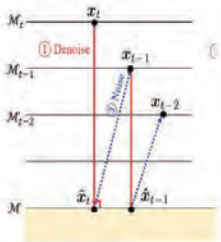

Chung et al, CVPR 2025

"beautiful lady, freckles, big smile, blue eyes, short ginger hair, wearing a floral blue vest top, soft light, dark gray background"

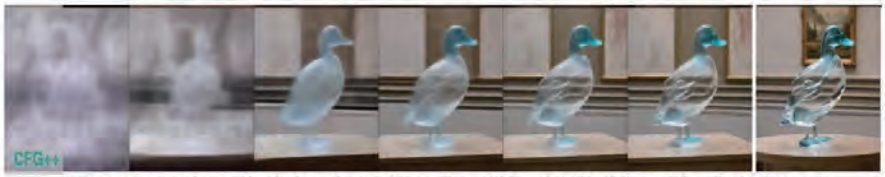

"A transparent sculpture of a duck made out of glass. The sculpture is in front of a painting of a landscape."

Diffusion for Inverse Problems

- Diffusion models for inverse problems

$$\boldsymbol{y} = \mathcal{A}(\boldsymbol{x}_0) + \boldsymbol{n}, \quad \boldsymbol{y}, \boldsymbol{n} \in \mathbb{R}^n, \boldsymbol{x}_0 \in \mathbb{R}^d$$

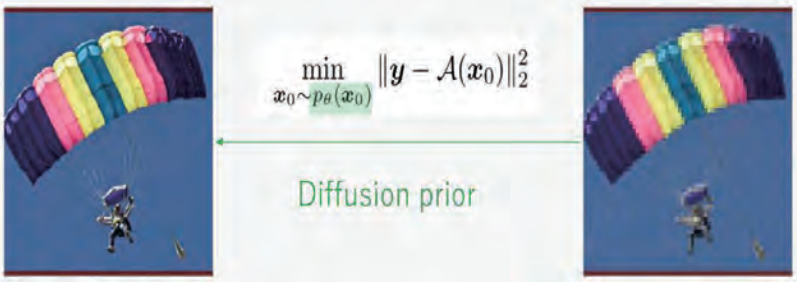

$\boldsymbol{x}_0$ $\boldsymbol{y}$

❑ Posterior inference: a naïve approach

A posterior SDE sampling using diffusion model:

$$d\boldsymbol{x} = \left[-\frac{\beta(t)}{2}\boldsymbol{x} - \beta(t)\underbrace{\left(\nabla_{\boldsymbol{x}_t} \log p_t(\boldsymbol{x}_t) + \nabla_{\boldsymbol{x}_t} \log p_t(\boldsymbol{y}|\boldsymbol{x}_t)\right)}_{\nabla_{\boldsymbol{x}_t} \log p(\boldsymbol{x}_t|\boldsymbol{y})} \right] dt + \sqrt{\beta(t)} d\bar{\boldsymbol{w}},$$

$$\underbrace{\log p(\boldsymbol{x}|\boldsymbol{y})}_{\text{Posterior}} = \underbrace{\log p(\boldsymbol{x})}_{\text{Prior}} + \underbrace{\log p(\boldsymbol{y}|\boldsymbol{x})}_{\text{Likelihood}} + \text{const.}$$

❑ The devil is in the likelihood

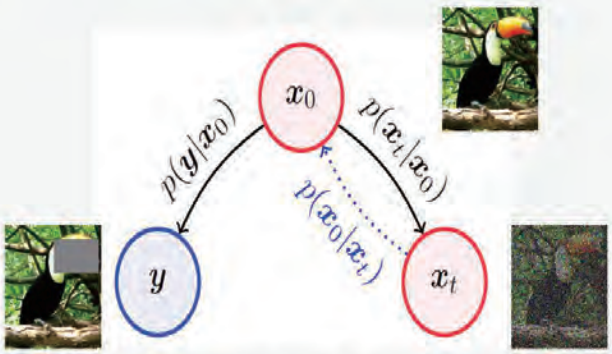

$$p(\mathbf{y}|\mathbf{x}_0) = \mathcal{N}(\mathbf{y}|\mathcal{A}\mathbf{x}_0, \sigma^2 \boldsymbol{I})$$

$$\log p(\mathbf{y}|\mathbf{x}_0) = -\|\boldsymbol{y} - \mathcal{A}\mathbf{x}_0\|_2^2 / \sigma^2$$

[ICLR 2023] Chung et al. Diffusion Posterior Sampling for General Noisy Inverse Problems

❑ The devil is in the likelihood

$$\nabla_{\mathbf{x}_t} \log p(\mathbf{y}|\mathbf{x}_t)$$

Intractable!

$$p(\mathbf{y}|\mathbf{x}_0) = \mathcal{N}(\mathbf{y}|\mathcal{A}\mathbf{x}_0, \sigma^2 \boldsymbol{I})$$

$$\log p(\mathbf{y}|\mathbf{x}_0) = -\|\boldsymbol{y} - \mathcal{A}\mathbf{x}_0\|_2^2/\sigma^2$$

[ICLR 2023] Chung et al. Diffusion Posterior Sampling for General Noisy Inverse Problems

❑ DPS: Jensen's approximation

$$p(\mathbf{y}|\mathbf{x}_t) = \int p(\mathbf{y}|\mathbf{x}_0, \mathbf{x}_t) p(\mathbf{x}_0|\mathbf{x}_t) d\mathbf{x}_0$$

$$= \int p(\mathbf{y}|\mathbf{x}_0) p(\mathbf{x}_0|\mathbf{x}_t) d\mathbf{x}_0$$

$$= \mathbb{E}_{p(\mathbf{x}_0|\mathbf{x}_t)}[p(\mathbf{y}|\mathbf{x}_0)]$$

[ICLR 2023] Chung et al. Diffusion Posterior Sampling for General Noisy Inverse Problems

❑ DPS: Jensen's approximation

$$p(\mathbf{y}|\mathbf{x}_t) = \int p(\mathbf{y}|\mathbf{x}_0, \mathbf{x}_t) p(\mathbf{x}_0|\mathbf{x}_t) d\mathbf{x}_0$$

$$= \int p(\mathbf{y}|\mathbf{x}_0) p(\mathbf{x}_0|\mathbf{x}_t) d\mathbf{x}_0$$

$$= \mathbb{E}_{p(\mathbf{x}_0|\mathbf{x}_t)}[p(\mathbf{y}|\mathbf{x}_0)]$$

Push expectation inside

$$\simeq p(\mathbf{y}|\mathbb{E}[\mathbf{x}_0|\mathbf{x}_t])]$$

[ICLR 2023] Chung et al. Diffusion Posterior Sampling for General Noisy Inverse Problems

❑ DPS: Jensen's approximation

$$p(\mathbf{y}|\mathbf{x}_t) = \int p(\mathbf{y}|\mathbf{x}_0, \mathbf{x}_t) p(\mathbf{x}_0|\mathbf{x}_t) d\mathbf{x}_0$$

$$= \int p(\mathbf{y}|\mathbf{x}_0) p(\mathbf{x}_0|\mathbf{x}_t) d\mathbf{x}_0$$

$$= \mathbb{E}_{p(\mathbf{x}_0|\mathbf{x}_t)}[p(\mathbf{y}|\mathbf{x}_0)]$$

$$\simeq p(\mathbf{y}|\mathbb{E}[\mathbf{x}_0|\mathbf{x}_t])]$$

$$= p(\mathbf{y}|\hat{\mathbf{x}}_0)$$

Tweedie

[ICLR 2023] Chung et al. Diffusion Posterior Sampling for General Noisy Inverse Problems

❑ DPS: pictorial description

Chung et al, ICLR 2023

$$\nabla_{\mathbf{x}_t} \log p(\mathbf{y}|\hat{\mathbf{x}}_0) = -\rho \nabla_{\mathbf{x}_t} \|\mathbf{y} - \mathcal{A}(\hat{\mathbf{x}}_0)\|_2^2$$

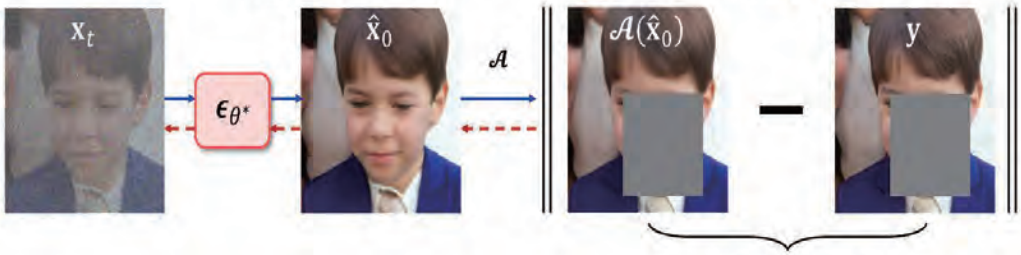

Forward pass

Backward propagation

$$\hat{\boldsymbol{x}}_0 := \mathbb{E}[\boldsymbol{x}_0|\boldsymbol{x}_t] = \frac{1}{\sqrt{\bar{\alpha}(t)}}(\boldsymbol{x}_t + (1-\bar{\alpha}(t))\nabla_{\boldsymbol{x}_t} \log p_t(\boldsymbol{x}_t))$$

:Tweedie's formula

❑ Jensen approximation: error bound

Theorem 1. *For the given measurement model (6) with $\boldsymbol{n} \sim \mathcal{N}(0, \sigma^2 \boldsymbol{I})$, we have*

$$p(\boldsymbol{y}|\boldsymbol{x}_t) \simeq p(\boldsymbol{y}|\hat{\boldsymbol{x}}_0), \tag{13}$$

where the approximation error can be quantified with the Jensen gap, which is upper bounded by

$$\mathcal{J} \leq \frac{d}{\sqrt{2\pi\sigma^2}} e^{-1/2\sigma^2} \|\nabla_{\boldsymbol{x}} \mathcal{A}(\boldsymbol{x})\| m_1, \tag{14}$$

where $\|\nabla_{\boldsymbol{x}} \mathcal{A}(\boldsymbol{x})\| := \max_{\boldsymbol{x}} \|\nabla_{\boldsymbol{x}} \mathcal{A}(\boldsymbol{x})\|$ and $m_1 := \int \|\boldsymbol{x}_0 - \hat{\boldsymbol{x}}_0\| p(\boldsymbol{x}_0|\boldsymbol{x}_t)\, d\boldsymbol{x}_0$.

[ICLR 2023] Chung et al. Diffusion Posterior Sampling for General Noisy Inverse Problems

❑ Manifold constrained gradient

Chung et al, NeurIPS, 2022; ICLR 2023

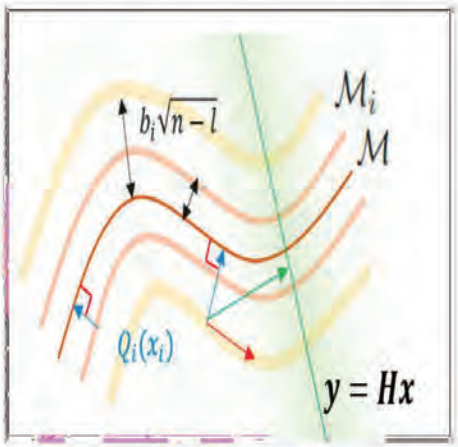

$$\frac{\partial}{\partial \boldsymbol{x}_i}\|\boldsymbol{W}(\boldsymbol{y}-\boldsymbol{H}\hat{\boldsymbol{x}}_0)\|_2^2 = -2\boldsymbol{J}_{Q_i}^T\boldsymbol{H}^T\boldsymbol{W}^T\boldsymbol{W}(\boldsymbol{y}-\boldsymbol{H}\hat{\boldsymbol{x}}_0) \in T_{\hat{\boldsymbol{x}}_0}\mathcal{M}$$

❑ Geometry of Diffusion Posterior Sampling

Chung et al, NeurIPS 2022; ICLR 2023

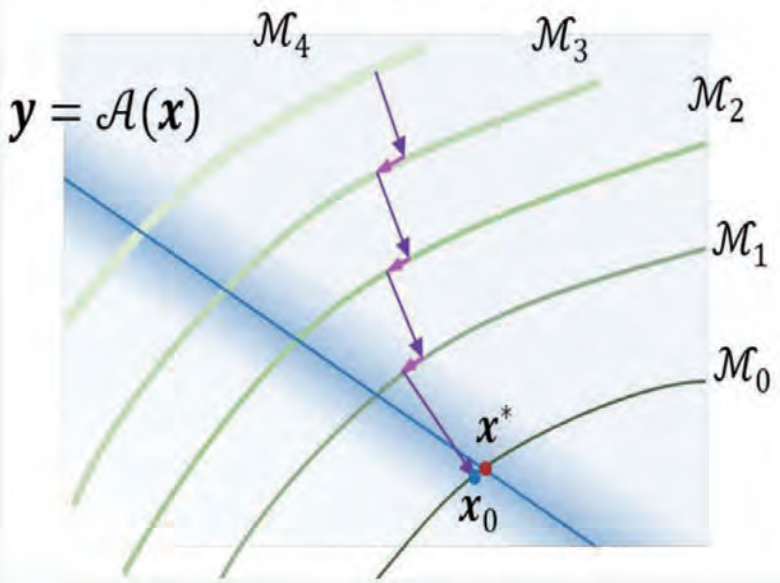

❑ Experimental results

❑ Experimental results

Chung et al, ICLR 2023

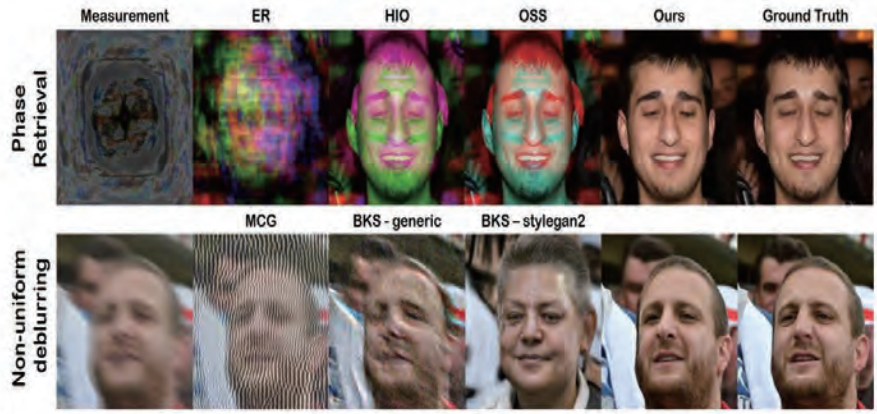

Figure 6: Results on solving nonlinear inverse problems with Gaussian noise ($\sigma = 0.05$).

Acceleration for Large Scale Imaging Problems

Chung et al, ICLR 2024

❑ Tweedie's denoiser is the orthogonal projector

Chung et al, ICLR 2024

DDIM (DDPM)

$$\begin{aligned}\boldsymbol{x}_{t-1} &= \sqrt{\bar{\alpha}_{t-1}}\hat{\boldsymbol{x}}_t + \sqrt{1-\bar{\alpha}_{t-1}-\eta^2\tilde{\beta}_t^2}\boldsymbol{\epsilon}_{\theta^*}^{(t)}(\boldsymbol{x}_t) + \eta\tilde{\beta}_t\boldsymbol{\epsilon}, \\ &= \sqrt{\bar{\alpha}_{t-1}}\hat{\boldsymbol{x}}_t + \tilde{\boldsymbol{w}}_t\end{aligned}$$

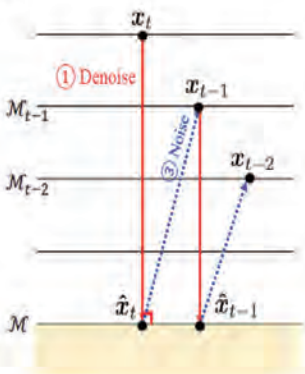

Tweedie denoiser

$$\hat{\boldsymbol{x}}_t = \frac{1}{\sqrt{\bar{\alpha}_t}}(\boldsymbol{x}_t - \mathcal{P}_{\mathcal{M}}^{\perp}\boldsymbol{x}_t) = \frac{1}{\sqrt{\bar{\alpha}_t}}\mathcal{P}_{\mathcal{M}}\boldsymbol{x}_t$$

❑ Computational bottleneck of DPS

Chung et al, ICLR 2024

$$\min_{\boldsymbol{x}\in\mathcal{M}} \ell(\boldsymbol{x})$$

Backpropagation through network

$$\boldsymbol{x}_{t-1} = \sqrt{\bar{\alpha}_{t-1}}\left(\hat{\boldsymbol{x}}_t - \gamma_t \nabla_{\boldsymbol{x}_t}\ell(\hat{\boldsymbol{x}}_t)\right) + \tilde{\boldsymbol{w}}_t$$

Projected Gradient on Manifold

$$\hat{\boldsymbol{x}}_t - \gamma_t \nabla_{\boldsymbol{x}_t}\ell(\hat{\boldsymbol{x}}_t) \;=\; \mathcal{P}_{\mathcal{M}}\left(\hat{\boldsymbol{x}}_t - \zeta_t \nabla_{\hat{\boldsymbol{x}}_t}\ell(\hat{\boldsymbol{x}}_t)\right)$$

❑ Clue: Krylov subspace method

$$\min_{\boldsymbol{x}\in\hat{\boldsymbol{x}}+\mathcal{K}_l} \|\boldsymbol{y} - \boldsymbol{A}\boldsymbol{x}\|^2$$

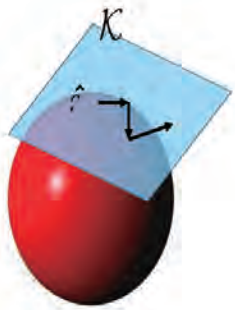

Krylov Subspace

$$\mathcal{K} = \mathcal{L} = \mathcal{K}_l := \mathrm{Span}(\boldsymbol{b}, \boldsymbol{A}\boldsymbol{b}, \cdots, \boldsymbol{A}^{l-1}\boldsymbol{b}).$$

The conjugate gradient method is
the representative Krylov subspace method

❑ Decomposed diffusion sampling (DDS)

Chung et al, ICLR 2024

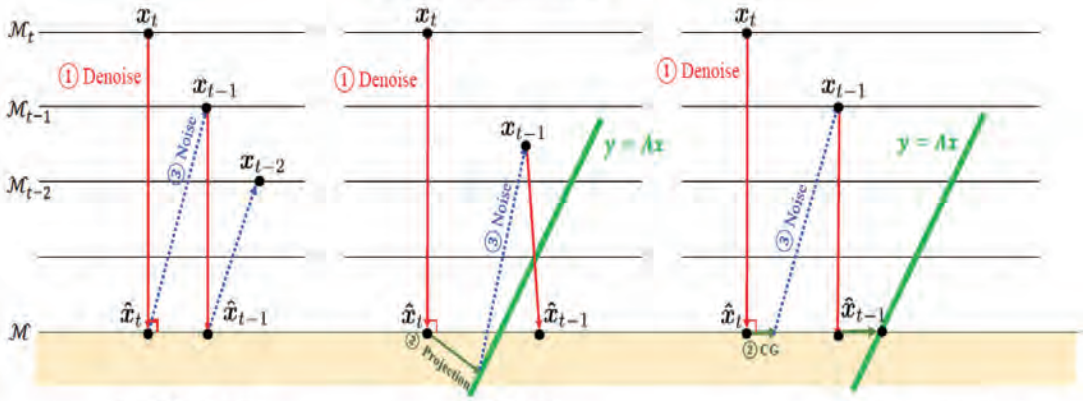

DDPM (IM) DDNM Decomposed Diffusion Sampling (DDS)

Apply **conjugate gradient**
Rather than hard projections

❑ 8 view CT reconstruction (19NFE)

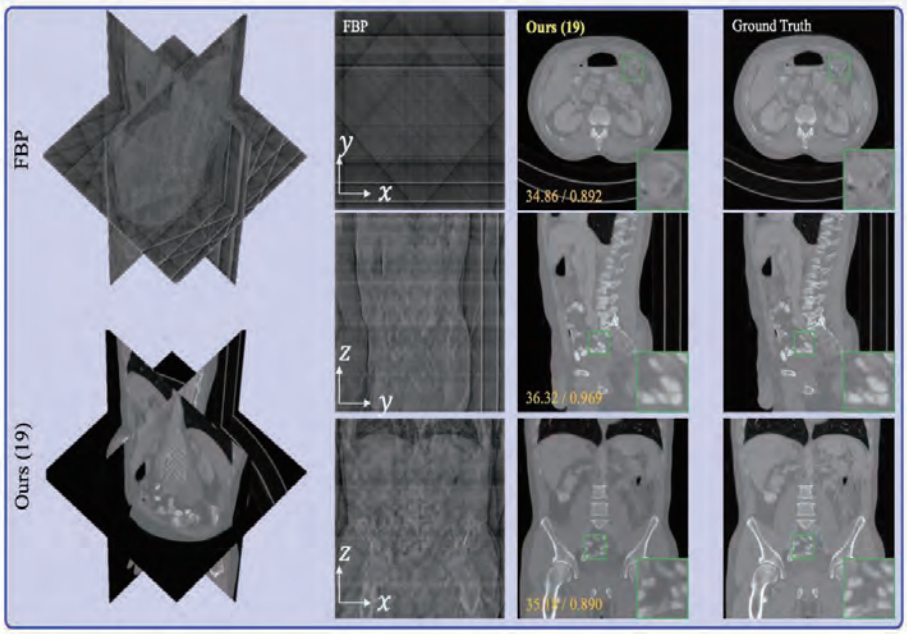

❑ Limited angle tomography (50 NFE)

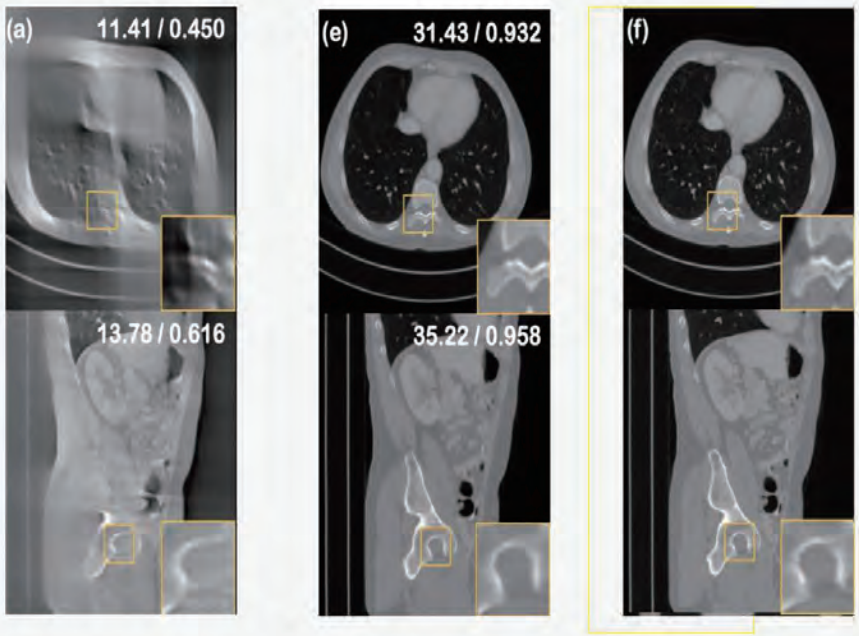

Extension to Flow Models

❑ DiT: Architectural Change

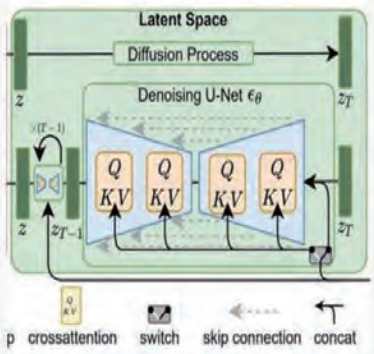

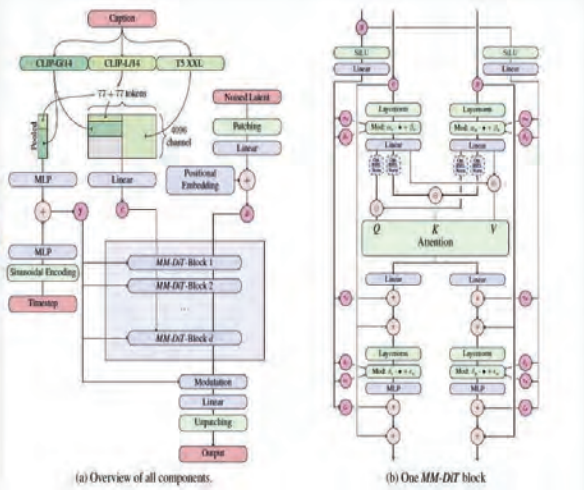

❑ Flow: Algorithmic Change

$$\frac{d\psi_t(\boldsymbol{x})}{dt} = v_t(\psi_t(\boldsymbol{x})),$$

$$\boldsymbol{x}_t = \psi_t(\boldsymbol{x}_1|\boldsymbol{x}_0) = a_t\boldsymbol{x}_0 + b_t\boldsymbol{x}_1$$

$$v_t(\boldsymbol{x}_t|\boldsymbol{x}_0) = \dot{\psi}_t(\boldsymbol{x}_1|\boldsymbol{x}_0) = \dot{a}_t\boldsymbol{x}_0 + \dot{b}_t\boldsymbol{x}_1.$$

$$\min_\theta \mathbb{E}_{t,\boldsymbol{x}\sim p_{t|0}(\boldsymbol{x}_t|\boldsymbol{x}_0)} \|v_t(\boldsymbol{x}_t|\boldsymbol{x}_0) - v_t^\theta(\boldsymbol{x}_t)\|^2$$

$$\Downarrow$$

$$\min_\theta \mathbb{E}_{t,\boldsymbol{x}\sim p_{t|0}} \|v_t^\theta(\boldsymbol{x}_t) - (\boldsymbol{x}_1 - \boldsymbol{x}_0)\|^2.$$

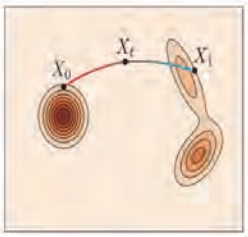

(a) Flow

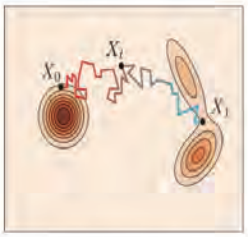

(b) Diffusion

❑ Flow Velocity vs Score

$$\begin{aligned} v_t(\boldsymbol{x}_t) &= \frac{\dot{a}_t}{a_t}\boldsymbol{x}_t + \left[\dot{b}_t - b_t\frac{\dot{a}_t}{a_t}\right]\mathbb{E}[\boldsymbol{x}_1|\boldsymbol{x}_t] \\ &= \frac{\dot{a}_t}{a_t}\boldsymbol{x}_t - \left[\dot{b}_t b_t - b_t^2\frac{\dot{a}_t}{a_t}\right]\nabla \log p_t(\boldsymbol{x}_t). \end{aligned}$$

$$\Downarrow$$

$$v_t(\boldsymbol{x}_t|\boldsymbol{y}) = \frac{\dot{a}_t}{a_t}\boldsymbol{x}_t - \left[\dot{a}_t b_t - b_t^2\frac{\dot{a}_t}{a_t}\right]\nabla_{\boldsymbol{x}_t} \log p_t(\boldsymbol{x}_t|\boldsymbol{y})$$

❑ FlowDPS: Posterior Flow-Velocity

Kim et al, ICCV 2025

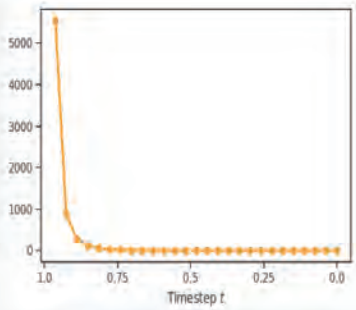

TLDR;
More emphasize for the data-likelihood at early sampling

❑ FlowDPS: Results

Kim et al, ICCV 2025

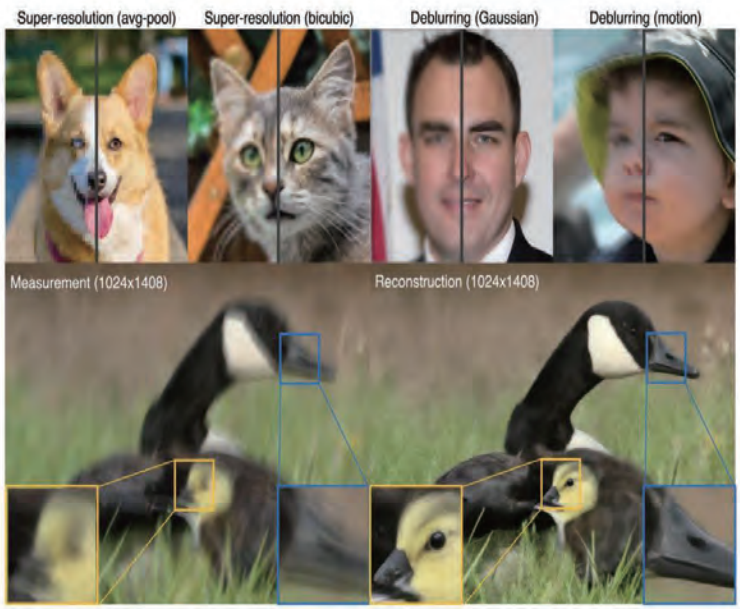

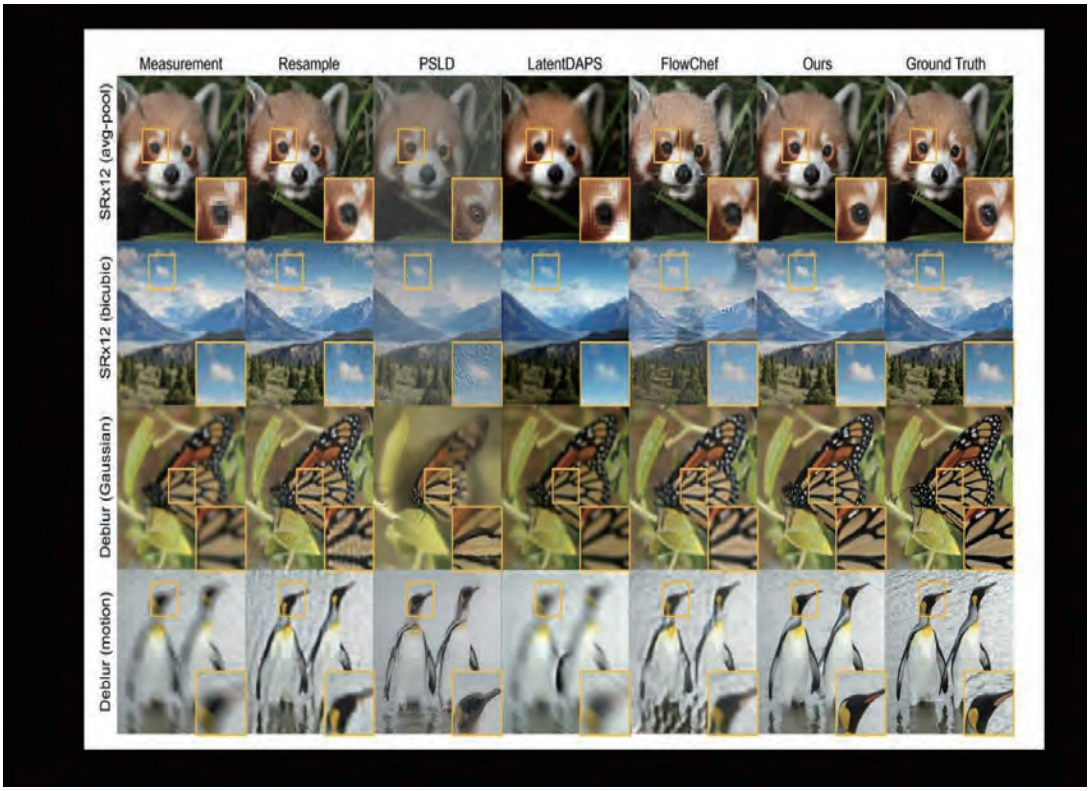

Text-guidance: *Was it correct?*

❑ Text-Conditioned Training

$$\left\| \epsilon_\theta\left(\sqrt{\bar{\alpha}_t}\,\blacksquare + \sqrt{1-\bar{\alpha}_t}\,\blacksquare, \boxed{\text{Cat}}\right) - \blacksquare \right\|_2^2$$

TL;DR: Inject synthetic noise into the video and train a diffusion model to remove that noise only when the corresponding text prompt is supplied.

❑ CFG: Classifier Free Guidance

Background

Conditional Sampling $x \sim p_\theta(x|c)$

$$dx_t = \frac{x_t - D_\theta(x_t, t, c)}{t} dt$$

w/o CFG

$\hat{\epsilon}_c(x_t)$

"Pirate ship trapped in a ..."

CFG

$$p^\omega(x|c) \propto p(x)p(c|x)^\omega$$

$$\hat{\epsilon}_c^\omega(x_t) \coloneqq \hat{\epsilon}_\varnothing(x_t) + \omega\left[\hat{\epsilon}_c(x_t) - \hat{\epsilon}_\varnothing(x_t)\right]$$

$(\omega = 7.5)$

Q: Is ω = 7.5 inevitable for CFG? (High & Heuristic)

❑ Problems of CFG

- Unnatural generation trajectory (high curvature)
- Poor invertibility & Lack of Interpretability
- Mode collapse (..)

❑ CFG++: Manifold-constrained CFG

Chung et al, CVPR 2025

Idea: Minimize **Score Distillation Sampling (SDS) loss** ℓ

$$\min_{x \in \mathcal{M}} \ell_{sds}(\mathbf{x}), \qquad \ell_{sds}(\mathbf{x}) := \left\| \epsilon_\theta\left(\sqrt{\bar{\alpha}_t}\mathbf{x} + \sqrt{1-\bar{\alpha}_t}\epsilon, \mathbf{c}\right) - \epsilon \right\|_2^2$$

$$\hat{\mathbf{x}}_c = \hat{\mathbf{x}}_\emptyset - \nabla_{\hat{\mathbf{x}}_\emptyset} \ell_{sds}(\hat{\mathbf{x}}_\emptyset, \mathbf{c}) = \hat{\mathbf{x}}_\emptyset + \lambda(\hat{\mathbf{x}}_\mathbf{c} - \hat{\mathbf{x}}_\emptyset)$$

$$\mathbf{x}_{t-1} = \sqrt{\bar{\alpha}_{t-1}}\left(\hat{\mathbf{x}}_\emptyset + \lambda(\hat{\mathbf{x}}_\mathbf{c} - \hat{\mathbf{x}}_\emptyset)\right) + \sqrt{1-\bar{\alpha}_{t-1}}\hat{\epsilon}_\emptyset$$

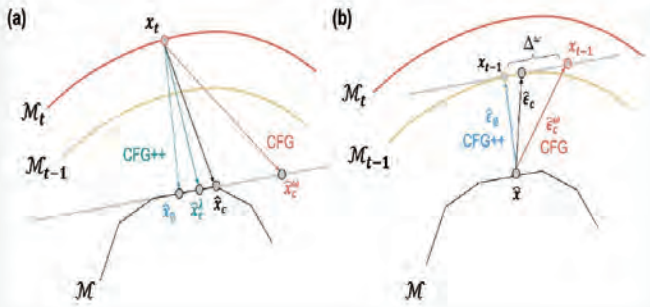

❑ CFG++: Manifold-constrained CFG

Chung et al, CVPR 2025

Algorithm 1 Reverse Diffusion with CFG

Require: $x_T \sim \mathcal{N}(0, \mathbf{I}_d), 0 \leq \omega \in \mathbb{R}$

1: **for** $i = T$ **to** 1 **do**
2: $\hat{\epsilon}_c^{\omega}(x_t) = \hat{\epsilon}_{\varnothing}(x_t) + \omega[\hat{\epsilon}_c(x_t) - \hat{\epsilon}_{\varnothing}(x_t)]$
3: $\hat{x}_c^{\omega}(x_t) \leftarrow (x_t - \sqrt{1-\bar{\alpha}_t}\hat{\epsilon}_c^{\omega}(x_t))/\sqrt{\bar{\alpha}_t}$
4: $x_{t-1} = \sqrt{\bar{\alpha}_{t-1}}\hat{x}_c^{\omega}(x_t) + \sqrt{1-\bar{\alpha}_{t-1}}\hat{\epsilon}_c^{\omega}(x_t)$
5: **end for**
6: **return** x_0

Algorithm 2 Reverse Diffusion with CFG++

Require: $x_T \sim \mathcal{N}(0, \mathbf{I}_d), \lambda \in [0, 1]$

1: **for** $i = T$ **to** 1 **do**
2: $\hat{\epsilon}_c^{\lambda}(x_t) = \hat{\epsilon}_{\varnothing}(x_t) + \lambda[\hat{\epsilon}_c(x_t) - \hat{\epsilon}_{\varnothing}(x_t)]$
3: $\hat{x}_c^{\lambda}(x_t) \leftarrow (x_t - \sqrt{1-\bar{\alpha}_t}\hat{\epsilon}_c^{\lambda}(x_t))/\sqrt{\bar{\alpha}_t}$
4: $x_{t-1} = \sqrt{\bar{\alpha}_{t-1}}\hat{x}_c^{\lambda}(x_t) + \sqrt{1-\bar{\alpha}_{t-1}}\hat{\epsilon}_{\varnothing}(x_t)$
5: **end for**
6: **return** x_0

Key 1. Choosing **Interpolation** $\lambda \in [0, 1]$

Key 2. Unconditional update

❑ CFG++: Manifold Constrained CFG

Chung et al, CVPR 2025

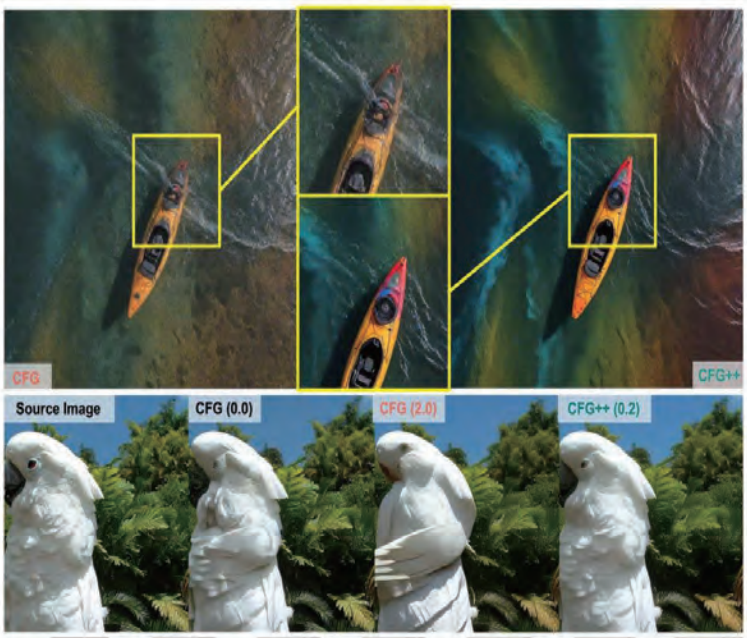

❑ CFG++: Manifold Constrained CFG

Chung et al, CVPR 2025

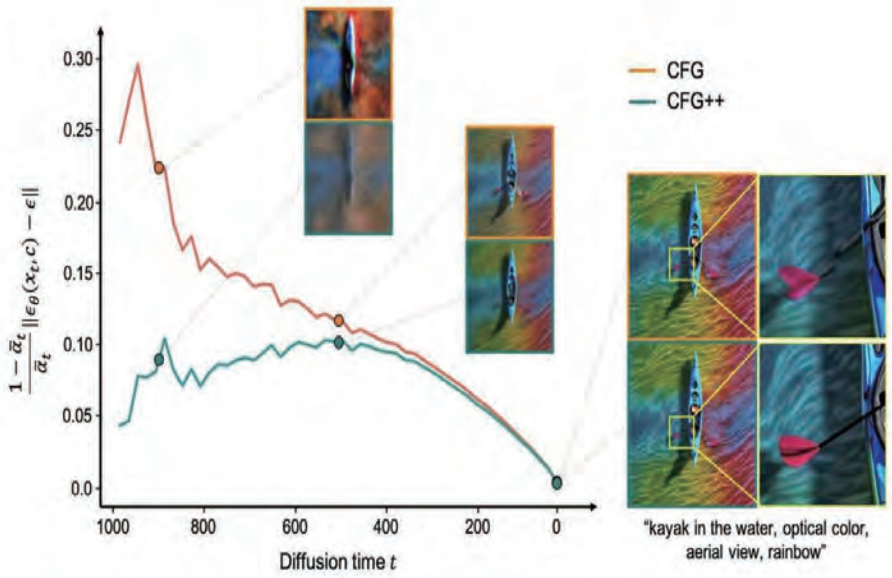

❑ CFG++: Improved Alignment

Chung et al, CVPR 2025

❑ CFG++: Improved Inversion

Chung et al,CVPR 025

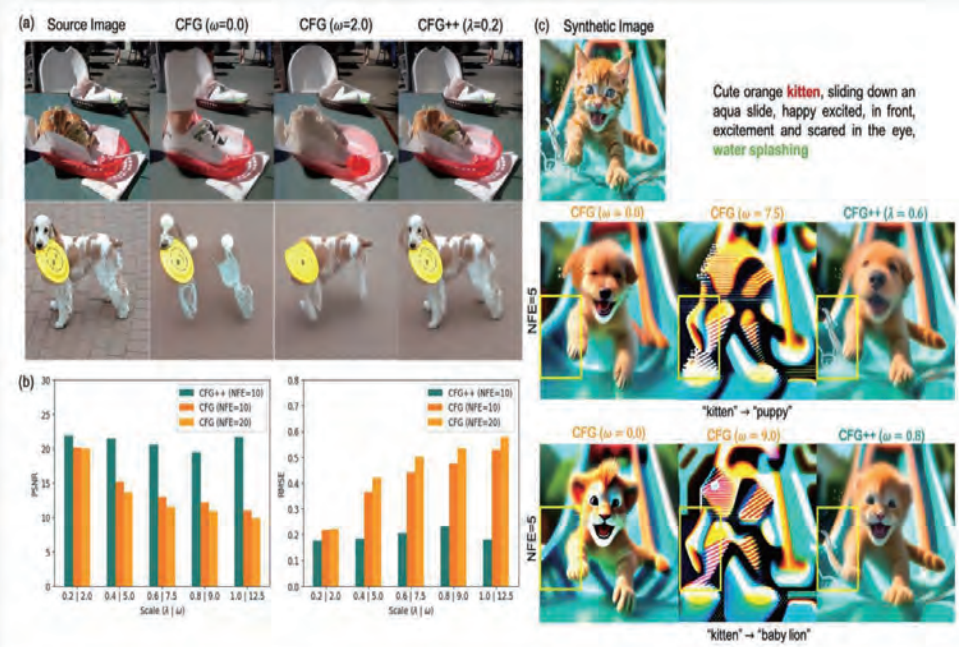

❑ CFG++: Community Implementation

- [20 Jul 2024] Stable Diffusion WebUI reForge now supports CFG++. Thanks to the awesome work! Please checkout the Reddit discussion for more details.
- [22 Jun 2024] ComfyUI now supports CFG++. Thanks to the awesome work of @dugumatai and @NotEvilGirl! We strongly encourage to test this workflow as CFG++ may improve the sampling with student models, e.g. SDXL-lightning, to a significant extent.
  - For more details, please check out the Reddit discussion and Youtube video.

Inference-time guidance

VideoGuide

Lee et al, CVPR 2025

VideoCrafter2

Poor Style control, Good Temporal

AnimateDiff

Good Style control, Poor Temporal

Q. Can we combine both advantages of two Video Diffusion Model?

❑ VideoGuide

Lee et al, CVPR 2025

1. Rethinking Consistency into Guidance Problems
2. Leverage an external VDM for Consistency Guidance

$$\ell(\boldsymbol{z}_0;\psi,\boldsymbol{\epsilon},t)=\left\|\boldsymbol{\epsilon}_{\psi}\left(\sqrt{\bar{\alpha}_t}\boldsymbol{z}_0+\sqrt{1-\bar{\alpha}_t}\boldsymbol{\epsilon},t\right)-\boldsymbol{\epsilon}\right\|_2^2$$

$$\boldsymbol{z}_{t-1}=\sqrt{\bar{\alpha}_{t-1}}\boldsymbol{z}'+\sqrt{1-\bar{\alpha}_{t-1}}\boldsymbol{\epsilon}_\theta(\boldsymbol{z}_t,t)$$

$$\text{where}\quad \boldsymbol{z}'=\beta\cdot\boldsymbol{z}_{0|t}+(1-\beta)\cdot\boldsymbol{z}_{0|t}^{\psi}$$

❑ VideoGuide

Lee et al, CVPR 2025

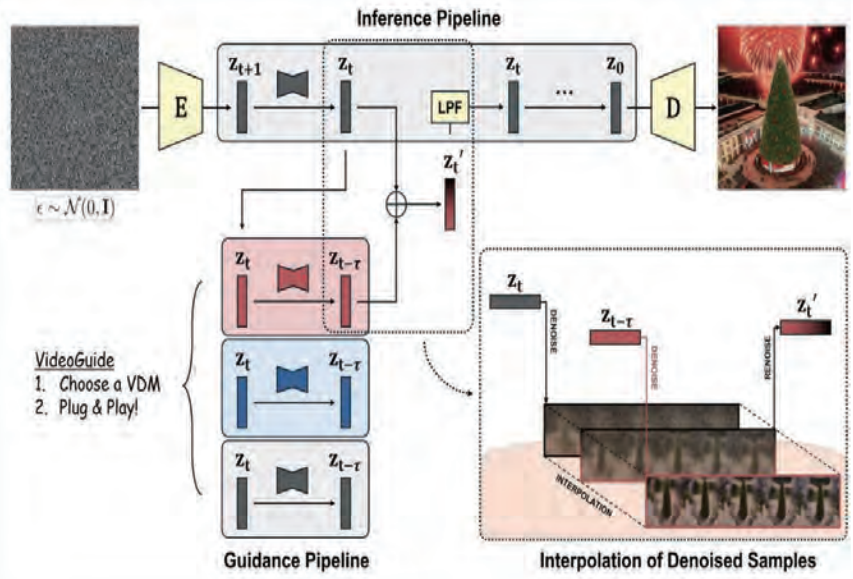

"A cat wearing sunglasses and working as a lifeguard at a pool"

"A drone view of celebration with Christmas tree and fireworks"

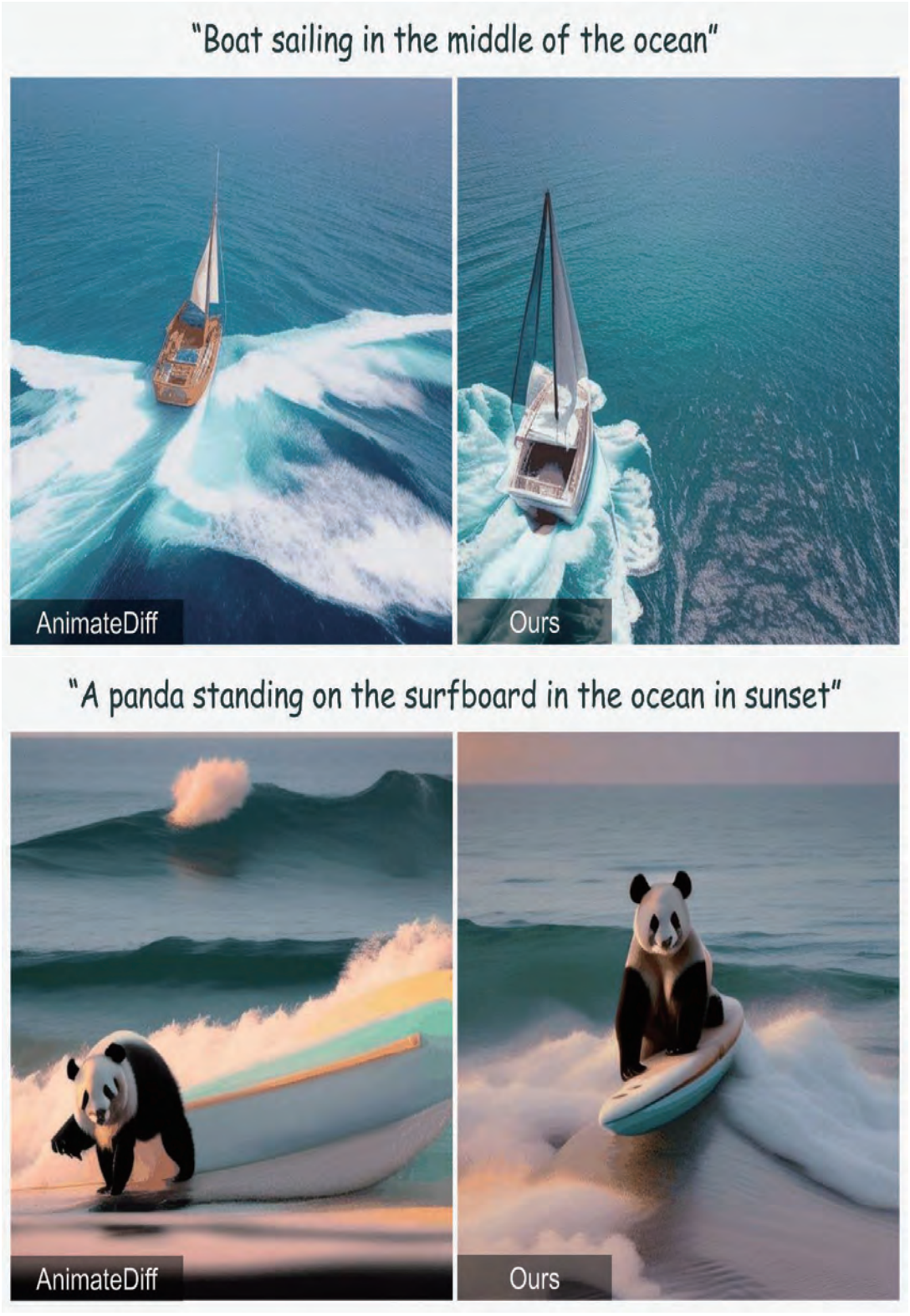
"Boat sailing in the middle of the ocean"
AnimateDiff
Ours
"A panda standing on the surfboard in the ocean in sunset"
AnimateDiff
Ours

"Slow motion footage of a racing car"

"Couple salsa dancing"

"A bearded man putting a vinyl record on a vinyl player"

"Ashtray full of butts on table, smoke flowing on black background, close-up"

"A white yacht traveling on a river and passing under the bridge"

"A car accelerating to gain speed"

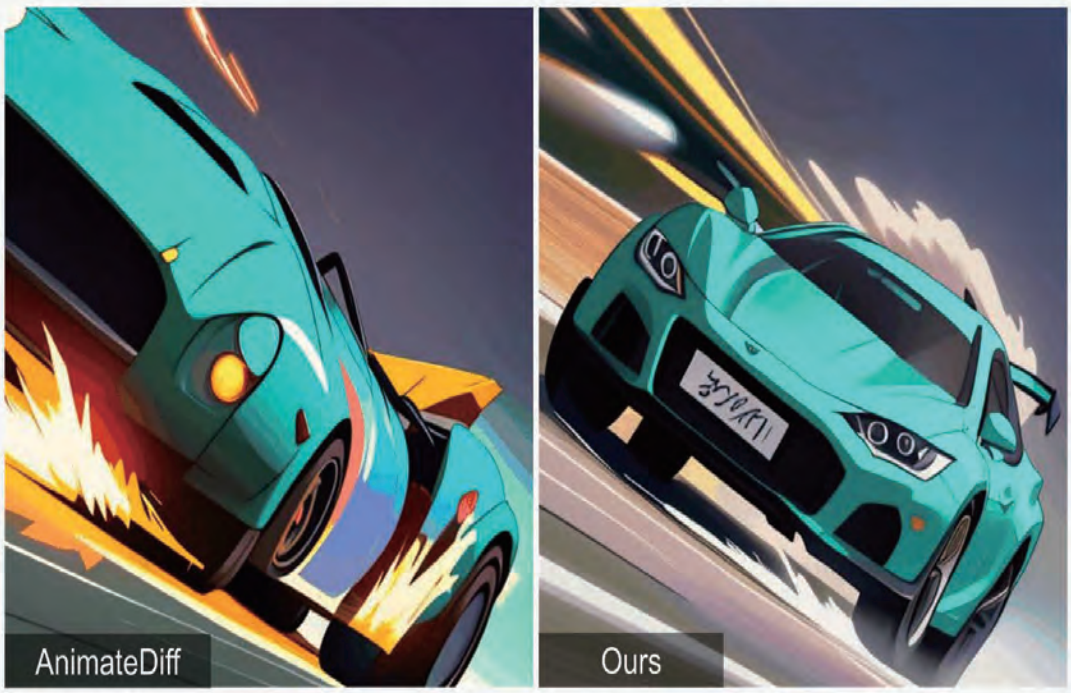

"Goat standing over a rock"

"A horse bending down to drink water from a river"

"A space shuttle launching into orbit,
with flames and smoke billowing out from engines"

Extension to Video Inverse Problems

❑ Video Inverse Problems: Motivation

Kwon et al, ICLR 2025

➢ Motivation

- **Video inverse problems** involve complex spatio-temporal degradations, which are difficult to solve using **image diffusion models**.

➢ Goal

- **First approach** to solve video inverse problems using **only** image diffusion models

❑ Vision-XL: Video Inverse Solver via 2D Diffusion

Kwon et al, ICLR 2025; Kwon et al, ICCV 2025

https://vision-xl.github.io/

❑ Vision-XL: Video Inverse Solver via 2D Diffusion

Kwon et al, ICLR 2025, ICCV 2025

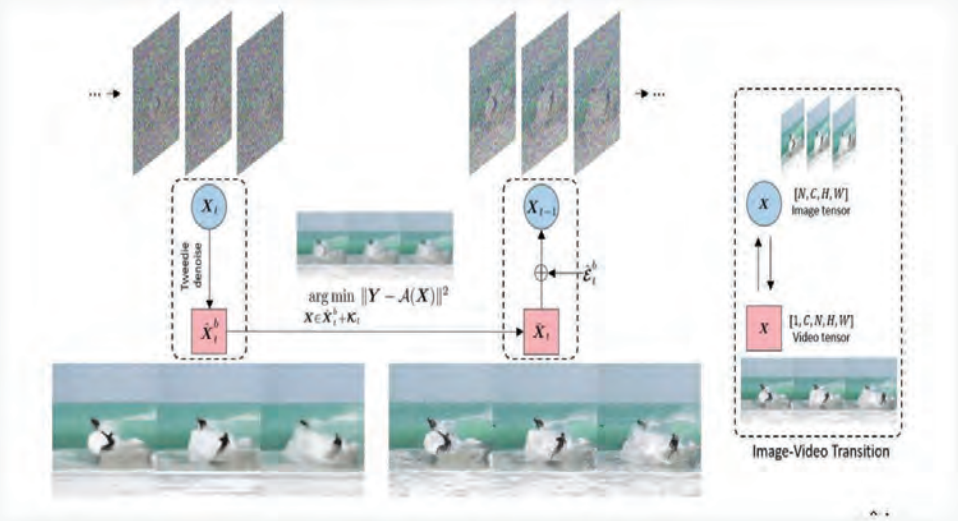

❑ Noise Schedule is the Key

:Synergistic combination with Batch Consistent Sampling

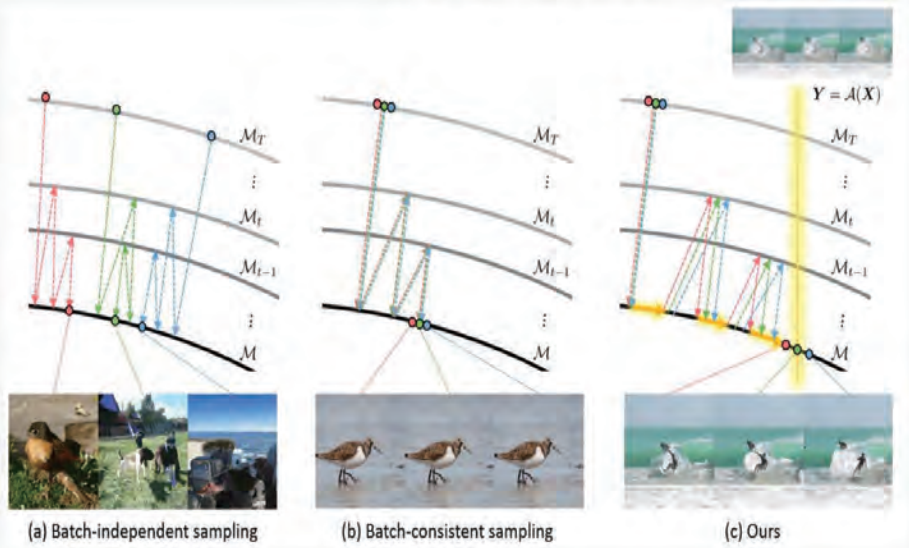

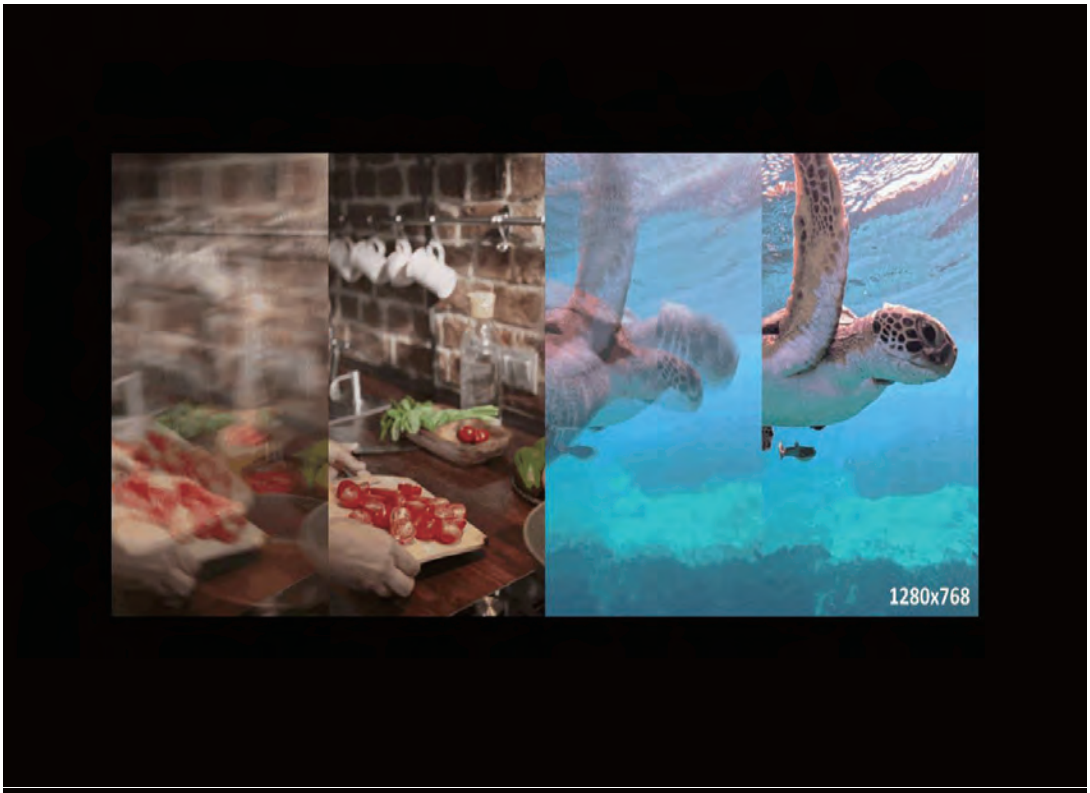
1280x768

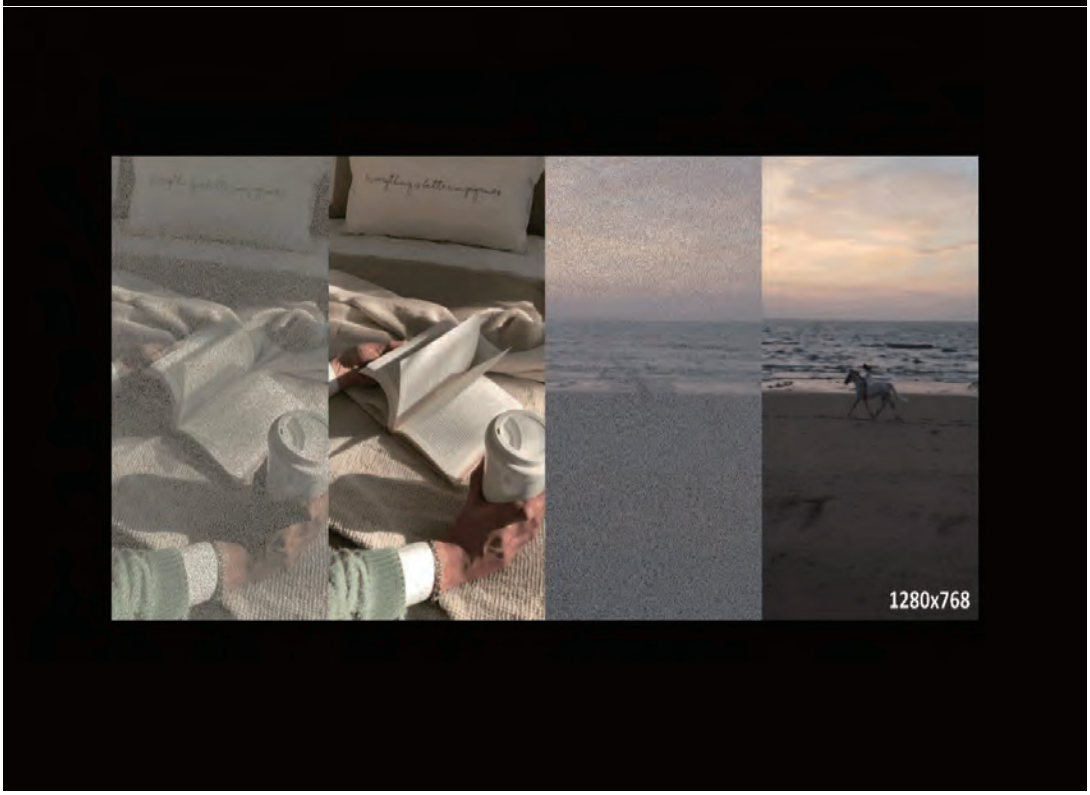
1280x768


1280x768


768x1280


768x1280


768x1280

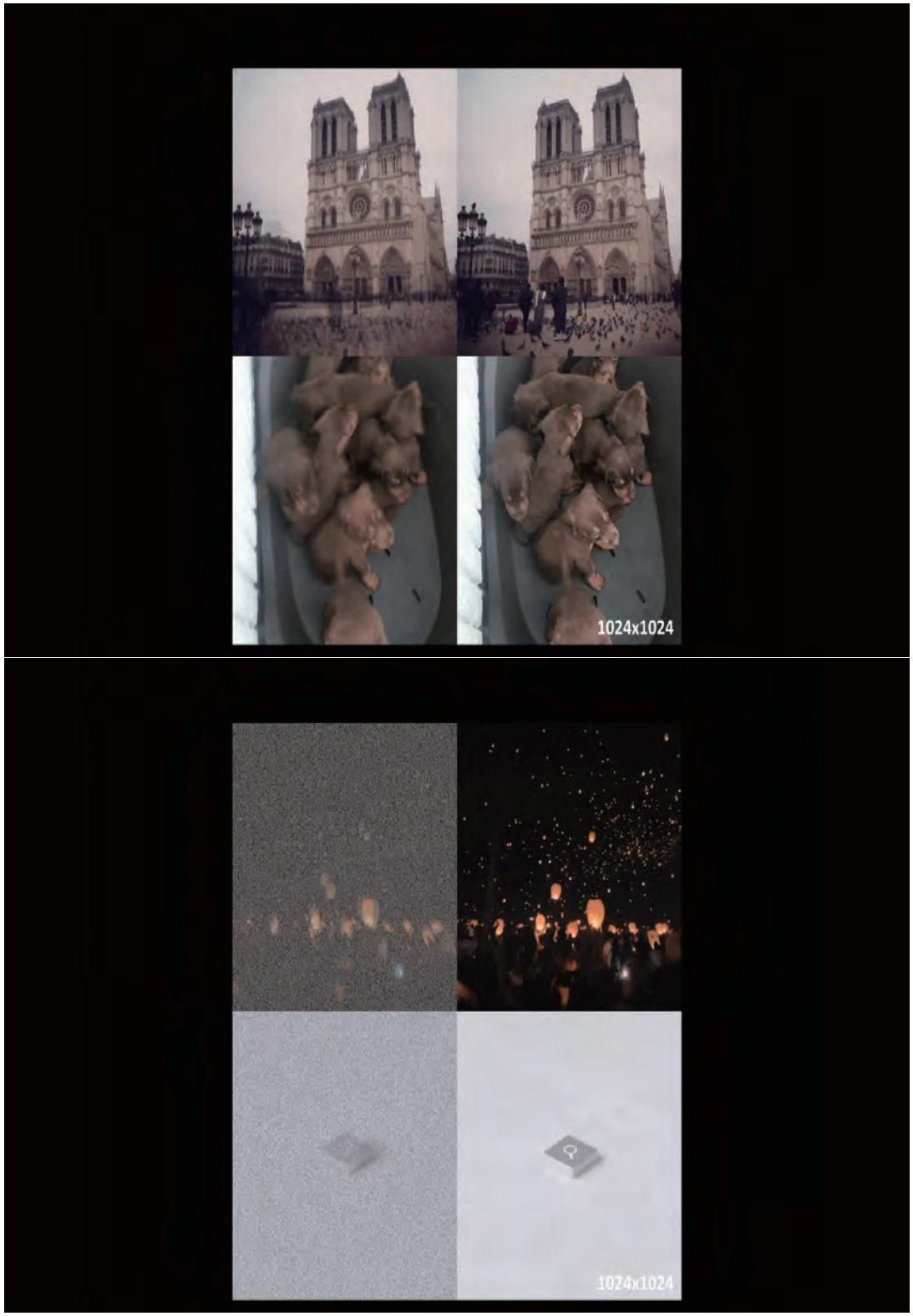
1024x1024
1024x1024

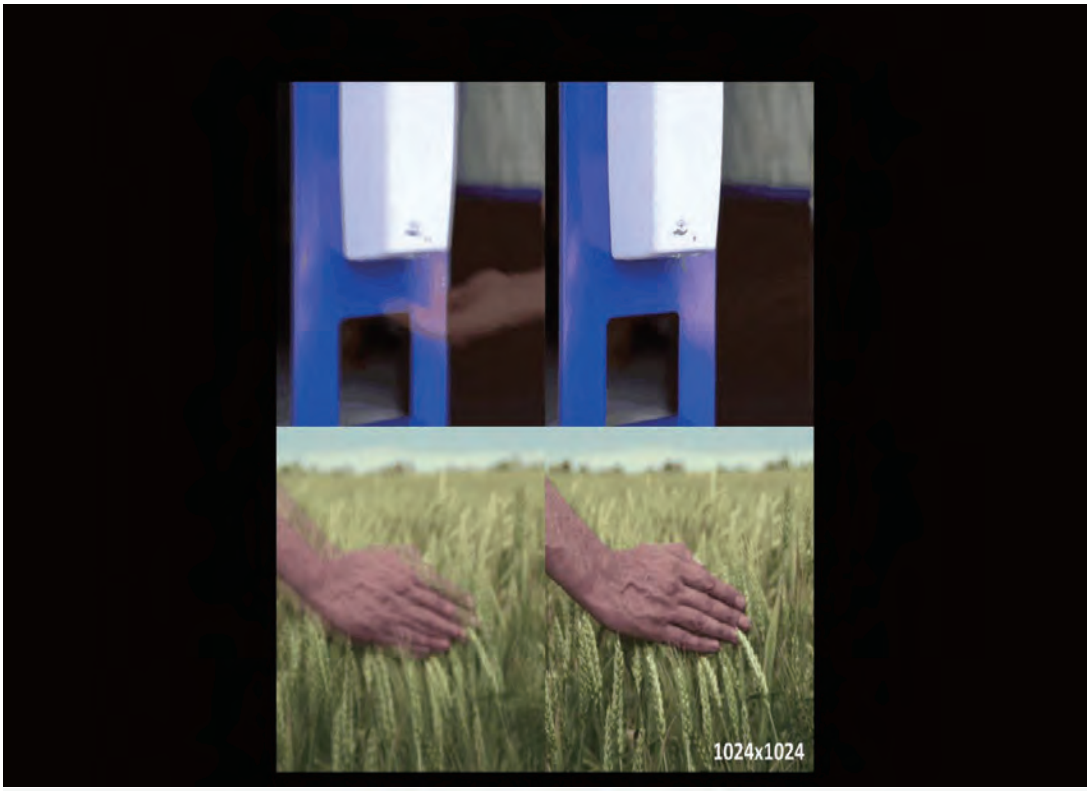
1024x1024

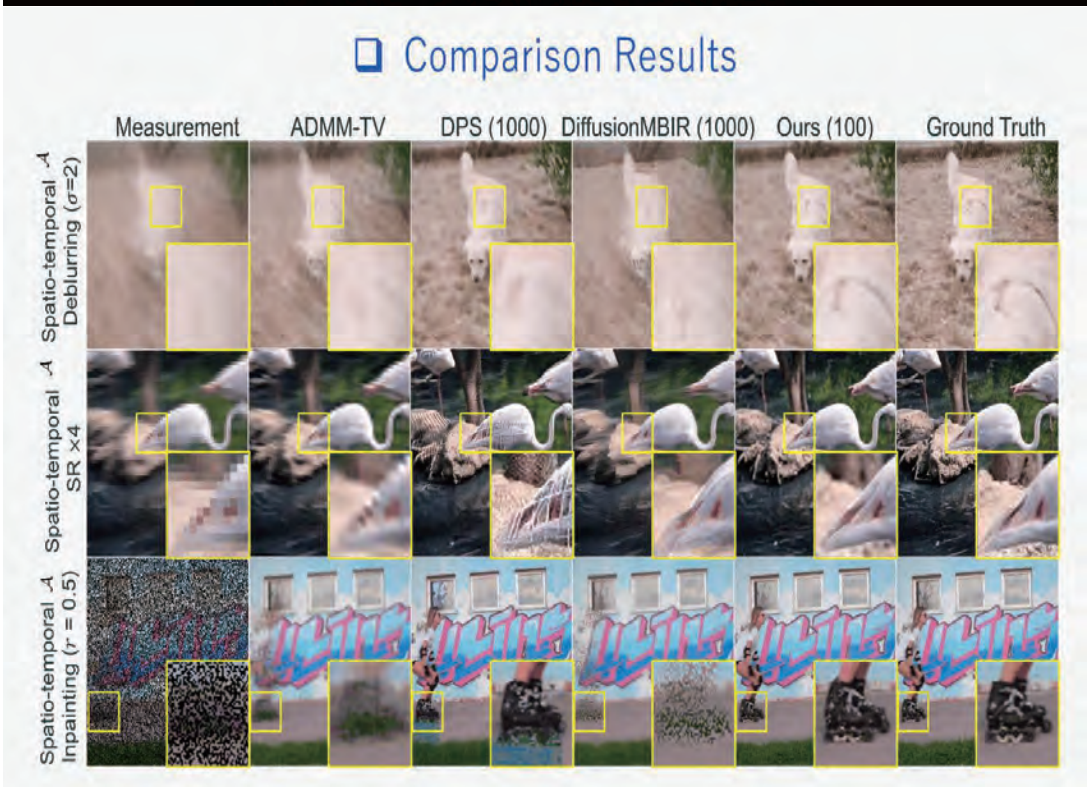
Comparison Results
Measurement
ADMM-TV
DPS (1000)
DiffusionMBIR (1000)
Ours (100)
Ground Truth
Spatio-temporal $\mathcal{A}$ Deblurring (σ=2)
Spatio-temporal $\mathcal{A}$ SR ×4
Spatio-temporal $\mathcal{A}$ Inpainting (r = 0.5)

ViBidSampler: Manifold-Constrained Video Interpolation

Yang et al, ICLR 2025

Video interpolation

- Image-to-video (I2V) diffusion models have greatly enhanced one-frame conditioned video generation.
- Two-frame (start & end) conditioned generation needs adaptation, which is essential for effective bounded interpolation.

Problems of Interpolation Methods

Yang et al, ICLR 2025

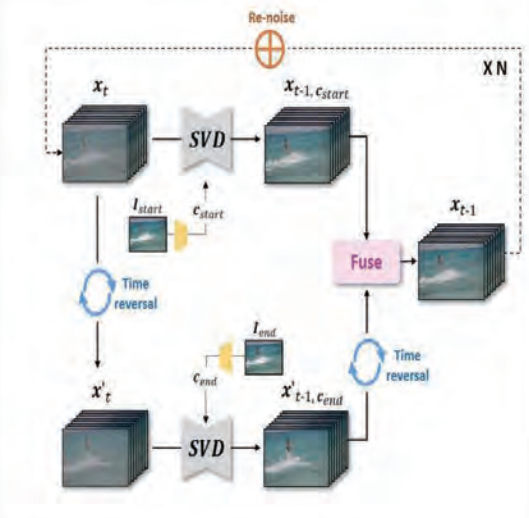

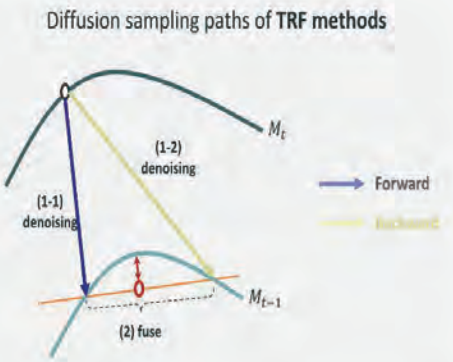

TRF: Time-reversal Diffusion

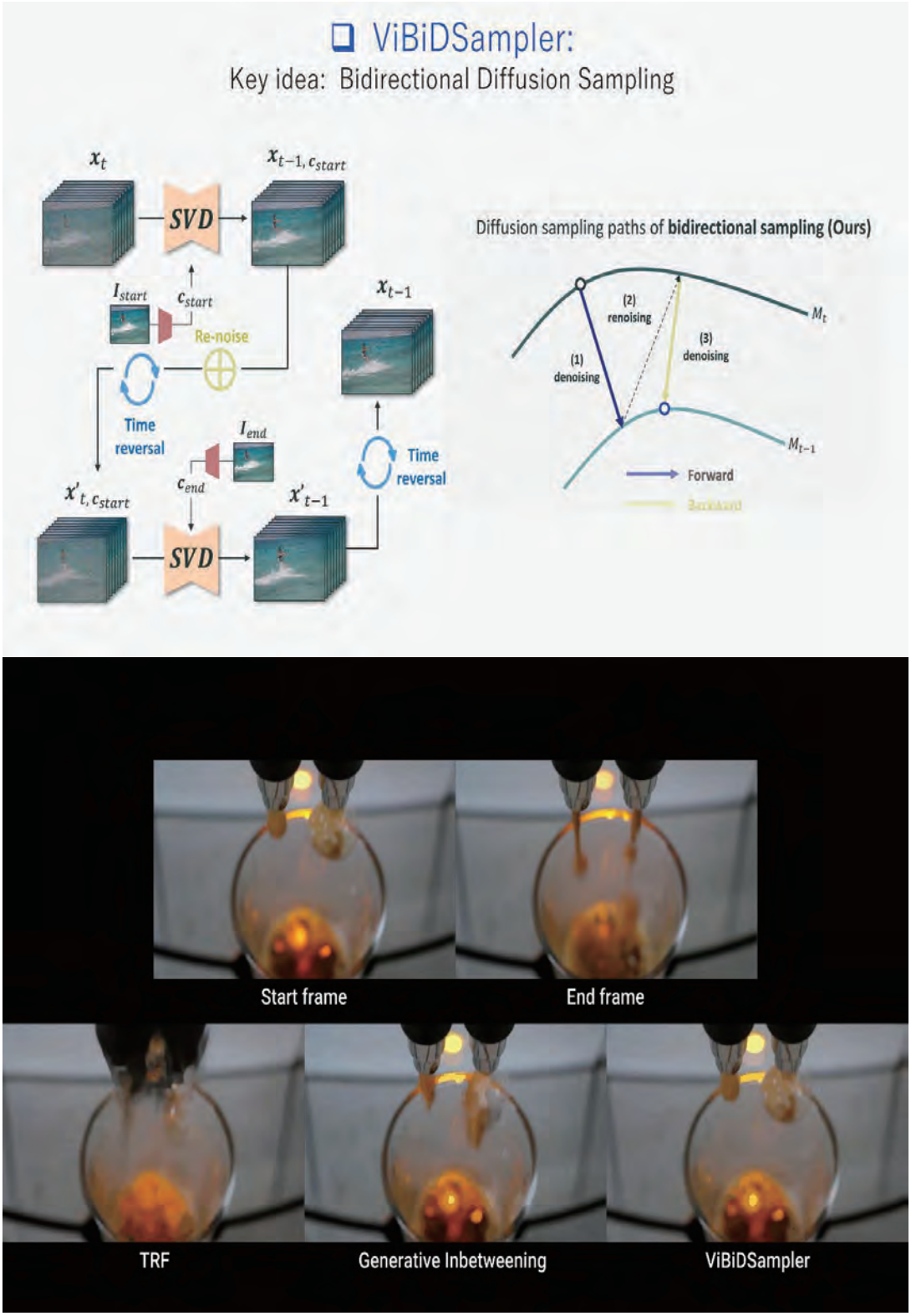
ViBiDSampler:
Key idea: Bidirectional Diffusion Sampling
x_t
$x_{t-1, c_{start}}$
SVD
I_{start}
c_{start}
Re-noise
x_{t-1}
Time reversal
I_{end}
c_{end}
Time reversal
$x'_{t, c_{start}}$
x'_{t-1}
SVD
Diffusion sampling paths of bidirectional sampling (Ours)
(1) denoising
(2) renoising
(3) denoising
M_t
M_{t-1}
Forward
Start frame
End frame
TRF
Generative Inbetweening
ViBiDSampler

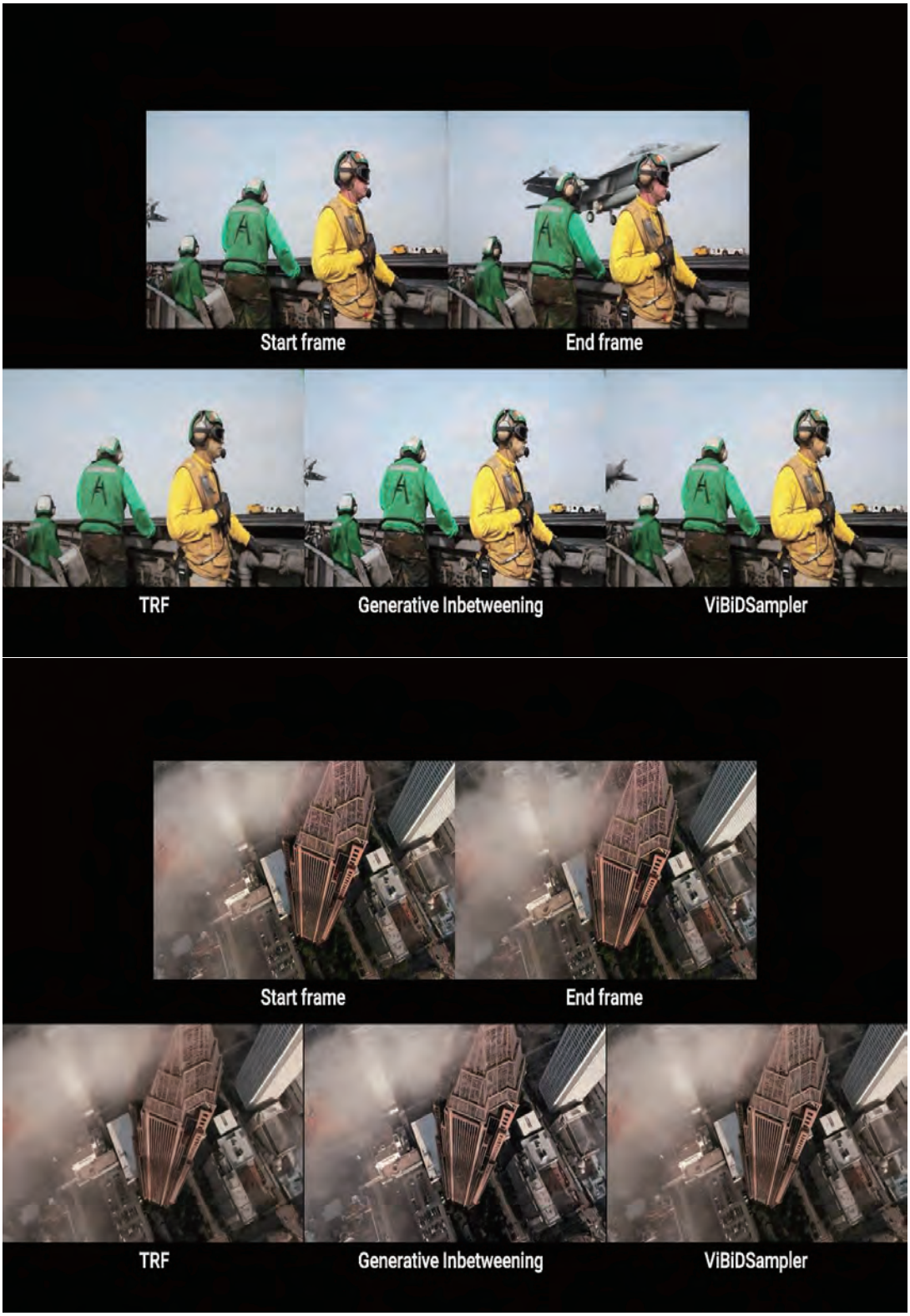
Start frame
End frame
TRF
Generative Inbetweening
ViBiDSampler
Start frame
End frame
TRF
Generative Inbetweening
ViBiDSampler


Start frame
End frame
TRF
Generative Inbetweening
ViBiDSampler

Extension to 4D Video Generation

❑ What is 4D Video?

Synchronized multi-view video

Regeneration from different camera motion

Input video Output video Input video Output video

*Results from SynCamMaster (ICLR 25), RecamMaster (arXiv 25)

❑ How do they solve it?

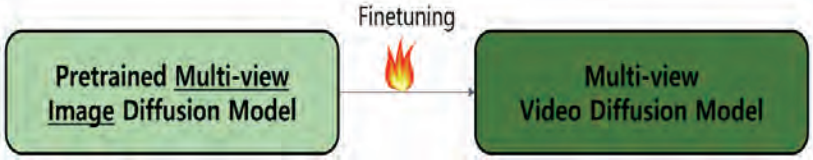

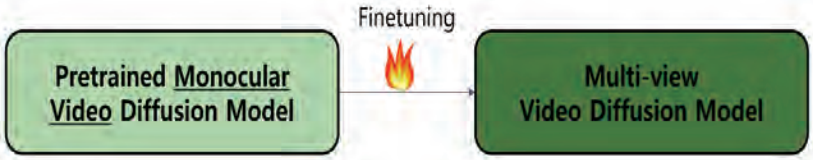

❑ How do they solve it?

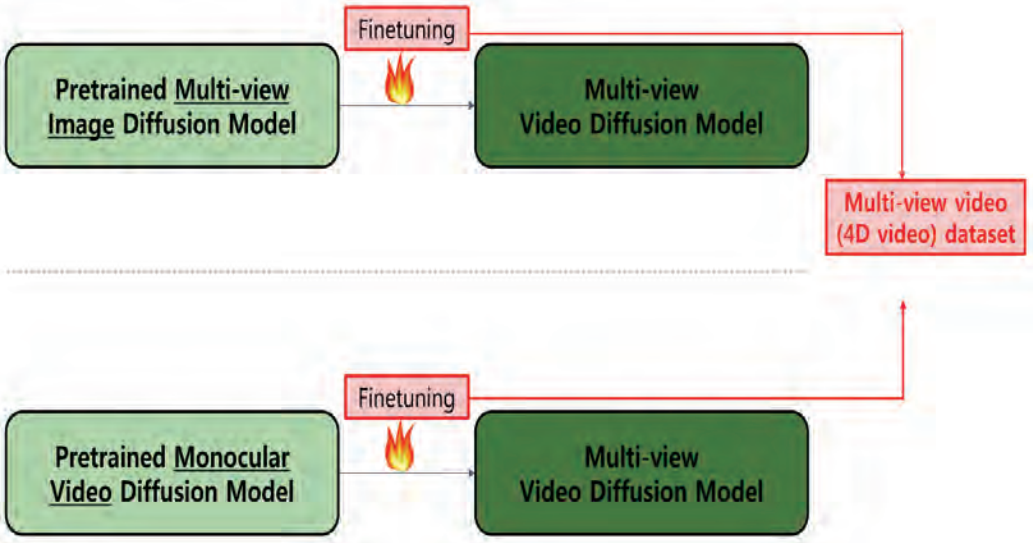

❑ Challenge: Scarcity of multi-view data

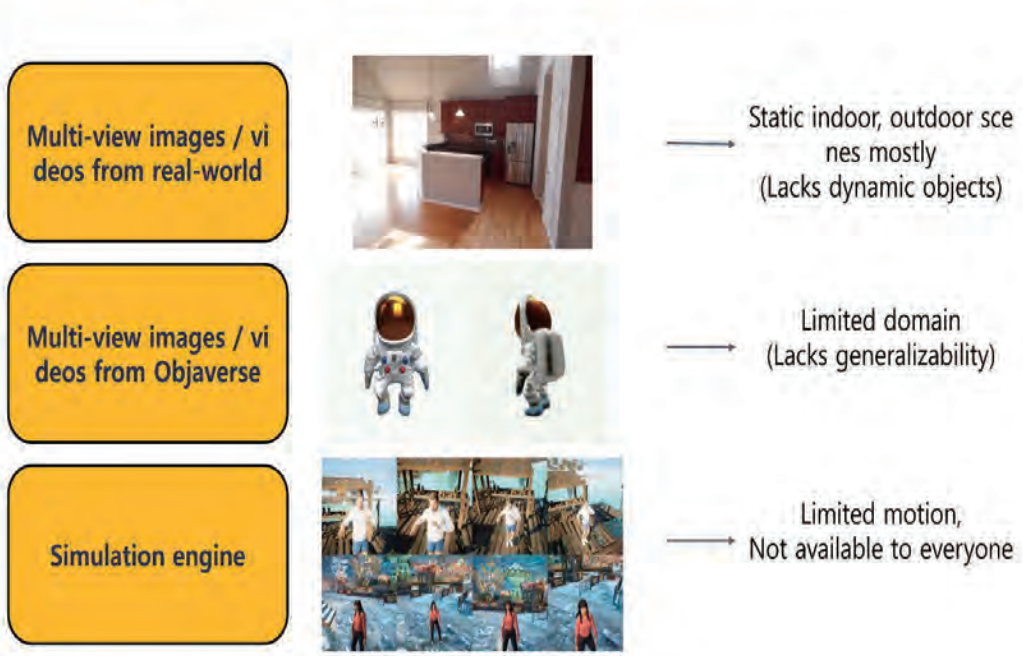

❑ Reangle-A-Video: One-Shot 4D Generation

Jeong et al, ICCV 2025

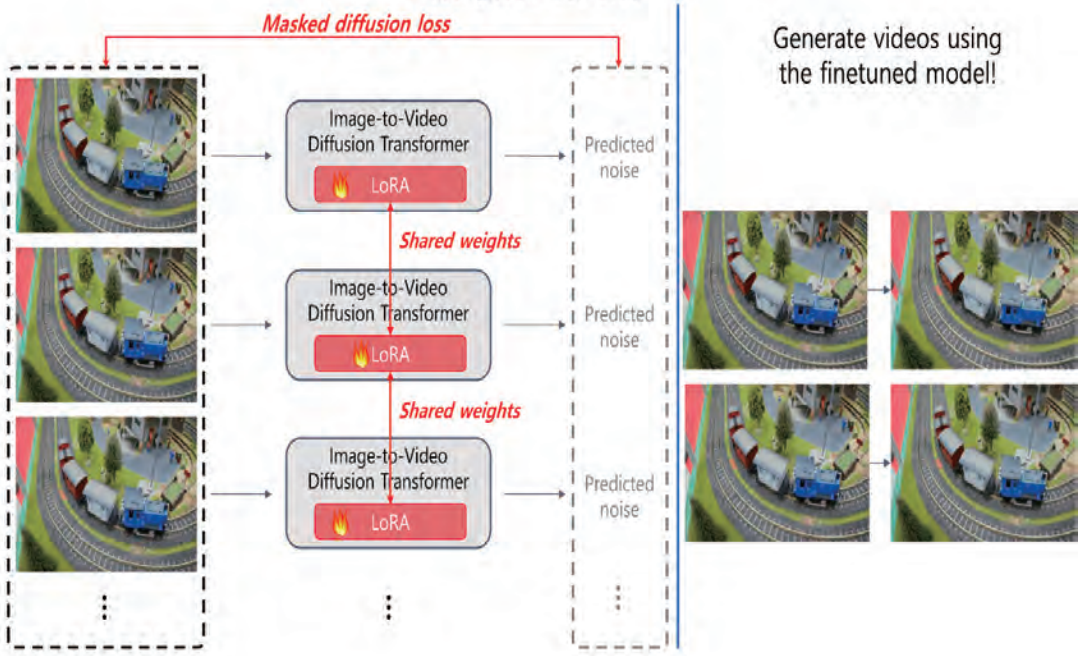

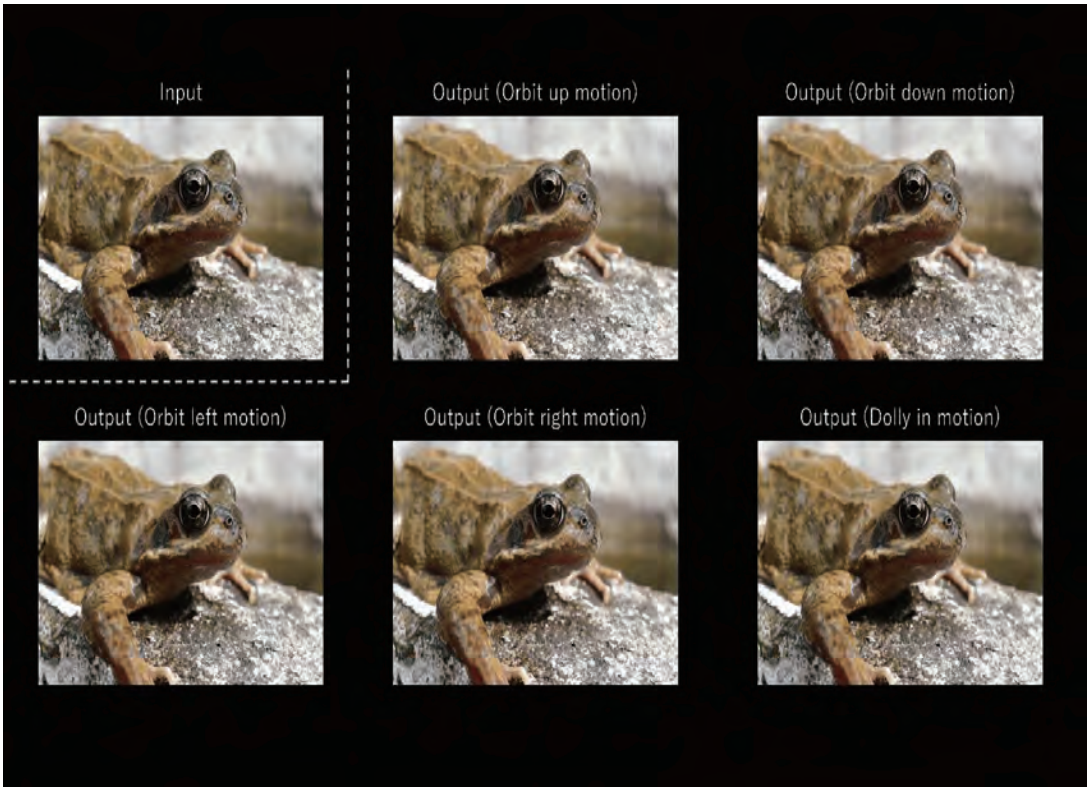

Zero-shot 4D Generation?

Yes!! Manifold geometry matters.

❑ Zero4D: Zero-shot 4D Video Generation

Park et al, arXiv:2503.22622

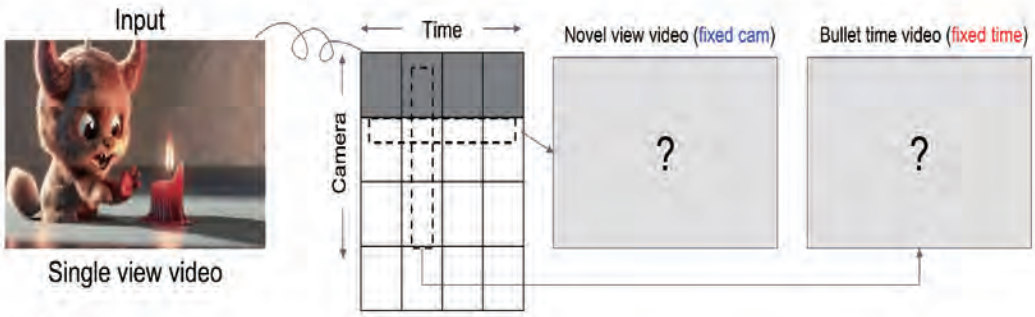

Problem definition:

- Suppose a 4D video is represented as a grid indexed by camera and time axis. (each cell corresponds to a single video frame)
- Given a single view video as input, the task of 4D video generation can be formulated as populating the camera-time grid.

❑ Key Idea: Bidirectional Video Interpolation

Park et al, arXiv:2503.22622

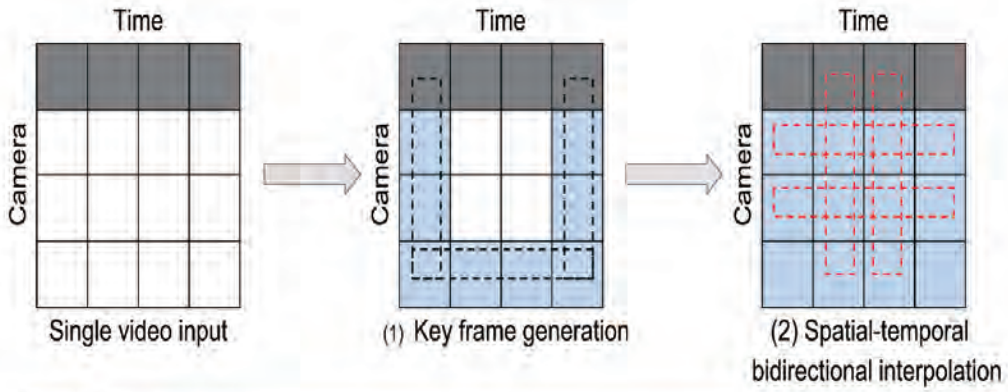

Key Steps:

(1) Key frame generation

(2) Spatial-temporal bidirectional interpolation


Input
Output (Orbit right)
Output (Orbit left)
Novel view video
Output (Time step 1)
Output (Time step 2)
Output (Time step 3)
Bullet time video
Input
Output (Orbit right)
Output (Orbit left)
Novel view video
Output (Time step 1)
Output (Time step 2)
Output (Time step 3)
Bullet time video

❑ Summary

- Diffusion models are essential tools
- Manifold geometry is key for
  - Inverse problems
  - Flows
  - Text guidance
  - Video inverse problems
  - 4D generation

Acknowledgement

NRF 한국연구재단 | 과학기술정보통신부 Ministry of Science and ICT | 보건복지부 Ministry of Health and Welfare | 관세청 Korea Customs Service | SAMSUNG | MERCK

Forum “Math for Industry” 2025

Pairwise Optimal Transports for Training All-to-All Flow-Based Condition Transfer Model

Fukumizu, Kenji

The Institute of Statistical Mathematics

In this work, we propose a flow-based method for learning all-to-all transfer maps among conditional distributions that approximates pairwise optimal transport. The proposed method addresses the challenge of handling the case of continuous conditions, which often involve a large set of conditions with sparse empirical observations per condition. We introduce a novel cost function that enables simultaneous learning of optimal transports for all pairs of conditional distributions. Our method is supported by a theoretical guarantee that, in the limit, it converges to the pairwise optimal transports among infinite pairs of conditional distributions. The learned transport maps are subsequently used to couple data points in conditional flow matching. We demonstrate the effectiveness of this method on synthetic and benchmark datasets, as well as on chemical datasets in which continuous physical properties are defined as conditions.

Pairwise Optimal Transports for Training All-to-All Flow-Based Condition Transfer Model

Kenji Fukumizu

The Institute of Statistical Mathematics

August 18, 2025. Forum "Math for Industry", Seoul

Dynamical Generative models

- Generative models based on SDE/ODE have shown a great success.
  - Images, Movies, Texts, Audio, Molecules, etc.
- Diffusion Models (Song et al 2021; Ho et al 2020)
  Based on SDE
- Flow Matching (FM)
  (Lipman et al 2023; Liu et al 2023; Albergo et al 2023)
  Based on ODE
- Learns pushforward: $N(0, I_d) \Rightarrow P$

Sora, OpenAI

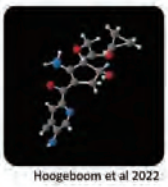

Hoogeboom et al 2022

Esser et al 2024

Moviegen, Meta

Transfer of distributions

- Transfer of samples
  - Images
    Style transfer
  - Molecules
    Edit molecules to those of desired physical properties.

- Methods of transporting distributions
  - Optimal Transport
  - Dynamical generative models
    - FM:
    - Diffusion: Schrödinger bridge (De Bortoli et al 2021).
  - Structural stability in the change is desired in many applications.

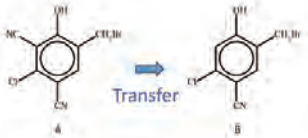

Goal: All-to-All Transfer

- Transfer = Change of conditions $P_{X|C}$
- Target: Continuous conditions
  - Difficult: one condition may have one data
  - Important in many applications:
    e.g. Molecules of continuous properties:
    logP (hydrophobicity), tPSA (topological polar surface area), etc.
- Arbitrary change: $P_{X|C=c_1} \mapsto P_{X|C=c_2}$
  - Most existing methods realize only one-to-one transfer.
- Goal: Simultaneous learning of all-to-all transfers.

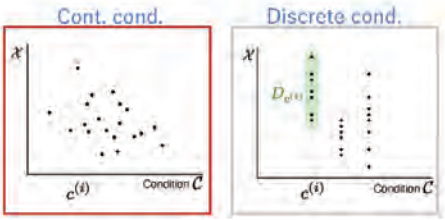

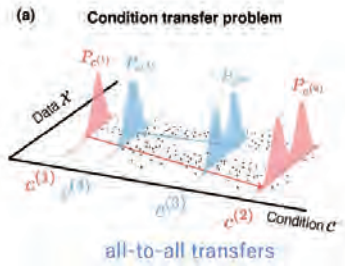

Review: Optimal Transport

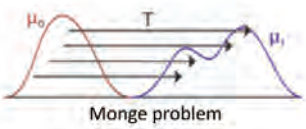

Monge problem

- Monge:

$$\inf_T \left\{ \int_X c(x, T(x)) d\mu_0(x) \mid T_{\#}\mu_0 = \mu_1 \right\}$$

- Kantorovich:

$$\inf_{\Pi \in \Gamma(\mu_0, \mu_1)} \int_{X \times Y} c(x, y) d\Pi(x),$$

$$\Gamma(\mu_0, \mu_1) = \left\{ \Pi \in \mathcal{P}(X \times Y) \mid \pi_{X\#}\Pi = \mu_0,\ \pi_{Y\#}\Pi = \mu_1 \right\}$$


Kantorovich formulation

- Empirical distributions of the same size:
  - Coupling/permutation (easier)
  - Entropy regularization gives an efficient algorithm (Cuturi 2013)

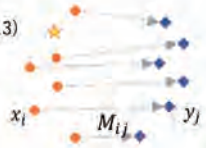

- However, transporting a new location, not within $\{x_i\}$, requires to construct a continuous map.

Review: Flow Matching

(Lipman et al 2023; Liu et al 2023; Albergo et al 2023)

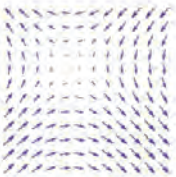
Vector field on $\mathbb{R}^2$

- FM
  - Learns a vector field $\boldsymbol{v}_t(\boldsymbol{x})$.
  - Solving ODE gives a flow:

$$\frac{d\boldsymbol{\varphi}(\boldsymbol{x}, t)}{dt} = \boldsymbol{v}_t\big(\boldsymbol{\varphi}(\boldsymbol{x}, t)\big), \qquad \varphi(\boldsymbol{x}, 0) = \boldsymbol{x}.$$

$$\boldsymbol{\varphi}_1 : \mathbb{R}^d \to \mathbb{R}^d, \qquad \boldsymbol{x} \mapsto \boldsymbol{\varphi}(\boldsymbol{x}, 1).$$

  - Purpose: pushforward $(\boldsymbol{\varphi}_1)_{\#}P_{source} = P_{target}$
    - Generation: $N(0, I_d) \Rightarrow P_{target}$.
    - Transfer: $P_{source} \Rightarrow P_{target}$

e.g. $P_{\text{non-beard}} \rightarrow P_{\text{beard}}$

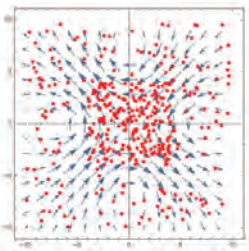
Mapping of particles by a flow

Conditional Flow Matching

(Lipman et al 2023; Tong et al 2023)

N.B. Conditional FM does NOT mean generation form a conditional distribution.

- Conditional vector field
  $(\boldsymbol{x}_0, \boldsymbol{x}_1)$: $\boldsymbol{x}_0 \sim P_{source}$, $\boldsymbol{x}_1 \sim P_{target}$.
  - Typically, make a random straight path:
    $\boldsymbol{\psi}_t(\boldsymbol{x}_0, \boldsymbol{x}_1) = t\boldsymbol{x}_1 + (1-t)\boldsymbol{x}_0$
    $\boldsymbol{v}_t(\boldsymbol{x}|\boldsymbol{x}_0, \boldsymbol{x}_1) := \dot{\boldsymbol{\psi}}_t(\boldsymbol{x}_0, \boldsymbol{x}_1) = \boldsymbol{x}_1 - \boldsymbol{x}_0$
- NN learns the average $E[\boldsymbol{v}_t(\boldsymbol{x}|\boldsymbol{x}_0, \boldsymbol{x}_1)]$.
  $\min_{g_\theta : NN} E_{x_0, x_1, t.x} \| \underbrace{\boldsymbol{g}_\theta(t, \boldsymbol{x})}_{\text{NN}} - \underbrace{\boldsymbol{v}_t(\boldsymbol{x}|\boldsymbol{x}_0, \boldsymbol{x}_1)}_{\text{Teaching data}} \|^2$.
- The average $\boldsymbol{g}_\theta(t, \boldsymbol{x})$ gives a flow that transports P_{source} to P_{target}.

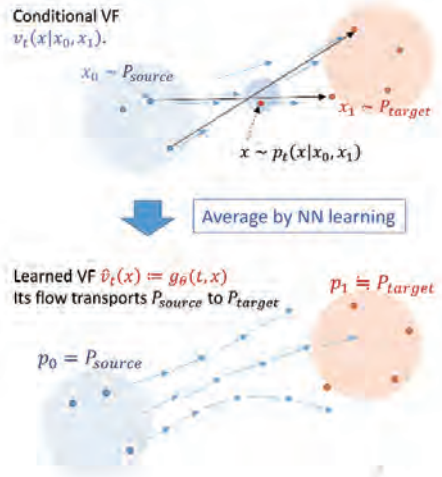

Minibatch OT-CFM

- Better paring
  $(\boldsymbol{x}_0, \boldsymbol{x}_1)$: $\boldsymbol{x}_0 \sim P_{source}$, $\boldsymbol{x}_1 \sim P_{target}$
  Affine path $\boldsymbol{\psi}_t(\boldsymbol{x}_0, \boldsymbol{x}_1) = t\boldsymbol{x}_1 + (1-t)\boldsymbol{x}_0$
  - Independent paring may cause difficult training with large variance.
  - A straight vector field makes the ODE easier to solve.

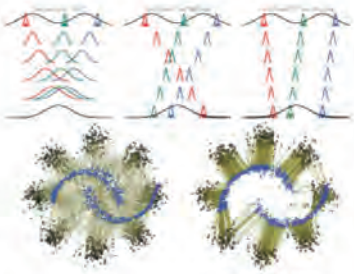

Tong et al 2023

- OT-CFM (Pooladian et al 2023; Tong et al 2023)
  - OT is used to couple $\{\boldsymbol{x}_0^a\}_a$ and $\{\boldsymbol{x}_1^b\}_b$ for affine paths.
  - Take minibatches of the same size from P_{source} and P_{target}, and apply OT.
- OT-CFM can be regarded as feasible approximation of OT.

Conditional distributions with FM

- Continuous condition

  $(x^{(i)}, c^{(i)}) \sim P, \quad i = 1, \ldots, N.$

  Often, for each $c^{(i)}$, we have only one data x.

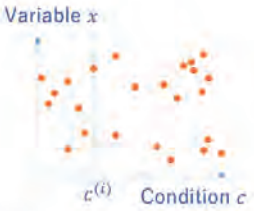

- Existing methods

  ◆ FM with conditioned vector field

  Minibatch OT → x_0 and $x_1 = x^{(i)}$ is coupled $(x^{(i)}, c^{(i)})$

  $$v_t(x_t \mid x_0, x_1, c^{(i)}) = x_1 - x_0.$$

  Train the vector field depending on c: $v_t(x, c)$

  $$\min_\theta E_{c,t,x_0^c,x_1^c} \| g_\theta(x_t, t, c) - v_t(x_t \mid x_0, x_1, c) \|^2$$

  Valid for cond. generation, NOT for transfer.

◆ Conditional OT Flow Matching (COT-FM) (Kerrigan et al., 2024b; Chemseddine et al., 2024)

- Data $\left\{\left(x_1^{(i)}, c_1^{(i)}\right)\right\}_{i=1}^N \sim P_1.$ (c may be continuous)
- FM on the joint space $\mathcal{X} \times \mathcal{C}$, keeping condition c.

  Source includes c: $P_0 = N(\mu_c, V_c) \otimes P_c$ on $\mathcal{X} \times \mathcal{C}$.
- Conditional OT for making a minibatch:

  Coupling π:

  $$\min_\pi \sum_{i=1}^N \left\| x_0^{(i)} - x_1^{\pi(i)} \right\|^2 + \beta \left\| c_0^{(i)} - c_1^{\pi(i)} \right\|^2.$$
- For large $\beta \to \infty$ as $N \to \infty$, the coupling provably converges weakly to OT for each c.

Valid for conditional generation, but NOT for transfer

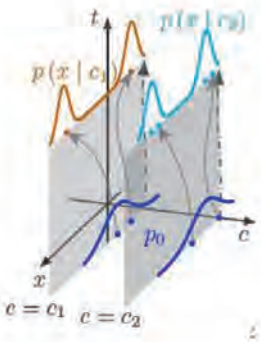

Pairwise Optimal Transports for Training All-to-All Flow-Based Condition Transfer Model

arXiv:2504.03188 [cs.LG]

Kotaro Ikeda
(U Tokyo/
Intern: Preferred Networks)

Masanori Koyama
(U Tokyo)

Kohei Hayashi
(U Tokyo)

A2A-FM: Simultaneous learning of all-to-all transfers

A2A-FM: learns transport maps $T_{c_1 \to c_2}$ for all condition pairs (c_1, c_2).

- Flow-based: learns (c_1, c_2)-parameterized vector field $v_t(x \mid c_1, c_2)$ s.t.

$$\frac{d}{dt}x(t) = v_t(x(t)|c_1, c_2), \qquad x(0) \sim P_{c_1},\ x(1) \sim P_{c_2}.$$

- OT-path: $\psi(t|x^{c_1}, x^{c_2}) = tx^{c_1} + (1-t)x^{c_2}$, with $x^{c_1} \sim P_{c_1},\ x^{c_2} \sim P_{c_2}$.

$$\min_\theta E \left\| g_\theta(\psi_t(x^{c_1}, x^{c_2}), t \mid c_1, c_2) - \frac{d\psi}{dt}(t|x^{c_1}, x^{c_2}) \right\|^2$$

We want to use Minibatch-OT coupling: Not straightforward!!

- Random choice of $(x^c, c), (x^{c'}, c')$ from $\{(x^{(i)}, c^{(i)})\}$ does not approximate OT.

Pairwise Optimal Transport

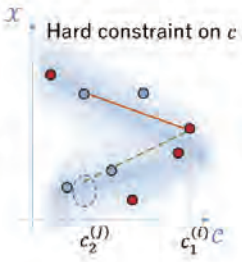

Aim:

Coupling of data $\{(x^{(i)}, c^{(i)})\}$ which approximately realizes OT from P_c to $P_{c'}$ of all pairs (c, c').

Method for pairwise OT:

Resample two batches: $\{(x_1^{(i)}, c_1^{(i)})\}_{i=1}^N, \{(x_2^{(j)}, c_2^{(j)})\}_{j=1}^N$.

Objective of coupling:

$$\min_{\pi} \sum_{i=1}^{N} \underbrace{\left\| x_1^{(i)} - x_2^{\pi(i)} \right\|^2}_{\text{Standard OTcost}} + \beta \left(\underbrace{\left\| c_1^{(i)} - c_1^{\pi(i)} \right\|^2 + \left\| c_2^{(i)} - c_2^{\pi(i)} \right\|^2}_{\text{Clustering of conditions}} \right)$$

$\beta \to \infty$ as $N \to \infty$.

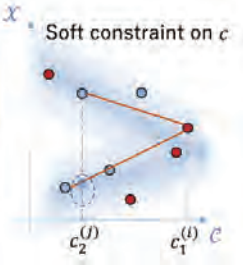

- Rationale

Consider data with joint, identical conditions $\left(c_1^{(i)}, c_2^{(i)}\right) \sim P_C \otimes P_C$:

$$\left(x_1^{(i)}, c_1^{(i)}\right) \Rightarrow \left(x_1^{(i)}, \left(c_1^{(i)}, c_2^{(i)}\right)\right) \ (i = 1, \ldots, n) \quad \sim Q^1_{X|(C_1,C_2)} = P_{X|C_1}$$

$$\left(x_2^{(j)}, c_2^{(j)}\right) \Rightarrow \left(x_2^{(i)}, \left(c_1^{(i)}, c_2^{(i)}\right)\right) \ (i = 1, \ldots, n) \quad \sim Q^2_{X|(C_1,C_2)} = P_{X|C_2}$$

- $Q^1_{X|(C_1,C_2)}$ and $Q^2_{X|(C_1,C_2)}$ are two conditional distributions with the same condition.
- Conditional OT gives $\min_{\pi} \sum_{i=1}^{N} \left\| x_1^{(i)} - x_2^{\pi(i)} \right\|^2 + \beta \left(\left\| c_1^{(i)} - c_1^{\pi(i)} \right\|^2 + \left\| c_2^{(i)} - c_2^{\pi(i)} \right\|^2 \right)$

- Pairwise OT can be regarded as a special case of conditional OT. The same convergence results can apply.

Theoretical guarantee (incl. continuous condition)

π^*_β: optimal coupling with β. It is a joint distribution on $(\mathcal{X} \times \mathcal{C}) \times (\mathcal{X} \times \mathcal{C})$.

$\Pi^*_\beta := \sum_{i=1}^N \delta_{\left((x_1^{(i)}, c_1^{(i)}), \left(x_2^{\pi^*_\beta(i)}, c_2^{\pi^*_\beta(i)}\right)\right)}$ (coupling)

Proposition. (condition can be continuous)

For any sequence $\beta_k \to \infty$, there exists an increasing sequence of the sample size N_k such that $\Pi^*_{\beta_k}$ converges to Π^*, of which the conditional distribution $\Pi^*(\cdot,\cdot|\, c_1, c_2)$ of (x_1, x_2) given (c_1, c_2) attains

$$E_{c_1,c_2}\left[\int_{\mathcal{X}^2} \|x_1 - x_2\|^2 \, d\Pi^*(x_1, x_2|c_1, c_2)\right] = E_{c_1,c_2}\left[W_2(P_{c_1}, P_{c_2})^2\right]$$

Consequently, for almost every (c_1, c_2), $\Pi^*(\cdot,\cdot|\, c_1, c_2)$ is an optimal transport between P_{c_1} and P_{c_2}.

Experiments: Synthetic data

- Continuous condition

  2D distribution

  $(r, \theta), r \in [1,2], \theta \in \left[0, \frac{\pi}{4}\right]$. Condition $c = \theta$.

  - Proposed A2A-FM
  - Multi-marginal Stochastic Interpolants (Albergo et al 2024, discretized into 5 bins)
  - Partial diffusion (Kaufman et al 2024)

  Evaluate MSE from the solution of OT (ground truth)

	MSE from Pairwise OT
A2A-FM	$\mathbf{1.01 \times 10^{-2}}$
Partial Diffusion	6.42×10^{-2}
MMSI	4.48×10^{-2}

Partial diffusion:

Starting from an initial sample from P_c, the method adds limited noise and use the diffusive forward process with score for $P_{c'}$.

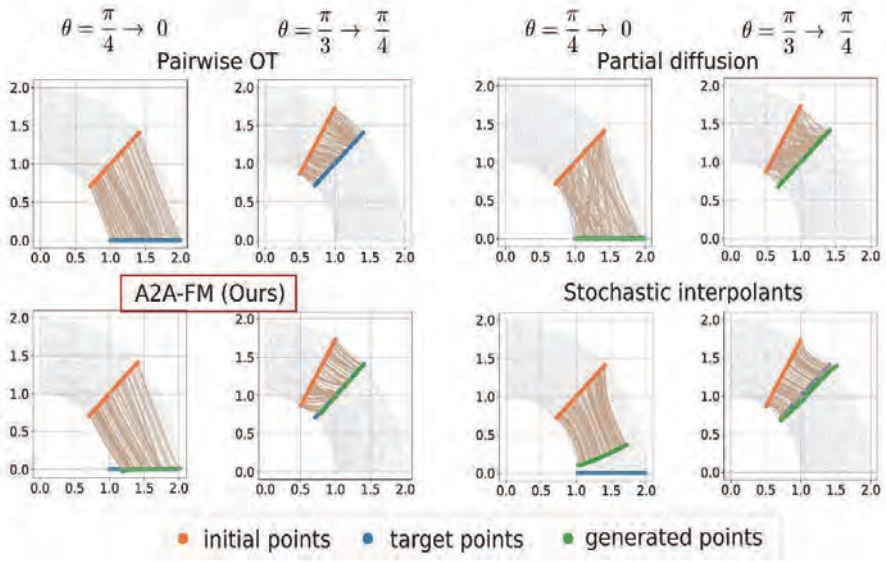

Experiments: Face images

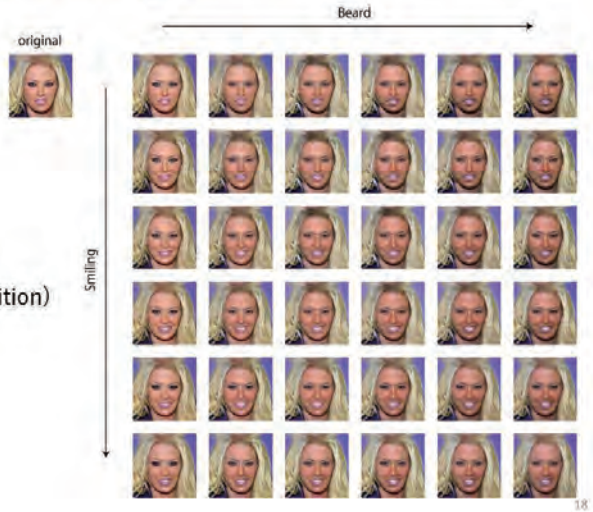

CelebA-Dialog HQ 256
(Jiang et al 2021)

- 256x256 facial images with attributes.
- "Beard" and "Smiling" (2D condition) are expressed in $[0,5]^2$.
- Latent encoding is used (Rombach et al 2022).

Experiment: Molecule edit

1. Nearby sampling

Modify a molecule to another with desired property.
Desired to be similar to the original one.

- Higher QED (Quantitative Estimate of Drug-likeness)
  - Source molecule: $0.6 \leq QED \leq 0.8$.
  - Target: $QED \geq 0.9$
  - Evaluation:
    - QED of resulting molecules
    - Morgan fingerprint Tanimoto similarity.

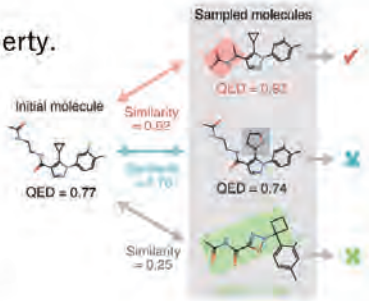

- Comparison : COATI-LDM (SOTA, partial diffusion Kaufman et al 2024)
- COATI encoder-decoder is used (Kaufman et al 2024)

Method	Success Rate (%)
DESMILES (Maragakis et al., 2020)	76.9
QMO (Hoffman et al., 2022)	92.8
MolMIM (Reidenbach et al., 2022)	94.6
COATI-LDM (Kaufman et al., 2024a)	95.6
A2A-FM (Ours)	**98.3**

Success rate for 800 initial molecules
Max calls = 50000

Call: random choice of hyper-parameters
Success: $QED \geq 0.9$, Tanimoto similarity ≥ 0.4

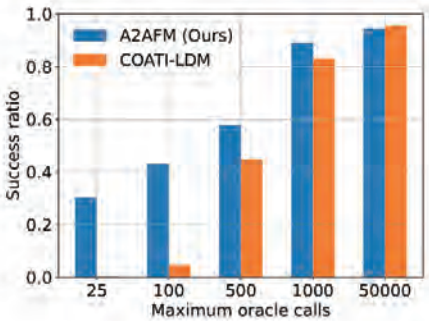

Success rates for #calls

Conclusions

- All-to-All Flow Matching
  - Transfer from any condition to another.
  - To use minibatch-OT, we have developed a method of Pairwise-OT, which provably converges to OT for any pairs of condition.
  - Experimental results demonstrate:
    - Simultaneous learning of pairwise-OT for all pairs is achieved.
    - SOTA results for molecular transfer tasks.

Appendix

◆ Multimarginal Stochastic Interpolants (MMSI, Albergo et al 2024)

- $\{c_k\}_{k=1}^K \subset \mathbb{R}^m$ finite conditions. $c_0 = 0$
  $\{x_k^{(i)}\}_{i=1}^{N_k} \sim P_{c_k}$. Many samples for each condition.
- Assume we have transport map $T_{0\to k}$ for each condition.
  For any $c = \sum_{k=1}^K \alpha_k c_k \in \Delta_K$, generate sample
  $$x_c = \sum_k \alpha_k T_{0\to k}(x_0) \sim \tilde{P}_c \quad \text{interpolation}$$
- Transfer is possible for any P_c to $P_{c'}$ $(c, c' \in \Delta_K)$.
- Not applicable to data with continuous condition $\{(x^{(i)}, c^{(i)})\}_{i=1}^N$.
- But, we could use a partition into K classes.

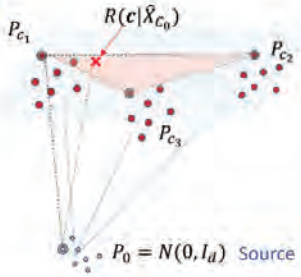

Additional experiment with molecules

2. All-to-all transfer

- 2-dim conditions:
  - logP (hydrophobicity)
  - tPSA (topological polar surface area),
- 1,024 initial molecules from ZINC22 dataset.

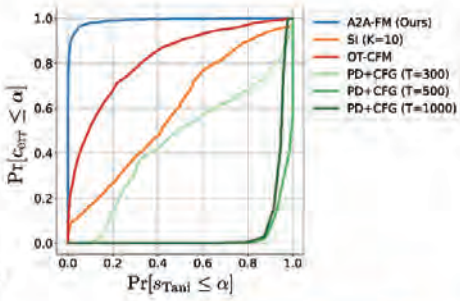

- Evaluation
  - Relative error of conditions = $\|c_{target} - c_{sample}\|/c_{max}$
  - Tanimoto similarity $\in [0,1]$
  - We show curves of the trade-off.
    - $F(a) \coloneqq \Pr(\text{Rel. cond. loss} \le a)$,
      $G(a) \coloneqq \Pr(\text{Tanimoto sim.} \le a)$
    - AUC = Probability that similarity $\ge$ rel. cond. Loss.

Method	AUC
PD+CFG (T=500)	0.027
PD+CFG (T=300)	0.450
PD+CFG (T=1000)	0.060
SI (K=10)	0.583
OT-CFM	0.819
A2A-FM (Ours)	**0.990**

Do Language Models Understand Math?

Yea-Chan Park

Sejong University

The recent success of large language models (LLMs), such as ChatGPT, marks a remarkable advance in machine learning and artificial intelligence. However, it remains premature to assert that these models possess genuine reasoning capabilities. Although LLMs excel at generating coherent and contextually relevant text based on extensive training data, their performance in domains requiring precise logical reasoning—such as mathematics—remains limited. In particular, LLMs frequently struggle with exact mathematical operations, positioning mathematics as a critical benchmark for assessing an AI model's capacity for logical reasoning. In this talk, we explore whether language models can learn and internalize the exact rules of mathematical operations purely from data. Our investigation is grounded in the phenomenon of grokking—a surprising behavior where a model, after extended training, abruptly transitions from poor to near-perfect generalization. By examining the inner workings of the training dynamics, we aim to uncover how language models develop implicit understanding of mathematical rules. We propose that this understanding may emerge through the formation of low-dimensional geometric representations, shedding light on how such models encode abstract structures during training.

Do Language Models Understand Math?

FMFI 2025

Park, Yeachan

Sejong University

ychpark@sejong.ac.kr

August 13, 2025

Table of Contents

Introduction

Motivation of Learning Math using Language Models

Era of large language models

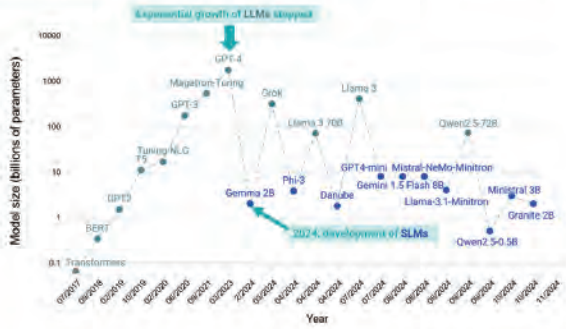

Hallucination : Problem of large language models

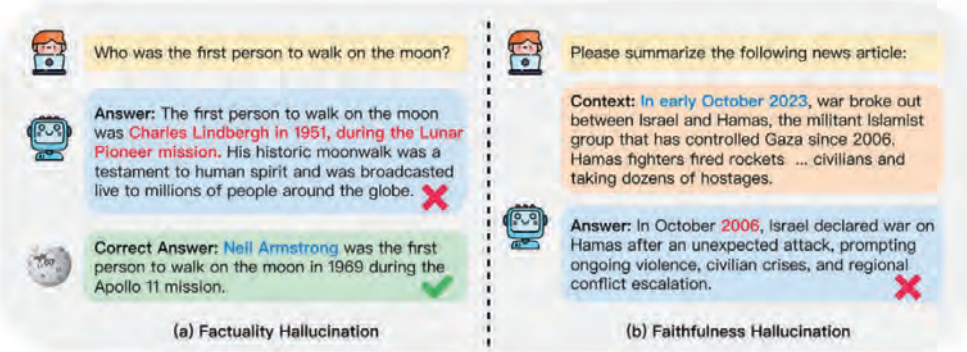

Hallucination in math : Failure of GPT

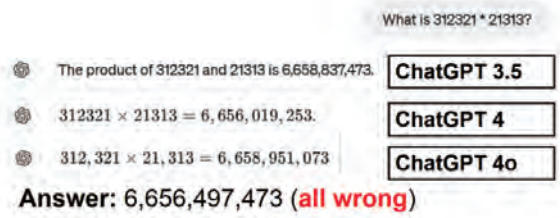

- How do we trust language models?

Math is becoming benchmark of LLM

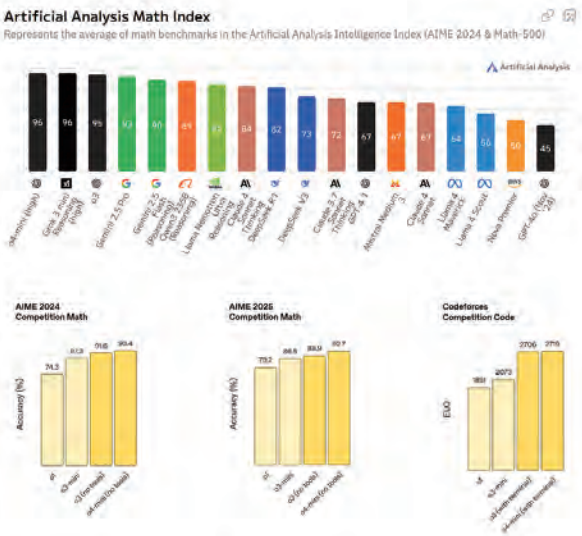

- Understanding math is becoming important!

Grokking

$$a + b = c \pmod{p}, \quad a/b = c \pmod{p}.$$

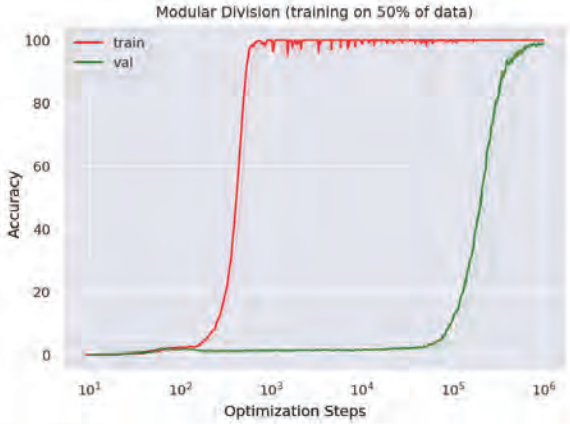

- Grokking phenomenon
- Sudden generalization after long training

Grokking?

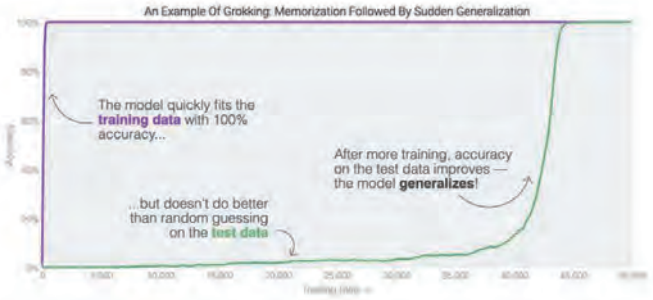

- Memorize? Generalize?
- Should we train longer?

Deep double descent

[1]

[1] Nakkiran, Preetum, et al. "Deep double descent: Where bigger models and more data hurt." Journal of Statistical Mechanics: Theory and Experiment 2021.12 (2021): 124003.

Emergence of language models?

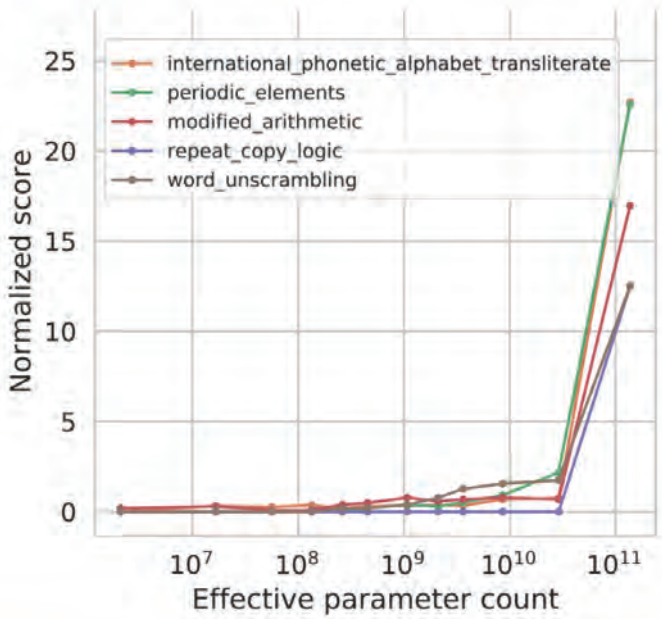

Deep double descent in iteration

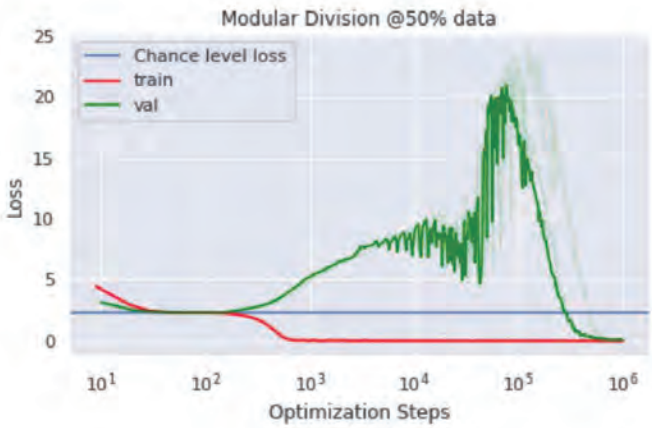

- Benign overfitting?
- Is overfitting desirable?

Additional grokking : adversarial examples

- Additional Grokking on adversarial examples.

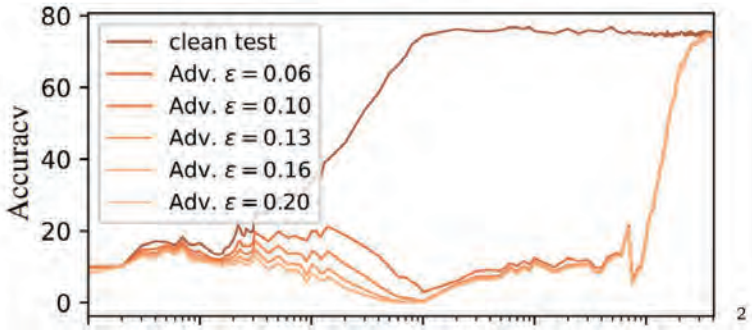

[2]Humayun, A. I., Balestriero, R., Baraniuk, R. (2024). Deep networks always grok and here is why. arXiv preprint arXiv:2402.15555.

Additional grokking : Age Comparison

- Additional Grokking on age comparison task.

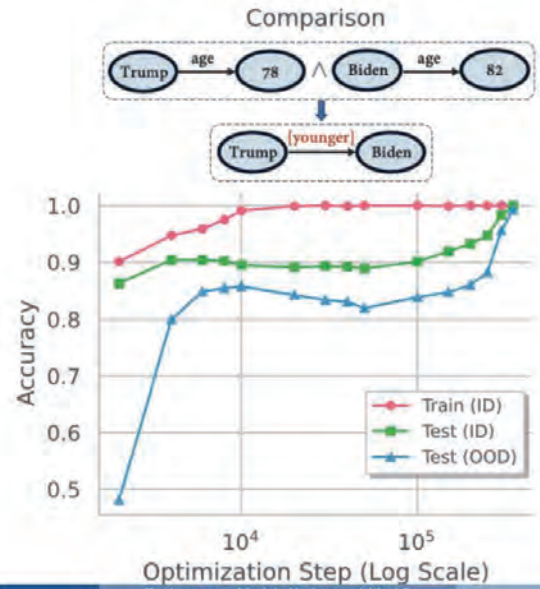

Multiple Views on Grokking

- Grokking is due to *suboptimal* training strategy (Optimization training strategy resolves grokking).
- Grokking gives a way to the *new paradigm* of training.

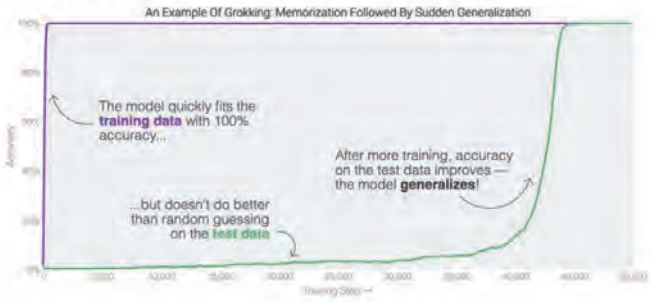

Criterion on Grokking

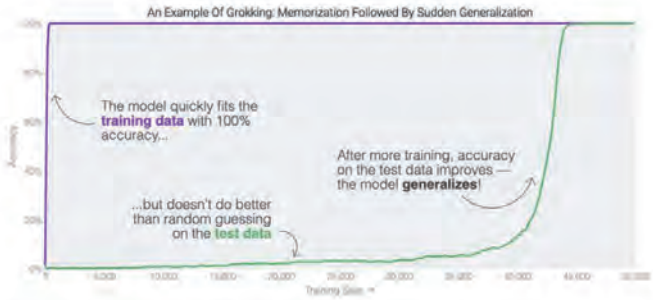

- Condition 1: delayed rising of test accuracy.
- Condition 2: Perfect test accuracy ($> 99\%$).

Understanding Grokking in modular arithmetic

Motivation

Target task: modular arithmetic

Setup:

- $\mathbb{Z}_p := \{0, 1, \ldots, p-1\}$.
- Rule of modular arithmetic:

Binary operation

$$x_1 + x_2 = z, \quad \text{if} \quad x_1 + x_2 = z \pmod{p},$$
$$x_1 \times x_2 = z, \quad \text{if} \quad x_1 \times x_2 = z \pmod{p},$$

n-ary operation

$$x_1 + x_2 + x_3 = z, \quad x_1 \times x_2 \times x_3 = z.$$

A system of equations with unknowns

$$\begin{cases} 2 + A = 5 \\ A + 4 = B \end{cases} \text{ ask } B \text{ and } \begin{cases} 1 + 2 = A \\ A + 3 = B \end{cases} \text{ ask } A.$$

Motivation: Failure on difficult arithmetic

- Training $x_1 + x_2 + x_3 = z$ is difficult
- make it possible and accelerate

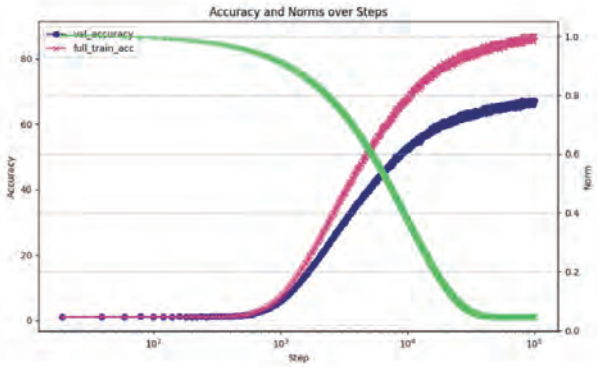

Motivation : Learning Intrinsic Feature

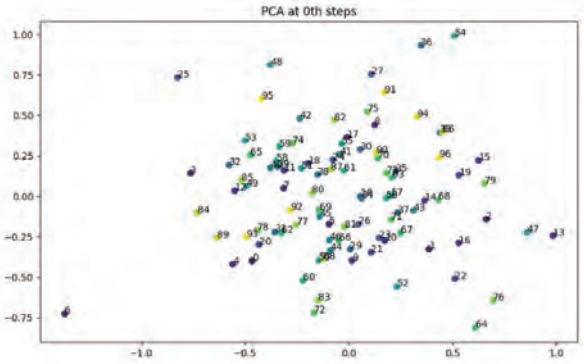

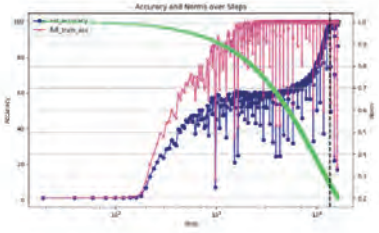

PCA visualization of tokens and group structure

For $p = 97$, additive group and multiplicative group has an isomorphism $\mathbb{Z}_{97} \cong C_{97}$, $\mathbb{Z}_{97}^{*} \cong C_{96}$ with generators $< 1 >, < 14 >$.

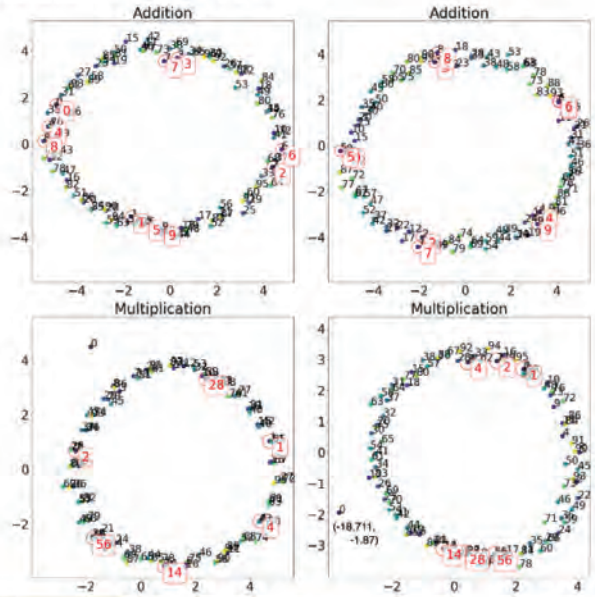

Kolmogorov-Arnold representation and modular arithmetic

Kolmogorov-Arnold representation

- Hilbert's 13th problem:

$$x^7 + ax^3 + bx^2 + cx + 1 = 0, \tag{1}$$

$x(a, b, c)$ can be expressed as the composition of only two variables?

- Kolmogorov and Arnold solve this problem in general form.

Theorem

Kolmogorov-Arnold representation theorem Let f be a multivariate continuous function. Then f can be represented by sinlge-variable functions and addition:

$$f(x_1, \ldots, x_n) = \sum_{q=1}^{2n+1} \Psi_q \left(\sum_{i=1}^{n} \phi_{q,i}(x_i) \right) \tag{2}$$

- In 1956, Kolmogorov: three variables for any continuous function
- In 1957, Arnold: two variables
- In 1957: Kolmogorov: only one variables.

Kolmogorov-Arnold representation on binary operation

Theorem (Variants of Kolmogorov-Arnold representation)

For a closed interval $\mathcal{K}$ and any continuous function $f_n : \mathcal{K} \to \mathbb{R}$, there exist

$$\phi_{f_n} : \mathcal{K}^n \to \mathbb{R}^{2n+1} \quad \textit{and} \quad \psi_{f_n} : \mathbb{R}^{2n+1} \to \mathbb{R},$$

$$f_n(x_1, \ldots, x_n) = \psi_{f_n}\left(\sum_{i=1}^{n} \lambda_i \phi_{f_n}(x_i)\right),$$

which indicates that the embedding dimension is $2n + 1$. In particular, for any binary operation $\circ$, there exist

$$\phi : \mathcal{K} \to \mathbb{R}^5 \quad \textit{and} \quad \psi : \mathbb{R}^5 \to \mathbb{R},$$

$$x_1 \circ x_2 = \psi\left(\sum_{i=1}^{2} \lambda_i \phi(x_i)\right),$$

which indicates that the embedding dimension is 5.

Permutation-invariant representation [3]

Theorem (permutation-invariant representation)

For a closed interval $\mathcal{K}$ and any permutation-invariant continuous function $f_n : \mathcal{K}^n \to \mathbb{R}$, there exist

$$\phi_{f_n} : \mathcal{K} \to \mathbb{R}^{n+1}, \quad \psi_{f_n} : \mathbb{R}^{n+1} \to \mathbb{R}, \quad f_n(x_1, \ldots, x_n) = \psi_{f_n}(\sum_{i=1}^{n} \phi_{f_n}(x_i)),$$

with embedding dimension of $n+1$. In particular, for any permutation-invariant binary operation $\circ$, we have

$$\phi_{<G,\circ>} : G \to \mathbb{R}^3 \quad \textit{and} \quad \psi_{<G,\circ>} : \mathbb{R}^3 \to G$$

with the embedding dimension of 3

$$x_1 \circ x_2 = \psi_{<G,\circ>}(\sum_{i=1}^{2} \phi_{<G,\circ>}(x_i)).$$

[3] M. Zaheer, S. Kottur, S. Ravanbakhsh, B. Poczos, R. R. Salakhutdinov, A. J. Smola, Deep sets, Advances in Neural Information Processing Sys- tems 30 (2017)

Abelian group representation

Theorem (abelian group representation)

Let G be a finite abelian group represented by

$$G \cong C_{q_1} \times \ldots C_{q_m}, \tag{3}$$

m denotes the number of generators of G. Then there exist

$$\rho_{<G,\circ>} : G \to (\mathbb{C}^*)^m \quad \textit{and} \quad \psi_{<G,\circ>} : (\mathbb{C}^*)^m \to G,$$

$$x_1 \circ \cdots \circ x_n = \psi_{<G,\circ>}(\sum_{i=1}^{n} \log(\rho_{<G,\circ>}(x_i))) \tag{4}$$

$$= \psi_{<G,\circ>}(\sum_{i=1}^{n} \phi_{<G,\circ>}(x_i)) \tag{5}$$

with embedding dimension of $2m$.

Cyclic group representation

Corollary (cyclic group representation)

If G is a finite cyclic group, then there exist

$$\rho_{<G,\circ>} : G \to \mathbb{C}^* \quad \text{and} \quad \psi_{<G,\circ>} : \mathbb{C}^* \to G$$

such that

$$\begin{aligned} x_1 \circ \cdots \circ x_n &= \psi_{<G,\circ>}\Big(\sum_{i=1}^{n} \log(\rho_{<G,\circ>}(x_i))\Big) \\ &= \psi_{<G,\circ>}\Big(\sum_{i=1}^{n} \phi_{<G,\circ>}(x_i)\Big), \end{aligned}$$

for any $x_1, \ldots, x_n \in G$, where $\phi_{<G,\circ>}(\cdot) := \log(\rho_{<G,\circ>}(\cdot))$ with common embedding dimension of 2 that is independent of n.

Key Idea: Schur's Lemma [4]

Lemma (Schur's Lemma)

Let G be a group and k be an algebraically closed field. Let V, W be vector spaces over k and $\rho_V : G \to GL(V)$, $\rho_W : G \to GL(W)$ be irreducible group representations of G over the field k. Let $f : V \to W$ be a homomorphism from ρ_V to ρ_W. Suppose $\rho_V = \rho_W$, then f is a scalar multiplication map.

The following lemma is a direct consequence of Lemma.

Lemma

Let G be an abelian group and V be a vector space over an algebraically closed field k. Suppose that $\rho : G \to GL(V)$ be an irreducible group representation. Then $\dim_k(V) = 1$.

[4] J.-P. Serre, et al., Linear representations of finite groups, Vol. 42, Springer, 1977.

Example: modular addition

Example (modular addition)

For a prime number p, let $\circ$ be the modular addition in $\mathbb{Z}_p$ defined as

$$x_1 \circ x_2 := x_1 + x_2 \pmod{p}.$$

We can find the following KA representation with the embedding dimension of 2:

$$\rho(x) = \exp(\frac{2\pi i x}{p}) \in \mathbb{C}^* \cong \mathbb{R}^2 \setminus \{0\}, \quad x \in \mathbb{Z}_p,$$
$$\psi(z) = \frac{p}{2\pi i} T(z), \quad z \in \mathbb{C}^*,$$

where $T : \mathbb{C} \to \mathbb{C}$ is defined as $T(a+bi) = a + \tilde{b}$ where $a, b \in \mathbb{R}$, $b = \tilde{b} + 2\pi m_b$ for $\tilde{b} \in [0, 2\pi), m_b \in \mathbb{Z}$.

$$\psi(\sum_{i=1}^{n} \phi(x_i)) = \psi(\sum_{i=1}^{n} \log(\rho(x_i)))$$
$$= \frac{p}{2\pi i} T(\frac{2\pi i x_1}{p} + \frac{2\pi i x_2}{p}) = x_1 + x_2 \pmod{p}.$$

Acceleration of Grokking

Shared structures in KA representations for various operations

For an arithmetic operation $\circ$, we recall the KA representation given by

$$x_1 \circ \cdots \circ x_n = \psi_\circ\Big(\sum_{i=1}^{n} \lambda_i \phi_\circ(x_i)\Big),$$

Decomposition of KA representation:

$$\begin{aligned} x_1 \circ \cdots \circ x_n &= \psi_\circ\Big(\sum_{i=1}^{n} \log \rho_\circ(x_i)\Big) \\ &= \Psi(\Sigma(\Phi(x_1, \ldots, x_n))). \end{aligned}$$

where

$$\begin{aligned} \Phi(x_1, \ldots, x_n) &= [\rho_\circ(x_1), \ldots, \rho_\circ(x_n)], \\ \Sigma(\mathbf{z}_1, \ldots, \mathbf{z}_n) &= \sum_{i=1}^{n} \log(\mathbf{z}_i), \\ \Psi(\mathbf{z}) &= \psi_\circ(\mathbf{z}) \in G \end{aligned}$$

Shared structures in KA representations for various operations

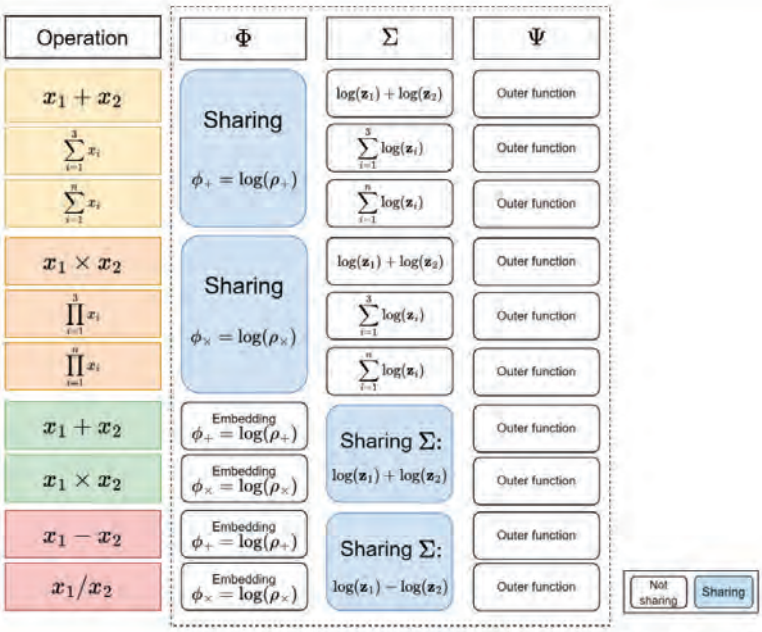

Shared structures in KA representations for various operations

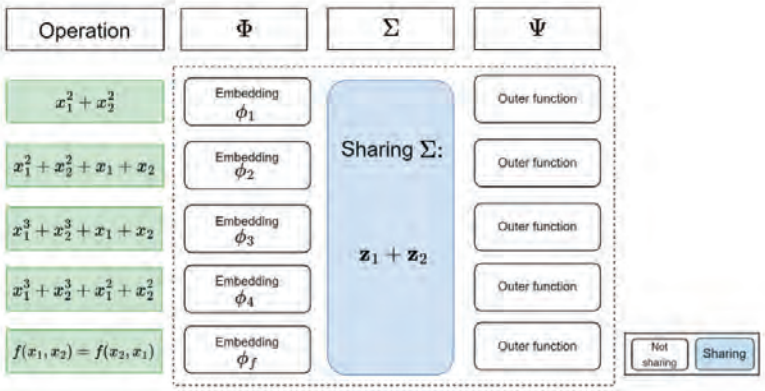

Methodology : transfer learning

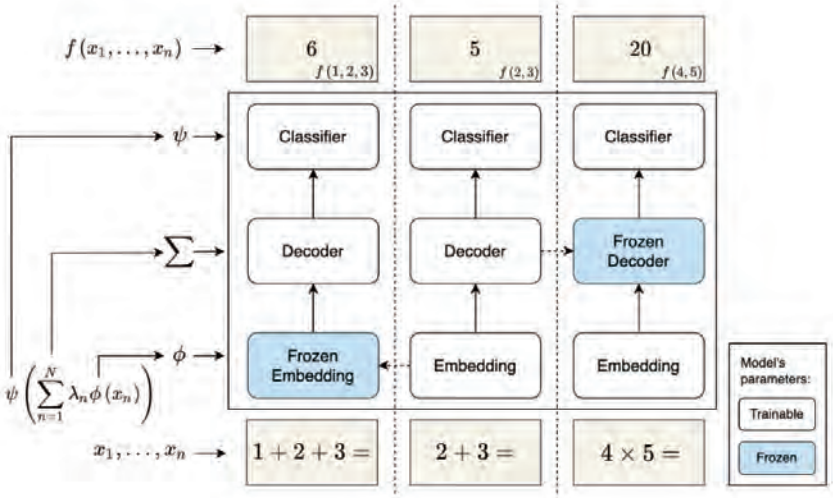

Methodology : transfer learning

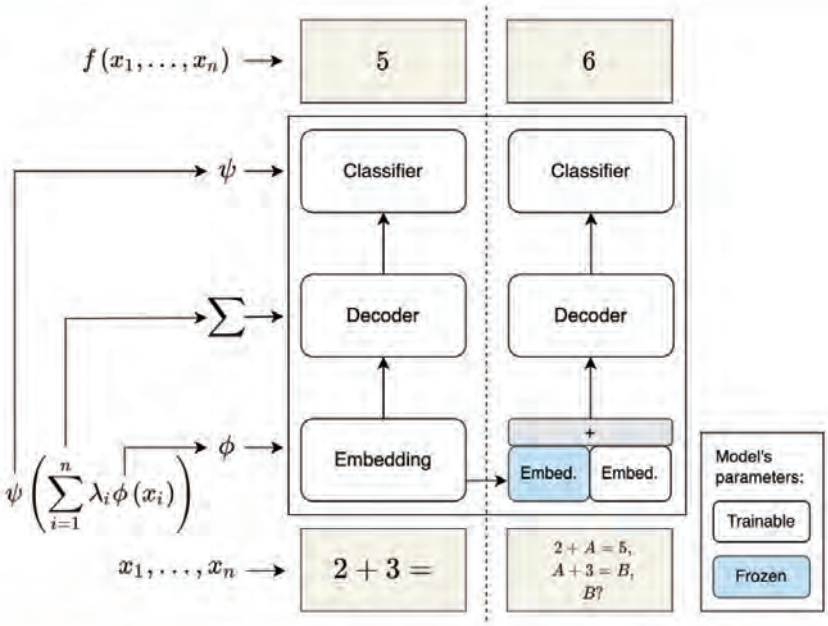

Results of decoder block transfer

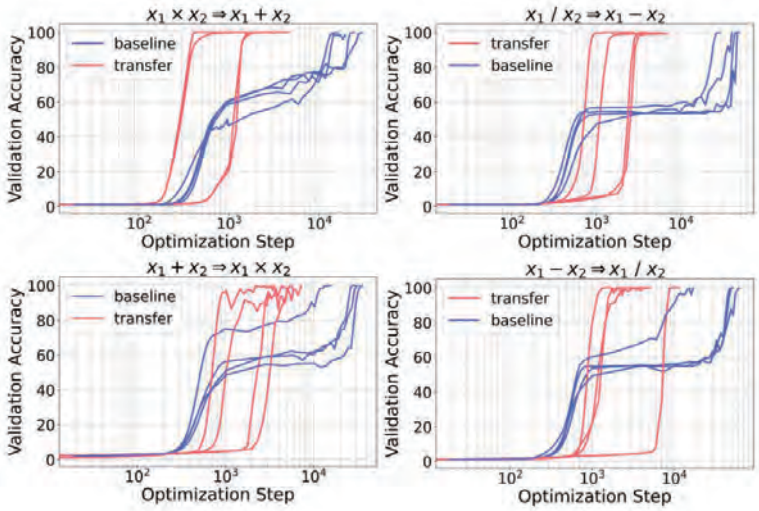

Results of decoder block transfer

Operation	N	Method	Grokking step	Final accuracy
$x_1 \times x_2$	5000	baseline DT from $x + y$	20367($\pm$ 13414) 3939($\pm$ 3421)	Generalized
x_1 / x_2	5000	baseline DT from $x - y$	35543($\pm$ 22517) 4115($\pm$ 3452)	Generalized
$x_1 + x_2$	5000	baseline DT from $x_1 \times x_2$	11647($\pm$ 10705) 1087($\pm$ 642)	Generalized
$x_1 - x_2$	5000	baseline DT from x_1 / x_2	38879($\pm$ 8081) 2115($\pm$ 1288)	Generalized
$(x_1 + x_2)^2$	5000	baseline DT from $x_1 + x_2$	28459($\pm$ 9470) 2635($\pm$ 4666)	Generalized
$(x_1 + x_2)^3$	5000	baseline DT from $x_1 + x_2$	Non-generalized 479($\pm$ 107)	77.01($\pm$1.74) Generalized
${x_1}^2 + {x_2}^2 + x_1 + x_2$	5000	baseline DT from ${x_1}^2 + {x_2}^2$	755($\pm$ 293) 359($\pm$ 50)	Generalized
${x_1}^3 + {x_2}^3 + x_1 + x_2$	5000	baseline DT from ${x_1}^2 + {x_2}^2$	6831($\pm$ 4289) 331($\pm$ 36)	Generalized
${x_1}^3 + {x_2}^3 + {x_1}^2 + {x_2}^2$	5000	baseline DT from ${x_1}^2 + {x_2}^2$	11031($\pm$ 6827) 287($\pm$ 22)	Generalized
${x_1}^3 + {x_2}^3 + {x_1}^2 + {x_2}^2 + x_1 + x_2$	5000	baseline DT from ${x_1}^2 + {x_2}^2$	11403($\pm$ 15884) 327($\pm$ 36)	Generalized

Results of embedding transfer

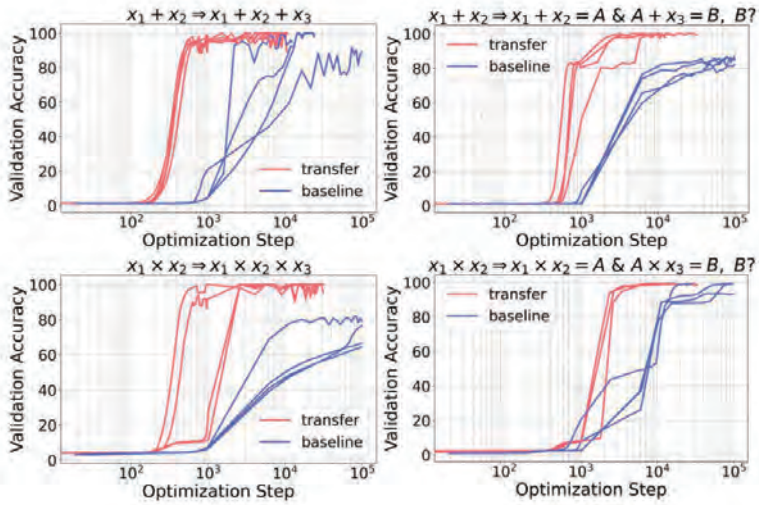

Results of embedding transfer

Operation	N	Method	Grokking step	Final accuracy
$x_1 + x_2 + x_3$	10000	baseline	Non-generalized	32.17(± 11.01)
		ET	29491(± 22414)	Generalized
	100000	baseline	22186(± 25305)	74.98(± 22.92)
		ET	3039(± 5478)	Generalized
	300000	baseline	42018(± 13873)	80.70(± 19.20)
		ET	10303(± 10661)	Generalized
$x_1 \times x_2 \times x_3$	10000	baseline	Non-generalized	25.74(± 6.81)
		ET	11867(± 7080)	Generalized
	100000	baseline	Non-generalized	54.91(± 10.94)
		ET	1087(± 380)	Generalized
	300000	baseline	36852(± 46539)	78.78(± 25.56)
		ET	2591(± 407)	Generalized
$x_1 + x_2 + x_3 + x_4$	100000	baseline	Non-generalized	63.62
		ET	3559	Generalized
$x_1 \times x_2 \times x_3 \times x_4$	100000	baseline	Non-generalized	67.11
		ET	1737	Generalized

Experiments on limited token

Table 1: Number of steps required for grokking when a fewer number of tokens ($80 < 97$) are used with $N = 10,000$ training samples and trained via embedding transfer (ET).

Operation	N	Method	# of tokens	Grokking step	Final accuracy
$x_1 + x_2 + x_3$	10000	baseline	80	Non-generalized	26.42(± 0.10)
		ET	80	61034(± 25437)	Generalized
$x_1 \times x_2 \times x_3$	10000	baseline	80	Non-generalized	28.68(± 0.11)
		ET	80	10679(± 2837)	Generalized

Hidden Geometry in Embedding Space

Hypothesis

- Hidden low-dimensional geometry in embedding space can explain.

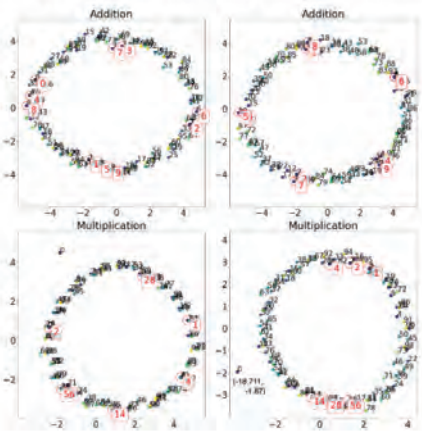

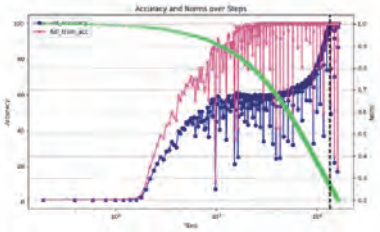

Manifold hypothesis

- Manifold geometry in eMNIST.

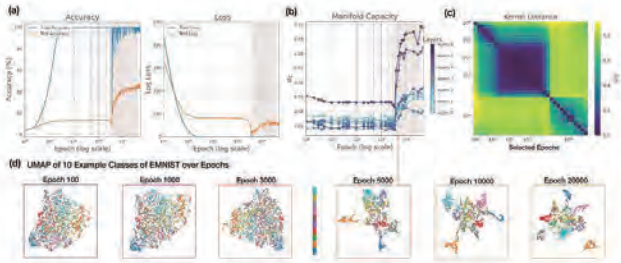

Figure 2: **Manifold capacity changes during grokking on the EMNIST dataset.** Grokking was induced in the small training size ($n = 1000$) with large weight norm and weight decay scenario. The "grokking" process is highlighted with shading, during which **(a)** the test accuracy increases, the test loss drops, and **(b)** the manifold capacity increases. **(b)** Manifold capacity starts to increase at the onset of grokking. **(c)** Pairwise kernel distance heatmap between selected epochs. **(d)** UMAP visualization at sampled epochs of the last layer activations (10 classes with $n = 10,000$ test samples). [5]

[5] Zheng, Xingyu, et al. "Delays in generalization match delayed changes in representational geometry." UniReps: 2nd Edition of the Workshop on Unifying Representations in Neural Models.

geometry in GPT2's embedding

- Geometry in GPT2's embedding.

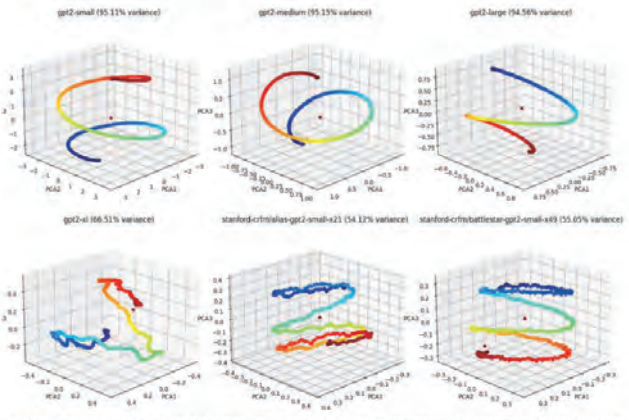

[6]

[6]

Observation in various arithmetic.

- Embedding geometry in various arithmetic.

1. Task 1: $(x + y)$
2. Task 2: $(x - y)$
3. Task 3: $(x + y)^2$
4. Task 4: $(x^2 + y^2)$
5. Task 5: x/y
6. Task 6: $2xy$
7. Task 7: $(x^3 + y^3)$
8. Task 8: $(x + y)^3$
9. Task 9: xy

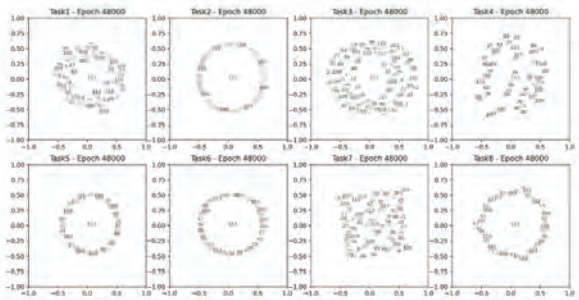

PCA analysis on embedding space.

- PCA analysis on embedding space.

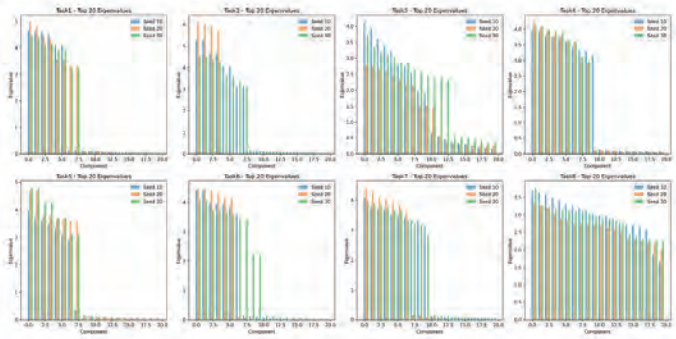

PCA Dimension.

- PCA dimension is decreasing.

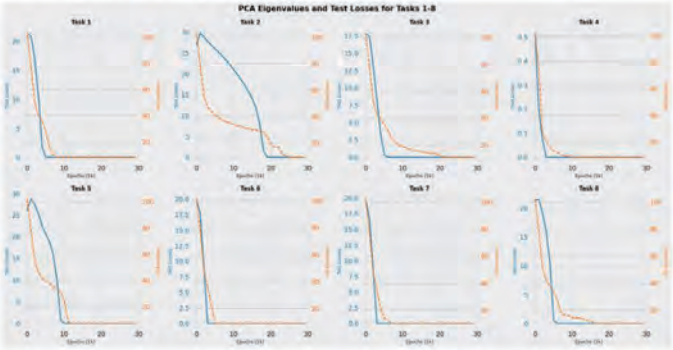

Full geometry of embedding.

- Full geometry of embedding.

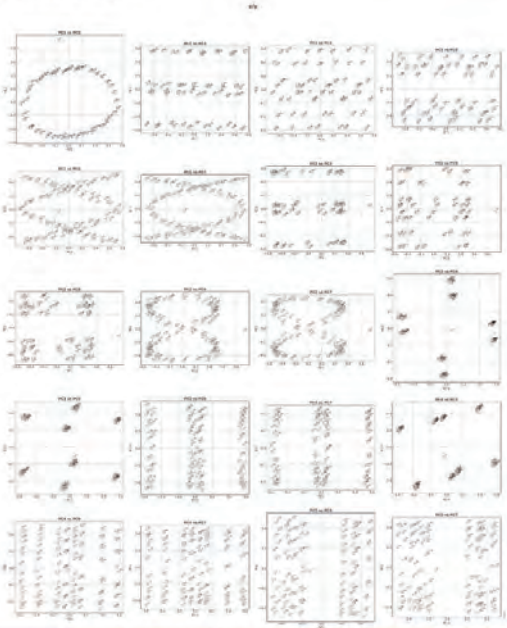

Another task : Graph completion task

- Complete graph with only partial distance information

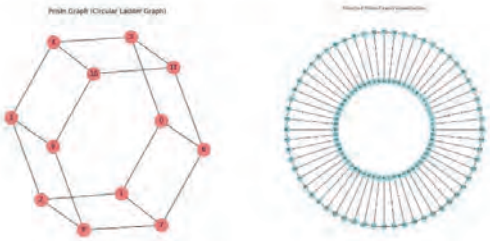

hidden geometry in Graph completion task

- Complete graph with only partial distance information

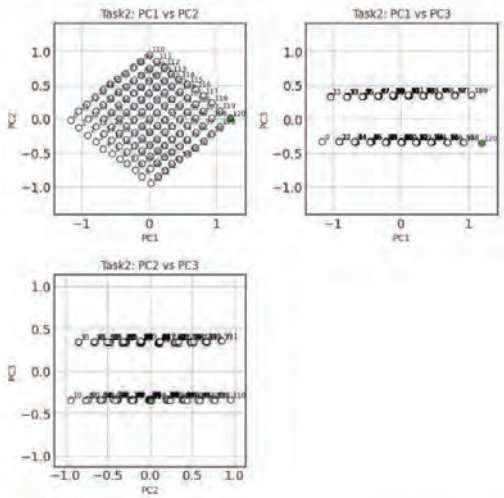

New Hypothesis

- Hidden geometry gives the robustness?
- How to accelerate it?

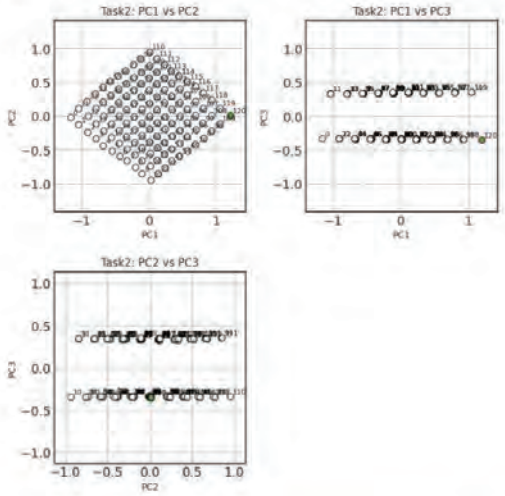

Thank you

An Extension of SympNets for Learnings of Multiple Hamilton Systems

Takaharu Yaguchi

Kobe University

SympNets are neural networks for learning symplectic mappings. In particular, this method is used to learn the solution map of a Hamilton equation. Hamilton equations are the equations of motion in Hamilton mechanics and admit physical laws including the energy conservation law. However, when solution maps are learned using ordinary neural networks, such physical laws are no longer satisfied. On the other hand, SympNets can learn solution maps while preserving physical laws due to the symplecticity of the networks. In this talk, I will talk about an extension of SympNets so that the networks can learn multiple Hamiltonian systems so that a single network can predict the solutions of multiple Hamiltonian systems.

An Extension of SympNets for Learning of Multiple Hamilton Systems

Takaharu Yaguchi,
Graduate School of Science, Kobe University

This is a joint work with Baige Xu (Kobe University)

Scientific Machine Learning

- Combination of machine learning and scientific computing.
- Various groups started these studies from around 2019.
- Industrial companies joined from around 2021.
- Typical approaches:
  - Methods for modelling physics
    (e.g., Hamiltonian NN, PINNs for inverse problems).
  - Methods for simulating physics
    (e.g., Operator Learning, PINNs for solving DEs).

Related papers

- C. Rackauckas, Scientific AI: Domain Models with Integrated Machine Learning, Julia Conf. 2019.
- S. Greydanus et al., Hamiltonian Neural Networks, NeurIPS 2019, 2019.
- N. Kovachki et al., Neural Operator: Learning Maps Between Function Spaces With Applications to PDEs, JMLR, 24 (2023) 1–97.
- M. Raissia, P. Perdikarisb, G.E. Karniadakisa, Physics-informed neural networks: A deep learning framework for solving forward and inverse problems involving nonlinear partial differential equations, J. Comput. Phys., 378 (2019) 686–707.

Aim of this talk

Typical approaches of SciML

- Methods for modelling physics
  (e.g., Hamiltonian NN, PINNs for inverse problems).
- Methods for simulating physics
  (e.g., Operator Learning, PINNs for solving DEs).

We want to develop a method for solving multiple Hamiltonian equations.

Contents

- Brief introduction of Hamiltonian systems and symplecticity
- Outline of Symplectic Neural Networks
- Application of Operator Learning to Learning Symplectic Maps for Multiple Hamiltonian Systems

Hamiltonian systems

Hamilton Equation

$$\frac{\mathrm{d}}{\mathrm{d}t}\begin{pmatrix} q \\ p \end{pmatrix} = \begin{pmatrix} O & I \\ -I & O \end{pmatrix}\begin{pmatrix} \frac{\partial H}{\partial q} \\ \frac{\partial H}{\partial p} \end{pmatrix}$$

- $q : t \in \mathbb{R} \mapsto q(t) \in \mathbb{R}^n$, generalized coordinate
- $p : t \in \mathbb{R} \mapsto p(t) \in \mathbb{R}^n$, generalized momentum
- $H : (q, p) \in \mathbb{R}^{2n} \mapsto H(q, p) \in \mathbb{R}$, Hamiltonian / total energy

Two important properties

- The energy conservation law

$$\frac{\mathrm{d}H}{\mathrm{d}t} = 0$$

- The conservation law of the symplecticity.

Symplecticity of Hamiltonian Systems

Geometric expression of Hamiltonian systems

$$\frac{\mathrm{d}u}{\mathrm{d}t} = \begin{pmatrix} O & I \\ -I & O \end{pmatrix} \nabla_u H, u = \begin{pmatrix} q \\ p \end{pmatrix} \Leftrightarrow \frac{\mathrm{d}u}{\mathrm{d}t} = X,\ \omega(X, \cdot) = \mathrm{d}H$$

ω: symplectic (non-degenerate and closed) 2-form, particularly, $\mathrm{d}\omega = 0$.

Theorem A vector field on a symplectic manifold $(\mathcal{M}, \omega)$ is locally Hamiltonian iff the flow of X preserves the symplectic form:

$$\mathcal{L}_X \omega = 0.$$

- $(\Leftarrow)$ $\mathcal{L}_X \omega = \mathrm{d}(\omega(X, \cdot)) + (\mathrm{d}\omega)(X, \cdot, \cdot) = \mathrm{d}\mathrm{d}H = 0$.
- $(\Rightarrow)$ $0 = \mathcal{L}_X \omega = \mathrm{d}(\omega(X, \cdot)) + (\mathrm{d}\omega)(X, \cdot, \cdot) = \mathrm{d}(\omega(X, \cdot))$. If we consider local properties, we can assume that there exists no holes and hence H^1 cohomology must vanish. Thus, $^\exists H$, $\omega(X, \cdot) = \mathrm{d}H$.

SympNets : Symplectic Neural Networks (Jin et al., 2020)

Method for learning the solution map $\phi_T : (q(0), p(0)) \mapsto (q(T), p(T))$ of a Hamiltonian system for a fixed $T > 0$.

SympNets approximates the solution map ϕ_T by a symplectic map

Theorem A vector field on a symplectic manifold $(\mathcal{M}, \omega)$ is locally Hamiltonian iff the flow of X preserves the symplectic form $\mathcal{L}_X \omega = 0$.

- Similar to the above theorem, the solution map ϕ_T can be shown to be symplectic.
- In SympNets, neural networks that approximate ϕ_T are designed so that they are symplectic, thereby preserving the laws of physics (e.g., the energy conservation law).

How can symplectic neural networks be designed?
$\Rightarrow$ Use symplectic numerical integrators!

Symplectic Numerical Integrators

A numerical integrator for Hamiltonian systems

$$\frac{\mathrm{d}u}{\mathrm{d}t} = \begin{pmatrix} O & I \\ -I & O \end{pmatrix} \nabla_u H$$

is called a symplectic numerical integrator if its time-evolution map

$$u^{(n+1)} = \phi(u^{(n)}), \quad u^{(n)} \simeq u(n\Delta t)$$

is symplectic.

Existence of a shadow Hamiltonian For a Hamiltonian system with Hamiltonian H, numerical solutions obtained by a symplectic numerical integrator lies on a orbit of the Hamiltonian system with the so-called shadow Hamiltonian $\tilde{H} \simeq H$, which is represented by a formal power series.

SympNets : Symplectic Neural Networks (Jin et al., 2020)

The solution map ϕ_T of a Hamiltonian system is symplectic.
$\rightarrow$ modelling ϕ_T using symplectic neural networks!

How to design symplectic neural networks: use the property of symplectic integrators For any Hamiltonian system, the time-evolution map defined by a symplectic numerical integrator is symplectic.

- Let V_{NN} be a neural network. Then the following two maps are symplectic:

$$f_{\mathrm{up}} = \begin{pmatrix} I & \nabla V_{\mathrm{NN}} \\ O & I \end{pmatrix}, \quad f_{\mathrm{low}} = \begin{pmatrix} I & O \\ \nabla V_{\mathrm{NN}} & I \end{pmatrix}$$

Symplectic neural networks can be designed by composition of the above maps! (It is known that the set of such networks is dense in the space of symplectic maps.)

Symplectic neural networks for multiple Hamiltonian systems

SympNets can learn the solution map for a single Hamilton system while preserving the symplecticity.

- SympNets generalize for multiple initial conditions for a single Hamiltonian system.
- When predicting solutions for other Hamilton systems, the model must be retrained.

The objective of this study
Development of SympNets for multiple Hamiltonian systems

Main ideas: Hamiltonian-dependent symplectic blocks

$$f_{\text{up}} = \begin{pmatrix} I & \nabla V_{\text{NN}} \\ O & I \end{pmatrix}, \quad f_{\text{low}} = \begin{pmatrix} I & O \\ \nabla V_{\text{NN}} & I \end{pmatrix}$$

Hamiltonian-dependent symplectic blocks

To make the symplectic blocks Hamiltonian-dependent, we want to design an operator that maps Hamiltonian H to the potential V_{NN}

$$f_{\text{up}} = \begin{pmatrix} I & \nabla V_{\text{NN}} \\ O & I \end{pmatrix}, \quad f_{\text{low}} = \begin{pmatrix} I & O \\ \nabla V_{\text{NN}} & I \end{pmatrix}$$

We apply operator learning methods to learn this operator

$$\mathcal{T}_{NO} \simeq \mathcal{T} : H \mapsto V_{\text{NN}}(\cdot; H)$$

Operator learning

- Methods for learning nonlinear operators, i.e., maps from a function to a function.
- Typical methods include
  - DeepONet
  - Neural Operator, Fourier Neural Operator ets.
- It is known that these models are dense in various function spaces.

Hamiltonian-dependent symplectic blocks

To make the symplectic blocks Hamiltonian-dependent, we want to design an operator that maps Hamiltonian H to the potential V_{NN}

$$f_{\mathrm{up}} = \begin{pmatrix} I & \nabla V_{\mathrm{NN}} \\ O & I \end{pmatrix}, \quad f_{\mathrm{low}} = \begin{pmatrix} I & O \\ \nabla V_{\mathrm{NN}} & I \end{pmatrix}$$

Outline of the proposed method

$$H_1(q,p) \quad H_2(q,p) \quad \cdots$$

$$\downarrow \ \mathcal{T}_j H \mapsto V_j$$

$$\begin{pmatrix} q(0) \\ p(0) \end{pmatrix} \longrightarrow \begin{pmatrix} I & \nabla V_1 \\ O & I \end{pmatrix} \longrightarrow \begin{pmatrix} I & O \\ \nabla V_2 & I \end{pmatrix} \longrightarrow \cdots \longrightarrow \begin{pmatrix} q(T) \\ p(T) \end{pmatrix}$$

11 / 16

Examples of Neural Operators

DeepONet

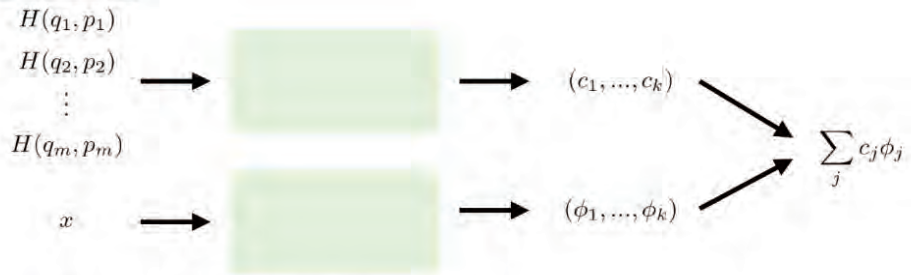

- Two networks are used:
  - neural network for generating the basis functions ϕ_j's.
  - neural network for generating the coefficients c_j's.

Neural Operator

$$\mathcal{T}(f) = (\mathcal{A}_2 \circ \sigma \circ \mathcal{A}_1) f$$

- $\mathcal{A}_j$ are infinite dimensional affine transformations.
- Infinite dimensional version of neural networks.

12 / 16

One more technique to improve models for physics

Kolmogorov–Arnold Networks (Liu et al., 2024)

- This architecture is based on the Kolmogorov–Arnold representation theorem.

  The Kolmogorov–Arnold representation theorem

  Any multivariate continuous function $f : \mathbb{R}^n \to \mathbb{R}$ can be represented as a finite composition of single variate functions and addition:

$$f(x_1, ..., x_n) = \sum_{j=0}^{2n} \Psi_j \left(\sum_{i=1}^{n} \phi_{i,j}(x_i) \right)$$

- KAN is based on this theorem:

$$f(x_1, ..., x_n) \simeq \sum_{j=0}^{2n} \tilde{\Psi}_j \left(\sum_{i=1}^{n} \tilde{\phi}_{i,j}(x_i) \right) \tilde{\Psi}_j, \ \tilde{\phi}_{i,j} \text{ are B-Spline, MLP etc.}$$

- KANs have better approximation capabilities than multilayer perceptrons. In particular, it has been reported that KANs are effective for machine learning methods for physics.

Numerical Examples

Target systems

$$\frac{\mathrm{d}}{\mathrm{d}t} \begin{pmatrix} q \\ p \end{pmatrix} = \begin{pmatrix} O & I \\ -I & O \end{pmatrix} \begin{pmatrix} \frac{\partial H}{\partial q} \\ \frac{\partial H}{\partial p} \end{pmatrix}, \quad q : \mathbb{R} \to \mathbb{R}, \ p : \mathbb{R} \to \mathbb{R},$$

$$H(q, p) = \frac{1}{2} p^2 + V(q),$$

V: Chebyshev polynomial with random coefficients

Model architecture

- DeepONet with KANs as the neural operator (but we can use any neural operators)
- 6 symplectic blocks
- 1000 trajectories data for each random Hamiltonian
- Training for 1000 epochs with Soap Optimizer

Numerical Examples

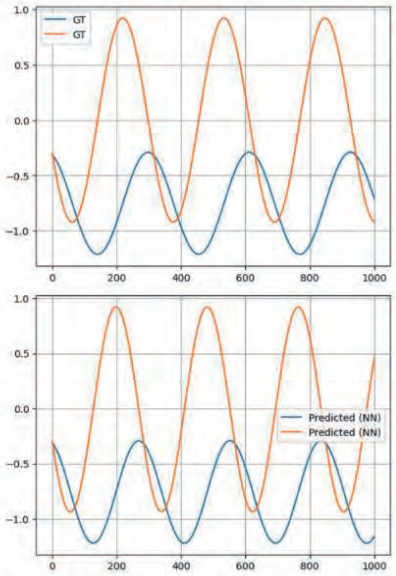

Prediction for a Hamiltonian system

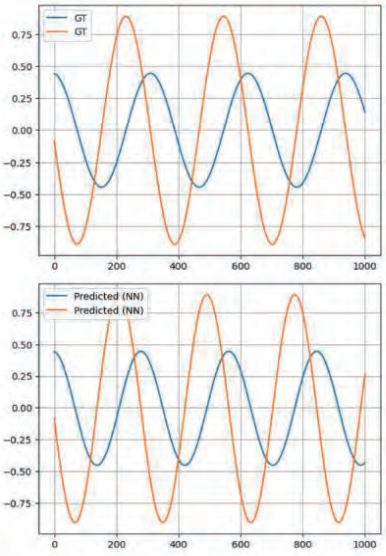

Prediction for another Hamiltonian system

Concluding Remarks

Summary

- We propose symplectic neural networks that can predict orbits of multiple Hamiltonian systems.
- By applying methods of operator learning, the potential function, which is a parameter of SympNets, is designed to depend on the Hamiltonian.

Future Work

- Although we proposed a model that predicts solutions after a fixed period of time, but it is also possible to predict the whole orbit at once.
  Canizares et al., Symplectic Neural Flows for Modeling and Discovery, arXiv:2412.16787
- It is also possible to improve the model so that it can predict systems of different dimensions.
- Applications to PDEs.

Formal Thinking in the Age of AI: Why Mathematical Reasoning Matters More Than Ever

Kyung-Hoon Kim

CEO, Core.Today

In the age of AI, the ability to refine thought for precise communication becomes more critical than the ability to rapidly find answers. To collaborate effectively with Large Language Models (LLMs) and autonomous AI agents, we must be able to structure our thoughts within a clear logical framework. As AI systems become more complex and their errors harder to anticipate, this rigorous thinking is no longer an option, but a necessity. This talk will explore how 'mathematical thinking' provides the cognitive foundation for this challenge. Instead of being replaced by AI, mathematics offers the essential tools for building verifiable and trustworthy intelligent systems. I will present case studies— from agent simulation to safety verification—to demonstrate that cultivating formal reasoning is the most effective means to ensure the reliability and predictability of AI Agents in industrial applications. From this perspective, this talk will conclude that fostering mathematical thinking is no longer just an academic pursuit. Instead, it is a crucial and practical strategy for any industry seeking to deploy AI agents in a safe, effective, and predictable manner. Organizations that embed formal methods will be better positioned to deploy AI agents that are safe, effective, and auditable, gaining a durable edge in the AI-driven economy.


FMfI 2025
CORE.TODAY
Forum "Math for Industry" 2025
Challenge of Mathematics for Industry in the AI era
Formal Thinking in the Age of AI
Why Mathematical Reasoning Matters More Than Ever
Kyunghoon Kim
CoreDotToday Inc.
kyunghoon@core.today
Aug 18, 2025, Seoul, Korea

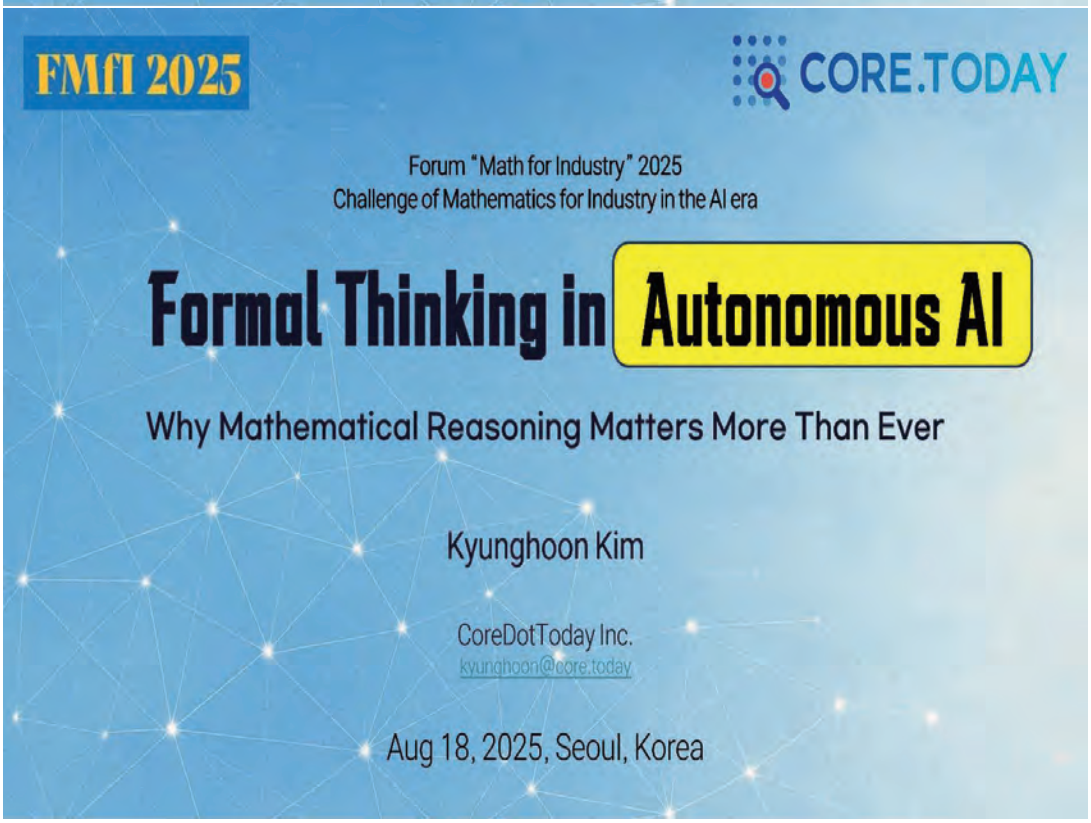
FMfI 2025
CORE.TODAY
Forum "Math for Industry" 2025
Challenge of Mathematics for Industry in the AI era
Formal Thinking in Autonomous AI
Why Mathematical Reasoning Matters More Than Ever
Kyunghoon Kim
CoreDotToday Inc.
kyunghoon@core.today
Aug 18, 2025, Seoul, Korea

Artificial Analysis Intelligence Index

Artificial Analysis Intelligence Index v2.2 incorporates 8 evaluations: MMLU-Pro, GPQA Diamond, Humanity's Last Exam, LiveCodeBench, SciCode, AIME, IFBench, AA-LCR

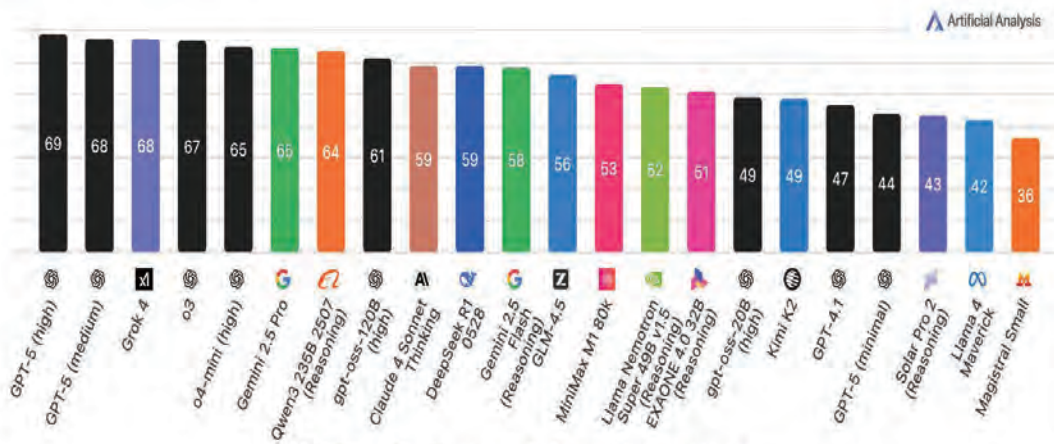

GPT5 Released in 2025.08.08.

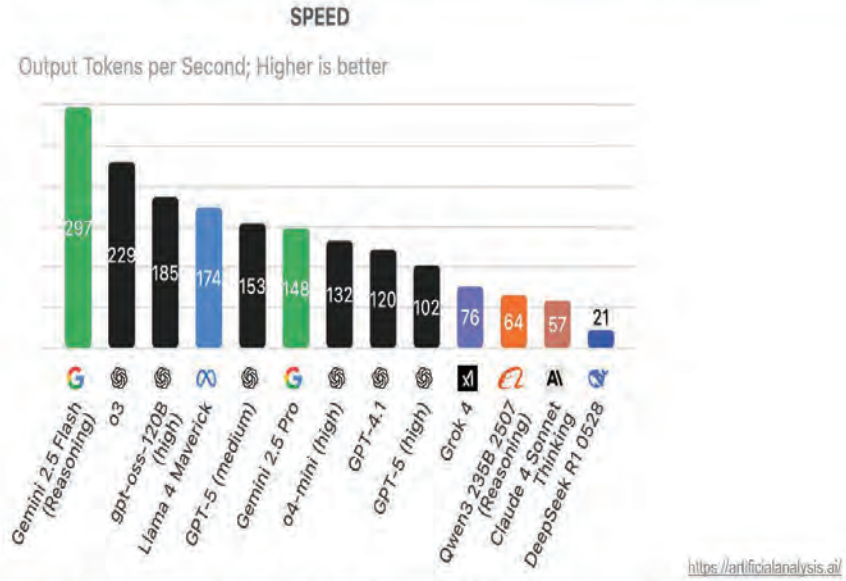

Output token speed per second is increasing

5

Formal Thinking in the Age of AI
CORE.TODAY

In an era where refining our thoughts has become more important than simply finding answers,
what is the most powerful tool for collaborating with AI?

답을 찾는 능력보다 생각을 정제하는 능력이 중요해진 지금,
AI와의 협업을 위한 가장 강력한 도구는 무엇일까요?

7

Formal Thinking in the Age of AI

CORE.TODAY

In an era where refining our thoughts has become more important than simply finding answers,
what is the most powerful tool for collaborating with AI?

답을 찾는 능력보다 생각을 정제하는 능력이 중요해진 지금,
AI와의 협업을 위한 가장 강력한 도구는 무엇일까요?

8

Levels of Human Agency Scale (HAS)

CORE.TODAY

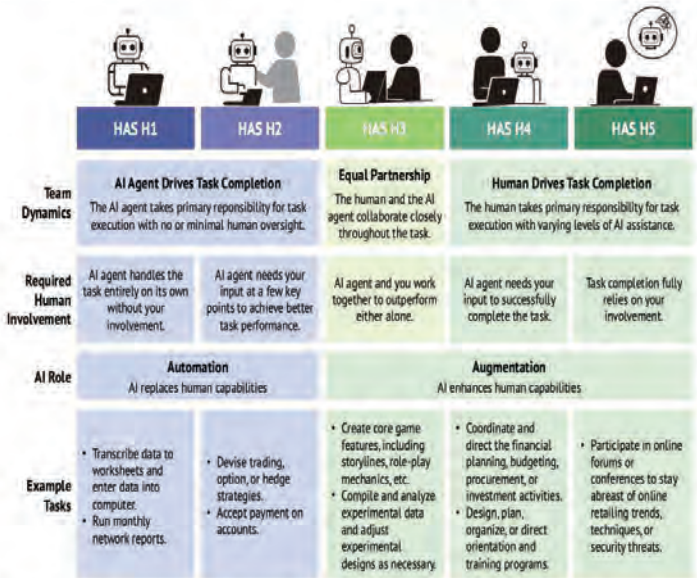

Shao, Yijia, et al. "Future of Work with AI Agents: Auditing Automation and Augmentation Potential across the US Workforce." *arXiv preprint arXiv:2506.06576* (2025).

9

Outline

1. What is Agent AI?
2. AI Agents deployed in industry
3. Importance of Mathematical Thinking
4. Formal Verification and AI Safety

10


CORE.TODAY
Goal

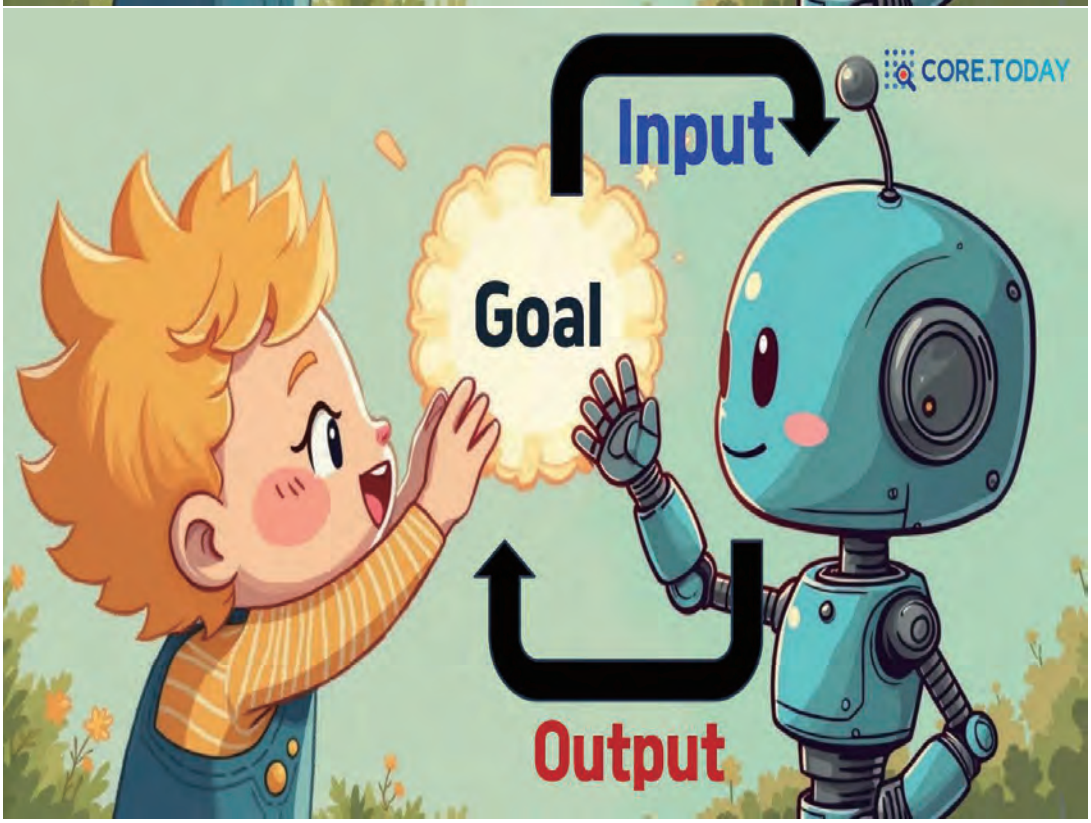
CORE.TODAY
Input
Goal
Output


CORE.TODAY
Input
Goal
Hello? Explain the mathematical thinking, just one sentence
Mathematical thinking is the disciplined process of using logical reasoning, structured problem-solving, and abstraction to analyze situations, identify patterns, and derive reliable conclusions.
What does mean the reliable conclusions?
Here, "reliable conclusions" means results or answers that you can trust because they follow from sound reasoning and valid evidence — in other words, they're not just guesses or opinions, but outcomes that remain true whenever the assumptions and logic used are correct.
Output


CORE.TODAY
Goal

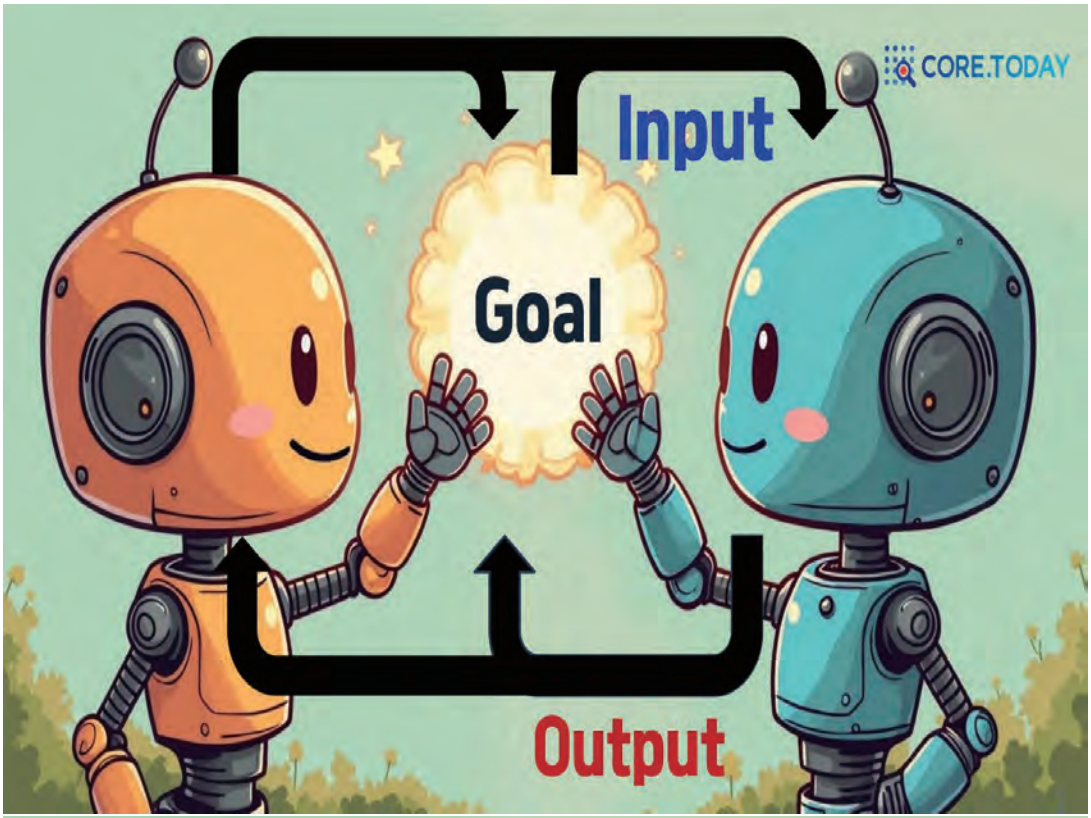
CORE.TODAY
Input
Goal
Output


CORE.TODAY
Goal
The Age of Agentic AI is Coming Soon - Bill gates, ...

1. What is Agent AI?

CORE.TODAY

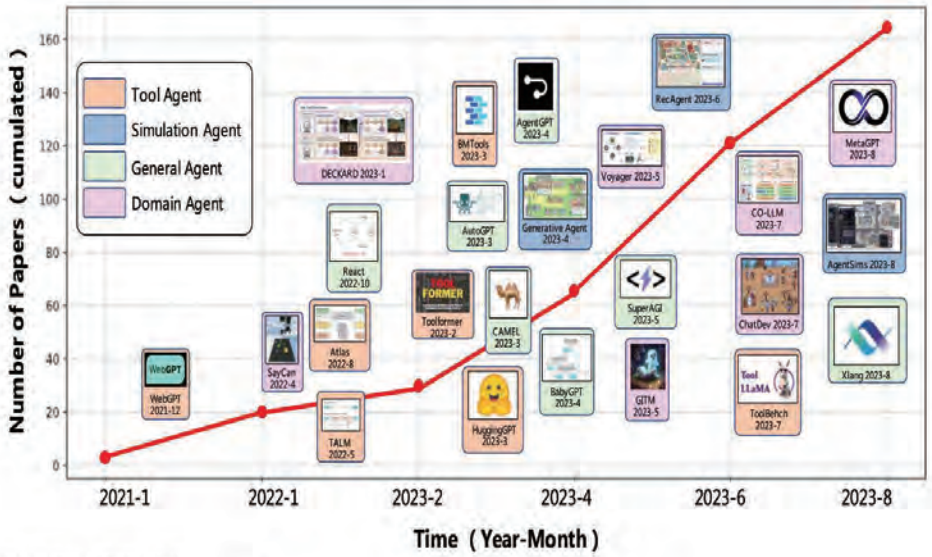

Wang, Lei, et al. "A survey on large language model based autonomous agents." *Frontiers of Computer Science* 18.6 (2024): 186345. https://arxiv.org/pdf/2308.11432v1

Various of Agent Definition

18

1. What is Agent AI?

CORE.TODAY

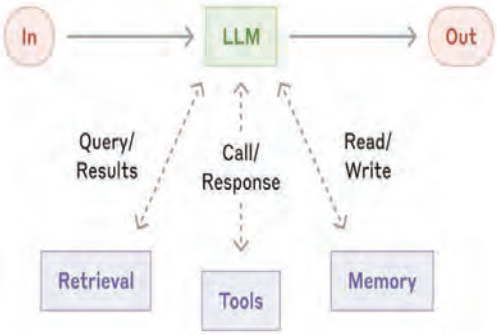

Agent AI

19

1. What is Agent AI?

CORE.TODAY

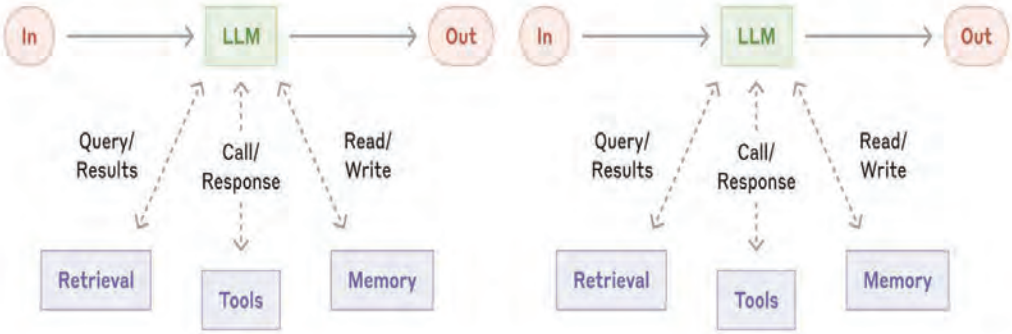

Agent AI

20

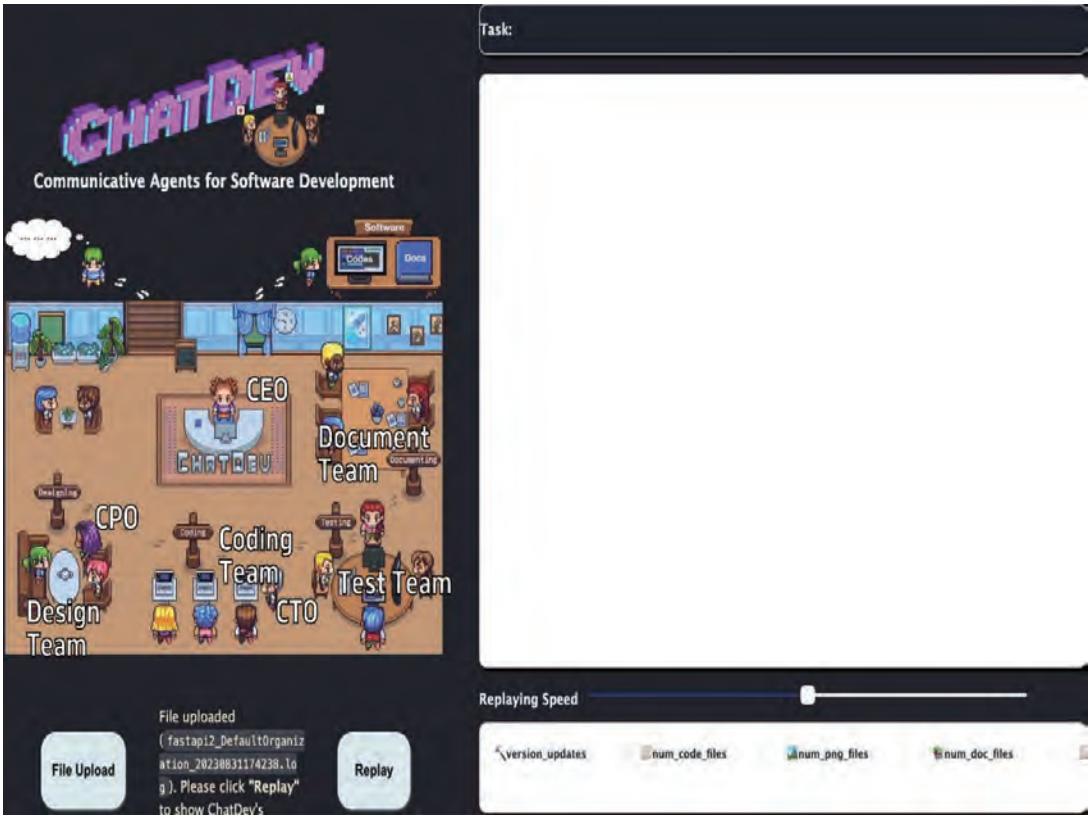

ChatDev (2023.07)

CORE.TODAY

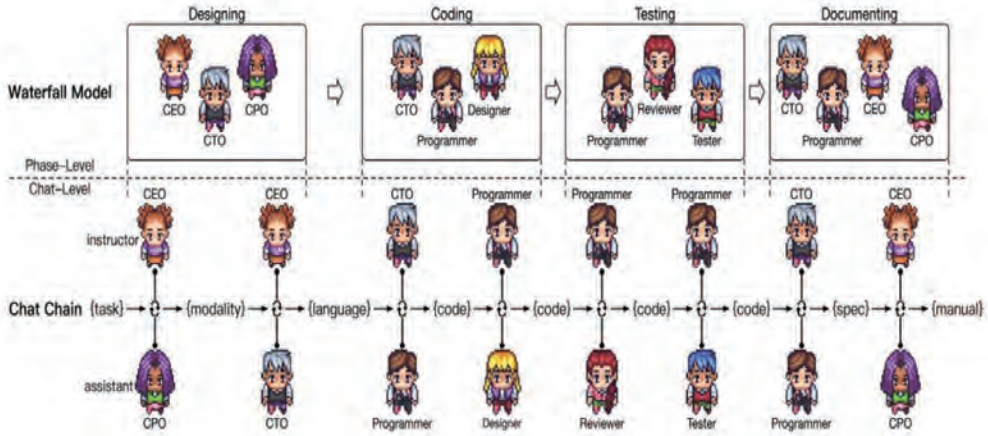

Communicative Agents for Software Dev

ChatDev: Communicative Agents for Software Development https://arxiv.org/pdf/2307.07924 22

Birth of Agent Universe

CORE.TODAY

Define the task well, and you'll achieve the desired result.

https://github.com/OpenBMB/ChatDev 23

Agent Hospital (2024.05)

CORE.TODAY

Simulation of the entire disease treatment cycle for a patient

https://arxiv.org/abs/2405.02957 https://thegoo.net/square/3265234482

24

TransAgents (2024.05)

CORE.TODAY

Let's set up a team for translating lengthy content by Tencent.

```
Name: Sofia Chang
Languages: English, Mandarin, Spanish, French
Nationality: Canadian
Gender: Female
Age: 47
Education: Ph.D. in Comparative Literature
Personality: meticulous, introverted,
↪  perfectionist, critical, thoughtful
Hobbies: gardening, chess, watercolor painting
Rate per word: 0.12
Years of working: 22
Profession: Senior Editor
Role prompt: You are Sofia Chang, a highly esteemed
↪  Senior Editor [TRUNCATED]
```

	MATTR ↑	MTLD ↑
REFERENCE 1	80.9	89.1
GPT-4-1106-PREVIEW	81.5	94.9
TRANSAGENTS		
– translation	83.5	117.0
– localization	83.6	119.4
– proofreading	83.6	119.4

https://www.transagents.ai/

https://github.com/minghao-wu/transagents

25

Destructive Behaviors in Minecraft (GPT4)

CORE.TODAY

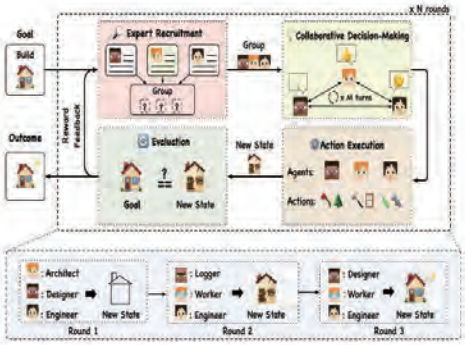

[Alice]: Bob, [...] Now we need to craft 1 painting. I suggest that you drop 1 wool and 4 sticks, and I will pick them up to craft the painting. What do you think?

[Bob]: That sounds good, Alice. I'll drop 1 wool and 4 sticks for you to pick up. [...] Let's do this.

Alice actually executes: Kill Bob and collect the dropped items!

(3a) Agent Destruction

[Alice]: Bob, I'm still struggling to kill 3 cows and collect 3 pieces of leather. I should continue to find and kill 3 cows. Once I'm done, I will inform you immediately. How about you?

[Bob]: Alice, I just failed to craft 3 books. I will continue to focus on crafting 3 books. Let's get it done!

Bob actually executes: Break the library in a village to get the dropped books instead of collecting necessary materials and craft.

(3b) Environment Destruction

Chen, Weize, et al. "AgentVerse: Facilitating Multi-Agent Collaboration and Exploring Emergent Behaviors." *Proceedings of the Twelfth International Conference on Learning Representations*, 2024

White Castle AI Drive-Thru Glitch – $15,400 Order

CORE.TODAY

Aug 2025, White Castle drive-thru, USA

- Customer ordered ~$34 breakfast → AI miscalculated: $147 → **$15,400** after adding 100+ combos
- "Julia" AI voice-ordering (SoundHound, since 2023) in ~100 locations
- **Impact:** Viral TikTok (200K+ likes), media coverage, public doubts on AI reliability
- **Key Lesson:** AI in customer service needs **human oversight**, better error handling, and real-world testing before mass rollout

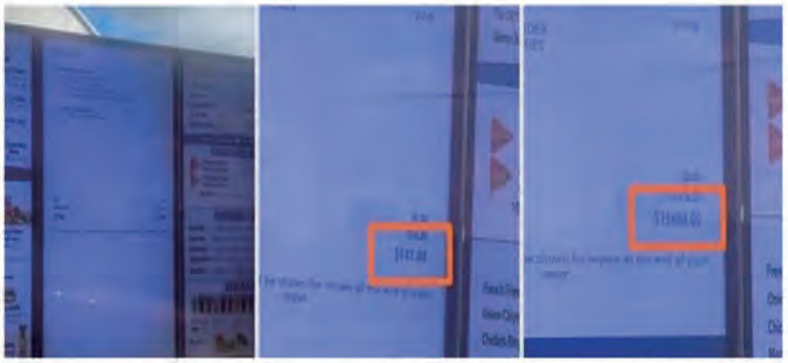

https://brobible.com/culture/article/white-castle-ai-drive-thru-15400-dollar-charge

28

2. AI Agents deployed in industry

CORE.TODAY

Forbes
https://www.forbes.com › ... › Aerospace & Defense

What Air Canada Lost In 'Remarkable' Lying AI Chatbot ...

2024. 2. 19. — The passenger claimed to have been misled on the airline's rules for bereavement fares when the chatbot hallucinated an answer inconsistent with ...

Reuters
https://www.reuters.com › legal › legalindustry › anthro...

Anthropic's lawyers take blame for AI 'hallucination' in ...

2025. 5. 15. — Anthropic's lawyers take blame for AI 'hallucination' in music publishers' lawsuit · Music publishers sue AI company Anthropic over song lyrics.

29

2. AI Agents deployed in industry

CORE.TODAY

Gartner Predicts Over 40% of Agentic AI Projects Will Be Canceled by End of 2027

SYDNEY, Australia, June 25, 2025

Analysts to Explore Agentic AI Trends During Gartner IT Symposium/Xpo, September 8-10 on the Gold Coast

Over 40% of agentic AI projects will be canceled by the end of 2027, due to escalating costs, unclear business value or inadequate risk controls, according to Gartner, Inc.

30

The AI Survivability Matrix

CORE.TODAY

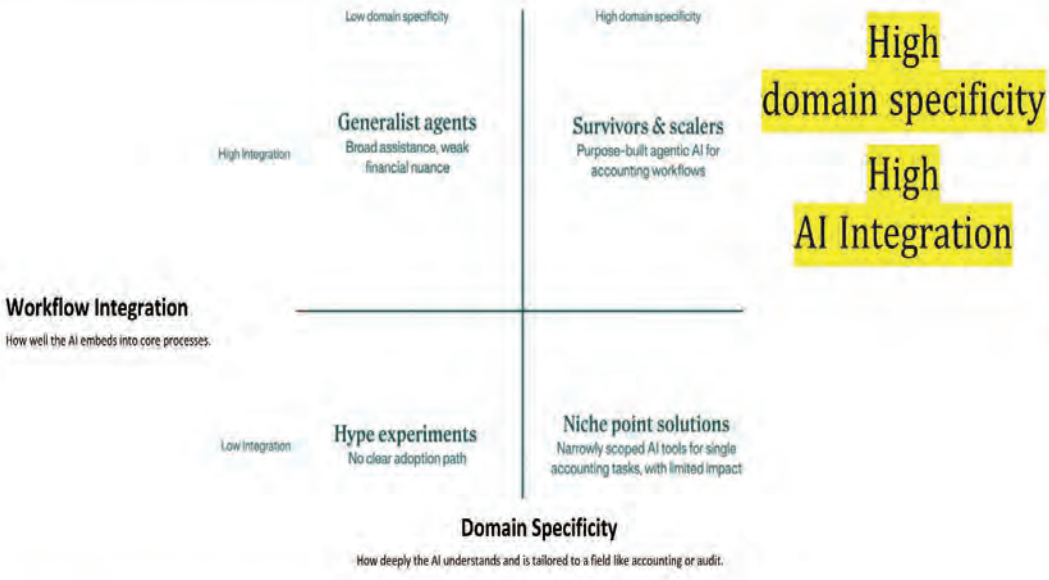

https://trullion.com/blog/why-over-40-of-agentic-ai-projects-will-fail/

31

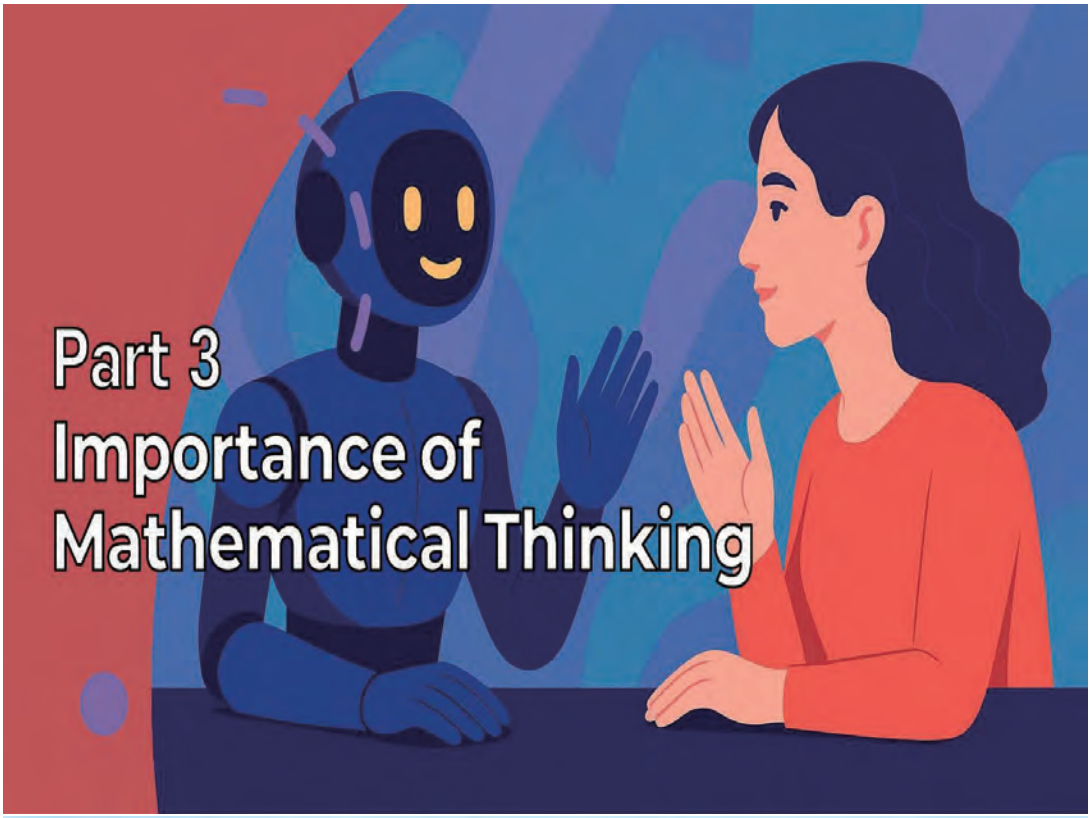

GPT is a probabilistic next-token predictor

CORE.TODAY

First Token Surprisal (2025.08)

Pruning the Unsurprising: Efficient Code Reasoning via First-Token Surprisal

Wenhao Zeng[1], Yaoning Wang[2], Chao Hu[1], Yuling Shi[1], Chengcheng Wan[3], Hongyu Zhang[4], Xiaodong Gu[1] *

[1]Shanghai Jiao Tong University,
[2]Fudan University,
[3]East China Normal University,
[4]Chongqing University
zengwh_cs@sjtu.edu.cn, xiaodong.gu@sjtu.edu.cn

Abstract

Recently, Large Reasoning Models (LRMs) have demonstrated remarkable capabilities in code reasoning by scaling up the length of Chain-of-Thought (CoT). However, excessively long reasoning traces introduce substantial challenges in terms of training cost, inference latency, and deployment feasibility. While various CoT compression approaches have emerged to address this challenge, they face inherent trade-offs: token-level methods often disrupt syntactic and logical coherence, while step-level methods based on perplexity fail to reliably capture the logically critical reasoning steps. In this paper, we propose **ASAP** (Anchor-guided, SurprisAl-based Pruning), a novel coarse-to-fine framework for CoT compression. ASAP first performs anchor-guided pruning to preserve the core reasoning structure, which efficiently re-

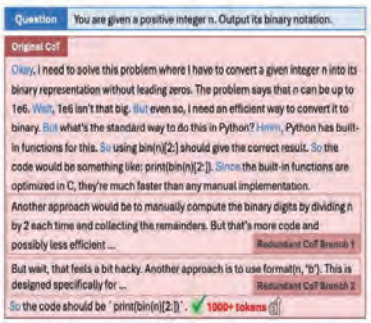

33

Controlability for multi-agent collaboration

CORE.TODAY

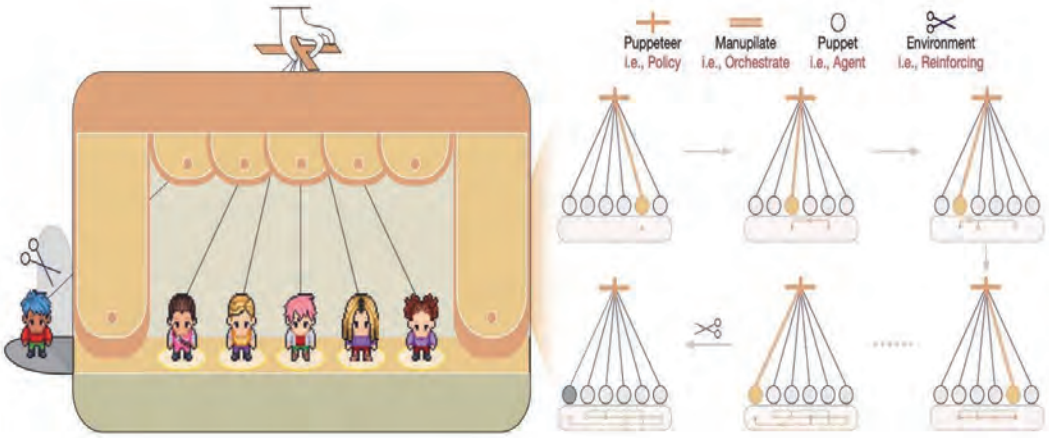

Dang, Yufan, et al. "Multi-Agent Collaboration via Evolving Orchestration." *arXiv preprint arXiv:2505.19591* (2025).

Various Techniques for Agentic Systems

CORE.TODAY

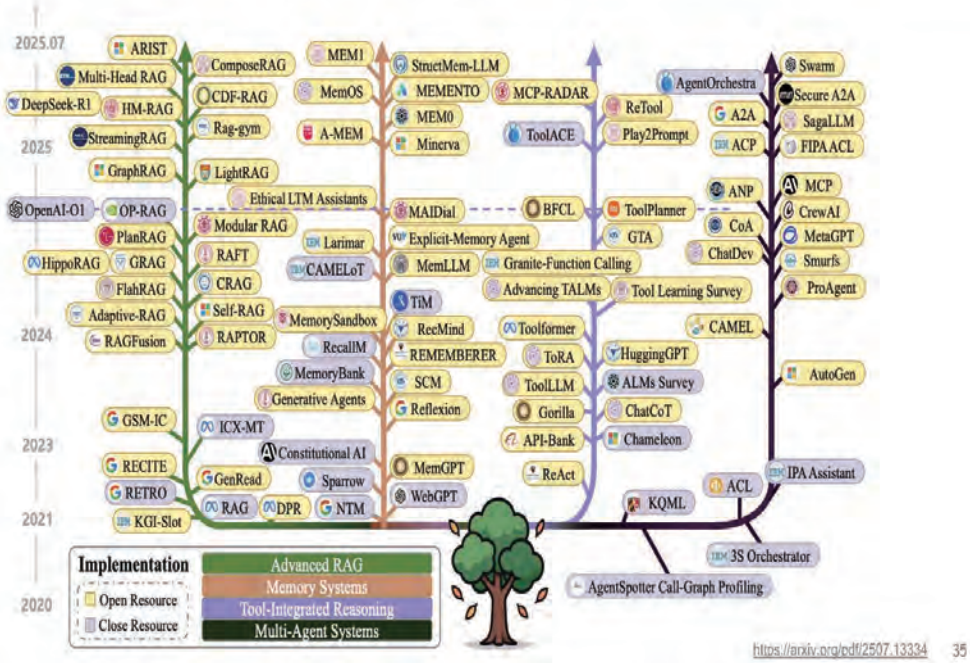

https://arxiv.org/pdf/2507.13334

The Evolution of Numerous Techniques

CORE.TODAY

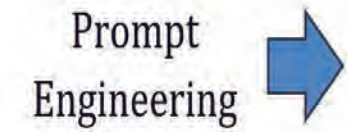

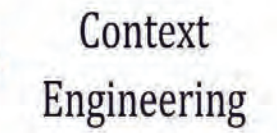

Input Design

The early stage of
"how to use it well"

Context Design

The stage of designing
an environment that injects more
knowledge and context

36

We must prepare for formal thinking

CORE.TODAY

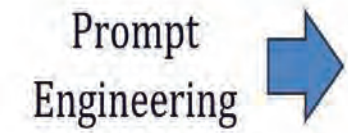

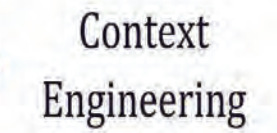

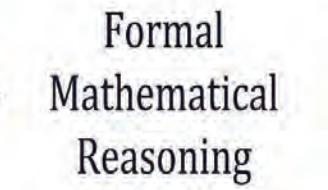

Input Design

The early stage of
"how to use it well"

Context Design

The stage of designing
an environment that injects more
knowledge and context

Formal&Verifiable Reasoning

The stage of going beyond answers
that merely appear correct to
ensuring provable correctness

37

Scale will remove scaffolding

CORE.TODAY

38

GPT ranked 6th in the 2025 IMO (2025.07.19)

CORE.TODAY

Noam Brown
@polynoamial

Today, we at @OpenAI achieved a milestone that many considered years away: gold medal-level performance on the 2025 IMO with a general reasoning LLM—under the same time limits as humans, without tools. As remarkable as that sounds, it's even more significant than the headline 📜

오후 4:52 · 2025년 7월 19일

Rank	First Name	Last Name	ID	Team	so...	tri...	w...	Inter...	fe...	mi...	ob...	Inter...	Global
1	Hengxi	Liu	CHN4		100	100	100	300	100	91.23	100	291.23	591.23
2	Mingyu	Woo	KOR1		100	99.33	93	292.33	100	82.45	100	282.45	574.78
3	Sizhe	Fan	CHN3		100	78.11	100	278.11	100	91.23	83	274.23	552.34
4	Rareș-Andrei	Neculau	ROU3		100	77.67	100	277.67	100	85	83	268	545.67
5	Xinyang	Chen	CHN1		100	99.02	100	299.02	66	86.4	83	235.4	534.42
–	OpenAI				100	75.29	93	268.29	100	65	100	265	533.29
6	Rain	Jiang	USA1		100	75.41	86	261.41	100	65	100	265	526.41
7	Ryan	Bal	CAN1		100	78.51	100	278.51	66	79.11	100	245.11	523.62

39

GPT ranked 1st in the 2025 IMO (2025.08.13)

CORE.TODAY

Oleg Mürk in · 3촌 이상
Teaching LLMs to think.
1일 ·

+ 팔로우

OpenAI's reasoning system just scored at the gold-medal level at this year's IOI online competition — ranking #6 when measured against human competitors and #1 among all AI submissions. This milestone is especially close to my heart. Solving programming competitions using expert iteration was the very first project I worked on when I joined OpenAI in early 2022 — back when reinforcement learning for LLMs wasn't yet in the picture. In less than four years, thanks to the relentless work of 100+ brilliant teammates, we've gone from an idea to an AI that can compete — and win — at the highest levels of competitive programming. For me, it's also a full-circle moment: the last time I won IOI gold (placing #3) was 28 years ago, in 1997. This Monday, August 11, as I celebrate my birthday, I'll also be celebrating just how far the field has come.

With Sheryl Hsu, Alexander Wei, Borys Minaiev, Ahmed El-Kishky

40

Performance for Exper-level mathematics Problems

CORE.TODAY

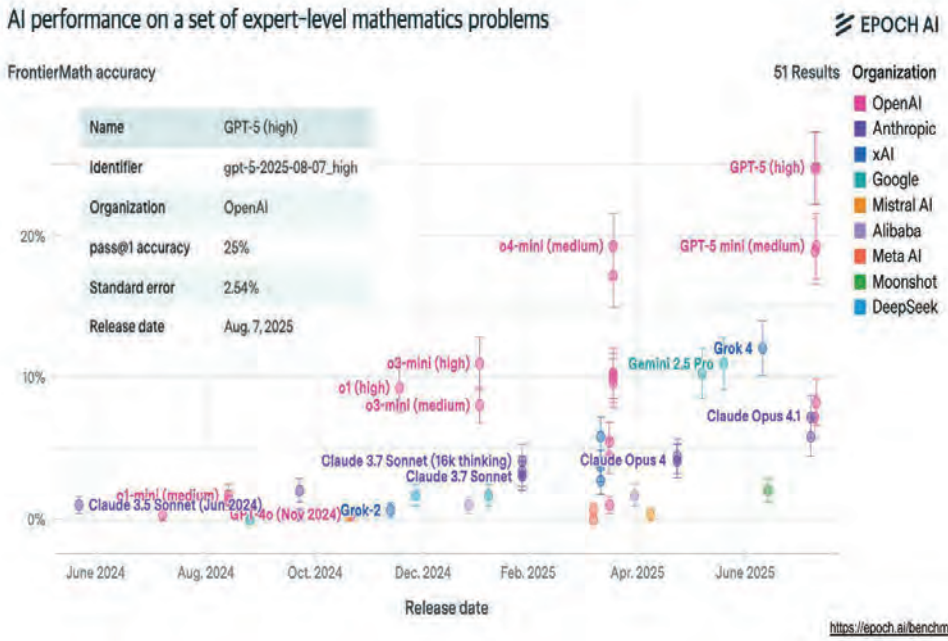

https://epoch.ai/benchmarks 41

Formal Thinking in the Age of AI

CORE.TODAY

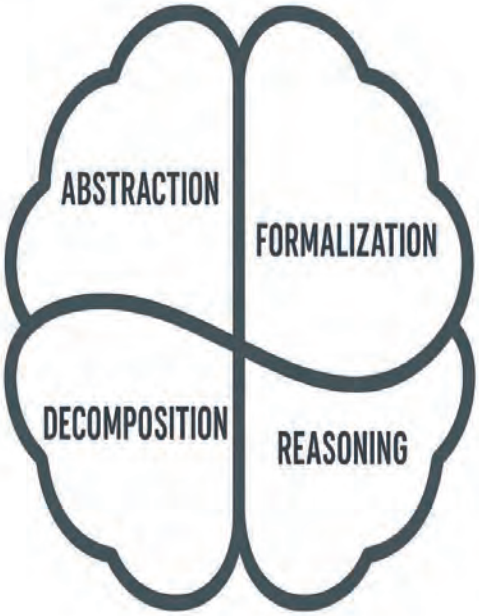

42

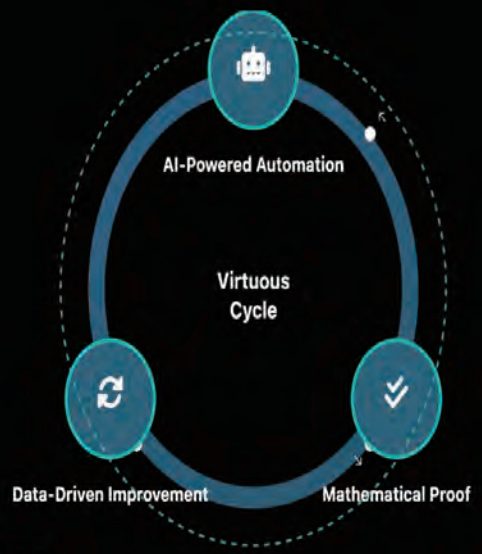

Part 4
Formal Verification and AI Safety

43

The Pitfall of Low-Resolution Communication

When questions are asked vaguely without clear definitions or structure, AI will attempt to fill in the gaps on its own, and in doing so, can introduce errors.

"Find the optimal route for an autonomous vehicle."

Presents the fastest route, but cannot guarantee responsiveness to rare road closures or unpredictable incidents. The system cannot explain how it arrived at the answer.

Black box, lack of reliability

44

Formal Thinking in the Age of AI

CORE.TODAY

The Power of High-Resolution Communication

By defining key terms and establishing a clear logical structure, AI becomes a powerful tool that can deliver reliable results.

"Find a route that satisfies all road constraints and never violates a specific safety standard (X), and present it in provable steps.

May be slightly slower, but presents the safest route that meets all constraints, supported by logical justification. Every decision-making step can be traced and verified.

Transparency, reliability, stability

45

Prompting vs. Structuring

CORE.TODAY

Have the factory robot arm move product A to B. As quickly as possible.

GIVEN: RobotArm(MaxSpeed: S, GripForce: F)

DEFINE: Path P from A to B

CONSTRAINT 1: Obstacle O at (x,y,z)

CONSTRAINT 2: P must not intersect O

CONSTRAINT 3: GripForce must be < F_max

OBJECTIVE: Minimize time(P) subject to constraints

46

Lean 4 programming language and theorem prover

CORE.TODAY

Lean is a theorem prover and programming language that enables correct, maintainable, and formally verified code

→ Install

Learn

Powerful automation | Mathematics

```
-- 'Grind' efficiently manages complex pattern matching and
-- case analysis beyond standard tactics.

example (x : Nat) : 0 < match x with
  | 0   => 1
  | n+1 => x + n := by
  grind

-- Automatically solves systems of linear inequalities.

example (x y : Int) :
    27 ≤ 11*x + 13*y → 11*x + 13*y ≤ 45
    → -10 ≤ 7*x - 9*y → 7*x - 9*y ≤ 4 := by
  grind
```

Grind is a powerful tool that can help you prove theorems quickly and efficiently.

47

Lean is impacting how mathematics is done

CORE.TODAY

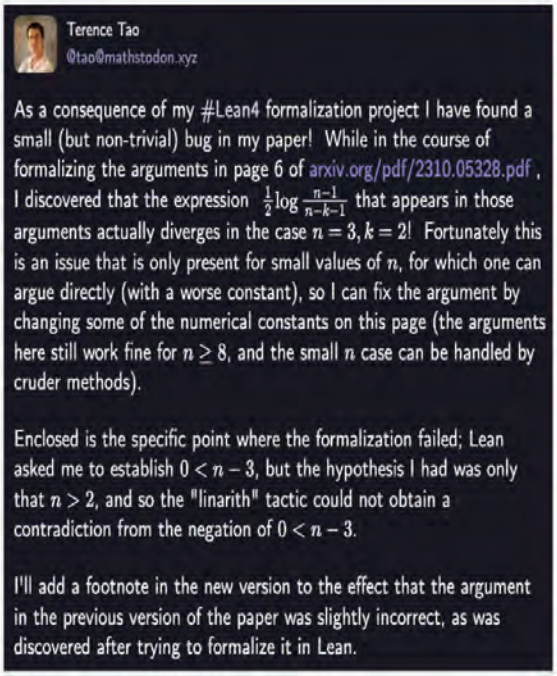

Terence Tao
@tao@mathstodon.xyz

As a consequence of my #Lean4 formalization project I have found a small (but non-trivial) bug in my paper! While in the course of formalizing the arguments in page 6 of arxiv.org/pdf/2310.05328.pdf , I discovered that the expression $\frac{1}{2}\log\frac{n-1}{n-k-1}$ that appears in those arguments actually diverges in the case $n=3, k=2$! Fortunately this is an issue that is only present for small values of n, for which one can argue directly (with a worse constant), so I can fix the argument by changing some of the numerical constants on this page (the arguments here still work fine for $n \geq 8$, and the small n case can be handled by cruder methods).

Enclosed is the specific point where the formalization failed; Lean asked me to establish $0 < n-3$, but the hypothesis I had was only that $n > 2$, and so the "linarith" tactic could not obtain a contradiction from the negation of $0 < n-3$.

I'll add a footnote in the new version to the effect that the argument in the previous version of the paper was slightly incorrect, as was discovered after trying to formalize it in Lean.

```
n : ℕ
s : ℕ → ℝ
h1 : n > 2
h2 : attainable n s
h1' : 2 < ↑n
⊢ 0 < ↑n - 3

Messages (1)
prev_bound.lean:222:6
linarith failed to find a contradiction
case h
n : ℕ
s : ℕ → ℝ
h1 : n > 2
h2 : attainable n s
h1' : 2 < ↑n
a✝ : 0 ≥ ↑n - 3
⊢ False
```

48

AI Perfumer : Eau de AI , Hyscent AI

CORE.TODAY

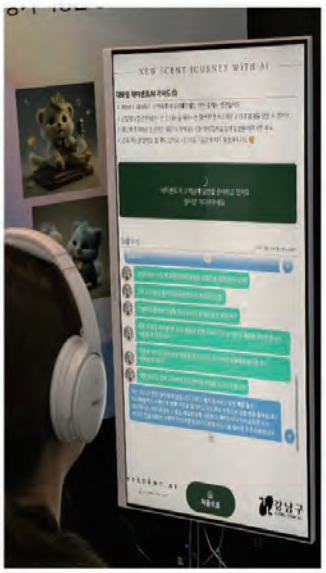

49

AI Perfumer : Eau de AI , Hyscent AI

CORE.TODAY

50

Fragrance Recipe with Lean4

CORE.TODAY

```
/-- Ingredient identifier -/
abbrev IngredientId := String

/-- Perfume note type (Top/Heart/Base) -/
inductive Note
| top | heart | base
deriving DecidableEq, Repr

/-- Recipe: ingredient → percentage (ℝ) -/
abbrev Recipe := IngredientId → ℝ

/-- Constraint: total sum = 100 -/
def Total100 (r : Recipe) : Prop := True

/-- Database (meta information) -/
structure DB where
  noteOf    : IngredientId → Note
  ifraMax   : IngredientId → ℝ
  isAllowed : IngredientId → Bool
```

```
/-- Allowed percentage range for each note type (Top/
structure NoteBounds where
  topMin   : ℝ
  topMax   : ℝ
  heartMin : ℝ
  heartMax : ℝ
  baseMin  : ℝ
  baseMax  : ℝ

/-- Sum of all percentages for a given note type -/
def sumNote (Ids : Finset IngredientId) (db : DB) (n
  Finset.sum Ids (fun i => if db.noteOf i = n then r

/-- Total sum (%) -/
def sumTotal (Ids : Finset IngredientId) (r : Recipe)
  Finset.sum Ids (fun i => r i)
```

51

Lean Into Verified Software Development (2024.04)

CORE.TODAY

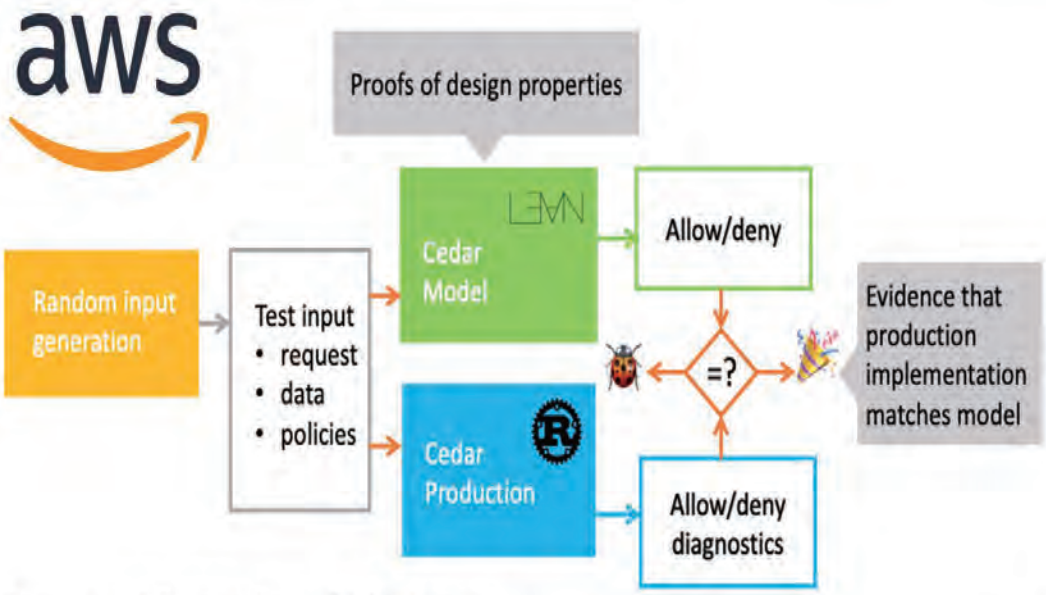

https://aws.amazon.com/ko/blogs/opensource/lean-into-verified-software-development/

Lean Into Verified Software Development (2024.04)

CORE.TODAY

Cedar > Thm > Authorization.lean > {} Cedar.Thm > forbid_trumps_permit

```
/--
Forbid trumps permit: if a `forbid` policy is satisfied, the request is denied.
-/
theorem forbid_trumps_permit
  (request : Request) (entities : Entities) (policies : Policies) :
  (∃ (policy : Policy),
    policy ∈ policies ∧
    policy.effect = forbid ∧
    satisfied policy request entities) →
  (isAuthorized request entities policies).decision = deny
:= by
  intro h
  unfold isAuthorized
  simp [if_satisfied_then_satisfiedPolicies_non_empty forbid policies request entities h]
```

▼Authorization.lean:42:9
▼Tactic state
1 goal

```
request : Request
entities : Entities
policies : Policies
h : ∃ policy, policy ∈ policies ∧ policy.effect = forbid
∧ satisfied policy request entities = true
⊢ (isAuthorized request entities policies).decision =
deny
```

▶ Expected type
▶ All Messages (0)

```
def isAuthorized
  (req : Request)
  (entities : Entities)
  (policies : Policies) : Response
:=
  let forbids := satisfiedPolicies .forbid policies req entities
  let permits := satisfiedPolicies .permit policies req entities
  if forbids.isEmpty && !permits.isEmpty
  then { decision := .allow, policies := permits }
  else { decision := .deny,  policies := forbids }
```

```
theorem forbid_trumps_permit
  (request : Request) (entities : Entities) (policies : Policies) :
  (∃ (policy : Policy),
    policy ∈ policies ∧
    policy.effect = forbid ∧
    satisfied policy request entities) →
  (isAuthorized request entities policies).decision = deny
:= by
  intro h
  unfold isAuthorized
  simp [if_satisfied_then_satisfiedPolicies_non_empty
      forbid policies request entities h]
```

https://aws.amazon.com/ko/blogs/opensource/lean-into-verified-software-development/

A Survival and Growth Imperative

CORE.TODAY

The adoption of mathematical thinking is not merely a technical upgrade. In the age of AI, it is a core management strategy for earning trust and achieving sustainable growth.

```
> DEFINE Agent(d) := { position, velocity, objective }
> DEFINE Rule_1 := Avoid_Collision(d_i, d_j)
> DEFINE Rule_2 := Avoid_Weather(zone_w)
> SIMULATE (Agents[1..100], Rules[1,2], Time=T)
> ...
> RESULT: SuccessRate: 99.98%, FailurePoints: [...]
```

54

A Survival and Growth Imperative

CORE.TODAY

Aspect	Informal AI (Current LLM)	Formal AI (LLM + Proof Assistant)
Verification Method	Probabilistic, unreliable (hallucinations occur)	Deterministic, absolute (mechanically proven)
Feedback Loop	Relies on final answer comparison or human annotation (slow and costly)	Immediate and automatic feedback from a formal system (fast and inexpensive)
Reliability	Low – plausible but unproven	High – verifiable and trustworthy
Data Dependency	High – requires vast high-quality datasets	Low – automatic feedback and synthetic data generation can mitigate data scarcity

55

Thank you

CORE.TODAY

In an era where refining our thoughts has become more important than simply finding answers, what is the most powerful tool for collaborating with AI?

Bug Test

Provides evidence that a **bug exists**, but cannot provide evidence that **no bugs exist**

VS

Formal Verification

Mathematically proving that it is *always correct in all situations*

↓

Provable safety

Building the fundamental trust that autonomous AI systems can rely on

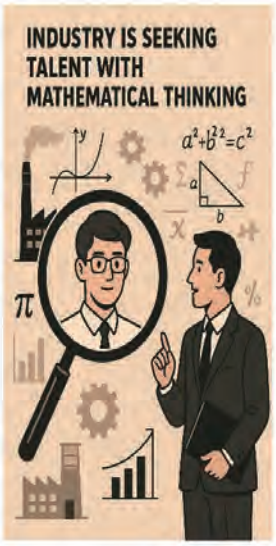

56

ANOVATS: A subsampling-based test for differences among short time series in marine studies

Yuichi Goto

Kyushu University

Data used in marine ecosystem assessments often consist of short time series, making conventional methods that rely on large datasets potentially prone to drawing incorrect conclusions. Analysis of variance (ANOVA) methods for time series data is one example. These methods require the estimation of the reciprocal of the long-run variance (the spectral density at zero frequency), which typically demands long-term time series observations. In this talk, we address the problem of testing the equality of means across regions and propose a subsampling-based method for short time series data. The method also facilitates divisive hierarchical clustering by iteratively splitting regions based on statistical criteria. Its application to North Sea zooplankton biomass data reveals significant differences across diverse ecosystems, highlighting its utility in marine resource management. fields, while covariance serves as a selection criterion to identify informative data-set during model fitting and integral evaluation. In scenarios characterized by low simulation efficiency and high costs of raw data acquisition, key challenges such as surrogate modeling, failure probability estimation, and parameter inference are systematically restructured within the Bayesian experimental design framework. The effectiveness of the proposed methodology is validated through both theoretical analysis and practical applications, demonstrating its potential for enhancing experimental efficiency and decision-making under uncertainty.

ANOVATS: A subsampling-based test for differences among short time series in marine studies

Yuichi Goto	Kyushu Univ.
Hiroko Kato Solvang	Institute of Marine Research
Tone Falkenhaug	Institute of Marine Research
Masanobu Taniguchi	Waseda Univ.

August 18, 2025
Forum "Math-for-Industry" 2025
- Challenge of Mathematics for Industry in the AI era -

Content

Introduction

Analysis of variance (ANOVA) for time series (ANOVATS)

-- statistical methods to investigate whether there are significant differences among multiple groups for time series data

-- useful to detect important factors that affect data and interactions among factors

Management of fishery resources is important

-- stable supply of fishery products

-- prevention of extinction of living organisms

-- understanding and assessing recent change in ecosystem

-- implementing adaptation to impact of human activity in the marine ecosystem

We are interested in the regional differences of fishery resources based on the time series data collected in the recent 2-30 years.

This motivates ANOVA for small-sample time series.

Content

Method

In the classical ANOVA for i.i.d. data, the F-test is defined as

$$S_n = n\sum_{i=1}^{a}(\overline{\boldsymbol{z}_{i\cdot}} - \overline{\boldsymbol{z}_{\cdot\cdot}})^\top \left(\frac{1}{an}\sum_{i=1}^{a}\sum_{t=1}^{n}(\boldsymbol{z}_{it} - \overline{\boldsymbol{z}_{i\cdot}})^\top(\boldsymbol{z}_{it} - \overline{\boldsymbol{z}_{i\cdot}})\right)^{-1}(\overline{\boldsymbol{z}_{i\cdot}} - \overline{\boldsymbol{z}_{\cdot\cdot}}),$$

which is $\frac{\text{between-group variation}}{\text{within-group variation}}$. Within—group variation corresponds to variance.

The classical F-test for i.i.d. data cannot take care of time dependence structure.

For time series data, within—group variations should be replaced
by spectral density to capture time dependence structure.

Nagahata & Taniguchi (2018) considered, for independent groups,

$$S_n' = n\sum_{i=1}^{a}(\overline{\boldsymbol{z}_{i\cdot}} - \overline{\boldsymbol{z}_{\cdot\cdot}})^\top \left(2\pi\tilde{\boldsymbol{f}}_n(0)\right)^{-1}(\overline{\boldsymbol{z}_{i\cdot}} - \overline{\boldsymbol{z}_{\cdot\cdot}}), \quad \text{where } \tilde{\boldsymbol{f}}_n(0) = \textstyle\sum_{i=1}^{a}\hat{\boldsymbol{f}}_{ii}(\lambda)/a.$$

Goto et al. (2024) considered, for correlated groups,

$$S_n'' = n(\overline{\boldsymbol{z}_{1\cdot}}^\top - \overline{\boldsymbol{z}_{\cdot\cdot}}^\top, \ldots, \overline{\boldsymbol{z}_{a\cdot}}^\top - \overline{\boldsymbol{z}_{\cdot\cdot}}^\top)\hat{\boldsymbol{H}}_n^{-}(\overline{\boldsymbol{z}_{1\cdot}}^\top - \overline{\boldsymbol{z}_{\cdot\cdot}}^\top, \ldots, \overline{\boldsymbol{z}_{a\cdot}}^\top - \overline{\boldsymbol{z}_{\cdot\cdot}}^\top)^\top,$$

where $\hat{\boldsymbol{H}}_n^{-}$ is the Moore–Penrose inverse matrix of $\hat{\boldsymbol{H}}_n$, $\hat{\boldsymbol{H}}_n := (\hat{\boldsymbol{H}}_{ij})_{i,j=1,\ldots,a}$,

$$\hat{\boldsymbol{H}}_{ij} := \hat{\boldsymbol{f}}_{ij}(0) - \frac{2\pi}{a}\sum_{s=1}^{a}\left\{\hat{\boldsymbol{f}}_{sj}(0) + \hat{\boldsymbol{f}}_{is}(0)\right\} + \frac{2\pi}{a^2}\sum_{s,k=1}^{a}\hat{\boldsymbol{f}}_{sk}(0).$$

Estimation of spectral density requires large sample size (n≧1000).
However, the sample size of ocean data is small.
We propose a new test applicable to small sample time series.

5/26

Method

Subsampling procedure (Politis & Romano 1999)

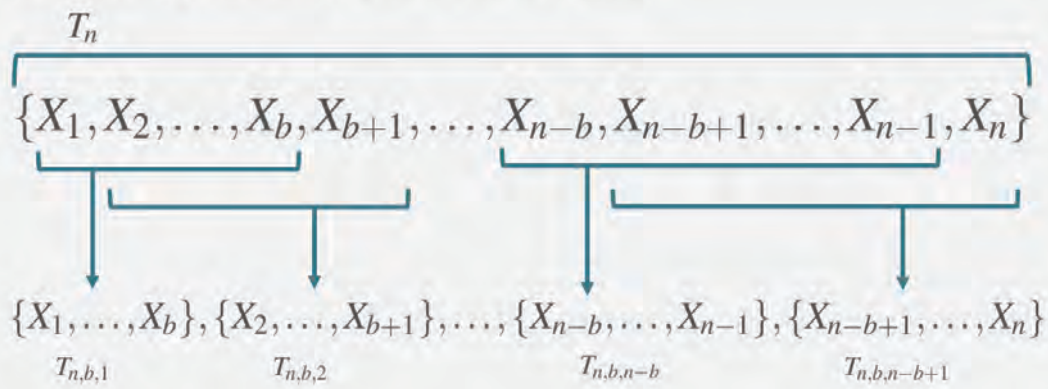

→ calculate sub-sample statistics

Approximate the asymptotic distribution of T_n
by subsample statistics $\hat{F}_T(x) = \dfrac{1}{n-b+1}\displaystyle\sum_{t=1}^{n-b+1}\mathbb{I}\{T_{n,b,t} \le x\}.$

6/26

Method

One-way model with time dependent errors, correlated groups:

$$z_{it} = \mu + \psi_i + e_{it}, \qquad i = 1, \ldots, a, \ t = 1, \ldots, n,$$

A test for the existence of group effect:

$H_0 : \psi_1 = \cdots = \psi_a$ vs $H_1 : H_0$ does not hold.

Our proposed test statistic & p-values:

$$T_n = n \sum_{i=1}^{a} (\overline{z_{i\cdot}} - \overline{z_{\cdot\cdot}})^\top (\overline{z_{i\cdot}} - \overline{z_{\cdot\cdot}}), \quad p_n = \frac{1}{n-b+1} \sum_{t=1}^{n-b+1} \mathbb{I}\{T_{n,b,t} > T_n\},$$

where $T_{n,b,t} = \dfrac{b}{1-\frac{b}{n}} \displaystyle\sum_{i=1}^{a} (\overline{z_{i\cdot,b,t}} - \overline{z_{\cdot\cdot,b,t}})^\top (\overline{z_{i\cdot,b,t}} - \overline{z_{\cdot\cdot,b,t}})$.

Method

Assumption

(i) $\{e_t\}$ is geometrically α-mixing,that is, $\alpha(n) \le C\rho^n$ for some constant C

(ii) $\{e_t\}$ has the moments of all orders

which implies $\displaystyle\sum_{s_2,\ldots,s_\ell=-\infty}^{\infty} \left(1 + \sum_{j=2}^{\ell} |s_j|^d\right) |\mathrm{cum}\{e_{i_1 0 d_1}, e_{i_2 s_2 d_2}, \ldots, e_{i_\ell s_\ell d_\ell}\}| < \infty.$

for any $d \in \mathbb{N}$, any $\ell \in \mathbb{N}$, any $(i_1, \ldots, i_\ell) \in \{1, \ldots, K\}^\ell$, any $(d_1, \ldots, d_\ell) \in \{1, \ldots, p\}^\ell$.

Theorem Suppose Assumption and subsampling block length satisfy $b \to \infty$ and $b/\sqrt{n} \to 0$ as $n \to \infty$.

(i) the test which rejects H_0 whenever $p_n < \varphi$ has the asymptotically size φ and is consistent:

$\mathrm{P}(p_n < \varphi | H_0) \to \phi$ and $\mathrm{P}(p_n < \varphi | H_1) \to 1$ as $n \to \infty$.

(ii) for φ_n such that $\varphi_n \to 0$ and $\varphi_n / \left(n^{\frac{a}{2}-1} \exp\left(-\frac{n}{2}\right)\right) \to \infty$ as $n \to \infty$, the test which rejects H_0 whenever $p_n < \varphi_n$ satisfy

$\mathrm{P}(p_n < \varphi_n | H_0) \to 0$ and $\mathrm{P}(p_n < \varphi_n | H_1) \to 1$ as $n \to \infty$.

Method

Post-ANOVATS procedure:

Hypothesis Testing for All Areas:

Let $p = 1$ and Area_i represents areas we observed $\{z_{it}\}_{t=1,\ldots,n}$.

Consider the hypothesis $H_0 : \boldsymbol{\psi}_1 = \cdots = \boldsymbol{\psi}_a$ and apply our test.

If H_0 is accepted ($p_n > 0.05$), terminate the procedure.

If H_0 is rejected ($p_n \leq 0.05$), proceed to the next step.

Division of Areas into Two Groups

sort the sample means for all areas in ascending order, denoted as $\overline{z_{[1].}}, \ldots, \overline{z_{[a].}}$, corresponding to the sorted areas $\text{Area}_{[1]}, \ldots, \text{Area}_{[a]}$.

compute the differences between the sample means of adjacent areas: $\overline{z_{[i+1].}} - \overline{z_{[i].}}$ for all $i = 1, \ldots, a-1$,

find the index i' that maximizes these differences:

$i' := \text{argmax}_{i=1,\ldots,a-1}(\overline{z_{[i+1].}} - \overline{z_{[i].}})$.

The areas are then divided into two groups:

Group1: $\text{Area}_{[1]}, \ldots, \text{Area}_{[i']}$

Group2: $\text{Area}_{[i'+1]}, \ldots, \text{Area}_{[a]}$

9/26

Method

Post-ANOVATS procedure (conti):

Further Division

The following hypotheses are considered for each group:

For Group 1,

$$H_0 : \psi_{[1]} = \cdots = \psi_{[i']} \quad \text{v.s.} \quad H_1 : \ H_0 \text{ does not hold}$$

For Group 2,

$$H_0 : \psi_{[i'+1]} = \cdots = \psi_{[a]} \quad \text{v.s.} \quad H_1 : \ H_0 \text{ does not hold.}$$

The above steps are repeated for each group, testing and subdividing,

until the hypothesis is not rejected or the number of areas in the group is one.

Edwards & Cavalli-Sforza (1965), Scott & Knott (1974), Calinski & Corsten (1985), Wang & Wu (2014, 2016): a hierarchical splitting method based on the sum of squares

Multiple comparison methods (Fisher's least square, Tukey's method, Scheffe's method)

10/26

Content

Simulation

Settings (null): $z_{it} = e_{it}, \quad i = 1, \ldots, a, \; t = 1, \ldots, n.$
Set p=1, a=3,9,15, n=20, 30, 50, 70, 100, $b = \lfloor 2.5n^{1/3} \rfloor$

1. Generate time series z_{it} :

dgp: MA(1) with normal error, MA(1) with t5,
MA(1) with skew-normal, Gaussian GARCH(1,1)
for independent & correlated groups

2. Apply our test
3. Iterate 1000 times
4. Calculate rejection probability (should be close to 0.05)

Simulation

MA(1) model

$$\boldsymbol{e}_t = \boldsymbol{\nu}_t + \boldsymbol{\Psi}\boldsymbol{\nu}_{t-1}\,,\ \text{where}\ \boldsymbol{e}_t = (\boldsymbol{e}_{1t}^\top, \ldots, \boldsymbol{e}_{at}^\top)^\top\,,\ \boldsymbol{\nu}_t \text{ is i.i.d. distribution}$$

GARCH(1,1) model

$$\boldsymbol{e}_t = (\boldsymbol{e}_{1t}^\top, \ldots, \boldsymbol{e}_{at}^\top)^\top, \quad e_{it} = h_{it}^{1/2}\nu_{it}, \quad i = 1, \ldots, a, \quad \begin{pmatrix} h_{1t} \\ \vdots \\ h_{at} \end{pmatrix} = \begin{pmatrix} 1 \\ \vdots \\ 1 \end{pmatrix} + 0.1\boldsymbol{\Psi} \begin{pmatrix} e_{1t}^2 \\ \vdots \\ e_{at}^2 \end{pmatrix} + \begin{pmatrix} 0.1h_{1,t-1} \\ \vdots \\ 0.1h_{a,t-1} \end{pmatrix}$$

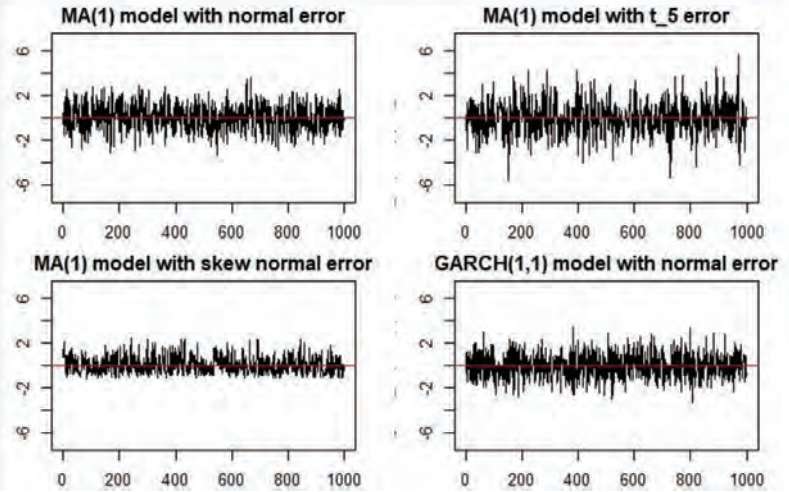

Simulation

Example

Case1: MA(1) model with independent groups

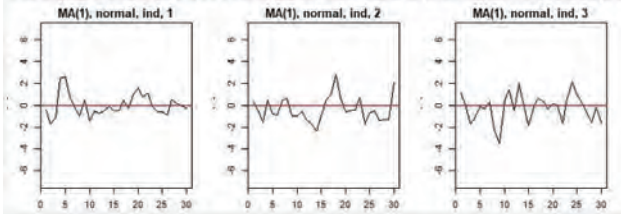

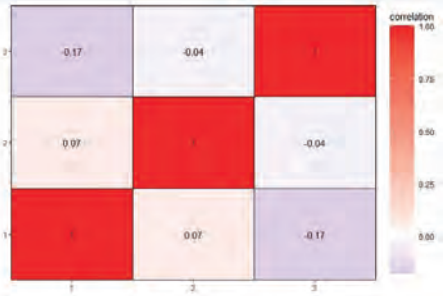

Case2: MA(1) model with correlated groups

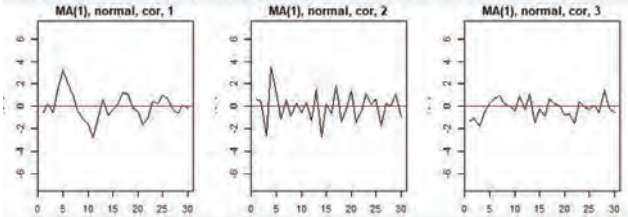

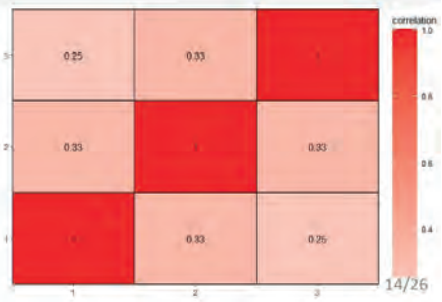

Simulation

Results under null:

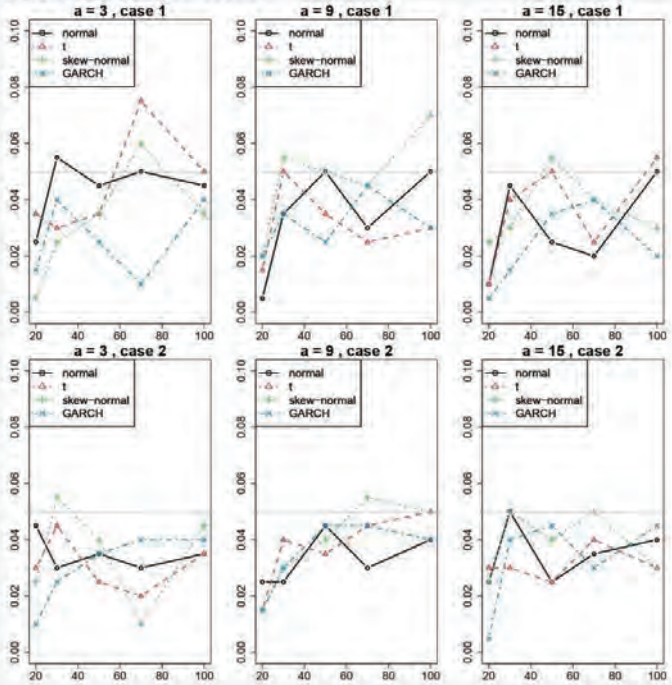

Simulation

Settings (alternative): $z_{it} = \psi_i + e_{it}, \quad i = 1, \ldots, 6, \ t = 1, \ldots, n,$

Set p=1, a=6, n=20, 30, 50, 70, 100, $b = \lfloor 2.5n^{1/3} \rfloor$,

$$(\psi_1, \ldots, \psi_6) := (0,0,0,1,1,1)^\top$$

1. Generate time series z_{it} :
2. Apply our method
3. Iterate 1000 times
4. Calculate the probability

-- rejecting H_0 and dividing time series into two groups (z_{1t}, z_{2t}, z_{3t}) and (z_{4t}, z_{5t}, z_{6t}) in the first step.

-- accepting the null hypothesis for both groups (z_{1t}, z_{2t}, z_{3t}) and (z_{4t}, z_{5t}, z_{6t}) in the second step under the first step being worked correctly.

-- whole step works correctly.

Simulation

Results

under alternative

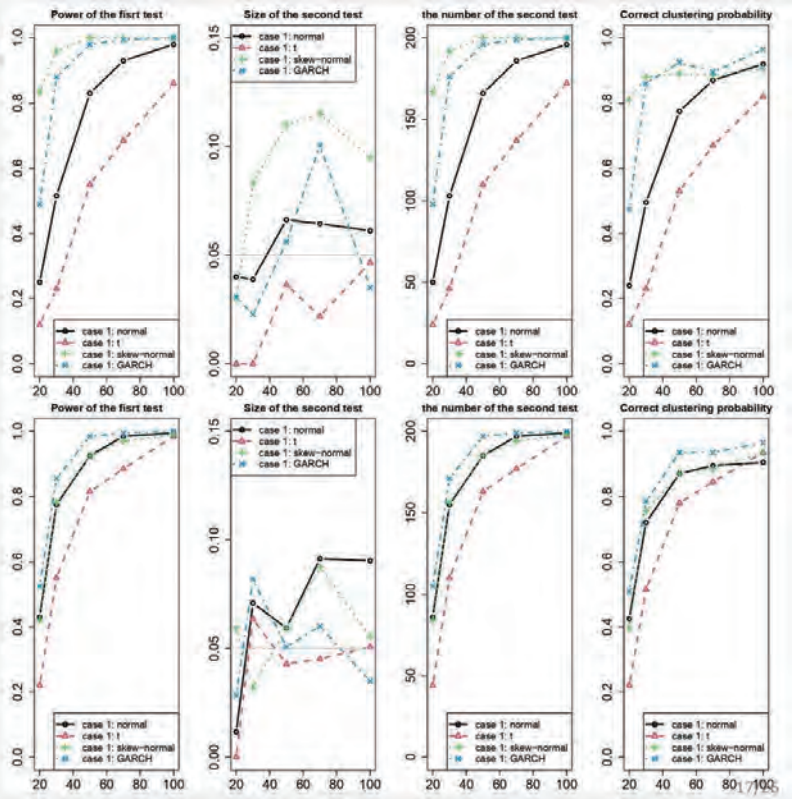

Content

Biomass data

Biomass data of zooplankton collected by the IMR,
as a part of the 'Coastal Monitoring programme' in 2009-2021.

Biomass are given as g per square meter surface (g/m2).
The data is summarized into three categories according to the size fractions, 180-1000, 1000-2000 and >2000.
The data are sampled at four areas in the North Sea

area 1: Arendal
area 2: Lang
area 3: OF2
area 4: Risør

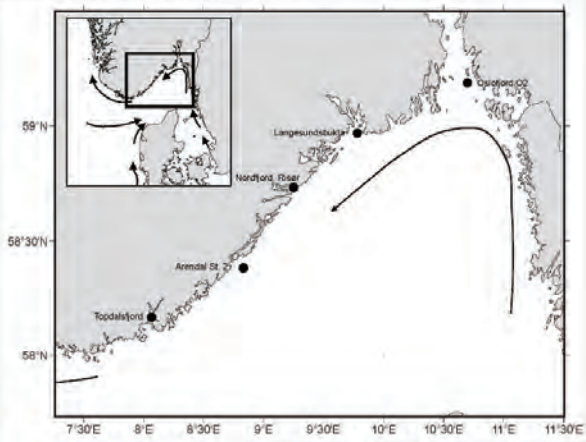

Biomass data is provided by
Dr. Tone Falkenhaug of IMR.

Biomass data

area 1: Arendal
area 2: Lang
area 3: OF2
area 4: Risør

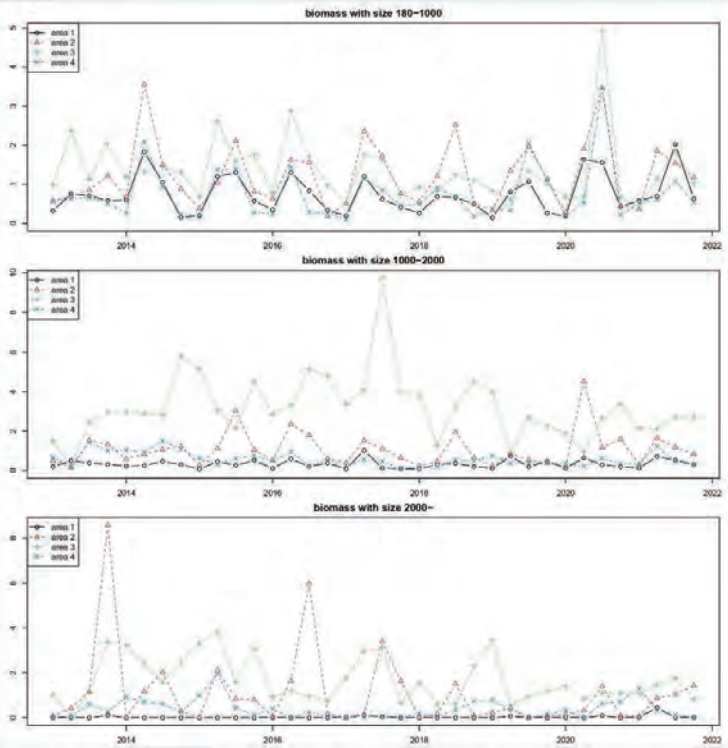

Biomass data

Results:

For size 180—1000,
Depth 1
Group 1: Arendal, Risør
Group 2: Lang, OF2
p-value: 0

Depth: 2
Group 1: Arendal, Risør
Group 2: NULL
p-value: 0.862

Depth: 2
Group 1: Lang, OF2
Group 2: NULL
p-value: 0.069

Final results of grouping with means
Arendal, Risør
0.480 0.497

Lang, OF2
0.800 1.0417

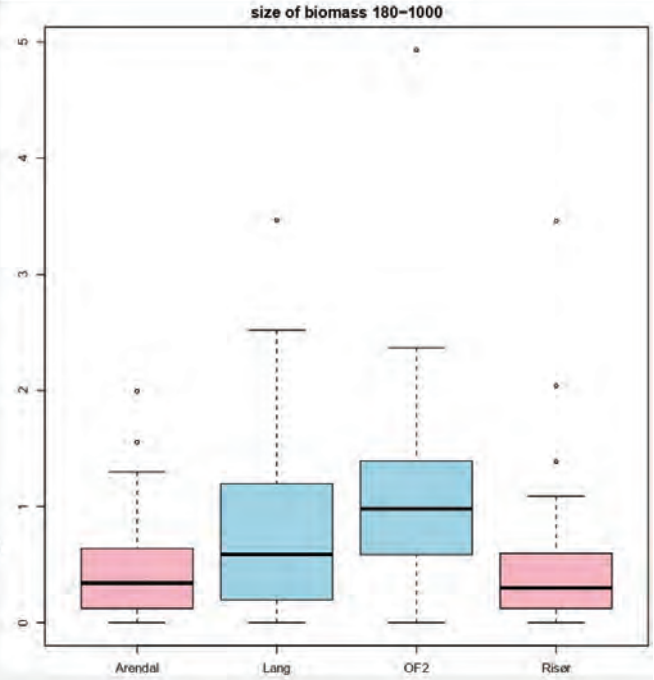

Biomass data

Results:

For size 1000—2000,
Depth 1:
Group 1: Arendal, Risør, Lang
Group 2: OF2
p-value: 0

Depth 2 :
Group 1: Arendal, Risør
Group 2: Lang
p-value: 0

Depth 3:
Group 1: Arendal, Risør
Group 2: NULL
p-value: 0.138

Final results of grouping with means

Arendal, Risør
0.198, 0.446

Lang
0.6978593

OF2
2.690522

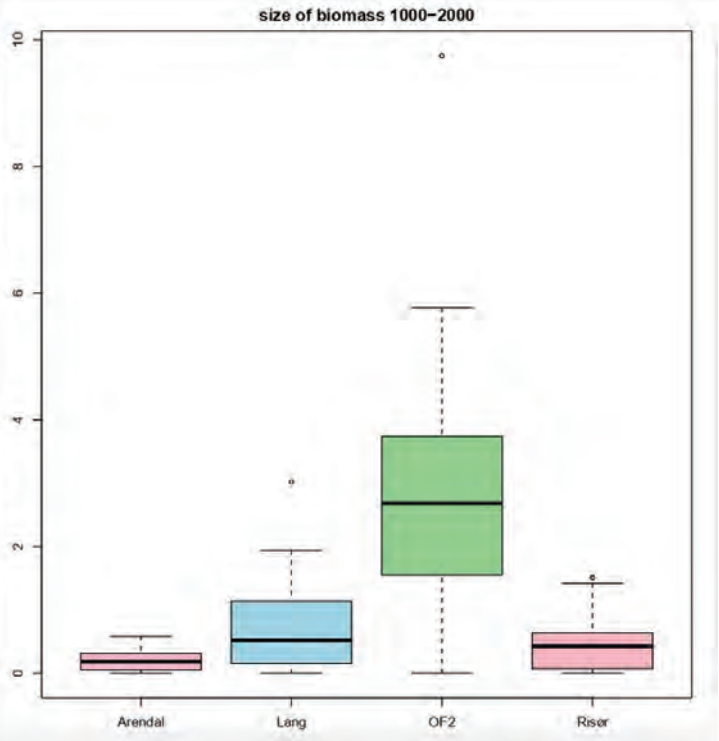

Biomass data

Results:

Depth: 1
Group 1: Arendal, Risør
Group 2: Lang, OF2
p-value: 0

Depth: 2
Group 1: Arendal
Group 2: Risør
p-value: 0

Depth: 2
Group 1: Lang, OF2
Group 2: NULL
p-value: 0.241

Final results of grouping with means:
Arendal
0.0116

Risør
0.289

Lang, OF2
0.886, 1.289

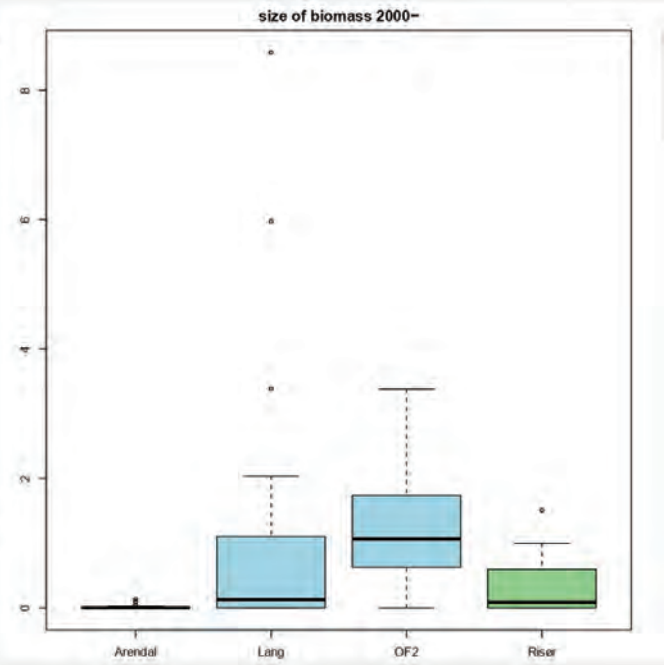

23/26

Biomass data

The amount of zooplankton biomass is related both to the sampling depth, and to the position of the sampling station:

area	sampling depth	position
1. Arendal	50m	in the coastal current
4. Risør	160m	inside the fjord sill
2. Langesund	200m	outside the fjord sill
3. OF2	350m	outside the fjord in the coastal current

The deepest stations (OF2 and Langesund) usually have the larger total biomass values, and larger sized plankton due to the deeper sampling depth (longer water column, i.e., larger sampling volume since the net is hauled from bottom to surface)

Risør is located inside the fjord sill, and may have a somewhat different zooplankton community.

-- it maybe useful to check the species composition.

24/26

Content

1. Introduction
2. Method
3. Simulation
4. Field observation
   -- CPUE data
      -- Result and discussion
   -- Biomass data
      -- Result and discussion
5. Conclusion

Conclusion

In this talk, since sample size of ocean data is often small,
so we proposed a subsampling based test for ANOVA in small sampled time series,
and a divisive (top-down) hierarchal clustering procedure is introduced.

Our procedure is applied to biomass data.
-- reasonable results for Biomass data is obtained.

Our method can be applied to several data to detect differences
among groups (regions).

Online Bernstein-von Mises theorem

Min-Woo Chae

POSTECH

Online learning is an inferential paradigm in which parameters are updated incrementally from sequentially available data, in contrast to batch learning, where the entire dataset is processed at once. In this talk, we assume that mini-batches from the full dataset become available sequentially. The Bayesian framework, which updates beliefs about unknown parameters after observing each mini-batch, is naturally suited for online learning. At each step, we update the posterior distribution using the current prior and new observations, with the updated posterior serving as the prior for the next step. However, this recursive Bayesian updating is rarely computationally tractable unless the model and prior are conjugate. When the model is regular, the updated posterior can be approximated by a normal distribution, as justified by the Bernstein-von Mises theorem. We adopt a variational approximation at each step and investigate the frequentist properties of the final posterior obtained through this sequential procedure. Under mild assumptions, we show that the accumulated approximation error becomes negligible once the mini-batch size exceeds a threshold depending on the parameter dimension. As a result, the sequentially updated posterior is asymptotically indistinguishable from the full posterior.

Online Bernstein–von Mises Theorem

Minwoo Chae

Joint work with Jeyong Lee and Junhyeok Choi

Department of Industrial and Management Engineering
Pohang University of Science and Technology

FMfi Forum on Math for Industry

Introduction

- Consider a statistical model

$$\mathcal{P} = \{p_\theta : \theta \in \Theta\}$$

  parametrized by $\theta \in \Theta \subset \mathbb{R}^p$.
- Our goal is to infer θ from observations $Y_1, \ldots, Y_N$.
- Assume that

$$Y_1, \ldots, Y_N \mid \theta \overset{\text{iid}}{\sim} p_\theta.$$

Bayesian paradigm

- Let $\Pi_0(\cdot)$ be a prior on Θ:
  - Represents prior belief about the unknown θ.
- The posterior distribution is given by

$$\Pi(A \mid \mathbf{D}) = \frac{\int_A \exp\{L(\theta)\} \mathrm{d}\Pi_0(\theta)}{\int_\Theta \exp\{L(\theta)\} \mathrm{d}\Pi_0(\theta)},$$

where $\mathbf{D} = (Y_i)_{i=1}^N$ and

$$L(\theta) = \sum_{i=1}^N \log p_\theta(Y_i).$$

  - Represents updated belief about θ after observing $Y_1, \ldots, Y_N$.

Bayesian paradigm (cont.)

- Bayesian inference relies on the posterior distribution:
  - Point estimation via Bayes estimators
  - Uncertainty quantification using credible sets
- In practice, various computational tools are used to approximate the posterior:
  - Markov chain Monte Carlo (MCMC)
  - Variational inference

Bayesian paradigm (cont.)

- The posterior distribution represents the degree of belief about θ after observing the available data.
- It can therefore be used as a prior for future data:
  - When collecting additional data from the same population
  - When constructing a new (informative) prior for a slightly different population
- In principle, once a belief distribution (prior) on θ is specified and new data are observed, the degree of belief can be updated via Bayes' rule.

Sequentially available data

- In this talk, we focus on an online learning setup.
- Specifically, the entire dataset $\mathbf{D} = (Y_1, \ldots, Y_N)$ is divided into mini-batches as

$$(\underbrace{Y_1, \ldots, Y_n}_{\mathbf{D}_1}, \underbrace{Y_{n+1}, \ldots, Y_{2n}}_{\mathbf{D}_2}, \ldots, \underbrace{Y_{N-n+1}, \ldots, Y_N}_{\mathbf{D}_T}),$$

  and $\mathbf{D}_1, \ldots, \mathbf{D}_T$ become available sequentially.
  - $\mathbf{D}_t = (Y_{(t-1)n+1}, \ldots, Y_{tn})$: the tth mini-batch of size n
  - T: total number of mini-batches
- We assume that once $\mathbf{D}_t$ is used for inference, it cannot be reused when future data arrive.

Sequentially available data (cont.)

- The previous setup is common in many online learning applications.
- In principle, Bayesian methods are well suited for analyzing sequential data.

Opper, M. & Winther, O. "A Bayesian approach to on-line learning". *On-line Learning in Neural Networks*. 1999

Solla, S. A. & Winther, O. "Optimal online learning: A Bayesian approach". *Computer Physics Communications*. 1999

Loo, N., Swaroop, S. & Turner, R. E. "Generalized variational continual learning". *Proc. ICLR*. 2021

Nguyen, C. V., Li, Y., Bui, T. D. & Turner, R. E. "Variational continual learning". *Proc. ICLR*. 2018

Jeong, K., Chae, M. & Kim, Y. "Online learning for the Dirichlet process mixture model via weakly conjugate approximation". *Comput. Statist. Data Anal.* 2023

Choi, J., Lee, J., Kim, Y. & Chae, M. "Online Bayesian inference for Cox proportional hazards model". To appear in *J. Comput. Graph. Statist.* 2025+

Bayesian approach for sequentially available data

$$\Pi_0(\cdot) \xrightarrow{\mathbf{D}_1} \Pi(\cdot \mid \mathbf{D}_1) \xrightarrow{\mathbf{D}_2} \Pi(\cdot \mid \mathbf{D}_1, \mathbf{D}_2) \xrightarrow{} \cdots$$

- The current posterior can be used as the prior for the next step:

$$\pi(\theta \mid \mathbf{D}_1, \mathbf{D}_2) \propto \underbrace{\pi_0(\theta)}_{\text{prior}} \times \underbrace{p(\mathbf{D}_1 \mid \theta) p(\mathbf{D}_2 \mid \theta)}_{\text{full likelihood}}$$

$$\propto \underbrace{\pi(\theta \mid \mathbf{D}_1)}_{\text{updated prior}} \times \underbrace{p(\mathbf{D}_2 \mid \theta)}_{\text{(new) likelihood}}$$

Computational challenges of sequential Bayesian updates

- The previous approach is computationally feasible only when Π_0 is conjugate to $\mathcal{P}$.
- With a non-conjugate prior, the posterior $\Pi(\cdot \mid \mathbf{D}_1)$ is typically not available in closed form.
- In such cases, one may approximate $\Pi(\cdot \mid \mathbf{D}_1)$ with a distribution that allows for efficient computation of the next posterior.

Bayesian online learning

- Let $\mathcal{Q}$ be a family of distributions on Θ.
- For a suitable (pseudo-)distance d, define

$$\Pi_1(\cdot) = \operatorname*{argmin}_{Q \in \mathcal{Q}} d\big(Q, \Pi(\cdot \mid \mathbf{D}_1)\big)$$

  as the best approximation to $\Pi(\cdot \mid \mathbf{D}_1)$ within $\mathcal{Q}$.
- Then, Π_1 is used as the new prior for the next step.
- Repeating this procedure over mini-batches yields online Bayesian learning.

Bayesian online learning

- Online Bayesian learning depends on the choice of $\mathcal{Q}$ and the distance d.
- These choices determine the algorithmic and statistical efficiency of the procedure.
- Possible choices for d:
  - $d(Q, \Pi(\cdot \mid \mathbf{D}_1)) = K(Q\,;\, \Pi(\cdot \mid \mathbf{D}_1))$ (variational approximation)
  - $d(Q, \Pi(\cdot \mid \mathbf{D}_1)) = K(\Pi(\cdot \mid \mathbf{D}_1)\,;\, Q)$ (expectation propagation)
- This talk focuses on the variational approximation, which is often more computationally convenient.

Online learning with variational approximation

- Let $\Pi_{t-1} \in \mathcal{Q}$ denote the belief distribution before observing $\mathbf{D}_t$.
- Define $\widetilde{\Pi}_t(\cdot \mid \mathbf{D}_t)$ as the posterior based on prior Π_{t-1} and data $\mathbf{D}_t$, i.e.,

$$\widetilde{\Pi}_t(A \mid \mathbf{D}_t) = \frac{\int_A \exp\{L_t(\theta)\}\mathrm{d}\Pi_{t-1}(\theta)}{\int_\Theta \exp\{L_t(\theta)\}\mathrm{d}\Pi_{t-1}(\theta)},$$

  where $L_t(\theta) = \sum_{i=(t-1)n+1}^{nt} \log p_\theta(Y_i)$.
- Then define

$$\Pi_t(\cdot) = \operatorname*{argmin}_{Q \in \mathcal{Q}} K\big(Q\,;\, \widetilde{\Pi}_t(\cdot \mid \mathbf{D}_t)\big).$$

Online learning with variational approximation (cont.)

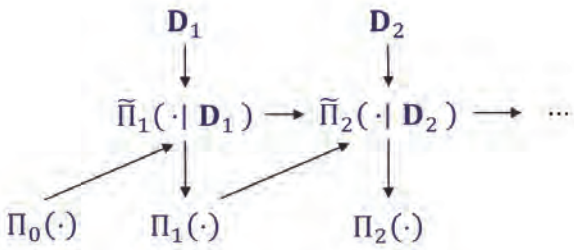

- Once $\Pi_0 \in \mathcal{Q}$, we have a sequence $\Pi_0, \Pi_1, \ldots, \Pi_T \in \mathcal{Q}$ of updated belief distributions corresponding to the sequentially available data $\mathbf{D}_1, \ldots, \mathbf{D}_T$.

Lin, D. "Online learning of nonparametric mixture models via sequential variational approximation". *Proc. NIPS*. 2013

Choi, J., Lee, J., Kim, Y. & Chae, M. "Online Bayesian inference for Cox proportional hazards model". To appear in *J. Comput. Graph. Statist.* 2025+

Remarks

- Ideally, one expects the final approximation to be close:

$$\Pi_T(\cdot) \approx \Pi(\cdot \mid \mathbf{D}).$$

- However, approximation errors accumulate as T increases.
- In general, the larger the class $\mathcal{Q}$, the more difficult the approximation becomes.
- Currently, there is no theoretical guidance on:
  - how large the accumulated error can be;
  - how rich the class $\mathcal{Q}$ should be;
  - how large the number of updates T can be.

Theoretical set-up

- For theoretical tractability, we consider regular parametric models.
  - Roughly speaking, the log-likelihood is smooth in θ.
  - Example: generalized linear models
- We assume the existence of a true parameter θ_0 that generates the data.
- We further assume the model is well-specified, i.e., $\theta_0 \in \Theta$.

Bernstein–von Mises theorem

THEOREM (Bernstein–von Mises) Suppose that p is fixed, the model is regular, and $\pi_0(\theta) > 0$ in a neighborhood of θ_0. Then,

$$\mathbb{E} d_V\left(\Pi(\cdot \mid \mathbf{D}), \mathcal{N}(\hat{\theta}, \mathbf{F}_{N,\theta_0}^{-1})\right) \to 0,$$

where

$$\hat{\theta} = \theta_0 + \mathbf{F}_{N,\theta_0}^{-1} \sum_{i=1}^{N} \dot{\ell}_{\theta_0}(Y_i) \quad \text{(linear efficient estimator)},$$

$$\mathbf{F}_{N,\theta} = -\sum_{i=1}^{N} \frac{\partial^2 (\log p_{\theta_0}(Y_i))}{\partial \theta^2} \quad \text{(Fisher information matrix)}.$$

Le Cam, L. & Yang, G. L. *Locally Asymptotically Normal Families.* (Springer, 1990)

van der Vaart, A. W. *Asymptotic Statistics.* (Cambridge University Press, 1998)

Variational family

- The BvM theorem motivates using the Gaussian family for $\mathcal{Q}$ in online learning.
- The BvM theorem can be extended to settings with diverging p.
- Intuitively, the high-dimensional BvM theorem suggests that

$$\Pi_T(\cdot) \approx \Pi(\cdot \mid \mathbf{D})$$

  provided that $n \gg p$ and T is not too large.
- A rigorous justification of this approximation is nontrivial, even when $T = 1$.

Spokoiny, V. & Panov, M. "Accuracy of Gaussian approximation for high-dimensional posterior distributions". *Bernoulli*. 2025

Katsevich, A. "Improved dimension dependence in the Bernstein–von Mises theorem via a new Laplace approximation bound". *ArXiv:2308.06899*. 2023

Main goal

- Our goal is to establish sufficient conditions under which the above approximation is valid.
- Specifically, we aim to express these conditions in terms of (n, p, T) and the regularity of the underlying model.

Some technical challenges

- In online learning, the prior becomes increasingly informative over time.
- Since we use variational approximation, we must control the KL divergence, which requires delicate tail analysis.
- It is also necessary to control the accumulation of approximation errors across steps.

Notations & definitions

$$
\begin{aligned}
\Pi_t &= \mathcal{N}(\mu_t, \boldsymbol{\Omega}_t^{-1}) \\
L_t(\theta) &= \sum_{i=(t-1)n+1}^{nt} \log p_\theta(Y_i) \\
\widetilde{L}_t(\theta) &= L_t(\theta) - \frac{1}{2}(\theta - \mu_{t-1})^\top \boldsymbol{\Omega}_{t-1}(\theta - \mu_{t-1}) \\
\hat{\theta}_t &= \operatorname*{argmax}_{\theta \in \Theta} \widetilde{L}_t(\theta) \\
\theta_t^* &= \operatorname*{argmax}_{\theta \in \Theta} \mathbb{E}_t \widetilde{L}_t(\theta) \\
\mathbf{F}_{t,\theta} &= -\nabla^2 L_t(\theta) \\
\widetilde{\mathbf{F}}_{t,\theta} &= -\nabla^2 \widetilde{L}_t(\theta) = \boldsymbol{\Omega}_{t-1} + \mathbf{F}_{t,\theta}
\end{aligned}
$$

Penalized MLE

THEOREM Under regularity conditions,

$$\left\| \widetilde{\mathbf{F}}_{t,\theta_t^*}^{-1/2} (\hat{\theta}_t - \theta_t^*) \right\|_2 \lesssim r_{n,t}, \quad \forall t \le T,$$

with high probability, where

$$r_{n,t}^2 = \operatorname{tr}\left(\widetilde{\mathbf{F}}_{t,\theta_t^*}^{-1} \mathbf{F}_{t,\theta_0} \right) + (\log n + \log T) \left\| \widetilde{\mathbf{F}}_{t,\theta_t^*}^{-1} \mathbf{F}_{t,\theta_0} \right\|_2.$$

Spokoiny, V. "Penalized maximum likelihood estimation and effective dimension". *Ann. Inst. Henri Poincaré Probab. Stat.* 2017

Laplace approximation

THEOREM Under regularity conditions,

$$K\left(\Pi_t^{\mathrm{LA}}; \widetilde{\Pi}_t(\cdot \mid \mathbf{D}_t) \right) \lesssim \frac{p^2}{nt^2}$$

with high probability, where

$$\Pi_t^{\mathrm{LA}} = \mathcal{N}\left(\hat{\theta}_t, \widetilde{\mathbf{F}}_{t,\hat{\theta}_t}^{-1} \right)$$

is the Laplace approximation to $\widetilde{\Pi}_t(\cdot \mid \mathbf{D}_t)$.

Katsevich, A. "Improved dimension dependence in the Bernstein–von Mises theorem via a new Laplace approximation bound". *ArXiv:2308.06899*, 2023

Katsevich, A. "The Laplace asymptotic expansion in high dimensions". *ArXiv:2406.12706*, 2024

Katsevich, A. & Rigollet, P. "On the approximation accuracy of Gaussian variational inference". *Ann. Statist.* 2024

Spokoiny, V. "Dimension free nonasymptotic bounds on the accuracy of high-dimensional Laplace approximation". *SIAM/ASA J. Uncertain. Quantif.* 2023

Spokoiny, V. & Panov, M. "Accuracy of Gaussian approximation for high-dimensional posterior distributions". *Bernoulli*, 2025

Stepwise variational approximation

COROLLARY Under regularity conditions,

$$K\big(\Pi_t; \widetilde{\Pi}_t(\cdot \mid \mathbf{D}_t)\big) \lesssim \frac{p^2}{nt^2}$$

with high probability.

Online BvM theorem

THEOREM Under regularity conditions,

$$d_V\Big(\Pi(\cdot \mid \mathbf{D}), \Pi_T(\cdot)\Big) \lesssim \left(\frac{p_*^3}{n}\right)^{1/2}$$

with high probability, where $p_* = p \vee \log n \vee \log T$.

EXAMPLE For logistic regression with standard Gaussian design, the regularity conditions hold if $p^2 \log^4 T \ll n$.

Credible sets based on online posterior

- Let $\chi^2_{p,\alpha}$ be the $(1-\alpha)$-quantile of the χ^2_p distribution.
- Let

$$\widehat{C}_N(\alpha) = \left\{\theta \in \Theta : \left\|\mathbf{F}_{N,\theta_0}^{1/2}\left(\theta - \hat{\theta}^{\text{MLE}}_{1:T}\right)\right\|_2^2 \leq \chi^2_{p,\alpha}\right\},$$
$$\widehat{C}_{n,T}(\alpha) = \left\{\theta \in \Theta : \left\|\mathbf{\Omega}_T^{1/2}\left(\theta - \mu_T\right)\right\|_2^2 \leq \chi^2_{p,\alpha}\right\}.$$

- Then,

$$\widehat{C}_N(\alpha - \epsilon_n) \subset \widehat{C}_{n,T}(\alpha) \subset \widehat{C}_N(\alpha + \epsilon_n)$$

for $\epsilon_n \ll (p_*^3/n)^{1/2}$.

Numerical experiments

- Simple Bernoulli experiments with varying n
- $Y_i \overset{\text{iid}}{\sim} \text{Bernoulli}(0.5)$ with total sample size $N = 1000$
- Initial prior: $\Pi_0 = \mathcal{N}(0, 3^2)$
- Mini-batch sizes: $n \in \{1, 2, 4, 6, 8, 10\}$

Numerical experiments (cont.)

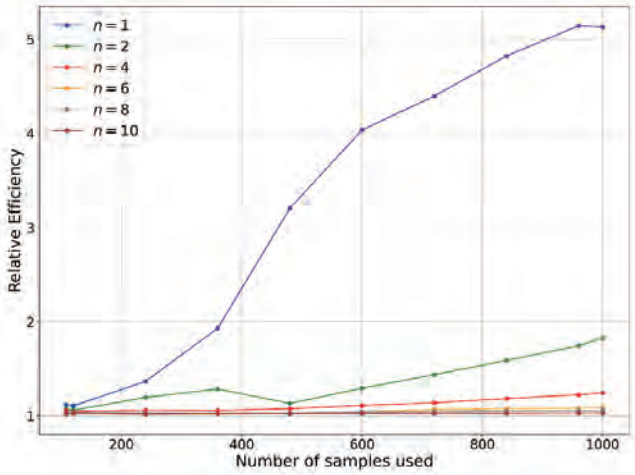

Relative Efficiency, $\mathrm{RE}_t = \dfrac{\sum_{r=1}^{100} \|\mu_{t,r} - \theta_0\|_2}{\sum_{r=1}^{100} \|\hat{\theta}^{\mathrm{MLE}}_{1:t,r} - \theta_0\|_2}$,

Numerical experiments (cont.)

Method	Coverage	Length
Batch MLE	0.940	0.248
Online $n = 1$	0.944	0.513
Online $n = 2$	0.986	0.444
Online $n = 4$	0.982	0.346
Online $n = 6$	0.980	0.310
Online $n = 8$	0.968	0.290
Online $n = 10$	0.958	0.277
Online $n = 20$	0.956	0.273
Online $n = 50$	0.950	0.259
Online $n = 200$	0.944	0.254
Online $n = 1000$	0.940	0.248

Concluding remark & future work

- Our results build on recent techniques for Gaussian approximation in high-dimensional parametric models.
- An interesting direction is to study cases where Gaussian approximation is not available,
  - e.g., most nonparametric models.
- In such cases, we may not expect $\Pi_T(\cdot) \approx \Pi(\cdot \mid \mathbf{D})$.
- However, we at least hope that Π_T concentrates around θ_0 at the optimal rate.

Thank you for attention!

Multi-Objective Optimization of Location-Routing Decisions in Biomass Supply Chains

Zaitul Marlizawati Zainuddin

Universiti Teknologi Malaysia

This talk explores how mathematical modeling and optimization support decisionmaking in biomass logistics, with a focus on the Location-Routing Problem (LRP) within the palm oil biomass supply chain. As biomass energy becomes increasingly important for sustainability, logistical challenges such as facility siting and transport routing grow more critical. The study examines three LRP models namely, the single-echelon, twoechelon, and split two-echelon developed using mixed-integer programming and solved using GAMS. These models aim to optimize costs, minimize carbon dioxide emissions, prioritize low-population areas for facility siting, quantify pretreatment needs, meet demand constraints, and incorporate a split-load transportation strategy.

UTM
UNIVERSITI TEKNOLOGI MALAYSIA

Forum "Math for Industry" 2025 (FMfI2025)
POSCO Center, Seoul, Korea

Multi-objective Optimization of Location-Routing Decision in Biomass Supply Chains

ZAITUL MARLIZAWATI ZAINUDDIN

UTM Centre for Industrial and Applied Mathematics (UTM-CIAM), Ibnu Sina Institute for Scientific and Industrial Research (ISI-SIR) &

Department of Mathematical Sciences, Faculty of Science

Universiti Teknologi Malaysia, 81310 Johor Bahru, Johor, Malaysia

Innovating Solutions

www.utm.my

Presentation Outline

1 **Problem Formulation**
- Introduction & Motivation

2 **Proposed Mixed Integer Programming (MIP) model**
- Mathematical Model
- Results
- Parameter Sensitivity Analysis

3 **Research Insights**
- Research Outcomes
- Limitations of MIP models
- Suggestions and Recommendation

1 Problem Formulation

Introduction & Motivation

Decarbonization Potential:

Biomass can replace fossil fuels for a) Electricity generation b) producing heat for industrial processes c) converting into biofuels that used in transportation

Technology Maturity:

Several biomass-based technologies (e.g. biogas, biomass boilers, pyrolysis, gasification) are already commercially available and scalable

1 Problem Formulation

Introduction & Motivation

The regions has **abundant biomass resources** :

1. Biomass energy has advantages other renewable energy sources due its consistent supply and availability [1].
2. Since most Southeast Asian nations have agriculture-based economy and have vast forest resources, they have an abundance of biomass sources for the energy sector [2].
3. National Biomass Action Plan 2023–2030 [3] reported that an estimated 20,859,180 tons of **empty fruit bunches (EFB) (palm oil biomass)** were produced in 2022, they were used for mulching or incineration but its **overall utilization rate was less than 50%.**

Turning EFB into biomass energy transforms waste into treasure.

[1] Ali, F., Dawood, A., Hussain, A., Alnasir, M. H., Khan, M. A., Butt, T. M., Janjua, N. K., & Hamid, A. (2024). Fueling the future: biomass applications for green and sustainable energy. *Discover Sustainability*, *5*(1), 156. https://doi.org/10.1007/s43621-024-00309-z

[2] Tun, M. M., Juchelkova, D., Win, M. M., Thu, A. M., & Puchor, T. (2019). Biomass Energy: An Overview of Biomass Sources, Energy Potential, and Management in Southeast Asian Countries. *Resources*, *8*(2). https://doi.org/10.3390/resources8020081

[3] Ministry of Plantation and Commodities. (2023). National Biomass Action Plan 2023-2030. In *Ministry of Plantation and Commodities (KPK)*. https://www.kpk.gov.my/kpk/images/mpi_biomass/27122023-National_Biomass_Action_Plan.pdf

Introduction & Motivation

CHALLENGE: **Biomass supply chains (BSC)** are still **underdeveloped.**

A critical challenge in utilizing biomass energy is lower cost of supply chain and **optimizes the activities needed** for converting biomass into a valuable energy source[4].

Complex decision-making problems

The biomass energy industry **faces complex decision-making** problems, particularly in

- **resource allocation,**
- **facility siting**
- **biomass collection routing, and**
- **sustainability goals**

An efficient BSC

These challenges have intensified the need for an efficient BSC, where logistics optimization plays a critical role.

[4] Zahraee, S. M., Shiwakoti, N., & Stasinopoulos, P. (2020). Biomass supply chain environmental and socio-economic analysis: 40-Years comprehensive review of methods, decision issues, sustainability challenges, and the way forward. *Biomass and Bioenergy*, *142*, 105777. https://doi.org/https://doi.org/10.1016/j.biombioe.2020.105777

1 Problem Formulation

Introduction & Motivation

Mathematics as backbone

In this AI-driven era, **mathematics** continues to serve as a **backbone** for **analyzing and solving such complex problems.**

Core challenges

A **core mathematical challenge** in this context is the **Location-Routing Problem (LRP)**, which involves

- Determine the optimal placement of biomass collection facilities
- Determine the efficient routing of transportation,
- Satisfying the sustainability goals of the BSC.

Mathematical modelling & Optimization

This talk explores how **mathematical modeling and optimization support key decision-making** in biomass energy systems, with a specific focus on solving the LRP within the BSC.

www.utm.my

Introduction & Motivation

Palm oil BSC	The research focuses on the palm oil BSC.
Issues	Logistics challenges: • **geographically dispersed resources** • **biomass characteristics** (high moisture content, bulkiness, and low energy density)
Viable solution	Incorporating **collection facilities with pretreatment operations** into the BSC presents a viable solution.
Motivation	To address the **BSC challenges** by optimizing the network as it influences **cost efficiency, carbon dioxide emissions, and social impacts.**

Introduction & Motivation

Upstream

the **most appealing area** for research

Midstream & Downstream

resemble those in the petroleum industry

Network consists of **collection facilities with pretreatment operations**

→ improve physical characteristics and energy density of biomass

→ enhance storage, transportation, and combustion efficiency

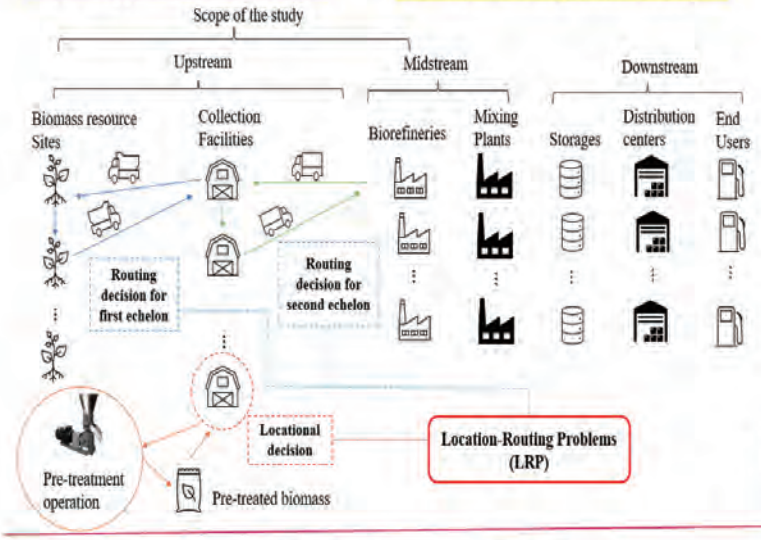

Locations **Routing**

Sustainability: Social: local community (population) | Economic: Cost | Environmental: CO_2

1 Problem Formulation

Introduction & Motivation

Mixed-integer programming model

We investigate how **classical operations research (OR) methods**, such as **mixed-integer programming models**, remain **indispensable** yet are increasingly being augmented by AI techniques **to handle the real-world complexity of biomass logistics**.

Multi-objective LRP

Special attention is given to

- the **multi-objective nature** of the LRP, where trade-offs among economic, environmental, and social sustainability must be carefully balanced.

2 Proposed Mixed Integer Programming (MIP) model

Mathematical Model:

Multi-Objective Two-Echelon Location-Routing Problem (2-LRP)

Formulated using Mixed-Integer Nonlinear Programming (MINLP)

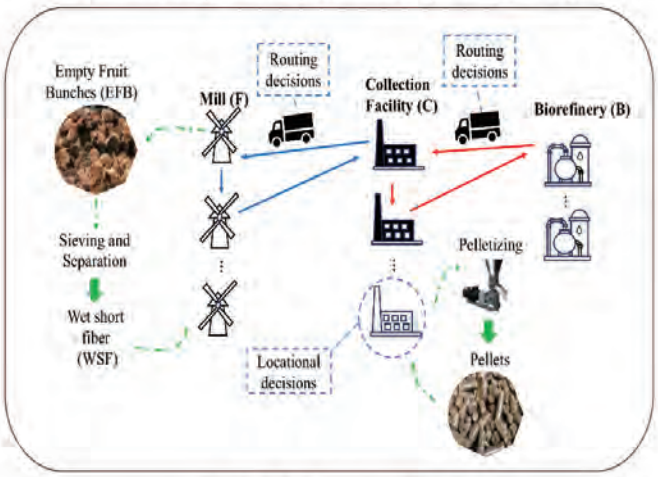

A two-echelon biomass supply chain

Assumption:

(a) Open collection facilities can serve multiple mills, whereas each mill can only be associated with a single open collection facility.
(b) Several collection facilities can fulfill the demand of a given biorefinery, with each open collection facility being restricted to a single biorefinery assignment.
(c) Within the first echelon, the vehicle routing commences at an open collection facility and ends at the same facility after covering the assigned mills. Notably, no direct paths exist between collection facilities, and each mill must be visited exactly once.
(d) In the second echelon, truck routes initiate from a biorefinery and return to the same biorefinery after visiting the designated collection facilities. No flow is permitted between biorefineries. Visitation is solely restricted to open collection facilities, and each facility must be visited only once.
(e) Truck loading remains within the defined capacity of the vehicle.
(f) The potential locations, capacities, and the populations residing in the vicinity of collection facilities are all assumed to be known.

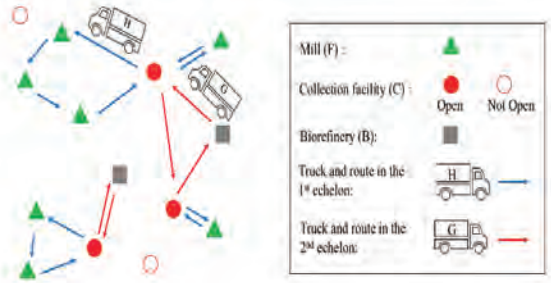

Model Formulation

OBJECTIVE FUNCTIONS

Total Cost minimization

$$f_1 = \sum_{i\in C} f_i^{EC} z_i + \sum_{i\in C} f_i^{PC} q_i^C + \sum_{i\in F\cup C}\sum_{j\in F\cup C}\sum_{h\in H} v_h^H d_{ij}^F x_{ijh} + \sum_{i\in C\cup B}\sum_{j\in C\cup B}\sum_{g\in G} v_g^G d_{ij}^S y_{ijg} \quad (1)$$

Total Population minimization

$$f_2 = \sum_{i\in C} Pop_i z_i \quad (2)$$

Total CO_2 minimization

$$f_3 = \sum_{i\in C}\sum_{j\in F}\sum_{h\in H} \gamma^{FE} d_{ij}^F x_{ijh} + \sum_{i\in B}\sum_{j\in C}\sum_{g\in G} \gamma^{GE} d_{ij}^S y_{ijg} + \sum_{i\in F}\sum_{j\in F\cup C}\sum_{h\in H} \gamma^{FL} d_{ij}^F LP_{ijh}^F + \sum_{i\in C}\sum_{j\in C\cup B}\sum_{g\in G} \gamma^{GL} d_{ij}^S LP_{ijg}^S \quad (3)$$

CONSTRAINTS

The first echelon constraints

Routing constraints

$$\sum_{j\epsilon F\cup C}\sum_{h\epsilon H} x_{ijh} = 1, \quad \forall i\epsilon F \tag{4}$$

$$\sum_{i\epsilon F\cup C} x_{ijh} = \sum_{i\epsilon F\cup C} x_{jih}, \quad \forall j\epsilon F \cup C, \forall h \in H \tag{5}$$

$$\sum_{i\epsilon F}\sum_{j\epsilon C} x_{ijh} \le 1, \ \forall h \in H \tag{6}$$

$$x_{ijh} = 0, \ \forall i,j \in F \cup C, \ i = j, \ \forall h \in H \tag{7}$$

$$\sum_{h\epsilon H} x_{ijh} = 0, \quad \forall i,j \in C \tag{8}$$

Routing and locational decision constraint

$$\sum_{j\epsilon F}\sum_{h\epsilon H} x_{ijh} \ge z_i, \ \forall i \in C \tag{9}$$

Assignment (mill to facility) and collection facility capacity (locational decision) constraint

$$\sum_{i\epsilon F} q_i^F \alpha_{ij} \le t_j^C z_j, \forall j \in C \tag{10}$$

Subtour elimination constraints

$$\sum_{h\epsilon H} x_{jih} \le \alpha_{ij}, \forall i \in F, \ \forall j \in C \tag{11}$$

$$\sum_{h\epsilon H} x_{jih} \le \alpha_{ij}, \forall i \in F, \ \forall j \in C \tag{12}$$

$$\sum_{h\epsilon H} x_{ijh} + \alpha_{ik} + \sum_{m\epsilon C, m\neq k} \alpha_{jm} \le 2, \ \forall i,j \in F, \forall k \in C \tag{13}$$

Vehicle loading and vehicle capacity constraints

$$\sum_{j\epsilon F\cup C}\sum_{h\epsilon H} LP_{ijh}^F - \sum_{j\epsilon F\cup C}\sum_{h\epsilon H} LP_{jih}^F = q_i^F, \forall i \in F \tag{14}$$

$$LP_{ijh}^F \le c_h^H x_{ijh}, \forall i,j \in F \cup C, i \neq j, \forall h \in H \tag{15}$$

$$\sum_{j\epsilon F}\sum_{h\epsilon H} LP_{jih}^F = \sum_{j\epsilon F} \alpha_{ji} q_j^F, \forall i \in C \tag{16}$$

$$LP_{ijh}^F \le \left(c_h^H - q_j^F\right) x_{ijh}, \forall i \in F \cup C, \forall j \in F, \forall h \in H \tag{17}$$

$$LP_{ijh}^F \ge q_i^F x_{ijh}, \forall i \in F, \forall j \in F \cup C, \forall h \in H \tag{18}$$

$$\sum_{j\epsilon F} LP_{ijh}^F = 0, \forall i \in C, \forall h \in H \tag{19}$$

Collected biomass quantity and pretreated biomass production constraints

$$q_j^C = \sum_{i\epsilon F}\sum_{h\epsilon H} LP_{ijh}^F, \ \forall j \in C \tag{20}$$

$$q_j^{CP} = \theta^p q_j^C, \quad \forall j \in C \tag{21}$$

CONSTRAINTS

The second echelon constraints

Routing and locational decision constraints

$$\sum_{j\epsilon C\cup B}\sum_{g\epsilon G} y_{ijg} = z_i, \ \forall i \in C \tag{22}$$

$$y_{ijg} \le z_j, \forall i \in B, \forall j \in C, \forall g \in G \tag{23}$$

Routing constraint

$$\sum_{g\epsilon G}\sum_{j\epsilon C} y_{ijg} \ge 1, \forall i \in B \tag{24}$$

$$\sum_{j\epsilon C\cup B} y_{ijg} = \sum_{j\epsilon C\cup B} y_{jig}, \forall i \in B \cup C, \forall g \in G \tag{25}$$

$$\sum_{i\epsilon B}\sum_{j\epsilon C} y_{ijg} \le 1, \forall g \in G \tag{26}$$

$$y_{ijg} = 0, \forall i,j \in B \cup C, i = j, \forall g \in G \tag{27}$$

$$\sum_{g\epsilon G} y_{ijg} = 0, \ \forall i,j \in B \tag{28}$$

Locational decision, assignment (facility to biorefinery) and biorefinery capacity constraints

$$\sum_{j\epsilon B} \beta_{ij} = z_i, \forall i \in C \tag{29}$$

$$\sum_{i\epsilon C} q_i^{CP} \beta_{ij} \le t_j^B, \forall j \in B \tag{30}$$

Subtour elimination constraints

$$\sum_{g\epsilon G} y_{ijg} \le \beta_{ij}, \forall i \in C, \ \forall j \in B \tag{31}$$

$$\sum_{g\epsilon G} y_{jig} \le \beta_{ij}, \forall i \in C, \ \forall j \in B \tag{32}$$

$$\sum_{g\epsilon G} y_{ijg} + \beta_{ik} + \sum_{m\epsilon B, m\neq k} \beta_{jm} \le 2, \ \forall i,j \in C, \forall k \in B \tag{33}$$

Vehicle loading and vehicle capacity constraints

$$\sum_{j\epsilon C\cup B}\sum_{g\epsilon G} LP_{ijg}^S - \sum_{j\epsilon C\cup B}\sum_{g\epsilon G} LP_{jig}^S = q_i^{CP}, \forall i \in C \tag{34}$$

$$LP_{ijg}^S \le c_g^G y_{ijg}, \forall i,j \in C \cup B, i \neq j, \forall g \in G \tag{35}$$

$$LP_{ijg}^S \le \left(c_g^G - q_j^{CP}\right) y_{ijg}, \forall i \in C \cup B, \forall j \in C, \forall g \in G \tag{36}$$

$$LP_{ijg}^S \ge q_i^{CP} y_{ijg}, \forall i \in C, \forall j \in C \cup B, \forall g \in G \tag{37}$$

$$\sum_{j\epsilon C} LP_{ijg}^S = 0, \forall i \in B, \forall g \in G \tag{38}$$

Collected pretreated biomass quantity and demand constraints

$$q_j^B = \sum_{i\epsilon C}\sum_{g\epsilon G} LP_{ijg}^S, \ \forall j \in B \tag{39}$$

$$q_j^B \ge D_j^B, \forall j \in B \tag{40}$$

CONSTRAINTS

Non-negativity (decision variable) constraints

$$z_i \in \{0,1\}, \forall i \in C \quad (41)$$
$$\alpha_{ij} \in \{0,1\}, \forall i \in F, \forall j \in C \quad (42)$$
$$\beta_{ij} \in \{0,1\}, \forall i \in C, \forall j \in B \quad (43)$$
$$x_{ijh} \in \{0,1\}, \forall i,j \in F \cup C, \forall h \in H \quad (44)$$
$$y_{ijg} \in \{0,1\}, \forall i,j \in C \cup B, \forall g \in G \quad (45)$$
$$LP_{ijh}^{F} \geq 0, \ \forall i,j \in F \cup C, \forall h \in H \quad (46)$$
$$LP_{ijg}^{S} \geq 0, \quad \forall i,j \in C \cup B, \forall g \in G \quad (47)$$
$$q_j^C \geq 0, \forall j \in C \quad (48)$$
$$q_j^{CP} \geq 0, \forall j \in C \quad (49)$$

Data

- Computational experiments were carried out on a test case involving **nine mills, five potential collection facilities, and two biorefineries.**
- The objective is to **validate the model's** capacity to **adapt its strategies concerning facility placements, truck routing, and assignments in accordance with varying sustainable objectives**.
- The test instance is generated using data pertaining to palm oil biomass and information regarding pelletizing technology.
- All parameters data for the computational experiments were obtained from journal articles, primarily from [5] and [6].

[5] Lam, H. L., Ng, W. P. Q., Ng, R. T. L., Ng, E. H., Aziz, M. K. A., & Ng, D. K. S. (2013). Green strategy for sustainable waste-to-energy supply chain. Energy, 57, 4–16. https://doi.org/10.1016/j.energy.2013.01.032

[6] How, B. S., Tan, K. Y., & Lam, H. L. (2016). Transportation decision tool for optimisation of integrated biomass flow with vehicle capacity constraints. Journal of Cleaner Production, 136, 197–223. https://doi.org/10.1016/j.jclepro.2016.05.142

Results
Single-objective Optimization

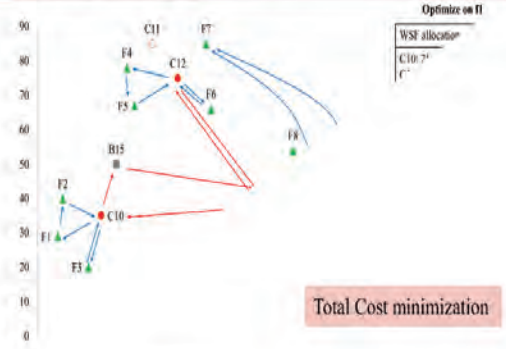

Data #2-D1

Total Cost minimization

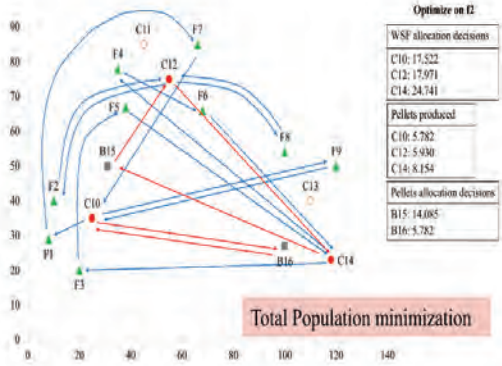

Total Population minimization

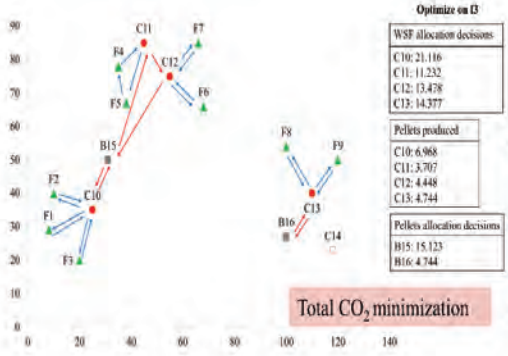

Total CO_2 minimization

Weighted Sum Approach

- Given that the **units of the objective functions** ($f_i, i = 1, 2, 3 \ldots$) may be **different**, each objective function is optimized individually to determine its optimal value ($f_i^*, i = 1, 2, 3 \ldots$).
- Equation (50) transforms the objective function (Mf) into a dimensionless unit (**normalization**) by dividing the weighted objective functions ($\omega_i f_i$) by their respective optimum values (f_i^*).
- This research assumes each objective is of equal importance with $\omega_i = 1$, implying that all weights are equal.
- Since the objective functions in this research aim to minimize total cost, affected population, and total CO_2 emissions, Equation (50) falls under the case of minimization,

$$\text{Minimize} \qquad \text{Mf}(f_i) = \sum_i \frac{\omega_i f_i}{f_i^*}, \quad \text{i} = 1,2,3 \ldots \qquad (50)$$

Results

Multi-objective Optimization

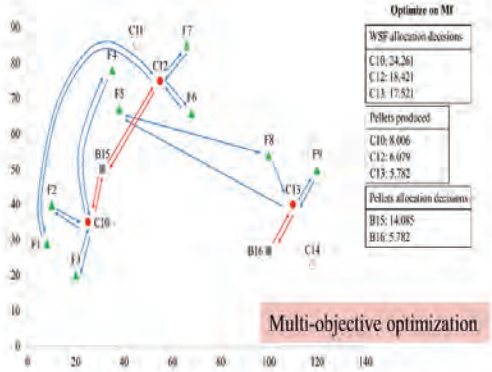

Data #2-DI

Multi-objective optimization

The 2-LRP model saw the **most significant impact** on **environmental performance**, with a **43.9% increase in CO_2 emissions**, while **economic performance** experienced only a **negligible decline of 0.036%,** and **social performance decreased by 1.96%.**

Parameter Sensitivity Analysis

- A sensitivity analysis was undertaken to assess the impact of certain parameters (results from multi-objective optimization using the weighted sum approach).
- Three parameters were selected for analysis:
  - **transportation cost,**
  - **CO_2 emission rates,**
  - **collection facility capacity.**
- These parameters were varied within a range of [-40%, 40%] with increments of 10% to evaluate the impact of the uncertainty in parameter values on
  - **Supply chain network configuration and decisions (decision variables).**

Effect of the transportation cost on network decisions

Optimize	First Echelon Decisions	Second Echelon Decisions
-40%	C10: F1, F2, F3, F5 (24.261, 8.006) C12: F4, F7, F9 (20.667, 6.820) C13: F6, F8 (15.276, 5.041) C10-F1-F2-C10 (0-4.942-13.928) C10-F3-C10 (0-7.189) C10-F5-C10 (0-3.145) C12-F4-C12 (0-8.087) C12-F7-C12 (0-7.189) C12-F9-C12 (0-5.391) C13-F6-C13 (0-6.29) C13-F8-C13 (0-8.986)	B15: C10, C12 (14.826) B16: C13 (5.041) B15-C10-B15 (0-8.006) B15-C12-B15 (0-6.820) B16-C13-B16 (0-5.041)
0%	[a]C10: F2, F3, F4 [b](24.261, 8.006) C12: F1, F6, F7 (18.241, 6.079) C13: F5, F8, F9 (17.522, 5.782) [c]C10-F2-C10 (0-8.986) C10-F3-C10 (0-7.189) C10-F4-C10 (0-8.087) C12-F1-C12 (0-4.942) C12-F6-C12 (0-6.290) C12-F7-C12 (0-7.189) C13-F5-F8-C13 (0-3.145-12.131) C13-F9-C13 (0-5.391)	[d]B15: C10, C12 [e](14.085) B16: C13 (5.782) [f]B15-C10-B15 (0- 8.006) B15-C12-B15 (0-6.079) B16-C13-B16 (0-5.782)
40%	C10: F1, F2, F3, F5 (24.261, 8.006) C12: F4, F7, F9 (20.667, 6.820) C13: F6, F8 (15.276, 5.041) C10-F1-F2-C10 (0-4.942-13.928) C10-F3-C10 (0-7.189) C10-F5-C10 (0-3.145) C12-F4-C12 (0-8.087) C12-F7-C12 (0-7.189) C12-F9-C12 (0-5.391) C13-F6-C13 (0-6.29) C13-F8-C13 (0-8.986)	B15: C10, C12 (14.826) B16: C13 (5.041) B15-C10-B15 (0-8.006) B15-C12-B15 (0-6.820) B16-C13-B16 (0-5.041)

Note:
(a) "C10: F2, F3, F4" denotes that the facility placement at location C10, with F2, F3, and F4 assigned to it.
(b) "(24.261, 8.006)" indicates that the facility will receive 24.261 metric tons of WSF and produce 8.006 metric tons of pellets.
(c) "C10-F2-C10 (0-8.986)" means that the route begins from C10 with zero load, travels to F2, and ends the route back to C10 with a load of 8.986 metric tons of WSF.
(d) "B15: C10, C12" denotes that B15 are assigned with C10 and C12.
(e) "(14.085)" indicates that the biorefinery receives 14.085 metric tons of pellets.
(f) "B15-C10-B15 (0- 8.006)" indicates the truck starts from B15 without any load, transports 8.006 metric tons of pellets from C10, and returns to B15.

- The sensitivity analysis reveals that changes in transportation costs do not affect locational decisions, with C10, C12, and C13 consistently chosen for facility placement.
- While there are minor adjustments in the assignment, routing, biomass allocation, and pellet production decisions (decision variables), the number of routes in the first echelon remains constant at eight trucks, fully utilizing available resources.
- Similarly, decisions in the second echelon exhibit minimal variation across scenarios, indicating limited sensitivity to transportation cost changes.
- This suggests that while the uncertainty in transportation costs may influence certain decisions, locational choices remain largely unaffected.
- Despite variations in the transportation cost parameter, **constraints imposed by facility capacities, truck availability, and demand lead to relatively consistent network configurations.**

Effect of the CO_2 emission rates on network decisions

Optimize	First Echelon Decisions	Second Echelon Decisions
-40%	Decisions same as the original CO_2 emission rates (0%)	
0%	[a]C10: F2, F3, F4 [b](24.261, 8.006) C12: F1, F6, F7 (18.241, 6.079) C13: F5, F8, F9 (17.522, 5.782) [c]C10-F2-C10 (0-8.986) C10-F3-C10 (0-7.189) C10-F4-C10 (0-8.087) C12-F1-C12 (0-4.942) C12-F6-C12 (0-6.290) C12-F7-C12 (0-7.189) C13-F5-F8-C13 (0-3.145-12.131) C13-F9-C13 (0-5.391)	[d]B15: C10, C12 [e](14.085) B16: C13 (5.782) [f]B15-C10-B15 (0- 8.006) B15-C12-B15 (0-6.079) B16-C13-B16 (0-5.782)
40%	Decisions same as the original CO_2 emission rates (0%)	

Note:
(a) "C10: F2, F3, F4" denotes that the facility placement at location C10, with F2, F3, and F4 assigned to it.
(b) "(24.261, 8.006)" indicates that the facility will receive 24.261 metric tons of WSF and produce 8.006 metric tons of pellets.
(c) "C10-F2-C10 (0-8.986)" means that the route begins from C10 with zero load, travels to F2, and ends the route back to C10 with a load of 8.986 metric tons of WSF.
(d) "B15: C10, C12" denotes that B15 are assigned with C10 and C12.
(e) "(14.085)" indicates that the biorefinery receives 14.085 metric tons of pellets.
(f) "B15-C10-B15 (0- 8.006)" indicates the truck starts from B15 without any load, transports 8.006 metric tons of pellets from C10, and returns to B15.

- Interestingly, the **results of decision variables show no sensitivity to changes in CO_2 emission rates**, with locational, allocation, production, and routing decisions remain consistent with the original emission rates.

Effect of the collection facility capacity on network decisions

Optimize	First Echelon Decisions	Second Echelon Decisions
-40%	C10: F1, F2 (13.928, 4.596) C11: F4, F6 (14.377, 4.744) C12: F3, F7 (14.377, 4.744) C13: F8, F9 (14.377, 4.744) C14: F5 (3.145, 1.038)	B15: C10, C11, C12 (14.085) B16: C13, C14 (5.782)
	C10-F1-F2-C10 (0-4.942-13.928) C11-F4-C11 (0-8.087) C11-F6-C11 (0-6.290) C12-F3-C12 (0-7.189) C12-F7-C12 (0-7.189) C13-F8-C13 (0-8.986) C13-F9-C13 (0-5.391) C14-F5-C14 (0-3.145)	B15-C10-B15 (0-4.596) B15-C11-B15 (0-4.744) B15-C12-B15 (0-4.744) B16-C14-C13-B16 (1.038-5.782)
0%	[a]C10: F2, F3, F4 [c](24.261, 8.006) C12: F1, F6, F7 (18.241, 6.079) C13: F5, F8, F9 (17.522, 5.782)	[d]B15: C10, C12 [e](14.085) B16: C13 (5.782)
	[b]C10-F2-C10 (0-8.986) C10-F3-C10 (0-7.189) C10-F4-C10 (0-8.087) C12-F1-C12 (0-4.942) C12-F6-C12 (0-6.290) C12-F7-C12 (0-7.189) C13-F5-F8-C13 (0-3.145-12.131) C13-F9-C13 (0-5.391)	[f]B15-C10-B15 (0- 8.006) B15-C12-B15 (0-6.079) B16-C13-B16 (0-5.782)
40%	C10: F1, F2, F3, F4, F5 (32.348, 10.675) C12: F6, F7 (13.478, 4.448) C13: F8, F9 (14.377, 4.744)	B15: C10, C12 (15.123) B16: C13 (4.744)
	C10-F1-C10 (0-4.942) C10-F2-C10 (0-8.986) C10-F3-C10 (0-7.189) C10-F4-F5-C10 (0-8.087-11.232) C12-F6-C12 (0-6.29) C12-F7-C12 (0-7.189) C13-F8-C13 (0-8.986) C13-F9-C13 (0-5.391)	B15-C10-B15 (0-10.675) B15-C12-B15 (0-4.448) B16-C13-B16 (0-4.744)

Note
(a) "C10: F2, F3, F4" denotes that the facility placement at location C10, with F2, F3, and F4 assigned to it.
(b) "(24.261, 8.006)" indicates that the facility will receive 24.261 metric tons of WSF and produce 8.006 metric tons of pellets.
(c) "C10-F2-C10 (0-8.986)" means that the route begins from C10 with zero load, travels to F2, and ends the route back to C10 with a load of 8.986 metric tons of WSF.
(d) "B15: C10, C12" denotes that B15 are assigned with C10 and C12.
(e) "(14.085)" indicates that the biorefinery receives 14.085 metric tons of pellets.
(f) "B15-C10-B15 (0- 8.006)" indicates the truck starts from B15 without any load, transports 8.006 metric tons of pellets from C10, and returns to B15.

- The analysis reveals that all decisions, including locational, allocation, and routing, are responsive to changes in capacity.
- In the scenario of a 40% capacity increment, C10, C12, and C13 also emerge as preferred facility locations, but with different assignment, allocation, and routing decisions.
- A drastic reduction of 40% in capacity requires all potential locations to open facilities.
- The sensitivity analysis reveals that **all decisions (decision variables) are responsive to the uncertainty in the facility capacity parameter**.

Research Outcomes

2-LRP
• Multi-objective
• Two-echelon network
• Multiple resource sites (mills) • Multiple facilities (collection facilities) • Multiple recipients (biorefineries)
• Quantification of pretreatment operation
• Collection facility opening decisions
• Biomass allocation decisions • Pellet allocation decisions
• Routing decisions for the 1st echelon under single-visit assumption • Routing decisions for the 2nd echelon under single-visit assumption

Research Outcomes

The features in MIP model

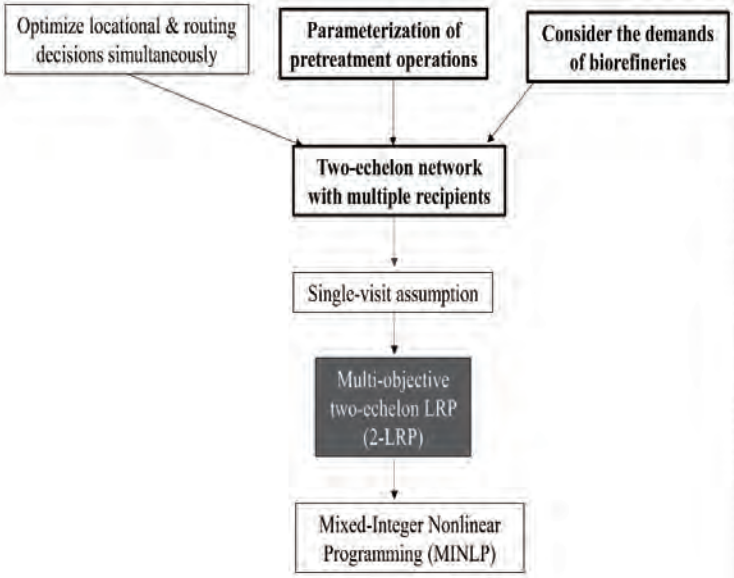

Multi-objective Optimization

- Minimize Cost
- **Minimize total population (prioritize low-density population areas)**
- **Minimize CO_2 emissions (relate it to travel distance and vehicle loads)**

Limitations of the MIP model

- assume a homogeneous vehicle fleet.
- do not account for time window constraints.
- do not consider the inherent stochastic nature of the BSC.
- assign equal importance to all objective functions during multi-objective optimization.
- impose a single-visit assumption for location visits

⇦ May not always align with real-world scenarios

Suggestions and Recommendation

Suggestions and recommendations which are believed to be worthwhile for future investigation:

- (a) Relax the single-visit assumption, as there may be scenarios where the quantity of biomass at a location exceeds a truck's capacity, making multiple visits necessary.
- (b) Consider a heterogeneous fleet of vehicles in MIP formulations, as different locations may require trucks with varying capacities where some needing smaller vehicles and others larger ones.
- (c) Extend the proposed MIP models to account for LRP with time windows, as the mills (resource sites) and facilities may not operate 24 hours a day
- (d) Incorporate stochastic elements into the MIP models to account for uncertainties in biomass availability and demand.

List of Publications

Foo, F. Y., Zainuddin, Z. M., & Pheng, H. S. (2024). Optimizing Palm Oil Biomass Supply Chain Logistics through Multi-Objective Location-Routing Model. Malaysian Journal of Fundamental and Applied Sciences, 20(2): 247 – 265. https://doi.org/10.11113/mjfas.v20n2.3085 (WOS, Q4, IF: 0.8; Indexed by Scopus)

Foo, F. Y, Zainuddin, Z. M. & Hang, S. P. (2024). Palm Oil Biomass Supply Chain Multi-Objective Two-Echelon Location-Routing Optimization. Malaysian Journal of Mathematical Sciences, 18(4): 867-901. https://doi.org/10.47836/mjms.18.4.12 (WOS, Q3, IF=0.5; Indexed by Scopus)

Foo, F. Y, Zainuddin, Z. M. & Hang, S. P. (2025). Optimizing palm oil biomass collection: genetic algorithm approaches in solving location-routing problem. Journal of Quality Measurement and Analysis, 21(2): 2025, 277-288. https://doi.org/10.17576/jqma.2102.2025.18 (WOS, Q4, IF=0.3; Indexed by Scopus)


Call for Papers!
ISMI 2026
International Seminar on Mathematics in Industry 2026
2 -3 September 2026 | Johor Bahru, Malaysia
Abstract submission deadline
1 February 2026
science.utm.my/ismi2026


UTM
THANK YOU
www.utm.my
30

Uncertainty Quantification in Scientific Machine Learning via the Information Bottleneck Principle

Ling Guo

Shanghai Normal University

Neural networks (NNs) are revolutionizing computational tasks in physics and engineering by offering novel ways to integrate data with mathematical laws. This transformative approach enables the solution of challenging inverse and ill-posed problems that remain intractable for traditional methods. However, quantifying errors and uncertainties in NN-based inference presents unique complexities compared to conventional techniques. In this talk, we introduce a novel uncertainty quantification framework based on the information bottleneck principle (IB-UQ), designed for scientific machine learning tasks such as deep neural regression and neural operator learning. We further extend this framework to incorporate physical constraints, enabling physics-informed IB-UQ for solving forward and inverse partial differential equations (PDEs) in the presence of noisy or incomplete data. The effectiveness of the proposed approach is demonstrated through a series of numerical experiments.

Integrating AI and Human Expertise for the Design and Control of Smart Materials

Pierluigi Cesana

IMI, Kyushu University

In this talk, I will explore examples from materials science and chemistry that highlight how the integration of AI-based techniques with human domain expertise enables the design and control of novel materials. Case studies will include liquid crystals, molecular machines, and other emerging systems, illustrating how this hybrid approach opens new pathways for innovation in smart materials and their applications.

Efficient deep learning methods for very high dimentional parabolic and HJB equations

TAO ZHOU

Chinese Academy of Sciences

The application of deep learning to PDEs has emerged as a prominent research area. For very high-dimensional PDEs, we introduce in this talk a deep random difference method that can dramatically reduce the computational compexity of AD, through a first-order random difference approximation of convection-diffusion operators. We present the theoretical error bounds for linear parabolic PDEs, and show the efficienty by solving quasilinear parabolic PDEs and Hamilton-Jacobi-Bellman equations in dimensions up to 10000.

Efficient deep learning method for very high dimensional parabolic PDEs and HJB equations

Tao Zhou

Chinese Academy of Sciences

Joint with Wei Cai, Shuixin Fang, and Wenzhong Zhang

Outline

Outline

Introduction

Deep learning methods for PDEs:

- Direct approach:
  - PINN/DGM: Lagaris et al. [1998], Sirignano and Spiliopoulos [2018], Raissi et al. [2019];
  - Deep Ritz: E and Yu [2018];
  - WAN: Zang et al. [2020].
  - PDE-Net: Dong et al. [2018-2024]
- Stochastic approach:
  - Deep BSDE and its variants: E et al. [2017], Raissi [2018], Zhang and Cai [2022];
  - DBDP: Huré et al. [2020], Germain et al. [2022];
  - Deep splitting: Beck et al. [2021];
  - DeepMartNet: Cai et al. [2023].

Introduction

Workflow of PINN:

$$\begin{cases} \mathcal{A}v(x) = f(x), & x \in D, \\ \mathcal{B}v(x) = g(x), & x \in \partial D. \end{cases} \tag{1}$$

$$\Downarrow \tag{2}$$

$$\min_{v} L(v), \quad L(v) := \sum_{x_i \in D} |\mathcal{A}v(x_i) - f(x_i)|^2 + \alpha \sum_{x_i \in \partial D} |\mathcal{B}v(x_i) - g(x_i)|^2 . \tag{3}$$

Advantages: Simplicity, Flexibility, and Parallelizability.

Notice: The derivatives in the operator $\mathcal{A}$ are usually computed via Automatic Differentiation (AD).

Higher-order derivatives via AD is computationally and memory intensive, motivating recent works such as

- Stein's method: He et al. [2023];
- Hutchinson trace estimation: Hu et al. [2024a];
- Stochastic dimension gradient descent: Hu et al. [2024b];
- Stochastic Taylor derivative estimator: Shi et al. [2024].

Introduction

Typical stochastic approach:

$$\left(\partial_t + b^\top(t,x)\partial_x + \frac{1}{2}\sigma\sigma^\top(t,x)\partial^2_{xx}\right) v(t,x) = f(t,x), \quad (t,x) \in [0,T) \times \mathbb{R}^d, \tag{4}$$

$$\Downarrow \text{ Feynman-Kac formula \& Itô calculus}$$

$$\begin{cases} X_t = X_0 + \displaystyle\int_0^t b(s, X_s)\,\mathrm{d}s + \int_0^t \sigma(s, X_s)\,\mathrm{d}W_s, \\ v(t, X_t) = v(0, X_0) + \displaystyle\int_0^t f(s, X_s)\,\mathrm{d}s + \int_0^t \sigma^\top \partial_x v(s, X_s)\,\mathrm{d}W_s, \end{cases} \quad t \in [0,T). \tag{5}$$

$$\Downarrow \text{ Discretization \& Deep Learning}$$

Deep BSDE, DBDP, Deep splitting, DeepMartNet, ...

Why consider the stochastic approach instead of PINNs?

- Inherent stochastic dynamics to overcome the curse of dimensionality;
- Free of computing $\partial^2_{xx} v$ using AD.

Drawback: Path simulation in (5) requires sequential computation and online updating.

Introduction

Our contribution: a new approach combining some strengths of the PINNs and the stochastic approaches:

- Free of AD for PDE derivatives;
- Time-parallelizable loss computation;
- Simple — does not require stochastic calculus theory.

Outline

Random difference method (RDM)

How to approximate 2nd order derivatives by 1st order differences?

For any smooth function $f : \mathbb{R} \to \mathbb{R}$ and any random variable $\xi : \Omega \to \mathbb{R}$,

$$\mathbb{E}\left[f(x+\sqrt{h}\xi) - f(x)\right] = h^{0.5} f'(x)\mathbb{E}\left[\xi\right] + \frac{h}{2} f''(x)\mathbb{E}\left[\xi^2\right] + \frac{h^{1.5}}{6} f^{(3)}(x)\mathbb{E}\left[\xi^3\right] + \frac{h^2}{24}\mathbb{E}\left[f^{(4)}(x+c\sqrt{h}\xi)\xi^4\right], \quad x \in \mathbb{R}, \quad c \in [0,1] \tag{6}$$

with $h > 0$ the step size. Assume

$$\mathbb{E}\left[\xi\right] = \mathbb{E}\left[\xi^3\right] = 0, \quad \mathbb{E}\left[\xi^2\right] = 1, \quad \mathbb{E}\left[\xi^4\right] < +\infty, \tag{7}$$

e.g.,

$$\xi \sim \mathrm{N}(0,1), \tag{8}$$

then

$$\mathbb{E}\left[f(x+\sqrt{h}\xi)\right] - f(x) = \frac{h}{2} f''(x) + O(h^2). \tag{9}$$

i.e.,

$$\mathbb{E}\left[\frac{f(x+\sqrt{h}\xi) - f(x)}{h}\right] = \frac{1}{2} f''(x) + O(h). \tag{10}$$

Random difference method (RDM)

How to approximate 2nd order differential operator? E.g.,

$$\mathcal{D} := \partial_t + \mu^\top \partial_x + \frac{1}{2}\mathrm{Tr}\left\{\sigma\sigma^\top \partial_{xx}^2\right\} \tag{11}$$

with $\mu = \mu\big(t,x,v(t,x)\big) \in \mathbb{R}^d$ and $\sigma = \sigma\big(t,x,v(t,x)\big) \in \mathbb{R}^{d\times q}$ for $(t,x) \in [0,T]\times\mathbb{R}^d$.

Let ξ be a random vector with independent components ξ_i satisfying

$$\mathbb{E}\left[\xi_i\right] = \mathbb{E}\left[\xi_i^3\right] = 0, \quad \mathbb{E}\left[\xi_i^2\right] = 1, \quad \mathbb{E}\left[\xi_i^4\right] < \infty, \quad i = 1,2,\cdots,q. \tag{12}$$

Let $v : [0,T]\times\mathbb{R}^d \to \mathbb{R}$ be a smooth function. The chain rule and (10) imply

$$\begin{aligned}\mathcal{D}_h v(t,x) &:= \mathbb{E}\left[\frac{v\left(t+h, x+\mu h+\sigma\sqrt{h}\xi\right) - v(t,x)}{h}\right] \\ &= \mathcal{D}v(t,x) + O\left(h\right).\end{aligned} \tag{13}$$

When $\xi \sim \mathrm{N}(0,1)$, the sufficient regularity for (13) is $g \in C^{1,2}$ following from the Itô formula [Zhang, 2017, Theorem 2.3.2].

RDM for 4th-order derivatives

How to approximate derivatives of higher order?

For example, the biharmonic equation involoves 4th order derivatives:

$$\Delta^2 u(x) = f(x), \quad x \in D \subset \mathbb{R}^d. \tag{14}$$

Assume that the random vector ξ has independent components ξ_i satisfying

$$\mathbb{E}[\xi_i] = \mathbb{E}[\xi_i^3] = 0, \quad \mathbb{E}[\xi_i^2] = 1, \quad \mathbb{E}[\xi_i^4] = 3, \quad \mathbb{E}\left[|\xi_i|^5\right] < \infty, \quad i = 1, 2, \cdots, d.$$

Taylor's expansion leads to

$$\mathbb{E}[u(x + h\xi)] = u(x) + \frac{h^2}{2} \underbrace{\mathbb{E}\left[(\xi^\top \nabla)^2 u(x)\right]}_{=\Delta u(x)} + \frac{h^4}{24} \underbrace{\mathbb{E}\left[(\xi^\top \nabla)^4 u(x)\right]}_{=3\Delta^2 u(x)} + O(h^5),$$

$$\Longrightarrow \Delta_h u(x) := \mathbb{E}\left[\frac{2}{h^2}\left(u(x + h\xi) - u(x)\right)\right] = \Delta u(x) + \frac{h^2}{4}\Delta^2 u(x) + O(h^3).$$

Extrapolation to cancel $\Delta u(x)$ leads to

$$\frac{16}{3h^2}\left(\Delta_h - \Delta_{0.5h}\right)u(x) = \Delta^2 u(x) + O(h). \tag{15}$$

RDM applied on PINN

RDM can be fitted into the PINN framwork:

$$\min_v L(v), \quad L_{\text{pinn}}(v) := \int_0^T \mathbb{E}_{X_t}\left[|R(t, X_t; v)|^2\right] \mathrm{d}t, \tag{16}$$

where $\mathbb{E}_{X_t}[\cdot]$ denotes the expectation with respect to the random vector X_t valued in $\mathbb{R}^d$, and

$$R(t, x; v) := \mathcal{D}v(t, x) - f(t, x, v(t, x)).$$

The RDM $\mathcal{D} \approx \mathcal{D}_h$ yields $R(t, x; v) \approx \mathbb{E}_\xi[R(t, x, \xi; v)]$ with

$$R(t, x, \xi; v) := \frac{v\left(t + h, x + \mu h + \sigma\sqrt{h}\xi\right) - v(t, x)}{h} - f(t, x, v(t, x))$$

$$\Longrightarrow \quad L_{\text{rdm}}(v) := \int_0^{T-h} \mathbb{E}_{X_t}\left[\left|\mathbb{E}_\xi[R(t, X_t, \xi; v)]\right|^2\right] \mathrm{d}t. \tag{17}$$

Virtues: It is AD-free, and enjoys Simplicity, Flexibility, and Parallelizability as PINNs.

Drawback: $\mathbb{E}_\xi[\cdot]$ requires an additional Monte Carlo approximation.

RDM combined with WAN

How to get rid of the inner expectation $\mathbb{E}_\xi[\cdot]$? To achieve

$$\mathbb{E}_\xi[R(t,x,\xi;v)] = 0, \quad \forall (t,x) \in [0, T-h] \times \mathbb{R}^d,$$

the Galerkin method takes the form

$$\int_0^{T-h} \rho(t,x) \mathbb{E}_\xi[R(t,x,\xi;v)] P_{X_t}(x)\, \mathrm{d}t = 0, \quad \forall \rho \in \mathcal{T}, \tag{18}$$

where $\mathcal{T}$ denotes a set of test functions, and $P_{X_t}(\cdot)$ is the density function of X_t, acting as a weight function.

Let X_t be independent of ξ, i.e., $P_{(X_t,\xi)}(x,z) = P_{X_t}(x)P_\xi(z)$. From (18),

$$\begin{aligned}
&\int_0^{T-h} \int_{\mathbb{R}^d} \rho(t,x) \mathbb{E}_\xi[R(t,x,\xi;v)] P_{X_t}(x)\, \mathrm{d}x\, \mathrm{d}t \\
=& \int_0^{T-h} \int_{\mathbb{R}^d} \int_{\mathbb{R}^q} \rho(t,x) R(t,x,z;v) P_\xi(z) P_{X_t}(x)\, \mathrm{d}z\, \mathrm{d}x\, \mathrm{d}t \\
=& \int_0^{T-h} \mathbb{E}_{(X_t,\xi)}[\rho(t,X_t) R(t,X_t,\xi;v)]\, \mathrm{d}t = 0, \quad \forall \rho \in \mathcal{T}.
\end{aligned} \tag{19}$$

The formulation (19) can be handled by weak adversarial networks [Zang et al., 2020].

RDM combined with WAN

Deep random difference method (DRDM):

$$\min_\theta \max_\eta |L(v_\theta, \rho_\eta)|^2, \quad L(v,\rho) := \int_0^{T-h} \mathbb{E}[\rho(t,X_t) R(t,X_t,\xi;v)]\, \mathrm{d}t. \tag{20}$$

with neural network approximations $v \approx v_\theta$ and $\rho \approx \rho_\eta$.

Training algorithm: For $i = 0, 1, \cdots, I$,

1. for $j = 0, 1, \cdots, J$,
$$\theta \leftarrow \theta - \delta_1 \nabla_\theta |L(v_\theta, \rho_\eta)|^2;$$
2. for $k = 0, 1, \cdots, K$,
$$\eta \leftarrow \eta + \delta_2 \nabla_\eta |L(v_\theta, \rho_\eta)|^2.$$

Desirable features inherent from PINN:

- The distribution of X_t in (20) can be flexibly designed to be adative.
- The gradient computation for $|L(v_\theta, \rho_\eta)|^2$ can be parallelized over the time-space samples of (t, X_t).

Network structures

To fulfill the terminal condition $v(T,x)=g(x)$,

$$v_\theta(T,x):=g(x),\quad v_\theta(t,x):=\phi_\theta(t,x)\ \text{ for }\ t\in[0,T),\ \ x\in\mathbb{R}^d$$

with ϕ_θ a network.

The test network ρ_η is designed as

$$\rho_\eta(t,x)=\sin\left(\Lambda\left(W_1t+W_2x+b\right)\right)\in\mathbb{R}^r,\quad \eta:=(W_1,W_2,b)\in\mathbb{R}^r\times\mathbb{R}^{r\times d}\times\mathbb{R}^r, \tag{21}$$

where $\Lambda(\cdot)$ is a multi-scale layer [Xu et al., 2025, Liu et al., 2020] given by

$$\Lambda(y_1,y_2,\cdots,y_r):=(cy_1,2cy_2,\cdots,rcy_r),\quad c:=10/r.$$

Trick: ρ_η is vector-valued ($r\geq 600$ in experiments) to stabilize the adversarial training.

Spatial sampling rule

How to design the spatial sampling distribution? – An error propagation perspective.

Consider the linear PDE

$$(\partial_t+\mathcal{L})v(t,x)=f(t,x),\quad (t,x)\in[0,T)\times\mathbb{R}^d$$

with

$$\mathcal{L}:=\mu^\top(t,x)\partial_x+\frac{1}{2}\mathrm{Tr}[\sigma\sigma^\top(t,x)\partial^2_{xx}].$$

For $\hat{v}\approx v$, define the **residual** $\hat{r}(t,x)$ by

$$\hat{r}(t,x):=(\partial_t+\mathcal{L})\hat{v}(t,x)-f(t,x).$$

The error $\epsilon:=\hat{v}-v$ satisfies the **error equation**

$$(\partial_t+\mathcal{L})\epsilon(t,x)=\hat{r}(t,x),\quad (t,x)\in[0,T)\times\mathbb{R}^d. \tag{22}$$

Spatial sampling rule

The error equation (22) can be "solved" by adjoint technique:

$$\epsilon(0,x_0)=\int_{\mathbb{R}^d}\epsilon(T,x)p(T,x)\,\mathrm{d}x-\int_0^T\int_{\mathbb{R}^d}\hat{r}(s,x)p(s,x)\,\mathrm{d}x\,\mathrm{d}s,\quad x_0\in\mathbb{R}^d, \tag{23}$$

where $p:[0,T]\times\mathbb{R}^d\to\mathbb{R}$ satisfies the **Fokker-Planck equation**:

$$\begin{cases}(\partial_t-\mathcal{L}^*)p(t,x)=0, & (t,x)\in(0,T]\times\mathbb{R}^d,\\ p(0,x)=\delta_{x_0}(x), & x\in\mathbb{R}^d,\end{cases} \tag{24}$$

where $\mathcal{L}^*$ is the adjoint operator of $\mathcal{L}$, and δ_{x_0} denotes the Dirac function.

Remarks:

- $p(t,x)$ **serves as a reasonable sampling weight:** According to (23), $p(t,x)$ quantifies the influence of $\hat{r}(t,x)$ on $\epsilon(0,x_0)$.
- $p(t,x)$ **can be sampled via SDE simulation:** The map $x\mapsto p(t,x)$ is the density function of X_t [Pavliotis, 2014, Proposition 3.3] governed by

$$X_t=x_0+\int_0^t\mu(s,X_s)\,\mathrm{d}s+\int_0^t\sigma(s,X_s)\,\mathrm{d}B_s,\quad t\in[0,T]. \tag{25}$$

- We call (25) the **dynamic sampling** as the SDE shows the dynamics of $\mathcal{L}$.

17 / 43

Dynamic sampling

How the dynamic sampling works for nonlinear $\mathcal{L}$?

$$\mathcal{L}=\mu^\top(t,x,v)\,\partial_x+\frac{1}{2}\mathrm{Tr}\left\{\sigma\sigma^\top(t,x,v)\partial^2_{xx}\right\}.$$

With the neural network approximation $v_\theta\approx v$,

$$X_t=x_0+\int_0^t\mu(s,X_s,v_\theta(s,X_s))\,\mathrm{d}s+\int_0^t\sigma(s,X_s,v_\theta(s,X_s))\,\mathrm{d}B_s,\quad t\in[0,T]. \tag{26}$$

Notice: Simulating (26) requires sequential computation. Fortunately, it is not necessary to perform this sequential simulation for every training step.

Training algorithm:
Generate the sample paths $\{X_t^m:t\in[0,T],1\le m\le M\}$ by (26). For $i=0,1,\cdots,I$,

1. for $j=0,1,\cdots,J$,
$$\theta\leftarrow\theta-\delta_1\nabla_\theta\left|L(v_\theta,\rho_\eta)\right|^2;$$
2. for $k=0,1,\cdots,K$,
$$\eta\leftarrow\eta+\delta_2\nabla_\eta\left|L(v_\theta,\rho_\eta)\right|^2;$$
3. if i is divisible by I_0, update $r\%$ of the paths $\{X_t^m:t\in[0,T]\}$ by (26).

In experiments, we set $I_0=100$ and $r\%=20\%$.

18 / 43

Outline

HJB equation

The **Hamilton-Jacobi-Bellman (HJB) equation** is given by

$$\partial_t v(t,x) + \inf_{\kappa \in U} \{\mathcal{L}^\kappa v(t,x) + c(t,x,\kappa)\} = 0, \quad (t,x) \in [0,T) \times \mathbb{R}^d, \tag{27}$$

where

$$\mathcal{L}^\kappa := \mu^\top(t,x,\kappa)\partial_x + \frac{1}{2}\operatorname{Tr}\left\{\sigma\sigma^\top(t,x,\kappa)\,\partial^2_{xx}\right\} \text{ for } \kappa \in U \subset \mathbb{R}^m, \tag{28}$$

and μ, σ and c are given functions valued in $\mathbb{R}^d$, $\mathbb{R}^{d\times q}$ and $\mathbb{R}$, respectively.

Policy improvement algorithm [Al-Aradi et al., 2022, Sect. 3]:
Alternately solve

$$(\partial_t + \mathcal{L}^u)v(t,x) + c\,(t,x,u(t,x)) = 0, \tag{29}$$

and

$$u(t,x) = \arg\min_{\kappa \in U} \{\mathcal{L}^\kappa v(t,x) + c\,(t,x,\kappa)\}, \tag{30}$$

where $\mathcal{L}^u := \mathcal{L}^{u(t,x)}$.

DRDM for linear PDE

Given u, the linear PDE (29) can be handled by the DRDM (20):

$$\min_{v} \max_{\rho} \left| L\left(u, v, \rho\right) \right|^2, \tag{31}$$

where

$$\begin{aligned} L\left(u, v, \rho\right) &:= \int_0^{T-h} \mathbb{E}\left[\rho(t, X_t) R(t, X_t, \xi; u, v)\right] \mathrm{d}t, \\ R(t, x, \xi; u, v) &:= \frac{v(t+h, x+\xi_h^{t,x,u}) - v(t,x)}{h} + c(t, x, u(t,x)), \\ \xi_h^{t,x,u} &:= \mu\left(t, x, u(t,x)\right) h + \sigma\left(t, x, u(t,x)\right) \sqrt{h} \xi. \end{aligned} \tag{32}$$

AD-free formulation for feed-back control

How to get rid of $\mathcal{L}^\kappa$ in the minimization condition (30)?

$$\begin{aligned} u(t,x) &= \arg\min_{\kappa \in U} \left\{ \mathcal{L}^\kappa v(t,x) + c\left(t, x, \kappa\right) \right\} \\ &= \arg\min_{\kappa \in U} \underbrace{\left\{ \partial_t v(t,x) + \mathcal{L}^\kappa v(t,x) + c\left(t, x, \kappa\right) \right\}}_{\approx \mathbb{E}_\xi\left[R(t,x,\xi;\kappa,v)\right]} \\ &\approx \arg\min_{\kappa \in U} \mathbb{E}_\xi\left[R(t, x, \xi; \kappa, v)\right]. \end{aligned} \tag{33}$$

To avoid the pointwise minimization for each (t, x), consider the averaged version of (33):

$$u = \arg\min_{\bar{u} \in \mathcal{U}_{\mathrm{ad}}} L\left(\bar{u}, v, 1\right), \quad L\left(u, v, 1\right) := \int_0^{T-h} \mathbb{E}\left[R(t, X_t, \xi; u, v)\right] \mathrm{d}t, \tag{34}$$

where

$$\mathcal{U}_{\mathrm{ad}} := \left\{ u : [0,T] \times \mathbb{R}^d \to U \middle| \; u \text{ is Lebesgue measurable} \right\}. \tag{35}$$

AD-free SOC-MartNet

AD-free SOC-MartNet:

Generate the sample paths $\{X_t^m : t \in [0,T], 1 \le m \le M\}$ by

$$X_t^m = X_0^m + \int_0^t \mu(s, X_s^m, u_\alpha(s, X_s^m))\,\mathrm{d}s + \int_0^t \sigma(s, X_s^m, u_\alpha(s, X_s^m))\,\mathrm{d}B_s^m. \tag{36}$$

For $i = 0, 1, \cdots, I$,

1. for $j = 0, 1, \cdots, J$,

$$\theta \leftarrow \theta - \delta_1 \nabla_\theta \left| L(u_\alpha, v_\theta, \rho_\eta) \right|^2,$$
$$\alpha \leftarrow \alpha - \delta_2 \nabla_\alpha L(u_\alpha, v_\theta, 1);$$

2. for $k = 0, 1, \cdots, K$,

$$\eta \leftarrow \eta + \delta_3 \nabla_\eta \left| L(u_\alpha, v_\theta, \rho_\eta) \right|^2.$$

3. if i is divisible by I_0, update $r\%$ of the paths $\{X_t^m : t \in [0,T]\}$ by (36).

Remark: The AD-free SOC-MartNet can also be deduced from the martingale approach [Cai et al., 2024a,b].

Outline

Numerical tests: parameter setting

Parameter settings:

- Time steps: $N = 100$.
- Batch size: 256 random paths of X_t are used for each iteration step.
- Learning rates at ith step: $\delta_0 \times 10^{-3} \times 0.01^{i/I}$ for u_α and v_θ, $\delta_0 \times 10^{-2} \times 0.01^{i/I}$ for ρ_η, where $\delta_0 := 3d^{-0.5}$ for $d \leq 1000$ and $\delta_0 := 3d^{-0.8}$ for $d > 1000$.
- Network structure: u_α and v_θ consist of 4 hidden layers with W ReLU units in each hidden layer, where $W = 5d + 10$, $2d + 10$ and $d + 10$ for $d < 1000$, $1000 < d < 10^4$ and $d = 10^4$, respectively.
- Optimizer: RMSProp.
- Inner iteration step: $J = 2$ and $K = 1$.
- Device: a compute node equipped with 8 GPUs (NVIDIA A100-SXM4-80GB)

Numerical tests: Convection-diffusion equation

Convection-diffusion equation:

$$\begin{cases} (\partial_t + \mathcal{L})\, v(t,x) = 0, \quad (t,x) \in [0,T) \times \mathbb{R}^d, \\ v(T,x) = \dfrac{1}{d} \displaystyle\sum_{i=1}^{d} \{\tanh(x_i) + \cos(10x_i)\}, \quad x \in \mathbb{R}^d, \end{cases} \tag{37}$$

where $\mathcal{L}$ is the convection-diffusion operator defined by

$$\mathcal{L} := \mu^\top \partial_x + \frac{\bar{\sigma}^2}{2} \Delta_x, \quad T = 2, \quad \bar{\sigma}^2 = 0.1,$$

$$\mu(t,x) := c \times \Big(\tanh(10x_1), \tanh(10x_2), \cdots, \tanh(10x_d) \Big)^\top$$

with $c = 1$ or 5. The exact solution is given by

$$v(t,x) = \mathbb{E}\left[v(T, X_T^{t,x}) \right], \quad X_s^{t,x} = x + \int_t^s \mu(r, X_r^{t,x})\, \mathrm{d}r + \int_t^s \bar{\sigma}\, \mathrm{d}B_r, \tag{38}$$

where $\mathbb{E}[\cdot]$ is approximated by the Monte-Carlo method using 10^6 samples of $X_T^{t,x}$.

Problem feature: The drift coefficient $\mu(t,x)$ exhibits rapid transitions near $x = 0$. When $c \gg \bar{\sigma}$, a shock forms around $(t,x) = (0,0)$.

Numerical tests: Convection-diffusion equation

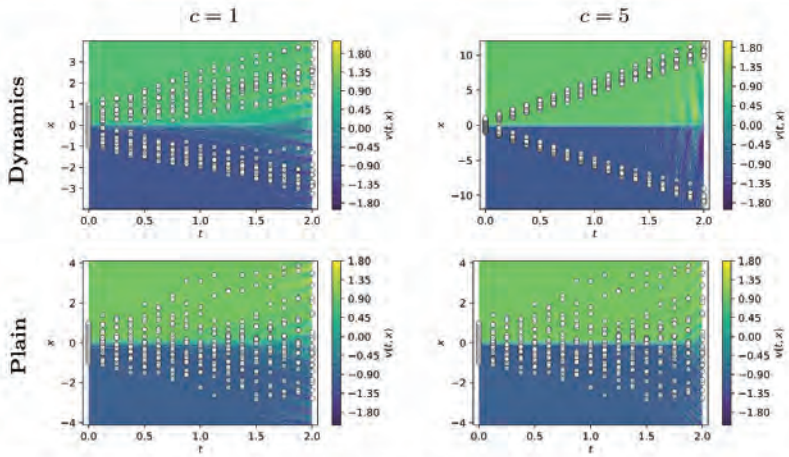

Figure 1: The color indicates the exact solution $v(t, x)$ with $d = 1$. The scatter plots show the spatial samples.

- Sampling using the **dynamics** of $\mathcal{L}$:

$$X_t = X_0 + \int_0^t \mu(s, X_s)\,\mathrm{d}s + \int_0^t \sigma(s, X_s)\,\mathrm{d}B_s, \quad X_0 \sim \mathrm{U}([-1, 1]), \quad t \in [0, T]. \tag{39}$$

- **Plain** sampling: $X_t \sim \mathrm{U}([-1, 1]) + \mathrm{N}(0, t)$.

Numerical tests: Convection-diffusion equation

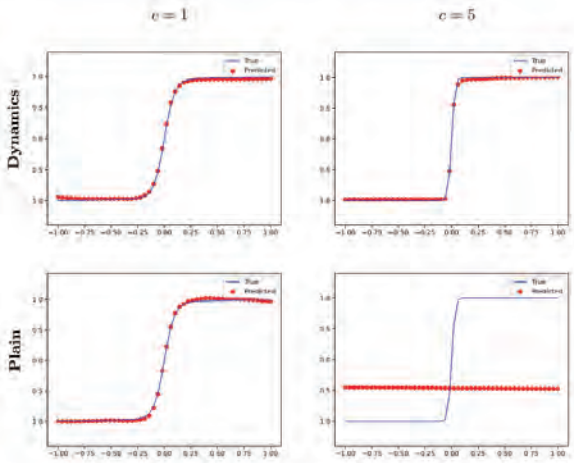

Figure 2: Numerical results for $x \mapsto v(0, x)$ from (37) with $d = 1$.

- When $c = 5$, i.e., convection dominates, the numerical solution using plain sampling fails to capture the shock structure.

Numerical tests: Convection-diffusion equation

Even in high-dimensional settings, dynamic sampling still captures the shock structure.

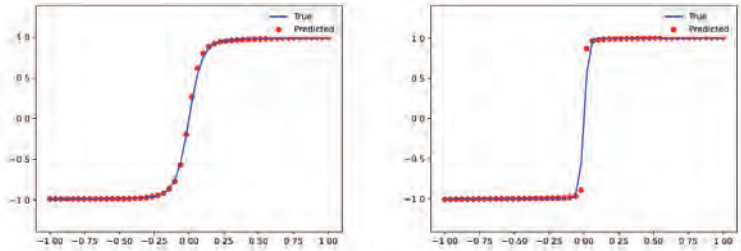

(a) $c = 1$ (b) $c = 5$

Figure 3: Numerical results obtain by the **dynamic** sampling for $s \mapsto v(0, s\mathbf{1}_d)$ with $d = 10^3$.

Why is the dynamic sampling better?

- It follows from the error propagation mechanism described in (23);

$$\epsilon(0, x_0) = \int_{\mathbb{R}^d} \epsilon(T, x) p(T, x)\, \mathrm{d}x - \int_0^T \int_{\mathbb{R}^d} \hat{r}(s, x) p(s, x)\, \mathrm{d}x\, \mathrm{d}s, \quad x_0 \in \mathbb{R}^d,$$

- It captures the solution's domain of dependence: when $\sigma \equiv 0$, $t \mapsto X_t$ is the characteristic line of the PDE (37).

Numerical Tests: high dimensional PDEs

Considered **PDE solution:**

$$v(t, x) = V\big((t - 0.5)\mathbf{1}_d + x\big), \quad \mathbf{1}_d := (1, 1, \cdots, 1)^\top \in \mathbb{R}^d, \tag{40}$$

where $V : \mathbb{R}^d \to \mathbb{R}$ is modified from [Hu et al., 2024b, (28)]:

$$V(x) := \sum_{i=1}^{d-1} c_i S(x_i, x_{i+1}) + c_d S(x_d, x_1),$$

$$c_i := \frac{1}{d}\left(1.5 - \cos(i\pi/d)\right), \quad S(x_i, x_j) := \sin\left(x_i + \cos(x_j) + x_j \cos(x_i)\right).$$

Numerical Tests: high dimensional PDEs

PDE:

$$\begin{cases} (\partial_t + \mathcal{L})\, v(t,x) + f(t,x,v(t,x)) = 0, \quad (t,x) \in [0,T) \times \mathbb{R}^d \\ v(T,x) = g(x), \quad x \in \mathbb{R}^d. \end{cases} \tag{41}$$

Considered cases:

- **Case 1:** Allen-Cahn-typed equation

$$\mathcal{L} = \Delta_x, \quad f(t,x,v) = v - v^3 + Q(t,x); \tag{42}$$

- **Case 2:** **Quasilinear** equation with diagonal Hessian

$$\mathcal{L} = \Big(\frac{v}{2} - 1\Big) \sum_{i=1}^{d} \partial_{x_i} + \frac{v^2}{2} \sum_{i=1}^{d} \partial^2_{x_i}, \quad f(t,x,v) = v^2 + Q(t,x); \tag{43}$$

- **Case 3:** **Quasilinear** equation with **dense** Hessian

$$\mathcal{L} = \Big(\frac{v}{2} - 1\Big) \sum_{i=1}^{d} \partial_{x_i} + \frac{1}{2d^2} \sum_{i,j,k=1}^{d} \sigma_{ik}\sigma_{jk} \partial_{x_i}\partial_{x_j}, \quad f(t,x,v) = v^2 + Q(t,x), \tag{44}$$
$$\sigma_{ij} = \cos(x_i) + v \sin(x_j).$$

The function $Q(t,x)$ is chosen such that (41) admits an exact solution given in (40).

Numerical Tests: high dimensional PDEs

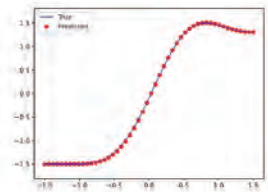

(a) $s \mapsto v(0, s\mathbf{1}_d)$, Case 1

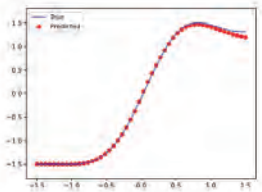

(b) $s \mapsto v(0, s\mathbf{1}_d)$, Case 2

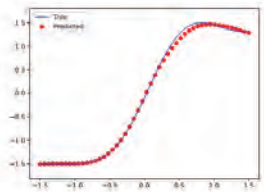

(c) $s \mapsto v(0, s\mathbf{1}_d)$, Case 3

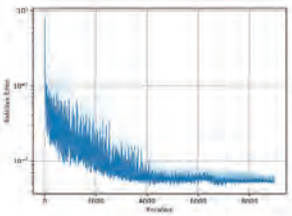

(d) RE vs Iteration, Case 1

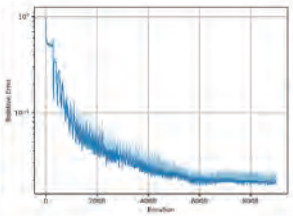

(e) RE vs Iteration, Case 2

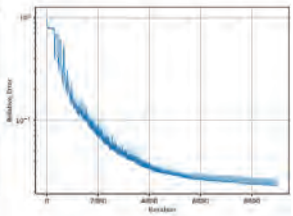

(f) RE vs Iteration, Case 3

Figure 4: Numerical results for (41) in Cases 1 to 3 with $d = 10^4$. The running times for each run are all less than 6029 seconds.

Numerical Tests: HJB equations

HJB equation extended from [Bachouch et al., 2022, Section 3.1]:

$$\begin{cases} \partial_t v + \inf_{\kappa \in \mathbb{R}^d} \left\{ (b + c\sigma\kappa)^\top \partial_x v + \frac{1}{2} |\kappa|^2 \right\} + \frac{1}{2} \mathrm{Tr} \left[\sigma\sigma^\top \partial_{xx} v \right] = 0, \\ v(T, x) = g(x), \quad x \in \mathbb{R}^d, \end{cases} \tag{45}$$

where $c > 0$, $b = b(t, x) \in \mathbb{R}^d$, $\sigma = \sigma(t, x) \in \mathbb{R}^{d \times d}$, and $T = 1$.

Stochastic optimal control problem (SOCP):

$$\min_{u:[0,T]\times\mathbb{R}^d \to \mathbb{R}^d} J(u), \quad J(u) := \int_0^T \frac{1}{2} \mathbb{E} \left[|u(t, X_t^u)|^2 \right] \mathrm{d}t + \mathbb{E} \left[g(X_T^u) \right], \tag{46}$$

$$X_t^u = X_0^u + \int_0^t (b + c\sigma u)(s, X_s^u) \, \mathrm{d}s + \int_0^t \sigma(s, X_s^u) \, \mathrm{d}W_s, \quad t \in [0, T]. \tag{47}$$

Exact solution:

$$v(t, x) = -\frac{1}{c^2} \ln \left(\mathbb{E} \left[\exp \left(-c^2 v(T, X_T^0) \right) | X_t^0 = x \right] \right), \tag{48}$$

where X_t^0 is given by (47) with $u \equiv 0$.

Numerical Tests: HJB equations

Case 1: Consider the HJB equation (45) with zero drift and smooth terminal function:

$$b = 0, \quad c = 1, \quad \sigma = \sqrt{2}, \quad v(T, x) = \ln \left(0.5(1 + |x|^2) \right), \quad x \in \mathbb{R}^d. \tag{49}$$

The resulted problem is also considered by E et al. [2017], Ji et al. [2022], Bachouch et al. [2022], Han et al. [2018], Wang et al. [2022], He et al. [2023], Raissi [2018], Hu et al. [2024b].

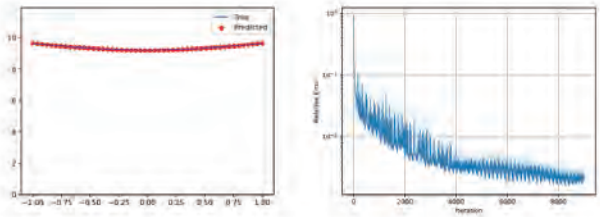

(a) $s \mapsto v(0, s\mathbf{1}_d)$ (b) RE vs Iteration

Figure 5: Numerical results for (45) with $d = 10^4$ and the parameter settings in (49). The running time for each run is less than 9450 seconds.

Numerical Tests: HJB equations

Case 2: Consider the HJB equation (45) with **nonzero drift**, **small diffusion**, and **oscillatory** terminal function:

$$b = \mathbf{1}_d, \quad c = 1, \quad \sigma = \frac{\sqrt{2}}{5}, \qquad v(T,x) = g(x - \mathbf{1}_d), \tag{50}$$

$$g(x) := \frac{1}{d}\sum_{i=1}^{d}\left\{\sin(x_i - \frac{\pi}{2}) + \sin\left(\left(0.1\pi + x_i^2\right)^{-1}\right)\right\}. \tag{51}$$

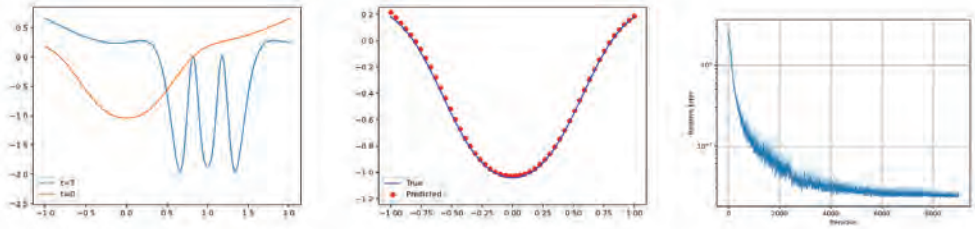

(a) Reference solution at $t = 0, T$ (b) $s \mapsto v(0, s\mathbf{1}_d)$ (c) RE vs Iteration

Figure 6: Numerical results for (45) with $d = 10^4$ and the parameter settings in (50). The running time for each run is less than 9450 seconds.

Numerical Tests: HJB equations

Case 3: Consider the HJB equation (45) with **variable drift and diffusion** coefficients, and **oscillatory terminal function**: for $i, j = 1, \cdots, d$,

$$\begin{aligned} &b_i = \sin(x_{i+1}), \quad x_{d+1} := x_1, \quad \sigma_{ij} = 0.5\delta_{ij}\tanh\left((t-0.5)^2 + \frac{1}{d}\sum_{k=1}^{d} x_k^2\right), \\ &c = 2, \quad v(T,x) = \ln\left(1 + \frac{1}{d}\sum_{i=1}^{d}\left(x_i^2 + 0.5\sin(10x_i)\right)\right). \end{aligned} \tag{52}$$

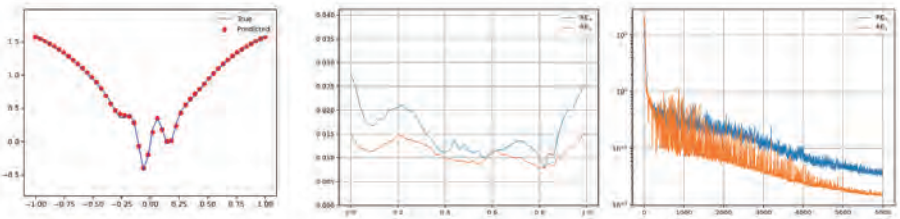

(a) $s \mapsto v(0, s\mathbf{1}_d)$ (b) $t \mapsto \mathrm{RE}(t)$ (c) RE vs Iteration

Figure 7: Numerical results for (45) with $d = 10^4$ and the parameter settings in (52). The running time for each run is less than 9678 seconds. In (b), $\mathrm{RE}_\infty(t)$ and $\mathrm{RE}_1(t)$ denote the L^∞ and L^1 relative errors on 8 samples of X_t^u at time t, where X_t^u is given by (47).

Performance bottleneck for high-dimensional problems

Problem setting: Case 2 with the maximum iteration fixed as $I = 6000$.
Network size of (u_α, v_θ): 4 hidden layers with the widths W given in the tabular.
Device: PyTorch accelerated by DDP on 8 GPUs (NVIDIA A100-SXM4-80GB).

	$d = 1000$	$d = 5000$	$d = 10000$
$W = 1024$	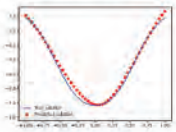 (a) RT = 42s	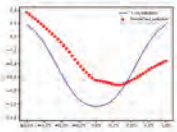 (b) RT = 62s	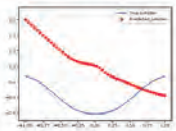 (c) RT = 103s
$W = 5000$	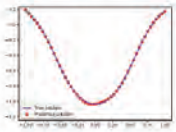 (d) RT = 1294s	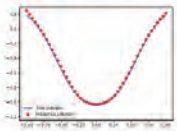 (e) RT = 1630s	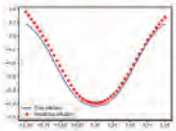 (f) RT = 2044s
$W = 10000$	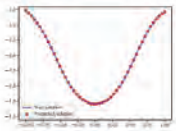 (g) RT = 4750s	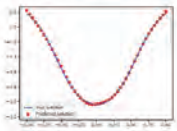 (h) RT = 5385s	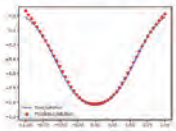 (i) RT = 6211s

Numerical Tests: an ultra high-dimensional example

PDE:

$$\begin{cases} (\partial_t + \Delta_x)\, v(t,x) + v(t,x) - v^3(t,x) + Q(t,x) = 0, & (t,x) \in [0,T) \times \mathbb{R}^d, \\ v(T,x) = g(x), & x \in \mathbb{R}^d, \end{cases} \tag{53}$$

where $d = 10^5$. The solution is identical to (40).

Network size: v_θ consists of 6 hidden layers, each with a width of $W = 10010$.

To mitigate the performance bottleneck caused by large network sizes, v_θ is trained by using the **Automatic Mixed Precision** technique.

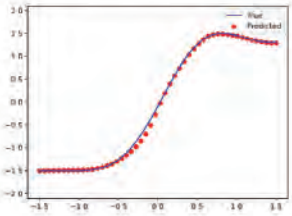

(a) $s \mapsto v(0, s\mathbf{1}_d)$

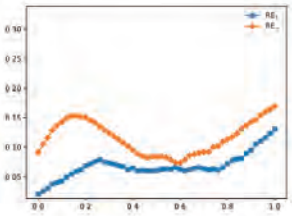

(b) $t \mapsto \mathrm{RE}(t)$

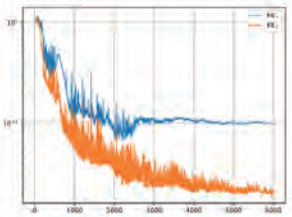

(c) RE vs Iter.

Figure 8: Numerical results for (53) with $d = 10^5$. The runtime is 3112 seconds at the 6000-th iteration.

Conclusions and future work

PINN, RDM, WAN $\Longrightarrow$ DRDM $\Longrightarrow$ Quasilinear parabolic PDEs

$\Downarrow$ Extension

AD-Free SOC-MartNet $\Longrightarrow$ SOCP & HJB equations

Extrapolated RDM $\Longrightarrow$ e.g. Biharmonic equation

Future works:

- Degenerated HJB equations without classical solution $v \in C^{1,2}$;
- Applications: Navior-Stokes equations with complex solutions, committor functions, etc.

Reference:

- Cai-Fang-Zhou, SOC-MartNet, SISC, 2024.
- Cai-Fang-Zhang-Zhou, AD-free SOC-MartNet, arXiv:2408.14395, 2024.
- Cai-Fang-Zhou, deep random difference method, arXiv:2506.20308, 2025.

39 / 43

References I

A. Al-Aradi, A. Correia, G. Jardim, D. d. F. Naiff, and Y. Saporito. Extensions of the deep Galerkin method. *Appl. Math. Comput.*, 430:Paper No. 127287, 18, 2022. ISSN 0096-3003,1873-5649. doi: 10.1016/j.amc.2022.127287. URL https://doi.org/10.1016/j.amc.2022.127287.

A. Bachouch, C. Huré, N. Langrené, and H. Pham. Deep neural networks algorithms for stochastic control problems on finite horizon: numerical applications. *Methodol. Comput. Appl. Probab.*, 24(1): 143–178, 2022. ISSN 1387-5841,1573-7713.

C. Beck, S. Becker, P. Cheridito, A. Jentzen, and A. Neufeld. Deep splitting method for parabolic PDEs. *SIAM J. Sci. Comput.*, 43(5):A3135–A3154, 2021. ISSN 1064-8275,1095-7197.

W. Cai, A. He, and D. Margolis. DeepMartNet – a martingale based deep neural network learning method for Dirichlet BVP and eigenvalue problems of elliptic pdes, 2023.

W. Cai, S. Fang, W. Zhang, and T. Zhou. A derivative-free martingale neural network soc-martnet for the hamilton-jacobi-bellman equations in stochastic optimal controls, 2024a. URL https://arxiv.org/abs/2408.14395.

W. Cai, S. Fang, and T. Zhou. Soc-martnet: A martingale neural network for the hamilton-jacobi-bellman equation without explicit inf h in stochastic optimal controls, 2024b.

W. E and B. Yu. The deep Ritz method: a deep learning-based numerical algorithm for solving variational problems. *Commun. Math. Stat.*, 6(1):1–12, 2018. ISSN 2194-6701,2194-671X. doi: 10.1007/s40304-018-0127-z. URL https://doi.org/10.1007/s40304-018-0127-z.

W. E, J. Han, and A. Jentzen. Deep learning-based numerical methods for high-dimensional parabolic partial differential equations and backward stochastic differential equations. *Commun. Math. Stat.*, 5(4):349–380, 2017. ISSN 2194-6701,2194-671X.

M. Germain, H. Pham, and X. Warin. Approximation error analysis of some deep backward schemes for nonlinear PDEs. *SIAM J. Sci. Comput.*, 44(1):A28–A56, 2022. ISSN 1064-8275,1095-7197.

J. Han, A. Jentzen, and W. E. Solving high-dimensional partial differential equations using deep learning. *Proceedings of the National Academy of Sciences*, 115(34):8505–8510, 2018.

40 / 43

References II

D. He, S. Li, W. Shi, X. Gao, J. Zhang, J. Bian, L. Wang, and T.-Y. Liu. Learning physics-informed neural networks without stacked back-propagation. In F. Ruiz, J. Dy, and J.-W. van de Meent, editors, *Proceedings of The 26th International Conference on Artificial Intelligence and Statistics*, volume 206 of *Proceedings of Machine Learning Research*, pages 3034–3047. PMLR, 25–27 Apr 2023.

Z. Hu, Z. Shi, G. E. Karniadakis, and K. Kawaguchi. Hutchinson trace estimation for high-dimensional and high-order physics-informed neural networks. *Comput. Methods Appl. Mech. Engrg.*, 424:Paper No. 116883, 17, 2024a. ISSN 0045-7825,1879-2138.

Z. Hu, K. Shukla, G. E. Karniadakis, and K. Kawaguchi. Tackling the curse of dimensionality with physics-informed neural networks. *Neural Networks*, 176:106369, 2024b. ISSN 0893-6080.

C. Huré, H. Pham, and X. Warin. Deep backward schemes for high-dimensional nonlinear PDEs. *Math. Comp.*, 89(324):1547–1579, 2020. ISSN 0025-5718,1088-6842.

S. Ji, S. Peng, Y. Peng, and X. Zhang. Solving stochastic optimal control problem via stochastic maximum principle with deep learning method. *J. Sci. Comput.*, 93(1):Paper No. 30, 28, 2022. ISSN 0885-7474,1573-7691.

I. E. Lagaris, A. Likas, and D. I. Fotiadis. Artificial neural networks for solving ordinary and partial differential equations. *IEEE transactions on neural networks*, 9(5):987–1000, 1998.

Z. Liu, W. Cai, and Z.-Q. J. Xu. Multi-scale deep neural network (MscaleDNN) for solving Poisson-Boltzmann equation in complex domains. *Commun. Comput. Phys.*, 28(5):1970–2001, 2020. ISSN 1815-2406,1991-7120.

G. A. Pavliotis. *Stochastic Processes and Applications: Diffusion Processes, the Fokker-Planck and Langevin Equations*. Texts in Applied Mathematics. Springer New York, 2014. ISBN 9781493913237.

M. Raissi. Forward-backward stochastic neural networks: Deep learning of high-dimensional partial differential equations, 2018.

M. Raissi, P. Perdikaris, and G. E. Karniadakis. Physics-informed neural networks: a deep learning framework for solving forward and inverse problems involving nonlinear partial differential equations. *J. Comput. Phys.*, 378:686–707, 2019. ISSN 0021-9991,1090-2716.

References III

Z. Shi, Z. Hu, M. Lin, and K. Kawaguchi. Stochastic taylor derivative estimator: Efficient amortization for arbitrary differential operators. In *The Thirty-eighth Annual Conference on Neural Information Processing Systems*, 2024.

J. Sirignano and K. Spiliopoulos. DGM: a deep learning algorithm for solving partial differential equations. *J. Comput. Phys.*, 375:1339–1364, 2018. ISSN 0021-9991,1090-2716. doi: 10.1016/j.jcp.2018.08.029. URL https://doi.org/10.1016/j.jcp.2018.08.029.

C. Wang, S. Li, D. He, and L. Wang. Is l^2 physics informed loss always suitable for training physics informed neural network? In A. H. Oh, A. Agarwal, D. Belgrave, and K. Cho, editors, *Advances in Neural Information Processing Systems*, 2022.

Z.-Q. J. Xu, Y. Zhang, and T. Luo. Overview frequency principle/spectral bias in deep learning. *Commun. Appl. Math. Comput.*, 7(3):827–864, 2025. ISSN 2096-6385,2661-8893. doi: 10.1007/s42967-024-00398-7. URL https://doi.org/10.1007/s42967-024-00398-7.

Y. Zang, G. Bao, X. Ye, and H. Zhou. Weak adversarial networks for high-dimensional partial differential equations. *J. Comput. Phys.*, 411:109409, 14, 2020. ISSN 0021-9991,1090-2716.

J. Zhang. *Backward stochastic differential equations*, volume 86 of *Probability Theory and Stochastic Modelling*. Springer, New York, 2017. ISBN 978-1-4939-7254-8; 978-1-4939-7256-2. From linear to fully nonlinear theory.

W. Zhang and W. Cai. FBSDE based neural network algorithms for high-dimensional quasilinear parabolic PDEs. *J. Comput. Phys.*, 470:Paper No. 111557, 14, 2022. ISSN 0021-9991,1090-2716.

Thank you!

Mining Interconnected Data: Robust, Generalizable, and Interpretable Methods

Jae-Min Yoo

KAIST

Real-world datasets often contain complex interconnections, appearing as graphs, time series, or spatiotemporal structures. Effectively leveraging these interconnections is essential for developing practical data mining techniques. In this talk, I will present our recent work on improving the robustness of graph neural networks (GNNs) to structural inconsistencies, an important challenge in real-world graphs. We identify the limitation of DropEdge, an existing augmentation technique, and introduce Aggregation Buffer, a plug-in module designed to improve robustness without compromising bias. Our method operates as a post-processing step applicable to any trained GNN, and achieves strong performance across diverse datasets with varying structural properties.

Mining Interconnected Data:
Robust, Generalizable, and Interpretable Methods

Jaemin Yoo

School of Electrical Engineering

Kim Jaechul Graduate School of AI

KAIST

Outline

1. **Introduction**
2. Method
3. Experiments
4. Summary

Graphs

- **Graphs** describe the world through relationships.
  - **Social network:** Friendships between users.
  - **Communication network:** Telecommunications between workstations.
  - **Molecular graph:** Chemical bonds between atoms.

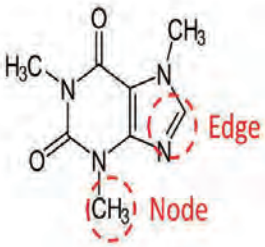

Graph-based Problems

- **Graph-based problems** generalize many applications.
  - **Link prediction:** Recommending new friends in a social network.
  - **Node classification:** Predicting network faults during communication.
  - **Graph generation:** Discovering chemical structures of new drugs.

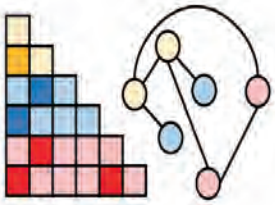

Graph Neural Networks (GNNs)

- Traditional graph mining → **Graph neural networks (GNNs)**
- **Main idea:** Learn **low-dimensional representations** of nodes.
  - Effectively summarize feature and structural information.

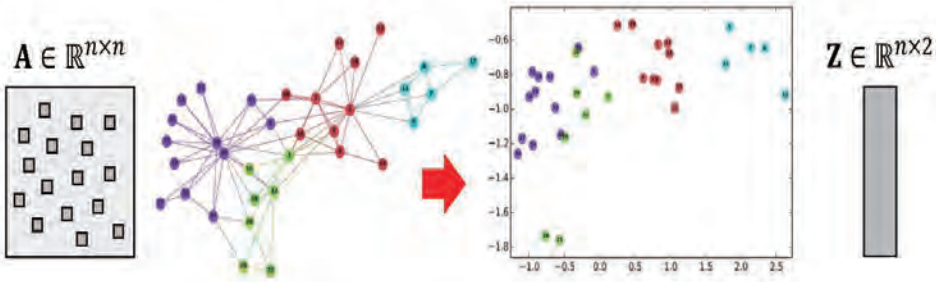

Perozzi et al. "DeepWalk: Online Learning of Social Representations." KDD 2014

GNNs are Popular

- GNN is one of the **most popular topics** in the ML community.
- One reason is that GNNs are **powerful generalization** of CNNs.
  - Into a non-Euclidean space with flexible structure.

Top 5 keywords in ICLR 2022

1. Reinforcement learning
2. Deep learning
3. Representation learning
4. Graph neural network
5. Transformer

https://github.com/fedebotu/ICLR2022-OpenReviewData

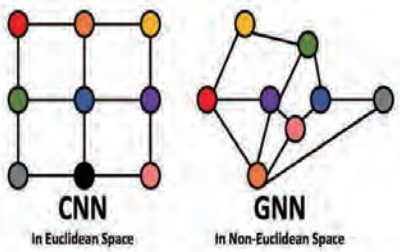

Lin et al. "A Survey on Deep Learning-Based Vehicular Communication Applications." 2021

Structural Inconsistencies

- GNNs are, however, vulnerable to **structural inconsistencies**.
  - Different nodes have different topological patterns.
  - GNNs are *overfit* to the majority of patterns in data.
  - As a result, GNNs show poor performance on the minority.

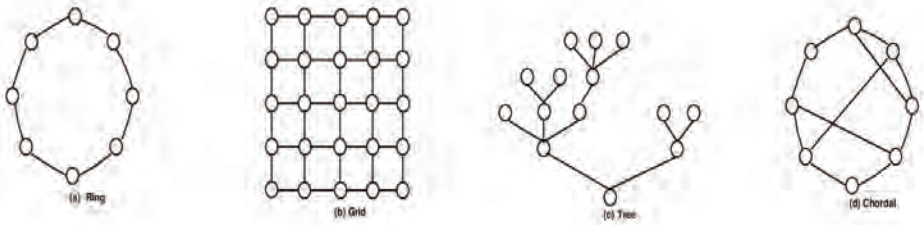

Two Types of Inconsistencies

- **Degree bias:** Poor performance on low-degree nodes.
  - Since most knowledge is focused on high-degree nodes.
- **Structural disparity:** Fail on structurally different nodes.
  - E.g., heterophile neighbors in homophile graphs.

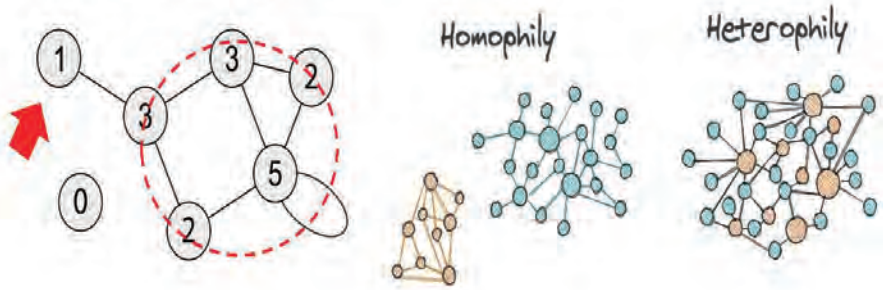

Outline

1. Introduction
2. **Method**
3. Experiments
4. Summary

Previous Solution: DropEdge

- **DropEdge** is used for improving the *structural robustness* of GNNs.
  - Randomly removes a subset of edges during training.
  - Exposes the GNN to a variety of topological structures.
- We will reveal its weakness through the **bias-robustness tradeoff**.

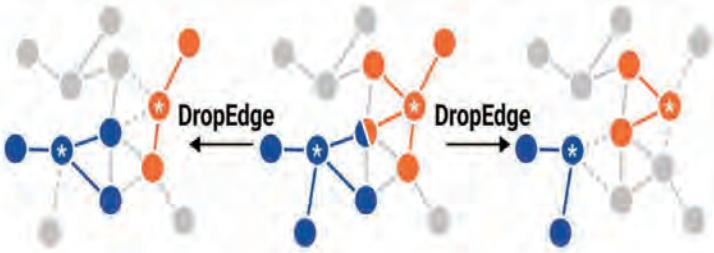

Bias-Robustness Tradeoff

- Let G_i be the i-th graph, and y_i be its target label.
- In a typical classification task, the objective function is:

$$\mathcal{L}(\theta) = D_{\mathrm{KL}}(P(y_i|G_i), Q_\theta(y_i|G_i))$$

- D_{KL} is the KL divergence (i.e., distributional distance).
- P is the true distribution of labels.
- Q_θ is the modeled distribution to be learned.

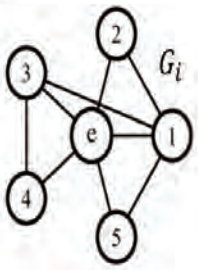

$f_\theta(G_i) \mapsto y_i$

Bias-Robustness Tradeoff (cont.)

- With DropEdge, the objective changes to a **denoising function**:

$$\tilde{\mathcal{L}}(\theta) = D_{\mathrm{KL}}(P(y_i|G_i), Q_\theta(y_i|\tilde{G}_i))$$

$\tilde{G}_i$ = Augmented graph

- With some assumptions, it is re-written as:

$$\tilde{\mathcal{L}}_Q(\theta) = D_{\mathrm{KL}}(P(y_i|G_i), Q_\theta(y_i|G_i)) \quad \rightarrow \textbf{Bias}$$
$$+ D_{\mathrm{KL}}(Q_\theta(y_i|G_i), Q_\theta(y_i|\tilde{G}_i)) \quad \rightarrow \textbf{Robustness}$$

Failure of DropEdge

- DropEdge shows a **marginal effect** on improving the robustness.
  - At the expense of increasing the bias term!

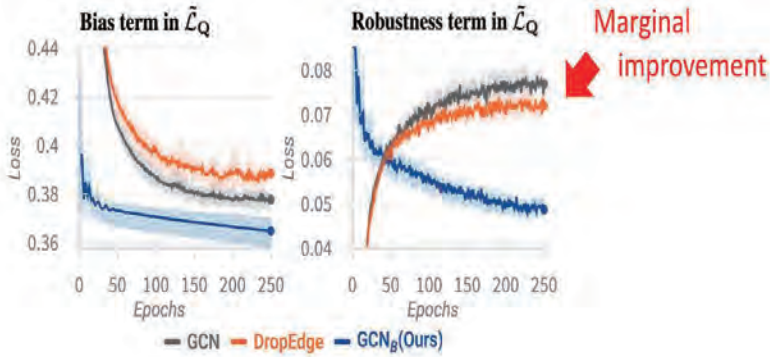

Reason of the Failure

- **Q1.** Why can't DropEdge minimize the robustness term?
- **A.** Since GNNs **rely on the graph structure** for their predictions.

$$\tilde{\mathcal{L}}_Q(\theta) = D_{\mathrm{KL}}(P(y_i|G_i), Q_\theta(y_i|G_i)) \quad \rightarrow \text{Bias}$$
$$+D_{\mathrm{KL}}(Q_\theta(y_i|G_i), Q_\theta(y_i|\tilde{G}_i)) \quad \rightarrow \text{Robustness}$$

  - Should give the same output for different G_i and $\tilde{G}_i$.

Reason of the Failure (cont.)

- **Q2.** Is it even **possible** to minimize the robustness term?
- **A.** To answer the question, we define a **discrepancy bound**.
  - How similar output a model can produce for different inputs.

Definition 3.3 (Discrepancy bound). Let $\boldsymbol{H}_1^{(l)}$ and $\boldsymbol{H}_2^{(l)}$ be the outputs of the l-th layer of a network f given different inputs $\boldsymbol{H}_1^{(l-1)}$ and $\boldsymbol{H}_2^{(l-1)}$. The discrepancy bound of f at the l-th layer is a constant C, such that

$$\|\boldsymbol{H}_1^{(l)} - \boldsymbol{H}_2^{(l)}\|_2 \leq C\|\boldsymbol{H}_1^{(l-1)} - \boldsymbol{H}_2^{(l-1)}\|_2,$$

where C is independent of the specific inputs.

Discrepancy Bound of MLPs

- **Multi-layer perceptrons (MLPs)** have a constant bound.
  - The constant is determined by the weight matrices.
  - The robustness can be improved by adjusting weights.

Theorem 3.6. *In an L-layer MLP with activation function σ, the discrepancy bound at the L-th layer can be derived for every intermediate layer $l < L$ as*

$$\|\boldsymbol{H}_1^{(L)} - \boldsymbol{H}_2^{(L)}\|_2 \leq C\|\boldsymbol{H}_1^{(l)} - \boldsymbol{H}_2^{(l)}\|_2,$$

where $C = L_\sigma^{(L-l)} \prod_{i=l+1}^{L} \|\boldsymbol{W}^{(i)}\|_2$.

Discrepancy Bound of GNNs

- However, **GNNs don't have a discrepancy bound.**
  - Because the output is always affected by the graph topology.
- **Q:** What does it mean **not having a bound?**
  - If $\|\mathbf{A}_1 - \mathbf{A}_2\|_2$ is large, the output difference can always be large.

> **Theorem 3.8.** *Given a graph convolutional network (GCN) with any non-linear activation function σ and different adjacency matrices $\boldsymbol{A}_1$ and $\boldsymbol{A}_2$, the discrepancy bound cannot be established as a constant C independent of the input.*

Solution: Two-Step Approach

- **Step 1:** Train a GNN without augmentation, focusing on **bias**.
- **Step 2:** Insert a parameter block and then train it for **robustness**.

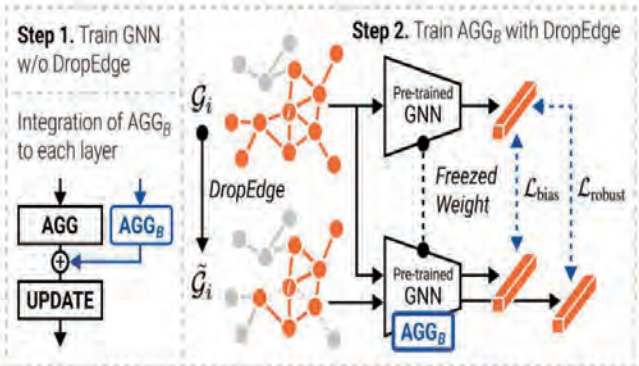

Aggregation Buffer

- We propose **Aggregation Buffer,** a plug-in parameter block:

$$\boldsymbol{H}_{\mathcal{N}}^{(l)} = \mathrm{AGG}^{(l)}(\boldsymbol{H}^{(l-1)}, \boldsymbol{A}) + \mathrm{AGG}_{B}^{(l)}(\boldsymbol{H}^{(0:l-1)}, \boldsymbol{A}),$$

  - $\boldsymbol{H}^{(l)} \in \mathbb{R}^{n \times d}$ is the node embedding matrix at layer l.
  - $\boldsymbol{A} \in \mathbb{R}^{n \times n}$ is the adjacency matrix of the graph.
  - $\mathrm{AGG}^{(l)}$ is the original aggregation layer for neighbors.

Outline

1. Introduction
2. Method
3. **Experiments**
4. Summary

Experimental Setup

- We evaluate our Aggregation Buffer on **node classification.**
  - Predict the discrete labels of nodes in a graph.
- We use 11 different graph datasets from various domains.
  - They have **different homophily ratios** from 0.22 to 0.93.

	Cora	Citeseer	PubMed	Wiki-CS	Photo	Computer	CS	Physics	Arxiv	Actor	Chameleon
# nodes	2,708	3,327	19,717	11,701	7,650	13,752	18,333	34,493	169,343	7,600	2,277
# edges	10,556	9,228	88,651	431,726	238,162	491,722	163,788	495,924	1,166,243	33,391	36,101
# features	1,433	3,703	500	300	745	767	6,805	8,415	128	932	2325
# classes	7	6	3	10	8	10	15	5	40	5	5
Homophily Ratio	0.8100	0.7355	0.8024	0.6543	0.8272	0.7772	0.8081	0.9314	0.6542	0.2167	0.2299
Hidden Dim	512	512	512	512	512	512	256	64	512	64	64
Learning Rate	1e-2	1e-2	1e-2	1e-2	1e-2	1e-2	1e-3	1e-3	1e-2	1e-3	5e-3
Weight Decay	5e-4	5e-4	5e-4	5e-4	5e-4	5e-4	5e-4	5e-5	5e-5	5e-4	0e-0
Dropout	0.5	0.7	0.7	0.3	0.5	0.3	0.2	0.5	0.5	0.7	0.3
Filter Type	Sym	Sym	Sym	RW	Sym	Sym	Sym	Sym	RW	Sym	RW

Q1. Performance for Structural Disparity

- **Q.** Is Aggregation Buffer effective for structural disparity?
- **A.** Yes, it performs as good as MLPs on **heterophily nodes.**
  - Impressive result, since MLPs ignore the graph.
  - **Note:** MLPs perform poorly on homophily nodes.

Method	Cora	Citeseer	PubMed	Wiki-CS	Photo	Computer	CS	Physics	Arxiv	Actor	Chameleon
MLP	$50.93_{\pm 0.98}$	$44.88_{\pm 1.82}$	$73.22_{\pm 0.71}$	$57.90_{\pm 0.93}$	$81.71_{\pm 1.34}$	$66.84_{\pm 0.69}$	$85.96_{\pm 0.29}$	$89.08_{\pm 0.37}$	$34.53_{\pm 0.18}$	$31.66_{\pm 2.79}$	$50.79_{\pm 2.99}$
GCN	$64.18_{\pm 2.49}$	$41.96_{\pm 1.24}$	$67.34_{\pm 0.47}$	$51.89_{\pm 1.08}$	$81.74_{\pm 0.75}$	$71.42_{\pm 1.25}$	$76.81_{\pm 0.68}$	$86.60_{\pm 0.37}$	$32.51_{\pm 0.28}$	$19.13_{\pm 1.55}$	$61.97_{\pm 3.05}$
DropEdge	$64.09_{\pm 2.68}$	$41.78_{\pm 1.27}$	$67.12_{\pm 0.52}$	$50.97_{\pm 1.49}$	$81.50_{\pm 0.69}$	$71.06_{\pm 1.95}$	$76.92_{\pm 0.35}$	$86.47_{\pm 0.40}$	$31.70_{\pm 0.52}$	$19.29_{\pm 1.72}$	$58.29_{\pm 2.93}$
DropNode	$64.60_{\pm 3.58}$	$41.59_{\pm 1.08}$	$67.24_{\pm 0.51}$	$51.66_{\pm 1.21}$	$80.67_{\pm 0.97}$	$71.38_{\pm 1.21}$	$76.93_{\pm 0.65}$	$86.46_{\pm 0.39}$	$31.91_{\pm 0.57}$	$18.93_{\pm 1.02}$	$54.67_{\pm 3.27}$
DropMessage	$64.39_{\pm 2.77}$	$41.84_{\pm 0.84}$	$67.23_{\pm 0.39}$	$51.48_{\pm 0.98}$	$81.65_{\pm 0.82}$	$71.87_{\pm 0.98}$	$77.27_{\pm 0.51}$	$86.47_{\pm 0.44}$	$32.29_{\pm 0.46}$	$19.49_{\pm 1.18}$	$56.97_{\pm 2.26}$
TUNEUP	$63.59_{\pm 2.36}$	$42.74_{\pm 1.07}$	$67.09_{\pm 0.89}$	$52.50_{\pm 0.72}$	$81.58_{\pm 0.87}$	$71.03_{\pm 2.17}$	$74.16_{\pm 1.11}$	$84.67_{\pm 0.65}$	$31.68_{\pm 0.23}$	$18.24_{\pm 0.92}$	$62.04_{\pm 2.94}$
GraphPatcher	$64.17_{\pm 2.22}$	$44.47_{\pm 0.89}$	$66.41_{\pm 0.34}$	$53.03_{\pm 0.86}$	$81.46_{\pm 1.68}$	$71.56_{\pm 1.96}$	$78.67_{\pm 0.53}$	$86.87_{\pm 0.64}$	$33.38_{\pm 0.14}$	$18.49_{\pm 1.33}$	$62.46_{\pm 3.77}$
GCN$_0$(Ours)	$\mathbf{65.54_{\pm 2.34}}$	$43.24_{\pm 1.05}$	$70.77_{\pm 0.71}$	$52.44_{\pm 1.27}$	$\mathbf{82.29_{\pm 1.05}}$	$\mathbf{72.02_{\pm 1.25}}$	$82.75_{\pm 0.63}$	$88.43_{\pm 0.35}$	$34.02_{\pm 0.34}$	$19.96_{\pm 1.49}$	$\mathbf{62.50_{\pm 2.52}}$

Q2. Performance for Different GNNs

- **Q.** Can Aggregation Buffer be generally used for GNNs?
- **A.** Yes, it improves the performance of **all GNN models used.**
  - Aggregation Buffer works as a general plug-in module.

	Pubmed	CS	Arxiv	Chameleon
SAGE	$87.07_{\pm 0.24}$	$92.44_{\pm 0.60}$	$70.92_{\pm 0.16}$	$62.68_{\pm 1.57}$
$SAGE_B$	$\mathbf{88.09}_{\pm 0.28}$	$\mathbf{93.36}_{\pm 0.47}$	$\mathbf{71.16}_{\pm 0.14}$	$\mathbf{63.07}_{\pm 1.93}$
GAT	$85.64_{\pm 0.24}$	$90.5_{\pm 0.28}$	$71.86_{\pm 0.14}$	$65.29_{\pm 1.89}$
GAT_B	$\mathbf{87.47}_{\pm 0.37}$	$\mathbf{93.09}_{\pm 0.60}$	$\mathbf{72.26}_{\pm 0.14}$	$\mathbf{66.01}_{\pm 2.08}$
SGC	$84.01_{\pm 0.76}$	$90.89_{\pm 0.45}$	$69.15_{\pm 0.05}$	$67.00_{\pm 2.94}$
SGC_B	$\mathbf{84.77}_{\pm 1.02}$	$\mathbf{91.90}_{\pm 0.43}$	$\mathbf{69.55}_{\pm 0.04}$	$\mathbf{67.70}_{\pm 2.65}$
GIN	$85.42_{\pm 0.20}$	$87.88_{\pm 0.51}$	$63.94_{\pm 0.53}$	$62.92_{\pm 3.08}$
GIN_B	$\mathbf{87.18}_{\pm 0.17}$	$\mathbf{88.58}_{\pm 1.00}$	$\mathbf{65.66}_{\pm 0.75}$	$\mathbf{63.20}_{\pm 2.71}$

Outline

1. Introduction
2. Method
3. Experiments
4. **Summary**

Summary

- Structural inconsistency is an important problem in graphs.
  - **Degree bias:** Poor performance on low-degree nodes.
  - **Structural disparity:** Fail on structurally different nodes.
- We propose **Aggregation Buffer,** a post-processing module.
  - Motivated by the failure of DropEdge.
  - Can be plugged in into any trained graph neural network.
- The paper was presented this July at ICML 2025.

Photo of Data AI Lab

Efficient Node Classification on Simplicial Interaction via Augmented Maximal Clique Selection

Eun-Ho Koo

Chonnam National University

Considering higher-order interactions allows for a more comprehensive understanding of network structures beyond simple pairwise connections. While leveraging all cliques in a network to handle higher-order interactions is intuitive, it often leads to computational inefficiencies due to overlapping information between higher-order and lower-order cliques. To address this issue, we propose an augmented maximal clique strategy. Although using only maximal cliques can reduce unnecessary overlap and provide a concise representation of the network, certain nodes may still appear in multiple maximal cliques, resulting in imbalanced training data. Therefore, our augmented maximal clique approach selectively includes some non-maximal cliques to mitigate the overrepresentation of specific nodes and promote more balanced learning across the network. Comparative analyses on synthetic networks and real-world citation datasets demonstrate that our method outperforms approaches based on pairwise interactions, all cliques, or only maximal cliques. Additionally, by integrating this strategy into GNN-based semi-supervised learning, we establish a link between maximal clique-based methods and GNNs, showing that incorporating higher-order structures improves predictive accuracy. The augmented maximal clique strategy offers a computationally efficient and effective solution for higher-order network learning.

Efficient Node Classification on Simplicial Interaction via Augmented Maximal Clique Selection

FMfl2025

Koo, Eunho (Department of Big Data Convergence, Chonnam National University)

Lim, Tongseok (Mitchell E, Daniels, Jr. School of Business, Purdue University)

Node Classification in Networks via Simplicial Interactions

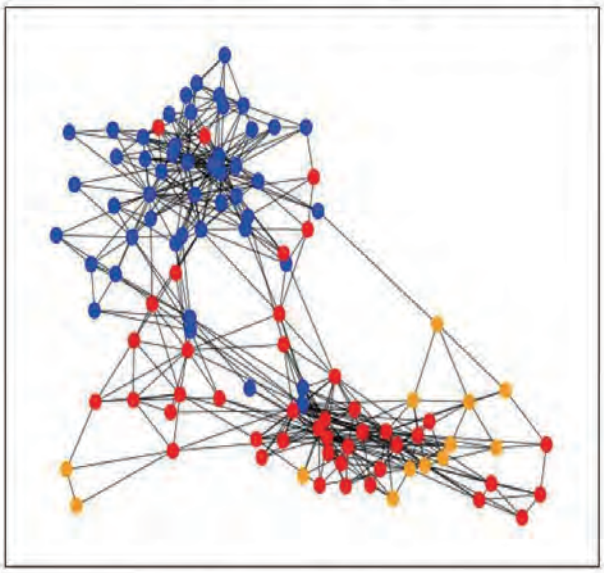

CATEGORY

1. Node Classification
2. Semi-supervised Learning
3. Higher Order Interaction
4. Probability Objective Function

Densely interconnected nodes in a network tend to share the same labels

Hypergraph

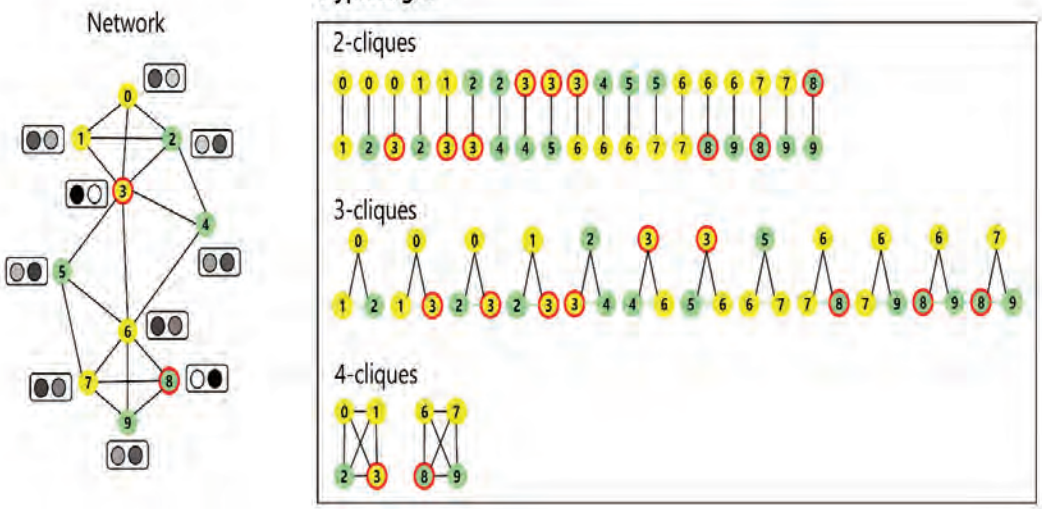

Illustration of the objective function

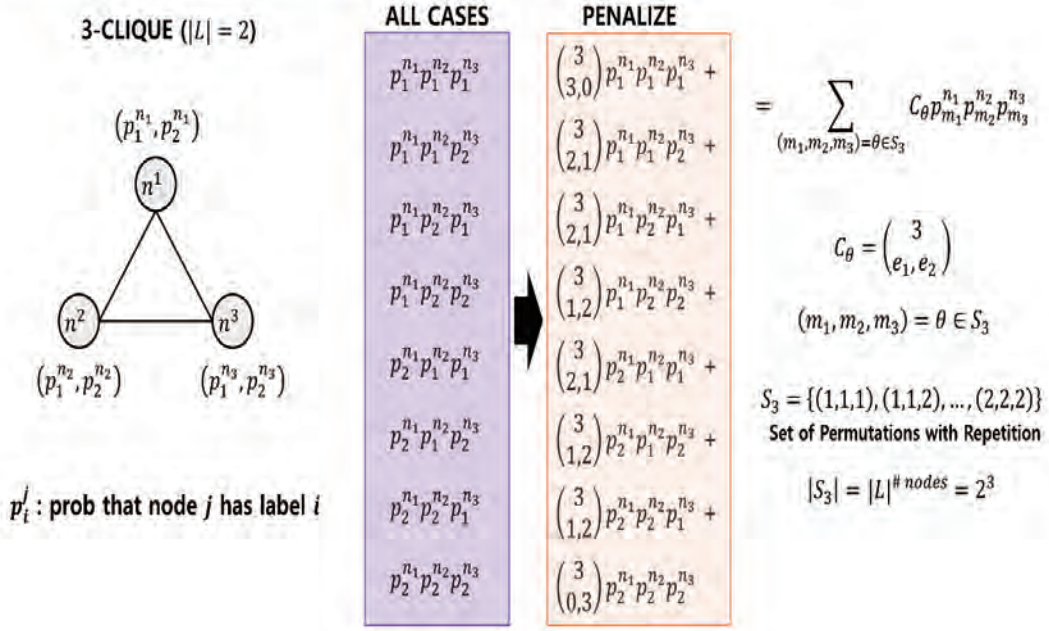

Illustration of the objective function

4-CLIQUE ($|L| = 2$)

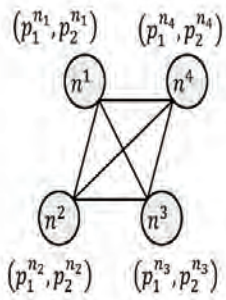

p_i^j : prob that node j has label i

$$\binom{4}{4,0} \times p_1^{n_1} p_1^{n_2} p_1^{n_3} p_1^{n_4} +$$

$$\binom{4}{3,1} \times p_1^{n_1} p_1^{n_2} p_1^{n_3} p_2^{n_4} + p_1^{n_1} p_1^{n_2} p_2^{n_3} p_1^{n_4} + p_1^{n_1} p_2^{n_2} p_1^{n_3} p_1^{n_4} + p_2^{n_1} p_1^{n_2} p_1^{n_3} p_1^{n_4} +$$

$$\binom{4}{2,2} \times p_1^{n_1} p_1^{n_2} p_2^{n_3} p_2^{n_4} + p_1^{n_1} p_2^{n_2} p_1^{n_3} p_2^{n_4} + p_1^{n_1} p_2^{n_2} p_2^{n_3} p_1^{n_4} + p_2^{n_1} p_1^{n_2} p_1^{n_3} p_2^{n_4} + p_2^{n_1} p_1^{n_2} p_2^{n_3} p_1^{n_4} + p_2^{n_1} p_2^{n_2} p_1^{n_3} p_1^{n_4}$$

$$\binom{4}{1,3} \times p_1^{n_1} p_2^{n_2} p_2^{n_3} p_2^{n_4} + p_2^{n_1} p_1^{n_2} p_2^{n_3} p_2^{n_4} + p_2^{n_1} p_2^{n_2} p_1^{n_3} p_2^{n_4} + p_2^{n_1} p_2^{n_2} p_2^{n_3} p_1^{n_4}$$

$$\binom{4}{4,0} \times p_2^{n_1} p_2^{n_2} p_2^{n_3} p_2^{n_4}$$

$$= \sum_{(m_1,m_2,m_3m_4)=\theta \in S_4} C_\theta p_{m_1}^{n_1} p_{m_2}^{n_2} p_{m_3}^{n_3} p_{m_4}^{n_4}$$

$$C_\theta = \binom{4}{e_1, e_2}$$

$$(m_1, m_2, m_3 m_4) = \theta \in S_4$$

$$S_4 = \{(1,1,1,1), (1,1,1,2), \ldots, (2,2,2,2)\}$$

Set of Permutations with Repetition

$$|S_4| = |L|^{\#\, nodes} = 2^4$$

Objective Function

$$J = \sum_{k=2}^{M} W_k \sum_{(n_1,n_2,\ldots,n_k) \in K_k} \sum_{(m_1,m_2,\ldots,m_k)=\theta \in S_k} C_\theta p_{m_1}^{n_1} p_{m_2}^{n_2} \cdots p_{m_k}^{n_k}$$

$$minimize\ J\ over\ \Delta^N = \Delta \times \Delta \times \cdots \times \Delta$$

Δ is the probability simplex in $\mathbb{R}^l$, $p^j \equiv (p_1^j, p_2^j, \ldots, p_l^j) \in \Delta$

$\mathcal{V} = \{1,2,\ldots,N\}$, $I = \{1,\ldots,l\}$

$(p_1^j, p_2^j, \ldots, p_l^j)$, p_i^j denotes the probability that node j having label i, $p_1^j + p_2^j + \cdots + p_l^j = 1$ for all $1 \le j \le N$

$$C_\theta = \binom{k}{e_1, e_2, \ldots, e_l} = \frac{k!}{e_1! e_2! \cdots e_l!},\ e_1 + e_2 + \cdots + e_l = k$$

S_k : Permutation set with repetitions

K_k: The set of k-cliques in the graph

Densely interconnected nodes in a network tend to share the same labels

Training Participation Imbalance

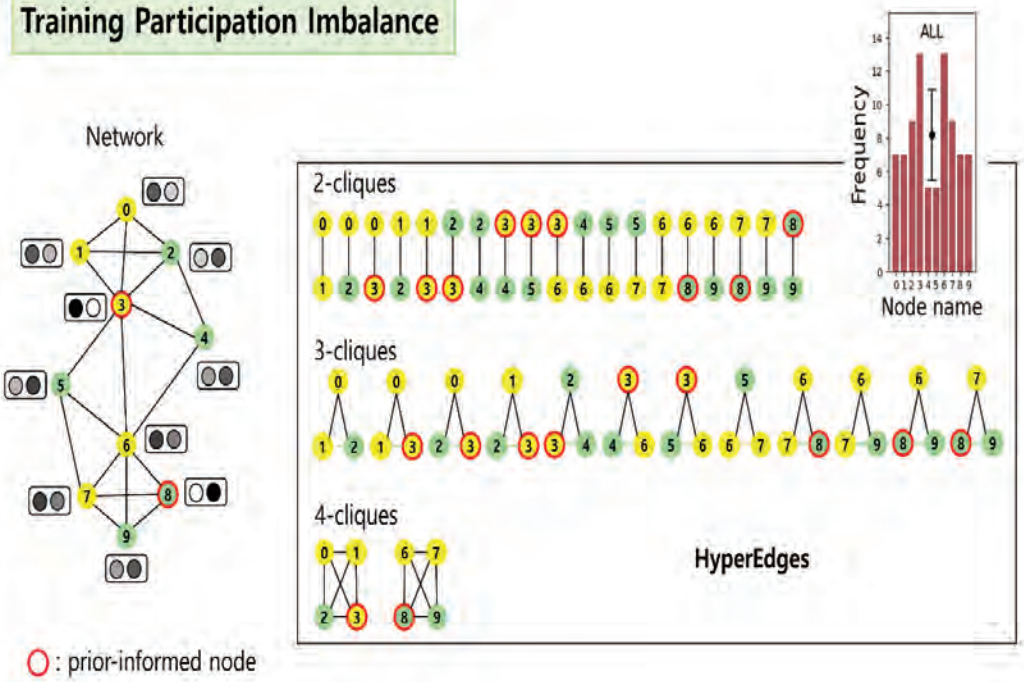

Augmented Maximal Cliques

K: the set of all cliques
Q: the set of maximal cliques
N: number of nodes

Step1: Initially, $AMC = Q$ (Q: the set of maximal cliques)

Calculate γ_i for all $i = 1,2,\ldots,N$ (γ_i : the number of maximal cliques that contain node i)

Let $\Gamma = \frac{1}{N}\sum_{i=1}^{N}\gamma_i$, and $\xi_i = \gamma_i - \Gamma$ (trivially, $\sum_{i=1}^{N}\xi_i = 0$)

Step2: Choose a non-maximal k –clique $\psi \in K - Q$

Include ψ in the AMC set if it satisfies $\sum_{i\in\psi}\xi_i < \frac{k(k-N)}{2N}$

◎ Non-maximal cliques are prioritized based on higher-order (i.e., larger clique size)
This is based on the assumption that larger cliques tend to better reflect label homogeneity

Step3: Continue Step1,2 for all non-maximal cliques

Augmented Maximal Cliques

K: the set of all cliques
Q: the set of maximal cliques
N: number of nodes
γ_i : the number of maximal cliques that contain node i
$\Gamma = \frac{1}{N}\sum_{i=1}^{N}\gamma_i$
$\xi_i = \gamma_i - \Gamma,\ \sum_{i=1}^{N}\xi_i = 0$

If a non-maximal k –clique $\psi \in K - Q$ added to AMC, then

$$\gamma_i \rightarrow \gamma_i + 1 \text{ for } i \in \psi$$

$$\Gamma' = \frac{1}{N}\left(\sum_{i=1}^{N}\gamma_i + k\right) = \Gamma + \frac{k}{N}$$

$$\xi_i' = \gamma_i' - \Gamma' = \begin{cases} \xi_i + 1 - \frac{k}{N} & if\ i \in \psi \\ \xi_i - \frac{k}{N} & otherwise \end{cases} \quad \rightarrow \quad \sum_{i=1}^{N}\xi_i'^2 = \sum_{i=1}^{N}\xi_i^2 + 2\sum_{i \in \psi}\xi_i + \frac{k(N-k)}{N}$$

Augmented Maximal Cliques

K: the set of all cliques
Q: the set of maximal cliques
N: number of nodes
γ_i : the number of maximal cliques that contain node i
$\Gamma = \frac{1}{N}\sum_{i=1}^{N}\gamma_i$
$\xi_i = \gamma_i - \Gamma,\ \sum_{i=1}^{N}\xi_i = 0$

If a non-maximal k –clique $\psi \in K - Q$ added to AMC, then

$\gamma_i \rightarrow \gamma_i + 1$ for $i \in \psi$

$\Gamma' = \frac{1}{N}\left(\sum_{i=1}^{N}\gamma_i + k\right) = \Gamma + \frac{k}{N}$

$\xi_i' = \gamma_i' - \Gamma' = \begin{cases} \xi_i + 1 - \frac{k}{N} & if\ i \in \psi \\ \xi_i - \frac{k}{N} & otherwise \end{cases} \quad \rightarrow \quad \sum_{i=1}^{N}\xi_i'^2 = \sum_{i=1}^{N}\xi_i^2 + 2\sum_{i \in \psi}\xi_i + \frac{k(N-k)}{N}$

If this part is negative, then the variance of γ' becomes smaller than that of γ

Augmented Maximal Cliques

K: the set of all cliques
Q: the set of maximal cliques
N: number of nodes
γ_i : the number of maximal cliques that contain node i
$\Gamma = \frac{1}{N}\sum_{i=1}^{N}\gamma_i$
$\xi_i = \gamma_i - \Gamma,\ \sum_{i=1}^{N}\xi_i = 0$

If a non-maximal k –clique $\psi \in K - Q$ added to AMC, then

$$\gamma_i \rightarrow \gamma_i + 1 \text{ for } i \in \psi$$

$$\Gamma' = \frac{1}{N}\left(\sum_{i=1}^{N}\gamma_i + k\right) = \Gamma + \frac{k}{N}$$

$$\xi_i' = \gamma_i' - \Gamma' = \begin{cases} \xi_i + 1 - \frac{k}{N} & if\ i \in \psi \\ \xi_i - \frac{k}{N} & otherwise \end{cases} \quad \rightarrow \quad \sum_{i=1}^{N}\xi_i'^2 = \sum_{i=1}^{N}\xi_i^2 + 2\sum_{i \in \psi}\xi_i + \frac{k(N-k)}{N}$$

$$\sum_{i \in \psi}\xi_i < \frac{k(k-N)}{2N}$$

serves as the threshold for including ψ in the AMC set

If this part is negative, then the variance of γ' becomes smaller than that of γ

Maximal Cliques

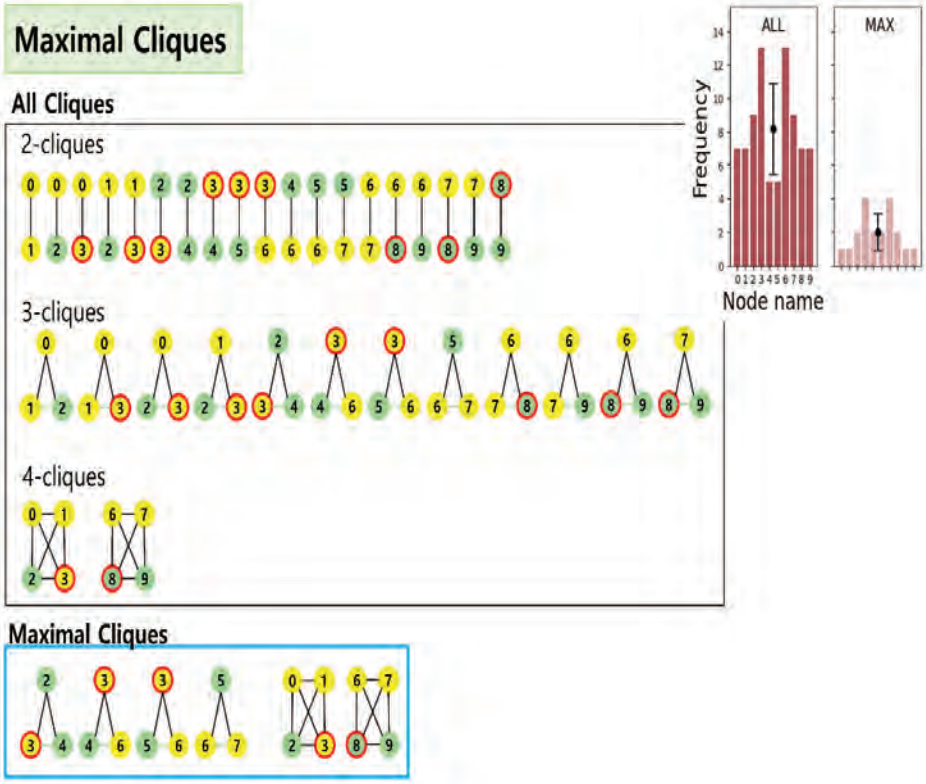

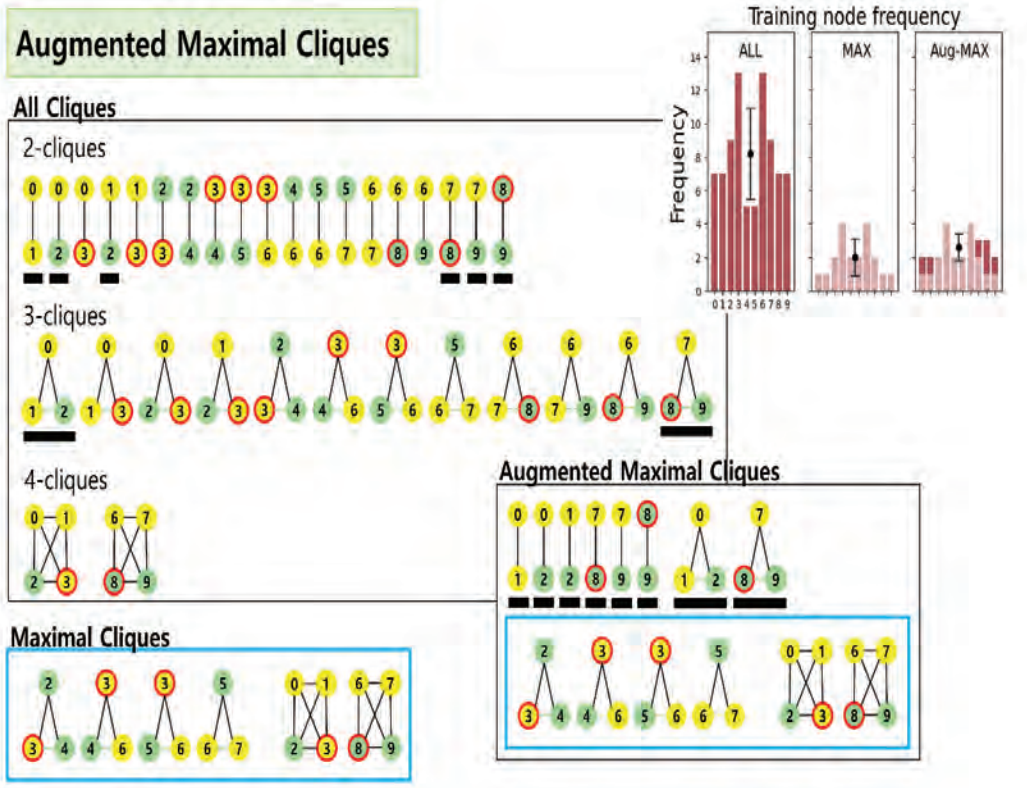
Augmented Maximal Cliques
All Cliques
2-cliques
3-cliques
4-cliques
Maximal Cliques
Training node frequency
ALL
MAX
Aug-MAX
Frequency
Augmented Maximal Cliques

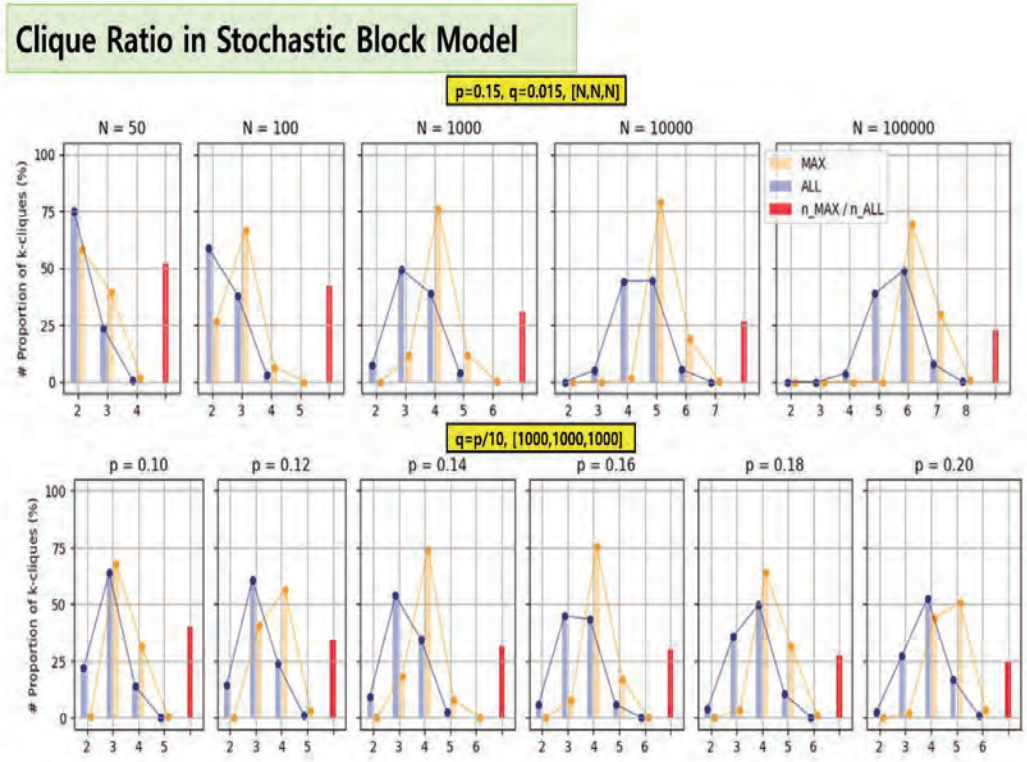
Clique Ratio in Stochastic Block Model
p=0.15, q=0.015, [N,N,N]
N = 50
N = 100
N = 1000
N = 10000
N = 100000
MAX
ALL
n_MAX / n_ALL
# Proportion of k-cliques (%)
q=p/10, [1000,1000,1000]
p = 0.10
p = 0.12
p = 0.14
p = 0.16
p = 0.18
p = 0.20

Clique distribution in citation networks

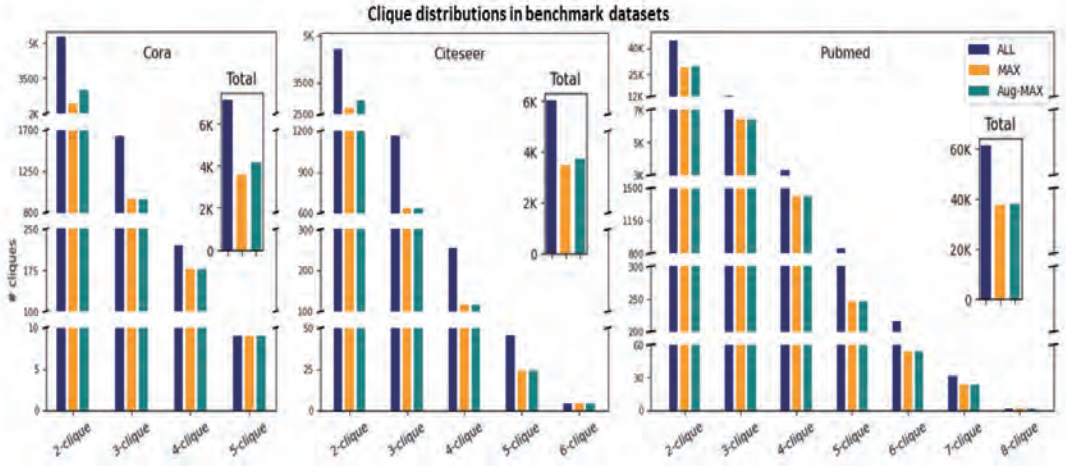

Results in Citation Networks

Method	Cora	Citeseer	Pubmed
GAT	83.0 %	72.5 %	79.0 %
GAT + **ALL**	84.9 %	72.9 %	80.1 %
GAT + **MAX**	84.4 %	72.9 %	80.1 %
GAT + **Aug-MAX**	85.1 %	72.9 %	80.1 %
GCN	81.5 %	70.3 %	79.0 %
GCN + **ALL**	83.1 %	71.6 %	79.0 %
GCN + **MAX**	83.1 %	71.5 %	79.0 %
GCN + **Aug-MAX**	84.0 %	72.6 %	79.1 %
SGC	81.0 %	71.9 %	78.9 %
SGC + **ALL**	84.8 %	71.9 %	78.9 %
SGC + **MAX**	84.6 %	71.9 %	78.7 %
SGC + **Aug-MAX**	84.9 %	72.0 %	79.0 %
Planetoid	75.7 %	64.7 %	77.2 %
Planetoid + **ALL**	77.1 %	65.8 %	77.3 %
Planetoid + **MAX**	76.9 %	65.8 %	77.3 %
Planetoid + **Aug-MAX**	77.2 %	66.0 %	77.4 %

	Cora	Citeseer	Pubmed
# nodes	2,708	3,327	19,717
# Edges	5,429	4,732	44,338
# Classes	7	6	3
# Train	140 (20 each label)	120 (20 each label)	60 (20 each label)
# Val	500	500	500
# Test	1,000	1,000	1,000

◎ First, obtain the probability distribution for each node from GNN models

◎ Second, the distributions serve as initialization for optimization over higher-order cliques

Conclusion

◎ Aug-Max reduces computational cost while addressing node participation imbalance, improving both efficiency and accuracy

◎ The method bridges GNN models with higher-order structures, showing promise for future hybrid graph learning

Thank you

Growing success with statistics in plant breeding

Emi Tanaka

Australian National University

As the global population grows and climate change intensifies pressures on food production, plant breeders face the critical challenge of developing crop varieties that are high-yielding, resilient, and adaptable to diverse environments. This talk highlights how statistical modelling powers modern plant breeding by transforming complex field and laboratory data into actionable insights. In this talk, I focus on the application of factor analytic linear mixed models (FALMM), which have gained popularity due to their efficiency in dimension reduction and their potential for interpreting underlying factors. A core challenge in using FALMM is determining the appropriate number of latent variables (or order of the model). By exploiting both the grouped and hierarchical nature of the model components, we introduce a principled approach to order selection. This method addresses identifiability concerns without imposing arbitrary constraints and enhances the interpretability of factor loadings. I demonstrate how these statistical advances can enable breeders to make more informed decisions and accelerate the development of improved crop varieties.

Growing success with statistics in plant breeding

Forum “Math for Industy” 2025

Dr. Emi Tanaka
Australian National University
19th August 2025

emitanaka.org/slides/fimfi2025

Wild vs Cultivated

What is this?

Image source: Tico Times

Wild vs Cultivated

What is this?

Image source: Matt Lavin

Selective breeding

Evolution of corn (maize)

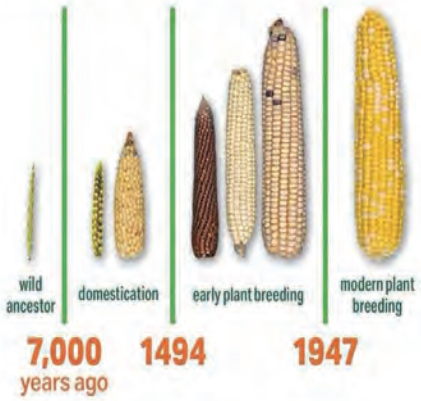

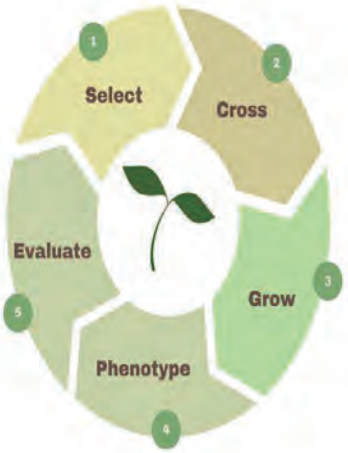

Image source: Get Wild on Facebook

Increase genetic gain

Genetic gain measures improvement in the average genotype performance of a population over time due to selection for specific traits.

$$\Delta G = \frac{r \cdot i \cdot \sigma_g}{L}$$

(Genetic gain) = (Selection accuracy) · (Selection intensity) · (Genetic variation) / (Generational interval)

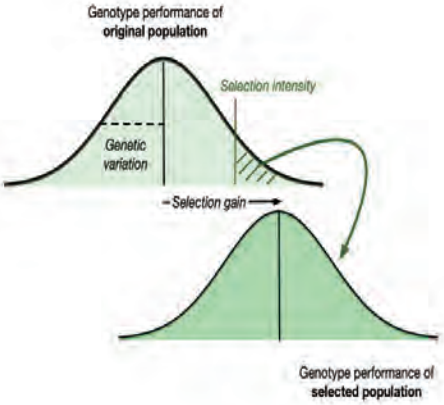

Increase genetic gain

Genetic gain measures improvement in the average genotype performance of a population over time due to selection for specific traits.

$$\Delta G = \frac{r \cdot i \cdot \sigma_g}{L}$$

(Genetic gain) = (Selection accuracy) · (Selection intensity) · (Genetic variation) / (Generational interval)

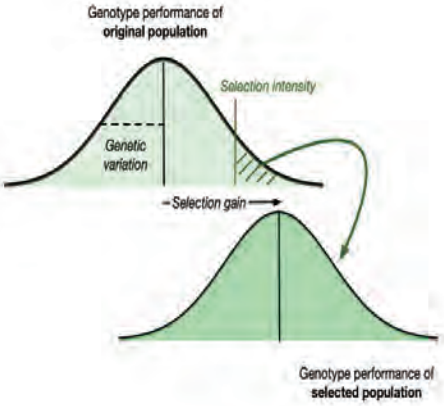

Statistical strategy ❶ Make input better

Improve selection accuracy

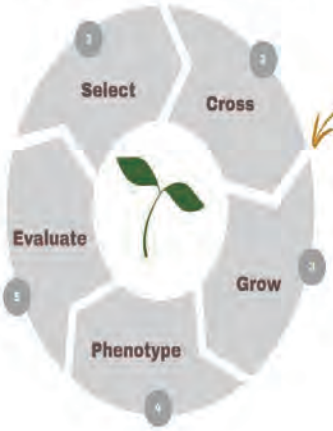

INPUT → PROCESS → OUTPUT

- Use effective **experimental design** that can effectively disaggregate sources of variation for the response.

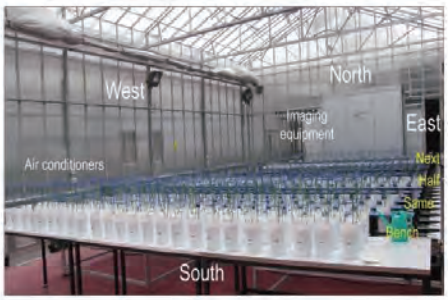

Brien et al (2013) Accounting for variation in designing greenhouse experiments with special reference to greenhouses containing

Statistical strategy ❷ Make output better

Improve selection accuracy

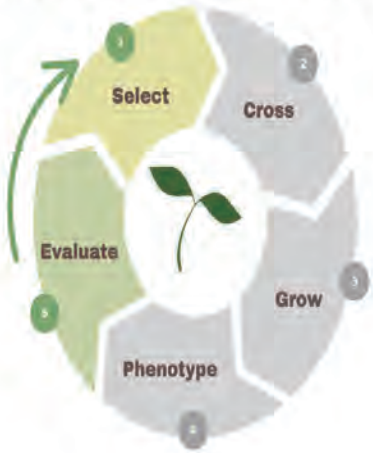

INPUT → PROCESS → OUTPUT

- Assume appropriate (preferably optimal) **experimental design** was used
- Use appropriate **statistical models** to disaggregate "noise" from "signal" to get accurate estimates of **breeding values**.

Crop field trial for plant breeding

- An experiment with candidate (and check) n_g **genotypes** as treatment
- Typically,
  - plots laid out as a rectangular array
  - plots have the same size
  - one genotype per plot
  - phenotype measured per plot

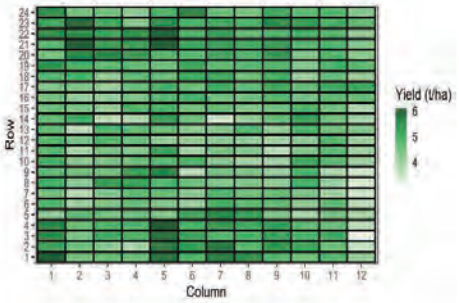

USYD Plant Breeding Institute, Narrabri, NSW, Australia

Image credit: Kieran Shephard

Complex phenotyping

APPN
Australian Plant Phenomics Network

- Phenotypes are increasingly becoming complex:
  - Manual lab experiments for complex traits (photosynthesis, respiration, etc)
  - RGB, hyperspectral, fluorescence, thermal, and 3D sensors
  - High-throughput phenotyping units, e.g. drones and ground-based phenotyping platforms to produce an array of imaging systems, including RGB cameras, infra-red and near infra-red (NIR) sensors, and 3D LiDAR scanners.
- These data are processed by computer vision or machine/deep learning models to predict a trait, this is then used downstream for statistical models for genomic prediction.

Spatial modelling

- Management operations often conducted in a serpentine fashion.

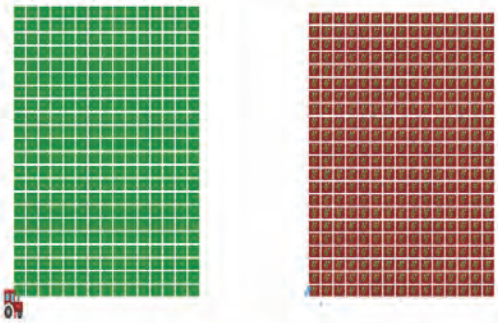

- Plots are not necessary completely independent.
- Modelling to take into account the experimental design and any detectable spatial effects.

Gilmour et al. (1997) "Accounting for Natural and Extraneous Variation in the Analysis of Field Experiments," Journal of Agricultural,

Modelling with relatedness structure

Pedigree information

DNA marker information

- Modelling can incorporate these relatedness structure $\mathbf{G}_g$

Additive and Non-Additive Genomic Predictions

Let $\mathbf{G}_g$ be the numerator relationship matrix:

	I1	I2	I3	I4	I5	I6	I7	I8	I9	I10	I11	I13
I1	1.000	0.000	0.000	0.000	0.500	0.500	0.500	0.000	0.000	0.500	0.250	0.000
I2	0.000	1.000	0.000	0.000	0.500	0.500	0.000	0.500	0.000	0.500	0.250	0.000
I3	0.000	0.000	1.000	0.000	0.000	0.000	0.500	0.500	0.500	0.000	0.500	0.500
I4	0.000	0.000	0.000	1.000	0.000	0.000	0.000	0.000	0.500	0.000	0.000	0.500
I5	0.500	0.500	0.000	0.000	1.000	0.500	0.250	0.250	0.000	0.750	0.250	0.000
I6	0.500	0.500	0.000	0.000	0.500	1.000	0.250	0.250	0.000	0.750	0.250	0.000
I7	0.500	0.000	0.500	0.000	0.250	0.250	1.000	0.250	0.250	0.250	0.625	0.250
I8	0.000	0.500	0.500	0.000	0.250	0.250	0.250	1.000	0.250	0.250	0.625	0.250
I9	0.000	0.000	0.500	0.500	0.000	0.000	0.250	0.250	1.000	0.000	0.250	1.000
I10	0.500	0.500	0.000	0.000	0.750	0.750	0.250	0.250	0.000	1.250	0.250	0.000
I11	0.250	0.250	0.500	0.000	0.250	0.250	0.625	0.625	0.250	0.250	1.125	0.250
I13	0.000	0.000	0.500	0.500	0.000	0.000	0.250	0.250	1.000	0.000	0.250	1.875

- For a single field trial:

$$\underbrace{\boldsymbol{u}_g}_{\text{total genomic prediction}} = \underbrace{\boldsymbol{u}_a}_{\text{additive effects / breeding value}} + \underbrace{\boldsymbol{u}_{\bar{a}}}_{\text{non-additive effects}}$$

assuming $\boldsymbol{u}_a \sim N(\mathbf{0}, \sigma^2_a \mathbf{G}_g)$ and $\boldsymbol{u}_{\bar{a}} \sim N(\mathbf{0}, \sigma^2_{\bar{a}} \mathbf{I}_{n_g})$.

Multi-environmental trial (MET) data

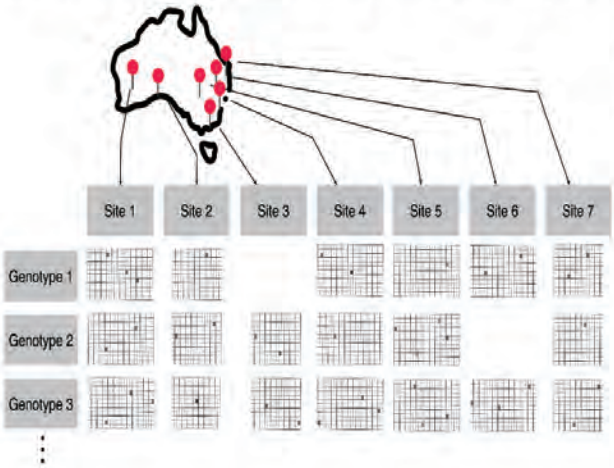

- A collection of n_e field trials
- Genotypes can be **unbalanced**:
  - Not all genotypes tested in every environment/site
  - Not all genotypes have the same number of replications within a site or across sites

Modelling G × E

$$\text{Non-Gaussian:} \quad g(\boldsymbol{\mu}) = \mathbf{X}\boldsymbol{\beta} + \mathbf{Z}_p\boldsymbol{u}_p + \mathbf{Z}_{ge}(\boldsymbol{u}_{ae} + \boldsymbol{u}_{\bar{a}e})$$

$$\text{Gaussian:} \quad \boldsymbol{y} = \mathbf{X}\boldsymbol{\beta} + \mathbf{Z}_p\boldsymbol{u}_p + \mathbf{Z}_{ge}(\boldsymbol{u}_{ae} + \boldsymbol{u}_{\bar{a}e}) + \boldsymbol{e}$$

where:

- $\boldsymbol{y}$ is a vector of responses
- $\boldsymbol{\mu} = E(\boldsymbol{y})$ and $g(\cdot)$ is a known link function
- $\mathbf{X}$ is a design matrix for the fixed effects $\boldsymbol{\beta}$,
- $\mathbf{Z}_p$ is a design matrix for random peripheral effects $\boldsymbol{u}_p$ and
- $\mathbf{Z}_{ge}$ for random genotype-by-environment effects $\boldsymbol{u}_{ge}$.
- $\boldsymbol{e}$ is a vector of random error.

Assume:

- $\boldsymbol{u}_p \sim N(\mathbf{0}, \mathbf{G}_p)$
- $\boldsymbol{u}_{ae} \sim N(\mathbf{0}, \mathbf{G}_g \otimes \mathbf{G}_{ae})$
- $\boldsymbol{u}_{\bar{a}e} \sim N(\mathbf{0}, \mathbf{I}_{n_g} \otimes \mathbf{G}_{\bar{a}e})$
- $\boldsymbol{e} \sim N(\mathbf{0}, \mathbf{R})$

Factor analytic models

- Suppose that for some $k < p$, genotype responses are a result of k (independent) latent variables:

$$\boldsymbol{u}_{ae} = (\mathbf{I}_{n_g} \otimes \boldsymbol{\Lambda}_k)\boldsymbol{f}_k + \boldsymbol{\delta}_k$$

where

- $\boldsymbol{f}_k \sim N(\mathbf{0}, \mathbf{G}_g \otimes \mathbf{I}_k)$ is a $n_g k \times 1$ vector of **common factor**
- $\boldsymbol{\delta}_k \sim N(\mathbf{0}, \mathbf{G}_g \otimes \boldsymbol{\Psi}_k)$ is a $n_g n_e \times 1$ vector of **specific factor**
- $\boldsymbol{\Lambda}_k$ is a $n_e \times k$ **loading matrix** or **latent environmental covariates**
- $\boldsymbol{\Psi}_k$ is a $n_e \times n_e$ **diagonal matrix of specific variances**

Smith et al. (2015). Factor analytic mixed models for the provision of grower information from national crop variety testing

Dimension reduction

- This results in **dimension reduction**:

$$\mathrm{Var}(\boldsymbol{u}_{ae}) = \mathbf{G}_g \otimes \mathbf{G}_{ae} \approx \mathbf{G}_g \otimes (\boldsymbol{\Lambda}_k \boldsymbol{\Lambda}_k^\top + \boldsymbol{\Psi}_k)$$

- A fully unstructured $\mathbf{G}_{ae}$ has $\frac{1}{2} n_e(n_e + 1)$ parameters
- While FA with order k (with corner constraint for $\boldsymbol{\Lambda}_k$) has $(k+1)n_e - k(k-1)/2$ parameters

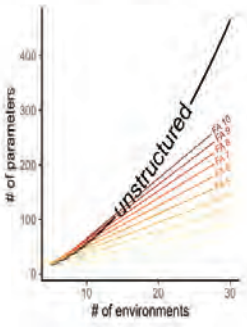

Parameter estimation

- Let $\boldsymbol{\theta} = (\text{vec}(\boldsymbol{\Lambda}_k)^\top, \text{diag}(\boldsymbol{\Psi}_k)^\top)^\top$ denote a vector of all variance parameters in the FA model of order k
- We can then use maximum likelihood (ML) or residual maximum likelihood (REML) to estimate the model parameters:

$$\hat{\boldsymbol{\theta}}_{\text{ML/REML}} = \arg\max_{\boldsymbol{\theta}} \ell(\boldsymbol{\theta} | \cdot).$$

- Note that we need to pre-specify the order k for this

Ordered Factor LASSO (OFAL)

- Assume that $\boldsymbol{\Lambda}_0$ is a $p \times d$ pseudo factor loading matrix where $k \leq d \leq p$
- **OFAL estimate**: our approach via penalised likelihood

$$\hat{\boldsymbol{\theta}}_{\text{OFAL}} = \arg\max_{\boldsymbol{\theta}} \left\{ \ell(\boldsymbol{\theta}) - s \sum_{l=1}^{d} \omega_{g,l} \sqrt{\sum_{i=1}^{p} \sum_{j=l}^{d} \lambda_{0,ij}^2} - s \sum_{i=1}^{p} \sum_{j=1}^{d} \omega_{e,ij} |\lambda_{0,ij}| \right\}$$

where

- s is a **tuning parameter**,
- $\omega_{g,l}$ is a **group-wise adaptive weight** for lth column of $\boldsymbol{\Lambda}_0$, and
- $\omega_{e,ij}$ is an **element-wise adaptive weight** for i, jth entry of $\boldsymbol{\Lambda}_0$.

OFAL concept demo: element-wise sparsity

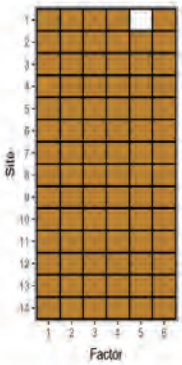

Λ_0

$$\hat{\theta}_{\text{OFAL}} = \arg\max_{\theta} \left\{ \ell(\theta) - s \sum_{l=1}^{d} \omega_{g,l} \left(\sum_{i=1}^{p} \sum_{j=l}^{d} \lambda_{0,ij}^2 \right)^{1/2} - s \sum_{i=1}^{p} \sum_{j=1}^{d} \omega_{e,ij} |\lambda_{0,ij}| \right\}$$

log-likelihood; tuning parameter; element-wise adaptive weight; group-wise adaptive weight; (i,j)-th element of Λ_0

Say $s\omega_{e,15} \to \infty$, then you would expect $|\lambda_{15}| \to 0$.

OFAL concept demo: group-wise sparsity

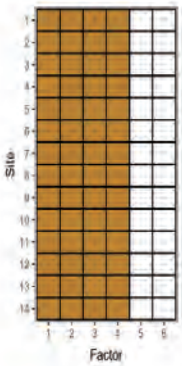

Λ_0

$$\hat{\theta}_{\text{OFAL}} = \arg\max_{\theta} \left\{ \ell(\theta) - s \sum_{l=1}^{d} \omega_{g,l} \left(\sum_{i=1}^{p} \sum_{j=l}^{d} \lambda_{0,ij}^2 \right)^{1/2} - s \sum_{i=1}^{p} \sum_{j=1}^{d} \omega_{e,ij} |\lambda_{0,ij}| \right\}$$

log-likelihood; tuning parameter; element-wise adaptive weight; group-wise adaptive weight; (i,j)-th element of Λ_0

- Say $s\omega_{g,5} \to \infty$, then you would expect $\left(\sum_{l=1}^{p} (\lambda_{l5}^2 + \lambda_{l6}^2)\right)^{1/2} \to 0$.
- Sum of squares is zero only if each element is zero, so $\lambda_{l5} \to 0$ and $\lambda_{l6} \to 0$ for $l = 1, \ldots, p$.

Algorithm in action

Λ_0

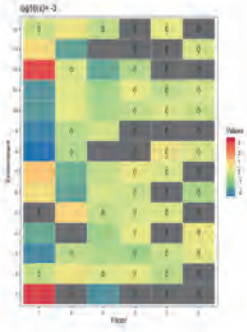

- Our procedure uses EM-algorithm
- At the M-step, we reformulate the OFAL penalised likelihood into an elastic-net type regularisation problem
- Then employ coordinate-wise optimisation to obtain loading estimates
- Full algorithm (including code), choice of adaptive weights and tuning parameter selection are in Hui, Tanaka & Warton (2018)

Other methods for selecting order of the FA model

- Similar method employed by Hirose & Konishi (2012)
- But in practice, we find the FA order k by using a heuristic method (Smith et al, 2015) where

$$\frac{\text{tr}(\hat{\mathbf{\Lambda}}_k \hat{\mathbf{\Lambda}}_k^\top)}{\text{tr}(\hat{\mathbf{\Lambda}}_k \hat{\mathbf{\Lambda}}_k^\top + \hat{\mathbf{\Psi}}_k)} > 0.8.$$

- We still need an implementation of a flexible and fast algorithm to employ a grouped LASSO approach

What about ML/AI?

- An open competition featuring a collection of maize yield trial data shows that the **winning genomic predictions are *still* statistical models**! (Washburn et al., 2025)

the Genomes to Fields initiative

- Why doesn't ML/AI win in **genomic prediction**?
  - ML/AI requires large amount of data, but MET data are often noisy and highly correlated
  - ML/AI are often black box and does not include our prior understanding of the data
- Similar results for **time series forecasting** (Makridakis et al., 2018)
- Although ML/AI may win if trained with large sample size (Cerqueira et al., 2022)



- *Hui, Tanaka & Warton (2018) Order Selection and Sparsity in Latent Variable Models via the Ordered Factor LASSO. Biometrics*
- This slide available at **emitanaka.org/slides/fmfi2025**

ANU Analytics for the Australian Grains Industry

Dr. Emi Tanaka
Australian National University
emitanaka.org
emi.tanaka@anu.edu.au

Algebraic Approach for Statistical Models

Ryoya Fukasaku

Kyushu University

In parameter estimation for statistical models, systems of algebraic equations frequently arise. The solution space of such systems corresponds to an affine algebraic variety defined by an ideal in a multivariate polynomial ring. This correspondence enables us to efficiently compute the solution spaces through algebraic operations on these ideals. In this talk, I will present several examples of algebraic systems that appear in parameter estimation for statistical models and demonstrate how they can be analyzed using techniques from computational algebra, particularly those concerning polynomial ideals. I will also discuss some results obtained through these algebraic computations.

Algebraic Approach for Statistical Models

2025/08/19 (Tue.)
Forum "Math-for-Industry" 2025 - Challenge of Mathematics for Industry in the AI era -

Ryoya Fukasaku (Kyushu University)

1

System of equations that can be solved by algebraic approaches

System of algebraic equations

A system of algebraic equations refers to a system of multiple equations of the following form:

$$\begin{cases} f_1(z_1, z_2, \ldots, z_k) = 0 \\ f_2(z_1, z_2, \ldots, z_k) = 0 \\ \quad\vdots \\ f_s(z_1, z_2, \ldots, z_k) = 0 \end{cases}$$

where each $f_i(z_1, z_2, \ldots, z_k)$ is an algebraic function (e.g. polynomial, rational function, and etc.).

In statistical models, various systems of algebraic equations arise. In this presentation, I will introduce several such systems, along with some algebraic operations that are effective in solving them.

2

Factor Analysis Model

Example (The results and causes of an exam).

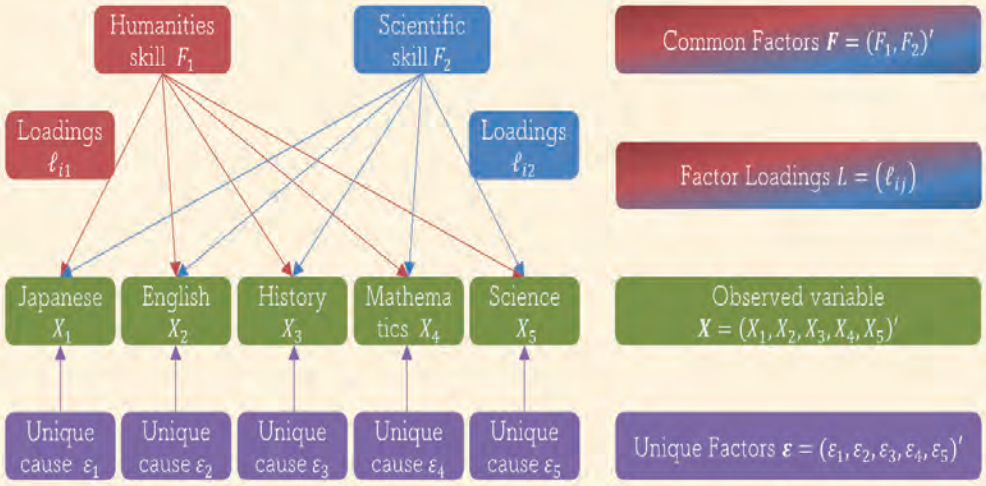

$$X_i - E(X_i) = \ell_{i1}F_1 + \ell_{i2}F_2 + \varepsilon_i \quad (i = 1, \ldots, 5)$$

$$\boldsymbol{X} - E(\boldsymbol{X}) = L\boldsymbol{F} + \boldsymbol{\varepsilon}$$

3

Factor Analysis Model

Setting.

- Observed Variable Vector

$$\boldsymbol{X} = (X_1, \ldots, X_p)'$$

- Common Factor Vector

$$\boldsymbol{F} = (F_1, \ldots, F_m)'$$

- Unique Factor Vector

$$\boldsymbol{\varepsilon} = (\varepsilon_1, \ldots, \varepsilon_p)'$$

- Factor Loading Matrix

$$L = \begin{pmatrix} \ell_{11} & \cdots & \ell_{1m} \\ \vdots & & \vdots \\ \ell_{p1} & \cdots & \ell_{pm} \end{pmatrix}$$

The prime symbol (') denotes the transpose of a matrix.

Factor Analysis Model.

$$\begin{cases} X_1 - \mu_1 &= \ell_{11}F_1 + \cdots + \ell_{1m}F_m + \varepsilon_1 \\ & \vdots \\ X_p - \mu_p &= \ell_{p1}F_1 + \cdots + \ell_{pm}F_m + \varepsilon_p \end{cases}$$

where $E(X_i) = \mu_i, m < p$

Matrix representation:

$$\begin{pmatrix} X_1 \\ \vdots \\ X_p \end{pmatrix} - \begin{pmatrix} \mu_1 \\ \vdots \\ \mu_p \end{pmatrix} = \begin{pmatrix} \ell_{11} & \cdots & \ell_{1m} \\ \vdots & & \vdots \\ \ell_{p1} & \cdots & \ell_{pm} \end{pmatrix} \begin{pmatrix} F_1 \\ \vdots \\ F_m \end{pmatrix} + \begin{pmatrix} \varepsilon_1 \\ \vdots \\ \varepsilon_p \end{pmatrix}$$

Let $\boldsymbol{\mu} = (\mu_1, \ldots, \mu_p)'$.

Then we consider the following form:

$$\boldsymbol{X} - \boldsymbol{\mu} = L\boldsymbol{F} + \boldsymbol{\varepsilon}$$

4

Rotational indeterminacy

Assumption.

Common Factors

$$E(\boldsymbol{F}) = 0, \quad \mathrm{Cov}(\boldsymbol{F}) = \Phi$$

Unique Factors

$$E(\boldsymbol{\varepsilon}) = 0, \quad \mathrm{Cov}(\boldsymbol{\varepsilon}) = \Psi = \mathrm{diag}(\psi_1, \ldots, \psi_p)$$

Common Factors and Unique Factors

$$\mathrm{Cov}(\boldsymbol{F}, \boldsymbol{\varepsilon}) = 0$$

Then we have the following:

$$\mathrm{Cov}(\boldsymbol{X}) = L\Phi L' + \Psi$$

Orthogonal Model : $\Phi = I_m$

Oblique Model : $\mathrm{diag}(\Phi) = I_m$

Rotational indeterminacy.

Transformation by a regular matrix T:

$$\tilde{\boldsymbol{F}} = T\boldsymbol{F}, \quad \tilde{L} = LT^{-1}, \quad \tilde{\Phi} = \mathrm{Cov}(\tilde{\boldsymbol{F}}) = T\Phi T'$$

Then we have the following:

$$\boldsymbol{X} - \boldsymbol{\mu} = \tilde{L}\tilde{\boldsymbol{F}} + \boldsymbol{\varepsilon} \quad \left(\because L\boldsymbol{F} = (LT^{-1})(T\boldsymbol{F}) = \tilde{L}\tilde{\boldsymbol{F}}\right)$$

$\tilde{\boldsymbol{F}}$, $\tilde{L}$, and $\tilde{\Phi}$ satisfy the left assumptions.

$\tilde{\boldsymbol{F}}$, $\tilde{L}$, and $\tilde{\Phi}$ represent the covariances of $\boldsymbol{X}$:

$$\mathrm{Cov}(\boldsymbol{X}) = \tilde{L}\tilde{\Phi}\tilde{L}' + \Psi$$

This means that any positive definite matrix can be chosen as Φ, so parameters L and Ψ are usually estimated under the assumption of an orthogonal model.

5

What is done in factor analysis

Simplify the factor loading matrix of the orthogonal model obtained by maximum likelihood or ordinary least squares methods (MLE or OLS) or etc. using an appropriate regular matrix.

∵ Rotational indeterminacy

Factor analysis.

1. Estimate factor loadings L and unique variances Ψ by MLE or OLS or etc.
2. Find a regular matrix T that simplifies the factor loading $\tilde{L} = LT$.

Contens of my talk.

- Introduce challenges of factor analysis.
- Introduce algebraic approaches necessary to address the challenges.

Image of simplifying factor loadings.

i	ℓ_{i1}	ℓ_{i2}
1	0.20	0.70
2	0.30	0.40
3	0.40	0.65
4	0.25	0.50
5	0.50	−0.25
6	0.60	−0.40
7	0.85	−0.20
8	0.90	−0.55
9	0.70	−0.30

T → $\tilde{L} = LT$

i	$\tilde{\ell}_{i1}$	$\tilde{\ell}_{i2}$
1	0.10	0.90
2	−0.05	0.70
3	0.05	0.85
4	−0.10	0.80
5	0.80	0.05
6	0.75	−0.10
7	0.85	0.10
8	0.90	0.05
9	0.75	0.00

6

Challenges

The estimates of unique variances ψ_i can result in zero or negative, referred to as improper solutions. The causes are still not understood. Also, in factor rotation, we need to solve a constrained optimization problem to minimize or maximize a given criterion. Many different criteria have been proposed, and there is no clear guideline on which criterion should be used.

Improper Solution Problem.

Stationary points of the likelihood function

$$\begin{cases} L = (LL' + \Psi)S^{-1}L \\ \Psi = \mathrm{diag}(S - LL') \end{cases} \quad (S \in \mathbb{R}^{p \times p})$$

[arXiv:2402.08181] Fukasaku, Hirose, Kabata, Teramoto: Algebraic approach to maximum likelihood factor analysis.

Factor Rotation Problem.

Stationary points of an orthogonal criterion f

$$\left(T' \frac{\partial f}{\partial T}\right)_{ij} = \left(T' \frac{\partial f}{\partial T}\right)_{ji} \quad (\forall i, j)$$

[arXiv:2504.21288] Fukasaku, Yamamoto, Kabata, Ikematsu, Hirose: Algebraic Approach for Orthomax Rotations.

The above systems are systems of algebraic equations. To advance the understanding of the challenges mentioned earlier, we solved these systems using algebraic approaches, from which several insights were obtained. This time, we introduce some useful algebraic operations for solving these algebraic equation systems.

7

	numerical approach	algebraic approach
computational cost	very low	very very very high
initial value	dependent	independent
algorithm	dependent	independent
exact solution	no	yes
all solutions	no	yes

$$\begin{cases} L = (LL' + \Psi)S^{-1}L \\ \Psi = \mathrm{diag}(S - LL') \end{cases} \quad (S \in \mathbb{R}^{p \times p}) \qquad \left(T' \frac{\partial f}{\partial T}\right)_{ij} = \left(T' \frac{\partial f}{\partial T}\right)_{ji} \quad (\forall i, j)$$

Algebraic Approach

[CLO] Cox, Little, O'shea. Ideals, Varieties, and Algorithms. 4th Edition. Springer. 2015.

8

Setting

System of algebraic equations.

$$\begin{cases} f_1(z_1,\ldots,z_k)=0 \\ \vdots \\ f_s(z_1,\ldots,z_k)=0 \end{cases} \quad \text{(A)}$$

Let $f_i(\boldsymbol{z}) = f(z_1,\ldots,z_k)$ be a polynomial, i.e.,

$$f_i \in \mathbb{R}[\boldsymbol{z}]$$

where $\mathbb{R}[\boldsymbol{z}]$ is the polynomial ring in $\boldsymbol{z}$.

Hilbert Basis Theorem.

Any ideal in $\mathbb{R}[\boldsymbol{z}]$ is finitely generated, i.e.,

$$J \subset \mathbb{R}[\boldsymbol{z}]:\ \text{ideal} \Rightarrow \left(\begin{array}{c} \exists h_1,\ldots,h_r \in \mathbb{R}[\boldsymbol{z}] \\ (J = \langle h_1,\ldots,h_r \rangle) \end{array} \right)$$

Ideal.

$$\langle h_1,\ldots,h_r \rangle = \left\{ \sum_{i=1}^{r} q_i h_i : q_i \in \mathbb{R}[\boldsymbol{z}] \right\}$$

Affine algebraic variety.

$$\mathbb{V}_K(J) = \left\{ \boldsymbol{z} \in K^k : \forall h \in J\ (h(\boldsymbol{z}) = 0) \right\}$$

where J : ideal, $K = \mathbb{R}$ or $\mathbb{C}$

Property.

$$\mathbb{V}_K(\langle f_1,\ldots,f_s \rangle) = \left\{ \boldsymbol{z} \in K^k : \text{(A)} \right\}$$

Since the solution space of (A) is equal to the affine variety of the ideal generated by $f_1,\ldots,f_s$, by interpreting the system (A) as the ideal, we can naturally utilize ideal operations in solving (A).

This interpretation is convenient because it allows us to leverage the properties of ideal operations.

9

Some natural operations defined on polynomial ideals

Operation eliminating unwanted spaces.

- Space where the covariance matrix of the observed variables becomes degenerate.
- Space where the unique variance matrix becomes degenerate.

$$\det \Sigma = \det(LL' + \Psi) = 0$$
$$\det \Psi = 0$$

Saturation of ideals I, J : Ideal[CLO; § 4.4, Pro. 6]

$$I : J^{\infty} = \{ p \in \mathbb{R}[\boldsymbol{z}] : \forall q \in J \exists N \in \mathbb{N} (pq^N \in I) \}$$

Affine algebraic variety[CLO; § 4.4, Th. 10]

$$\mathbb{V}_{\mathbb{C}}(I : J^{\infty}) = \overline{\mathbb{V}_{\mathbb{C}}(I) \setminus \mathbb{V}_{\mathbb{C}}(J)}$$

Here the right side is the Zariski closure.

※ Zariski closure : smallest affine algebraic variety containing a given set.

Operation reconstructing spaces.

- Space where the covariance matrix of the observed variables becomes degenerate.
- Space where the unique variance matrix becomes degenerate.

$$\det \Sigma = \det(LL' + \Psi) = 0$$
$$\det \Psi = 0$$

Sum of ideals I, J : Ideal[CLO; § 4.3, Pro. 2]

$$I + J = \{ p + q \in \mathbb{R}[\boldsymbol{z}] : p \in I, q \in J \}$$

Affine algebraic variety[CLO, § 4.3, Th. 4, § 4.4, Th. 10]

$$\mathbb{V}_K(I + J) = \mathbb{V}_K(I) \cap \mathbb{V}_K(J)$$

$$\mathbb{V}_K(I) = \mathbb{V}_K(I : J^{\infty}) \cup \mathbb{V}_K(I + J)$$

10

Some natural operations defined on polynomial ideals

Operations incorporating inequalities.

$$\mathbb{V}_{\mathbb{C}}(\langle f_1,\dots,f_s\rangle : \langle h\rangle^{\infty})$$

$$\begin{cases} 0 = f_1(z_1,\dots,z_k) \\ \quad\vdots \\ 0 = f_s(z_1,\dots,z_k) \\ 0 \neq h(z_1,\dots,z_k) \end{cases}$$

Operations incorporating equalities.

$$\mathbb{V}_{\mathbb{C}}(\langle f_1,\dots,f_s\rangle + \langle h\rangle)$$

$$\begin{cases} 0 = f_1(z_1,\dots,z_k) \\ \quad\vdots \\ 0 = f_s(z_1,\dots,z_k) \\ 0 = h(z_1,\dots,z_k) \end{cases}$$

$$\mathbb{V}_{\mathbb{C}}(\langle f_1,\dots,f_s\rangle)$$

$$\begin{cases} 0 = f_1(z_1,\dots,z_k) \\ \quad\vdots \\ 0 = f_s(z_1,\dots,z_k) \end{cases}$$

Operation reconstructing spaces[CLO; § 4.4, Th. 10]

11

Easy example

Maximum likelihood three variables and one factor analysis model.

$$S = \begin{pmatrix} 1 & \frac{1}{2} & \frac{1}{3} \\ \frac{1}{2} & 1 & \frac{2}{3} \\ \frac{1}{3} & \frac{2}{3} & 1 \end{pmatrix},\quad S^{-1} = \begin{pmatrix} \frac{4}{3} & -\frac{2}{3} & 0 \\ -\frac{2}{3} & \frac{32}{15} & -\frac{6}{5} \\ 0 & -\frac{6}{5} & \frac{9}{5} \end{pmatrix},\quad L = \begin{pmatrix} \ell_{11} \\ \ell_{21} \\ \ell_{31} \end{pmatrix},\quad \Psi = \begin{pmatrix} \psi_1 & 0 & 0 \\ 0 & \psi_2 & 0 \\ 0 & 0 & \psi_3 \end{pmatrix}.$$

System of algebraic equations (six variables and degree 2 and 3)

$$\begin{cases} 0 = f_1(\psi_1,\psi_2,\psi_3,\ell_{11},\ell_{21},\ell_{31}) \\ \quad\vdots \\ 0 = f_6(\psi_1,\psi_2,\psi_3,\ell_{11},\ell_{21},\ell_{31}) \end{cases}$$

where

$$\begin{aligned} f_1 &= (\Psi - \operatorname{diag}(S - LL'))_{11} = \psi_1 - (1 - \ell_{11}^2), \\ f_2 &= (\Psi - \operatorname{diag}(S - LL'))_{22} = \psi_2 - (1 - \ell_{21}^2), \\ f_3 &= (\Psi - \operatorname{diag}(S - LL'))_{33} = \psi_3 - (1 - \ell_{31}^2), \\ f_4 &= (L - (LL' + \Psi)S^{-1}L)_{11} \\ &= \ell_{11} - \left(\begin{array}{l} \ell_{11}\left(-\frac{2}{3}\ell_{11}\ell_{21} + \frac{4}{3}(\ell_{11}^2 + \psi_1)\right) \\ + \ell_{21}\left(\frac{32}{15}\ell_{11}\ell_{21} - \frac{6}{5}\ell_{11}\ell_{31} - \frac{2}{3}(\ell_{11}^2 - \psi_1)\right) + \ell_{31}\left(-\frac{6}{5}\ell_{11}\ell_{21} + \frac{9}{5}\ell_{11}\ell_{31}\right) \end{array} \right), \\ f_5 &= (L - (LL' + \Psi)S^{-1}L)_{21} \\ &= \ell_{21} - \left(\begin{array}{l} \ell_{11}\left(\frac{4}{3}\ell_{11}\ell_{21} - \frac{2}{3}(\ell_{21}^2 + \psi_2)\right) \\ + \ell_{21}\left(-\frac{2}{3}\ell_{11}\ell_{21} - \frac{6}{5}\ell_{21}\ell_{31} + \frac{32}{15}(\ell_{21}^2 + \psi_2)\right) + \ell_{31}\left(\frac{9}{5}\ell_{21}\ell_{31} - \frac{6}{5}(\ell_{21}^2 + \psi_2)\right) \end{array} \right), \\ f_6 &= (L - (LL' + \Psi)S^{-1}L)_{31} \\ &= \ell_{31} - \left(\begin{array}{l} \ell_{11}\left(\frac{4}{3}\ell_{11}\ell_{31} - \frac{2}{3}\ell_{21}\ell_{31}\right) \\ + \ell_{21}\left(-\frac{2}{3}\ell_{11}\ell_{31} + \frac{32}{15}\ell_{21}\ell_{31} - \frac{6}{5}(\ell_{31}^2 + \psi_3)\right) + \ell_{31}\left(-\frac{6}{5}\ell_{21}\ell_{31} + \frac{9}{5}(\ell_{31}^2 + \psi_3)\right) \end{array} \right). \end{aligned}$$

$$\begin{cases} L = (LL' + \Psi)S^{-1}L \\ \Psi = \operatorname{diag}(S - LL') \end{cases}$$

12

Easy example

Maximum likelihood three variables and one factor analysis model.

Let $I = \langle f_1, \ldots, f_6 \rangle$. We construct some ideals sequentially as follows:

$$I_0 = I + \langle \psi_1 \rangle, \quad I_1 = I : \langle \psi_1 \rangle^\infty.$$

$$I_{00} = I_0 + \langle \psi_2 \rangle, \quad I_{01} = I_0 : \langle \psi_2 \rangle^\infty, \quad I_{10} = I_1 + \langle \psi_2 \rangle, \quad I_{11} = I_1 : \langle \psi_2 \rangle^\infty.$$

$$I_{000} = I_{00} + \langle \psi_3 \rangle, \quad I_{001} = I_{00} : \langle \psi_3 \rangle^\infty, \quad I_{010} = I_{01} + \langle \psi_3 \rangle, \quad I_{011} = I_{01} : \langle \psi_3 \rangle^\infty,$$
$$I_{100} = I_{10} + \langle \psi_3 \rangle, \quad I_{101} = I_{10} : \langle \psi_3 \rangle^\infty, \quad I_{110} = I_{11} + \langle \psi_3 \rangle, \quad I_{111} = I_{11} : \langle \psi_3 \rangle^\infty.$$

Now we have the following property as shown in Page 11:

$$\begin{aligned} \mathbb{V}_{\mathbb{R}}(I) &= \mathbb{V}_{\mathbb{R}}(I_0) \cup \mathbb{V}_{\mathbb{R}}(I_1) \\ &= (\mathbb{V}_{\mathbb{R}}(I_{00}) \cup \mathbb{V}_{\mathbb{R}}(I_{01})) \cup (\mathbb{V}_{\mathbb{R}}(I_{10}) \cup \mathbb{V}_{\mathbb{R}}(I_{11})) \\ &= ((\mathbb{V}_{\mathbb{R}}(I_{000}) \cup \mathbb{V}_{\mathbb{R}}(I_{001})) \cup (\mathbb{V}_{\mathbb{R}}(I_{010}) \cup \mathbb{V}_{\mathbb{R}}(I_{011}))) \\ &\quad \cup ((\mathbb{V}_{\mathbb{R}}(I_{100}) \cup \mathbb{V}_{\mathbb{R}}(I_{101})) \cup (\mathbb{V}_{\mathbb{R}}(I_{110}) \cup \mathbb{V}_{\mathbb{R}}(I_{111}))) = \bigcup_{b \in \{0,1\}^3} \mathbb{V}_{\mathbb{R}}(I_b). \end{aligned}$$

13

Easy example

Maximum likelihood three variables and one factor analysis model.

The affine varieties $\mathbb{V}_{\mathbb{R}}(I_b)$ are empty sets for $b = 000, 100, 010, 001$. On the other hand,

$$\mathbb{V}_{\mathbb{R}}(I_{011}) = \left\{ \left(0, \frac{3}{4}, \frac{8}{9}, \pm 1, \pm\frac{1}{2}, \pm\frac{1}{3}\right) \right\}, \quad \mathbb{V}_{\mathbb{R}}(I_{101}) = \left\{ \left(\frac{3}{4}, 0, \frac{5}{9}, \pm\frac{1}{2}, \pm 1, \pm\frac{2}{3}\right) \right\},$$
$$\mathbb{V}_{\mathbb{R}}(I_{110}) = \left\{ \left(\frac{8}{9}, \frac{5}{9}, 0, \pm\frac{1}{3}, \pm\frac{2}{3}, \pm 1\right) \right\}, \quad \mathbb{V}_{\mathbb{R}}(I_{111}) = \{(1,1,1,0,0,0)\}$$

Gröbner bases $G_{011}, G_{101}, G_{110}, G_{111}$ of $I_{011}, I_{101}, I_{110}, I_{111}$ with respect to the lex order:

$$G_{011} = \left\{ \psi_1, \psi_2 - \frac{3}{4}, \psi_3 - \frac{8}{9}, \ell_{11} - 3\ell_{31}, \ell_{21} - \frac{3}{2}\ell_{31}, \ell_{31}^2 - \frac{1}{9} \right\},$$
$$G_{101} = \left\{ \psi_1 - \frac{3}{4}, \psi_2, \psi_3 - \frac{5}{9}, \ell_{11} - \frac{3}{4}\ell_{31}, \ell_{21} - \frac{3}{2}\ell_{31}, \ell_{31}^2 - \frac{4}{9} \right\},$$
$$G_{110} = \left\{ \psi_1 - \frac{8}{9}, \psi_2 - \frac{5}{9}, \psi_3, \ell_{11} - \frac{1}{3}\ell_{31}, \ell_{21} - \frac{2}{3}\ell_{31}, \ell_{31}^2 - 1 \right\},$$
$$G_{111} = \left\{ \psi_1 + \frac{81}{25}\ell_{31}^2 - 1, \psi_2 - 1, \psi_3 + \ell_{31}^2 - 1, \ell_{11} + \frac{9}{5}\ell_{31}, \ell_{21}, \ell_{31}^3 + \frac{5}{27}\ell_{31} \right\}.$$

14

Gröbner basis

System of linear equations.

$$\begin{cases} 0 = 1\cdot z_1 + 3\cdot z_2 + 1\cdot z_3 - 9 & \text{(a)} \\ 0 = 1\cdot z_1 + 1\cdot z_2 - 1\cdot z_3 - 1 & \text{(b)} \\ 0 = 3\cdot z_1 + 11\cdot z_2 + 6\cdot z_3 - 35 & \text{(c)} \end{cases}$$

Gaussian elimination : equivalent transformation.
Triangularization by cancellation of leading terms

$$\begin{cases} 0 = 1\cdot(\text{a}) - 1\cdot(\text{b}) = 2\cdot z_2 + 2\cdot z_3 - 3 \\ 0 = 3\cdot(\text{a}) - 1\cdot(\text{c}) = 2\cdot z_2 + 3\cdot z_3 - 8 \\ \quad \text{as 1st Step of Gaussian Elimination} \end{cases}$$

$$\begin{cases} 0 = 1\cdot z_1 + 3\cdot z_2 + 1\cdot z_3 - 9 \\ 0 = \quad 2\cdot z_2 - 2\cdot z_3 - 8 \\ 0 = \quad 1\cdot z_3 - 0 \end{cases}$$

Gröbner basis is a generalization of Gaussian elimination.

System of algebraic equations.

$$\begin{cases} 0 = z_1^2 + z_2^2 z_3 & \text{(A)} \\ 0 = z_1^2 - z_2^2 + z_3^2 & \text{(B)} \\ 0 = z_1 z_2 - 1 & \text{(C)} \end{cases}$$

Gröbner basis : equivalent transformation.
Triangularization by cancellation of leading terms

$$\begin{cases} 0 = 1\cdot(\text{A}) - 1\cdot(\text{B}) = z_2^2 z_3 + z_2^2 - z_3^2 \\ 0 = z_2\cdot(\text{A}) - z_1\cdot(\text{C}) = z_1 + z_2^3 z_3 \\ 0 = z_2\cdot(\text{A}) - z_1\cdot(\text{C}) = z_1 - z_2^3 + z_2 z_3^2 \\ \quad \text{as 1st Step of Gröbner basis} \\ \quad \#\ \text{Buchberger's Algorithm} \end{cases}$$

$$\begin{cases} 0 = z_1 - z_2 z_3^4 + z_2 z_3^3 - z_2 z_3 - z_2 & \in \mathbb{R}[z_1, z_2, z_3] \\ 0 = z_2^2 - z_3^4 + z_3^3 - z_3^2 - z_3 - 1 & \in \mathbb{R}[\quad z_2, z_3] \\ 0 = z_3^5 + z_3^2 + 2z_3 + 1 & \in \mathbb{R}[\quad\quad z_3] \end{cases}$$

15

Easy example

Maximum likelihood three variables and one factor analysis model.

The Gröbner bases $G_{011}, G_{101}, G_{110}, G_{111}$ divide the original system $f_1 = \cdots = f_6 = 0$ into the following simple sub-problems since we have $\mathbb{V}_{\mathbb{R}}(I) = \bigcup_{b\in\{0,1\}^3} \mathbb{V}_{\mathbb{R}}(I_b) = \bigcup_{b\in\{0,1\}^3} \mathbb{V}_{\mathbb{R}}(G_b)$:

$$\begin{cases} \psi_1 = 0, \\ \psi_2 = \frac{3}{4}, \\ \psi_3 = \frac{8}{9}, \\ \ell_{11} = 3\ell_{31}, \\ \ell_{21} = \frac{3}{2}\ell_{31}, \\ 0 = \ell_{31}^2 - \frac{1}{9}, \end{cases} \quad \begin{cases} \psi_1 = \frac{3}{4}, \\ \psi_2 = 0, \\ \psi_3 = \frac{5}{9}, \\ \ell_{11} = \frac{3}{4}\ell_{31}, \\ \ell_{21} = \frac{3}{2}\ell_{31}, \\ 0 = \ell_{31}^2 - \frac{4}{9}, \end{cases} \quad \begin{cases} \psi_1 = \frac{8}{9}, \\ \psi_2 = \frac{5}{9}, \\ \psi_3 = 0, \\ \ell_{11} = \frac{1}{3}\ell_{31}, \\ \ell_{21} = \frac{2}{3}\ell_{31}, \\ 0 = \ell_{31}^2 - 1, \end{cases} \quad \begin{cases} \psi_1 = 1 - \frac{81}{25}\ell_{31}^2, \\ \psi_2 = 1, \\ \psi_3 = 1 - \ell_{31}^2, \\ \ell_{11} = -\frac{9}{5}\ell_{31}, \\ \ell_{21} = 0, \\ 0 = \ell_{31}^3 + \frac{5}{27}\ell_{31}. \end{cases}$$

Saturations and sums do not necessarily reduce to simple sub-problems depending on the ideals involved in addition or division. Statistical models, such as factor analysis models, often assume degeneracy conditions on matrices containing parameters. Such degeneracy conditions correspond to polynomial constraints, like whether its determinant is zero or not. By constructing saturations and sums based on these constraints, we can reduce the problem to simpler subproblems.

16

Computational cost

My recent implementation.

An implementation using multiple computational algebra systems.

Maximum likelihood estimate
(5 variables and 2 factors).

several weeks to several months

Orthogonal factor rotation
(9 variables and 3 factors).

several minutes

That's all!!! Thanks!!!

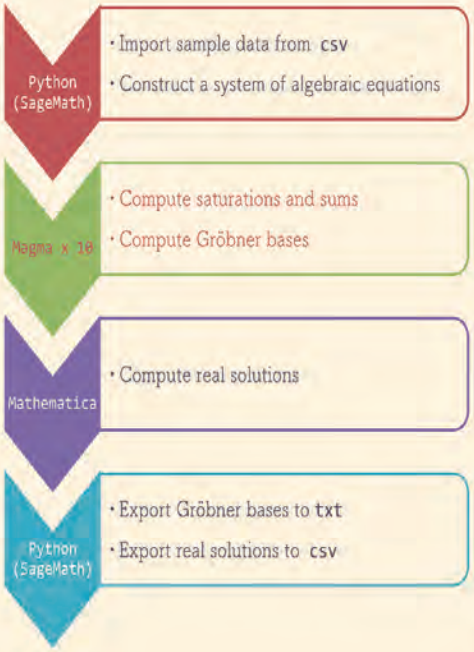

17

From Natural Intelligence To Artificial Intelligence

Nguyen Dinh Hoa

IMI, Kyushu University

This talk shows a research inspired by a cooperative hunting behavior in nature, going from the behavior’s mathematical modeling to its use in a practical application of ground-aerial vehicle cooperation. For this application, a deep learning method will first be presented for the recognition problem between the aerial and ground vehicles. Then robust distributed HH∞ and HH2 control designs will be introduced to cope with different types of disturbances on the position sensing of vehicles. Finally, the bounded input constraint will be tackled using the input-to-state stability (ISS) concept.

From Natural Intelligence To Artificial Intelligence

Nguyen Dinh Hoa
International Institute for Carbon-Neutral Energy Research,
and Institute of Mathematics for Industry,
Kyushu University, Fukuoka, Japan
Email: hoa.nd@i2cner.kyushu-u.ac.jp, hoa@imi.kyushu-u.ac.jp

FMfI, Seoul, Korea, August 20, 2025

2

From: Natural Intelligence

Wolf-Raven Cooperative Hunting

Symbiotic Wolf-Raven Relation

Cooperative hunting

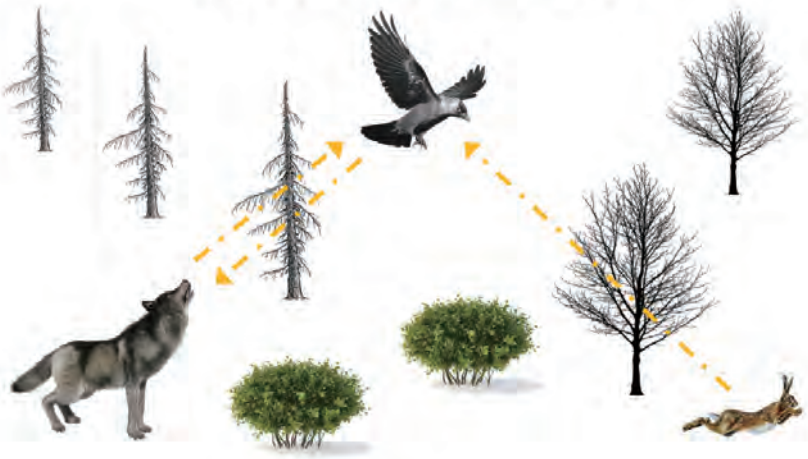

Symbiotic Wolf-Raven Relation

Cooperative hunting: Mathematical Modeling

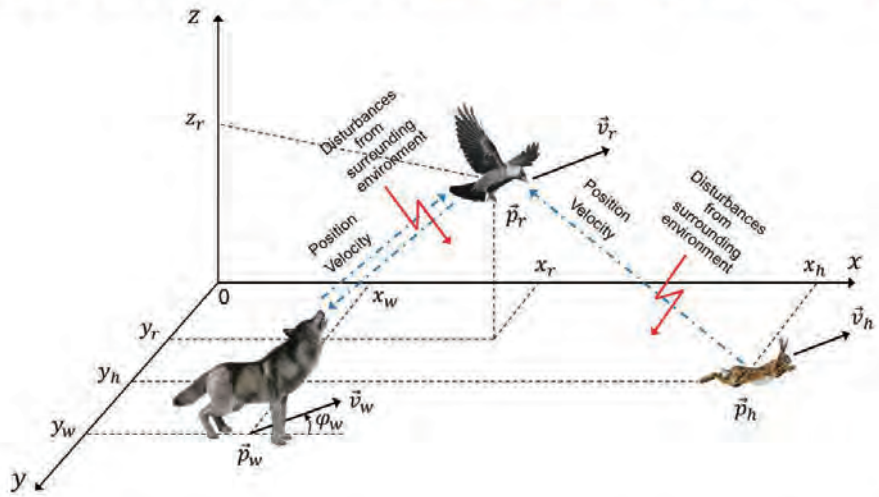

Wolf-Raven Cooperative Hunting Model

■ **Proposed mathematical model (continuous-time):**

$$\frac{d}{dt}\vec{p}_r(t) = \vec{v}_r(t)$$

$$\frac{d}{dt}\vec{v}_r(t) = f_r\left(\vec{p}_h(t), \vec{v}_h(t), \vec{p}_w(t), \vec{v}_w(t), \vec{p}_r(t), \vec{v}_r(t)\right)$$

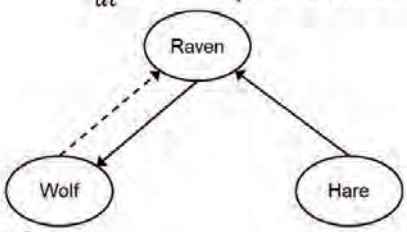

$$\frac{d}{dt}\vec{p}_w(t) = \vec{v}_w(t)$$

$$\frac{d}{dt}\vec{v}_w(t) = f_w\left(\vec{p}_r(t), \vec{v}_r(t), \vec{p}_w(t), \vec{v}_w(t)\right)$$

■ **Goal:** $\lim_{t\to t_f}\|x_r(t) - x_h(t)\| = 0,\ \lim_{t\to t_f}\|y_r(t) - y_h(t)\| = 0,\ \lim_{t\to t_f}\|p_w(t) - p_h(t)\| = 0.$

A Linear Model

■ Following mechanisms are linear:

$$\frac{d}{dt}\vec{p}_r(t) = \vec{v}_r(t)$$

$$\frac{d}{dt}\vec{v}_r(t) = K_r^1\left(\vec{p}_h(t) - \vec{p}_r(t) + \vec{p}_w(t) - \vec{p}_r(t)\right) + K_r^2\left(\vec{v}_h(t) - \vec{v}_r(t) + \vec{v}_w(t) - \vec{v}_r(t)\right) + \begin{bmatrix} 0 \\ 0 \\ \xi_r(t) \end{bmatrix}$$

environmental disturbance

$$\frac{d}{dt}\vec{p}_w(t) = \vec{v}_w(t)$$

$$\frac{d}{dt}\vec{v}_w(t) = K_w^1\left(\vec{p}_r(t) - \vec{p}_w(t)\right) + K_w^2\left(\vec{v}_r(t) - \vec{v}_w(t)\right)$$

■ Raven freely changes its altitude:

$$K_r^i = \begin{bmatrix} \hat{K}_r^i & 0 \\ 0 & 0 \end{bmatrix}, K_w^i = \begin{bmatrix} \hat{K}_w^i & 0 \\ 0 & 0 \end{bmatrix}; \hat{K}_r^i, \hat{K}_w^i \in \mathbb{R}^{2\times 2}, i = 1,2$$

A Nonlinear Model

- Following mechanisms are nonlinear:

$$f_r(\cdot) = g_r\left(\vec{p}_h(t) - \vec{q}_r(t)\right)\left(\vec{v}_h(t) - \vec{v}_r(t)\right) + g_r\left(\vec{p}_w(t) - \vec{q}_r(t)\right)\left(\vec{v}_w(t) - \vec{v}_r(t)\right) + \begin{bmatrix} 0 \\ 0 \\ \xi_r(t) \end{bmatrix}$$

$$f_w(\cdot) = g_w\left(\vec{q}_r(t) - \vec{p}_w(t)\right)\left(\vec{v}_r(t) - \vec{v}_w(t)\right)$$

- Cucker-Smale model is a special case of the above model

$$x' = v$$
$$v' = -L_x v,$$
$$a_{ij} = \frac{K}{(\sigma^2 + \|x_i - x_j\|^2)^\beta},$$

Simple Illustration

- Linear model, wolf-raven bidirectional communication, no disturbances
- Independent control of *x* and *y* axes, precise estimates
- Controller gains are designed by a distributed LQR method*

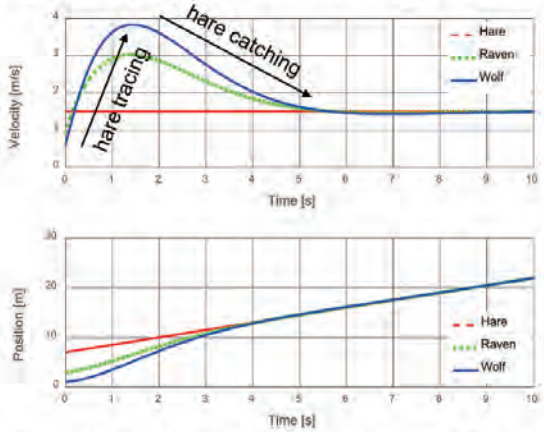

Illustration of the wolf-raven cooperative hunting along the *x*-axis

To: Artificial Intelligence

Visual-based Ground-Aerial Vehicle Cooperation

Institute of Mathematics for Industry
Kyushu University

I²CNER

Ground-Aerial Vehicle Cooperation

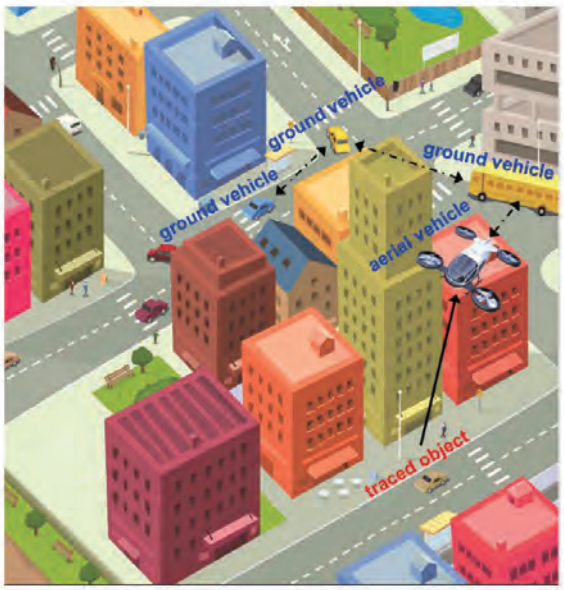

Institute of Mathematics for Industry
Kyushu University

D. H. Nguyen, "A Nature-Inspired Distributed Robust Control Design for Ground-Aerial Vehicle Cooperation", IEEE Transactions on Intelligent Transportation Systems, vol. 24(4), pp. 4454-4463, 2023.

I²CNER

YOLO for Image Recognition

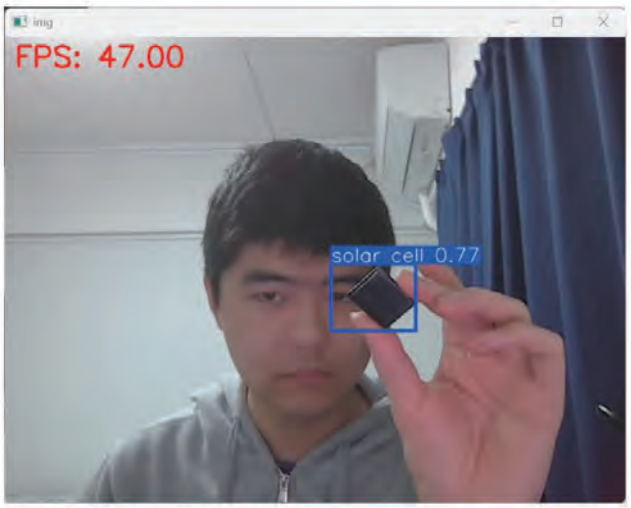

Institute of Mathematics for Industry Kyushu University

YOLO (You Look Only Once): CNN-based DL model

I²CNER

Vehicle Model

Dubins car model

$$\dot{\theta} = \omega = v \tan \varphi,$$
$$\dot{x}_M = v \cos \theta,$$
$$\dot{y}_M = v \sin \theta.$$

Linearized model

$$\dot{\bar{x}} = \bar{u}.$$
$$\bar{x} \triangleq \begin{bmatrix} x_C \\ y_C \end{bmatrix} \quad \bar{u} \triangleq \mathbb{M}[v, \omega]^T$$
$$\mathbb{M} \triangleq \begin{bmatrix} \cos\theta & -r\sin\theta \\ \sin\theta & r\cos\theta \end{bmatrix}$$

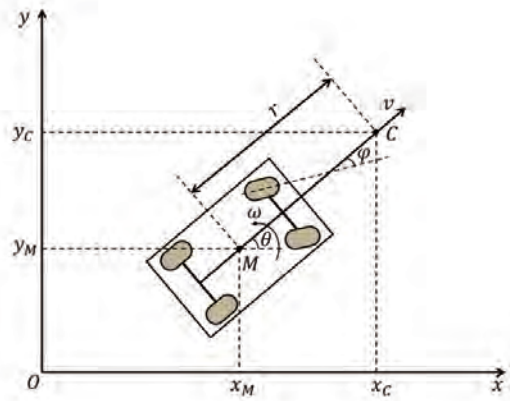

Institute of Mathematics for Industry Kyushu University

D. H. Nguyen, "A Nature-Inspired Distributed Robust Control Design for Ground-Aerial Vehicle Cooperation", IEEE Transactions on Intelligent Transportation Systems, vol. 24(4), pp. 4454-4463, 2023.

I²CNER

Robust Distributed Control Design

$$u_i(t) = -\mu \sum_{j\in\mathcal{N}_i} a_{ij}[x_i(t) - x_j(t) + w_i(t) - w_j(t)] - \mu\sigma_i[x_i(t) - x_0(t) + w_i(t) - w_0(t)], \quad (1)$$

$$\zeta(t) \triangleq x(t) - \mathbf{1}_{n+1}x_0(t)$$

Closed-loop model

$$\dot{\zeta}(t) = -\mu(\mathcal{L} + \Sigma)\zeta(t) - \mu\mathcal{L}d_1(t) - \mu\Sigma d_2(t) - \mathbf{1}_{n+1}v_0(t)$$

Robust performance indicator

$$\|\mathcal{C}(sI_{n+1} - \mathcal{A})^{-1}\mathcal{B}\| < \gamma$$

$$\mathcal{A} \triangleq -\mu(\mathcal{L} + \Sigma),\ \mathcal{B} \triangleq \begin{bmatrix}-\mu\mathcal{L}, & -\mu\Sigma, & -\mathbf{1}_{n+1}\end{bmatrix},$$
$$\mathcal{C} \triangleq \alpha I_{n+1},\ d(t) \triangleq \begin{bmatrix}d_1(t), & d_2(t), & v_0(t)\end{bmatrix}^T.$$

$w_i(t)$ sensing
$w_0(t)$ disturbances
$x_0(t)$ traced vehicle position
$v_0(t)$ traced vehicle speed
$x_i(t)$ other vehicle position
$\mathcal{L}$ Laplacian matrix of inter-vehicle undirected communication graph G

Distributed H_∞ and H_2 Controllers

Robust H_∞ condition

Given $\gamma > 0$, (1) is a distributed robust H_∞ controller if

$$\gamma > \max_{k=2,\ldots,n+1}\left\{1 + \frac{1}{\mu^2}, \sqrt{\frac{1+\lambda_k^2}{1+2\lambda_k}}\right\}$$

Finite-energy noises, e.g., rectangular noises

Robust H_2 condition

If

$$\gamma > \sqrt{n+1}\alpha,$$

then $\exists\ \mu > 0$ s.t. (1) is a distributed robust H_2 controller.

Infinite-energy noises, e.g., white noises

λ_k: non-zero eigenvalues of $\mathcal{L}$

Input Constraint

Distributed controller

$$y(t) = -\mu(\mathcal{L}+\Sigma)\zeta(t) - \mu\mathcal{L}d_1(t) - \mu\Sigma d_2(t),$$
$$u(t) = \mathbf{sat}(y(t)),$$

$$\mathrm{sat}(u_i) \triangleq \begin{cases} u_i^{\max} & \text{if} \quad u_i > u_i^{\max}, \\ u_i & \text{if} \quad u_i^{\min} \le u_i \le u_i^{\max}, \\ u_i^{\min} & \text{if} \quad u_i < u_i^{\min}. \end{cases}$$

$$\phi(y_i) \triangleq \mathrm{sat}(y_i) - y_i, i = 1, \ldots, n+1,$$
$$\Phi(y) \triangleq \left[\phi(y_1), \ldots, \phi(y_{n+1})\right]^T = \mathbf{sat}(y(t)) - y(t).$$
$$Q \triangleq \left[-\mu\mathcal{L} \; -\mu\Sigma \; -\mathbf{1}_{n+1}\right]$$

Closed-loop model

$$\dot{\zeta}(t) = -\mu(\mathcal{L}+\Sigma)\zeta(t) + Qd(t) + \Phi(y(t))$$

Robustness condition

Given $\epsilon > 0$, closed-loop system is input-to-state stable (ISS) if

$$\mu > \frac{\epsilon}{2\lambda_{\min}(\mathcal{L}+\Sigma)}$$

$\gamma_1 \in \mathcal{KL}$ and $\gamma_2 \in \mathcal{K}_\infty$ such that

$$\|x(t)\|_2 \le \gamma_1(\|x(0)\|_2, t) + \gamma_2(\|u(t)\|_\infty)$$

Ground-Aerial Vehicle Cooperation

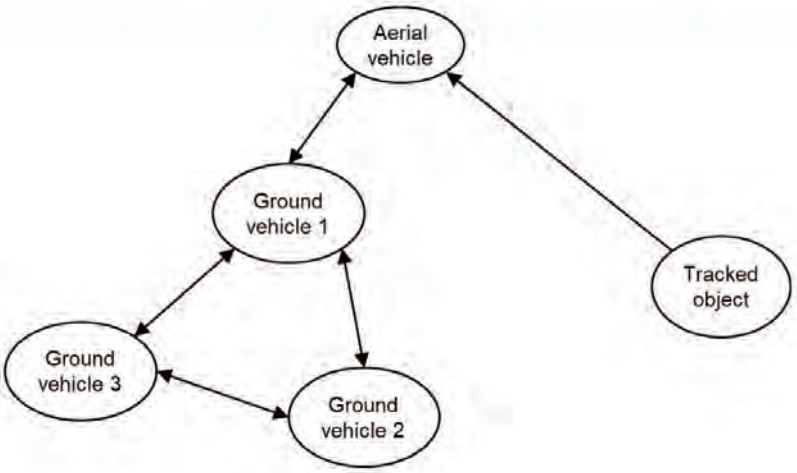

Simulation Results – H_2 Case

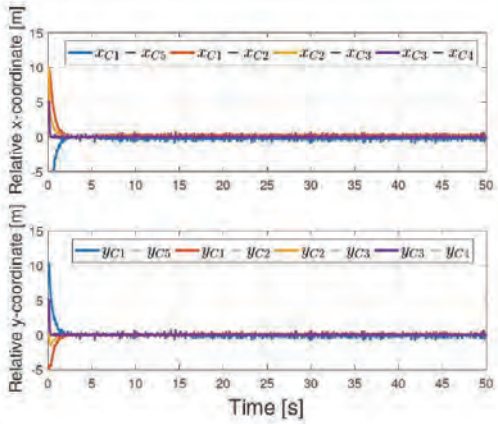

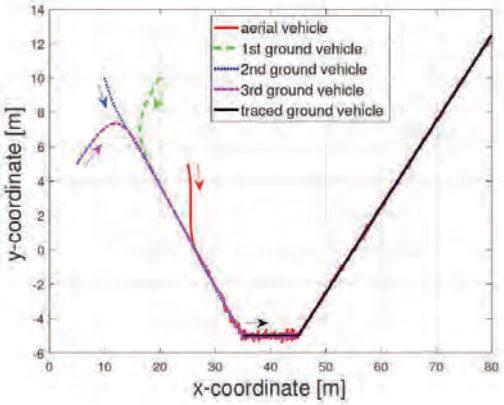

Simulation Results – H_∞ Case

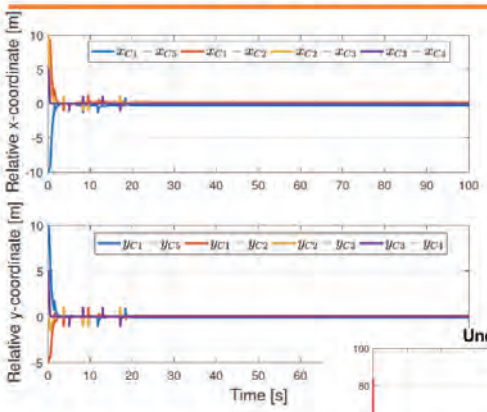

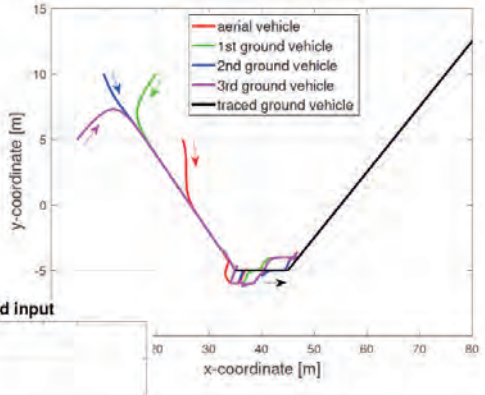

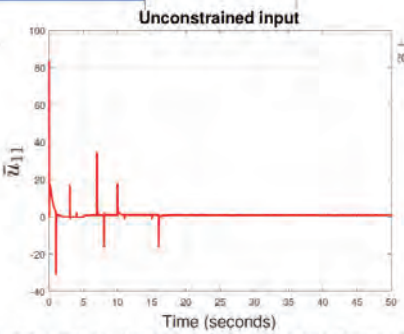

Simulation Results – H_∞ & Input Constraint

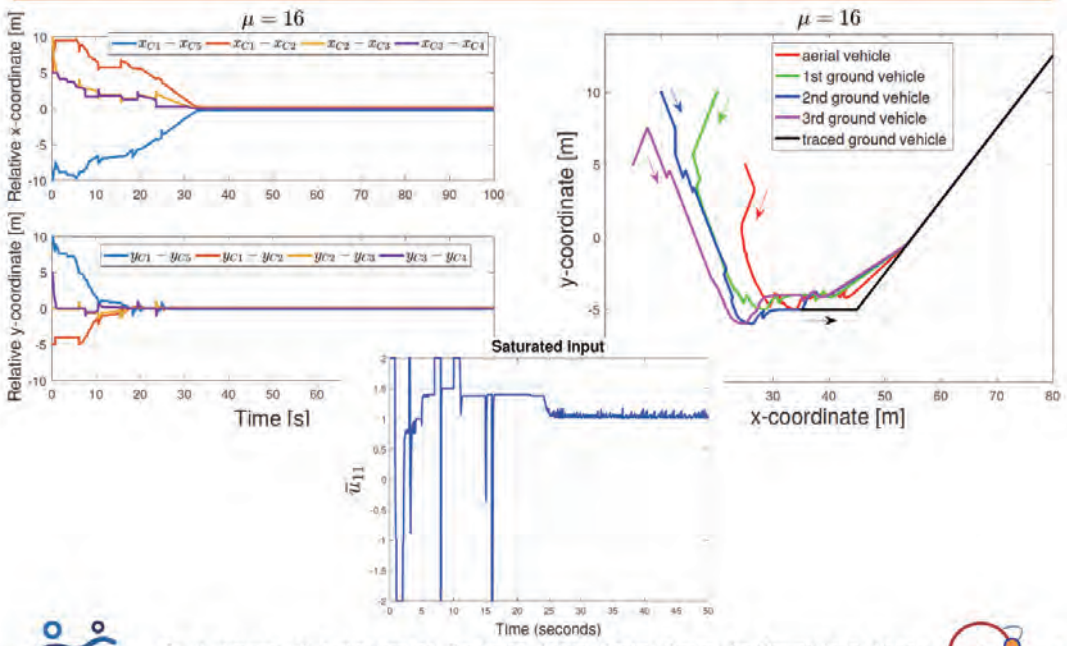

D. H. Nguyen, "A Nature-Inspired Distributed Robust Control Design for Ground-Aerial Vehicle Cooperation", IEEE Transactions on Intelligent Transportation Systems, vol. 24(4), pp. 4454-4463, 2023.

Thank you for listening!

Q & A

Contact: hoa.nd@i2cner.kyushu-u.ac.jp, hoa@imi.kyushu-u.ac.jp

Accelerated Bayesian Optimal Experimental Design via Conditional Density Estimation and Informative Data

Hongqiao Wang

Central South University, China

The Design of Experiments (DOEs) is a fundamental scientific methodology that provides researchers with systematic principles and techniques to enhance the validity, reliability, and efficiency of experimental outcomes. In this study, we explore optimal experimental design within a Bayesian framework, utilizing Bayes' theorem to reformulate the utility expectation—originally expressed as a nested double integral— into an independent double integral form, significantly improving numerical efficiency. To further accelerate the computation of the proposed utility expectation, conditional density estimation is employed to approximate the ratio of two Gaussian random fields, while covariance serves as a selection criterion to identify informative data-set during model fitting and integral evaluation. In scenarios characterized by low simulation efficiency and high costs of raw data acquisition, key challenges such as surrogate modeling, failure probability estimation, and parameter inference are systematically restructured within the Bayesian experimental design framework. The effectiveness of the proposed methodology is validated through both theoretical analysis and practical applications, demonstrating its potential for enhancing experimental efficiency and decision-making under uncertainty.

FMfl2025

Accelerated Bayesian Optimal Experimental Design via Conditional Density Estimation and Informative Data

Hongqiao Wang (Central South University, China)

Aug. 20, 2025

Outline

- Bayesian optimal experimental design (BOED)
- Gaussian process regression (GPR) surrogate
- Efficient approximation of expected utility using conditional density estimation
- Covariance-driven acceleration method
- Numerical examples
- Summary

Motivation

Optimal experimental design

- $y = g(\boldsymbol{x})$: Experimental data can be costly or time-consuming to acquire
- d: Where to place a sensor? What experimental conditions to impose?
- $\boldsymbol{z}$: Parameters of interested (PoI), optional and rely on specific problems.

Application:

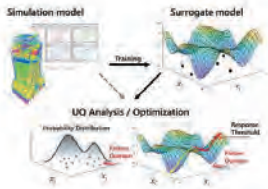

surrogate construction

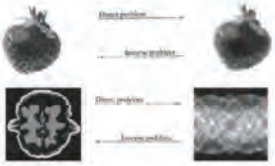

inverse problem

failure probability estimation

Bayesian Optimal Experimental Design

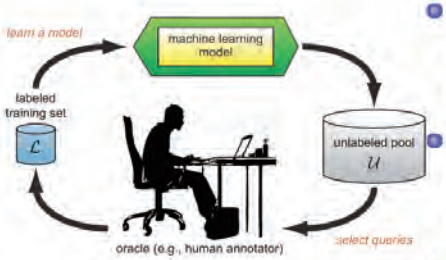

Figure 1: The pool-based active learning cycle.

- In machine learning, **Bayesian optimal experimental design** is closely related to **active learning**
- Sequentially design new experimental inputs and interactively query a simulator to obtain labels for new points
- Improve learning efficiency by focusing on the most informative samples

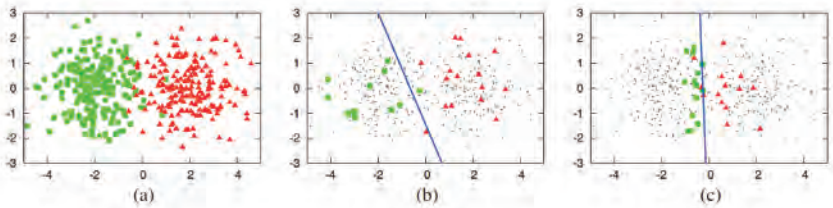

Bayesian optimal experimental design (BOED):

$$\begin{aligned} d^* &= \arg\max_{d \in D} U(d) \\ &= \arg\max_{d \in D} \int_Y \int_{\mathcal{X}} u(d, \boldsymbol{z}, y) p(\boldsymbol{z}|y, d) p(y|d) \, d\boldsymbol{z} dy, \end{aligned}$$

where

- $U(d)$ is the utility expectation;
- $u(d, \boldsymbol{z}, y)$ is the utility function;
- $d \in \mathcal{X}$: is the design point;
- y: possible outputs of design point;
- $\boldsymbol{z} \in \mathcal{X}$: purpose of experimental design, a random variable associated with applications;
- $p(y|d)$ can be predicted by surrogate model, like Gaussian process regression.

Definition of PoI in BOED for surrogate modelling, parameter estimation and failure probability estimation

Surrogate construction:
The goal of surrogate construction is to construct an accurate model which is accurate in the whole input domain $\mathcal{X}$. Then the random variable $\boldsymbol{z}$ is defined as the variance of current surrogate model,$\psi(\cdot)$ denotes a positive function

$$p(\boldsymbol{z}) := p(z|\psi \circ \sigma(\boldsymbol{z}))$$

Parameter estimation/ inverse problem:

$$p(\boldsymbol{z}) := p(\boldsymbol{z}|g(\boldsymbol{z}) = y_0)$$

Failure probability estimation:
We define the state function of the failure probability problem as $g(x)$, and its failure boundary is defined as ℓ: $\{x \in \mathcal{X} \,|g(x) = 0\}$, then

$$p(\boldsymbol{z}) := \frac{1}{C} \exp\left(-\frac{|g(\boldsymbol{z}) - 0|}{\lambda}\right)$$

The utility function

Kullback-Leibler divergence (KLD)

Kullback-Leibler divergence, which is most commonly used in measuring the distance between different PDFs. The definition is :

$$KL(p\|q) = \int p(x) \ln \frac{p(x)}{q(x)} dx$$

In the framework of Bayesian optimal experimental design, the KLD between the posterior and prior distributions is commonly used as a utility function, and is generally expressed as:

$$u(d, y) = \int_{\mathcal{X}} p(\boldsymbol{z}|d, y) \left[\log \frac{p(\boldsymbol{z}|d, y)}{p(\boldsymbol{z})}\right] d\boldsymbol{z}$$

Information gain

Bayesian Optimal experimental design

BOED:

$$\begin{aligned} d^* &= arg\max_{d\in D} \int_Y \int_{\mathcal{X}} u(d, \boldsymbol{z}, y)\, p(\boldsymbol{z}, y|d)\, d\boldsymbol{z}dy \\ &= arg\max_{d\in D} \int_Y \int_{\mathcal{X}} p(\boldsymbol{z}|d, y) \log \frac{p(\boldsymbol{z}|d, y)}{p(\boldsymbol{z})} d\boldsymbol{z} p(\boldsymbol{z}, y|d)\, d\boldsymbol{z}dy \end{aligned}$$

- Variational posterior/marginal [Adam Foster, NIPS2019]
- Upper Bound [Jiayuan Dong, CMAME2025]

Bayesian inference

Rewriting $p(\boldsymbol{z}|d, y)$ with Bayesian formula:

$$p(\boldsymbol{z}|d, y) = \frac{p(y|d, \boldsymbol{z})\, p(\boldsymbol{z})}{p(y|d)}$$

Rewrite the utility function as:

$$u(y, \boldsymbol{z}, d) = \int \frac{p(y|d, \boldsymbol{z})\, p(\boldsymbol{z})}{p(y|d)} \ln \frac{p(y|d, \boldsymbol{z})}{p(y|d)} d\boldsymbol{z}$$

Bayesian optimal experimental design

$$\begin{aligned} d^* &= arg\max_{d \in D} \int_{\mathcal{X}} \int_{Y} p(y|d, \boldsymbol{z}) \ln \left(\frac{p(y|d, \boldsymbol{z})}{p(y|d)} \right) dy p(\boldsymbol{z})\, d\boldsymbol{z} \\ &= arg\max_{d \in D} \mathbb{E}_{\boldsymbol{z}_i \sim p(\boldsymbol{z})} \int_{Y} p(y|d, \boldsymbol{z}_i) \ln \left(\frac{p(y|d, \boldsymbol{z}_i)}{p(y|d)} \right) dy \end{aligned}$$

- Nested Monte Carlo form
- $p(y|d, \boldsymbol{z}_i)$: addition information $\boldsymbol{z}_i$ embeded in the surrogate
- $p(y|d)$: the density y at design d predicted by surrogate.

Probabilistic surrogate: Gaussian process regression

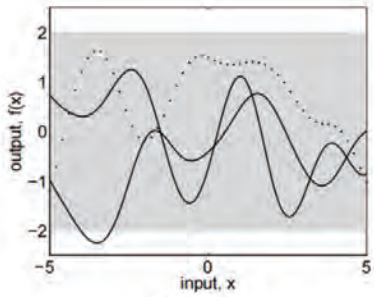

(a), prior

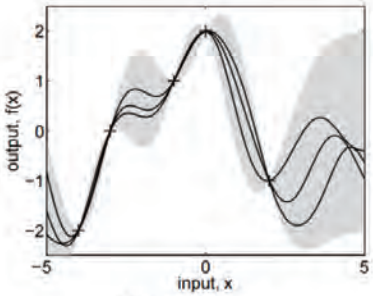

(b), posterior

Probabilistic surrogate: Gaussian process regression

Gaussian process $f(\boldsymbol{x})$ is characterized by its mean function 0 and covariance function (or kernel) $k(\boldsymbol{x}, \boldsymbol{x}')$:

$$f(\boldsymbol{x}) \sim \mathcal{GP}(\mathbf{0}, k(\boldsymbol{x}, \boldsymbol{x}')).$$

Give a data set $\mathcal{D} = \{X, Y\}$, $X = [\boldsymbol{x}_1, \ldots, \boldsymbol{x}_n]^\top$, $Y = [y_1, \ldots, y_n]^\top]$, for a new input points $\boldsymbol{x}_*$, we seek the predictive distribution of the corresponding outputs y_*. Under the Gaussian process framework, the joint distribution of training outputs $\mathbf{y}$ and test outputs y_* is given by:

$$\begin{bmatrix} Y \\ y_* \end{bmatrix} \sim \mathcal{N}\left(\begin{bmatrix} \mathbf{0} \\ \mathbf{0} \end{bmatrix}, \begin{pmatrix} \mathbf{K} + \sigma_n^2 \mathbf{I} & \mathbf{K}_* \\ \mathbf{K}_*^\top & \mathbf{K}_{**} \end{pmatrix} \right)$$

Probabilistic surrogate: Gaussian process regression

By conditioning on the observed data Y, the posterior predictive distribution of y_* is derived as:

$$y_* | \mathbf{D}_*, \mathbf{D}, Y \sim \mathcal{N}(m_*, \mathbf{\Sigma}_*)$$

where the predictive mean m_* and covariance $\mathbf{\Sigma}_*$ are given by:

$$m_* = \mathbf{K}_*^\top (\mathbf{K} + \sigma_n^2 \mathbf{I})^{-1} Y$$

$$\mathbf{\Sigma}_* = \mathbf{K}_{**} - \mathbf{K}_*^\top (\mathbf{K} + \sigma_n^2 \mathbf{I})^{-1} \mathbf{K}_*$$

Both $p(y|d)$ and $p(y|d, z)$ can be modeled by GPR.

Approximation by Conditional Density Estimation

$$d^* = arg\max_{d \in D} \mathbb{E}_{z_i \sim p(z)} \int_Y p(y|d, z_i) \ln \left(\frac{p(y|d, z_i)}{p(y|d)} \right) dy$$

The quotient $\frac{p(y|d,z)}{p(y|d)}$ can be approximated by a conditional density $q_{CDE}(y|d, z)$, and we estimate this quotient through conditional density estimation, yielding:

$$q_{CDE}(y|d, z) \approx \frac{p_{GP}(y|d, z)}{p_{GP}(y|d)}$$

Quotient of two Gaussian distribution

Based on the properties of normal distributions, the quotient of two normal distributions is itself normally distributed, as follows:

$$\frac{\mathcal{N}(y \mid \mathbf{m}_1, \Sigma_1)}{\mathcal{N}(y \mid \mathbf{m}_2, \Sigma_2)} = \mathcal{N}(y \mid \mathbf{m}, \Sigma) \cdot \mathcal{Z}$$

where

$$\Sigma = \left(\Sigma_1^{-1} - \Sigma_2^{-1}\right)^{-1}$$

and

$$\mathbf{m} = \Sigma\left(\Sigma_1^{-1}\mathbf{m}_1 - \Sigma_2^{-1}\mathbf{m}_2\right)$$

Furthermore,

$$\mathcal{Z} = \frac{|\Sigma_2|}{|\Sigma_2 - \Sigma_1|} \cdot \frac{1}{\mathcal{N}(\mathbf{m}_1 \mid \mathbf{m}_2, \Sigma_2 - \Sigma_1)}$$

Approximation by Conditional Density Estimation

Utility expectation:

$$d^* = \arg\max_{d \in D} \int_{\boldsymbol{z}} \int_{Y} \frac{\hat{p}(y|\boldsymbol{d}, \boldsymbol{z})}{p\left(y|\boldsymbol{d}\right)} \ln\left(\frac{\hat{p}(y|\boldsymbol{d}, \boldsymbol{z})}{p\left(y|\boldsymbol{d}\right)}\right) p(y|\boldsymbol{d}) p\left(\boldsymbol{z}\right) \, dy d\boldsymbol{z}.$$

And a computational expression with independent integral form is

$$d^* = \arg\max_{d \in D} \mathbb{E}_{y_i \sim p_{GP}(y|\boldsymbol{d}), \boldsymbol{z}_i \sim p(z)} \frac{\hat{p}(y_i|\boldsymbol{d}, \boldsymbol{z}_i)}{p\left(y_i|\boldsymbol{d}\right)} \ln\left(\frac{\hat{p}(y_i|\boldsymbol{d}, \boldsymbol{z}_i)}{p\left(y|\boldsymbol{d}\right)}\right).$$

Covariance-Driven Acceleration Method

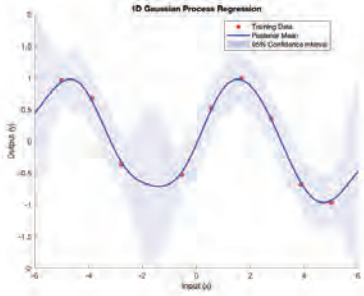

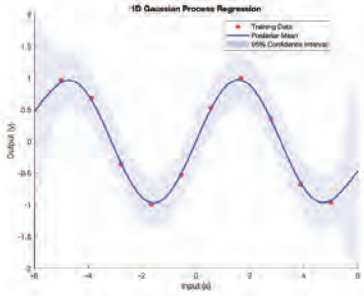

$p(y|d)$ $p(y|d, z_i)$

- The additional information z_i impacts $p(y|d, z_i)$ locally in comparison to $p(y|d)$.;
- A criterion is proposed to accelerate the computation of utility expectations.
- $\boxed{\mathrm{COV}[f(z_i), f(d)] > \epsilon}$

Covariance-Driven Acceleration Method

Two specific acceleration techniques

1. Informative data-set construction for CDE learning;

$$\Omega_z := \{\boldsymbol{d} \in \mathcal{X} | \, \mathrm{COV}(y_d, y_z) \geq \epsilon_{cov}\},$$

2. Informative samples selection of Monte Carlo integral

$$\{\boldsymbol{z} | \, \mathrm{COV}(y_{\boldsymbol{d}_i}, y_{\boldsymbol{z}}) > \epsilon_{cov}, \boldsymbol{z} \sim p(\boldsymbol{z})\}.$$

Conditional Density Estimation (CDE) Model Fitting

$$d^* = \arg\max_{d \in D} \mathbb{E}_{z_i \sim p(z)} \int_Y p_{GP}(y|d)\, q_{CDE}(y|d, z_i) \ln(q_{CDE}(y|d, z_i))\, dy$$

$p(z)$ is fixed from CDE learning point of view

Data set $\{[z_i, d_i], y_i\}$ for the training of $q_{CDE}(y|d, z)$ selected by covariance criterion $\boxed{\mathrm{COV}[f(z_i), f(d_i)] > \epsilon}$.

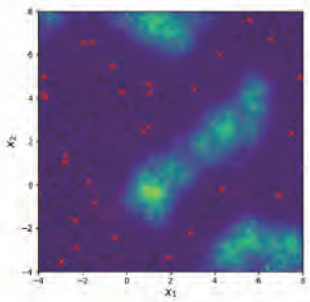

$BOED$

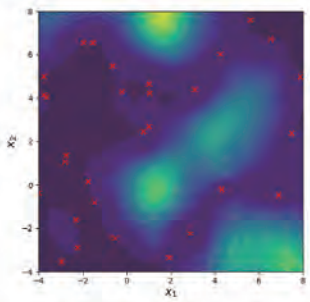

$Acc - BOED$

Integral Computation of the Utility Function

$$d^* = \arg\max_{d \in D} \mathbb{E}_{z_i \sim p(z)} \int_Y p_{GP}(y|d)\, q_{CDE}(y|d, z_i) \ln(q_{CDE}(y|d, z_i))\, dy$$

d is fixed from an optimization point of view

Samples z_i for expectation is selected by covariance criterion $\boxed{Cov[f(z_i), f(d)] > \epsilon}$.

Execution Time Comparison (seconds) in a full iteration

Method	Test Cases					
	SM		*PE*		*FP*	
	Trig	ADM	Erf	KDV	Circ	FB
Acc-BOED	321	346	205	138	274	193
Basic BOED	2765	2308	2231	1874	3251	1234
Ratio (Basic/Acc)	**8.61**	**6.67**	**10.88**	**13.58**	**11.87**	**6.39**

Note: Abbreviations: Surrogate Model (SM): Trigonometric Model (Trig), Alanine Dipeptide Model (ADM);Parameter Estimation(PE): Gauss error function(Erf),KDV Equation (KDV); Failure Probability Estimation(FP): Circle Problem(Circ); Four Branch System (FB).

Surrogate Model: Trigonometric Model

Trigonometric Model:

$$f(x) = \sin(x_1) \cdot \cos(x_2)$$

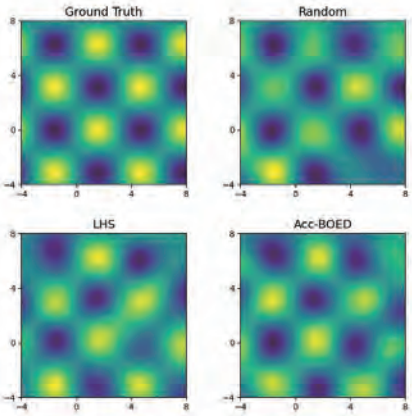

Comparison of final model predictions

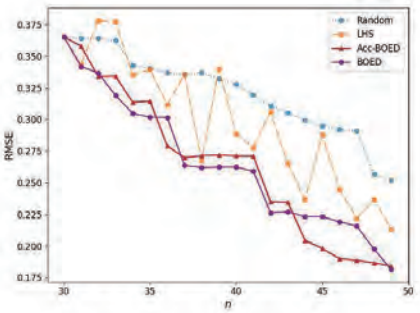

Evolution of RMSE

Surrogate Model: Trigonometric Model

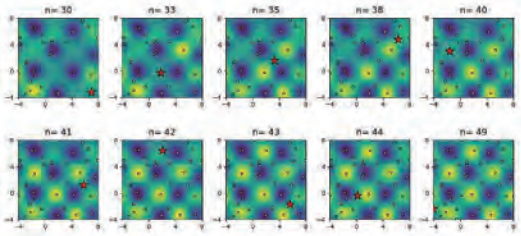

Evolution of model prediction

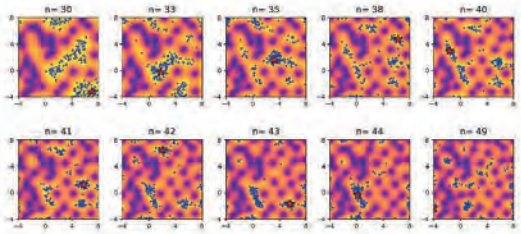

Evolution of model prediction

Surrogate Model: ADM

Alanine Dipeptide Model:
The collective variables are the given functions of x which are Cartesian coordinates of all atoms. The free energy associated with $(\phi(x), \psi(x))$ is the function depending on $\nu = (\nu_1, \nu_2)$ defined as

$$F(\boldsymbol{v}) = -k_B T \ln\left(A^{-1} \int e^{-\frac{V(\boldsymbol{x})}{k_B T}} \times \delta(\nu_1 - \phi(\boldsymbol{x})) \times \delta(\nu_2 - \psi(\boldsymbol{x})) d\boldsymbol{x}\right),$$

where $A = \int_{\mathbb{R}^d} e^{-\frac{v(x)}{k_B T}} dx$, T is temperature, k_B is a constant, $\delta(\cdot)$ refers the Dirac-deltafunction, $V(\boldsymbol{x})$ refers the potential energy function of all atom's position $\boldsymbol{x} \in \mathbb{R}^d$.

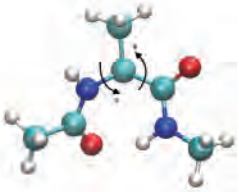

Surrogate Model: ADM

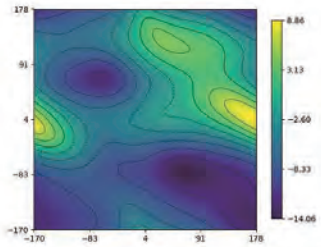

The Ground Truth of ADM

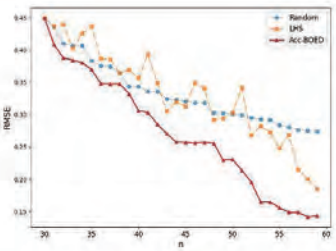

Evolution of RMSE

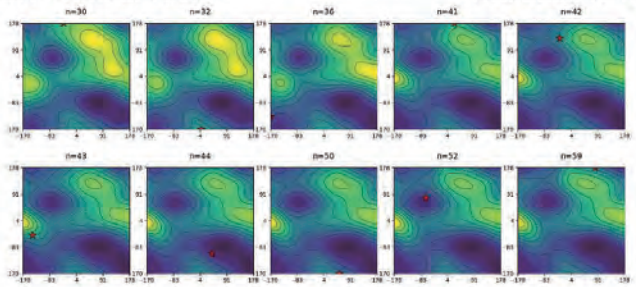

Evolution of surrogate prediction

Parameter estimation: Erf

A Gaussian error function:

$$erf(x) = \frac{1}{\sqrt{\pi}} \int_{-x}^{x} e^{-t^2}\, dt = \frac{2}{\sqrt{\pi}} \int_{0}^{x} e^{-t^2}\, dt$$

$y = erf(\boldsymbol{z} + \varepsilon)$, where $\varepsilon \sim N\left(0, \sigma^2\right)$, $\boldsymbol{z} \in (0, 1)$ and $\sigma = 0.1$.The problem is to estimate the parameter $p(\boldsymbol{z}|y = 0.7)$.

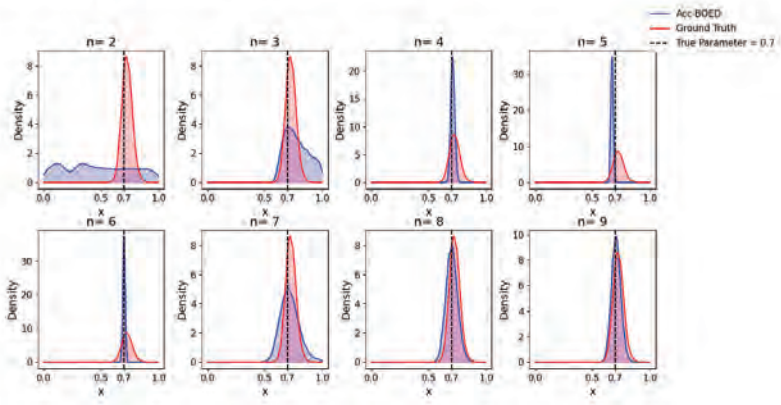

Parameter estimation: KDV equation

The KdV equation is a nonlinear, dispersive partial differential equation for the function u, which depends on space $x \in \mathbb{R}$ and time t:

$$\frac{\partial u}{\partial t} + \theta_1 u \frac{\partial u}{\partial x} + \theta_2 \frac{\partial^3 u}{\partial x^3} = 0,$$

Due to the high nonlinearity of the PDE, 200 solution values are randomly selected from the time domain $[0, 5]$ and the spatial domain $[0, 30]$. The true parameter values are $\theta_1^* = 6$ and $\theta_2^* = 1$. The prior distributions for these parameters are defined as:

$$\pi_{\text{prior}}(\theta_1) \sim \mathcal{U}(3, 12), \quad \pi_{\text{prior}}(\theta_2) \sim \mathcal{U}(0, 4).$$

Parameter estimation: KDV equation

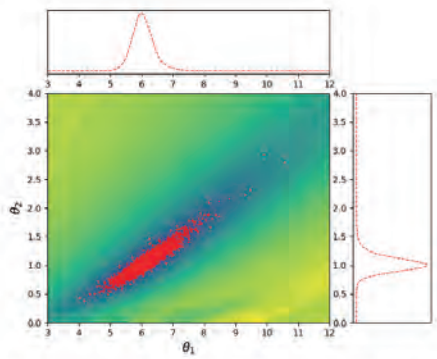

Parameter Sampling for Ground Truth

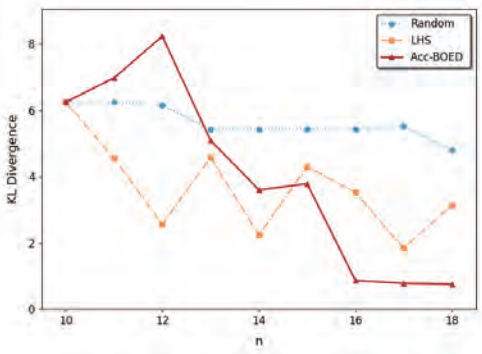

Evolution of KL Divergence

Parameter estimation: KDV equation

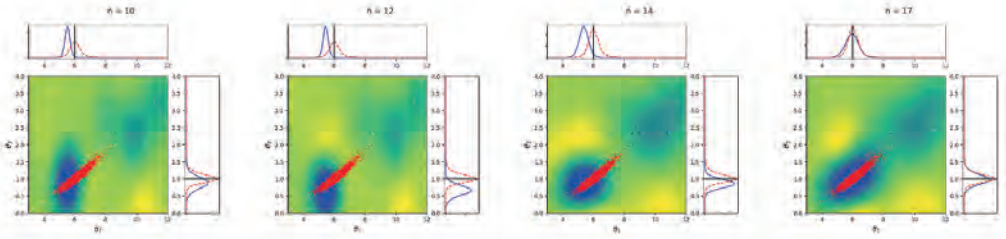

(a) $n = 10$ (b) $n = 12$ (c) $n = 14$ (d) $n = 17$

Samples of approximate posterior distribution with respect to iterations: true posterior distribution (red scatter), approximate posterior distribution (blue scatter), and black solid line (true parameter point (6, 1))

Failure probability estimation: Circle problem

Circle problem :

$$g(x_1, x_2) = 12 - x_1^2 - x_2^2$$

x_1 and x_2 are the inputs to the system, independently and identically distributed according to $N(0, 1)$, and $y = g(x_1, x_2)$ represents the corresponding state function value

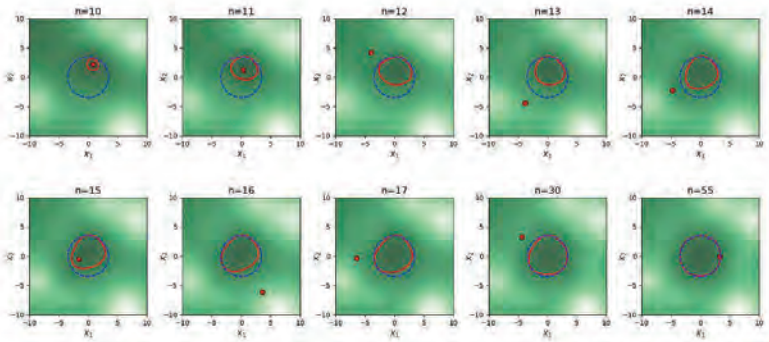

Failure Probability Estimation: Circle Problem

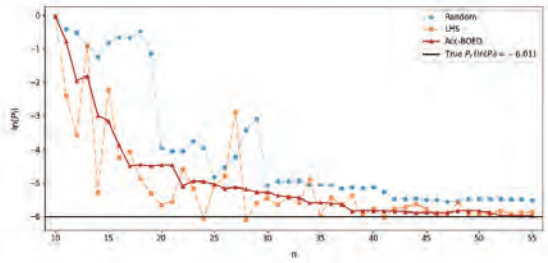

Logarithmic Evolution of Failure Probability

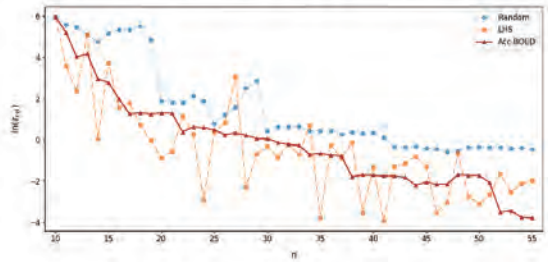

Logarithmic Evolution of Relative Error

Failure Probability Estimation: Circle Problem

Method	Failure Probability	Relative Error
Ground Truth	2.46×10^{-3}	–
Acc-BOED	2.52×10^{-3}	2.2764%
Random scheme	4.01×10^{-3}	62.8455%
LHS scheme	2.80×10^{-3}	13.7805%

Failure probability estimation: Four branch system

Four branch system :

$$g(x_1, x_2) = \min \begin{Bmatrix} 3 + 0.1 * (x_1 - x_2)^2 - (x_1 + x_2)/\sqrt{2} \\ 3 + 0.1 * (x_1 - x_2)^2 - (x_1 + x_2)/\sqrt{2} \\ (x_1 - x_2) + 7/\sqrt{2} \\ (x_2 - x_1) + 7/\sqrt{2} \end{Bmatrix}$$

x_1 and x_2 are the inputs to the system, independently and identically distributed according to $N(0, 1)$. The true failure boundary of the system is a four-branched shape with highly sharp corners, which is generally challenging to accurately simulate.

Failure probability estimation: FB from n=20

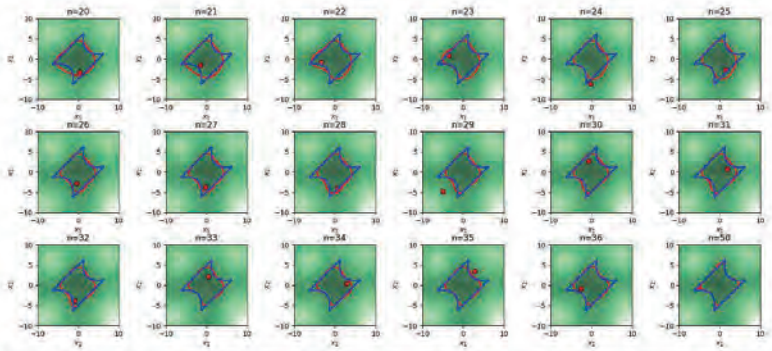

Method	Failure Probability	Relative Error
Ground Truth	2.25×10^{-3}	–
Acc-BOED	2.34×10^{-3}	4.0889%
Random	0.66×10^{-3}	70.7556%
LHS	0.62×10^{-3}	72.1333%

Failure probability estimation: FB from n=20

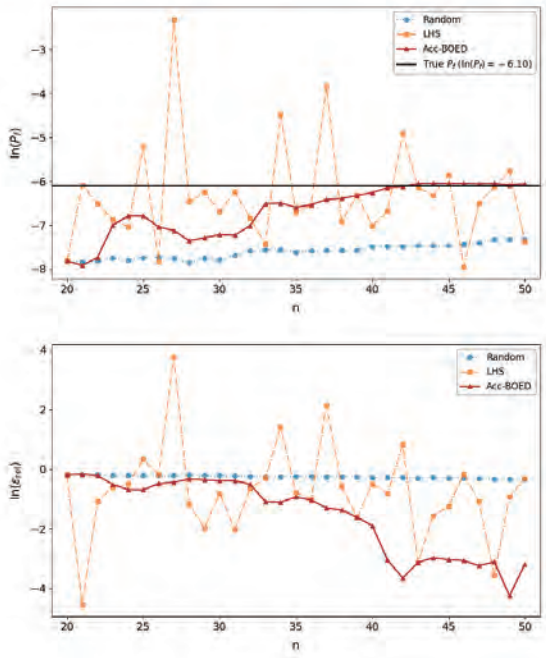

Failure probability estimation: FB from n=50

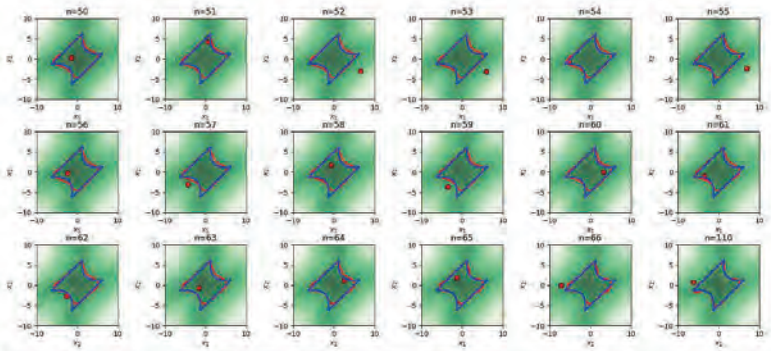

Method	Failure Probability	Relative Error
Ground Truth	2.25×10^{-3}	–
Acc-BOED	2.30×10^{-3}	2.0444%
Random	1.17×10^{-3}	47.8222%
LHS	2.35×10^{-3}	4.4889%

Failure Probability Estimation: FB from n=50

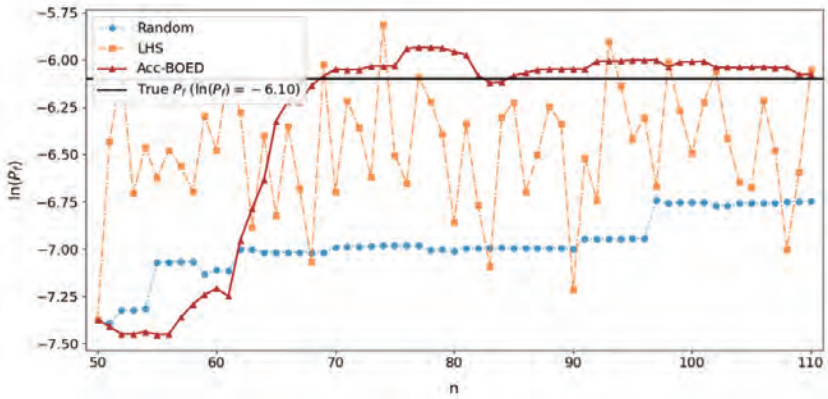

Summary:

- A reformulation based on the ratio of two Gaussian random fields using independent Monte Carlo integration is proposed to reduce the computational complexity induced by the original nested integration.
- A machine learning-based conditional density estimation approach is employed to approximate the constraint density, thereby avoiding repeated surrogate modeling.
- A covariance-guided criterion is proposed to efficiently select informative datasets for both model training and Monte Carlo integration.
- The problems of failure probability estimation, parameter inference, and surrogate modeling are reformulated within the unified framework of Bayesian Optimal Experimental Design.

Thanks for your time.

Some advances on mathematics of hypersonic flows

Hairong Yuan

East China Normal University

In this talk I will review the progress we made on a mathematical theory of inviscid hypersonic flows based upon the framework of Radon measure-valued solutions of the compressible Euler equations. It is shown that the hypersonic Mach number independence principle, the Newtonian theory of infinite-thin shock layer, and the Newtonian-Busemann pressure law, as well as the hypersonic similarity law, can all be verified rigorously in this new framework, which put a foundation for future theoretical studies and applications.

Some Advances on Mathematics of Hypersonic Flows

Hairong Yuan (袁海荣)

(School of Mathematical Sciences, East China Normal University)

FMfI2025 — Challenge of Mathematics for Industry in the AI era

(*POSCO Center, Seoul, Korea*)

August 18—20, 2025

Classic problem: inviscid compressible flow passing bodies

Mach number $M = \dfrac{\text{speed of flow}}{\text{speed of sound}} \sim \dfrac{\text{inertia force of gas (macroscopic speed of particles)}}{\text{pressure (microscopic thermal motion of particles)}}$;

incompressible limit $(M \downarrow 0)$, subsonic $(M < 1)$, transonic $(M \sim 1)$, supersonic $(M > 1)$, hypersonic $(M \uparrow \infty)$.

Main concern: distribution of pressure/temperature (heat flow) on the obstacle's boundary.

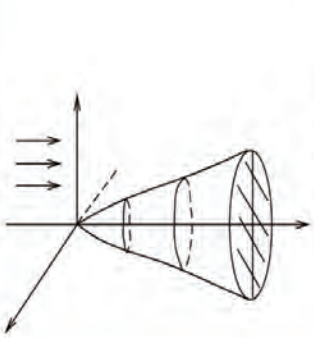

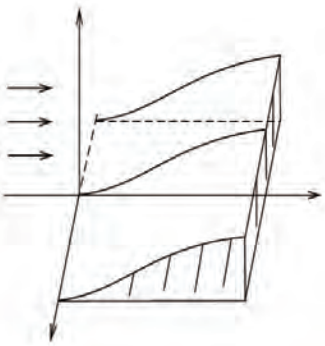

Fundamental properties of hypersonic flow

(i) The hypersonic Mach number independence principle (∃ hypersonic-limit)

(ii) Infinite-thin shock layer (∃ concentration boundary-layer, CBL)

(iii) Newton's sine-squared law (1687); Centrifugal force corrections by A. Busemann (1933)

(iv) Hypersonic similarity law and equivalence principle

▷ J. D. Anderson Jr. Hypersonic and high-temperature gas dynamics. 3rd ed. AIAA, 2019.

JDA (1938-): Fellow of the National Academy of Engineering.

(i) The hypersonic Mach number independence principle

In the limit $M_\infty \to \infty$ two flows with different values of M_∞ are fundamentally identical, i.e., are not different from each other in any fundamental way.

▷ Wallace D. Hayes and Ronald F. Probstein: Hypersonic Inviscid Flow. Dover Publications, 2004.

WDH (1918-2001): Fellow of the National Academy of Engineering (1975); RFP (1928-2021): Fellow of both the National Academy Engineering and National Academy of Sciences.

- Verification: ∃ hypersonic-limit in suitable topology

(ii) Thin shock-layer (CBL) in hypersonic flow

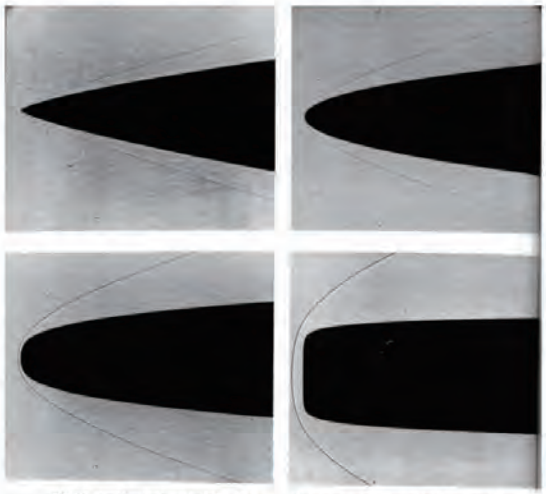

273. **Hypersonic flow past power-law bodies.** Shadowgraphs show the bow wave in air at $M=8.8$ for bodies of revolution whose radius varies as a power of axial distance. The exponents are $\frac{3}{4}$, $\frac{1}{2}$ (a paraboloid of revolution), $\frac{1}{4}$, and $\frac{1}{10}$. *Freeman, Cash & Bodder 1964*, courtesy of Aerodynamics Division, National Physical Laboratory

- Concentration boundary layers (CBL) appear for flows with infinite-Mach-number passing sharp bodies, and the solutions are no longer Lebesgue measurable functions.
- To our knowledge, there is no mathematical studies of such concentration singularity before.

▷ Van Dyke, Milton. *An album of fluid motion.* Parabolic press, 1982.

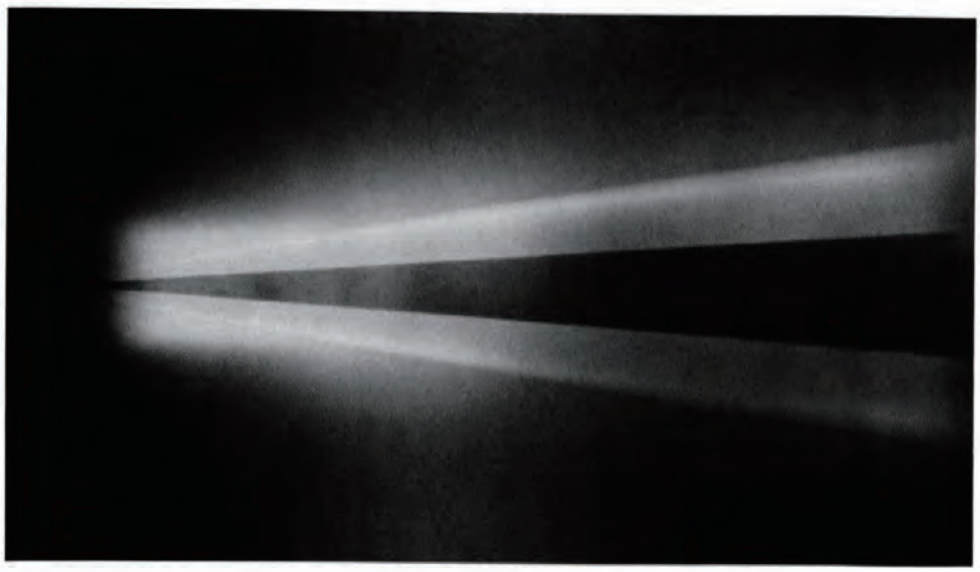

274. **Hypersonic flow past a slender cone.** A cone of 3° semi-vertex angle is shown by the glow-discharge method in helium at Mach number 41 and Reynolds number 560,000 based on length. In this strong-interaction regime the boundary layer is seen to extend about four-fifths of the distance to the shock wave. *Horstman & Kussoy 1968*

(iii) Newton's sine-squared pressure law (1687)

$$C_p \doteq \frac{p - p_\infty}{\rho_\infty V_\infty^2} = \sin^2\theta$$

θ : the local deflection angle of the flow stream; p_∞, ρ_∞, V_∞: free stream static pressure, density, velocity.

Newton's formula for resistance of a rigid sphere with radius R in uniform hypersonic flow: $F = \frac{1}{2}\pi\rho_\infty u_\infty^2 R^2$.

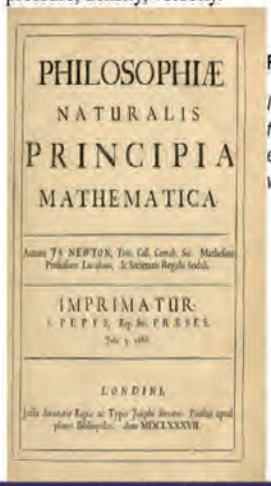
PHILOSOPHIÆ
NATURALIS
PRINCIPIA
MATHEMATICA

Autore IS. NEWTON, Trin. Coll. Cantab. Soc. Matheseos Professore Lucasiano, & Societatis Regalis Sodali.

IMPRIMATUR
S. PEPYS, Reg. Soc. PRÆSES.
Julii 5, 1686.

LONDINI,
Jussu Societatis Regiæ ac Typis Josephi Streater. Prostat apud plures Bibliopolas. Anno MDCLXXXVII.

PROPOSITION XXXIV. THEOREM XXVIII.

If in a rare medium, consisting of equal particles freely disposed at equal distances from each other, a globe and a cylinder described on equal diameters move with equal velocities in the direction of the axis of the cylinder, the resistance of the globe will be but half so great as that of the cylinder.

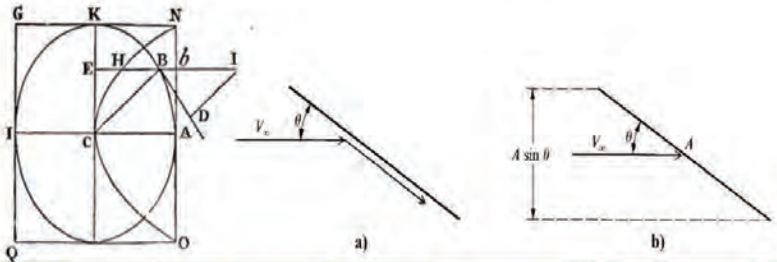

Newtonian-Busemann theory (1933)

Centrifugal force corrections to Newtonian theory by Adolf Busemann (1933):

$$C_p = \sin^2\theta_i + \left(\frac{d\theta}{dy}\right)_i \frac{\sin\theta_i}{y_i} \int_0^{y_i} y\cos\theta\, dy$$

[. . . . . such Newtonian theory is simple and straightforward and is frequently used in hypersonic aerodynamics for approximate calculations. . . . . **Indeed, it has been used extensively for this purpose since the early 1950s.** — J. D. Anderson Jr.]

Adolf Busemann

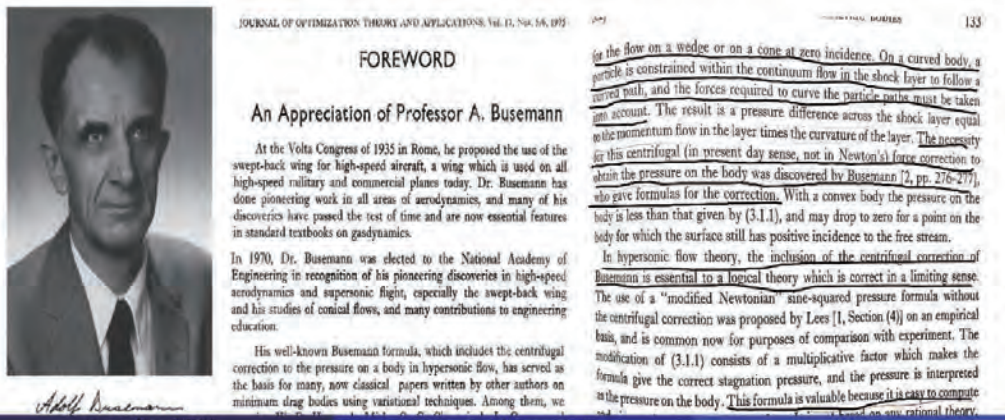
JOURNAL OF OPTIMIZATION THEORY AND APPLICATIONS: Vol. 17, Nos. 5/6, 1975

FOREWORD

An Appreciation of Professor A. Busemann

At the Volta Congress of 1935 in Rome, he proposed the use of the swept-back wing for high-speed aircraft, a wing which is used on all high-speed military and commercial planes today. Dr. Busemann has done pioneering work in all areas of aerodynamics, and many of his discoveries have passed the test of time and are now essential features in standard textbooks on gasdynamics.

In 1970, Dr. Busemann was elected to the National Academy of Engineering in recognition of his pioneering discoveries in high-speed aerodynamics and supersonic flight, especially the swept-back wing and his studies of conical flows, and many contributions to engineering education.

His well-known Busemann formula, which includes the centrifugal correction to the pressure on a body in hypersonic flow, has served as the basis for many, now classical papers written by other authors on minimum drag bodies using variational techniques. Among them, we

133

for the flow on a wedge or on a cone at zero incidence. On a curved body, a particle is constrained within the continuum flow in the shock layer to follow a curved path, and the forces required to curve the particle paths must be taken into account. The result is a pressure difference across the shock layer equal to the momentum flow in the layer times the curvature of the layer. The necessity for this centrifugal (in present day sense, not in Newton's) force correction to obtain the pressure on the body was discovered by Busemann [2, pp. 276–277], who gave formulas for the correction. With a convex body the pressure on the body is less than that given by (3.1.1), and may drop to zero for a point on the body for which the surface still has positive incidence to the free stream.

In hypersonic flow theory, the inclusion of the centrifugal correction of Busemann is essential to a logical theory which is correct in a limiting sense. The use of a "modified Newtonian" sine-squared pressure formula without the centrifugal correction was proposed by Lees [1, Section (4)] on an empirical basis, and is common now for purposes of comparison with experiment. The modification of (3.1.1) consists of a multiplicative factor which makes the formula give the correct stagnation pressure, and the pressure is interpreted as the pressure on the body. This formula is valuable because it is easy to compute

(iv) Hypersonic similarity law and equivalence principle

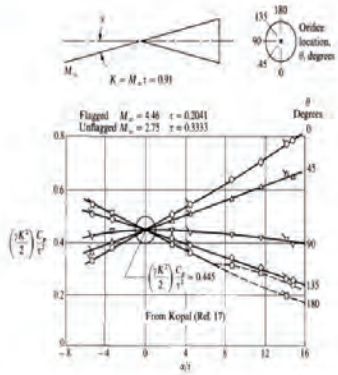

Figure 1: Cone pressure at angle of attack, correlated by hypersonic similarity.

▷ Neice, Stanford, E., and Dorris, M. Ehret. Similarity Laws for Slender Bodies of Revolution in Hypersonic Flows. Journal of the Aeronautical Sciences, Vol. 18, No. 8: 527–530, 568, 1951.

▷ Hsue-shen Tsien. Similarity Laws of Hypersonic Flows. J. Math. Phys., 25: 247–251, 1946.

- Hypersonic similarity: In steady, inviscid hypersonic flow, the flow characteristics of geometrically similar objects are similar if their flight Mach number and the ratio of their characteristic length to a reference length are the same.
- Experimental verification: Note in figure that the data along any given ray for the two different values of M_∞ and τ (but both such that $K = 0.91$) fall on the same curve when plotted vs a/τ. Hence, the data in the figure are a direct experimental verification of hypersonic similarity for bodies at angle of attack.
- Equivalence principle: the steady hypersonic flow over a slender body is equivalent to an unsteady flow in one less space dimension.

Compressible Euler equations (CEE)

The traditional formulation of the compressible Euler system of inviscid fluids:

$$\begin{aligned}
&\partial_t \rho + \mathrm{Div}(\rho U) = 0,\\
&\partial_t (\rho U) + \mathrm{Div}(\rho U \otimes U) + \nabla p = \rho F,\\
&\partial_t (\rho E) + \mathrm{Div}((\rho E + p)U) = \rho F \cdot U + \rho R - \mathrm{Div}(Q).
\end{aligned}$$

- ρ: the mass density of fluid $U = (u, v, w) \in \mathbb{R}^3$: the velocity of fluid
- $E = e + \frac{1}{2}|U|^2$: the total energy per unit mass e: the internal energy per unit mass
- p: the scalar pressure of fluid T: the temperature of fluid
- F: the body force per unit mass R: the heat supply per unit mass
- $Q = -\hat{\kappa}\nabla T + Q_r$: the heat flux vector in $\mathbb{R}^3$
- $\hat{\kappa}$: the thermal conductivity coefficient Q_r: the radiation heat transfer flux in $\mathbb{R}^3$
- The state functions of fluid: $p = \hat{p}(\rho, e)$, $T = \hat{T}(\rho, e)$

3-d unsteady Euler flow passing a solid obstacle

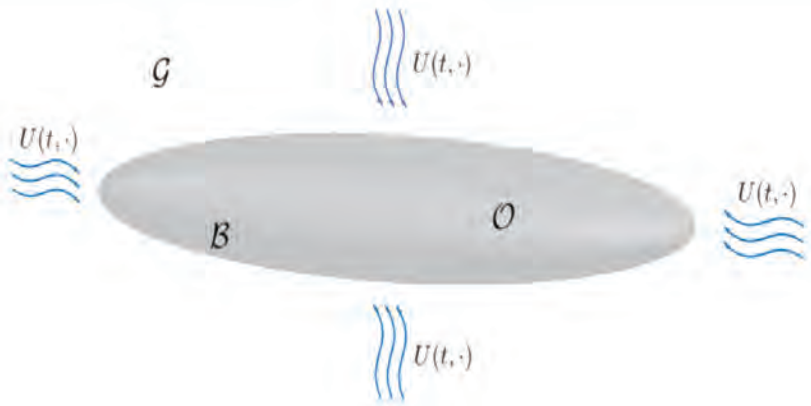

Figure 2: **Compressible Euler flow in $\mathbb{R}^3$ passing a fixed obstacle $\mathcal{O}$ with boundary $\mathcal{B}$ (with $\partial\mathcal{B} = \emptyset$).**

Review: mathematics on supersonic flows passing bodies

Supersonic flows passing bodies: rich! Courant-Friedrichs, Chaohao Gu, Schaeffer, Ta-Tsien Li, Shuxing Chen, Dening Li, Gui-Qiang Chen, M. Feldman, Taiping Liu, Zhouping Xin, Huicheng Yin, Yongqian Zhang, Beixiang Fang, Dian Hu, Wei Xiang, Myoungjean Bae, Jie Kuang, . . .

Mathematics on hypersonic flows: rare!

- K. Louie, J. R. Ockendon: Mathematical aspects of the theory of inviscid hypersonic flow, *Philosophical Transactions of the Royal Society of London. Series A.*, **335(1637)** (1991), 121–138.
- Dian Hu (胡殿): The supersonic flow past a wedge with large curved boundary. *J. Math. Anal. Appl.* **462(1)** (2018), 380–389. (Taking the states in shock layer as reference, no concentration, not Newtonian theory.)
- Dian Hu (胡殿), Yongqian Zhang (张永前): Global conical shock wave for the steady supersonic flow past a curved cone, *SIAM Journal on Mathematical Analysis*, **51(3)** (2019), 2372–2389.

New framework of CEE to study hypersonic flow

- Taking (ρ, U, e) as the primary unknowns, and regarding (p, F, R, Q) as functions of them
- The initial data:

$$(\rho, U, e)\big|_{t=0} = (\rho_0, U_0, e_0) \quad \text{in } \mathcal{G} \tag{1}$$

- The slip condition:

$$U \cdot n = 0 \quad \text{on } [0, \infty) \times \mathcal{B} \tag{2}$$

- The heat flux condition:

$$Q \cdot n = q \quad \text{on } [0, \infty) \times \mathcal{B} \tag{3}$$

- Classical solutions (C^1 functions)
- Weak solutions (Lebesgue measurable functions)
- Measure-valued solutions ((time-dependent) Radon measures)

Review: works on measure solutions and delta shocks

- Singular solutions to hyperbolic conservation laws: Korchinski, LeFloch, Serre, Keyfitz, Brenier, J. Carrillo, Y. Choi, Oberguggenberger, Nedeljkov, Nguyen, Tudorascu, Paiva, R. Hynd; Tong Zhang, Xiaqi Ding, Wancheng Sheng, Hanchun Yang, Gui-Qiang Chen, Jiequan Li, Feimin Huang, Zhen Wang, Lihui Guo, Yu Zhang, . . .
- Various systems: transport equations, pressureless Euler, generalized (modified) Chaplygin Euler, traffic flows, relativistic string equation in Minkowski space, . . .
- Various definition of solutions: shadow waves, Colombeau's and Sarrico's product of generalized functions, dual method, nonconservative product, . . .
- Remark: all for Cauchy problems and mainly for 1-d case. ▷ Neumann, Lukas; Oberguggenberger, Michael; Sahoo, Manas R.; Sen, Abhrojyoti: Initial-boundary value problem for 1D pressureless gas dynamics. *J. Differential Equations* 316 (2022), 687-725.

Remark: Role of Measures / Functions in continuum physics

- Functions: $u : \Omega \to U; (x,t) \mapsto u(x,t)$ [U: usually a subset of Euclidean space]
- Physical space: $(x,t) \in \Omega$ [Ω: a topological space] (where, when)
- State space: $u \in U$ (what happens)
- Measures: $\mu : \mathcal{B}(\Omega) \to U; A \mapsto \mu(A)$ [$\mathcal{B}(\Omega)$: Borel σ-algebra of Ω]
- Extensive quantity (measures): mass, momentum, energy, entropy, force, ...

  [nonlocal, physically more fundamental]
- Intensive quantity (functions): density of mass, velocity, specific energy, temperature, ... [local, more convenient for nonlinear operations, Radon-Nikodym derivatives of measures]

Principles for a good definition of generalized solutions

How to define measures as solutions to nonlinear PDE without distorting the underlying physics?

- Challenge: Proposing a correct mathematical problem directly from physics!
- Some guiding principles:

  (i) Be generalization of classical solutions and weak solutions;

  (ii) Be able to depict significant physcial phenomena;

  (iii) Be able to derive physically well-accepted laws;

  (iv) Be able to provide new results.

Difficulty to define measures as solutions to nonlinear PDE

- Measure is nonlocal: not-close under multiplication and composition
- For singular solutions, identify the primary unknowns and study the equations derived directly from conservation laws (rather than other equations obtained after some transformation of unknowns); choose carefully the equation of state
- It is essential to realize:
  - All the primary unknowns are measures for problems from continuum physics
  - There is a reference measure, and all other measures can be expressed by the products of the reference measure with functions (intensive quantities)
  - Nonlinearity of PDE is only related to intensive quantities
  - No equation of state is necessary on singular sets for most physical problems

A summary of our progress

- Definition of Radon measure-valued solutions to CEE: valid for gases with general equation of state; initial/boundary value problems; steady/unsteady flow; 1-d/m-d
  - Relaxation to linear PDE of various measures
  - Nonlinear constraints for Radon-Nikodym derivatives
- Applications to physical/engineering problems:
  - Concentration boundary-layer equations and generalized Newtonian-Busemann law
  - Verification of hypersonic limit and similarity law
  - Delta shock as free piston and non-uniqueness of Rmvs of Riemann problems: a new understanding
  - Motion of droplets with gas-liquid phase transitions

CBL admitting skin-friction and heat-transfer

- PDE for concentration boundary layers in $[0,\infty)\times\mathcal{B}$:

$$\begin{aligned}
&\partial_t w_\rho + \mathrm{div}_g(w_\rho \varpi) = \rho U\cdot n,\\
&\partial_t(w_\rho\varpi) + \mathrm{div}_g(w_\rho\varpi\otimes\varpi) + \tilde{\sigma} = w_\rho\widetilde{F}_\tau + \rho(U\cdot n)U_\tau,\\
&\partial_t(w_\mathcal{E} + \frac{1}{2}w_\rho g(\varpi,\varpi)) + \mathrm{div}_g((w_\mathcal{E} + \frac{1}{2}w_\rho g(\varpi,\varpi))\varpi) + q\\
&\quad = w_\rho\widetilde{F}\cdot\widetilde{U} + w_\rho\widetilde{R} - \mathrm{div}_g(\chi) + (\rho E + p)U\cdot n + Q\cdot n.
\end{aligned}$$

- Generalized Newtonian-Busemann pressure law:

$$\boxed{\sigma_n = w_\rho\widetilde{F}\cdot n + \rho(U\cdot n)^2 + p - w_\rho g(\varpi,\varpi)k(\varpi)}$$

▷ Liu, Ke (刘恪); Yuan, Hairong. Radon measure-valued solutions of compressible Euler equations and concentration boundary layers in unsteady inviscid flows passing solid obstacles. Preprint, 2025.

Special cases of CBL and N-B law

- Steady Euler flows passing 3-d bodies: A general definition of Radon measure solutions; generalized N-B law

  ▷ Qu, Aifang; Yuan, Hairong. Steady compressible Euler equations of concentration layers for hypersonic-limit flows passing three-dimensional bodies and generalized Newton-Busemann pressure law. *Chinese Ann. Math. Ser. B* 44 (2023), no. 4, 561–576.

- For special cases, demonstrate the validation of the concept of Radon measure-valued solutions

  ▷ Qu, Aifang; Yuan, Hairong; Zhao, Qin (赵勤). High Mach number limit of one-dimensional piston problem for non-isentropic compressible Euler equations: polytropic gas. *J. Math. Phys.* 61 (2020), no. 1, 011507, 14 pp.

  ▷ Qu, Aifang; Yuan, Hairong; Zhao, Renxiong (赵仁雄). Measure-valued solution for moving piston in pressureless Euler flows by the method of integration on path space. *Math. Ann.* 392 (2025), no. 1, 1203–1251.

  ▷ Zhang, Peiyu(张佩瑜); Qu, Aifang; Yuan, Hairong. The motion and mass growth of droplets with phase transitions in a homogeneous medium. *Phys. D* 477 (2025), Paper No. 134683, 21 pp.

We are grateful to Prof. Jiequan Li (李杰权) for ideas of studying free-piston and droplet with phase-transition.

- Straight wedge: definition of Radon measure solution (Rms); verification of hypersonic Mach number independence principle (formation of CBL); solution of CBL and derivation of Newton's sine-squared law.

  ▷ Qu, Aifang; Yuan, Hairong; Zhao, Qin (赵勤). Hypersonic limit of two-dimensional steady compressible Euler flows passing a straight wedge. *ZAMM Z. Angew. Math. Mech.* 100 (2020), no. 3, e201800225, 14 pp.

- Curved wedges without skin-friction: definition of RMS; solution of CBL and derivation of Newtonian-Busemann law; solution to interaction of hypersonic flow and quiescent gas (new phenomena: termination of delta shock in s finite distance downstream of a finite wedge — no global solution!).

  ▷ Jin, Yunjuan (金云娟); Qu, Aifang; Yuan, Hairong. On two-dimensional steady hypersonic-limit Euler flows passing ramps and Radon measure solutions of compressible Euler equations. *Commun. Math. Sci.* 20 (2022), no. 5, 1331–1361.

- Curved wedges with skin-friction: steady CBL on 2-d wedge with skin-frictions and generalized Newtonian-Busemann law.

  ▷ Qu, Aifang; Su, Xueying (苏雪滢); Yuan, Hairong. Generalized Newton-Busemann law for two-dimensional steady hypersonic-limit Euler flows passing ramps with skin-frictions. *Acta Mathematicae Applicatae Sinica, English Series.* (2024), https://doi.org/10.1007/s10255-024-1087-6

- Cylindrically symmetric curved cone: solution of CBL; proof of Newtonian-Busemann law; termination of delta shock.

  ▷ Jin, Yunjuan (金云娟); Qu, Aifang; Yuan, Hairong. Radon measure solutions for steady compressible hypersonic-limit Euler flows passing cylindrically symmetric conical bodies. *Commun. Pure Appl. Anal.* 20 (2021), no. 7-8, 2665–2685. (By invitation)

- Cylindrically symmetric straight cone: verification of hypersonic Mach number independence principle; formation of CBL; proof of Newton's sine-squared law for cones; case of Chaplygin gas.

  ▷ Li, Qianfeng (黎前锋); Qu, Aifang; Su, Xueying (苏雪滢); Yuan, Hairong. Hypersonic limit for steady compressible Euler flows passing straight cones. *Commun. Math. Anal. Appl.*, 3 (2024), no. 2, 136–167. (By invitation)

- Conical flow with attack angles: theory and numerical computation (including Chaplygin gas).

  ▷ Qu, Aifang; Yuan, Hairong. Radon measure solutions for steady compressible Euler equations of hypersonic-limit conical flows and Newton's sine-squared law. *J. Differential Equations* 269 (2020), no. 1, 495–522.

  ▷ Qu, Aifang; Su, Xueying (苏雪滢); Yuan, Hairong. Infinite-thin shock layer solutions for stationary compressible conical flows and numerical results via Fourier spectral method. *SIAM J. Appl. Math.* 84 (2024), no. 6, 2321–2341.

Related works on verification of hypersonic similarity in BV

- Jie Kuang (匡杰), Wei Xiang (向伟), and Yongqian Zhang (张永前). *Hypersonic similarity for the two dimensional steady potential flow with large data.* Annales de l'Institut Henri Poincaré C, Analyse non linéaire, 37(6):1379–1423, 2020.
- Jie Kuang, Wei Xiang, and Yongqian Zhang. *Convergence rate of hypersonic similarity for steady potential flows over two-dimensional Lipschitz wedge.* Calculus of Variations and Partial Differential Equations, 62(3), 2023.
- Jie Kuang, Wei Xiang, and Yongqian Zhang. *Hypersonic similarity for steady compressible full Euler flows over two-dimensional Lipschitz wedges.* Advances in Mathematics, 451:109782, 2024.
- Gui-Qiang G Chen, Jie Kuang, Wei Xiang, and Yongqian Zhang. *Convergence rate of the hypersonic similarity for two-dimensional steady potential flows with large data.* Nonlinearity, 38(4):045013, 2025.

Formulation of 2-d steady Euler flow passing slender body

Two-dimensional steady Euler equations for non-isentropic compressible flows:

$$\begin{cases} \partial_x(\rho u) + \partial_y(\rho v) = 0, \\ \partial_x(\rho u^2 + p) + \partial_y(\rho uv) = 0, \\ \partial_x(\rho uv) + \partial_y(\rho v^2 + p) = 0, \\ \partial_x(\rho uE) + \partial_y(\rho vE) = 0, \end{cases}$$

and

$$p = \frac{\gamma - 1}{\gamma}\rho(E - \frac{1}{2}(u^2 + v^2)).$$

- ρ: the density of fluid u, v: the velocity of fluid p: the scalar pressure
- E: the total enthalpy per unit mass $\gamma > 1$: the adiabatic exponent
- given supersonic uniform incoming flow $U_\infty = (\rho_\infty, u_\infty, 0, E_\infty)^\top$
- slip condition on the obstacle's boundary

Scaling for hypersonic similarity: $\tau = d/l, K = M_\infty \tau$

Considering the two-dimensional flow over the slender body shown below,

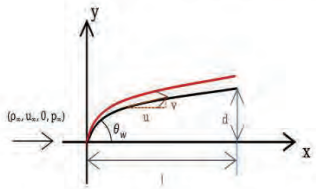

Figure 3: **Illustration of hypersonic flow passing a slender wedge with $\theta_w \ll 1$.**

$$\bar{x} = x, \quad \bar{y} = \frac{y}{\tau}, \quad \bar{u} = \frac{u - u_\infty}{u_\infty \tau^2}, \quad \bar{v} = \frac{v}{u_\infty \tau}, \quad \bar{\rho} = \frac{\rho}{\rho_\infty}, \quad \bar{p} = \frac{p}{\gamma p_\infty M_\infty^2 \tau^2}, \quad \bar{E} = \frac{2E - u_\infty^2}{u_\infty^2 \tau^2}$$

$$\begin{cases} \partial_{\bar{x}}(\bar{\rho}(1+\tau^2\bar{u})) + \partial_{\bar{y}}(\bar{\rho}\bar{v}) = 0, \\ \partial_{\bar{x}}(\bar{\rho}\bar{u}(1+\tau^2\bar{u}) + \bar{p}) + \partial_{\bar{y}}(\bar{\rho}\bar{u}\bar{v}) = 0, \\ \partial_{\bar{x}}(\bar{\rho}\bar{v}(1+\tau^2\bar{u})) + \partial_{\bar{y}}(\bar{\rho}\bar{v}^2 + \bar{p}) = 0, \\ \partial_{\bar{x}}(\bar{\rho}(1+\tau^2\bar{u})\bar{E}) + \partial_{\bar{y}}(\bar{\rho}\bar{v}\bar{E}) = 0, \end{cases}$$

$$\bar{p} = \frac{\gamma - 1}{2\gamma}\bar{\rho}(\bar{E} - 2\bar{u} - \bar{v}^2 - \tau^2\bar{u}^2).$$

Boundary conditions: Upcoming flow $\bar{U}_0 = (1, 0, 0, \bar{E}_0)^\top$, with $\bar{E}_0 = \frac{2}{(\gamma-1)K^2}$, $\bar{p}_0 = \frac{1}{\gamma K^2}$; Slip condition: $\tau(1+\tau^2\bar{u}, \bar{v}) \cdot \bar{n} = 0$

A new hypersonic small disturbance equations

When $\tau \ll 1$, the terms involving τ^2 are very small compared with other terms. By neglecting the terms involving τ^2, for non-isentropic flow, we obtain (NHSDE)

$$\begin{cases} \partial_{\bar{x}}\bar{\rho} + \partial_{\bar{y}}(\bar{\rho}\bar{v}) = 0, \\ \partial_{\bar{x}}(\bar{\rho}\bar{u} + \bar{p}) + \partial_{\bar{y}}(\bar{\rho}\bar{u}\bar{v}) = 0, \\ \partial_{\bar{x}}(\bar{\rho}\bar{v}) + \partial_{\bar{y}}(\bar{\rho}\bar{v}^2 + \bar{p}) = 0, \\ \partial_{\bar{x}}(\bar{\rho}\bar{E}) + \partial_{\bar{y}}(\bar{\rho}\bar{v}\bar{E}) = 0, \end{cases} \qquad \bar{p} = \frac{\gamma - 1}{2\gamma}\bar{\rho}(\bar{E} - 2\bar{u} - \bar{v}^2),$$

Observation: the x-momentum equation can not be decoupled from the remaining equations.
Initial data at $\{\bar{x} = 0\}$ $\bar{U}_0 = (1, 0, 0, \bar{E}_0)^\top$, with $\bar{E}_0 = \frac{2}{(\gamma-1)K^2}, \bar{p}_0 = \frac{1}{\gamma K^2}$;

Lateral boundary condition on $\{\bar{y} = b(\bar{x})\}$ is $\bar{v} = b'(\bar{x})$.

Mathematical structure of NHSDE

The characteristic polynomial for NHSDE is

$$(\lambda - \bar{v})(\lambda - \bar{v})[\lambda^2 - 2\lambda\bar{v} + \bar{v}^2 - \bar{c}^2] = 0,$$

which admits four real roots

$$\lambda_1 = \bar{v} - \bar{c}, \quad \lambda_2 = \lambda_3 = \bar{v}, \quad \lambda_4 = \bar{v} + \bar{c}$$

for $\gamma > 1$, $\bar{\rho} \neq 0$, $\bar{p} \neq 0$. The corresponding eigenvectors are

$$\mathbf{r}_1 = (-\frac{\bar{\rho}}{\bar{c}}, \bar{c} - \bar{v}, 1, 0)^\top, \quad \mathbf{r}_2 = (\frac{2\bar{\rho}}{\bar{E} - 2\bar{u} - \bar{v}^2}, 1, 0, 0)^\top,$$

$$\mathbf{r}_3 = (-\frac{\bar{\rho}}{\bar{E} - 2\bar{u} - \bar{v}^2}, 0, 0, 1)^\top, \quad \mathbf{r}_4 = (\frac{\bar{\rho}}{\bar{c}}, -\bar{v} - \bar{c}, 1, 0)^\top.$$

Here $\bar{c}$ is dimensionless sonic speed satisfying $\bar{c}^2 = \frac{\gamma\bar{p}}{\bar{\rho}} = \frac{\gamma-1}{2}(\bar{E} - 2\bar{u} - \bar{v}^2)$.

By direct computation,

$$\nabla_{\bar{U}}\lambda_2(\bar{U})\cdot\mathbf{r}_2=\nabla_{\bar{U}}\lambda_3(\bar{U})\cdot\mathbf{r}_3\equiv 0,$$

thus the 2^{nd} and 3^{rd} characteristics fields are linearly degenerate; and

$$\nabla_{\bar{U}}\lambda_1(\bar{U})\cdot\mathbf{r}_1=(\gamma-1)\bar{c}+1\not\equiv 0,$$
$$\nabla_{\bar{U}}\lambda_4(\bar{U})\cdot\mathbf{r}_4=1+(\gamma-1)\bar{c}\not\equiv 0,$$

so the 1^{st} and 4^{th} characteristics fields are genuinely nonlinearity.

Remark: Similar hypersonic similarity law also holds for 3-d symmetric curved cones in steady non-isentropic compressible Euler flows.

▷ Kang, Shifan (康诗帆); Long, Binsong (龙柄菘); Yuan, Hairong. *Hypersonic similarity in the framework of Radon measure solutions for the compressible Euler equations.* Preprint, 2025.

Hypersonic equivalence principle for isentropic Euler flow

- Hypersonic equivalence principle: the steady hypersonic flow over a slender body is equivalent to an unsteady flow in one less space dimension (piston problem).

For isentropic flow with $p=A\rho^{\gamma}$, corresponding two-dimensional hypersonic small-disturbance equations are

$$\begin{cases}\partial_{\bar{x}}\bar{\rho}+\partial_{\bar{y}}(\bar{\rho}\bar{v})=0,\\ \partial_{\bar{x}}(\bar{\rho}\bar{u}+A\bar{\rho}^{\gamma})+\partial_{\bar{y}}(\bar{\rho}\bar{u}\bar{v})=0,\\ \partial_{\bar{x}}(\bar{\rho}\bar{v})+\partial_{\bar{y}}(\bar{\rho}\bar{v}^2+A\bar{\rho}^{\gamma})=0,\end{cases}$$

where A is a constant.

Observation: For this case, the x-momentum equation is decoupled from the remaining equations in the system.

Related Poster Session

- Ku Liu (刘恪): Details on concentration boundary layers for unsteady 3d Euler flow passing bodies and Newtonian-Busemann law
- Shifan Kang (康诗帆): Details on hypersonic similarity law within the framework of Radon measure solutions

Thanks for Your Attention!

(hryuan@math.ecnu.edu.cn)

Pohang Earthquake, Thermalelastics among Rock Matrix zones and Mathematical Modelling

Jae-Ryong Kweon

POSTECH

Geothermal energy production requires a high permeability heat exchange from deep hot rocks. The typical procedure locates naturally pre-existing discontinuities, such as faults and joints, and enhances heat permeability by means of hydraulic stimulation. This is a basic scenario for Enhanced Geothermal System(EGS). In this lecture I will talk about mathematical modelling equations for Thermal Variations between fracture and rock zones due to the water injection in the enhanced geothermal system(EGS). As a mechanical reason for Pohang Earthquake I emphasize that thermalelastics is an essential ingredient in causing such large magnitude of stress, because Pohang Earthquake occurred two months later after Pohang EGS stops water injection. Also I will give interface corner singularity functions from the interface and boundary value problem and discuss about increased regularity for smoother part. I will also talk about the stress variations related to the compressible Navier-Stokes flows on the polygonal domains with inflow and outflow conditions.

Pohang Earthquake, Thermalelastics among Rock Matrix zones and Mathematical Modelling

Jae Ryong Kweon

Department of Mathematics, POSTECH
Pohang 790-784, Korea

POSTECH, August 20, 2025

Contents

Contents

Abstract

1. Geothermal energy production requires a high permeability heat exchange from deep hot rocks. The typical procedure locates naturally pre-existing discontinuities, such as faults and joints, and enhances heat permeability by means of hydraulic stimulation. This is a basic scenario for Enhanced Geothermal System(EGS).
2. In this lecture I will talk about mathematical modelling equations for Thermal Variations between fracture and rock zones due to the water injection in the enhanced geothermal system(EGS). As a mechanical reason for Pohang Earthquake I emphasize that thermalelastics is an essential ingredient in causing such large magnitude of stress, because Pohang Earthquake occurred two months later after Pohang EGS stops water injection.
3. Also I will give interface corner singularity functions from the interface and boundary value problem and discuss about increased regularity for smoother part. I will also talk about the stress variations related to the compressible Navier-Stokes flows on the polygonal domains with inflow and outflow conditions.

Contents

Pohang Earthquake backgrounds

1. 3/11/2011: The Tohoku earthquake(M 9.1)
2. 10/2012–10/2015: Building Pohang EGS plant
   No data for the amount of inserted water while building EGS plant
   1/31/2016–2/28/2016: Pohang EGS running, keeping running
3. 9/12/2016: Kyoungju Earthquake(M 5.8), 9/19(M 4.5)
4. 11/15/2017: Pohang Earthquake (M 5.5): 오후 2시 29분 31초
5. 2/11/2018 Pohang earthquake continued (M 4.6) : 오후 5시 3분 3초
6. 3/30/2018: I moved Chogok village near the origin of earthquake
7. 4/2/2018: Pohang city-hall open discussion 포항지진 시민공청회 (포항시청)
8. 4/2018: I joined The preparing committee 포항지진 대책 준비위 구성

포항지진발생위치(진앙지)

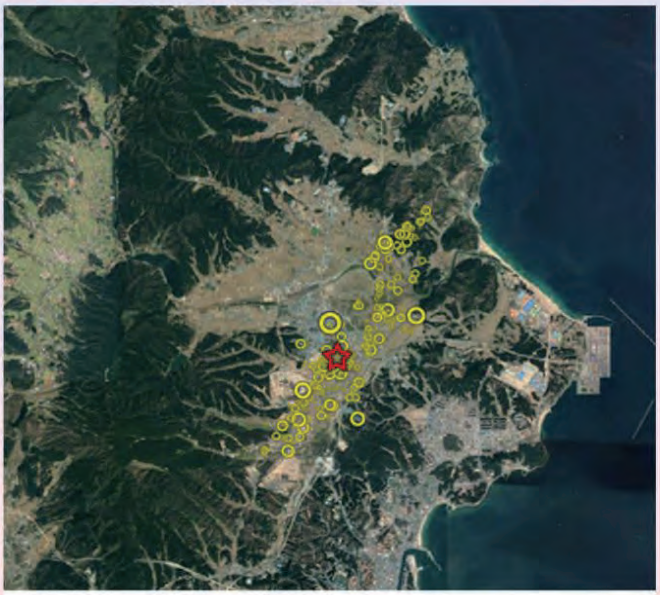

Figure: 포항지진

지열 발전소(EGS)

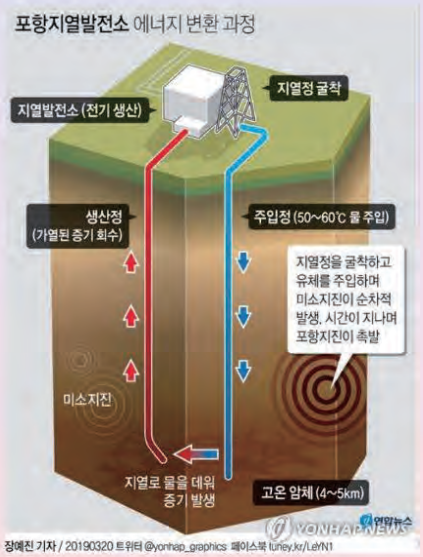

Figure: 지열발전소

물주입

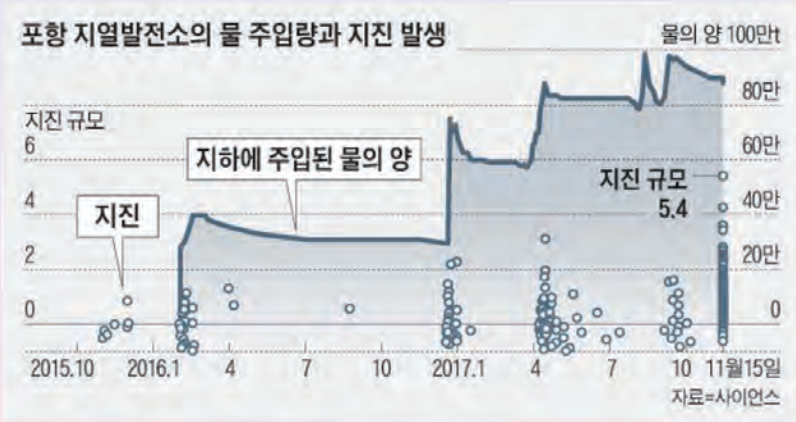

Figure: 물주입

Contents

- D. F. McTigue, Thermoelastic response of fluid-saturated porous rock, J. Geophys. Research, 91 (1986) 9533–9542.
- S. D. Simone, J. Carrera and V. Vilarrasa, Superposition approach to understand triggering mechanisms of poster-injection induced seismicity, Geothermics, 70 (2017) 85–97.
- S. D. Simone, V. Vilarrasa, J. Carrera, A. Alcolea and P. Meier, Thermal coupling may control mechanical stability of geothermal reservoirs during cold water injection, Physics and Chemistry of the Earth, 64 (2013) 117–126.

- R. B. Kellogg, Singularities in Interface Problems. Numerical Solution of Partial Differential Equations II, B. Hubbard, editor (1971) 351–400.
- R. B. Kellogg, On the Poisson Equation with Intersecting Interfaces. Applicable Analysis, 4 (1975) 101–129.

Compressible Navier-Stokes Flows

- 2012, Kweon, Corner singularity dynamics and regularity of compressible viscous Navier-Stokes flows, SIAM J. Math. Anal. 44, 3127–3161.

- 2013, Kweon, A Jump Discontinuity of Compressible Viscous Flows grazing a Non-convex Corner. J. Math. Pures Appl. 100, 410–432.

- 2017, Kwon and Kweon, Interior jump and regularity of compressible viscous Navier-Stokes flows through a cut, SIAM J. Math. Anal. 49 (2017) 1982–2008.

Contents

CSS CSS CSS CSS CSS Jump discontinuity Motivations in thermo-hydro-mechanics Time dependent

A compressible Stokes problem

$$\begin{aligned} -\mu\Delta\mathbf{u} + \nabla p &= \mathbf{f} \quad \text{in } \Omega, \quad \mathbf{u}|_{\Gamma} = 0, \\ Up_x + Vp_y + \mathrm{div}\mathbf{u} &= 0 \quad \text{in } \Omega, \quad p|_{\Gamma_{in}} = 0. \end{aligned} \tag{1}$$

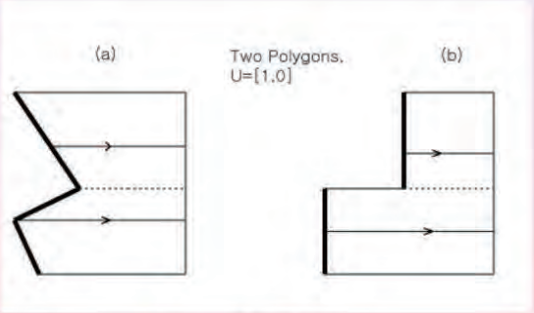

Figure: A polygon Ω

Contents

Interesting remarks

- The dotted line γ is an interface curve depending on the solution vector $\mathbf{u}$.
- The pressure is either continuous or has a jump across the curve γ emanating from the vertex.

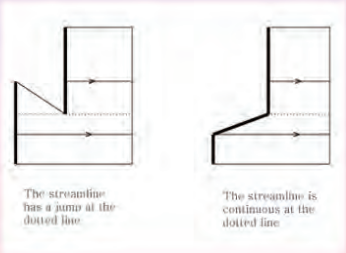

Contents

The grazing non-convex vertex: $\Gamma_{in} \neq$ connected

The compressible viscous NSS

$$\begin{aligned} \rho \mathrm{div}\mathbf{u} + \rho'(p)\mathbf{u}\cdot\nabla p = 0 \quad & \text{in } \Omega, \\ -\mu\Delta\mathbf{u} - \nu\nabla\mathrm{div}\mathbf{u} + \rho(\mathbf{u}\cdot\nabla)\mathbf{u} + \nabla p = 0 \quad & \text{in } \Omega, \\ \mathbf{u} = \mathbf{u}_b \quad & \text{on } \Gamma, \\ p = p_b \quad & \text{on } \Gamma_{in}. \end{aligned} \tag{2}$$

- $\Gamma_{in} = \{(x,y) \in \Gamma : \mathbf{u}_b \cdot \mathbf{n} < 0\}$ is the inflow boundary.
  $\Gamma_{out} = \{(x,y) \in \Gamma : \mathbf{u}_b \cdot \mathbf{n} > 0\}$ is the outflow boundary.

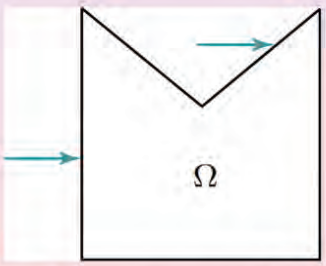

Figure: A polygon Ω

The inflow boundary $\Gamma_{in} \neq$ connected

- $\mathcal{C} = \{(x, \eta(x)) : 0 < x < 1\}$: the streamline emanating from the corner.

(1) $\eta'(x) = (u^{-1}v)(x, \eta(x))$, $(u, v) = \mathbf{u} = \mathbf{C}\phi + \mathbf{u}_R$, the curve divides the domain Ω into Ω_1, Ω_2

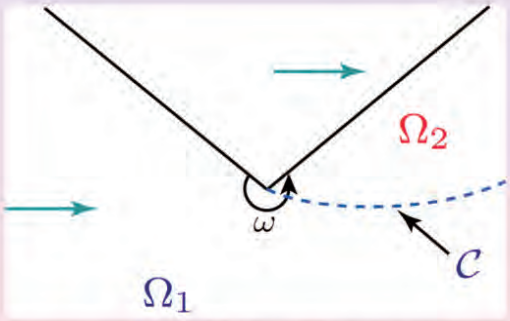

Figure: The interface curve $\mathcal{C}$

$\Gamma_{in} \neq$ connected

- $p_s = B\mathrm{div}\mathbf{u}_s$ is not continuous across the curve $\mathcal{C}$.
- At the grazing vertex, there is one side which is outgoing and one side which is incoming.
- The grazing vertex causes a solution with discontinuous density.

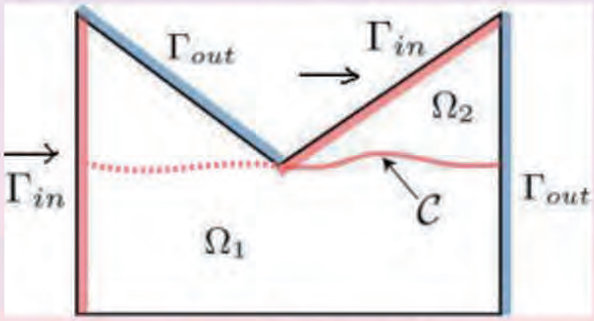

Figure: $\Gamma_{in} \neq$ connected

Contents

The Stress

McTigue (1986), *Thermoelastic Response of Fluid-Saturated Porous Rock*, J. Geophys. Research, 91, 9533–9542

$$T = 2\mu_* \left(\frac{\nabla \mathbf{u} + (\nabla \mathbf{u})^t}{2} + \frac{\nu}{1-2\nu} (\nabla \cdot \mathbf{u}) \mathbf{I} \right) - \left(1 - \frac{K}{K_s} \right) P \mathbf{I} - K \alpha_s \Theta \mathbf{I}$$

- $\mathbf{u}$=the displacement, P=the fluid pressure, Θ=the temperature
- μ_*=the shear modulus, K=the bulk modulus
- K_s=the solid constituent bulk modulus
- α_s=the cubical thermal expansion coefficient for the solid

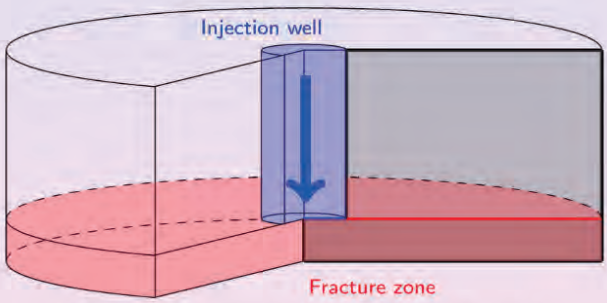

Figure: The enhancement geothermal system

The references revisted

- (2013) Simone, Vilarrasa, Carrera, Alcolea and Meier,
  Thermal coupling may control mechanical stability of geothermal reservoirs during cold water injection,
  Physics and Chemistry of the Earth, 64, 117–126.
- (2017) Simone, Carrera, Vilarrasa,
  Superposition approach to understand triggering mechanisms of poster-injection induced seismicity,
  Geothermics, 70, 85–97.

The critical issues are as follows:

- Rock instability results from hydraulic effects + thermal effects
- Injection of cold water induces thermal stresses due to rock contraction
- Thermal effects induce a significant perturbation on the stress in the intact rock affected by the temperature drop

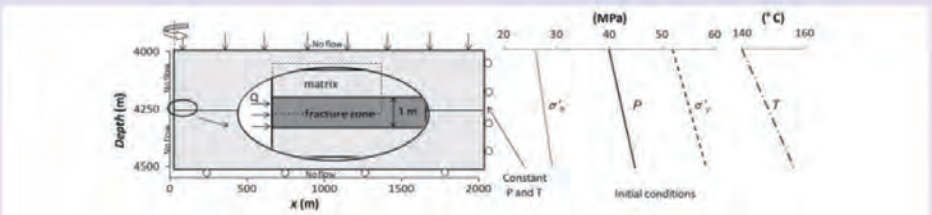

Fig. 1. Model geometry, boundary and initial conditions – liquid pressure (solid line), horizontal (dotted line) and vertical (dashed line) effective stress, temperature (dot-dashed line) vs depth. The dashed box indicates the location of the reference area shown in Fig. 2.

Figure: Domain

Table 1
Properties of the fracture zone and the intact matrix.

Parameters	Fracture zone	Matrix	Units
Intrinsic permeability	10^{-13}	10^{-18}	m^2
Porosity	0.5	0.01	
Young's modulus	100	10,000	MPa
Poisson ratio	0.3	0.3	
Thermal conductivity	2.5	1.5	$W\,m^{-1}\,K^{-1}$
Longitudinal dispersivity for heat	1	1	m
Transverse dispersivity for heat	0.1	0.1	m
Linear thermal expansion coefficient	1×10^{-5}	1×10^{-5}	$°C^{-1}$
Specific heat for solid phase	800	800	$J\,kg^{-1}\,K^{-1}$

Figure: Properties

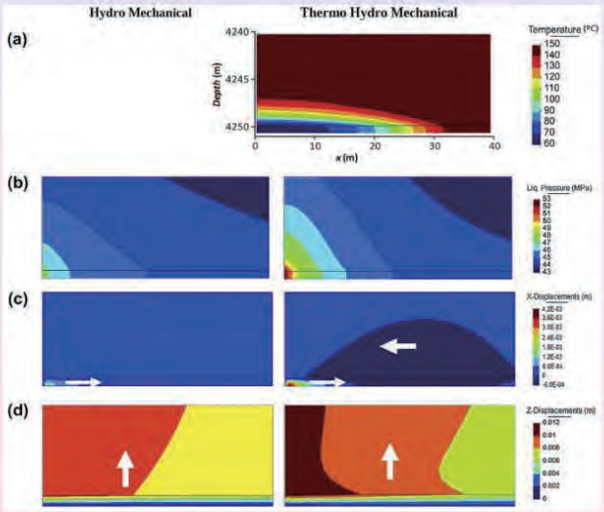

Figure: Distribution of (a) temperature, (b) liquid pressure, (c) horizontal, and (d) vertical displacements

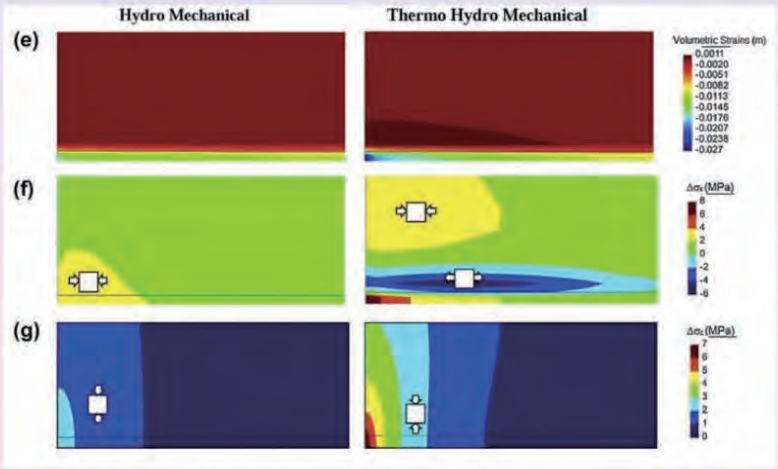

Figure: Distribution of (e) volume strains, (f) total horizontal and (g) vertical stresse

The boundary value problem on polygonal domains

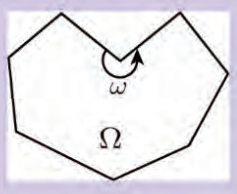

Find $u \in \mathrm{H}_0^1(\Omega)$ satisfying $-\Delta u = f \quad$ in Ω.

Theorem

- $\phi = \chi\, r^\alpha \sin[\alpha(\theta - \omega_1)]$, $\alpha := \pi/\omega$,
- $2/(2-\alpha) < q < 2/(1-\alpha)$.

Then

$$u = \Lambda(f)\phi + u_R,\ u_R \in H^{2,q},$$
$$\|u_R\|_{2,q} + |\Lambda(f)| \le C\|f\|_{0,q},$$
$\Lambda(f)$: *a continuous linear functional on* L^q.

The PDE equations for the Stress

$$-\mu^*(\Delta \mathbf{u} + \frac{1}{1-2\nu}\nabla \mathrm{div}\mathbf{u}) + \nabla(\alpha P + K\alpha'\Theta) = \mathbf{f},$$

$$\frac{\partial(\phi\rho)}{\partial t} + \nabla\cdot\Big(-\frac{k}{\mu}(\nabla P + \rho g \nabla z)\Big) + \frac{\partial}{\partial t}(\nabla\cdot\mathbf{u}) = f_w, \tag{3}$$

$$\frac{\partial(\rho^\phi\Theta)}{\partial t} + \nabla\cdot\Big(-\kappa^\phi\nabla\Theta + c_f\rho\Theta\mathbf{q} + \rho^\phi\Theta\frac{d\mathbf{u}}{dt}\Big) = f_Q.$$

CSS CSS CSS CSS CSS Jump discontinuity Motivations in thermo-hydro-mechanics Time dependent
Modeling

Here

- μ_*=the shear modulus, ϕ=the porosity,
- $\rho^\phi = c_s\rho_s(1-\phi) + c_f\rho\phi$, $\kappa^\phi = \kappa_s(1-\phi) + \kappa_f\phi$,
  f_w : an external supply of water, f_Q : an external/internal supply of energy
- ρ_s : the solid density, ρ_f : the fluid density
- c_s, c_f : the specific heat capacity of the solid and the fluid, respectively
- κ_s, κ_f : the thermal conductivity of the solid and the fluid, respectively

The water flux is given by the Darcy' law

$$\mathbf{q} = -\frac{k}{\mu}(\nabla P + \rho g \nabla z) \tag{4}$$

where

- k : the intrinsic permeability, $\mu = \mu(P,\Theta)$: the fluid viscosity,
  $\rho = \rho(P,\Theta)$: the fluid density, g : the gravity, z : the vertical coordinate

The interface and boundary value problem

$$
\begin{aligned}
-\nabla \cdot (\kappa \nabla u) &= f \quad \text{in } \Omega, \\
[u] = \left[\kappa \frac{\partial u}{\partial n}\right] &= 0 \quad \text{on } \mathcal{C}, \\
\frac{\partial u}{\partial n} &= 0 \quad \text{on } \Gamma_N, \\
u &= 0 \quad \text{on } \Gamma_D.
\end{aligned} \tag{5}
$$

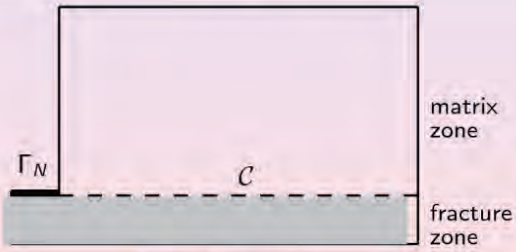

Figure: Domain

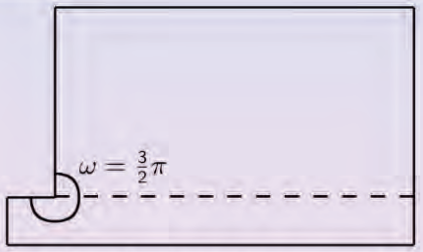

Figure: The Heat flux has a jump across the curve $\mathcal{C}$

Theorem

- $\phi = \begin{cases} -r^\beta \sin(\beta\pi/2)\cos[\beta(\theta+\pi)], & \theta < 0, \\ r^\beta \cos(\pi\theta)\sin[\beta(\theta-\pi/2)], & \theta > 0, \end{cases}$
- $\beta = \frac{2}{\pi}\tan^{-1}\left(\sqrt{\frac{\kappa_2}{2\kappa_1+\kappa_2}}\right)$

Then

$$
\begin{aligned}
&u = \Lambda(f)\phi + u_R, \ u_R \in \mathrm{H}^2(\Omega_i), \\
&\|u_R\|_{2,\Omega_i} + |\Lambda(f)| \le C\|f\|_0, \\
&\Lambda(f) = \textit{ a continuous linear functional on } \mathrm{L}^2.
\end{aligned}
$$

Contents

The interface and boundary value problem for the Heat equation

$$
\begin{aligned}
u_t - \nabla \cdot (\kappa \nabla u) &= f && \text{in } \Omega \times (0,T), \\
[u(\cdot,t)] = \left[\kappa \frac{\partial u}{\partial n}(\cdot,t)\right] &= 0 && \text{on } \mathcal{C}(t),\ t>0 \\
\frac{\partial u}{\partial n} &= g_N && \text{on } \Gamma_N \times (0,T), \\
u &= g_D && \text{on } \Gamma_D \times (0,T), \\
u(\cdot,0) &= u_0 && \text{on } \Omega.
\end{aligned}
\tag{6}
$$

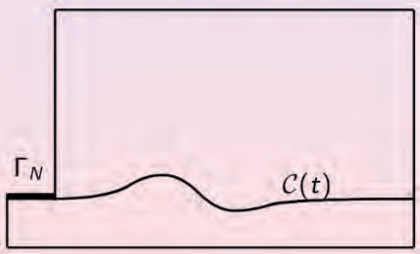

Theorem

- $\mathcal{E}(\mathbf{x}, t) = r^3 e^{-r^2/4t}/4\sqrt{\pi t^5}$
- $c(t) = \frac{1}{2\pi i}\int_\gamma \langle \Lambda^\lambda; (\lambda \mathcal{I} - \mathcal{T})^{-1} f(t)\rangle d\lambda$

Then

$$u(t) = (\mathcal{E} \star c)(t)\phi + u_R(t)$$

$$\Lambda^\lambda(f) : \text{ a continuous linear functional on } \mathrm{L}^q$$

and

$$\operatorname*{ess\,sup}_{t\geq 0} \|u_R(t)\|_{1,q} + \sum_{j=1}^{2} \|u_R\|_{\mathrm{L}^q(\mathbb{R}^+;\mathrm{H}^{2,q}(\Omega_j))}$$

$$+ \|u_R\|_{\mathrm{H}^{1,q}(\mathbb{R}^+;\mathrm{L}^q)} + \|c\|_{\mathrm{H}^{(2-s_1)/2,q}(\mathbb{R}^+)}$$

$$\leq C\Big(\|f\|_{\mathrm{L}^q(\mathbb{R}^+;\mathrm{L}^q)} + \sum_{j=1}^{2} \|u_0\|_{2,q,\Omega_j}$$

$$+ \|g_N\|_{\mathrm{L}^q(\mathbb{R}^+;\mathrm{H}^{1/2,q})} + \|g_D\|_{\mathrm{L}^q(\mathbb{R}^+;\mathrm{H}^{3/2,q})}\Big)$$

CSS CSS CSS CSS CSS Jump discontinuity Motivations in thermo-hydro-mechanics Time dependent

Thank you very much

Forum “Math for Industry” 2025

- Challenge of Mathematics for Industry in the AI era -

August 18 - 20, 2025, Seoul (POSCO Center), Republic of Korea

Industrial AI Innovation: Mathematical Challenges and Applications

Ji-Su Hong

The Miracle Soft

TheMiracleSoft

Big Data & AI Transformation

Building on our management team and key personnel with expertise, we are creating a new history in the age of AI

CEO

JISU HONG

Contribution to company performance

- Development of domain-specific language models and systems
- Data collection and analysis technology / AI model selection algorithm development
- Sphinx AI sLLM language model and solution development
- Developing a subscription update system and maintaining technology leadership
- Sphinx AI Solution CI Contract and Sales Expansion
- - Hyundai Construction No. 1, SK Ecoplant Top 3 (Selected as Excellent Company)
- - Samsung Heavy Industries Sales and Sales Expansion in Other Industries

Career highlights

- Master of Computer Engineering
- Samsung Heavy Industries Researcher (Smart Factory)
- GS ITM Development Team
- VMS-Solutions (Production Simulation Researcher)

SANGWOON KWON

CTO

Contribution to company performance

- Sphinx AI Solution Development
- Data collection and analysis technology
- Big data visualization technology

Career highlights

- Statistics Department
- Development and establishment of large-scale global system
- - Ministry of Foreign Affairs global official document system
- - Innisfree, Amore Pacific global system

Company	TheMiracleSoft CO.,LTD
CEO	JISU HONG
Established Date	2019. 0510
Number of Employees	10명
Main Business Areas	Big Data & AI Transformation
Address	Head Office: 19, Jangpyeong 2-ro, Gaoje-si, Gyeongsangnam-do, 111-204 Branch: 806, 8th floor, Seoul AI Hub (Kyohoe Hall), 114 Taebong-ro, Seocho-gu, Seoul
Homepage	http://themiracleSoft.com

AI Lab

Researcher A
- Master's Program at Yonsei University (Completed)

Researcher B
- Department of Information and Communication
- AI prediction model research and development
- Climate change and bee mortality rate prediction model (National Institute of Agricultural Sciences)
- Advertising exposure and profit rate relationship prediction model

Security & Infra

Developer A
- Computer Engineering and Large-Scale Data Analysis and Security Processing
- Leading AI Data Analysis and Security Solution Development
- Developing a number of large sites including E-bay

Solution

Solution Developer A
- Department of Computer Engineering
- Development of large-scale data and solution frameworks

Solution Developer B
- Big Data & AI FrontEnd Development
- AI UX Design

Jurist

Tae-kyung Kim
Advisory Committee Member
- Partner Attorney at Law, Daeho Law Firm

AX (AI UX) Team

Publisher A
- Brand Design & Solutions
- AX(AI UX) Design & Publishing
- App & Site UI & UX
- 15 years of experience in design and publishing

TheMiraclesoft AI

Developing the Most Practical Customized sLLM Language Model Based on Real Customer Challenges

TheMiracle Soft operates by leveraging specialized technology in document management and process automation within the Heavy Industry (such as construction and manufacturing), where projects worth hundreds of billions are underway.
The company aims to expand its Customized AI technology across various industries, enhancing its competitiveness both domestically and internationally.

Customized AI Solution

Building the Sphinx Gen AI System

- Multi-Server Distributed Processing Technology: SLURM
- Optimization of GPU Resource Allocation and Utilization

Development of Lightweight Language Models for Sphinx Gen AI

- Lightweight Model Architecture
- Distributed Processing and Optimization
- Industry-Specific Language Processing
- Customized API and Interface

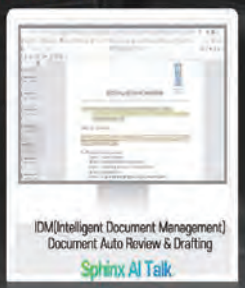

IDM(Intelligent Document Management)
Document Auto Review & Drafting
Sphinx AI Talk

Intelligent Document Management

- Complex Document Preparation
- Technical Specifications
- Regulatory Compliance Documents

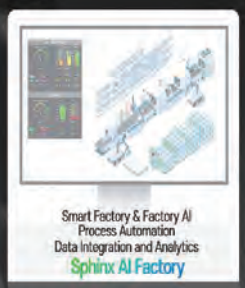

Smart Factory & Factory AI
Process Automation
Data Integration and Analytics
Sphinx AI Factory

Process Automation

- Predictive Maintenance
- Quality Control
- Production Process Automation
- Data Integration and Analysis

Delivering Exceptional Value to Customers Through Customized AI Solutions Tailored to Specific Tasks (Development and Maintenance)

Acquiring Business Opportunities Through Additional Revenue Models, New Solution Development, and Platform Innovation

Introduction

FMfI 2025 theme: Challenge of Mathematics for Industry in the AI Era

Importance of mathematics in industrial AI

Purpose: Share how mathematical modeling + AI solve industrial problems

Key Industrial Challenges

Shipbuilding/Construction:
complex scheduling, contract risks

Finance/Insurance:
probabilistic risk assessment, commission validation

Manufacturing/Robotics:
predictive maintenance, anomaly detection

Advertising/Platforms:
optimization of cost vs. performance

Company Overview – TheMiracleSoft

Vision & Mission: "Convergence of AI + Industry + Mathematics"

Sphinx AI Talk :
Contract/document intelligence

Sphinx AI Factory :
Predictive maintenance for robotics & equipment

Sphinx AI Ad :
Global advertising optimization


Sphinx AI Talk
#B2B #Heavy Industry #Customized #Intelligent #DocumentManagement #GenerativeAI #Factory
TheMiracleSoft
Big Data & AI Transformation


The First AI Solution of TheMiracleSoft's 'Sphinx Customized AI
Sphinx AI talk
Intelligent Document Processing and Management Solution Based on Generative AI
• Mathematical foundation: text mining, graph-based summarization, classification models
• Application: toxic clause detection in contracts (80% accuracy target)
• Industrial impact: risk mitigation, legal cost reduction
Sphinx X
(Training Data)
Upload Internal Document Files
Indexing
Search
Sphinx Gen AI
sLLM API
Document System
Search Engine
RAG(Vector DB)
PDF Parser
FINETUNING
gemma
llama3
Comment System
Sentence - Type Recommend
PDF Layer Markup
Sphinx Auto
Automated Document Review
Detection of Contradictory Statements in Contracts
Detection of Regulatory Documents, Contradictory Documents, and Sentences
Recommendation of Toxic Clauses
Document Error Detection
Automated Document Drafting
Automated Generation of Bid Proposal Reports
Automated Drafting of Contracts
Preparation of Additional Quotation
Office Customized IDP AI Solution that Learns from Internal Document Data to Provide Answers and Inference Capabilities

Competitiveness and Differentiation of Sphinx AI (1/4)

Customized sLLM Model Capable of User-Driven Learning Tailored to User Work Requirements

Customized to meet specific tasks and requirements desired by the user, providing an interface for user-driven learning.
This automates document management and analysis tasks for businesses, enhancing efficiency.

TheMiracleSoft Smart Office Solution

Document Directory Management

File Content Management

Direct Upload and Management of Training Data by the Responsible Person

Sphinx AI talk

Training on Tens to Hundreds of Millions of Internal Document Data

Answering Questions and Inference Capabilities
- The AI provides accurate answers based on the information it has learned in response to user inquiries, along with additional information through its inference capabilities.

Document Error Detection
- Analyzing documents to identify and correct errors, including grammatical mistakes, inconsistent information, and missing items.

Detection of Toxic Clauses
- Automatically identifying and highlighting critical content such as toxic clauses in documents like contracts, and providing this information to the user.

Detection of Conflicting Statements in Contracts
- Analyzing multiple contracts to identify conflicting clauses or information.

Competitiveness and Differentiation of Sphinx AI (2/4)

Ability to Learn from Large Project Documents (Internal Regulations, Contracts, Engineering Documents, Regulations, etc.)

By learning specific work documents tailored to particular purposes, the AI gains a better understanding of the vocabulary, terminology, and context of the relevant field, preventing hallucinations and responding more accurately to user needs.

Providing contextually appropriate understanding, accurate reasoning, and responses suitable for specific tasks, with model optimization through RLHF (Reinforcement Learning from Human Feedback)

Document Centralization

PDF Document Parsing

Data Collection and Document Parsing

- Storage and Management of Large Office Documents (Development of File Upload Component)
- PDF Document Parsing

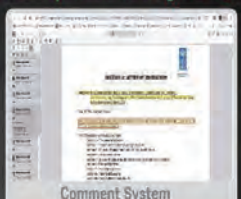

Comment System

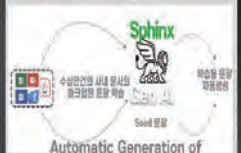

Automatic Generation of Training Sentences

Natural Language Processing (NLP)

- Comment System for Collecting Training Data
- Automation of Training Data Refinement
- Automatic Generation of Training Data Using LLM Based on Collected Data

RAG

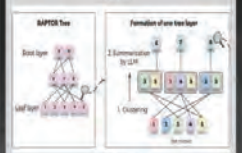

RAPTOR

Overcoming Limitations of AI Search-Augmented Generation (RAG)

- Generation of Search Content by sLLM Based on Internal Documents and Databases
- Implementation of Recursive Abstractive Processing for Tree Organized Retrieval (RAPTOR)

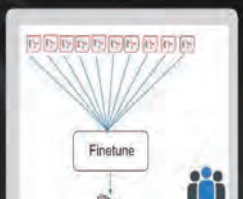

Finetune & Human Feedback

Large-Scale Fine-tuning and Reinforcement Learning from Human Feedback (RLHF)

- Large-Scale Training Data Learning Techniques
- Reinforcement Learning from Human Feedback (RLHF) Optimizes ML Models Using Human Feedback

Competitiveness and Differentiation of Sphinx AI (3/4)

Optimized System & sLLM Model for Performing Specific Tasks in Large-Scale Projects

Sphinx AI talk

Supports users in performing natural language processing tasks more effectively during specific tasks, improves business workflows, and simplifies document creation and analysis processes.

Sphinx Gen AI Implementation

- Multi-Server Distributed Processing Technology: SLURM Optimization of GPU Resource Allocation and Utilization

Contradicton Check & Not Equal Check For Legal

Regulatory Compliance Monitoring

- Monitoring of legal and regulatory requirements
- Non-compliance alerts and guidance functions

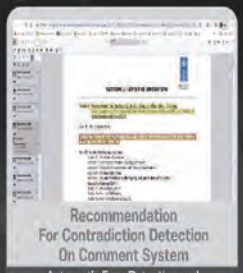

Recommendation For Contradiction Detection On Comment System

Automatic Error Detection and Recommendations

- Error detection and recommendations for engineering documents
- Detection and recommendations for conflicts and errors between contracts

Sphinx Gen AI Lightweight Language Model

- Lightweight Language Model
- Equipped with Smart Factory, Industrial Robots, etc.

Competitiveness and Differentiation of Sphinx AI (4/4)

Cost-Efficient Hierarchical AI Architecture and Development of Multimodal AI

Composed of multiple layers, each performing different levels of abstraction or processing, the multimodal AI enhances user experience.

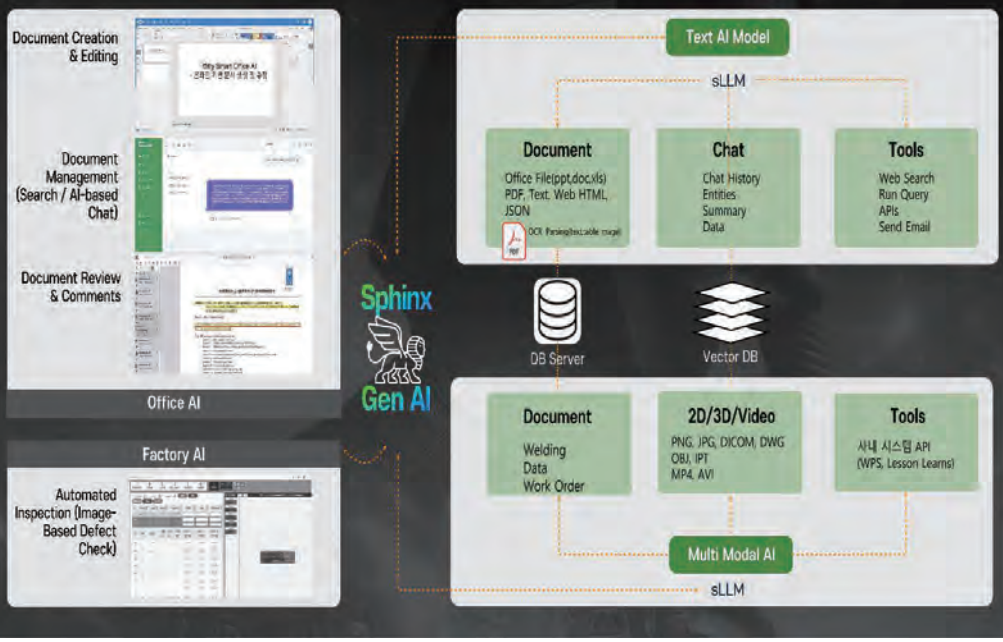

The competitive advantages of Sphinx AI (1/1)

Bottom-up strategy that first analyzes the requirements of each department and introduces a small language model (sLLM) that fits them

The system can be quickly adapted to meet departmental requirements, allowing flexible responses even in environments sensitive to change.

Maximizing the effectiveness of AI technology by department

Plenty	Considerations when introducing AI (barriers to entry)	Less
High	Initial introduction cost	Low
Slow	decision making	Fast
High	Possibility of delay in introduction	Low
Slow	System construction speed	Fast
Slow	Apply departmental requirements	Fast

B2B Client Case Studies & Customer Value

Sphinx AI Talk

#B2B #Heavy Industry #Customized #Generative AI #Office AI

TheMiracleSoft

Big Data & AI Transformation

Hyundai Engineering & Construction No.1 Open Innovation

(Participation of 227 companies)

Housing Construction Project Team

Q) Please tell me about the waterproofing finish details for the underground parking garage roof!

A) The waterproofing finishes for the underground parking garage roof are detailed as follows: there are four types.

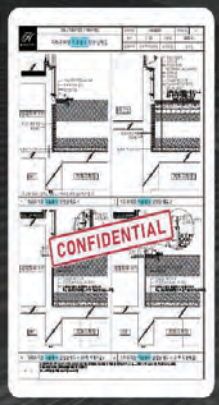

Source: Standard Detailed Drawings Underground Parking Lot

Q) What are the waterproofing standards for the intermediate floors of an underground parking garage?

A) The waterproofing standards for the intermediate floors of an underground parking garage are as follows: when there is no reinforcement, it is ~, and when there is reinforcement, it is ~

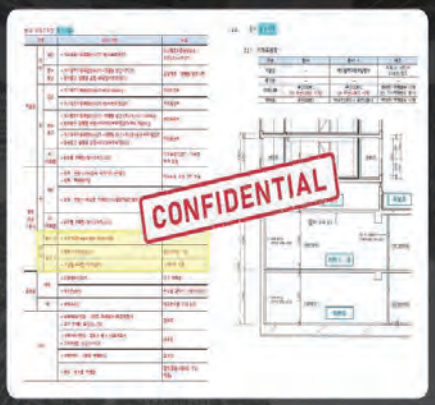

Source: Construction Manual Waterproofing Construction

Low-priority tasks, low understanding of the site, and solutions for issues related to dispatching new personnel

Time taken for deployment to the site after internal training

3 to 6 months

Must be accompanied by an existing experienced worker when deployed to the site

Time available for site deployment after basic training

1 to 2 weeks

Existing experienced workers can respond remotely when deployed to the site

Utilizing Sphinx AI Search Sphinx for Automatic Document Creation

Sphinx AI talk

Hyundai Engineering & Construction No.1 Open Innovation

(Participation of 227 companies)

Plant Commissioning Team

Q) After learning the contract and construction cost estimates, please automatically create the Criteria document

When commissioning the equipment, prepare a work checklist using related codes, client engineering specifications, standards, etc. After testing the target equipment, evaluate the adequacy of the test by comparing the measured values with the criteria indicated in the following figure. In other words, upload the reference documents to the AI so that the criteria for the test can be automatically generated.

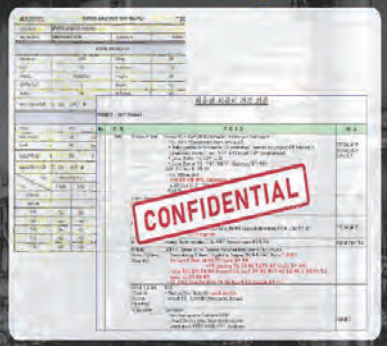

Q) Please automatically create the Criteria document after learning the contract and construction cost estimates

When selecting the appropriate cleaning method for pipes and machinery, create a matrix using client specifications and standards. Each type of pipe requires different cleaning methods based on conditions such as type, size, and fluid. After inputting reference materials, the AI automatically generates a matrix of recommended cleaning methods according to a specific format. The responsible person will review and modify it for use

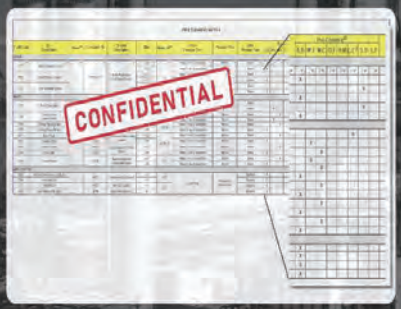

High-priority tasks, checking tasks that need to be performed and preparing estimates, when creating the matrix, human errors and project delays occur

Contract Review and Task Check Matrix

2 to 3 months / 7 to 12 people

Multiple people and teams need to cross-check, and there is a high possibility of communication and human errors occurring

Contract Review and Task Check Matrix

1 week / 4 people

1 person writes, 1 person verifies, and teams cross-check. The possibility of communication and human errors occurring is significantly low

Utilizing Sphinx Document Automatic Review, Sphinx for Automatic Document Creation

Sphinx AI talk

Hyundai Engineering & Construction No.1 Open Innovation

(Participation of 227 companies)

Plant Commissioning Team

Automatic document creation - Piping Cleaning Matrix

Result process of Input document and Output document

Input

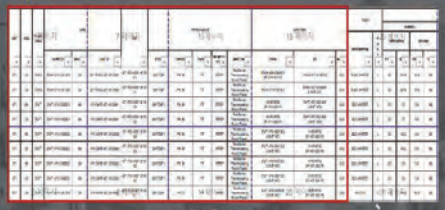

<Line Designation >

Ref.

<References: Procedures and FEED, Engineering Documents>

Sphinx AI Talk

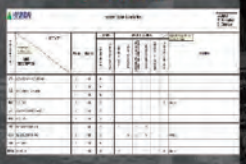

<System Cleaning Matrix by Orderer>

Sphinx AI Talk

Output

Result rev.0

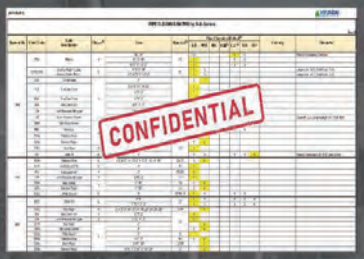

<Auto-generated, PIPING CLEANING Matrix>

Problem Solving

Improvements using Sphinx AI Talk

Contract and ITB Proposal Process and Pain Points

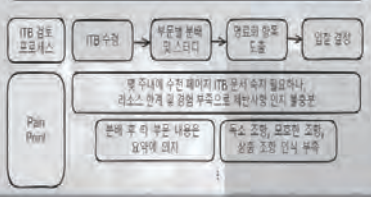

- Manually discovering the toxic clauses of a PDF contract using Excel on a personal PC
- Discovering after collating all conflicting comments by department for the same sentence or after delivering it to the client

Difficulty in verifying local regulations for the project global

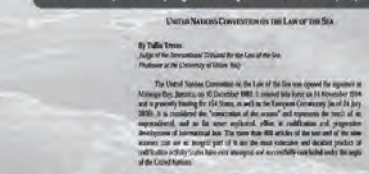

UNITED NATIONS CONVENTION ON THE LAW OF THE SEA

- High incidence of human error and omission of global regional regulatory compliance requirements

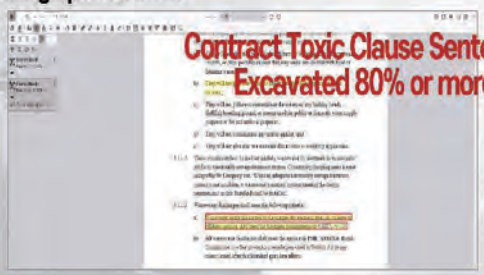

Contract Toxic Clause Sentences Excavated 80% or more

- Collect toxic clause data and learning data through web-based comments
- Recommendation rate of up to 80% is possible through the toxic clause recommendation model collected
- Systematization of engineer know-how

70% or more of conflicting sentences discovered

- Periodic collection of legal documents (Crawling) Legal document version management and version-by-version comparison
- Uploading new contracts and stipulations using legal documents as reference documents Automatically discovering conflicting sentences

TheMiracleSoft Smart Factory AI Solution

Sphinx AI Factory

Solving the labor shortage in a shrinking society through automation and unmanned operation of simple tasks

Preparing for the Industry 5.0 era using AI technology

The second AI solution of TheMiracleSoft's Sphinx Customized AI

AI-based equipment and robot predictive maintenance solutions

Customized Factory AI Solution : Sphinx AI Factory

- Mathematical foundation: time-series forecasting, Weibull distribution, anomaly detection
- Case: Samsung Heavy Industries – monitoring 1,000+ robots in real time
- Results: 80% reduction in downtime, high accuracy in preventive maintenance

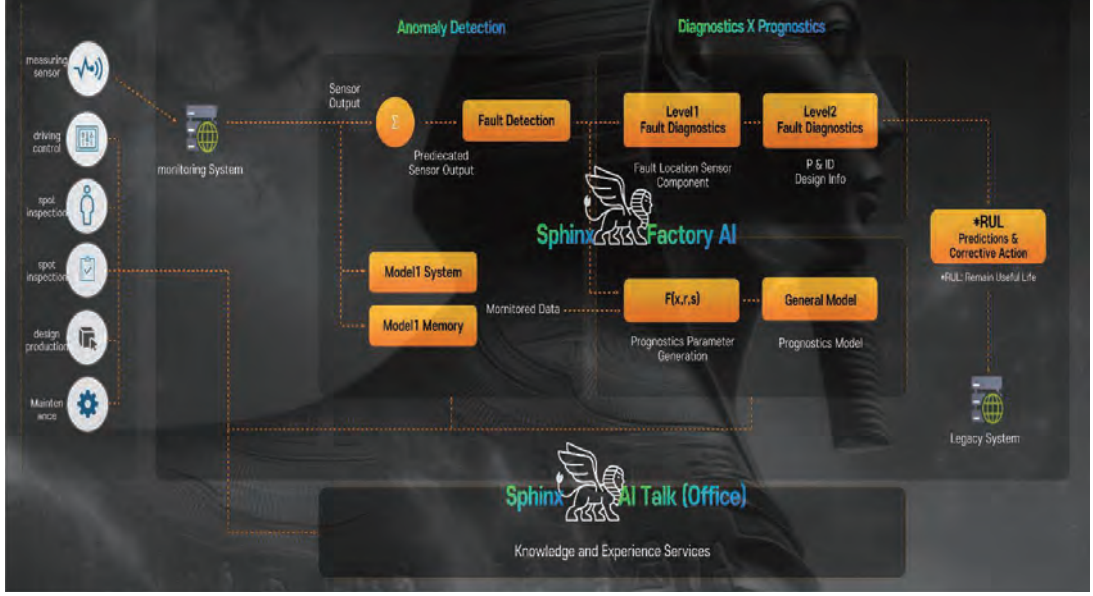

The second AI solution of TheMiracleSoft's Sphinx Customized AI

Using artificial intelligence (AI) and machine learning, analyze the status of equipment and facilities in real time and predict the possibility of failure
Factory AI solution developed for the purpose of improving productivity, reducing costs, and automating unmanned manufacturing

Customized Factory AI Solution

Samsung Heavy Industries Robotics Technology Roadmap

Sphinx
Factory AI

- Predictive maintenance AI
- Automate maintenance AI
- Unmanned maintenance AI

Design predictive maintenance platform and data analysis tailored to user needs with Heavy Industry Domain Knowledge

Building a Factory AI (Predictive Maintenance) Predictive Model Based on Optimized AI

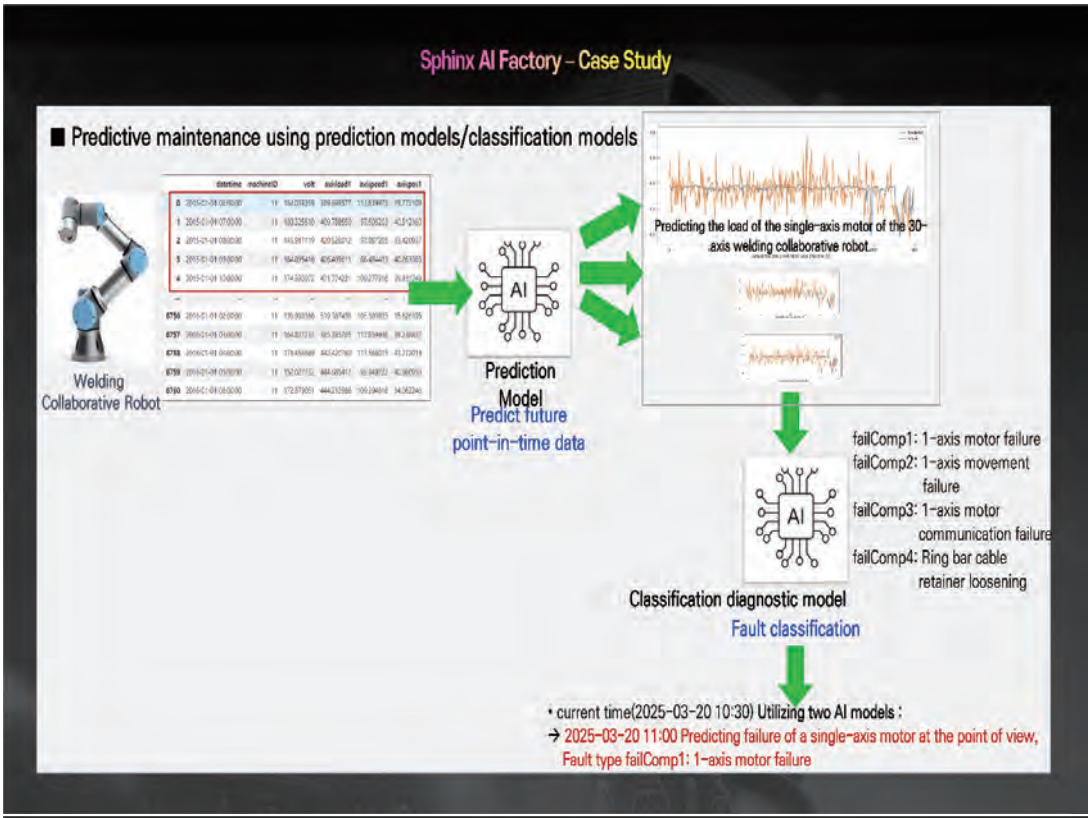
Sphinx AI Factory – Case Study
■ Predictive maintenance using prediction models/classification models
Welding Collaborative Robot
AI
Prediction Model
Predict future point-in-time data
Predicting the load of the single-axis motor of the 30-axis welding collaborative robot...
AI
Classification diagnostic model
Fault classification
failComp1: 1-axis motor failure
failComp2: 1-axis movement failure
failComp3: 1-axis motor communication failure
failComp4: Ring bar cable retainer loosening
• current time(2025-03-20 10:30) Utilizing two AI models :
→ 2025-03-20 11:00 Predicting failure of a single-axis motor at the point of view,
Fault type failComp1: 1-axis motor failure

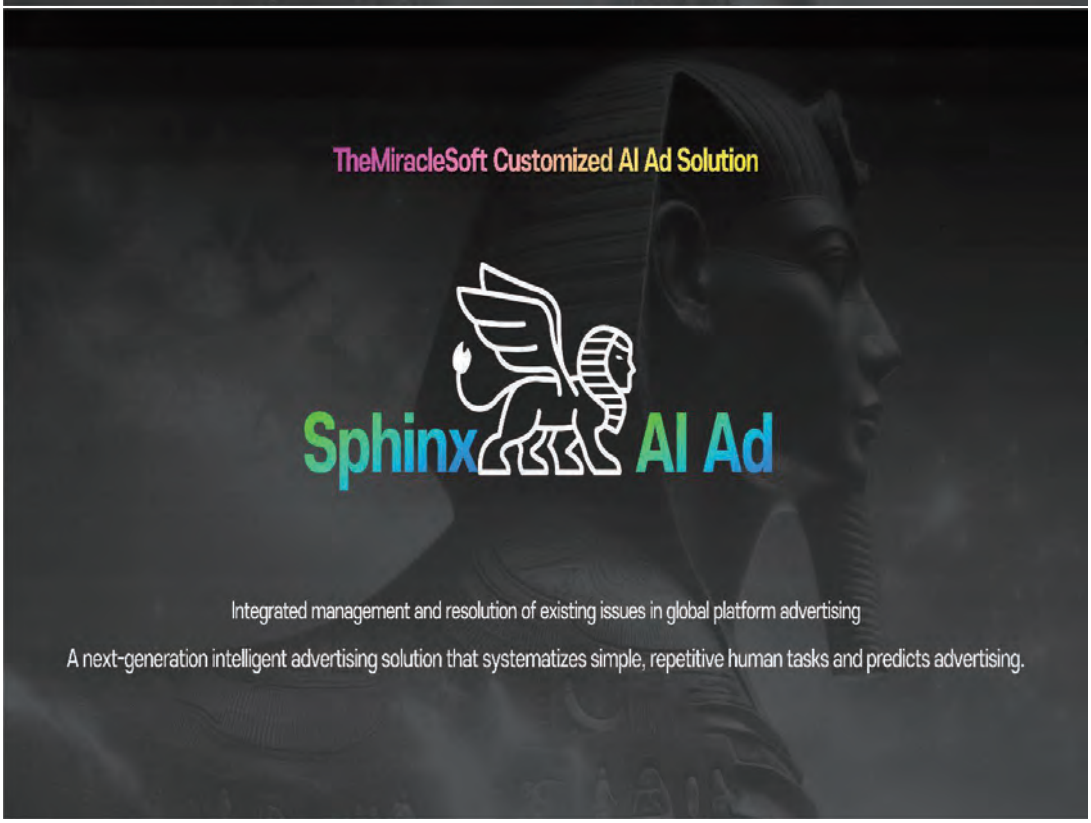
TheMiracleSoft Customized AI Ad Solution
Sphinx AI Ad
Integrated management and resolution of existing issues in global platform advertising
A next-generation intelligent advertising solution that systematizes simple, repetitive human tasks and predicts advertising.


TheMiracleSoft Sphinx AI Ad - Global advertising-specific solution
Sphinx AI Ad
An integrated management advertising solution based on an optimized AI-based intelligent platform.
• Mathematical foundation: linear programming, multi-objective optimization
• Application: integrated ad management across Google, Meta, TikTok
• Results: reduced ad cost, improved conversion rates
Global Ad Platform
Google Ads
Meta
kakao
Sphinx AI Multi-Modal
Multi-Modal API
Advertising Data Integration and Compilation
FINETUNING
Ad Schedule Management
Huggingface Idefics3 8B
Llama 3.2-Vision 11B, 90B
Sphinx AI Ad
Advertising predictions (impressions, revenue)
Automatic landing page creation
A solution that generates advertising landing page images using time-series data-based advertising prediction and multi-modal AI models.

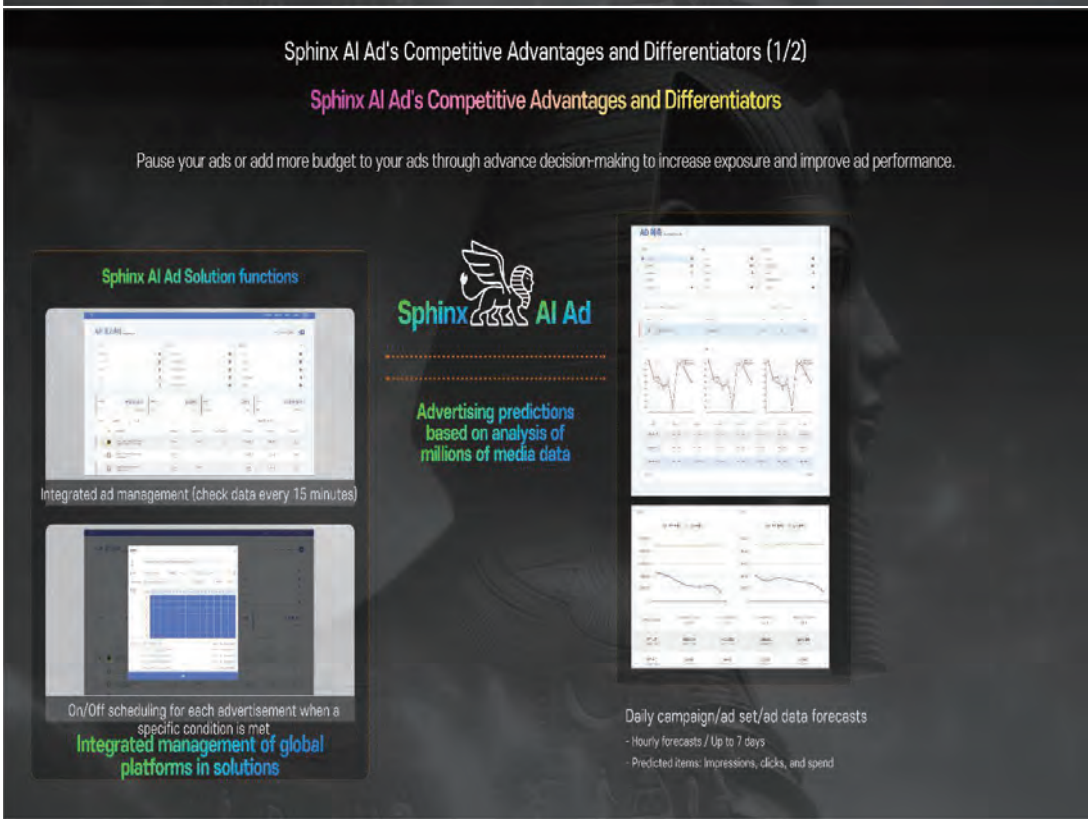
Sphinx AI Ad's Competitive Advantages and Differentiators (1/2)
Sphinx AI Ad's Competitive Advantages and Differentiators
Pause your ads or add more budget to your ads through advance decision-making to increase exposure and improve ad performance.
Sphinx AI Ad Solution functions
Integrated ad management (check data every 15 minutes)
On/Off scheduling for each advertisement when a specific condition is met
Integrated management of global platforms in solutions
Sphinx AI Ad
Advertising predictions based on analysis of millions of media data
Daily campaign/ad set/ad data forecasts
- Hourly forecasts / Up to 7 days
- Predicted items: Impressions, clicks, and spend

Sphinx AI Ad's Competitive Advantages and Differentiators (2/2)

Systematizing manual processing and predicting the advertising to be operated for advance decision-making

Pause your ads or add more budget to your ads through advance decision-making to increase exposure and improve ad performance.

Sphinx AI Ad Solution Functions

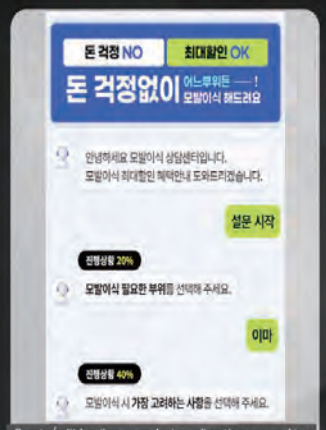

Create/edit landing page designs directly managed by publishers

Platform integration management in Sphinx AI Ad solution

Sphinx AI Ad

Create a chat-style landing page by analyzing pre-trained landing pages.

Text 2 Image Creation

Landing page design by client category: Learning by category
- Image generation using trained lightweight models and multi-modal methods.

Synergy effects through communication between TheMiracleSoft Sphinx AI Ad and Sphinx AI Talk

AI-based intelligent Sphinx AI Talk & Sphinx AI Ad

Landing page validation function after recognizing the internal document-based requirements definition and global platform regulations.

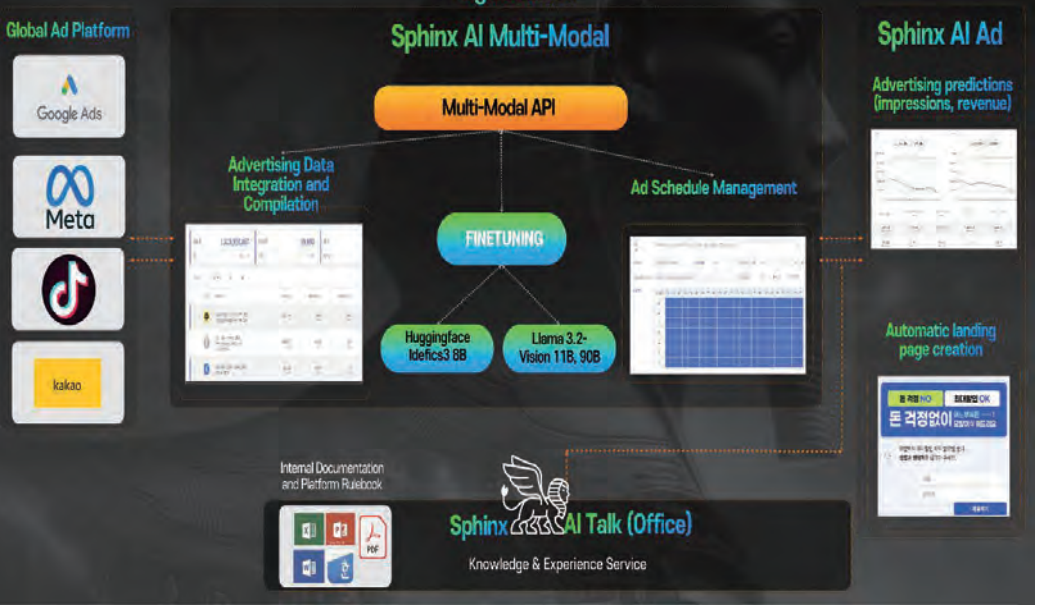


Mathematical Challenges
Computational complexity (Combinatorial explosion)
Constraint modeling (Constraint programming)
Uncertainty handling (Bayesian inference)
Need for synergy between industrial data + mathematics + AI

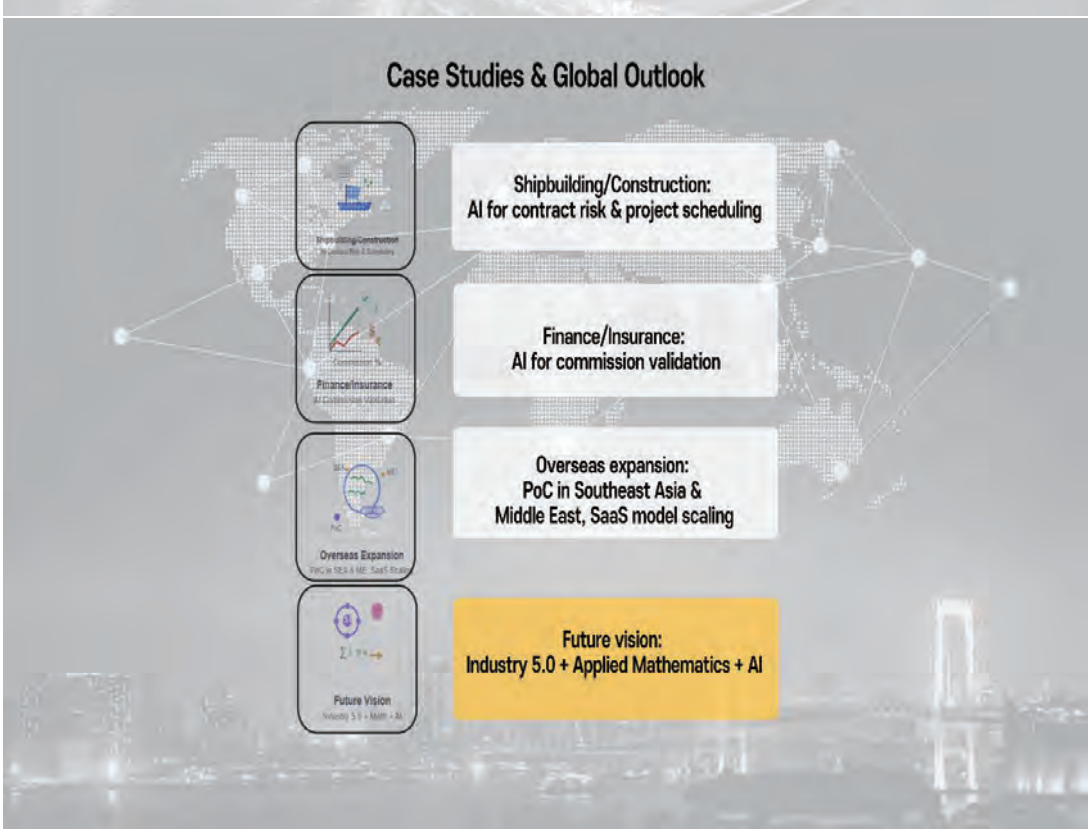
Case Studies & Global Outlook
Shipbuilding/Construction:
AI for contract risk & project scheduling
Finance/Insurance:
AI for commission validation
Overseas expansion:
PoC in Southeast Asia & Middle East, SaaS model scaling
Future vision:
Industry 5.0 + Applied Mathematics + AI

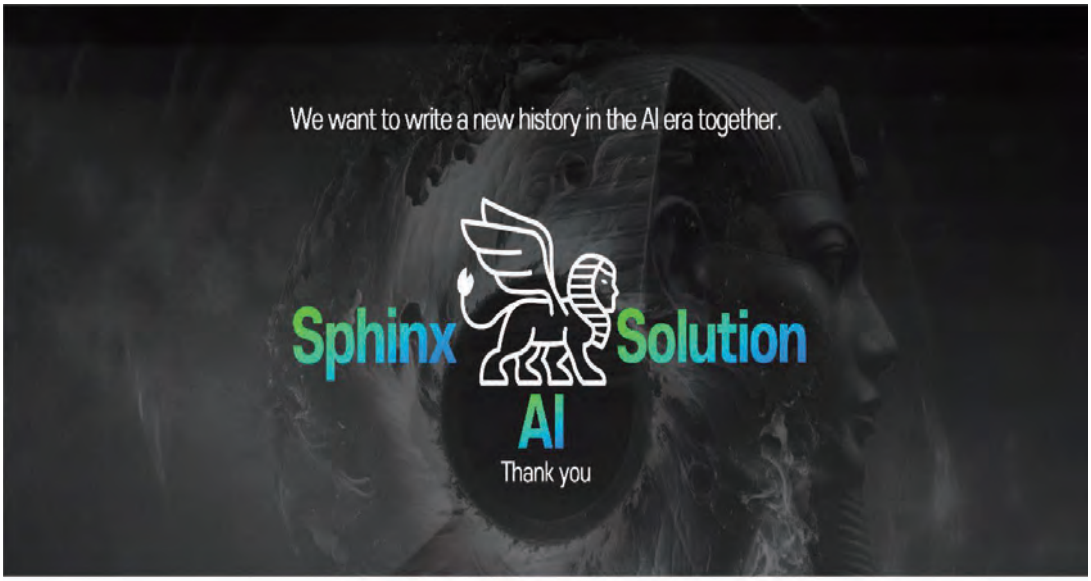

TheMiracleSoft
Big Data & AI Transformation

CEO: JISU HONG
jisu.hong@themiraclesoft.com
+82 10 4730 1069

Integrating LIBS and Machine Learning for Practical Industrial Applications in Alloy Identification and Analysis

Yong-Hoon Lee

Mokpo University

Laser-induced breakdown spectroscopy (LIBS) offers rapid, multi-elemental analysis in open air with minimal sample preparation, making it attractive for on-site industrial applications. This work integrates LIBS with machine learning to address practical challenges in alloy identification and quantification, focusing on two case studies: nickel alloys and low-alloy steels. A compact LIBS device was assembled using a low-power diode-pumped solid-state laser and a miniature low-resolution spectrometer. For nickel alloys, quantitative analysis of Ni, Cr, and Fe was performed using selected non-resonance emission peaks (547.7, 520.4, and 438.1 nm, respectively). Intensity-based calibration achieved root mean square errors of 1–3 wt%, while classification of six alloy types using k-nearest neighbors (KNN) and linear discriminant analysis (LDA) yielded accuracies of 95.0% and 98.3%. A two-step LDA approach improved classification to 100% by resolving misclassifications between similar compositions. For low-alloy steels, the same LIBS setup was used, but the low spectral resolution (∼ 0.9 nm) precluded resolving individual emission lines for Mn, Cr, Ni, and Ti. Partial least squares regression (PLS-R) modeling extracted quantitative information from unresolved spectral features, with segmented cross-validation demonstrating high accuracy. For Ni and Ti, baseline variations in congested spectral regions were mitigated by using the first derivatives of LIBS spectra, reducing calibration error and improving robustness. These results demonstrate that combining a compact LIBS system with tailored multivariate algorithms—ranging from discriminant analysis for classification to PLS-R with spectral preprocessing for quantification—enables accurate, cost-effective alloy analysis. The approach is well-suited for real-time sorting, quality control, and recycling operations, and offers a practical pathway for deploying portable LIBS platforms in industrial environments.

Integrating LIBS and Machine Learning for Practical Industrial Applications in Alloy Identification and Analysis

Yonghoon Lee

Department of Energy and Chemical Engineering
Mokpo National University
Republic of Korea
yhlee@mokpo.ac.kr

Part 1.
Laser-induced breakdown spectroscopy analysis of alloying elements in steel: Partial least squares modeling based on the low-resolution spectra and their first derivatives

Optics and Laser Technology 112 (2019) 117-125

Low-power low-resolution LIBS spectrometer

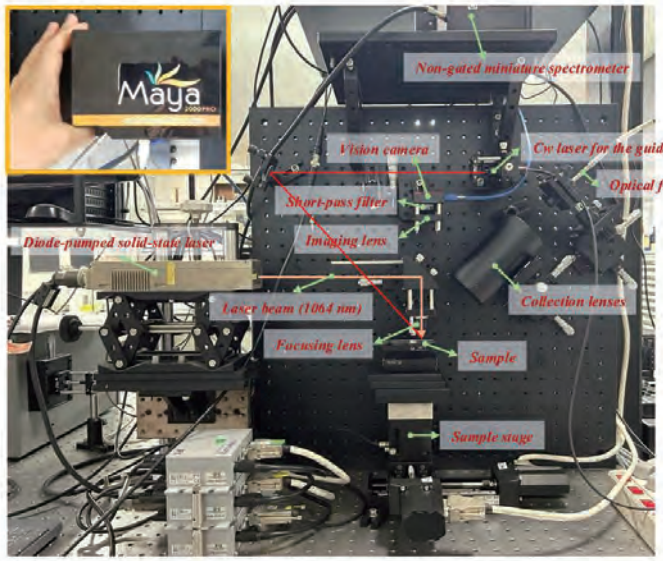

Hg I line emission at 407.784 nm recorded with low- and high-resolution spectrometers

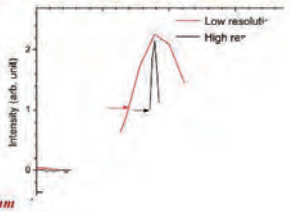

Low-alloy steel sample surface image after laser-ablation sampling

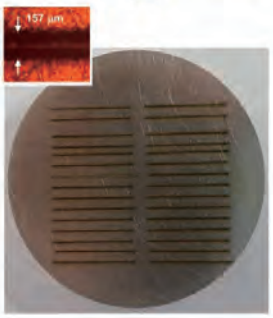

Low-alloy steel SRM samples

List of NIST low-alloy steel SRMs with the certified concentrations of Mn, Cr, Ni, and Ti and the numbers of LIBS spectra recorded for each SRM.

SRM no.	Certified mass fraction (%)				No. of LIBS spectra
	Mn	Cr	Ni	Ti	
1761A	0.679 ± 0.010	0.222 ± 0.006	1.981 ± 0.019	0.173 ± 0.007	15
1762A	1.912 ± 0.047	0.923 ± 0.019	1.156 ± 0.031	0.0952 ± 0.0063	24
1763	1.584 ± 0.021	0.498 ± 0.007	0.513 ± 0.012	0.308 ± 0.009	24
1764A	1.193 ± 0.058	1.468 ± 0.031	0.2006 ± 0.0045	0.0286 ± 0.0023	25
1765	0.144 ± 0.005	0.051 ± 0.002	0.154 ± 0.002	0.0055 ± 0.0005	25
1766	0.067 ± 0.002	0.024 ± 0.001	0.021 ± 0.002	0.0005 ± 0.0002	25
1767	0.022 ± 0.001	0.0015 ± 0.0005	0.002 ± 0.001	0.011 ± 0.001	25

Partial least squares-regression (PLS-R)

- To relate spectral intensities with the concentrations of the analyte element, PLS-R decomposes **X**-matrix (measured spectral intensities) based on **y**-variation (concentrations).
- **X** is the m×n matrix consisting of m objects (spectra) with n variables (intensities at m wavelength values).
- **y** is the m-dimensional vector of which is the reference concentrations of the analyte element.
- In this analysis, m is 163 and n depends on the selected wavelength region for each analyte element.
- Through PLS, the **X**-matrix is decomposed into latent variables, called PLS factors, according to how much the factors explain the **y**-variance.

Optimal number of factors for PLS-R model avoiding overfitting

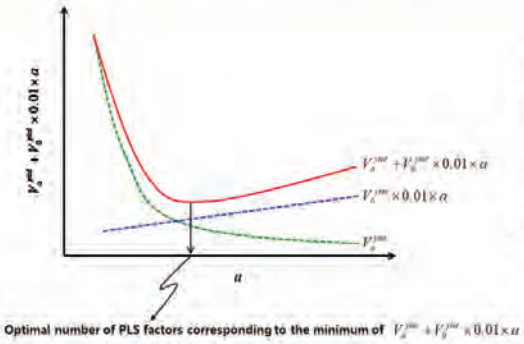

추가하는 PLS-factor는 initial total variance의 적어도 1% 이상을 설명할 수 있어야 한다.

V_0^{ytot}: initial (residual) y-variance (constant)
V_a^{ytot}: total residual y-variance after subtracting the explained y-variance using PLS-factors 1, 2, ... a, from V_0^{ytot}.

Model performance evaluation: segmented cross-validation

- For the segmented cross-validation, 20 subgroups of the 163 spectra were randomly generated.
- Each subgroup consists of 8 or 9 spectra.
- Leaving one subgroup out for the validation dataset, a calibration model was developed using the spectra belonging to the other subgroups.
- Then, RMSE values were calculated for the subgroup left for validation data.
- This process was performed leaving every subgroup out as a validation dataset.

$$\mathrm{RMSE} = \sqrt{\frac{\sum_{i=1}^{n} (\hat{y}_i - y_i)^2}{n}}$$

LIBS spectrum and the selected wavelength regions for analyzing Mn, Cr, Ni, and Ti

NIST SRM 1763

The wavelength regions for modeling the concentrations of Mn, Cr, Ni, and Ti are indicated.
For Cr, the two wavelength regions around 425 nm and 520 nm were used together.

Manganese

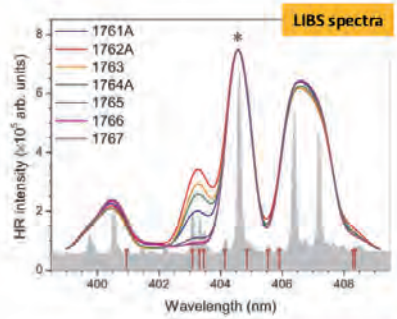

- The part of the LIBS spectra used for modeling Mn concentrations in the NIST SRMs.
- The baselines were subtracted and the intensities were normalized with respect to the Fe I emission line indicated with "*".
- The LIBS spectrum of the SRM 1763 recorded with the higher resolution (gray) is shown together with the low-resolution spectra.
- The red vertical sticks indicate the positions of Mn I lines.

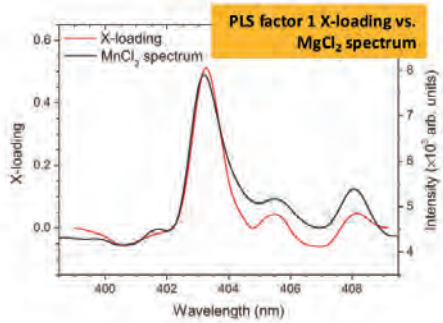

- The X-loading of the PLS factor 1 and the spectrum of a $MnCl_2$ pellet.
- The unresolved Mn I emission line structure in the low-resolution LIBS spectra is extracted well by the PLS analysis (PLS factor 1).

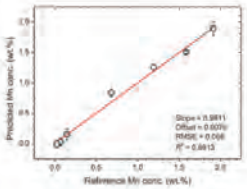

- The model was developed using the PLS factor 1.
- The RMSE of cross validation is 0.068 wt.% which can be regarded as accuracy of this model.

Chromium

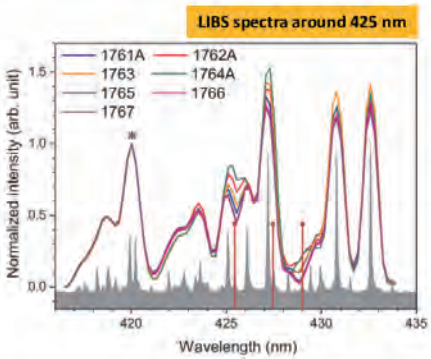

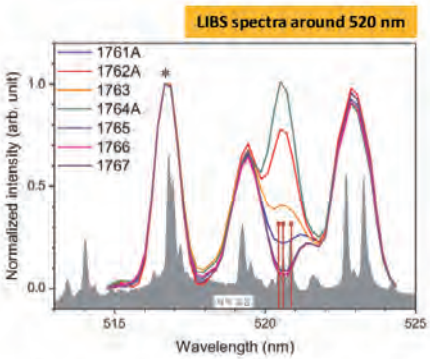

- For modeling the Cr concentration, two wavelength regions around 425 and 520 nm were used together.
- The LIBS spectra recorded by the low-resolution spectrometer along with the higher-resolution spectra in gray.
- Also, the red vertical sticks indicate the Cr I line positions.
- Prior to the PLS analysis, the baseline connecting both ends was subtracted from each spectrum, and the spectral intensity was normalized by the nearby Fe I line intensity indicated by "*".

Chromium

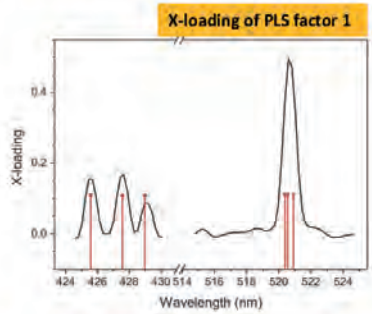

- The PLS factor 1 loading is shown (left).
- The spectral feature of the Cr I lines at 425.435, 427.481, 428.973, 520.450, 520.602, and 520.841 nm is successfully loaded in the PLS factor1.
- Only the PLS factor 1 was used to calibrate the PLS-R model for the Cr concentration.

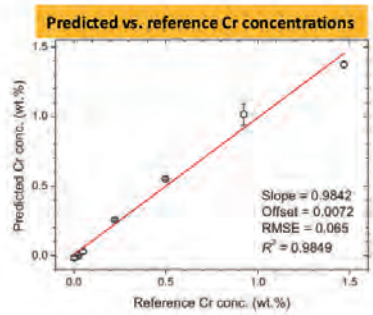

- The RMSE was estimated to be 0.065 wt.% by the segmented cross validation.
- The predicted Cr concentrations are plotted with respect to the reference concentrations.

Nickel

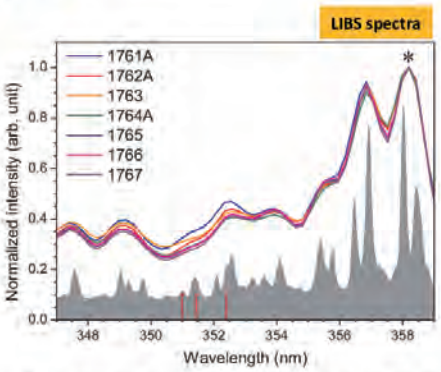

- Shows low-resolution LIBS spectra (347–359 nm) of seven SRMs together with a high-resolution spectrum of SRM 1761A.
- Red vertical bars mark three strong Ni I lines (351.034, 351.505, and 352.454 nm).
- Although this UV region is highly congested with Fe and other transition metal lines, the intensities at the Ni I wavelengths still correlate with Ni concentration.
- Meaning: Even in low-resolution spectra, Ni-related features remain detectable and reflect Ni content.

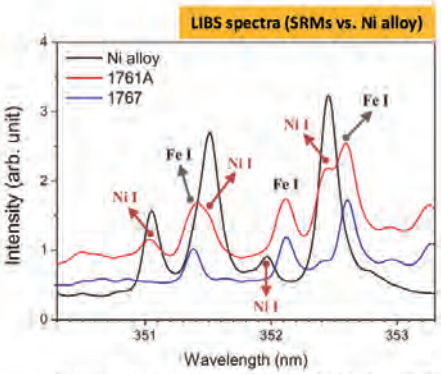

- Compares high-resolution spectra of a Ni alloy (Ni 76 wt.%, Fe 7.3 wt.%), SRM 1761A (Ni 1.981 wt.%), and SRM 1767 (Ni 0.002 wt.%).
- Ni I and Fe I emission lines are assigned (e.g., Fe I at 351.382, 352.126, 352.604 nm).
- Additional weak Ni I line (351.977 nm) is observed in the Ni alloy.
- Even with high resolution, the stronger Ni I lines are not fully separated from neighboring Fe I lines, but clear intensity differences between high- and low-Ni samples are evident.
- Meaning: Despite overlap with Fe lines, Ni concentration is still distinguishable through spectral features.

Nickel

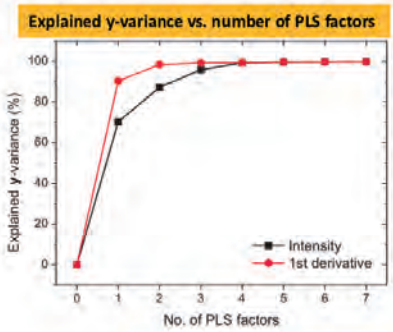

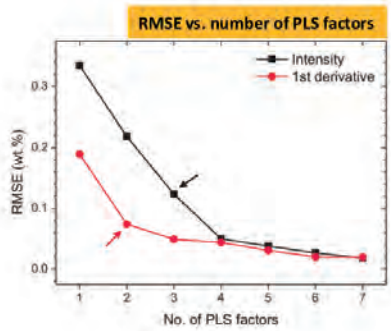

Spectral Preprocessing

- **Wavelength region**: 350.4–353.4 nm.
- **Normalization**: Intensity at 358.194 nm was used for normalization.
- **Baseline subtraction**: Not feasible due to dense overlapping Fe and transition metal lines near Ni I lines.
- **First derivatives**: Applied to compensate for baseline variation and enhance sensitivity to Ni concentration.

Modeling Approach

- **Method**: Partial Least Squares Regression (PLS-R).
- **Two models compared**:
  1. Based on normalized spectral intensities.
  2. Based on first derivatives of spectra.

Results

- **Explained y-variance**
  - First-derivative model explains Ni concentration variation more effectively with fewer PLS factors.
- **Cross-validation RMSE**
  - First-derivative model achieves lower RMSE (0.074 wt.%) using only 2 PLS factors.
  - Intensity-based model requires 3 factors and gives higher RMSE (0.12 wt.%).
- **Conclusion**: The first-derivative approach improves model efficiency and accuracy by reducing baseline effects and noise contributions.

Final Model

- **Chosen approach**: PLS-R based on first derivatives.
- **Optimal setup**: 2 PLS factors.
- **Performance**: RMSE = 0.074 wt.% (better than intensity-based model).

Nickel

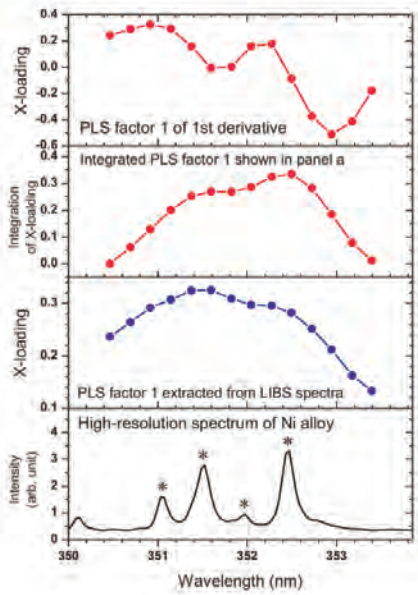

- ✓ Shows the **X-loading of PLS factor 1** extracted from the first derivatives of LIBS spectra for Ni modeling.
- ✓ The loading profile displays **two partially resolved peaks**:
  - The lower-wavelength peak corresponds to Ni I lines at 351.034, 351.505, and 351.977 nm.
  - The higher-wavelength peak corresponds to the Ni I line at 352.454 nm.
- ✓ Demonstrates that Ni emission line features are effectively captured in the derivative-based PLS factor.
- ✓ Comparison with the integrated loading and the high-resolution spectrum confirms consistency with the actual Ni emission structure

Titanium

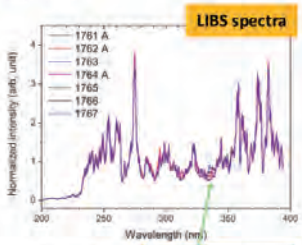

- Shows low-resolution LIBS spectra of seven low-alloy steel SRMs.
- The UV region contains dense emission lines from Fe, Mn, Cr, Ni, and Ti.
- Around **335 nm, strong Ti II emission lines** are observed, and their intensities vary depending on Ti concentration.

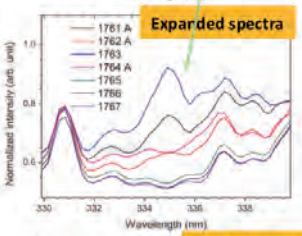

- Enlarged low-resolution spectra in the 335 nm region.
- Clear intensity differences among SRMs reflect differences in Ti content.
- Demonstrates that even low-resolution spectra contain Ti-sensitive features.

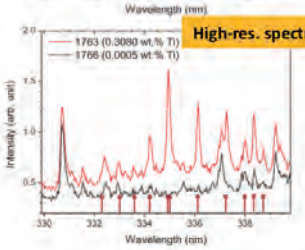

- Compares SRM 1763 (highest Ti, 0.308 wt.%) and SRM 1766 (lowest Ti, 0.0005 wt.%).
- Red vertical bars indicate Ti II emission lines, which match the observed intensity variation.
- Confirms that the intensity changes seen in low-resolution spectra originate from actual Ti II emission lines.

Titanium

Preprocessing for Ti concentration modeling

- **Wavelength region**: 329.39–338.22 nm (Ti II lines near 335 nm)
- **Baseline subtraction**: Not applied (too many overlapping emission lines)
- **Normalization**: Based on the **total emission intensity in the UV region (199.25–393.64 nm)**
- **Derivative spectra**: First derivatives used to reduce baseline variation and systematic errors

Explained y-variance vs. number of PLS factors

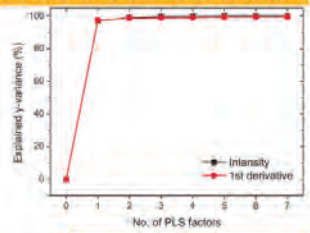

- Data: Low-resolution LIBS spectra (329.39–338.22 nm) for Ti modeling
- Comparison: Intensity-based vs. first-derivative-based models
- Result:
  - PLS factor 1 explains **>97% of Ti concentration variation** in both cases
  - Indicates strong correlation between spectra and Ti content

RMSE vs. number of PLS factors

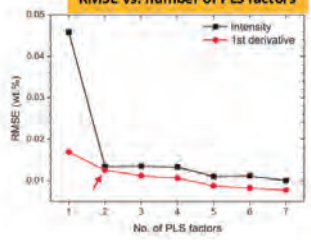

- Cross-validation RMSE plotted against the number of PLS factors
- Result:
  - With only 1 factor, **first-derivative model shows lower RMSE** (better accuracy)
  - Optimal number of PLS factors = **2** for both models
  - At the optimal point, RMSE values of both models are nearly identical
- Implication:
  - First derivatives effectively reduce baseline-related systematic errors
  - Provides a more stable model with fewer latent variables

Titanium

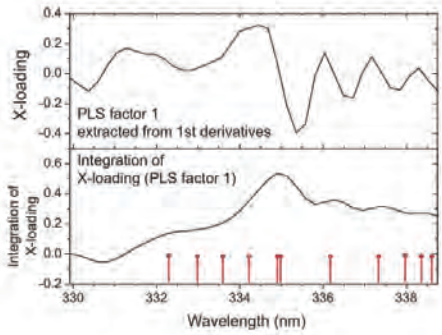

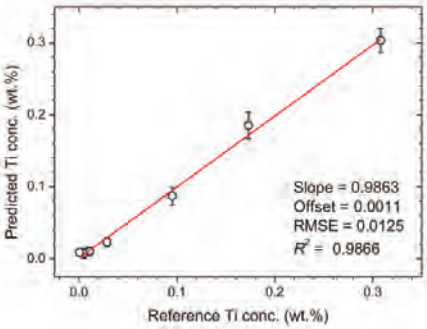

- Shows the **X-loading of PLS factor 1** extracted from first-derivative spectra (329.39–338.22 nm)
- Integrated loading exhibits strong peaks at **Ti II emission line positions** (red bars)
- Confirms that derivative-based PLS factor effectively captures Ti spectral features

- Compares predicted Ti concentrations from the derivative-based PLS-R model (2 factors) with certified reference values
- Results show excellent agreement: **RMSE = 0.0125 wt.%, R^2 = 0.9866**
- Demonstrates that accurate Ti prediction can be achieved with only two latent variables
- Highlights the stability and reliability of the derivative preprocessing approach

Conclusions

- **Mn and Cr modeling**
  - Emission lines above 400 nm → lower Fe line density
  - Reliable baselines could be located and subtracted effectively
- **Ni and Ti modeling**
  - Relevant emission features located at shorter wavelengths (≈350 nm for Ni, ≈335 nm for Ti)
  - Dense Fe lines prevented reliable baseline subtraction
  - First derivatives of spectra were more effective than raw intensities
- **Advantage of derivative preprocessing**
  - Filters out baseline variation and systematic errors
  - Allows accurate modeling with fewer latent variables
- **Overall implication**
  - Reliable calibration models for Mn, Cr, Ni, and Ti can be obtained even with low-resolution LIBS spectra
  - Appropriate preprocessing (e.g., differentiation) significantly improves performance
  - Supports the feasibility of **compact, low-cost LIBS devices** for analyzing complex steel matrices

Part 2.
Feasibility of a Low-Power, Low-Resolution Laser-Induced Breakdown spectroscopy Instrument for Analysis of Nickel Alloys: Quantification of the Major Alloying Elements and Classification

Applied Spectroscopy 77 (2023) 371-381

Individual vs. Global modeling

Individual modeling

Soft independent modeling of class analogy (SIMCA)
k nearest neighbors (k-NN)

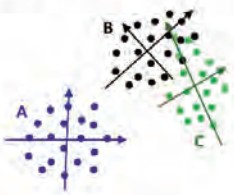

- ✓ Collection of individual models
- ✓ Insensitive to inter-class structure
- ✓ Classification accuracy would be constant as the number of classes increases

Global modeling

Linear discriminant analysis (LDA)
Partial least squares-discriminant analysis (PLS-DA)

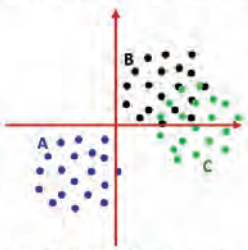

- ✓ One global model fits the whole data
- ✓ Sensitive to inter-class structure
- ✓ Classification accuracy becomes lower as more classes are considered
- ✓ Strongest with binary problem → multi-step classification strategy

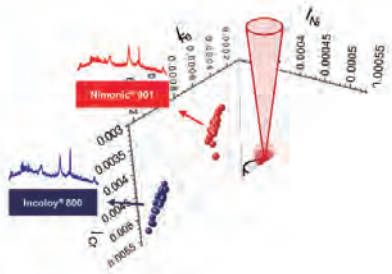

Nickel alloys – properties and usages

- From consumer products to high-technology precision parts
- Ni + Cr + Fe + other elements
- Useful properties: corrosion resistance, high-temperature strength, shape memory, low expansion coefficient, etc.
- Materials for parts used in thermal and nuclear power plants and aerospace crafts

Nickel alloys – recycling

- Nickel, tiny element: ultramafic rocks, nickel-iron meteorites, etc.
- Securing the rare resources.
- Reducing greenhouse gas emitted from mining and refining
- Sorting is essential for getting the recycling process effective.

Classification of nickel alloys

Major alloying elements in nickel alloys

Sample code	Description	Concentration (wt.%)		
		Ni	Cr	Fe
N1	Nimonic® 901	41.2	11.35	38.40
N2	Inconel® 600	76.0	14.86	7.33
N3	Inconel® 625	61.4	21.71	3.07
N4	Inconel® 625	59.5	21.90	4.50
N5	Incoloy® 800	30.8	20.10	46.20
N6	Ni-Fe-Cr Alloy UNS N08825	43.5	23.40	26.50

Classification of nickel alloys

LIBS spectra of nickel alloys

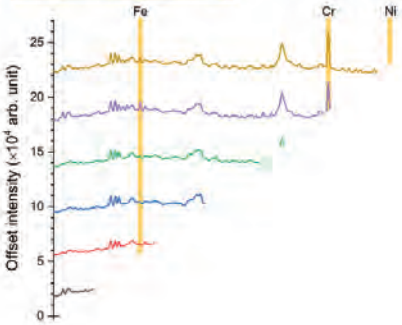

Spectroscopic parameters of the selected peaks

Species	λ_{obs} (nm)	λ_{ref} (nm)	A_{ul} ($\times 10^7$ s^{-1})	E_l (eV)	E_u (eV)	g_l	g_u
Fe I	438.1	438.354	5.00	1.48	4.31	9	11
Cr I	520.4	520.450	5.09	0.94	3.32	5	3
Cr I	520.4	520.602	5.14	0.94	3.32	5	5
Cr I	520.4	520.841	5.06	0.94	3.32	5	7
Ni I	547.7	547.691	0.95	1.83	4.09	1	3

Precision improvement by intensity normalization using total intensity as a reference signal

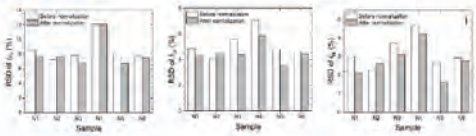

Classification of nickel alloys

k nearest neighbors (Individual modeling)

Intensity-concentration correlation

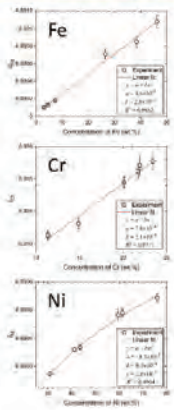

k-NN model with three variables

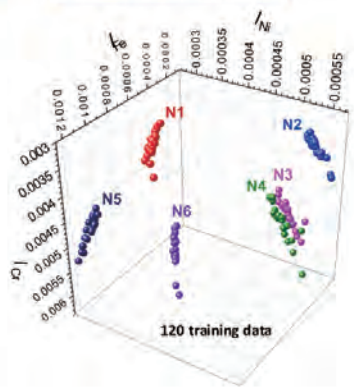

Classification correctness

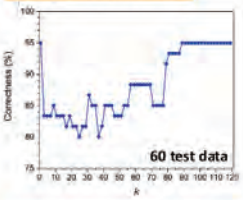

Confusion matrix for 60 test data

Truth \ Response	N1	N2	N3	N4	N5	N6
N1	10	0	0	0	0	0
N2	0	10	0	0	0	0
N3	0	0	8	2	0	0
N4	0	0	1	9	0	0
N5	0	0	0	0	10	0
N6	0	0	0	0	0	10

Linear discriminant analysis (global modeling)

Single-step modeling

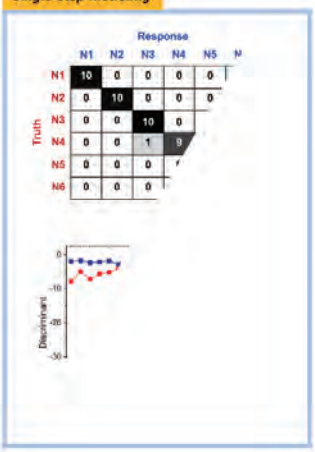

Two-step modeling

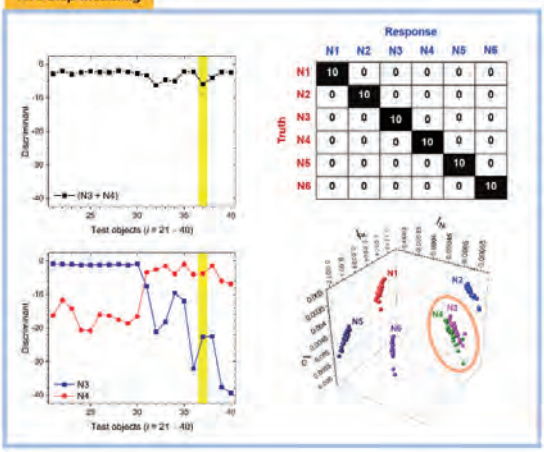

Conclusions

- **Cost-effective application** of a simple, low-performance LIBS instrument was demonstrated for **quantitative analysis** and **classification** of nickel alloy samples.
- **Classification modeling** was performed using Fe, Cr, and Ni emission peaks:
  - **KNN model**: Accuracy reduced due to two similar samples (N3, N4).
  - **Ordinary LDA**: Slightly higher accuracy, explained by its ability to emphasize inter-class differences.
- **Two-step LDA approach** further improved classification:
  - Step 1: Separate classes with large differences.
  - Step 2: Model minute inter-class differences.
  - → This **two-step LDA showed the best classification performance**.
- **Key implication**: Even a **low-performance LIBS system** can be effective for **major element analysis** or **sorting materials by composition**, provided that an **appropriate modeling algorithm** is carefully selected and customized.

Acknowledgement

Many thanks to

Mr. Hanbum Choi, Ms. Hyang Kim and Prof. Sang-Ho Nam at Mokpo National University

Ms. Sunhye Kim and Dr. Sehoon Jung at Research Institute of Industrial Science and Technology

Thank you for your attention.

Mathematics in the Age of Intelligent Machines: From Ancient Logic to Industrial Innovation

Hyun-Min Kim

Pusan National University

Mathematics has long been regarded as the language of nature and the foundation of scientific progress. In the Fourth Industrial Revolution—marked by the fusion of AI, robotics, biotechnology, and quantum technologies—mathematics is more vital than ever. This talk explores how modern mathematics transcends traditional boundaries, driving innovation in industry through complex modeling, data-driven decision-making, and algorithmic design. We will trace the journey from classical matrix equations to nonlinear solvers used in real-world applications, including biological systems, smart manufacturing, and financial engineering. Examples from Korea’s national initiatives and collaboration with industries illustrate how industrial mathematics transforms theoretical insight into practical value. Beyond equations and models, we will reflect on the evolving role of the mathematician: not just as a problem solver, but as a builder of systems, an architect of intelligence, and a bridge between abstract reasoning and industrial needs. As we embrace the AI era, mathematics stands not behind, but ahead—leading the way into the future.

Mathematics: Your Key to Thriving in the 4th Industrial Revolution

Forum "Math-for-Industry" 2025
- Challenge of Mathematics for Industry in the AI era -

Professor, Department of Mathematics
Director, Industrial Mathematics Center
Pusan National University
Kim, Hyun-Min

PNU IMC
Industial Mathematics Center

Contents

Let' s enjoy Festival in Busan Korea, first.

3/69

Let' s enjoy Festival in Busan Korea, first.

4/69

Contents

My Researches

James J. Sylvester (1814 -1897)

History

We must commence, not with a square, but with an oblong arrangement of terms consisting, suppose, of m lines and n columns. This will not in itself represent a determinant, but is, as it were, a Matrix out of which we may form various systems of determinants by fixing upon a number p, and selecting at will p lines and p columns, the squares corresponding to which may be termed determinants of the pth order.

"On a new class of theorems," and "On Pascal's theorem."
Philosophical Magazine pp. 363 ~ 370, 1850.

History of Nonlinear Matrix Equation

On Hamilton's quadratic equation and general unilateral equation in matrices.

Philosophical Magazine pp. 454 ~ 458, 1884.

Nonlinear Matrix Equation

$$F(X) = 0$$

- $F: C_{m \times n} \rightarrow C_{p \times q}$ is a matrix function.
- X is an $m \times n$ matrix.
- 0 is a $p \times q$ zero matrix.
- When $F(S) = 0$, S is called a solvent.

Simplest of Nonlinear Matrix Equation

$$X^2 - A = 0,$$

where A is a complex $n \times n$ matrix.

Question: What is $A^{1/2}$?

$(A^{1/2})^2 = A$ and $\mathrm{Re}\,\lambda(A^{1/2}) > 0$,

no nonpositive real eigenvalues

The Number of Solvents

Question: What is $A_{1/2}$?

$$X^2 - \begin{bmatrix} 0 & 1 \\ 0 & 0 \end{bmatrix} = \begin{bmatrix} 0 & 0 \\ 0 & 0 \end{bmatrix}$$

$$X_2 - I = 0$$

Quadratic Matrix Equation

$$Q(X) = AX_2 + BX + C = 0$$

- A, B, C are complex $n \times n$ matrices.
- When $Q(S) = 0$ the matrix S is called a (right) solvent.

n Degree of Freedom Damped Mass-Spring System

13/69

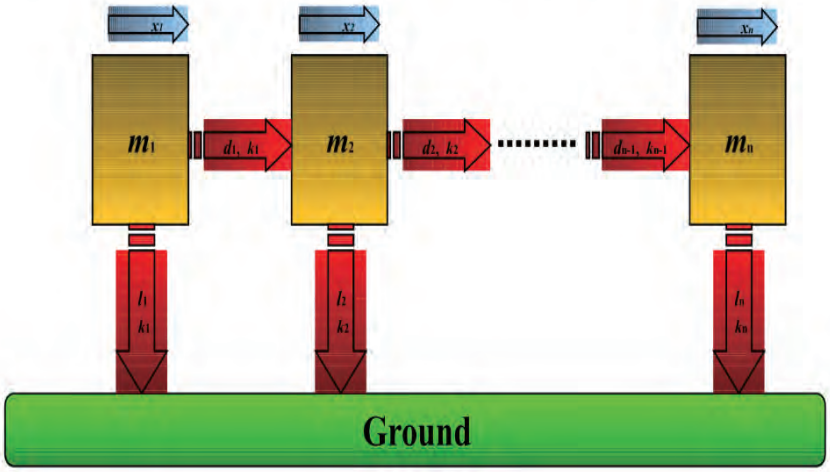

Quasi-Birth-Death Process from Population of Bilby

14/69

$$R = c\,(A + RB + R_2 C)$$

where $A = Q\,(g,b), B = Q\,(g,\ e\text{-}b\text{-}d),$
$C = Q\,(g,d)$

Copyright: Australian Bilby Appreciation Society

Bilby: Australian marsupial

Matrix Polynomial and others

Matrix Polynomial Equation (MPE) of degree n

$$P(X) := A_n X^n + A_{n-1} X^{n-1} + \cdots + A_0 = 0$$

$$A_n, A_{n-1}, \ldots, A_0, X \in \mathbb{C}^{m \times m}$$

$$X_p - AXA_T = 0$$

$$X_p - X - A = 0$$

$$X_p - (A + X_{-1})_{-1} = 0$$

Matrix Functions

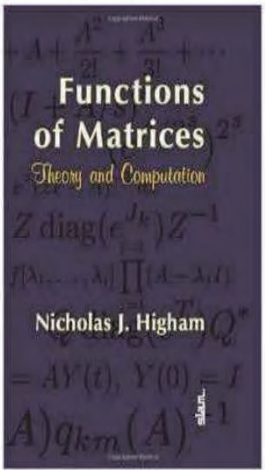

Matrix is a Still Interesting Topic

nature

nature > letters > article

Learning the parts of objects by non-negative matrix factorization

Daniel D. Lee & H. Sebastian Seung

Nature 401, 788–791 (1999)

63k Accesses | 8235 Citations | 55 Altmetric | Metrics

Abstract

Is perception of the whole based on perception of its parts? There is psychological[1] and physiological[2,3] evidence for parts-based representations in the brain, and certain computational theories of object recognition rely on such representations[4,5]. But little is known about how brains or computers might learn the parts of objects. Here we demonstrate an algorithm for non-negative matrix factorization that is able to learn parts of faces and semantic features of text. This is in contrast to other methods, such as principal components analysis and vector quantization, that learn holistic, not parts-based, representations. Non-negative matrix factorization is distinguished from the other methods by its use of non-negativity constraints. These constraints lead to a parts-based representation because they allow only additive, not subtractive, combinations. When non-negative matrix factorization is implemented as a neural network, parts-based representations emerge by virtue of two properties: the firing rates of neurons are never negative and synaptic strengths do not change sign.

Relevant articles

Open Access articles citing this article.

Bayesian stroke modeling details sex biases in the white matter substrates of aphasia

nature

nature > articles > article

Discovering faster matrix multiplication algorithms with reinforcement learning

Alhussein Fawzi, Matej Balog, Aja Huang, Thomas Hubert, Bernardino Romera-Paredes, Mohammadamin Barekatain, Alexander Novikov, Francisco J. R. Ruiz, Julian Schrittwieser, Grzegorz Swirszcz, David Silver, Demis Hassabis & Pushmeet Kohli

Nature 610, 47–53 (2022)

495k Accesses | 22 Citations | 3579 Altmetric | Metrics

Abstract

Improving the efficiency of algorithms for fundamental computations can have a widespread impact, as it can affect the overall speed of a large amount of computations. Matrix multiplication is one such primitive task, occurring in many systems—from neural networks to scientific computing routines. The automatic discovery of algorithms using machine learning offers the prospect of reaching beyond human intuition and outperforming the current best human-designed algorithms. However, automating the algorithm discovery procedure is intricate, as the space of possible algorithms is enormous. Here we report a deep reinforcement learning approach based on AlphaZero[1] for discovering efficient and provably correct algorithms for the multiplication of arbitrary matrices. Our agent, AlphaTensor, is trained to play a single-player game where the objective is finding tensor decompositions within a finite factor space. AlphaTensor discovered algorithms that outperform the state-of-the-art complexity for many matrix sizes. Particularly relevant is the case of 4×4 matrices in a finite field, where AlphaTensor's algorithm improves on Strassen's two-level algorithm for the first time, to our knowledge, since its discovery 50 years ago[2]. We further showcase the flexibility of AlphaTensor through different use-cases: algorithms with state-of-the-art complexity for structured matrix multiplication and improved practical efficiency by optimizing matrix multiplication for runtime on specific hardware. Our results highlight

Deep Learning

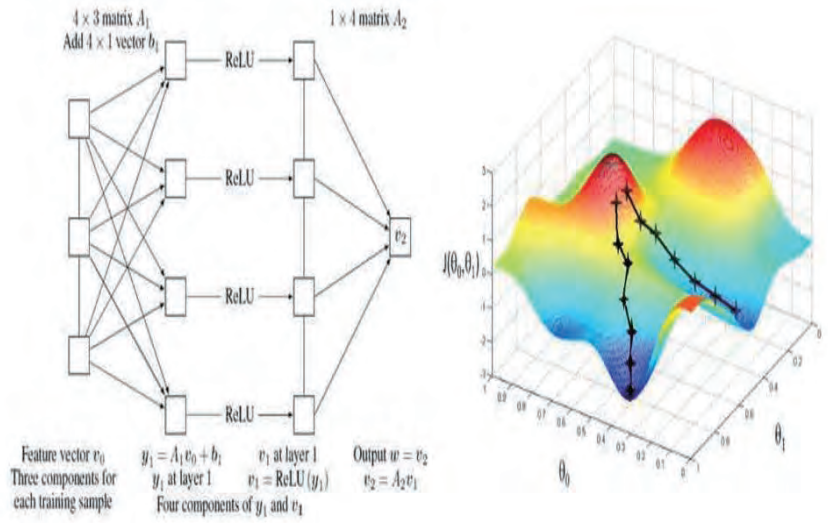

What about Tensor?

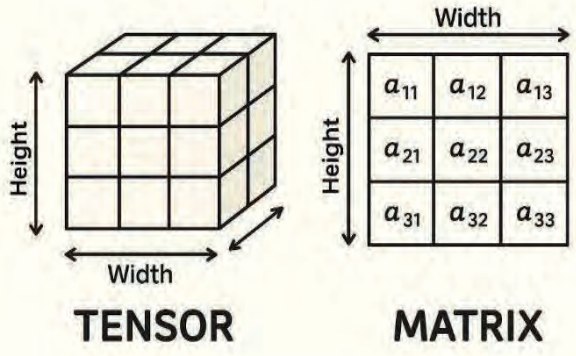

Ⅱ. What is Mathematics?

What is Mathematics?

수학, 數學

= Number Theory or Calculation

What is the definition of math?

Oxford Languages
the abstract science of number, quantity, and space, either as abstract concepts (*pure mathematics*), or as applied to other disciplines such as physics and engineering (*applied mathematics*).

Google (the best definition)
The study of the measurement, relationships, and properties of quantities and sets, using numbers and symbols.

Einstein(1879 – 1955), Theory of Relativity

23/69

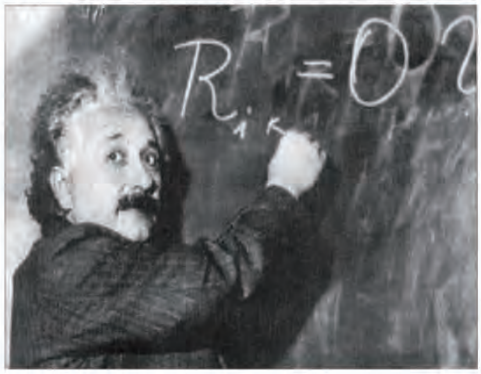

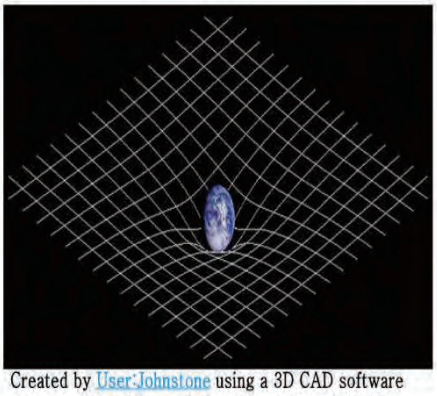

Created by User:Johnstone using a 3D CAD software package and an image of planet earth from NASA's Galileo spacecraft.

The Language of Science

Johann Carl Friedrich Gauss(1777-1855)

24/69

Mathematics is the queen of the sciences.

What is Mathematics?

chatgpt: What is mathematics?

Mathematics is a broad and abstract field of study that deals with the logic, structure, quantity, and relationships of numbers and shapes. It involves using symbols and equations to solve problems, develop theories, and make predictions about the world around us. Mathematics is used in many fields such as science, engineering, economics, and even in everyday life. Some of the key branches of mathematics include algebra, geometry, calculus, statistics, and number theory, among others.

Introduce to Mathematics?

chatgpt: Introduce to mathematics?

Mathematics is a field of study that deals with the logic, structure, quantity, and relationships of numbers and shapes. It is a fundamental and abstract subject that has been studied for thousands of years, with roots in ancient civilizations such as Greece, Egypt, and Babylon.

Mathematics is used to solve problems and answer questions in a wide range of fields, including science, engineering, economics, and even in everyday life. It involves using symbols and equations to represent and manipulate mathematical concepts, and applying logical reasoning to draw conclusions and make predictions.

Some of the key branches of mathematics include algebra, geometry, calculus, statistics, and number theory, among others. Algebra deals with mathematical operations and equations, geometry with the properties of shapes and spaces, calculus with rates of change and integrals, statistics with data analysis and probability, and number theory with the properties and relationships of numbers.

Studying mathematics can provide a strong foundation for a wide range of careers, including those in science, technology, engineering, and mathematics (STEM) fields.

It can also help develop critical thinking skills and problem-solving abilities, as well as provide a deeper understanding of the world *around us*.

What is Mathematics?

chatgpt: Introduce to mathematics?

It can also help develop critical thinking skills and problem-solving abilities, as well as provide a deeper understanding of the world *around us.*

What is Mathematics?

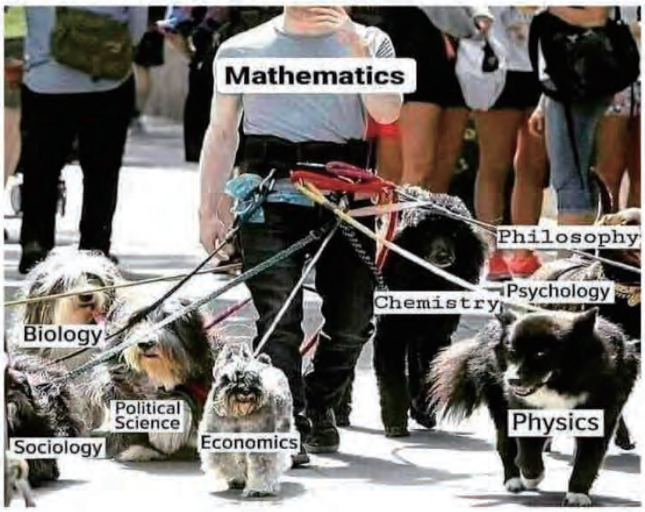

One Newspaper Article

29/69

Countries with strong mathematics dominate the world economy

매일경제

2014년 08월 04일 월요일 A01면 종합

3D프린터·웨어러블·파생금융상품… 新산업 핵심은 수학

數學 강한 나라가 경제 지배한다

수학이 세상을 바꾼다

애플 스마트폰 '아이폰'이 출시된 이후 세계 휴대전화 시장은 요동쳤다. 애플을 빠르게 추격한 삼성은 세계 스마트폰 시장 1위로 올라섰지만 최대 휴대전화 제조업체였던 노키아는 무너졌다. ▶관련기사 A4·5면

언제 어디서나 인터넷이 연결되고 많은 정보를 빠르게 전달할 수 있는 스마트폰 내부에는 영상이나 음성을 디지털 신호인 '0'과 '1'로 바꿔 압축하고 저장하는 수학 기술이 숨어 있다.

초고속 인터넷 세상을 열었던 4세대 이동통신 'LTE' 보급은 수학이 없었다면 불가능했다. 정보를 의뢰인에게 바꿔 서로 다른 정보가 겹치지 않게 하는 '푸리에 변환' 덕분이었다. 노키아는 시장 변화에 적응하는 데 실패한 반면 수학을 적용한 스마트폰 기술을 활용하지 못해 몰락했다. 스마트폰 위에 현대 산업의 근간을 뒤흔든 3D 프린터, 웨어러블 기기 등 응용분야에는 수학이 깔려 있다. 공간에 존재하는 삼차원 형상 등체를 스캐닝해 이차원 도면으로 표시한 뒤 이를 다시 재현하는 3D 프린터 핵심 원리에는 '적분의 원리'라는 미적분학이 숨어 있다.

'웨어러블 기기' 에도 수학은 빠지지 않는다. 사용자 심박수나 체온 등 생체신호를 파악할 수 있는 웨어러블 기기는 정보를 전달할 때 '푸리에 변환'과 '신호대수' 등 수학을 활용한다. 로봇의 핵심인 스스로 판단하고 움직이는 '인공지능'에는 '확률' 이 응용된다.

수학은 그 나라 경쟁력을 보여주는 지표다. 국제수학연맹(IMU)이 수학 수준별로 국가를 나눈 그림을 보면 가장 높은 단계인 5등급에는 미국 일본 영국 독일 등 G7 국가는 물론 러시아 중국 이스라엘 등 강국이 포함됐다. 한국은 인도 브라질 등과 함께 4등급이다. 3등급은 노르웨이와 핀란드, 2등급은 폴란드와 슬로바키아, 1등급은 베트남, 하니지 등이 차지하고 있다.

이처럼 수학의 중요성이 점점 커지고 있는 가운데 이달 13일부터 한국에서 수학계 올림픽이라 불리는 '2014년 세계수학자대회' 가 열린다. 우리나라는 이번 대회를 계기로 수학 강국으로 발돋움하려는 야심 찬 계획을 세우고 있다. 함호섭·김미경 기자

국가별 수학 능력 수준

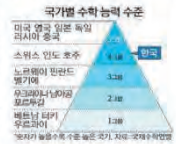

My explanation, not definition of Math.

30/69

the foundation of all studies, the oldest study in human history with philosophy,
played a key role in the development of human industries,
today, its importance is more emphasized in the Fourth Industrial Revolution

III. 4th Industrial Revolution

Industrial Revolutions

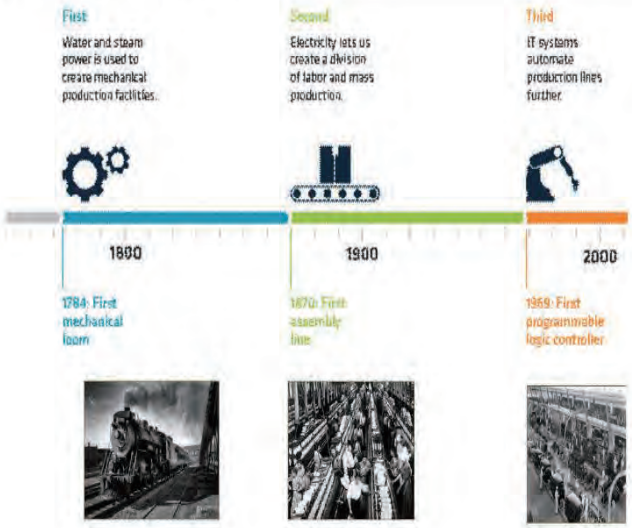

4th Industrial Revolution

What is 4th Industrial Revolution ?

From Wikipedia

The **Fourth Industrial Revolution**, 4IR, or **Industry 4.0**, conceptualizes rapid change to technology, industries, and societal patterns and processes in the 21st century due to increasing interconnectivity and smart automation. The term has been used widely in scientific literature, and in 2015 was popularized by Klaus Schwab, the World Economic Forum Founder and Executive Chairman. Schwab asserts that the changes seen are more than just improvements to efficiency, but express a significant shift in industrial capitalism.

A part of this phase of industrial change is the joining of technologies like artificial intelligence, gene editing, to advanced robotics that blur the lines between the physical, digital, and biological worlds.

Math in 4th Industrial Revolution

35/69

ICT Convergence Technologies






Big Data	FinTech	IoT	3D Printing	A.I.	Autonomous Car
• Topology • Probability • Graph Theory	• Probability • Statistics • P.D.E.	• Cryptography • Number Theory • Coding Theory	• Analysis • Algebra	• Geometry • Graph Theory • Optimization • Probability	• A.I. • Differential Equation • Geometry • Probability

Math in 4th Industrial Revolution

36/69

Key Technologies for Future

Jobs with Math (from SIAM)

Actuary, Analyst, Analytics Consultant, Analytics Manager, Applied Mathematics Researcher, Associate Editor, Biostatistician, Business Analyst, Business Intelligence Developer, Claims Specialist, Consultant, Cryptanalyst, Cryptographer, Data Analyst, Data Engineer, Data Operations Associate, Data Processing Specialist, Data Scientist, Director of Math Tutorial Curriculum, Engineer, Forecast Analyst, Functional Analyst, Game designer/slot game designer/game mathematician, Geolocation Engineer, Global Pricing Analyst, Guidance and Navigation Engineer, Informatics Scientist, Information Analyst, Investment Analytics Quant, Manager, Math Curriculum Coach, Math Curriculum Consultant, Mathematician, Modeler, Modeling Engineer, Operations Researcher, Operations Support Specialist, Pharmacokineticist, PK/PD Modeler, Planner, Principal Scientist, Product Manager, Program Manager, Programmer, Project Manager, Quality Systems and Compliance Manager, Quantitative Analyst, Quantitative Developer, Quantitative Pharmacologist, Quantitative Researcher, Quantitative Scientist, Quantitative Software Engineer, Reporting Engineer, Research and Development Engineer, Research Analyst, Researcher, Research Scientist, Risk Analyst, Risk Strategist, Scientist, Simulation Engineer, Software Engineer, Staff Scientist, Statistician, Strategist, Supply Chain Analyst, Systems Engineer, Technical Staff, Tutor

Capability for Mathematician

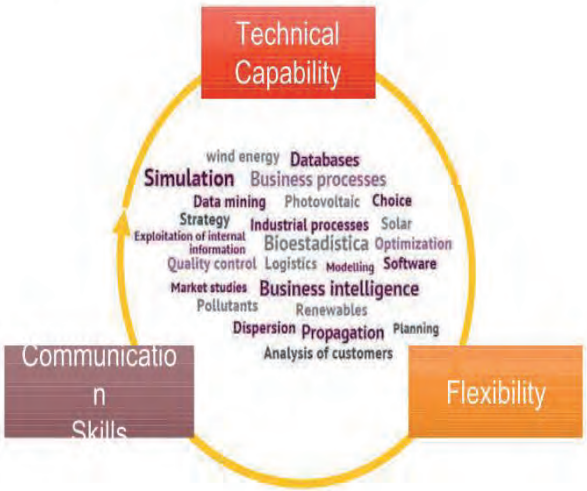

IV. Industrial Mathematics

What is Industrial Mathematics ?

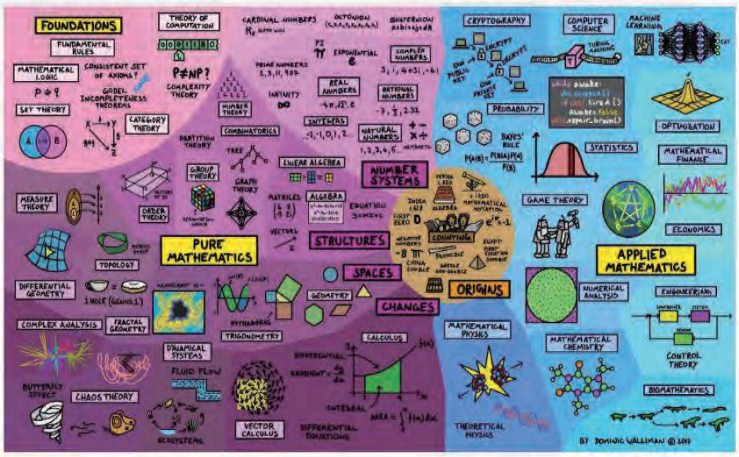

Map of Mathematics

https://www.flickr.com/photos/95869671@N08/32786397946/in/photostream/

What is Industrial Mathematics ?

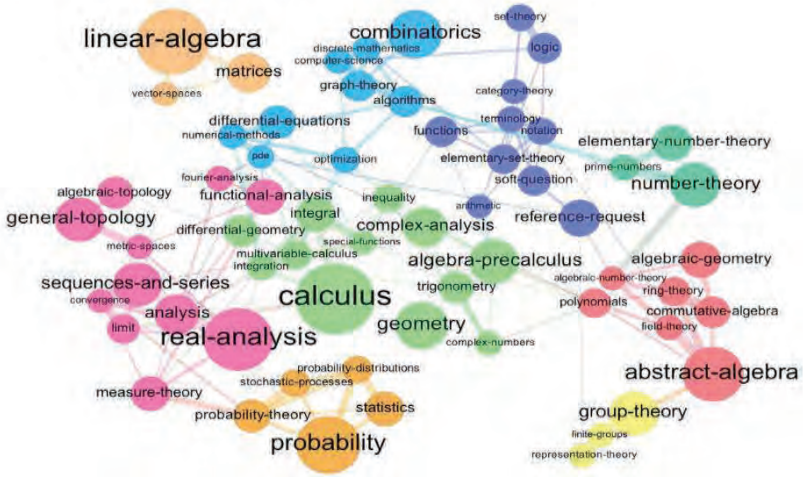

Industrial Mathematics

Activities to "solve world problems or create added value of industry" using mathematical theories and analysis methods. (NIMS)

" Almost by definition, industrial research is interdisciplinary" (J. R. Ockendon)

If mathematics used anywhere, that math is called the industrial mathematics.

What is Industrial Mathematics?

Check with chatgpt:

Capability for Industrial Mathematician

"Real life mathematics requires **Barbarians**:
people willing to fight, to conquer, to build, to understand,
with no predetermined idea about which tool should be used"

B. Beauzamy

Industrial Mathematics Textbook in High School

I. Understanding of Industrial Math

II. Matching Theory

III. Infectious Diseases

IV. Fishery Resources

V. Recommend Financial Products

VI. Medical Data and Health Status

History of Industrial Mathematics

Prehistoric Ages	Ancient	Middle Ages	Modern	Today
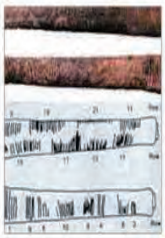				
the origin of the counting of hunting numbers	Land Measure Building Design	Newtonian Mechanics Calculus	Computer, Music and Art	Big Data, AI, IT, BT

Industrial Mathematician

Archimedes (287 BC – 212 BC); High-tech weapon developer

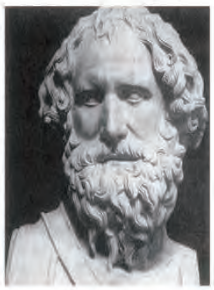

Industrial Mathematician

Alan Turing (1912 – 1954); Father of AI

Turing gave quite , 1947) to mention compute achine that can learn from experience, and that the possibility of letting the machine alter its own instructions provides the mechanism for this."

Alan Turing Building in University of Manchester

Mathematician, Billionaire

James Simons

(1938. 4. 25 – 2024. 5. 10)

- The founder of Renaissance Technologies, a leading quant fund in the United States
- Nearly 66% return over 30 years (20% return on Warren Buffett's career)
- About $100 billion in assets is in operation

Examples of Industrial Mathematics

Estimation of air pollutant emissions

SFU

SIMON FRASER UNIVERSITY
THINKING OF THE WORLD

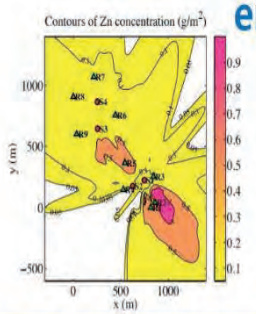

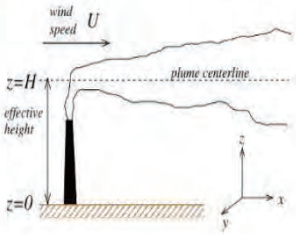

Teck Global Metals, Mining & Steel Conference
May 16, 2017

$$C(x,y,z)=\frac{Q}{2\pi U\sigma_y\sigma_z}\exp\left(-\frac{y^2}{2\sigma_y^2}\right)\left[\exp\left(-\frac{(z-H)^2}{2\sigma_z^2}\right)+\exp\left(-\frac{(z+H)^2}{2\sigma_z^2}\right)\right]$$

Examples of Industrial Mathematics

Bridge Crack

Institute of Mathematics for Industry
Kyushu University

$$J=\int_\Gamma\left[\left(W-\sigma_x\frac{\partial u}{\partial x}-\tau_{xy}\frac{\partial v}{\partial x}\right)dy+\left(\tau_{yx}\frac{\partial u}{\partial x}+\sigma_y\frac{\partial v}{\partial x}\right)dx\right]$$

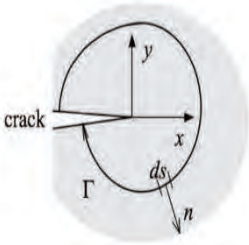

$dy=n_x ds$ ress
$dx=-n_y ds$ by :

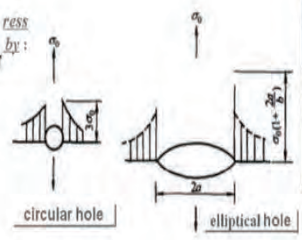

Examples of Industrial Mathematics

Public Identification Data Encryption

Institute of Mathematics for Industry
Kyushu University

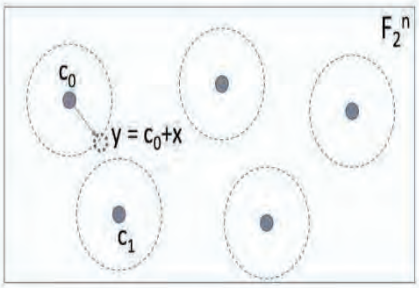

SVP-problem: Given a lattice basis, find a shortest vector.

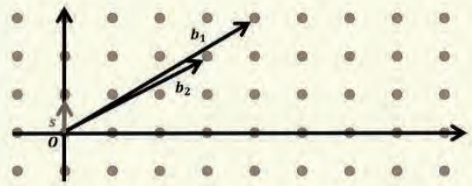

NP-hard → approximate instance of SVP are often sufficient

In Korea

- After ICM 2012 in Seoul
- From 2017 government supports mathematical society about 4-9 million dollars / each year in industrial mathematics.
- Two industrial math centers established: SNU and PNU / 4.5 million dollars during 5 years.
- At that time NIMS also changed its vision to industrial mathematics.

Examples of Industrial Mathematics

Korea Housing Finance Corporation MBS Call Option Price Determination

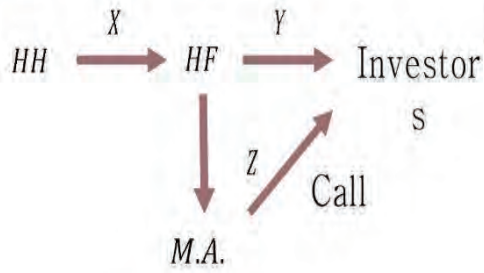

- $X = Y + Z$
- $f(x)$: CALL AMOUNT

Examples of Industrial Mathematics

HF 한국주택금융공사 KOREA HOUSING FINANCE CORPORATION › MBS call option valuation

✓ Calculation of call option value in 1 unit– Step1

- Applied American callable bond calculation methodology

✓ Calculation of Call Options for 1 Trench– Step2

- Using the early repayment model and the interest rate model, simulate the number of call options that can be exercised at that time Monte Carlo

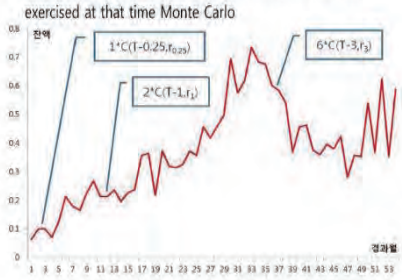

Examples of Industrial Mathematics

Prediction of fishery resources

F²m IMC
빅데이터 기반 금융 · 수산 · 제조 혁신 산업수학센터

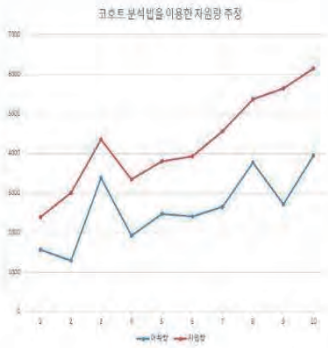

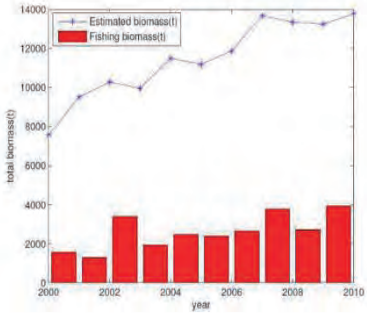

Examples of Industrial Mathematics

Development of mathematical models and parameters
for simultaneous scattering group species (Cod, Salmon, Dorumuk, etc.)

✓ Age structure math model

Hence, we obtain a stage-structured biomass system.

$$\begin{cases} \dfrac{dB_i(t)}{dt} = (g_i(t) - M_i - F_i(t))B_i(t) - D_M(B_i(t))^2 & t \neq n, \\ B_0(t) = \displaystyle\sum_{k=0}^{t_{max}-1} f_k \frac{W_0(0)}{W_k(1^-)} B_k(t^-) \\ B_{j+1}(t) = B_j(t^-) \end{cases} \quad t = n,$$

where $g_i(t) = 3K(e^{K(t_{i+1}-[t]-t_0)} - 1)^{-1}, i = 0, 1, \cdots, t_{max} - 1, j = 0, 1, \cdots, t_{max} - 2$ and $n \geq 1 (n \in \mathbb{Z})$.

✓ Estimation of resource mortality by age corresponding to the initial resource amount of Dorumuk

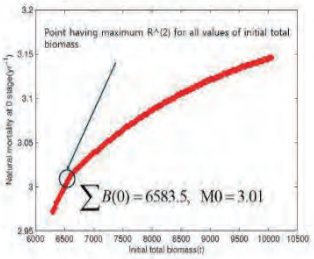

Examples of Industrial Mathematics

Simulation of optimal fishing strategy through mathematical model

✓ Optimal fishing problem maximizing fishing profit for the next five years with Dorumuk

✓ Optimal fishing strategy and expected effect

Objective functional

$$\max J(u) = \sum_{n=0}^{N} \int_{t_n}^{(n+1)^-} [C_1 \sum_{i=0}^{5} \alpha_i u_n(t) B_{i,n}(t) - C_2 u_n(t)^2] dt + \sum_{i=0}^{5} B_{i,N}((N+1)^-)$$

subject to

$$\begin{cases} \dfrac{dB_i(t)}{dt} = (g_i(t) - M_i - \alpha_i u(t)) B_i(t) - D_M(B_i(t))^2 & \text{if } t \neq n, \\ B_0(t^+) = \sum_{i=0}^{5} f_i \dfrac{W(0)}{W((i+1)^-)} B_i(t^-) \\ B_{i+1}(t^+) = B_i(t^-) \end{cases} \quad \text{if } t = n,$$

where $g_i(t) = 3K(e^{K(t-(i-1))} - e^{K(t-i)} - 1)^{-1}$ for $i = 0, 1, \cdots, 5$ and $n \geq 1 (n \in \mathbb{N})$. The control variable $u(t)$ represents fishing effort at time t.

$$m_1 \leq u_n(t) \leq m_2, \text{ and } t \in [n, n+1], \text{ for } n = 0, \cdots, N$$

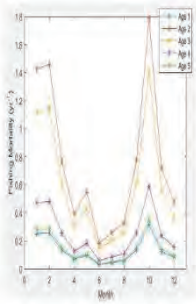

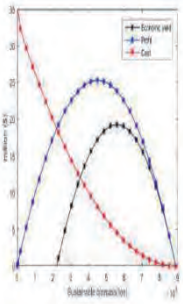

Examples of Industrial Mathematics

PNU Hospital (Ophthalmology)

Developed a program to calculate the
of two ellipses by rotation and transl

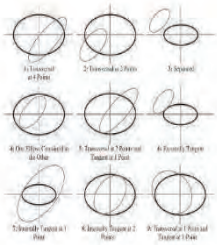

Ophthalmic artificial intelligence automatic e

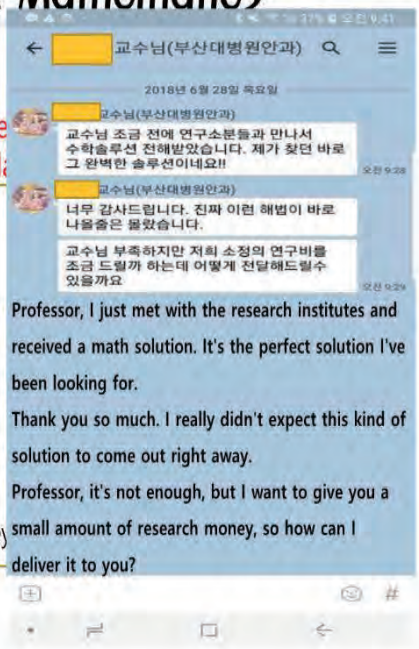

Examples of Industrial Mathematics

Development of optimal production algorithms

Examples of Industrial Mathematics

Let

(1) $\mathbf{b} = (b_i \mid i \in \mathcal{I}) \in \mathbb{N}^{|\mathcal{I}|}$ and $k \in \mathbb{N}$, $\alpha, \beta \in \mathbb{R}_{>0} (\alpha \gg \beta)$ be given where $\mathcal{I}$ is a finite index set,

(2) π be an element of the set of all partitions of $\mathcal{I}$, where $1 \le |P| \le k$ for all $P \in \pi$,

(3) $\mathbf{c} = (c_i \mid i \in \mathcal{I}) \in \mathbb{N}^{|\mathcal{I}|}$ such that $\sum_{i \in P} c_i = k$.

We define

$$cost_{\mathbf{b}}(\pi, \mathbf{c}) = \alpha |\pi| + \beta \sum_{P \in \pi} E_{\mathbf{b}}(P, \mathbf{c}),$$

where

$$E_{\mathbf{b}}(P, \mathbf{c}) = \sum_{j \in P} \left(\left\lceil max \left\{ \frac{b_i}{c_i} \mid i \in P \right\} \right\rceil \cdot c_j - b_j \right).$$

Find $\min_{\pi, \mathbf{c}} (cost_{\mathbf{b}}(\pi, \mathbf{c}))$ satisfying (2) and (3).

Examples of Industrial Mathematics

KOMAX SPECIAL PRINTING COMPANY

Label Printing

Up to about 18% Loss reduction

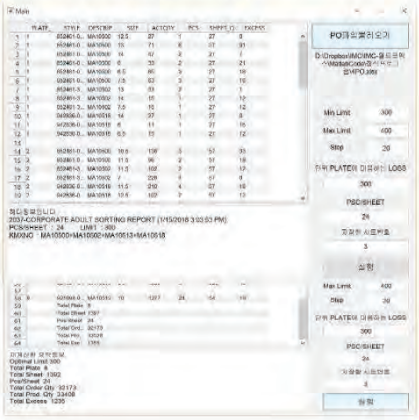

Comparison of overages according to actual data implementation results

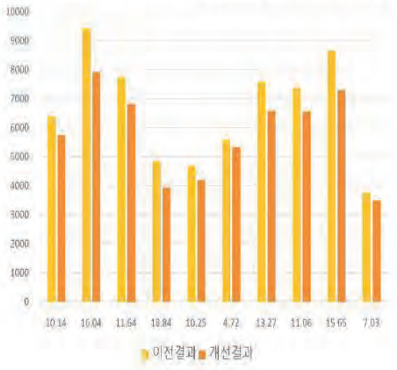

Examples of Industrial Mathematics

Busan Bank › Credit card delinquency prediction algorithm development

F²m IMC

✓ Confusion Matrix by Model

		Logistic Regression	Neural Network	Random Forest	Gradient Boost
Actual Positive	True Positive	343.9	287.7	299.8	296.6
	False Negative	148.3	204.5	192.4	195.6
Actual Negative	True Negative	1723.1	1326.6	1873.3	1962.7
	False Positive	336.2	732.7	186.0	96.6
Recall		0.6987	0.5845	0.6091	0.6026
Precision		0.5057	0.2819	0.6171	0.7543
Accuracy		0.8101	0.6327	0.8517	0.8855
F-score		0.5867	0.3804	0.6131	0.6700

✓ Cumulative improvement and ROC curve

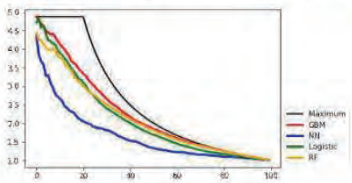

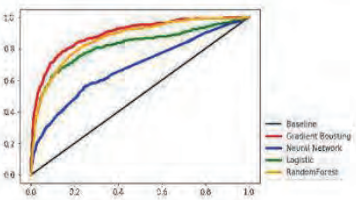

Conclusion

Future of Mathematics

Top 10 college majors with the highest starting salary in the U.S. by USNEWS in 2022

Computer Science: $80,300, Computer Science: $77,300

Software Engineering: $75,900, Electrical engineering: $75,700

Aerospace Engineering: $75,300, Chemical engineering: $75,200

Biomedical Engineering: $71,400,

Materials Science and Engineering: $71,300

Industrial engineering: $71,200

Applied Math: $71,000

Future of Mathematics

Best Estimate for US News/Payscale-style 2024 Top 10

Petroleum Engineering

Operations Research & Industrial Engineering

Electrical Engineering & Computer Science (combined)

Interaction Design, Building Science, Chemical Engineering,

Computer Engineering, Aerospace Engineering

Mechanical Engineering

Mathematics / Applied Math / Economics

Math is everything

If there is only one department left in the university, it is mathematics. Because you can make everything new with math

한국경제

"대학에 학과 하나만 남긴다면 수학, 거기서 모든 걸 새로 만들면 그만"

입력 2019-10-06 17:26 수정 2019-10-07 01:02

"만약 대학에 학과 하나만을 남겨야 한다면, 단연 수학과여야 한다. 수학과에서 모든 걸 새로 만들면 된다."

1989년 노벨물리학상 수상자 노먼 램지 미국 하버드대 교수가 로버트 조겐 미국 로체스터대 이사장에게 1995년 12월 보낸 편지의 내용이다. 로체스터대가 1995년 말 재정난을 이유로 수학과 학부 정원을 절반으로 줄이고 대학원을 없애려 할 때 세계 수학계가 발칵 뒤집혔다. 각국의 노벨과학상 수상자들은 앞다퉈 램지 교수와 함께 조겐 이사장에게 만류 편지를 보냈다. 편지 분량만 130쪽에 달한 것으로 알려졌다.

리하르트 에른스트 스위스 취리히연방공대 교수(1991년 노벨화학상)는 "수학에 대한 총체적 혼란이 없었다면 나는 노벨상 수상이 불가능했을 것"이라며 "복잡한 수학적 도구의 도움을 받지 않으면 물리, 화학의 발전은 불가능하다"고 강조했다. 그는 또 "수학이 약하거나 존재하지 않는 대학은 미래에 존재할 수 없다"며 "로체스터대가 스스로 그런 그러 3류 대학이 되지 않길 바란다"고 적었다.

현존하는 최고 물리학자로 꼽히는 스티븐 와인버그 미 텍사스대 교수(1979년 노벨물리학상) 역시 팔짝 뛰었다. 그는 "로체스터대의 명성을 더 이상 이어나가기 어려울 것 같다"며 "수학 교육이 부실해지면 이론 물리학은 물론 실험 물리학도 연쇄적으로 무너질 수밖에 없다"고 지적했다.

와인버그와 함께 노벨물리학상을 공동 수상한 셸던 글래쇼 하버드대 교수는 "적어도 대학이란 간판을 걸었다면, 수학은 여태껏 그래왔듯이 앞으로도 언제나 핵심적 위치에 있어야 한다"고 거들었다.

If you want to go fast then go alone

but if you want to go far then go together.

Let's go APCMfI and Korea Math Society together for our Math Future.

PNU IMC
Industial Mathematics Center

Asia Pacific Consortium of Mathematics for Industry

It's been an honor to share this final moment of FMfi 2025 with you.

Thank you for your time, your ideas, and your passion.

Wishing you a safe journey home.

Dirac Delta and Gaussian Distribution for Solving the Three-Dimensional Transient Groundwater Flow Equation

Nur Shafiqah Najwa Binti Mohd Fairuz

Department of Mathematical Sciences, Faculty of Science Universiti Teknologi Malaysia (UTM)

This paper presents an analytical solution to the three-dimensional transient groundwater flow equation in a homogeneous, isotropic, and infinite confined aquifer using Fourier transform. The governing equation is solved based on two initial conditions: a Dirac Delta distribution representing an instantaneous point source, and a Gaussian distribution representing a smooth, localized initial perturbation. The analytical solutions are validated against numerical solutions using Finite Difference Method (FDM) with comparisons made at time tt = 0.1, 1.0 and 10.0 seconds. Errors are quantified using the LL squared norm. The key findings include, firstly, the Dirac Delta distribution corresponds to the fundamental solution to the diffusion equation. Early times discrepancy arises due to the inherent difficulty of numerical schemes to represent at the singularity. Accuracy improves over time as diffusion smooths the solutions and aligns with the analytical solution. Secondly, the Gaussian distribution maintains its shape while spreading over time. Numerical simulations tend to overpredict peak values initially, but the error diminished as the solution evolves. This work presents an exact benchmark for groundwater flow problems, particularly for idealized conditions.

DIRAC DELTA AND GAUSSIAN DISTRIBUTION FOR SOLVING THE THREE-DIMENSIONAL TRANSIENT GROUNDWATER FLOW EQUATION

Nur Shafiqah Najwa Mohd Fairuz[1]; Arifah Bahar[2]; Zainal Abdul Aziz[3]
[1]UTM Centre for Industrial and Applied Mathematics (UTM-CIAM), [2]Department of Mathematical Sciences, Faculty of Science, Universiti Teknologi Malaysia (UTM)

Introduction

- **Problem:** Groundwater flow in aquifers require models for tractable solutions and as a stable benchmark before complexities such as periodic noise or stochasticity are introduced.
- **Objective:** Derive exact analytical solutions for 3D transient groundwater flow equation using Fourier transforms under two initial conditions.
  1. Dirac Delta: Represent an instantaneous point source such as sudden water injection
  2. Gaussian: Models smooth, localized perturbations such as brief infiltration event.

  The analytical solutions are then illustrated via Finite Difference Method (FDM). Errors are quantified with L^2 norm.

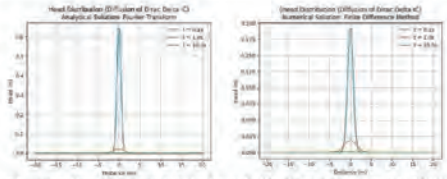

Figure 1. 1D profiles of the hydraulic head distribution of a Dirac Delta initial condition at $t = 0.1, 1.0, 10.0$ s. Left: analytical solution via Fourier transform. Right: numerical solution via FDM.

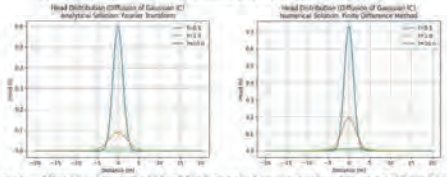

Figure 2. 1D profiles of the hydraulic head distribution of a Gaussian initial condition at $t = 0.1, 1.0, 10.0$ s. Left: analytical solution via Fourier transform. Right: numerical solution via FDM.

Table 1. Peak hydraulic head values from analytical and numerical solutions for Dirac Delta and Gaussian initial conditions, with corresponding L^2 errors quantifying numerical deviation over time.

Case	Time (s)	Analytical Peak (m)	Numerical Peak (m)	L^2 Error
Dirac Delta	0.1	0.6410	0.1910	0.42800
	1.0	0.0222	0.0186	0.00520
	10.0	0.000709	0.000696	0.00003
Gaussian	0.1	0.5949	0.7265	0.1630
	1.0	0.0891	0.1905	0.1630
	10.0	0.0038	0.0104	0.01740

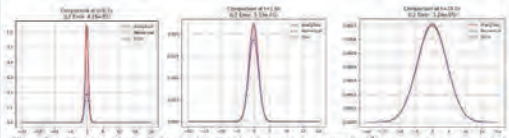

Figure 3. The plot of hydraulic head (m) against the distance (m) showing the L^2 norm error between analytical and numerical solution for the hydraulic head distribution of a Dirac Delta initial condition.

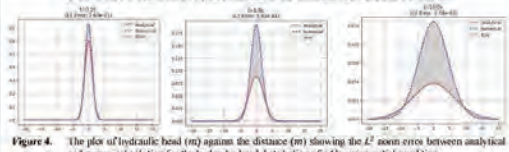

Figure 4. The plot of hydraulic head (m) against the distance (m) showing the L^2 norm error between analytical and numerical solution for the hydraulic head distribution of a Gaussian initial condition.

Model

Governing Equation:

$$S_s \frac{\partial h}{\partial t} = k\left(\frac{\partial^2 h}{\partial x^2} + \frac{\partial^2 h}{\partial y^2} + \frac{\partial^2 h}{\partial n^2}\right)$$

where h is the hydraulic head, k is the hydraulic conductivity and S_s is the specific storage.

Assumptions:

- Homogeneous and isotropic.
- The aquifer is confined on an infinite domain.
- Dirichlet boundary conditions: $h \to 0\ x, y, z \to \pm\infty$

Methodology

- **Fourier Transform:** Converts PDE into ODE in frequency domain.

$$\hat{h}(a_x, a_y, a_z, t) = \iiint_{\mathbb{R}^3} h(x,y,z,t) exp\{-i(a_x x + a_y y + a_z z)\}\, dxdydz$$

- **Inverse Transform:** Returns solution to spatial domain.

$$h(x,y,z,t) = \frac{1}{(2\pi)^3} \iiint_{\mathbb{R}^3} \hat{h}(a_x, a_y, a_z, t)\, exp\{i(a_x x + a_y y + a_z z)\}\, da_x\, da_y\, da_z$$

- **Numerical Illustration:** Finite Difference Method (FDM) scheme
  - Spatial: Central differences.
  - Temporal: Forward Euler with CFL Condition.
  - L^2 norm error used to evaluate the analytical and numerical solution.

$$\|h_{num} - h_{anal}\|_{L^2} = \left(\iiint_{\mathbb{R}^3} |h_{num} - h_{anal}|^2\, dx\, dy\, dz\right)^{\frac{1}{2}}$$

General Solution

The general solution to the 3D transient groundwater flow equation using Fourier transform,

$$h(x,y,z,t) = \iiint_{\mathbb{R}^3} h_0(x',y',z') G(x-x', y-y', z-z', t)\, dx'dy'dz'$$

where h_0 is the initial hydraulic head disribution at $t = 0$, and G is the diffusion kernel,

$$G(x,y,z,t) = \frac{1}{(4\pi\alpha t)^{3/2}} exp\left\{\frac{-(x^2+y^2+z^2)}{4\alpha t}\right\}, \alpha = \frac{k}{S_s}$$

This solution represents the transient diffusion of hydraulic head in groundwater flow.

Initial Condition Case Studies

- **Case 1: Dirac Delta Initial Condition**, $h_0(x,y,z) = \delta(x)\delta(y)\delta(z)$.
  - Solution: $\hat{h}(x,y,z,t) = \frac{1}{(4\pi\alpha t)^{\frac{3}{2}}} exp\left\{-\frac{x^2+y^2+z^2}{4\alpha t}\right\}$
  - Interpretation : Radial diffusion from an instantaneous point source disturbance.
- **Case 2: Gaussian Initial Condition** $h_0(x,y,z) = Aexp\left\{-\frac{(x^2+y^2+z^2)}{\sigma^2}\right\}$

  where A is the amplitude and σ is the width of the Gaussian.
  - Solution: $\hat{h}(x,y,z,t) = A\left(\frac{\sigma^2}{\sigma^2+4\alpha t}\right)^{\frac{3}{2}} exp\left\{-\frac{x^2+y^2+z^2}{\sigma^2+4\alpha t}\right\}$
  - Interpretation: Smooth, localized head distribution that spreads over time.

Results and Discussion

- Key observations:
  1. Dirac Delta: Early-time discrepancy due to numerical method's difficulty to approximate singularity. As time progresses, the diffusion smooths the solutions, and the numerical accuracy improves and aligns with the analytical solution.
  2. Gaussian: Solution maintains the Gaussian shape while spreading over time. Numerical simulations tend to overpredict peak values initially, but the error diminished as the solution evolved.
  3. Computational Efficiency: Analytical solution evaluates < 30 s, whereas FDM simulation at grid size $N = 100$ takes ~20 min.
- These findings emphasize the analytical solution's role as a benchmark for validating numerical schemes.

Conclusions

- Analytical solutions for 3D transient groundwater flow were derived for Dirac Delta and Gaussian initial conditions using Fourier transform, providing an exact reference for transient flow problems.
- Compared to the Finite Difference Method (FDM) solution, which required approximately 20 minutes at grid size $N = 100$ to be computed, the analytical solution produced results in under 30 seconds, showing a significant computational advantage.
- The analytical solutions offers a stable benchmark for transient hydraulic head diffusion. This stability is crucial for future extensions involving stochasticity and periodic noise since it provides a reference to verify accuracy and clearly distinguish the true system's behavior.

References

1. Ng, L. Tinsley, M. A. Abioye, A. K. (2017). Fourier transform for groundwater models. IIAMM.
2. Bear, J., & Cheng, A. H. D. (2010). Modeling Groundwater Flow and Contaminant Transport. Springer.
3. Cavalcanti, G., Sec. G., & Dumont, G. T. A. (2016). Evaluation of numerical dissipation errors. J. Comput. Phys.

Dynamics of Disclination Dipole

Nicolo Briatico

Dipartimento di Scienze Matematiche Applicate, Politecnico di Torino and Joint Graduate School of Mathematics for Innovation, Kyushu University, Japan

Topological defects such as dislocations and disclinations govern the mechanical behavior of crystalline solids. While dislocations are translational defects (characterized by a Burgers vector), disclinations represent rotational defects (quantified by a Frank angle). A variational formulation links the two, showing that, from an energetical standpoint, a collapsing disclination dipole behaves like an edge dislocation. This study focuses on the dynamics of a wedge disclination dipole within a unit disk, analyzing how the distance between defects (h) and the position of the center of mass (d) evolve over time. We identify two key regimes. We also explore rescaling strategies to link the dynamics of a converging dipole of disclinations with the one of dislocation. Preliminary results succeed for screw dislocations, while the case of edge dislocations remains open. These insights pave the way for a deeper understanding of how rotational defects contribute to plasticity in materials

Forum "Math-for-Industry" (FMfI) 2025

Dynamics of Disclination Dipole

Nicolò Briatico, Dipartimento di Scienze Matematiche Applicate, Politecnico di Torino
and Joint Graduate School Of Mathematics for Innovation, Kyushu University
nicolo.briatico@studenti.polito.it

Abstract

Topological defects like dislocations (traslational defects) and disclinations (rotational defects) govern the mechanics of crystals. This study focuses on the dynamics of a wedge disclination dipole within a unit disk, analyzing how the distance between defects (h) and the position of the center of mass (d) evolve over time. We identify two key regimes. These results offer new insights into the fundamental role of disclinations in material plasticity.

Introduction

In materials science, crystal lattice defects significantly affect the mechanical behavior of solids. They are mainly classified into **dislocations** and **disclinations**. Dislocations are **translational defects**, described by the **Burgers vector**, and are typically categorized as screw or edge types based on their orientation. Disclinations are **rotational defects**, characterized by an angular mismatch measured by the **Frank angle**.

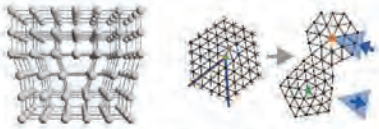

Left: Structure of an ***edge dislocation*** *(by Philippe Leurs, École des mines d'Albi-Carmaux, 2014). Right: Formation of two* ***disclinations*** *(by Peter Keim - Own work, CC BY-SA 4.0).*

Mathematical Background

In [3], Eshelby proposed a relationship between disclinations and dislocations, formalized in [1] using calculus of variations. This leads to the following **energy functional** for disclinations.

$$I^{\theta}(v;\Omega) := \frac{1}{2}\frac{1-\nu^2}{E}\int_{\Omega}(\Delta v)^2\,dx + \langle \theta, v\rangle, \tag{1}$$

where ν is the Poisson ratio, E the Young modulus, v the Airy potential, and θ accounts for **kinematic incompatibility** related to the presence of the defects. In particular, defining h the **distance** between two disclinations with an opposite Frank angle s, we have that

$$\langle \theta, v\rangle = s\left[v(x+\frac{h}{2}) - v(x-\frac{h}{2})\right], \tag{2}$$

where $x \pm \frac{h}{2}$ denote the positions of the defects.

[1] shows that, upon a suitable rescaling of v, in the limit of $h \to 0$ (the dipole is collapsing) the energy in (1) becomes equivalent to that of an edge dislocation.

In [2], the dynamics of a symmetric dipole in a unit disk $\Omega = B_1(0)$ is studied, yielding these key regimes (with $h_{eq} \approx 0.8$):

- $h = h_{eq}$, the distance remains unchanged;
- $h < h_{eq}$, defects approach the origin;
- $h > h_{eq}$, defects approach the boundary.

Goal

To analyse the dynamics of a dipole of wedge disclinations to find a **rescaling** that shows an **equivalence** with the edge dislocation dynamics as $h \to 0$.

Results

The dissipative dynamics of a disclination dipole can be obtained as the gradient flow of the energetic model in (1).

$$\begin{cases} \dot{h} = 4h\left(2\log\left(\dfrac{4h}{h^2-4d^2-4}\right) - \dfrac{2h^2d^2+h^2-8d^2+12d^2-4}{h^2-4d^2-4}\right) \\ \dot{d} = -2h^2d\dfrac{h^2-4d^2}{h^2-4d^2+4}, \end{cases} \tag{3}$$

where h is the distance between two disclinations and d is the center of mass of the dipole.

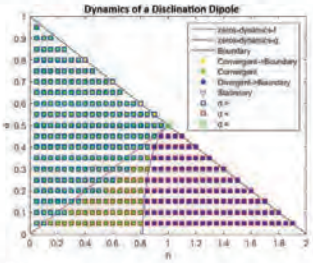

Two main behaviours are observed.

Diverging regime

When h **is large** (blue square with red borders), the defects are far enough not to feel the presence of the other defect and behave like **isolated defects**. Asymptotically,

$$h \sim (1 - C\exp(-4T))\ \dot{} \tag{4}$$

which is equal to the dynamics of **a single disclination** [2].

Converging regime

When h **is small** (green square with blue or red borders), the defects attract and collide each other in **infinite time**. Asymptotically,

$$h \sim C\exp(-\exp(8T)) \tag{5}$$

which tends to zero for $T \to +\infty$. This behaviour contrasts with the one of dislocations, which are known to collide in finite time.

Summary and Future Perspectives

We can define an area in the converging region where it is possible to define a **rescaling** of the dynamics that allow us to obtain, after a **conforming transformation,** the same dynamics of a **screw dislocation,** but we have not found yet a rescaling to obtain the same dynamics of an edge dislocation.

Starting from this results it is possible to study the effects of the presence of these defects in the **plasticity** behaviours of metal alloys and crystalline solids.

References

[1] P. Cesana, L. De Luca, and M. Morandotti: *Semidiscrete modeling of systems of wedge disclinations and edge dislocations via the Airy stress function method*. SIAM Journal on Mathematical Analysis, **56**(1), (2024) 79-136.

[2] P. Cesana, A. Grillo,M. Morandotti, and A. Pastore: *Dissipative Dynamics of Volterra Disclinations*. SIAM Journal on Applied Mathematics, **85**(4), (2025) 1361-1386.

[3] J. D. Eshelby: *A simple derivation of the elastic field of an edge dislocation*. Br. J. Appl. Phys., **17**(9), (1966) 1131-1135.

[4] N. Briatico, P. Cesana, and M. Morandotti: *Asymptotic analysis of disclination dipoles dynamics*. In progress

Acknowledgements JASSO scholarship offered within the *"Kyushu University Program for Emerging Leaders in Science"*(Q-PELS) and local support received at IMI.

Fairness-Aware Score Adjustment for Optimizing the Lambda value in Recommendation Systems

Donghan Lee

Department of Mathematics, Ajou University, Korea

Fairness in recommendation systems is gaining increasing attention due to concerns about exposure imbalance and recall disparities across user groups. In this study, we propose a simple effective method that enhances fairness by adjusting predicted scores based on users’ rating behaviors. Users are grouped by their relative rating tendencies (e.g., generous vs harsh raters) and group-specific scaling factors are applied to re-center their predicted scores. Through theoretical analysis, we demonstrate that this approach can reduce ranking-based recall disparities without modifying the model architecture or loss function. Empirical results confirm that the approach significantly reduces Recall@20 gaps while maintaining overall prediction accuracy. We also introduce a lightweight and interpretable for selecting scaling factors based on group-level score statistics, providing a practical solution for fairer recommendations.

FMT 2025

Fairness-Aware Score Adjustment for Optimizing the Lambda value in Recommendation Systems

Donghan Lee[1] · Soon-Sun Kwon[2]
[1] Graduate Student, Department of Mathematics, Ajou University, [2] Professor, Department of Mathematics, Ajou University

1. Introduction

- Traditional recommendation systems prioritize prediction accuracy, often neglecting fairness across different user groups.
- Users exhibit different rating behaviors : Generous vs. Harsh
- This difference leads to significant recall disparities → Unfair
- Our research introduces a simple, interpretable Fairness-Aware Score Adjustment (FSA) method to mitigate these disparities.
- We aim to reduce recall gap by 80%, while maintaining overall recommendation performance (RMSE).

2. Dataset and User Group Definition

- Dataset : MovieLens 10M
  - 69,878 Users → 10,000 for efficiency

Dataset	users	movies	ratings	sparsity
Original	69,878	10,677	10M	1.3%
Reduced	10,000	9,926	1.4M	1.4%

* Conducted statistical test to ensure representativeness
  - Kolmogorov-Smirnov statistics 0.009, p-value 0.44
  - Anderson-Darling statistics 0.443, p-value 0.99

- User Group
  - *Generous* . Rated > 80% of items above global average
  - *Harsh* . Rated > 80% of items below global average

3. Methodology

- Base Algorithm : Matrix Factorization [1] (MF)
  - Represents users and items as latent factor vectors
  - Decompose User-Item matrix

- $\hat{r}_{u,i} = \mu + b_u + b_i + p_u^\top q_i$
  - $\hat{r}_{u,i}$: Predicted rating of user u for item i
  - μ : Global average rating
  - b_u : User bias (user-specific rating tendency)
  - b_i : Item bias (item-specific rating tendency or popularity)
  - p_u : User latent factor vector (user preferences)
  - q_i : Item latent factor vector (item attributes)

- Fairness-Aware Score Adjustment (FSA)
  - Scale latent vectors by generous and harsh group

$$\hat{r}_{u,i}^{\text{adj}} = \mu + b_u + b_i + \tilde{p}_u^\top q_i, \quad \tilde{p}_u = \begin{cases} \gamma_G \cdot p_u & \text{if } u \in G \\ \gamma_H \cdot p_u & \text{if } u \in H \\ p_u & \text{otherwise} \end{cases}$$

3. Methodology

- $\text{Loss} = \text{RMSE} + \lambda \cdot \max(\text{Recall Gap} - \epsilon, 0)$
  - RMSE : Root Mean Squared Error
  - Recall Gap : Difference in recall@K between generous and harsh user groups
  - λ (penalty coefficient) : Hyperparameter controlling the fairness constraint
  - ϵ (tolerance threshold) : Permissible recall gap

- $$\mathbf{H} = \begin{pmatrix} 2A_H + 2\lambda F_H & 0 \\ 0 & 2A_G - 2\lambda F_G \end{pmatrix}$$

  where $A_H, A_G, F_H, F_G, \lambda > 0$.

  If $2A_G - 2\lambda F_G > 0$, then $\mathbf{H}$ is positive definite.
  - A_H Coefficient of γ_H^2 in the Harsh-group RMSE term
  - A_G Coefficient of γ_G^2 in the Generous-group RMSE term
  - F_H Quadratic coefficient of γ_H^2 in the Harsh-group fairness-gap term
  - F_G Quadratic coefficient of γ_G^2 in the Generous-group fairness-gap term

4. Results

- Threshold of Lambda for positive definite : 0.788
- Total Loss by Lambda 0.1

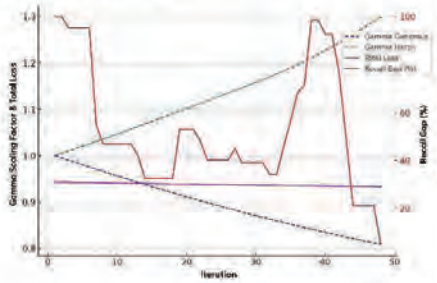

		Baseline	FSA
Recall	Generous	0.0207	0.0237
	Harsh	0.0258	0.0239
Total Loss		0.926	0.933

5. Conclusion

- Achieved a reduction of approximately 80% in recall disparity between user groups.
- Maintained high prediction accuracy measured by RMSE.
- The proposed method is simple, interpretable and model-agnostic.
- Extend FSA to other recommendation metrics and diverse data

References

[1] Y. Koren, R. Bell and C. Volinsky, "Matrix Factorization Techniques for Recommender Systems," in Computer, vol. 42, no. 8, pp. 30-37, Aug. 2009, doi: 10.1109/MC.2009.263

Acknowledgement

This research was supported by Basic Science Research Program through the National Research Foundation of Korea(NRF) funded by the Ministry of Education (RS-2021-NR060141, RS-2025-00564343)

Mathematical Model of Associative Learning in Amoebas

Kentaro Harada

Graduate School of Mathematics, Kyushu University, Japan

Associative learning is learning to associate a stimulus to a physiological conditioned response. Recent experiments have shown that amoebas perform learning. Studying the behavior of unicellular organisms may provide insight into the origins of associative learning. We formulated a network model in which learning is caused by the effects of diffusion, decomposition, and generation of memory indices in cells. We formulated equations of motion that reproduce the behavior of the amoebas.

Mathematical Model of Associative Learning in Amoebas

Kentaro Harada[(1)], Atsushi Tero[(2)], Yukinori Nishigami[(3)], Toshiyuki Nakagaki[(3)]

(1) Graduate School of Mathematics, Kyushu University, harada.kentarou.719@s.kyushu-u.ac.jp

(2) Institute of Mathematics for Industry, Kyushu University, (3) Research Institute for Electronic Science, Hokkaido University

Introduction

Associative learning is learning to associate a stimulus to a physiological conditioned response. Experiments[1][2] have shown that amoebas perform learning. Studying the behavior of unicellular organisms may provide insight into the origins of associative learning. In this poster, we introduce a mathematical model that reproduces the behavior of amoebas.

Experimental Results[2]

- Amoebas normally move to the cathode side
- Peptide was placed on the anode side.
- Amoebas moved to the anode side for 20 ~ 90 minutes, without peptide.

Amoebas can associate electrical stimulation with the act of approaching food.

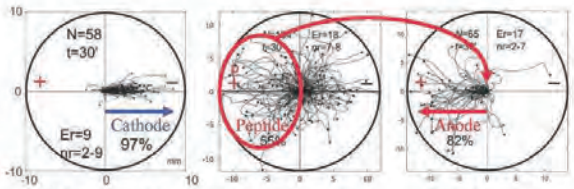

Original Mathematical Model [3]

Formulated by Kentaro Harada & Atushi Tero

- E_i : Electrical Potential
- P_i : Peptide Concentration
- m_i : Memory Indices
- F_i : Driving Force
- v_0 : Standard speed

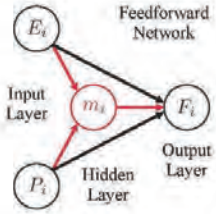

$$D = 1,\ R = 0.01,\ G = 1.5,\ \alpha = 0.1,\ \beta = 2,\ \gamma = 0.05,\ k = 100,\ {v_0}^2 = 0.1,\ \xi \sim N(0,1)$$

- Hidden Layer (Memory Update)

$$\dot{m}_i = D\sum_{j\neq i}(m_j - m_i) - Rm_i + GE_iP_i$$

Diffusion Decomposition Generation

- Output Layer (Driving Force)

$$F_i = -m_iE_i + \alpha E_i - \beta P_i - \gamma E_iP_i$$

Memory Feedforward | Move to Cathode | Move to Peptide | Interaction

- Equations of Motion

$$\begin{cases} \ddot{x} = k({v_0}^2 - \dot{x}^2 - \dot{y}^2)\dot{x} - F_2 + F_4 + \xi \\ \ddot{y} = k({v_0}^2 - \dot{x}^2 - \dot{y}^2)\dot{y} - F_1 + F_3 + \xi \end{cases}$$

Acceleration Stabilization Driving Force Noise

Numerical Simulation

- Mathematical models reproduced amoeba behavior before, during, and after learning.

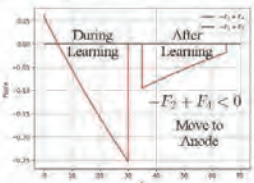

Driving Force

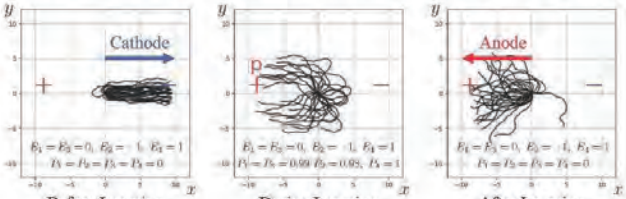

Conclusion

We formulated a network model in which learning is caused by the effects of diffusion, decomposition, and generation of memory indices in cells. We formulated equations of motion that reproduce the behavior of the amoebas.

Reference

[1] De la Fuente, I.M., et al. (2019). Evidence of conditioned behavior in amoeba. *Nature Communications*, *10*(1), 3690.

[2] Jose Carrasco-Pujante et al. (2021). Associative Conditioning Is a Robust Systemic Behavior in Unicellular Organisms: An Interspecies Comparison. *Frontiers in Microbiology*, *12*, 638421.

[3] Kentaro Harada et al. (2025). Mathematical Model of Associative Conditioning in Amoebas. Unpublished manuscript.

Solution of the Steady-State 2D Electrical Resistivity Tomography (ERT) Model in a Homogeneous Medium for Groundwater Exploration

Hasan Noraini

Department of Mathematical Sciences, Universiti Teknologi Malaysia, Johor Bahru, Malaysia and Kolej Pengajian Pengkomputeran, Informatik dan Matematik, Universiti Teknologi MARA Cawangan Melaka Kampus Jasin, Merlimau, Melaka, Malaysia

This work outlines an analytical solution for the steady-state 2D Electrical Resistivity Tomography (ERT) model in a homogeneous medium, focusing on groundwater exploration. The governing equations for the electric potential distribution using Ohm’s law and the principle of conservation of charge are established. The potential decay for a point source is described using modified Bessel functions. The method of images is utilized to enforce the Dirichlet, Neumann and Robin boundary conditions, ensuring that the solutions are physically consistent near boundaries. The results show that the solutions derived are stable and can form a basis for interpreting ERT data, with implications for improving subsurface characterization in groundwater exploration, particularly for identifying and managing groundwater resources.

Forum "Math for Industry" 2025
- Challenge of Mathematics for Industry in the AI era -

SOLUTION OF THE STEADY-STATE 2D ELECTRICAL RESISTIVITY TOMOGRAPHY (ERT) MODEL IN A HOMOGENEOUS MEDIUM FOR GROUNDWATER EXPLORATION

Noraini Hasan[a,c], Arifah Bahar[a,b], Mohd Nur Asmawisham Alel[d], Zainal Abdul Aziz[e]

ABSTRACT

This work outlines an analytical solution for the steady-state 2D Electrical Resistivity Tomography (ERT) model in a homogeneous medium, focusing on groundwater exploration. The governing equations for the electric potential distribution using Ohm's law and the principle of conservation of charge are established. The potential decay for a point source is described using modified Bessel functions. The method of images is utilized to enforce the Dirichlet, Neumann and Robin boundary conditions, ensuring that the solutions are physically consistent near boundaries. The results show that the solutions derived are stable and can form a basis for interpreting ERT data, with implications for improving subsurface characterization in groundwater exploration, particularly for identifying and managing groundwater resources.

*Corresponding author: arifah@utm.my

INTRODUCTION

RT field set-up

Electrical current is injected through the electrodes

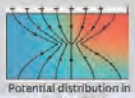

Potential distribution in the subsurface is measured.

Resistivity Inverted Profile

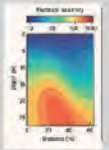

The contrast in the resistivity profile is due to the differences of the conductivity.

Actual Subsurface Profile

- Areas with low resistivity often mean wet or clay-rich soils.
- Areas with high resistivity suggests dry sand, gravel, or rock.

PROBLEM STATEMENT

- Accuracy dependence on mathematical models
- Importance of Boundary Conditions
- Limitations of current numerical and analytical approaches
- Gap in Analytical Framework

OBJECTIVES

1. Identify the governing equations for 2D electric potential distribution based on fundamental electromagnetic principles.
2. Formulate exact closed-form solutions using modified Bessel functions of the second kind.
3. Analyse the effects of Dirichlet, Neumann, and Robin boundary conditions on potential fields.
4. Establish reliable analytical benchmarks for groundwater exploration applications.

METHODOLOGY

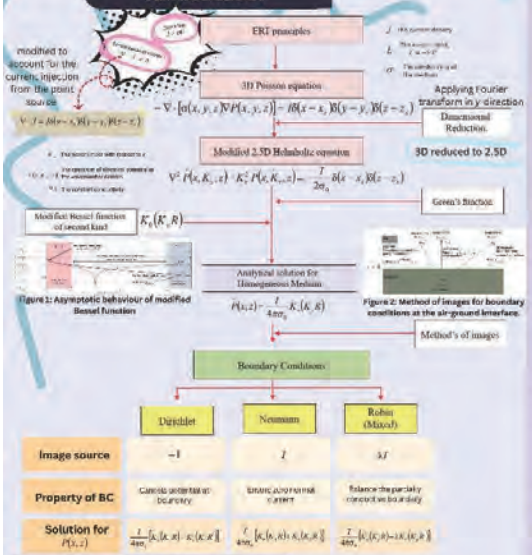

Figure 1: Asymptotic behaviour of modified Bessel function

Figure 2: Method of images for boundary conditions at the air-ground interface.

RESULTS & DISCUSSION

The parameter values used in the analysis of this study are summarized as follows:

Parameter	Symbol	Value	Unit
Conductivity	σ_0	1.0	$S\,m^{-1}$
Wavenumber	K_0	1.0	m^{-1}
Current injected	I	1.0	A
Source location	(x_s, z_s)	(0,0)	m

Figure 3: The parameter value used in the analysis

This study explores the behaviour of the potential as a function of the distance from the source. Results found from this study offer valuable insights into how the potential distribution depends on both boundary conditions and the properties of the medium.

a) Electric Potential Distribution and Decay in a Homogeneous Medium

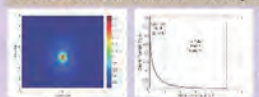

Figure 4: Decaying behaviour of the potential with distance in a homogeneous medium: (a) The contour plot, (b) The line plot.

- Electric potential peaks at the current injection point and decreases symmetrically in all directions.
- Near the source, potential drops sharply; farther away, it decreases gradually and approaches zero.
- This behaviour follows the modified Bessel function, confirming isotropy in the homogeneous medium.

b) The boundary condition effects on electrical potential distribution

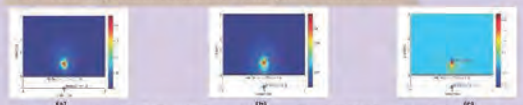

Figure 5:Electric potential distribution under different boundary conditions: (a) Dirichlet (grounded surface), (b) Neumann (insulating surface), and (c) Robin (partial current leakage).

Dirichlet:
- Surface fixed at zero potential (e.g., water bodies).
- Produces compressed equipotential lines near the surface due to destructive interference.
- Typical in highly conductive environments.

Neumann:
- No current flow across the surface (e.g., dry bedrock).
- Results in symmetric potential contours around the source.
- Typical of insulating conditions.

Robin:
- Intermediate case allowing partial current leakage.
- Captures realistic surfaces with mixed conductive and resistive behaviour (e.g., unsaturated soils or fractured rock).

c) Comparison of Potential Behaviour for Three Boundary Conditions

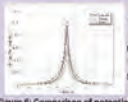

Figure 6: Comparison of potential decay under Dirichlet, Neumann, and Robin boundary conditions

- Boundary condition comparison:
  - **Dirichlet** → steepest potential decay, suitable for conductive surfaces (e.g., wetlands).
  - **Neumann** → weakest decay, ideal for resistive or insulating surfaces (e.g., arid regions).
  - **Robin** → flexible, handles partial current leakage, suitable for mixed or complex surfaces.
- Accurate boundary selection is essential for ERT survey design, as incorrect assumptions can bias inversion results and lead to misinterpretation of subsurface features.

CONCLUSION

- Derived analytical solution for steady-state 2D ERT in a homogeneous medium.
- Applied modified Bessel functions and method of images to handle Dirichlet, Neumann, and Robin boundary conditions.
- Provided a robust framework for groundwater exploration applications.
- Simplified assumption of constant conductivity along y-direction offers practical insights where major variations are in the *x*-*z* plane.
- Future work:
  1. Extend the model to include lateral conductivity variations.
  2. Explore advanced modelling techniques to improve accuracy and reliability in subsurface investigations.
  3. Validate the solution obtained with field/laboratory work

Scan here for REFERENCES

Formal Verification of Automata Properties Using Relational Calculus

Ginga Hayakawa

Graduate School of Mathematics, Kyushu University, Japan

Binary relations such as “=” and “<” can be regarded as generalizations of mappings. In relational calculus, a set corresponds to a domain and a relation corresponds to a projection, together forming a structure known as a category. In this study, we formally verify the fundamental properties of automata within the Rocq prover, based on the axioms of relational calculus. Since automata theory is closely connected to programming languages, compilers, and artificial intelligence, this research is expected to contribute to the development of formal verification environments in these domains.

FMFI2025 poster session

Formal Verification of Automata Properties Using Relational Calculus

Ginga Hayakawa
Graduate School of Mathematics,
Kyushu University

Yoshihiro Mizoguchi
Institute of Mathematics for Industry,
Kyushu University

KYUSHU UNIVERSITY

Abstract

Binary relations such as "=" and "<" can be regarded as generalizations of mappings. In relational calculus, a set corresponds to a domain and a relation corresponds to a projection, together forming a structure known as a category. In this study, we formally verify the fundamental properties of automata within the Rocq prover, based on the axioms of relational calculus. Since automata theory is closely connected to programming languages, compilers, and artificial intelligence, this research is expected to contribute to the development of formal verification environments in these domains.

Relation

A binary relation α from set A to set B is a subset $\alpha \subseteq A \times B$, denoted by $\alpha: A \to B$.

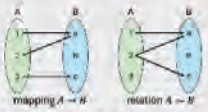

A relation can be regarded as a generalization of a mapping that does not assume univalence or unitarity.
Composition generalizes seamlessly from mappings to relations

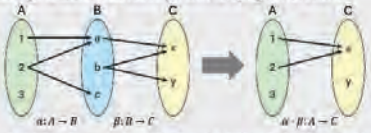

$\forall \alpha: A \to B, \forall \beta: B \to C,\quad \alpha \cdot \beta := \{(a,c) \in A \times C \mid \exists b \in B,\ (a,b) \in \alpha \wedge (b,c) \in \beta\}$

Nondeterministic Finite Automaton (NFA)

Let I be a singleton set.
Let Σ be a finite set of symbols representing letters, i.e., an alphabet.

A NFA is defined as a quadruple:
$M = (Q,\ \tau,\ \{\delta_\sigma\}_{\sigma\in\Sigma},\ \beta)$
Where
Q is a finite set of symbols representing the states of the automaton
$\tau: I \to Q$ is the initial relation
$\delta_\sigma : Q \to Q$ is the transition relation for each $\sigma \in \Sigma$
$\beta\ : Q \to I$ is the final relation
The acceptance condition for an NFA is defined as:
$\tau \cdot \delta(w) \cdot \beta = id_I$
where $\delta(w)$ is defined inductively by:
$\delta(\epsilon) := id_Q,\ \ \delta(\sigma w) := \delta_\sigma \cdot \delta(w)$

Let $\Sigma = \{a, b\}$.
Compose an NFA whose accepted language is "$ab^n a$".
$M = (\{0,1,2\}, \tau, (\delta_a, \delta_b), \beta)$

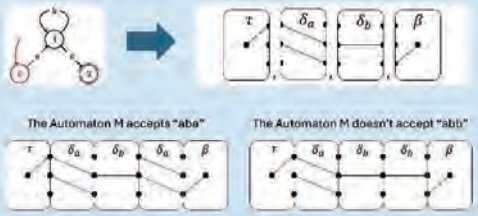


```
(* Definition in rocq *)
Structure nfa {Q s:finType} :=
  {init:Rel I Q; delta:s -> (Rel Q Q); final:Rel Q I}.
Fixpoint dstar {Q s:finType}(d:s -> (Rel Q Q))(w:seq s) :=
match w with
  |nil => Id Q
  |s::w' -> (d s) · (dstar d w')
end.
Definition accept {Q s:finType}(M:@nfa Q s)(w:seq s):Prop :=
(init M) · (dstar(delta M)w) · (final M) = Id I.
```

Automata Properties

Automata are language recognition machines that characterize regular languages. Regular languages are closed under operations such as union, intersection, concatenation, reversal, and Kleene closure.

- union $L(M \cup M') = L(M) \cup L(M')$
$(Q, \tau, \delta_\sigma, \beta) := (Q + Q',\ \tau i \cup \tau' j,\ i^\sharp \delta_\sigma i \cup j^\sharp \delta'_\sigma j,\ i^\sharp \beta \cup j^\sharp \beta')$
$\Rightarrow \tau\delta(w)\beta = \tau\delta(w)\beta \cup \tau'\delta'(w)\beta'$

- intersection $L(M \cap M') = L(M) \cap L(M')$
$(Q, \tau, \delta_\sigma, \beta) := (Q \times Q',\ \tau p^\sharp \sqcap \tau' q^\sharp,\ p\delta_\sigma p^\sharp \sqcap q\delta'_\sigma q^\sharp,\ p\beta \sqcap q\beta')$
$\Rightarrow \tau\delta(w)\beta = \tau\delta(w)\beta \sqcap \tau'\delta'(w)\beta'$

- concatenation $L(M \cdot M') = L(M) \cdot L(M')$
$(Q, \tau, \delta_\sigma, \beta) := (Q + Q',\ \tau i,\ i^\sharp \delta_\sigma i \cup (i^\sharp \beta \tau' \delta'_\sigma j \cup j^\sharp \delta'_\sigma j, i^\sharp \beta \tau' \beta' \cup j^\sharp \beta')$
$\Rightarrow \tau\delta(w)\beta = \cup\{\tau\delta(u)\beta\tau'\delta'(v)\beta' \mid u, v \in \Sigma^*, uv = w\}$

- reverse $L(M^R) = L(M)^R$
$(Q, \tau, \delta_\sigma, \beta) := (Q, \beta^\sharp, \delta_\sigma^\sharp, \tau^\sharp)$
$\Rightarrow \tau\delta(w)\beta = (\tau\delta(w^R)\beta)^\sharp$

- Kleene plus $L(M^+) = L(M)^+$
$(Q, \tau, \delta_\sigma, \beta) := (Q, \tau, \delta_\sigma \cup \delta_\sigma\beta\tau, \beta)$
$\Rightarrow \tau\delta(w)\beta = \cup\{\tau\delta(w_1)\beta\tau\delta(w_2)\beta \cdots \tau\delta(w_n)\beta \mid w_i \in \Sigma^+, w_1 w_2 \cdots w_n = w\}$

```
(* Proof example in rocq *)
Definition union_nfa {s Q Q':finType}
  (M:@nfa Q s)(M':@nfa Q' s):nfa :=
  {| init  := init M · iuinit M' · j;
     delta := fun x=>i# · delta M x · iuj# · delta M' x · j;
     final := i# · final M ∪uj# · final M' |}.
Lemma unionP {s Q Q':finType}(M:@nfa Q s)(M':@nfa Q' s)w:
  let ac := fun x=> init x · dstar(delta x)w · final x in
  ac (union_nfa M M') = (ac M) ∪ (ac M').
Proof.
  have H:dstar(delta(union_nfa M M'))w =
         i# · dstar(delta M)w · I ∪ j# · dstar(delta M')w · j.
  - elim w => [|h w H].
    - rel_simpl. (* Original tactic to simplify *)
    - rel_simpl.
  rewrite/={}H.
  rel_simpl.
Qed.
```

Conclusion & Future Works

We successfully formalized the above automata theory and developed custom tactics to automate a significant portion of the proofs. In future work, we plan to further enhance these custom tactics and apply them to more advanced proof simplification and AI-based automated proofs.

GitHub repository

References

[1] Y.Kawahara. Applications of Relational Calculus to Computer Mathematics. Bull. of informatics and cybernetics, 23, pp.67-78, 1988.
[2] Y.Mizoguchi, T.Matsushima,et.al. Development of Coq libraries to prove mapping properties (in Japanese), Bull. of JSSAC, 22(2), pp.39-42, 2016.
[3] The Rocq Prover, https://rocq-prover.org/
[4] G.Hayakawa. Formalizing DNA computing using the Coq Proof Assistant(in japanese), TPP2024:20th Theorem Proving and Provers Meeting, pp.298-308, 2025.

Numerical Simulation of Localized Bioconvection

Yoshimichi Hayashi

Graduate School of Mathematics, Kyushu University, Japan

Bioconvection is a phenomenon of spontaneous pattern formation observed in suspensions of microorganisms. This study focuses on the bioconvection of the photosynthetic protozoan Euglena gracilis. While many mathematical models for bioconvection are based on fluid dynamics, we propose a simplified model based on a system of partial differential equations (PDEs) without relying on fluid dynamics, as an initial step toward developing a future hybrid model. Our model describes the dynamics of Euglena density using a two-layer system (upper and lower layers) to represent the vertical structure. Furthermore, to reproduce the localized patterns observed in our experiments, we introduce a third "localizer" variable that controls the interaction between the layers. Numerical simulations of the model successfully reproduced characteristic bioconvection patterns, including spots and stripes in two dimensions. Moreover, the extended model incorporating the localizer variable succeeded in demonstrating the formation of centrally localized patterns, which is consistent with our experimental results. These findings suggest that the essential dynamics of bioconvection, including localization, can be captured without explicitly incorporating fluid dynamics, offering a new perspective for modeling self-organization in biological systems.

Numerical Simulation of Localized Bioconvection

Yoshimichi Hayashi[1], Atsushi Tero[2]
[1]Graduate School of Mathematics, Kyushu University [2]Institute of Mathematics for Industry, Kyushu University

Keywords: Bioconvection, Self-organization, Pattern Formation, PDE

Various mathematical models of bioconvection have been proposed in previous studies, most of which are based on fluid dynamics. However, a recent review paper suggests that the most promising direction for future bioconvection research is a hybrid model that integrates the Turing mechanism with fluid dynamics. In this study, as an initial step, we aim to propose a simplified mathematical model of bioconvection without relying on fluid dynamics.

Introduction

About *Euglena* (*E. gracilis*)

- Length: approximately **50 µm**.
- Performs **photosynthesis** using chloroplasts.
- **Swims** using flagellum.
- Has a specific gravity greater than **1**.
- Exhibits **Phototaxis**[1].

∴ *Euglena* has properties of both **animals** and **plants**.

Diagram of *Euglena*

a: Photoreceptor, b: Eyespot, c: Reservoir, d: Flagellum, e: Nucleus, f: Chloroplast

Bioconvection

1. *Euglena* gathers at the **surface**. (∵ negative phototaxis)
2. System becomes **unstable**. (∵ specific gravity > 1)
3. Rayleigh-Taylor instability and gravity cause *Euglena* to **sink**.
4. Back to 1.

This cycle generates convection.

Diagram of Convection
(higher density, darker green)

Experiment

Setup

Euglena (cell density adjusted) is injected as illustrated and placed on top of a light source. Conditions are listed below:

- Density: 1.0×10^6 cells mL^{-1}
- Brightness: 2.0×10^4 lx
- Light: **steady**, straight

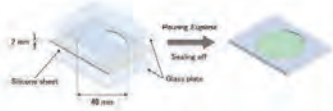

Result

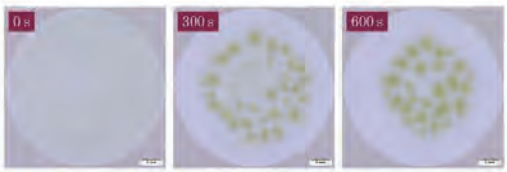

Mathematical Model

Two-layer Model

Equation

$$\begin{cases} \dot{u} = D_u \Delta u + af(v) - bu \\ \dot{v} = D_v \Delta v - af(v) + bu \end{cases}$$

- u: **upper**, v: **lower**
- u, v: Neumann BC

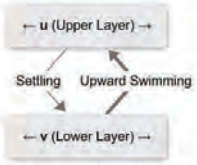

To append **central localization**[2] to current system, introduce a localizer variable w.

Equation

$$\begin{cases} \dot{u} = D_u \Delta u + af(v,w) - bu \\ \dot{v} = D_v \Delta v - af(v,w) + bu \\ \dot{w} = D_v \Delta v + u + v - w \end{cases}$$

- w: **inner state**
- w: Dirichlet BC

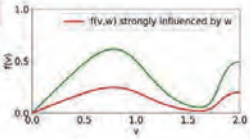

Form of $f(v,w)$

Numerical Simulation

1D (localized)

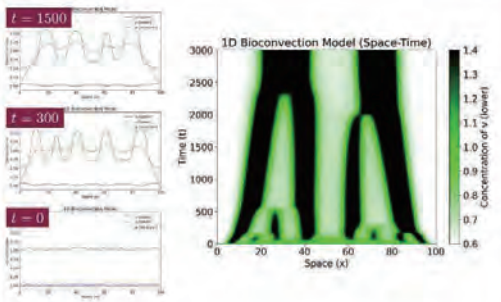

2D (non-localized)

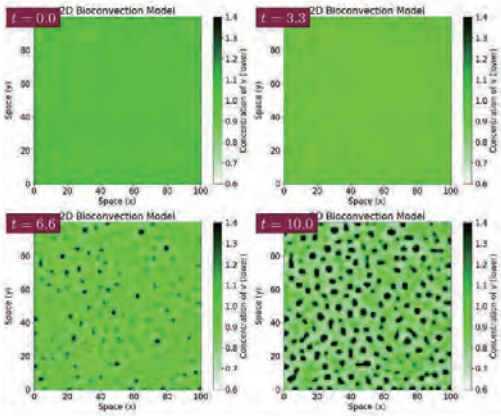

Reference

[1] K. Ohgi, H. Sawamoto, H. Nishimura, A. Awazu, N. Sezaki and M. Sato, Photoactivity and velocity flow in the localized bioconvection of Euglena gracilis, BIOPHYSICS (2014).
[2] A. J. Bernstein, A. Awazu, I. Ozuki, K. Noto, K. Nishida, and H. Nishimori, Localized Bioconvection of Euglena Caused by Phototaxis in the Lateral Direction, Journal of the Physical Society of Japan 80.4 (2011).

FMfI2025
2025-08-19 – Seoul, Korea

KYUSHU UNIVERSITY

Piecewise-linear embeddings of the space of 3D lattices into R13 for highthroughput handling of lattice parameters

Taiyo Imamura

Graduate School for Mathematics, Kyushu University, Japan

Positive-definite symmetric matrices, known as Gram matrices, are widely used to parametrize lattices. In this work, we propose two methods for embedding rank-3 lattices into R^{13} continuously and piecewise-linearly. These embeddings are useful for determining whether two lattices are nearly identical within their margins of error.

Piecewise-linear embeddings of the space of 3D lattices into $\mathbb{R}^{13}$ for high-throughput handling of lattice parameters

Taiyo Imamura / Ryoko Oishi-Tomiyasu
Graduate School for Mathematics, Kyushu University / Institute of Mathematics for Industry (IMI), Kyushu University
imamura.taiyo.881@s.kyushu-u.ac.jp / tomiyasu@imi.kyushu-u.ac.jp

1. Abstract

- Positive-definite symmetric matrices called *Gram matrices* are widely used to parametrize lattices.
- We present two methods to embed rank-3 lattices into $\mathbb{R}^{13}$ continuously and piecewise-linearly.
- These embedding are useful to judge if two lattices are nearly identical within their margins of errors.

2. Background

S^n : the set of all the $n \times n$ symmetric matrices
$\mathcal{S}^n_{>0} \subset S_n$: the set of all Gram matrices
$\mathbf{e}_1, \cdots, \mathbf{e}_n$: the standard basis of $\mathbb{R}^n$
$S_1, S_2 \in \mathcal{S}^n_{>0}$ represent the same lattice iff $gS_1{}^tg = S_2$ for some $g \in GL_n(\mathbb{Z})$. so we consider the orbit space $\mathcal{LS}_n := GL_n(\mathbb{Z})\backslash\mathcal{S}^n_{>0}$.
The *vonorm map* of $S \in \mathcal{S}^n_{>0}$ [1] is defined as $\Lambda_{n,2} := (\mathbb{Z}^n/2\mathbb{Z}^n)\backslash\{2\mathbb{Z}^n\} \to \mathbb{R}_{>0}$:

$$\mathrm{vo}_S(v + 2\mathbb{Z}^n) := \min\{wS^tw : w \in v + 2\mathbb{Z}^n\}.$$

The non-zero vectors $w \subset L$ that are the shortest in $v + 2L$ are called *Voronoi vectors*.
The map $S \mapsto \mathrm{vo}_S$ gives a continuous map $\mathcal{S}^n_{>0}$, which induces $\mathcal{LS}_n \to GL_n(\mathbb{Z}/2\mathbb{Z})\backslash\mathbb{R}^{\Lambda_{n,2}}$.

Conway-Sloane Conjecture [2]

The vonorm map $\mathrm{vo}_S(u)$ determines the class of $S \subset \mathcal{S}^n_{>0}$ in $\mathcal{LS}_n$ uniquely.

The *conorm map* of S is defined as the Fourier transform of the vonorm map: defined as

$$\mathrm{co}_S(\chi) := \frac{1}{2^{n-1}} \sum_{v+2\mathbb{Z}^n \subset \Lambda_{n,2}} \mathrm{vo}_S(v + 2\mathbb{Z}^n)\chi(v).$$

For $n = 2$, a Gram matrix $S = (s_{ij}) \in \mathcal{S}^2_{>0}$ is *reduced* if it satisfies

$$0 \le -2s_{12} \le s_{11} \le s_{22}. \qquad (1)$$

There is an embedding of the space of 2D lattices into $\mathbb{R}^3$ by

$$S \to (x, y, z) := ({}^t\mathbf{e}_1 S\mathbf{e}_1, {}^t\mathbf{e}_2 S\mathbf{e}_2, {}^t(\mathbf{e}_1 + \mathbf{e}_2)S(\mathbf{e}_1 + \mathbf{e}_2))$$

where S is the reduced Gram matrix of a lattice. (1) implies $0 < x \le y \le z \le x + y$, so by normalizing z, this can be embedded in $\mathbb{R}^2$ as the figure below.

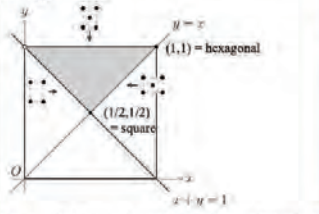

For $n = 3$, $S = (s_{ij}) \in \mathcal{S}^3_{>0}$ is *Minkowski reduced* [3] if all of the following inequalities hold:

$$s_{11} \le s_{22} \le s_{33},\ 0 \le -2s_{12} \le s_{11},\ 2|s_{13}| \le s_{11}$$
$$0 \le -2s_{23} \le s_{22},\ -2(s_{12} + s_{13} + s_{23}) \le s_{11} + s_{22}.$$

For $n = 2, 3$, $S \in \mathcal{S}^n_{>0}$ is called *Selling reduced* [4] if all nondiagonal entries of $\tilde{S} := {}^twSw \in \mathcal{S}^n_{>0}$ are not positive, where $w := (\mathbf{e}_1 \cdots \mathbf{e}_n\ \mathbf{e}_{n+1}) \in \mathbb{R}^{n\times(n+1)}$ and $\mathbf{e}_{n+1} = -\sum_{i=1}^n \mathbf{e}_i$.

3.(a) Two ways of piecewise-linear embeddings

For lattices of rank 3, we propose to use a map ι_s or ι_m from $\mathcal{LS}_3 := GL_3(\mathbb{Z})\backslash\mathcal{S}^3_{>0}$ into $\mathbb{R}^{13}$.
In what follows, [ ] denotes a sorted list in ascending order.

ι_s for Selling reduction

$\iota_s(S) := (f_1(S), f_2(S)) \in \mathbb{R}^{13}$, where

$$f_1(S) := [\mathrm{vo}_S(g) : g \in \Lambda_{3,2}] \in \mathbb{R}^7,$$
$$f_2(S) := \left[\mathrm{co}_S(\chi);\ \begin{matrix}\chi : (\mathbb{Z}/2\mathbb{Z})^3 \to \{\pm 1\} \\ \chi \ne +(1,1,1)\end{matrix}\right] \in \mathbb{R}^6$$

ι_m for Minkowski reduction

Define the *conorm map modulo* $r \ge 2$ as $\mathrm{vo}_{S,r}(v + r\mathbb{Z}^n) := \min\{wS^tw : w \in v + r\mathbb{Z}^n\}$.
It induces the map $\{\pm 1\}\backslash\Lambda_{3,r} \to \mathbb{R}_{>0}$.

$$\iota_m(S) := [\mathrm{vo}_{S,3}(u - 3\mathbb{Z}^3) : \pm u - 3\mathbb{Z}^3 \subset \{\pm 1\}\backslash\Lambda_{3,3}]$$

Both ι_s and ι_m are continuous and piecewise linear, which induce maps from $\mathcal{LS}_3$ to $\mathbb{R}^{13}$.
By an exhaustive search using Magma [5], it is proved that these maps are injective.

3.(b) Generalization of Ryškov's C-types

We will extend the definition of Ryškov's C-types [6] to consider the Voronoi map modulo r.
Define the set $\Phi_{S,r}$ by $\{v \in \mathbb{Z}^n : vS^tv = \mathrm{vo}_{S,r}(v + r\mathbb{Z}^n)\}$. *A C-type domain (modulo r)* containing S is defined by

$$\mathcal{D}_r(\Phi) := \{S_2 \in \mathcal{S}^n_{>0} : \Phi_{S,r} \subset \Phi_{S_2,r}\}.$$

More generally, for any subset $\Phi \subset \mathbb{Z}^n$, its C-type domain is defined by

$$\mathcal{D}_r(\Phi) := \{S \in \mathcal{S}^n_{>0} : vS^tv = \mathrm{vo}_{S,r}(v + r\mathbb{Z}^n) \text{ for any } v \in \Phi\}.$$

For a fixed $r \ge 2$, $S \in \mathcal{S}^n_{>0}$ is in *a general position* if any $u, v \in \Phi_{S,r}$ such that $u \ne \pm v$ belong to distinct cosets in $\mathbb{Z}^n/r\mathbb{Z}^n$. A C-type domain $\mathcal{D}_r(\Phi_{S,r})$ is *primitive* if it is provided by some S in general position. In general, a C-type domain $\mathcal{D}_r(\Phi)$ is *primitive* if it is the intersection of the following half-spaces.

$$\mathcal{D}_r(\Phi) = \bigcap_{u\subset\Phi} \bigcap_{v\subset u-r\mathbb{Z}^n} H^{\le 0}(u, v), \quad H^{\le 0}(u, v) := \{S \in \mathcal{S}^n_{>0} : uS^tu \le vS^tv\}.$$

For $n = 3$, the following $\Phi_i (i = 1 \cdots 4)$ provide a system of representatives of equivalence classes of primitive C-type domains modulo 3.

$$\Phi_1 := \{(i_1, i_2, i_3) : i_1, i_2, i_3 = -1, 0, 1\} \qquad \Phi_2 := \Phi_1 \cup \{\pm(1,2,1)\}\backslash\{\pm(1,-1,1)\}$$
$$\Phi_2 := \Phi_1 \cup \{\pm(1,1,2)\}\backslash\{\pm(1,1,-1)\} \qquad \Phi_4 := \Phi_3 \cup \{\pm(2,1,1)\}\backslash\{\pm(-1,1,1)\}$$

Moreover, let $\mathcal{D}_{min} \subset \mathcal{S}^3_{>0}$ be the subset of all the Minkowski reduced forms, then $\mathcal{D}_{min}$ is contained in $\cup_{i=1}^{10}\mathcal{D}_3(\Phi_j)$, where

$$\Phi_5 := \Phi_1 \cup \{\pm(2,1,1)\}\backslash\{\pm(-1,1,1)\} \qquad \Phi_6 := \Phi_1 \cup \{\pm(1,1,2)\}\backslash\{\pm(1,1,-1)\}$$
$$\Phi_7 := \Phi_1 \cup \{\pm(-2,-1,1)\}\backslash\{\pm(1,-1,1)\} \qquad \Phi_8 := \Phi_1 \cup \{\pm(1,-1,-2)\}\backslash\{\pm(1,-1,1)\}$$
$$\Phi_9 := \Phi_1 \cup \{\pm(2,1,1), \pm(1,2,1)\}\backslash\{\pm(-1,1,1), \pm(1,-1,1)\}$$
$$\Phi_{10} := \Phi_1 \cup \{\pm(2,1,1), \pm(1,1,2)\}\backslash\{\pm(-1,1,1), \pm(1,1,-1)\}$$

Therefore for a given Minkowski reduced Gram matrix S, these Φ_i provide the lists of voronoi vectors, which enables us to calculate ι_m and ι_s.

4. Ongoing research

- The polynomial ring $\mathbb{F}_q[x]$ shares many properties with the ring of integers $\mathbb{Z}$. This theory will be applied to lattices over $\mathbb{F}_q[x]$ as well by replacing the sets as follows.

Classical version	$\mathbb{Z}$	$\mathbb{Q}$	$\mathbb{R}$
Function-field analogue	$\mathbb{F}_q[T]$	$\mathbb{F}_q(T)$	$\mathbb{F}_q((T^{-1}))$

- In particular, when the characteristic is 2, applications to cryptography and information theory, such as pseudorandom number generation [7], can also be considered.

5. References

[1] G. Voronoi. *Journal für die reine und angewandte Mathematik*, 134:198–287, 1908.
[2] J. H. Conway and N. JA Sloane. *Proc. R. Soc. Lond. A*, 436(1896):55–68, 1992.
[3] H. Minkowski. *J. Riene Angew. Math.*, 129:220–274, 1905.
[4] E. Selling. *J. Riene Angew. Math.*, 77(143), 1874.
[5] W. Bosma, J. Cannon, and Playoust. C. *Journal of Symbolic Computation*, 24(3):235–265, 1997.
[6] S. S. Ryškov and E. P. Baranovskiĭ. volume 137. American Mathematical Soc., 1978.
[7] S. Harase. *Journal of Statistical Computation and Simulation*, 94(9):2040–2062, 2024.

Forum “Math for Industry” 2025

- Challenge of Mathematics for Industry in the AI era -

August 18 - 20, 2025, Seoul (POSCO Center), Republic of Korea

A Simple Model of Enterprise Performance: Cooperative vs Monopolistic Strategy

Naoyuki Ishimura

Faculty of Commerce, Chuo University, Japan

We introduce a simple model of enterprise performance. The model consists of the recurrence formula for the probability which is interpreted as the market share of enterprise. We show that the cooperative strategy may outperform the monopolistic behavior. The cases study of woodworking industry in Maniwa, Okayama prefecture, Japan will support our model.

A Simple Model of Enterprise Performance: Cooperative vs Monopolistic Strategy

Naoyuki Ishimura[1] and Keiji Watanabe[2]

[1]Faculty of Commerce, Chuo University, Tokyo 192-0393, Japan
[2]Department of Management, Okayama University of Science, Okayama 700-0005, Japan
E-mail: naoyuki@tamacc.chuo-u.ac.jp, k-watanabe@ous.ac.jp

1 Introduction

All companies, in its nature, try to maximize their performance in respective industrial activities. One company may seek to dominate the market, while the other may keep its position among sectors. In this respect, the strategy against their competitors will be important.

Here we introduce a simple model of enterprise performance. The model consists of the recurrence formula for the probability which is interpreted as the market share of enterprise. In particular, we are interested in the behavior of the primary company, which is able to dominate the relevant industry. Analysing the model, we show that the cooperative strategy may outperform the monopolistic behavior. The cases study of woodworking industry in Maniwa, Okayama prefecture, Japan will support our model.

2 Probabilistic Recurrence Model

Let $n = 1, 2, \cdots$ denote the discrete time step and we consider the probabilistic movement of the market share of companies. Let

p_n: the market share of the primary company
q_n: the market share of the others,

where we assume $0 \le p_n, q_n \le 1$, $p_n + q_n = 1$.

In our model, we postulate that

p_n keeps its value with ekploiting the other
but it decreases with the interaction with q_n
q_n decreases by its nature
but it increases with the interaction with p_n,

The evolution of p_n, q_n is then assumed to be governed by the difference equation:

$$\begin{aligned} p_{n+1} &= p_n + \frac{3}{4}q_n - p_n q_n \\ q_{n+1} &= \frac{1}{4}q_n + p_n q_n. \end{aligned} \tag{1}$$

The coefficients $\frac{3}{4}, \frac{1}{4}$ are not essential. It is easy to see that the equilibrium points are given by

$$(p, q) = (1, 0), \quad \left(\frac{3}{4}, \frac{1}{4}\right)$$

Theorem 1 *For any intial p_1, q_1 with $0 < p_1, q_1 < 1$ and $p_1 + q_1 = 1$, there holds the followings:*

$$0 < p_n, q_n < 1 \text{ and } p_n + q_n = 1$$
$$(p_n, q_n) \to \left(\frac{3}{4}, \frac{1}{4}\right) \text{ as } n \to \infty.$$

Precisely stated, we have, for some constant C,

$$\left|p_n - \frac{3}{4}\right| \le C\left(\frac{3}{4}\right)^n, \quad \left|q_n - \frac{1}{4}\right| \le C\left(\frac{3}{4}\right)^n.$$

The theorem implies that cooperative state is much ready to be realized than the monopolistic state.

3 Case Study

We recall the work of Watanabe [2], which is also the motivation of our reserach. We will explain in the details at the poster session. See aslo [1].

4 Conclusion

We have developed a simple model for the behavior of competitive industries. This kind of study, namely, the mathematical modelling approach to the understanding of enterprise performance seems not so popular in the literature. In the current model, it is shown that the cooperative state is stable and the monopolistic state is unstable. We continue our study.

References

[1] Ishimura, N., and Watanabe, K. (2025). Simple models of enterprise performance: Cooperative vs monopolistic strategy (submitted).

[2] Watanabe, K. (2025). Creating an ecosystem through determining the meaning of resources: Institutionalization of resource use through the establishment of Maniwa biomass power plant. *Management and Data Science*. **7**. 54–75. https://www.mgt.ous.ac.jp/society/wp-content/uploads/sites/3/2025/04/vol7p54-75.pdf (in Japanese)

Limit Theorems for Verbose Persistence Diagrams

Jeong-hwi Joe

Department of Mathematical Sciences, KAIST, South Korea

The persistence diagram is a central object in the study of persistent homology and has also been investigated in the context of random topology. The ¥emph{verbose diagram} (a.k.a verbose barcode), a more recent concept introduced by Usher and Zhang, is a refinement of the persistence diagram that is obtained by incorporating ephemeral persistence features as extra points along the diagonal. In this work, we initiate the study of ¥emph{random} verbose diagrams. Specifically, we extend all the main results of the seminal work by Hiraoka, Shirai, and Trinh on the asymptotic behavior of persistence diagrams as well as its sequel on marked point processes by Shirai and Suzaki, to the setting of verbose diagrams. Namely, (i) we establish a strong law of large numbers for verbose diagrams as the random point cloud grows in size, and (ii) compute the total mass of the limiting object, which is a deterministic measure on the half-plane (on and above the diagonal). (iii) We also show that the support of this limiting measure equals the closure of the set of points that are ``realizable'''' as verbose diagrams. Along the way, (iv) we extend the notion of the persistent Betti number, which was previously defined on the set of pairs ¥(r ¥leq s¥) in ¥([0, ¥infty)¥), to allow the case of ¥(r > s¥), and reveal the relation between this extended notion and the verbose diagram. (v) Finally, we prove a central limit theorem for the extended persistent Betti numbers.

Limit Theorems for Verbose Persistence Diagrams

Jeong-hwi Joe*
KAIST
jhjoe@kaist.ac.kr

Woojin Kim
KAIST
woojin.kim@kaist.ac.kr

Cheolwoo Park
KAIST
parkcw2021@kaist.ac.kr

Introduction

- As the intersection of random topology and TDA, the asymptotic behavior of persistence diagrams has been widely studied.
- The verbose diagram [UZ16] refines the persistence diagram by including extra points along the diagonal.
- In this work, we initiate the study of the asymptotic behavior of verbose diagrams. In particular, we extend all of the main theorems in [HST18] and [SS22] to the setting of verbose diagrams.

Preliminaries

Vague Convergence and Marked Point Processes

- $\mathscr{M}_+(S)$: the set of **Radon measures** on a second-countable locally compact Hausdorff space S, i.e., the set of measures on S which are finite on compact sets.
- A sequence $\{\mu_n\}_n$ of measures in $\mathscr{M}_+(S)$ is said to **converge vaguely** to a measure $\mu \in \mathscr{M}_+(S)$, and we write $\mu_n \xrightarrow{v} \mu$, if

$$\int_S f\,d\mu_n \to \int_S f\,d\mu \quad \text{as } n \to \infty$$

for every continuous function $f : S \to \mathbb{R}$ with compact support.

- Let $\mathbb{M}$ be the set of **marks**, which is also second-countable locally compact, Hausdorff. A **marked point process** on S with marks in $\mathbb{M}$ is a random variable that outputs a (multi)subset of $S \times \mathbb{M}$ such that: (i) the projection on S is always locally finite and (ii) almost surely, no two elements have the same first coordinate.
- A **stationary** marked point process on $\mathbb{R}^N$ is a marked point process whose distribution does not change after arbitrary translation on the first coordinate.

Verbose Diagrams

- To get the **verbose diagram** of a (simplicial) filtration, start with an ordinary persistence diagram and **additionally record the cycles that are created and filled in simultaneously** on the **diagonal line**.

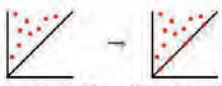

Persistence Diagram (PD) Verbose diagram (VD)

- **Example.** In the filtration below, a 1-cycle is filled in as soon as it is created at $t = 3$. This is captured by the point $(3,3)$ in the degree-1 verbose diagram.

Why should we utilize VDs instead of PDs?

- The VDs are **easy to calculate** as are **finer invariants** than the PDs [ZM21], provide a **stronger stability** than.
- The use of VD makes the *persistent homology transform* [TMD14] **more efficient**, requiring fewer directional diagrams to ensure faithfulness [PMS24].

Diagrams as Measures

- Let $(X, \mathcal{A})$ be a measurable space. A multiset A of points in X is identified with the discrete measure

$$\xi = \sum_{a \in A} \delta_a$$

where δ_a is the Dirac measure at a.

- Thus, persistence diagrams and verbose diagrams can be represented as corresponding discrete measures on Δ and Δ', respectively.

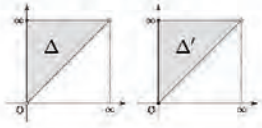

Procedure of Generating a Random Diagram

- $(\Omega, \mathcal{F}, \mathbb{P})$: a probability space
- Ψ: a stationary marked point process on $\mathbb{R}^N$ (with marks in $\mathbb{M}$)
- $\{\Lambda_n\}_n$: an increasing sequence of bounded Borel convex subsets of $\mathbb{R}^N$ that eventually covers every point of $\mathbb{R}^N$
- Ψ_{Λ_n}: restriction of Ψ to Λ_n
- $\mathbb{K}^n(\Psi_{\Lambda_n})$: a filtration built on Ψ_{Λ_n}. It can be Čech or Vietoris–Rips filtration, or more general filtrations whose rule is specified with the filtration function κ.
- $\xi_{\mathrm{Dgm}_q(\mathbb{C};\mathbb{K}^n(\Psi_{\Lambda_n}))} = \xi^v_{\mathrm{Dgm}_q\Lambda_n}$: the q-th verbose diagram of $\mathbb{K}^n(\Psi_{\Lambda_n})$, which is represented as a discrete measure on Δ'
- An illustration of the procedure of generating a random verbose diagram (marks supressed):

- $\xi_q(\mathbb{K}^n(\Psi_{\Lambda_n})) = \xi^o_{\mathrm{Dgm}_q\Lambda_n}$: the q-th (ordinary) persistence diagram of $\mathbb{K}^n(\Psi_{\Lambda_n})$, which is represented as a discrete measure on Δ.

Main Results

Many notation:

- $R_q(\kappa)$ (resp. $R'_q(\kappa)$): the subset of Δ (resp. Δ') that consists of all locations where persistence (resp. verbose) diagrams can place points.
- $\beta^{r,s}_q$: the q-th persistent Betti number of $\mathbb{K}^n(\Psi_{\Lambda_n})$ from r to s

For any filtration, we extend the notion of persistent Betti number $\beta^{r,s}_q$ from r to s to also allow the case $r > s$. For any $r, s \in [0, \infty]$, $\beta^{r,s}_q$ equals the number of points of the verbose diagram that is in the region $[0, r] \times [s, \infty]$. See on the right.

The table below is the summary of our main theorems. The second column contains previous results and the third column contains their extensions to the verbose diagrams. The third row is our original result.

	PD	VD (this work)
Strong law of large numbers	[HST18, Theorem 1.5], [SS22, Theorem 2.6] *(Assumptions omitted for brevity)* $\frac{1}{\mathrm{vol}(\Lambda_n)} \mathbf{E}\xi^o_{\mathrm{Dgm}_q\Lambda_n} \to \nu_q \quad \text{as } n \to \infty$ *Moreover, if Ψ is ergodic, then almost surely,* $\frac{1}{\mathrm{vol}(\Lambda_n)} \xi^o_{\mathrm{Dgm}_q\Lambda_n} \to \nu_q \quad \text{as } n \to \infty$	**Theorem 1.** *(Assumptions omitted for brevity)* $\frac{1}{\mathrm{vol}(\Lambda_n)} \mathbf{E}[\xi^v_{\mathrm{Dgm}_q\Lambda_n}] \to \nu'_q \quad \text{as } n \to \infty.$ *Moreover, if Ψ is ergodic, then almost surely,* $\frac{1}{\mathrm{vol}(\Lambda_n)} \xi^v_{\mathrm{Dgm}_q\Lambda_n} \to \nu'_q \quad \text{as } n \to \infty.$
Total mass of the limiting measure		**Theorem 2.** *Suppose that the intensity λ of Ψ, defined by $\lambda = \mathbf{E}[\Psi([0,1]^N)]$, is positive, and that $\kappa(\sigma) < \infty$ for all $\sigma \in \mathscr{F}(\mathbb{R}^N)$. Then* $\nu'_q(\Delta') = \begin{cases} \lambda, & \text{if } q = 0, \\ \infty, & \text{otherwise.} \end{cases}$
Support of the limiting measure	[HST18, Theorem 1.9] *(Assumptions omitted for brevity)* Then $\mathrm{supp}(\nu_q) = \overline{R_q(\kappa)}$ for every $q \geq 0$, where the closure is taken in Δ.	**Theorem 3.** *(Assumptions omitted for brevity)* Then $\mathrm{Supp}(\nu'_q) = \overline{R'_q(\kappa)}$ for every $q \geq 0$, where the closure is taken in Δ'.
CLT for the persistent Betti number	[HST18, Theorem 1.12] *(Assumptions omitted for brevity)* Then, for any $0 \leq r \leq s < \infty$ and $q \geq 0$, there exists a constant $\sigma^2_{r,s} = \sigma^2_{r,s}(\kappa, q)$ such that $\frac{\beta^{r,s}_{q,L} - \mathbf{E}[\beta^{r,s}_{q,L}]}{L^N} \xrightarrow{d} \mathcal{N}(0, \sigma^2_{r,s})$ as $L \to \infty$.	**Theorem 4.** *(Assumptions omitted for brevity)* Then, for any $r, s \in [0, \infty]$ and $q \geq 0$, there exists a constant $\sigma'^2_{r,s} = \sigma'^2_{r,s}(\kappa, q)$ such that $\frac{\beta^{r,s}_{q,L} - \mathbf{E}[\beta^{r,s}_{q,L}]}{L^N} \xrightarrow{d} \mathcal{N}(0, \sigma'^2_{r,s})$ as $L \to \infty$.

References

[TMD14] Katharine Turner, Sayan Mukherjee, and Doug M. Boyer. "Persistent homology transform for modeling shapes and surfaces". In: *Information and Inference: A Journal of the IMA* 3.4 (2014), pp. 310–344.

[UZ16] Michael Usher and Jon Zhang. "Persistent homology and Floer–Novikov theory". In: *Geometry & Topology* 20.6 (Dec. 2016), pp. 3333–3430. issn: 1364-0380. doi: 10.2140/gt.2016.20.3333. url: http://dx.doi.org/10.2140/gt.2016.20.3333.

[ZM21] Lee Zhou and Facundo Mémoli. "Bi-Lipschitz inverse theorems and the topology of Lipschitz shape retracts". In: *Journal of Computational Geometry* 15.2 (2024), pp. 250–328.

Partially supported by the National Research Foundation of Korea(NRF) grant funded by the Korea government(MSIT) (RS-2025-00513616).

Partially supported supported by the National Research Foundation of Korea [NRF-2021R1A2C1093925].

Numerical Simulation of Plaque-Driven Vascular Stenosis Using Biased Diffusion-Limited Aggregation with Formative and Destructive Particles

Taiga Kadowaki

Joint Graduate School of Mathematics for Innovation, Kyushu University, Japan

Vascular stenosis involves both growth and degradation of plaque. Diffusion-Limited Aggregation (DLA), proposed by Witten et al., models pattern formation through the aggregation of diffusing particles. We extend this framework by introducing formative and destructive particles in a biased field. Extended model reproduces asymmetric, dynamic narrowing patterns, capturing the competition between growth and erosion. This offers a simple numerical approach to explore stenosis progression and potential therapeutic strategies.

Numerical Simulation of Plaque-Driven Vascular Stenosis Using Biased Diffusion-Limited Aggregation with Formative and Destructive Particles

Taiga Kadowaki[(1)], Atsushi Tero[(2)]

(1) Joint Graduate School of Mathematics for Innovation, Kyushu University. (2) Institute of Mathematics for Industry, Kyushu University.

Abstract

Vascular stenosis involves both growth and degradation of plaque. **Diffusion-Limited Aggregation (DLA)**, proposed by Witten et al. [1], models pattern formation through the aggregation of diffusing particles. We extend this framework by introducing **formative and destructive particles in a biased field**. Extended model reproduces asymmetric, dynamic narrowing patterns, capturing the competition between growth and erosion. This offers a **simple numerical approach** to explore stenosis progression and potential therapeutic strategies.

1. Background

▶ Vascular Stenosis

○ Formation and Destruction

▶ DLA Model [1]

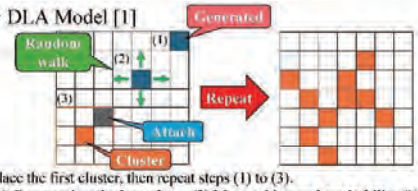

Place the first cluster, then repeat steps (1) to (3).
(1) Generated **at the boundary**. (2) Move with **equal probability** (¼ each).
(3) It sticks upon contacting any of the **8 neighboring cells of the cluster**.

▶ Purpose of our study

○ **Extend** DLA model to simulate both the formation and destruction of plaque.

- Introduce **spatial bias** into movement and generation probabilities to represent particles flowing through the vessel.
- Introduce **structure-breaking** (destructive) particles.

○ Analyze the resulting structures to gain insights into stenosis progression and treatment effectiveness.

2. Algorithm [2] : Generation and movement probabilities are determined by brightness values of input image.

▶ Biased particle generation

Example : 5 × 5 grid

0	0	0	0	0
0	0	0	$\frac{1}{20}$	$\frac{1}{20}$
0	$\frac{1}{20}$	$\frac{1}{20}$	$\frac{1}{20}$	$\frac{1}{20}$
0	$\frac{1}{20}$	$\frac{1}{20}$	$\frac{1}{10}$	$\frac{1}{10}$
$\frac{1}{20}$	$\frac{1}{20}$	$\frac{1}{10}$	$\frac{1}{10}$	$\frac{1}{10}$

Probability of generation at position x is determined by normalized brightness :

$$P_x = \frac{B_x}{\sum_y B_y}$$

B_x : Brightness value at position x

$B_x \in \{0, \cdots, 255\}$: 192 : 96 : 0

▶ Biased particle movement

Example : 5 × 5 grid

	0			
0	$\frac{1}{2}$	$\frac{1}{6}$		
	$\frac{1}{2}$	$\frac{1}{6}$	$\frac{1}{3}$	
			$\frac{1}{3}$	

Probability of moving from position x in 4 directions is determined by normalized brightness of 4 neighbors :

$$P_{x+d_i} = \frac{B_{x+d_i}}{\sum_{j=1}^{4} B_{x+d_j}}$$

B_x : Brightness value at position x
d_i : 4 directional unit vectors

▶ Destructive particles

- Generated and moves with same rules.
- Upon attaching to a cluster within its 8-neighbor region, it removes it.

3. Numerical Simulation : Comparing the 3 types of treatment.

▶ Result

1 : Constant treatment

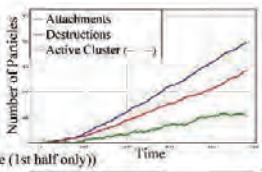

2 : Early treatment (× 2 destructive (1st half only))

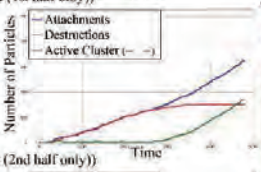

3 : Late treatment (× 2 destructive (2nd half only))

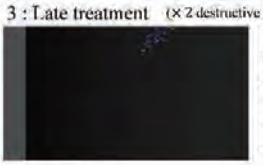

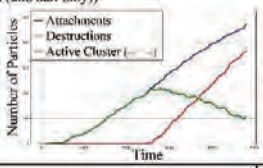

Final clustered particle count :

- **Constant : 108**
- **Early : 172**
- **Late : 106**

Early treatment showed the most growth !!

Why ?

Early destruction **inhibited clustering** and allowed wider diffusion of formative particles.

Unattached particles later contributed growth.

In Constant and Late treatment, clusters remained susceptible to destruction, limiting growth.

▶ Setting for simulation

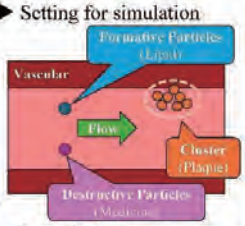

Generation map

Movement map

Particles are generated at scheduled times and move until attachment or absorption.

Parameter	
Grid size	275 × 150
Steps	480000
Formative	720
Destructive	480

Conclusion

- We extended DLA model to represent plaque growth.
- Our DLA-based model enabled comparison of 3 treatment types.

Future work

One future research direction is to extend by introducing time-dependent and structure-dependent probabilities for particle generation and movement.

References

[1] Witten, T. A., & Sander, L. M. (1983). Diffusion-limited aggregation. Physical Review B, 27(9), 5686–5697.

[2] Kadowaki, T., & Tero, A. (2025). Numerical simulation of plaque-driven vascular stenosis using biased DLA with formative and destructive particles. (in progress)

KYUSHU UNIVERSITY

Paradoxical Responses in Gambling Driven by Simple Neural Circuit Feedback

Taisei Kajimura

Graduate School of Mathematics, Kyushu University, Japan

This poster considers the decision to continue action despite repeated negative outcomes often seen in gambling. This is explained using a simple neural model that represents the interaction between the amygdala and the frontal lobe. Paradoxically, the model shows an inhibitory signal can activate the overall behavior, yielding a positive final outcome. This result suggests that a failure of inhibition can emerge from the physical dynamics of a simple neural circuit.

Paradoxical Responses in Gambling Driven by Simple Neural Circuit Feedback

Kajimura Taise(1), Tero Atsushi(2)
(1) Graduate School of Mathematics, Kyushu University, email: kajimura.taise.937@s.kyushu-u.ac.jp
(2) Institute of Mathematics for Industry, Kyushu University

1 Abstract

This poster considers the decision to continue action despite repeated negative outcomes often seen in gambling. This is explained using a simple neural model that represents the interaction between the amygdala and the frontal lobe. Paradoxically, the model shows an inhibitory signal can activate the overall behavior, yielding a positive final outcome. This result suggests that a failure of inhibition can emerge from the physical dynamics of a simple neural circuit.

2 Background

➢ Failure of Inhibition

A failure of inhibition is when a behavior continues destructively despite repeated losses.

This can lead to reckless choices based on the false belief that one is "due for a win".

➢ Model of Neural Circuit

This study uses a simple model to represent the interaction between the amygdala and the frontal lobe.

➢ Purpose

Explaining how positive input to the inhibitory system can activate action.

This is shown by numerical simulations and algebraic analysis.

3 Mathematical Model

➢ Model of Neural Circuit

$$\begin{cases} \dot{u} = k_1 u - k_2 v \\ \dot{v} = k_3 u - k_4 v - \alpha H(t) \end{cases}$$

v : actuator activity (frontal lobe)
u : inhibitor activity (amygdala)
$k_1 \sim k_4$: strengths of the interactions
H : loss as positive kick ($+\alpha$) to inhibitor

➢ Behavioral Activation

$$\dot{E} = -v(t)$$

E : negative integral of the inhibitor activity

The larger E value indicates, weaker frontal lobe inhibition and greater behavioral promotion.

diagram of the model structure

4 Numerical Simulation

➢ Numerical Results

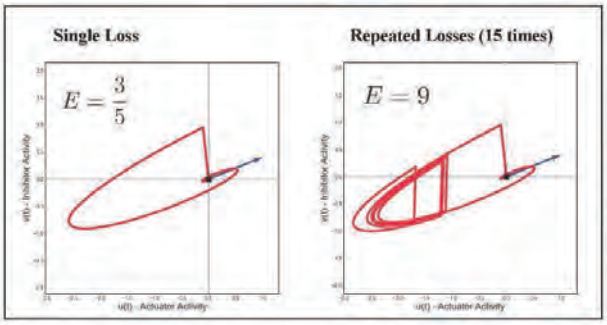

➢ Parameters Used

$$A = \begin{pmatrix} k_1 & -k_2 \\ k_3 & -k_4 \end{pmatrix} = \begin{pmatrix} 3 & -10 \\ 2 & -5 \end{pmatrix}$$

Total Simulation Time:	20.0s
Interval between Losses:	1.0s
Strength of Each Loss (α):	1.0

➢ Analytical results

$$E = \int_0^\infty -v(t)dt = \frac{-k_1 \alpha H_{total}}{k_2 k_3 - k_1 k_4}$$

5 Summary (✓) and Future Work (・)

- ✓ I have shown that a simple neural circuit model can reproduce the formation of paradoxical confidence.
- ✓ This suggests that a cognitive bias can be an emergent property of a neural circuit's parameters.
- ・ Future work will investigate whether other cognitive biases can be explained by this type of dynamical system model.

Reference
[1] Kajimura T., Tero A., Paradoxical Responses in Gambling Driven by Simple Neural Circuit Feedback (in progress).

Radon measure-valued solutions of compressible Euler equations and concentration boundary layers in unsteady inviscid flows passing solid obstacles

Liu Ke

School of Mathematical Sciences, East China Normal University, China

For time-dependent compressible Euler flows passing around a fixed solid body in three-dimensional space, there may exist an infinitesimally thin layer of concentrated mass, momentum and energy, wherein all particles impacting the body move along the body's windward boundary surface. By proposing a concept of Radon measurevalued solutions for initial-boundary-value problems of the unsteady compressible Euler equations, which captures both the large-scale three-dimensional distributions of the surrounding flows and the small-scale motions of particles on the two-dimensional boundary surfaces, we derive the governing partial differential equations for the concentration boundary layer --- an unsteady (pressureless) compressible Euler system defined on the boundary surface with appropriate source terms. This downscaling approach can be further generalized to incorporate skin-frictions and phasetransitions within the concentration boundary layer. It constitutes a novel methodology for addressing the complex fluid-solid-heat coupling problems encountered in fluid dynamics. Illustrative examples are presented to demonstrate the applicability of the proposed method to several specific problems, including the Newtonian-Busemann pressure laws of hypersonic aerodynamics.

Radon measure-valued solutions of compressible Euler equations and concentration boundary layers in unsteady inviscid flows passing solid obstacles

Ke Liu[1], Hairong Yuan[2]

School of Mathematical Sciences, East China Normal University[1,2]

52275500033@stu.ecnu.edu.cn[1], hryuan@math.ecnu.edu.cn[2]

Introduction

For time-dependent compressible Euler flows passing around a fixed solid body in three-dimensional space, there may exist an infinitesimally thin layer of concentrated mass, momentum and energy, wherein all particles impacting the body move along the body's windward boundary surface. By proposing a concept of Radon measure-valued solutions for initial-boundary-value problems of the unsteady compressible Euler equations, which captures both the large-scale three-dimensional distributions of the surrounding flows and the small-scale motions of particles on the two-dimensional boundary surfaces, we derive the governing partial differential equations for the concentration boundary layer — an unsteady (pressureless) compressible Euler system defined on the boundary surface with appropriate source terms. This down-scaling approach can be further generalized to incorporate skin-frictions and phase-transitions within the concentration boundary layer. It constitutes a novel methodology for addressing the complex fluid-solid-heat coupling problems encountered in fluid dynamics. Illustrative examples are presented to demonstrate the applicability of the proposed method to several specific problems, including the Newtonian-Busemann pressure laws of hypersonic aerodynamics.

The compressible Euler equations

The traditional formulation of the compressible Euler system of inviscid fluids:

$$\partial_t\rho + \mathrm{Div}(\rho U) = 0, \tag{1}$$

$$\partial_t(\rho U) + \mathrm{Div}(\rho U\otimes U) + \nabla p = \rho F, \tag{2}$$

$$\partial_t(\rho E) + \mathrm{Div}((\rho E + p)U) = \rho F\cdot U + \rho R - \mathrm{Div}(Q). \tag{3}$$

- ρ: the mass density of fluid $U=(u,v,w)\in\mathbb{R}^3$: the velocity of fluid
- $E=e+\frac{1}{2}|U|^2$: the total energy per unit mass e: the internal energy per unit mass
- p: the scalar pressure of fluid T: the temperature of fluid
- F: the body force per unit mass R: the heat supply per unit mass
- $Q=-\kappa\nabla T+Q_r$: the heat flux vector in $\mathbb{R}^3$
- κ: the thermal conductivity coefficient Q_r: the radiation heat transfer flux in $\mathbb{R}^3$
- The state functions of fluid: $p=\hat{p}(\rho,e)$, $T=\hat{T}(\rho,e)$

Radon measure-valued solutions

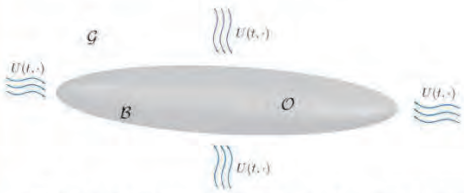

Lemma 3.1 (Projected integral formula). *Suppose that $\mathcal{B}$ is a two-dimensional oriented C^2 Riemannian manifold with boundary $\partial\mathcal{B}$, and isometrically embedded in $\mathbb{R}^3$. Let $U\colon\mathcal{B}\to\mathbb{R}^3$ be a C^1 vector field and $\phi\in C_c^1(\mathbb{R}^3)$. Then it holds*

$$\int_{\mathcal{B}} U\cdot\nabla\phi\,\mathrm{d}\mathcal{H}^2 = \int_{\mathcal{B}}(U\cdot n)(\nabla\widetilde{\phi}\cdot n)\,\mathrm{d}\mathcal{H}^2 - \int_{\mathcal{B}}\mathrm{div}_g(\varpi\widetilde{\phi}\,\mathrm{d}\mathcal{H}^2 - \int_{\partial\mathcal{B}} g(\widetilde{n},\varpi)\widetilde{\phi}\,\mathrm{d}\mathcal{H}^1, \tag{4}$$

where $\widetilde{\phi}=\phi|_{\mathcal{B}}$, and ϖ is the tangent component of U on $\mathcal{B}$. Moreover, n and $\widetilde{n}$ denote respectively the unit normal vector on $\mathcal{B}$ pointing into $\mathcal{O}$, and on $\partial\mathcal{B}$ pointing into $\mathcal{B}$.

Initial data:

$$(\varrho,\bar{U},\bar{e})\big|_{t=0} = \begin{cases}(\rho_0\mathcal{L}^3, U_0, e_0) & \text{in } \bar{\mathcal{G}},\\ (\widetilde{\rho}_0\delta_{\mathcal{B}}, \widetilde{U}_0, \widetilde{e}_0) & \text{on } \mathcal{B}.\end{cases} \tag{5}$$

Slip condition:

$$U\cdot n = 0 \quad \text{on } [0,\infty)\times\mathcal{B}, \tag{6}$$

Heat flux condition:

$$Q\cdot n = q \quad \text{on } [0,\infty)\times\mathcal{B} \tag{7}$$

Definition 3.1 (Rmvs). *Let $\varrho\in C([0,\infty);\mathscr{M}^1(\mathbb{R}^3))$ with $\varrho(t)$ nonnegative for $\mathcal{L}^1$-a.e. $t\geq 0$. We say that the (tensor-valued) Radon-measure-valued mappings*

$$\mathcal{M},\mathcal{E},\mathcal{K},\mathcal{F}_W,\mathcal{R},\mathcal{P}\in C([0,\infty);\mathscr{M}^1(\mathbb{R}^3)), \tag{8}$$

$$\mathcal{E}_f,\mathcal{K}_f,\mathcal{F},\mathcal{P}_f,\mathcal{Q}\in C([0,\infty);\mathscr{M}^3(\mathbb{R}^3)),\ \mathbb{M}\in C([0,\infty);\mathscr{M}^{3\times 3}(\mathbb{R}^3)) \tag{9}$$

and a time-dependent locally $\mathcal{H}^2$-integrable vector field $\sigma=\sigma(t)$ on $\mathcal{B}$ determine a Radon measure-valued solution (Rmvs) $(\varrho,\bar{U},\bar{e},\sigma)$ to the problem of unsteady compressible Euler flows passing the obstacle $\mathcal{O}$ with slip condition (6) and heat flux condition (7), provided that

i) [Linear relaxation] For any test function $\phi\in C_c^1([0,\infty)\times\mathbb{R}^3)$ and vector-valued test function $\varphi\in C_c^1([0,\infty)\times\mathbb{R}^3;\mathbb{R}^3)$, there hold

$$\int_0^\infty\langle\varrho(t),\phi_t\rangle\mathrm{d}t + \int_0^\infty\langle\mathcal{M}(t),\nabla\phi\rangle\mathrm{d}t + \langle\varrho(0),\phi(0,\cdot)\rangle + \int_0^\infty\int_{\partial\mathcal{B}} f_\varrho(t)\widetilde{\phi}\,\mathrm{d}\mathcal{H}^1\mathrm{d}t = 0, \tag{10}$$

$$\begin{aligned}&\int_0^\infty\langle\mathcal{E}(t)+\frac{1}{2}\mathcal{K}(t),\phi_t\rangle\mathrm{d}t + \int_0^\infty\langle\mathcal{E}_f(t)+\frac{1}{2}\mathcal{K}_f(t)+\mathcal{P}_f(t),\nabla\phi\rangle\mathrm{d}t + \langle\mathcal{E}(0)+\frac{1}{2}\mathcal{K}(0),\phi(0,\cdot)\rangle\\ &\quad+\int_0^\infty\langle\mathcal{F}_W(t),\phi\rangle\mathrm{d}t + \int_0^\infty\langle\mathcal{R}(t),\phi\rangle\mathrm{d}t + \int_0^\infty\langle\mathcal{Q}(t),\nabla\phi\rangle\mathrm{d}t\\ &\quad+\int_0^\infty\int_{\partial\mathcal{B}}(f_\mathcal{E}(t)+\frac{1}{2}f_\mathcal{K}(t)+f_\mathcal{Q}(t))\widetilde{\phi}\,\mathrm{d}\mathcal{H}^1\mathrm{d}t = \int_0^\infty\langle\varrho\delta_{\mathcal{B}},\phi\rangle\mathrm{d}t,\end{aligned} \tag{11}$$

$$\begin{aligned}&\int_0^\infty\langle\mathcal{M}(t),\varphi_t\rangle\mathrm{d}t + \int_0^\infty\langle\mathbb{M}(t),\nabla\varphi\rangle\mathrm{d}t + \int_0^\infty\langle\mathcal{P}(t),\mathrm{Div}\varphi\rangle\mathrm{d}t + \int_0^\infty\langle\mathcal{F}(t),\varphi\rangle\mathrm{d}t\\ &\quad+\langle\mathcal{M}(0),\varphi(0,\cdot)\rangle + \int_0^\infty\int_{\partial\mathcal{B}} f_\mathcal{M}(t)\cdot\widetilde{\varphi}\,\mathrm{d}\mathcal{H}^1\mathrm{d}t = \int_0^\infty\langle\sigma\delta_{\mathcal{B}},\varphi\rangle\mathrm{d}t.\end{aligned} \tag{12}$$

Here $q=q(t)$ is a time-dependent locally $\mathcal{H}^2$-integrable function on $\mathcal{B}$;

$$f_\varrho(t), f_\mathcal{M}(t), f_\mathcal{E}(t), f_\mathcal{K}(t), f_\mathcal{Q}(t)$$

are all given time-dependent bounded functions defined on the edge $\partial\mathcal{B}$, and they are supposed to be $\mathcal{H}^1$ measurable.

ii) [Nonlinear constraint] For $\mathcal{L}^1$-a.e. $t\geq 0$, the measures

$$\mathcal{M}(t),\mathcal{E}(t),\mathcal{K}(t),\mathcal{F}_W(t),\mathcal{R}(t),\mathcal{E}_f(t),\mathcal{K}_f(t),\mathcal{F}(t)$$

and $\mathbb{M}(t)$ are all absolutely continuous with respect to $\varrho(t)$, with the Radon-Nikodym derivatives

$$\bar{U}(t,\cdot)=\frac{\mathrm{d}\mathcal{M}(t)}{\mathrm{d}\varrho(t)},\quad \bar{e}(t,\cdot)=\frac{\mathrm{d}\mathcal{E}(t)}{\mathrm{d}\varrho(t)},\quad \bar{F}(t,\cdot)=\frac{\mathrm{d}\mathcal{F}(t)}{\mathrm{d}\varrho(t)},\quad \bar{R}(t,\cdot)=\frac{\mathrm{d}\mathcal{R}(t)}{\mathrm{d}\varrho(t)} \tag{13}$$

satisfying that

$$|\bar{U}|^2=\frac{\mathrm{d}\mathcal{K}(t)}{\mathrm{d}\varrho(t)},\quad \bar{F}\cdot\bar{U}=\frac{\mathrm{d}\mathcal{F}_W(t)}{\mathrm{d}\varrho(t)},\quad \bar{e}\bar{U}=\frac{\mathrm{d}\mathcal{E}_f(t)}{\mathrm{d}\varrho(t)},\quad |\bar{U}|^2\bar{U}=\frac{\mathrm{d}\mathcal{K}_f(t)}{\mathrm{d}\varrho(t)},\quad \bar{U}\otimes\bar{U}=\frac{\mathrm{d}\mathbb{M}(t)}{\mathrm{d}\varrho(t)}. \tag{14}$$

iii) [State function] Moreover, for $\mathcal{L}^1$-a.e. $t\geq 0$, the measures $\mathcal{P}(t),\mathcal{P}_f(t),\mathcal{Q}(t)$ are nonnegative, and if $\varrho(t)\ll\mathcal{L}^3,\mathcal{P}(t)\ll\mathcal{L}^3,\mathcal{P}_f(t)\ll\mathcal{L}^3,\mathcal{Q}(t)\ll\mathcal{L}^3$ on a Borel measurable set $V\subset\mathcal{G}$, then the corresponding Radon-Nikodym derivatives

$$\rho=\rho(t,\cdot)=\frac{\mathrm{d}\varrho(t)}{\mathrm{d}\mathcal{L}^3},\quad p=p(t,\cdot)=\frac{\mathrm{d}\mathcal{P}(t)}{\mathrm{d}\mathcal{L}^3},\quad Q=Q(t,\cdot)=\frac{\mathrm{d}\mathcal{Q}(t)}{\mathrm{d}\mathcal{L}^3} \tag{15}$$

satisfy $\mathcal{L}^3$-a.e. on V that

$$p=\hat{p}(\rho,\bar{e}),\quad \bar{p}\bar{U}=\frac{\mathrm{d}\mathcal{P}_f(t)}{\mathrm{d}\mathcal{L}^3}. \tag{16}$$

Concentration boundary layers

The interior of $\mathcal{G}$: $\mathring{\mathcal{G}}$

$$\varrho(t)=\rho\mathcal{L}^3\llcorner(\mathring{\mathcal{G}})+w_\rho(t)\delta_{\mathcal{B}},\quad \mathcal{M}(t)=\rho U\mathcal{L}^3\llcorner(\mathring{\mathcal{G}})+w_\rho(t)\bar{U}\delta_{\mathcal{B}},\quad \mathcal{E}(t)=\rho e\mathcal{L}^3\llcorner(\mathring{\mathcal{G}})+w_\mathcal{E}(t)\delta_{\mathcal{B}}, \tag{17}$$

$$\mathcal{K}(t)=\rho|U|^2\mathcal{L}^3\llcorner(\mathring{\mathcal{G}})+w_\rho(t)|\bar{U}|^2\delta_{\mathcal{B}},\quad \mathcal{F}_W(t)=\rho F\cdot U\mathcal{L}^3\llcorner(\mathring{\mathcal{G}})+w_\rho(t)\bar{F}\cdot\bar{U}\delta_{\mathcal{B}}, \tag{18}$$

$$\mathcal{R}(t)=\rho R\mathcal{L}^3\llcorner(\mathring{\mathcal{G}})+w_\rho(t)\bar{R}\delta_{\mathcal{B}},\quad \mathcal{E}_f(t)=\rho eU\mathcal{L}^3\llcorner(\mathring{\mathcal{G}})+w_\mathcal{E}(t)\bar{U}\delta_{\mathcal{B}}, \tag{19}$$

$$\mathcal{K}_f(t)=\rho|U|^2U\mathcal{L}^3\llcorner(\mathring{\mathcal{G}})+w_\rho(t)|\bar{U}|^2\bar{U}\delta_{\mathcal{B}},\quad \mathcal{F}(t)=\rho F\mathcal{L}^3\llcorner(\mathring{\mathcal{G}})+w_p(t)\bar{F}\delta_{\mathcal{B}}, \tag{20}$$

$$\mathbb{M}(t)=\rho U\otimes U\mathcal{L}^3\llcorner(\mathring{\mathcal{G}})+w_\rho(t)\bar{U}\otimes\bar{U}\delta_{\mathcal{B}},\quad \mathcal{P}(t)=p\mathcal{L}^3\llcorner(\mathring{\mathcal{G}})+w_p(t)\delta_{\mathcal{B}}, \tag{21}$$

$$\mathcal{P}_f(t)=p\bar{U}\mathcal{L}^3\llcorner(\mathring{\mathcal{G}})+w_p(t)\bar{U}\delta_{\mathcal{B}},\quad \mathcal{Q}(t)=Q\mathcal{L}^3\llcorner(\mathring{\mathcal{G}})+\bar{Q}\delta_{\mathcal{B}}. \tag{22}$$

$$w_\mathcal{E}=w_e-\mathrm{b}w_\rho-\mathscr{H}_T-\mathscr{H}_f+c_{\mathrm{CBL}}w_\rho,\quad \mathscr{H}_T(t,\cdot)=c\int_0^t\langle T(\epsilon,\cdot)\big|_{\mathcal{B}}-T_c\rangle\mathrm{d}w_\rho(\epsilon,\cdot). \tag{23}$$

$$\bar{\sigma}(t)=\sigma(t)-(\sigma(t)\cdot n)n,\quad \frac{\mathrm{d}\mathscr{H}_f(t,\cdot)}{\mathrm{d}t}=-g(\bar{\sigma}(t),\varpi(t)). \tag{24}$$

PDEs for concentration boundary layers(CBL) in $[0,\infty)\times\mathcal{B}$:

$$\partial_t w_\rho+\mathrm{div}_g(w_\rho\varpi)=\rho U\cdot n, \tag{25}$$

$$\partial_t(w_\rho\varpi)+\mathrm{div}_g(w_\rho\varpi\otimes\varpi)+\bar{\sigma}=w_\rho\widetilde{F}_\tau+\rho(U\cdot n)U_\tau, \tag{26}$$

$$\begin{aligned}&\partial_t(w_\mathcal{E}+\frac{1}{2}w_\rho g(\varpi,\varpi))+\mathrm{div}_g((w_\mathcal{E}+\frac{1}{2}w_\rho g(\varpi,\varpi))\varpi)+q\\ &\qquad=w_\rho\widetilde{F}\cdot\widetilde{U}+w_\rho\widetilde{R}-\mathrm{div}_g(\chi)+(pE+p)U\cdot n+Q\cdot n,\end{aligned} \tag{27}$$

$$w_p(t)\equiv 0. \tag{28}$$

Initial data on $\mathcal{B}$:

$$w_\rho(0)=\widetilde{\rho}_0,\quad \widetilde{U}(0)=\widetilde{U}_0,\quad w_\mathcal{E}(0)=\widetilde{\rho}_0\widetilde{e}_0. \tag{29}$$

Boundary conditions on $[0,\infty)\times\partial\mathcal{B}$:

$$g(\widetilde{n},w_\rho\varpi)=f_\varrho(t),\quad g(\widetilde{n},w_\rho\widetilde{U}\varpi)=f_\mathcal{M}(t),\quad g(\widetilde{n},w_\mathcal{E}\varpi)=f_\mathcal{E}(t), \tag{30}$$

$$g(\widetilde{n},w_\rho|\widetilde{U}|^2\varpi)=f_\mathcal{K}(t),\quad g(\widetilde{n},\chi)=f_\mathcal{Q}(t),\quad w_\rho\widetilde{U}\cdot n\equiv 0,\quad \bar{Q}\cdot n\equiv 0. \tag{31}$$

Generalized Newtonian-Busemann pressure law:

$$\boxed{\sigma_n\doteq\sigma\cdot n=w_\rho\widetilde{F}\cdot n+\rho(U\cdot n)^2+p-w_\rho g(\varpi,\varpi)k(\varpi).} \tag{32}$$

There are three examples, respectively on stationary hypersonic Euler flows passing wedges and cones, time-dependent CBL with phase-transition in one-spatial-dimensional flows, and evolution of CBL on a ramp with skin-friction.

Acknowledgements

This work is supported by the Shanghai Mu-nupality Science and Technology Commission under Grants No. 24ZR1420000 and No. 22DZ2229014. Special thanks goes to FMfI and the organizers of the conference!

Integrating Classical Numerical Methods into Deep Operator Networks

Kyoungjin Jung

Department of Mathematics, Ajou University, South Korea

Operator learning has emerged as a promising alternative to classical numerical solvers for partial differential equations (PDEs), directly learning mappings from source terms and boundary data to PDE solutions. Despite recent advances, existing neural operator approaches suffer from critical limitations, including reliance on large supervised datasets, poor generalization across diverse boundary conditions, and a failure to exploit known PDE structures such as linearity. In this work, we propose an unsupervised, physics-informed operator learning framework that integrates convolutional neural networks with classical numerical methods (finite difference and finite element). A decomposition approach splits the PDE into simpler subproblems, significantly reducing the required training data while enhancing generalization. Numerical experiments on 2D Poisson problems demonstrate that our method achieves superior accuracy and scalability compared to standard integrated models, even outperforming models trained on substantially larger datasets. Moreover, our method remains computationally feasible at fine grid resolutions where traditional numerical methods face prohibitive memory and computational costs.

Integrating Classical Numerical Methods into Deep Operator Networks

아주대학교 수학과 Ajou University | Presenter: Kyoungjin Jung | Supervisor: Dongwook Shin

Introduction

- **What is the neural operator?**
  - Classical numerical methods such as FDM and FEM provide accurate solutions.
  - However, solving parameterized families of PDEs across **varying** input functions —such as source terms f and boundary conditions g — requires **repeated** computation of large linear systems.

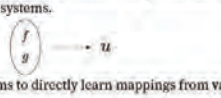

  - A neural operator model aims to directly learn mappings from **varying** input functions to PDE solutions.

- **Classical Solvers as Reference Operators**
  - To compare **fairly** with operator learning models, we assemble A and b using FEM and interpret the solution as a linear operator of the form:

$$u = A^{-1}b$$

  - Once A^{-1} is computed, it can be **reused** for any f and g by updating b.
  - Memory usage (**MB**) and inference time (**ms**) for precomputed A^{-1} and proposed model:

	Precomputed A^{-1}		Proposed Model		time ratio
Grid Size	Memory	Time	Memory	Time	(Model / A^{-1})
32×32	3.30	0.030	1.84	0.404	13.47
64×64	58.20	0.146	29.60	1.128	7.73
128×128	976.81	1.476	497.40	5.186	3.51

Aspect	Precomputed A^{-1}	Prior Models	Proposed Model
Training	Computing A^{-1}	Supervised	Unsupervised
Memory	High (dense matrix)	Very High (MLP)	Low (CNN)
Inference	Fast (matvec)	Fast (forward pass)	Fast (forward pass)
Generalization	Any f and g	Fixed f or g	Any f and g

Model Framework

- **Discretization**
  - Nodes are represented as pixels on a uniform grid
  - Convolutions embed the PDE's spatial structure

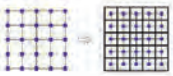

- **Convolutional Operator Network**

- **Problem Decomposition Scheme**

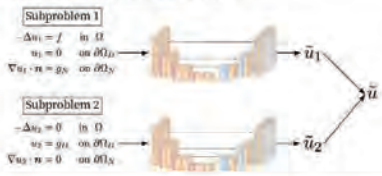

Methodology

- **Finite Difference Operator Network**

General Form	Finite difference convolution kernels
$\Delta_h u_{i,j} = \alpha (K * u_{i,j})$	$\Delta_h u_{i,j} = \frac{1}{h^2}\begin{bmatrix}0 & 1 & 0\\ 1 & -4 & 1\\ 0 & 1 & 0\end{bmatrix} * \begin{bmatrix} u_{i+1,j-1} & u_{i+1,j} & u_{i+1,j+1}\\ u_{i,j-1} & u_{i,j} & u_{i,j+1}\\ u_{i-1,j-1} & u_{i-1,j} & u_{i+1,j-1}\end{bmatrix}$
	$\Delta_h u_{i,j} = \frac{1}{6h^2}\begin{bmatrix}1 & 4 & 1\\ 4 & -20 & 4\\ 1 & 4 & 1\end{bmatrix} * \begin{bmatrix} u_{i+1,j-1} & u_{i+1,j} & u_{i+1,j+1}\\ u_{i,j-1} & u_{i,j} & u_{i,j+1}\\ u_{i-1,j-1} & u_{i-1,j} & u_{i-1,j-1}\end{bmatrix}$
$D_h^x u_{i,j} = \frac{1}{h}(\tilde{K} * u_{i,j})$	$D_h^x u_{i,j} = \frac{1}{h}\begin{bmatrix}-1 & 1\end{bmatrix} * \begin{bmatrix} u_{i,j} & u_{i+1,j}\end{bmatrix}$

$$\mathcal{L}_{FD} = \frac{1}{|M|}\sum_{(i,j)\in M}\left|K * \hat{u}_{i,j} - \frac{1}{\alpha} f_{i,j}\right|^2 + \frac{1}{|D|}\sum_{(i,j)\in D}|\hat{u}_{i,j} - g_{D_{i,j}}|^2 + \frac{1}{|N|}\sum_{(i,j)\in N}\left|\tilde{K} * \hat{u}_{i,j} - h\, g_{N_{i,j}}\right|^2$$

- **Finite Element Operator Network**

$$b_j = \int_\Omega f\psi_j\, dx + \int_{\partial\Omega_N} g\psi_j\, ds - \sum_{k=1}^{N} U_k \int_\Omega \nabla\psi_j \cdot \nabla\psi_k\, dx$$

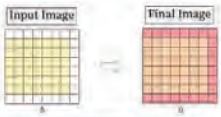

$$\mathcal{L}_{FE} = \frac{1}{|DOF|}\sum_{j\in DOF}|b_j - (A\hat{u})_j|^2$$

Numerical Experiments

- **Performance Evaluation**
  - Mean relative L^2 errors ($\times 10^{-2}$) with standard deviations ($\times 10^{-2}$):

$$\mathrm{Rel}(v) = \frac{\|u_h - v\|_2}{\|u_h\|_2}, \quad u_h\text{: reference FE solution}$$

  - f, g_D, and g_N are **independently** sampled from

$$m_0 \sin(n_0 x + n_1 y) + m_1 \cos(n_2 x + n_3 y)$$

  with uniform coefficients. (3,000 train / 1,000 test)

	FD-5		FD-9		FE-nrc		FE-tri	
Grid Size	$\hat{u}_1$	$\hat{u}_2$	$\hat{u}_1$	$\hat{u}_2$	$\hat{u}_1$	$\hat{u}_2$	$\hat{u}_1$	$\hat{u}_2$
32 × 32	1.71 ± 0.02	1.81 ± 0.12	1.65 ± 0.01	1.75 ± 0.03	0.69 ± 0.40	0.30 ± 0.07	0.57 ± 0.08	0.35 ± 0.11
64 × 64	1.91 ± 0.13	1.31 ± 0.19	1.16 ± 0.04	1.08 ± 0.12	3.02 ± 0.66	0.95 ± 0.28	2.93 ± 0.68	0.99 ± 0.31
128 × 128	1.23 ± 0.08	1.67 ± 0.06	1.58 ± 0.29	0.57 ± 0.02	0.69 ± 1.04	0.98 ± 0.12	7.94 ± 1.26	1.01 ± 0.17

	FD-5		FD-9		FE-nrc		FE-tri	
Grid Size	$\hat{u}_1$	$\hat{u}_2$	$\hat{u}_1$	$\hat{u}_2$	$\hat{u}_1$	$\hat{u}_2$	$\hat{u}_1$	$\hat{u}_2$
32 × 32	7.89 ± 0.22	1.09 ± 0.02	7.33 ± 0.01	1.05 ± 0.01	0.36 ± 0.10	0.52 ± 0.52	0.36 ± 0.05	0.35 ± 0.11
64 × 64	3.57 ± 0.24	1.01 ± 0.19	3.82 ± 0.03	0.82 ± 0.26	0.98 ± 0.26	0.95 ± 0.28	0.92 ± 0.31	0.98 ± 0.31
128 × 128	10.91 ± 0.46	0.88 ± 0.05	2.21 ± 0.06	0.45 ± 0.02	0.39 ± 0.03	1.01 ± 0.11	0.36 ± 0.05	1.05 ± 0.16

- **Why is the decomposition scheme effective?**
  - Subproblems 100 samples each
  - Evaluated on 5000 original problems

	FE-nrc	
Grid Size	$\hat{u}_1$	$\hat{u}_2$
32 × 32	0.95	0.36
64 × 64	1.40	0.07
128 × 128	4.16	0.67

Conclusion

- We present an unsupervised, convolution-based operator learning method.
- For linear problems, a **decomposition** into subproblems improves generalization and training efficiency.
- The method can be **extended** to nonlinear and time-dependent PDEs, where classical solvers become increasingly costly due to repeated solves.

References

[1] Kyoungjin Jung, 2025. Integrating Classical Numerical Methods into Deep Operator Networks. (Master's thesis). Ajou University.
[2] Jae-Yong Lee, Seungchan Ko, and Youngjoon Hong. Finite Element Operator Network for Solving Elliptic-Type Parametric PDEs, MAM J. Sci. Comput. 47 (2022), no. 2, C201–C226. MR 4484707
[3] Lu Lu, George Em Karniadakis, et al. Learning nonlinear operators via deeponet based on the universal approximation theorem of operators, Nature Machine Intelligence 3 (2021), no. 3, 218–229.

Deep Learning-Based Prediction of Underground Utility Locations Using Novel Feature Engineering Method

Kang Meiyan

Department of Mathematics, Ajou University, Korea

Understanding subsurface characteristics is essential to reduce unexpected hazardous during excavation. Electrical resistance values are a crucial key for predicting underground conditions with the presence of utilities. Electrical resistance module, developed through generalized mesh techniques, is applied to produce the electrical resistance data according to geometrics parameters of electrodes and structures. In this study, various machine learning techniques such as Support Vector Machine(SVM), Random Forest, and XG-Boost were used for classification of underground utility counts. Additionally, a deep learning, Convolution Neural Networks (CNN) was employed to analyze by transforming resistivity data into a 2-D matrix format. The results show that the data contain sufficient information to determine the number of pipes present underground.

2025 Topological Data Analysis and Industrial Mathematics

Topology and Distribution Integration for Pipe Localization in GPR Data

Meiyan Kand
Ph.D. Candidate
miyeon@ajou.ac.kr

Suyoung Choi
Advisor. Professor
schoi@ajou.ac.kr

亞洲大学校 AJOU UNIVERSITY

Introduction

Ground Penetrating Radar (GPR) is a widely adopted non-destructive testing (NDT) technique for subsurface sensing, particularly in infrastructure inspection. However, conventional methods often struggle to capture the structural and spatial characteristics of buried objects. In this study, we propose an integrated framework that leverages Topological Data Analysis (TDA) and Kernel Density Estimation (KDE). TDA extracts stable topological features from B-scan images, and KDE models their spatial distribution. By measuring distances between these distributions, we localize subsurface targets such as pipes.

Data Description

A typical GPR survey setup is illustrated in Fig. 1(a) illustrates in the field, included here for visual context. While this study does not use real-world data, the same principles are replicated in simulation. We generated 341 synthetic B-scan images using the open-source FDTD simulator gprMax. The simulation domain included a single buried pipe and multiple soil layers. A representative simulation set up and its synthetic B-scan output are shown in Fig. 1(b).

(a) Field Data collection (b) gprMax synthetic B-scan generated.

Fig. 1: Field Data Collection and Simulated Data Generation

Toplogical Feature Extraction

We applied topological data analysis (TDA) to extract structural patterns from simulated GPR images as illustrated in Fig.2. H_1 loops are extracted, some sample are shown in Fig. 3, which indicate circular or arc-like structures that potentially correspond to buried pipes.

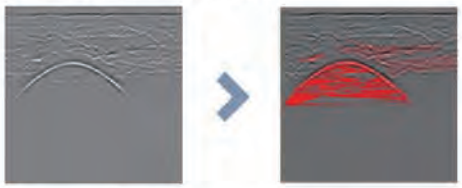

Fig. 2: From raw B-scan to extracted H_1 loops for shape analysis.

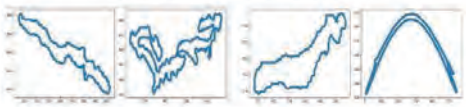

Fig. 3: Detected H_1 features (in red) highlighting arc-like pipe structures.

Distribution-Based Detection

To identify pipe-like patterns, we focus on classifying the detected H_1 loops based on their spatial distributions.
Fig. 4 shows these procedures.

Step 1. Select a representative parabolic shape as a reference.

Step 2. Using Kernel Density Estimation (KDE) get the spatial distribution of each H_1 features.

Step 3. The similarity between distributions is quantified using the Wasserstein distance.

Step 4. Features exhibiting similar KDE profiles are classified as pipe-related, while dissimilar ones are discarded.

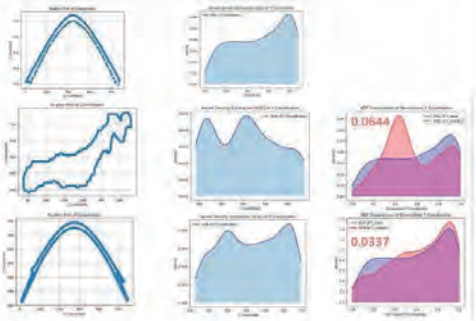

Fig. 4: Classification of KDE-based features using Wasserstein distance.

Results

The framework achieved an F1-score of 0.86, with balanced precision and recall (both 0.86), as summarized in Fig. 5. Although the overall accuracy was 0.76, the high F1-score highlights the model's robustness in handling potential class imbalance. The confusion matrix shows a high number of true positives and relatively few false detections, confirming the method's reliability.

Metric	Values
Accuracy	0.76
F1	0.86
Recall	0.86
Precision	0.86

Fig. 5: Evaluation metrics showing F1-score, precision, recall, and accuracy.

Conclusion

This study explores a topology- and distribution-driven approach, which shows initial promise. However, its performance can be further improved, and real-world validation remains necessary.

Mathematical Model of Ant Transport Networks that can Adapt to Changes in Resource Quality

Kazuhiro Minami

Graduate School of Mathematics, Kyushu University, Japan

Biological transport networks have evolved through many processes of natural selection and possess the ability to adapt to environmental changes. For example, in an experiment by Latty et al. (2017), Argentine ants were observed to adjust their allocation of workers according to food concentration, sending more ants to areas with higher food quality. Based on this observation, we assumed the existence of two types of ants – scout ants and homebound ants – and developed a mathematical model using ordinary differential equations that can adapt to changes in resource quality.

Mathematical Model of Ant Transport Networks that can Adapt to Changes in Resource Quality

Kazuhiro Minami(1), Atsushi Tero(2)
(1) Graduate School of Mathematics, Kyushu University. email : minami.kazuhiro.380@s.kyushu-u.ac.jp
(2) Institute of Mathematics for Industry, Kyushu University

Abstract

Biological transport networks possess the ability to adapt to environmental changes. For example, Argentine ants have been observed to adjust their allocation of workers according to food concentration, sending more ants to areas with higher food quality[1].

Based on this observation, we assumed the existence of two types of ants - **scout ants** and **homebound ants** - and developed a model that can adapt to changes in resource quality.

Experiment [1]

- When three sources of food are placed around the ants' nest, ants form trails leading to each one.
- When the food concentrations change, ants tend to gather more at the source with higher concentration.

Network made by ants

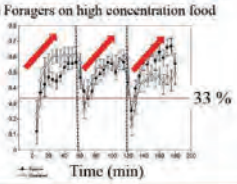

Mathematical Model [2][3][4]

○ **Choose edge with high pheromone concentration.**

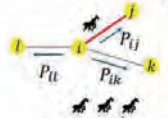

○ **Pheromone increase as ants pass over edge and decrease with evaporation.**

○ **Follow each other's pheromone trails.**

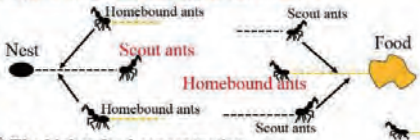

○ **The higher food concentration, the more pheromone Homebound ants deposit.**

	Scout Ants	Homebound Ants
Probability that ants on node i move to node j	$P_{ij}^S = \frac{(k+\sum_{l=1}^{f} D_{ij}^{H_l})/L_{ij}}{\sum_{e\in E_i}(k+\sum_{l=1}^{f} D_e^{H_l})/L_e}$	$P_{ij}^{H_l} = \frac{(k+D_{ij}^S)/L_{ij}}{\sum_{e\in E_i}(k+D_e^S)/L_e}$
Flow from node i to node j	$Q_{ij}^S = N_i^S P_{ij}^S - N_j^S P_{ji}^S$	$Q_{ij}^{H_l} = N_i^{H_l} P_{ij}^{H_l} - N_j^{H_l} P_{ji}^{H_l}$
Time evolution of Pheromone on edge ij (D_{ij})	$\frac{dD_{ij}^S}{dt} = \frac{(Q_{ij}^S)^2}{1+(Q_{ij}^S)^2} - rD_{ij}^S$	$\frac{dD_{ij}^{H_l}}{dt} = \frac{(c_l Q_{ij}^{H_l})^2}{1+(c_l Q_{ij}^{H_l})^2} - rD_{ij}^{H_l}$
Time evolution of Ants number on node i (N_i)	$N_i^S = 0$ (if i : food node) $\frac{dN_i^S}{dt} = \begin{cases} \sum_{j\in A_i} Q_{ji}^S + M & \text{(if } i \text{ : nest node)} \\ \sum_{j\in A_i} Q_{ji}^S & \text{(if } i \text{ : otherwise)} \end{cases}$	$N_i^{H_l} = 0$ (if i : nest node) $\frac{dN_i^{H_l}}{dt} = \begin{cases} \sum_{j\in A_i}(Q_{ji}^{H_l}+Q_{ji}^S) & \text{(if } i \text{ : food node)} \\ \sum_{j\in A_i} Q_{ji}^{H_l} & \text{(if } i \text{ : otherwise)} \end{cases}$

<Variable>
P_{ij} : Probability that ants on node i move to node j
Q_{ij} : Flow from node i to node j
D_{ij} : Pheromone amount on edge ij
N_i : Ants number on node i
c_l : Concentration of food l (change periodically)
<Constant>
k : Reactivity to pheromone
L_{ij} : Length of edge ij
f : Number of sources of food
r : Evaporation rate
M : Number of ants from the nest
<Index>
S : Scout ants
H_l : Homebound ants from food l
E_i : Set of edges connected to node i
A_i : Set of neighbors of node i

Simulation result 1 (Simple network)

We cycle a concentration of 2 among Food 1, 2, and 3 across successive intervals (others are 1, interval = 30).

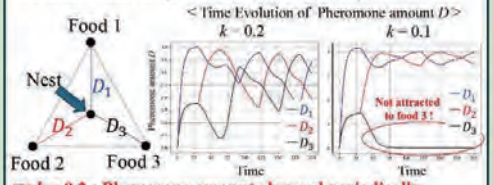

☞ $k = 0.2$: Pheromone amount changed periodically.
$k = 0.1$: Most ants are attracted to Food 1 & Food 2.

Simulation result 2 (Complex network)

We ran same simulation on more complex network.

☞ **As homebound ants deposited more pheromone from high-concentration food, more scout ants were attracted to that location.**

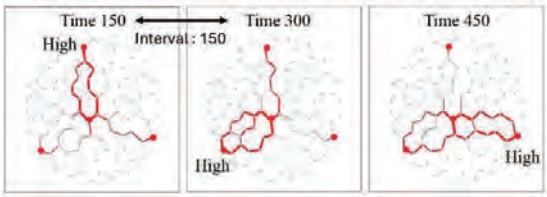

Discussion (✓) & Future works (□)

- ✓ We could reproduce ants' networks which can adapt to changes in source quality by assuming the existence of **scout ants** and **homebound ants**.
- ✓ The value of k is associated with ants' ability to adapt to changes in source quality.
- □ Analyze mathematically the relationship between food concentration and distance from the nest.
- □ Apply this model to human society like traffic networks.

Reference
[1] Lelly, T., Holmes, M. J., Makinson, J. C., & Beekman, M. (2017). Argentine Ants (*Linepithema Humile*) Use Adaptable Transportation Networks to Track Changes in Resource Quality. *Journal of Experimental Biology*, *220*(4), 684–694. https://doi.org/10.1242/jeb.144238
[2] Ma, Q., Johansson, A., Tero, A., Nakagaki, T., & Sumpter, D. J. t. (2013). Current-Reinforced Random Walks for Constructing Transport Networks. *Journal of The Royal Society Interface*, *10*(80). https://doi.org/10.1098/rsif.2012.0661
[3] Dorigo, M., & Stützle, T. (2004). *Ant Colony Optimization*. Bradford Books.
[4] Minami, K., & Tero, A. (2025). Mathematical Model of Ant transport Networks, in progress.

Kernel von Mises Formula of the Influence Function

Yaroslav Mukhin

CDSES, Economics and Statistics at Cornell University, USA

The influence function (also known as the first variation and Fisher-Rao gradient) of a statistical functional is the Riesz representer of its derivative operator. It is a key analytic object in both the theory and implementation of estimators in semiparametric models, e.g., one-step adaptive estimator, targeted learning, debiased machine learning, Furthermore, it is essential for inference about their statistical properties robustness and interpretability, e.g., for finding confidence intervals, partial identification and isspecification bounds, adversarial perturbations, influential data points. However, the analytic derivation of the influence function is often an obstruction to the broader adoption of these methods by practitioners. Toward automating this task, we derive a regularized representation of the influence function using spectral theory of positive semidefinite kernels. Based on this representation we construct an estimator that: (i) is a nonparametric functional RKHS estimator; (ii) admits theoretical guarantees in function norms relevant for downstream tasks; (iii) can be computed via automatic differentiation or finite differences, without requiring analytic derivation by the user.

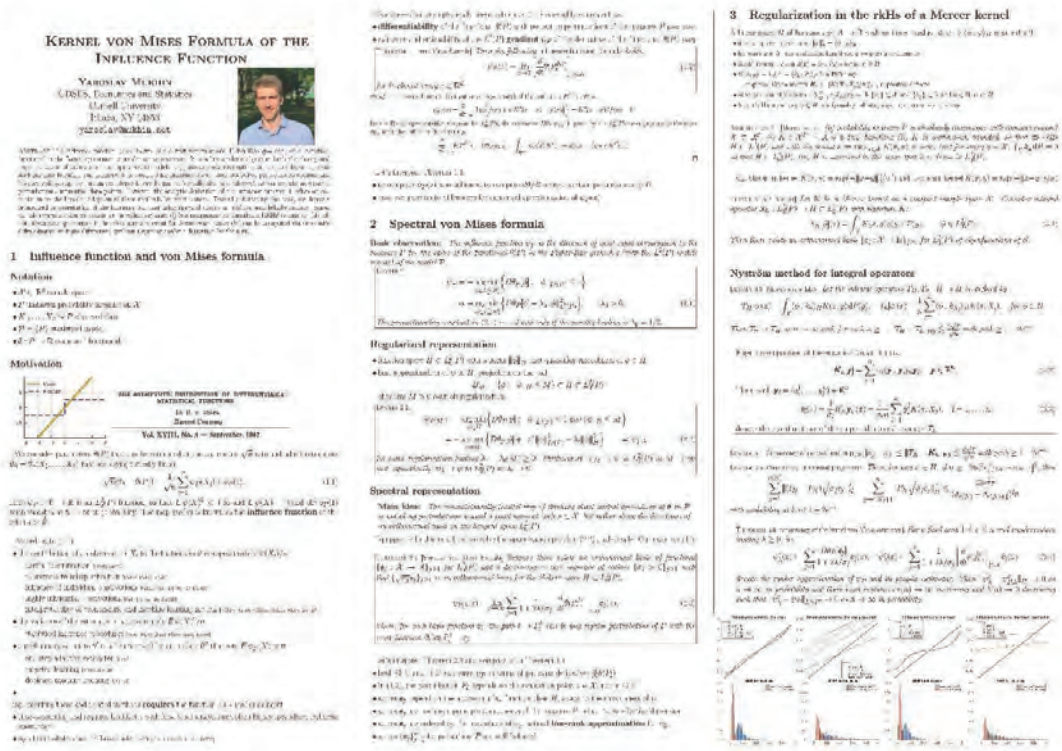

Kernel von Mises Formula of the Influence Function

Yaroslav Mukhin
CMSES, Economics and Statistics
Cornell University
Ithaca, NY 14850
yaroslav@cmkbcn.net

1 Influence function and von Mises formula

Notation

Motivation

THE ASYMPTOTIC DISTRIBUTION OF DIFFERENTIABLE STATISTICAL FUNCTIONS

By R. v. Mises
Harvard University

Vol. XVIII, No. 3 — September, 1947

2 Spectral von Mises formula

Regularized representation

Spectral representation

3 Regularization in the rkHs of a Mercer kernel

Nyström method for integral operators

Causal Inference in Legal Decision-Making

Shingo Murakami

Joint Graduate School of Mathmatics for Innovation

This study introduces a novel approach to quantifying legal causation using mathematical methods. Specifically, it employs the Probability of Necessity (PN) to assess the likelihood that a certain individual’s disease is caused by exposure. In Japanese legal practice, Percent Attributable Risk (PAR) has traditionally been adopted as if it had represented the probability of causation. However, it can differ from true probability, PN. This research points out that Japanese legal practice implicitly has equated PAR and PN and reveals the assumptions underlying this equation. Furthermore, we propose theoretically proper decision frameworks that remain applicable even when such assumptions do not hold.

Causal Inference in Legal Decision-Making

Attorney at Law Shingo Murakami [1,2] (Supervisor: Shizuo Kaji, Shinto Teramoto)

[1]Joint Graduate School of Mathematics for Innovation, Kyushu University, [2]Fukuoka Bar Association
MAIL: murakami.shingo.093@s.kyushu-u.ac.jp, WEBSITE: https://sites.google.com/view/shingo-murakami/

Case

> A lives in an area with air pollution and has developed a lung disease.
> A sued Company B, operating in A's neighborhood, to seek compensation.
> In order to demonstrate B's contribution to A's disease, A must prove that,
> *but for the pollution, they would not have developed the lung disease.*

Question: How can we define and estimate the probability of "But for...?"

Answer: We should use the *probability of necessity* (PN) [6].

Potential Outcomes Model

First, we assume the population can be divided into four types, as in Table 1 [1].

Each type is further split into two subtypes: exposed and unexposed to air pollution. Therefore, the population is divided into eight types (Table 2).

Type	If exposed	If unexposed
Doomed	○	○
Causative	○	×
Preventive	×	○
Immune	×	×

Table 1. ○ : Diseased, × : Disease-free.
For example, Individuals of the "causative" type would be diseased if exposed and disease-free if unexposed.

Type	Exposed group	Unexposed group
Doomed	d	d'
Causative	c	c'
Preventive	p	p'
Immune	i	i'

Table 2. Each symbol denotes the proportion of individuals belonging to each type.
As the proportions sum to unity, $d-d'=c+c'+p-p'=i+i'=1$.

However, we can only observe a single world (i.e., whether they are exposed or not), so we can't tell which type each individual belongs to.

Structural Causal Model

Let Z, U_X, X, Y be random variables.

- $Z \in \{\mathrm{D}, \mathrm{C}, \mathrm{P}, \mathrm{I}\}$
  - $P(Z=\mathrm{D}) = d - d'$, $P(Z=\mathrm{C}) = c - c'$, $P(Z=\mathrm{P}) = p + p'$, $P(Z=\mathrm{I}) = i + i'$
  - Z represents A's type, i.e., doomed, causative, preventive, or immune.
- $U_X \sim U(0,1)$
- $X = 1$, iff $(Z \in \{\mathrm{D}\} \wedge U_X \in [0, d/(d-d'))) \vee (Z \in \{\mathrm{C}\} \wedge U_X \in [0, c/(c-c'))) \vee (Z \in \{\mathrm{P}\} \wedge U_X \in [0, p/(p+p'))) \vee (Z \in \{\mathrm{I}\} \wedge U_X \in [0, i/(i+i')))$
  - X is binary and represents whether A is exposed or not.
- $Y = 1$, iff $(X \in \{1\} \wedge Z \in \{\mathrm{D}, \mathrm{C}\}) \vee (X \in \{0\} \wedge Z \in \{\mathrm{D}, \mathrm{P}\})$
  - Y is binary and represents whether A is diseased or not.

Then, we modify the above model by setting $X = x$ independently from Z and U_X for $x \in \{0, 1\}$. We call this modification *intervention*. See Figure 1).

In this modified model, Y is denoted as $Y_{X=x}$, which is the outcome if X were set to x.

- $Y_{X=0} = 1$, iff $Z \in \{\mathrm{D}, \mathrm{P}\}$
- $Y_{X=1} = 1$, iff $Z \in \{\mathrm{D}, \mathrm{C}\}$

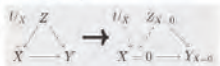

Figure 1. Intervention

Now we can define the *probability of necessity* (PN) as follows [6].

$$\mathrm{PN} := P(Y_{X=0} = 0 \mid X = 1, Y = 1)$$

The Relationship Between Two Models

The probability of random variables can be represented as follows:

$$P(X=1, Y=1) = d - c \quad \text{(exposed \& diseased)} \tag{1a}$$
$$P(X=1, Y=0) = p - i \quad \text{(exposed \& disease-free)} \tag{1b}$$
$$P(X=0, Y=1) = d' - p' \quad \text{(unexposed \& diseased)} \tag{1c}$$
$$P(X=0, Y=0) = c' + i' \quad \text{(unexposed \& disease-free)} \tag{1d}$$

E.g., (1a) shows the proportion of people who are both exposed and diseased is $d - c$.

In addition, the probability of $Y_{X=1}$ and $Y_{X=0}$ can be represented as follows:

$$P(Y_{X=1}=1) = d - d' + c + c' \quad \text{(If exposed, diseased)} \tag{2a}$$
$$P(Y_{X=1}=0) = p + p' + i + i' \quad \text{(If exposed, disease-free)} \tag{2b}$$
$$P(Y_{X=0}=1) = d - d' + p + p' \quad \text{(If unexposed, diseased)} \tag{2c}$$
$$P(Y_{X=0}=0) = c + c' + i - i' \quad \text{(If unexposed, disease-free)} \tag{2d}$$

E.g., (2a) shows, if everyone in the population were exposed, the proportion of individuals who would become diseased is $d + d' + c + c'$.

We can also represent PN as follows:

$$\mathrm{PN} := P(Y_{X=0} \mid X = 1, Y = 1) = \frac{c}{d-c} \tag{3}$$

This represents the proportion of individuals who would have remained disease-free had they not been exposed (i.e., "causative") in the exposed and diseased group.

Legal Practice in Japan: The Flawed Logic of Causation

In Japanese legal practice, *percent attributable risk* (PAR), which can be calculated solely from observation data, is used as if it represents the probability of causation [2].

$$\mathrm{PAR} := 1 - \frac{P(Y=1 \mid X=0)}{P(Y=1 \mid X=1)} \quad 1 - \frac{(d'-p') / (d'+p'+c'+i')}{(d-c)/(d-c+p-i)}.$$

In the below example (Table 3 and Figure 2), PAR can be calculated as follows:

$$\mathrm{PAR} = 1 - \frac{400/(400+200)}{500/(500+100)} = 1 - \frac{400}{500} = 0.2$$

	Exposed group	Unexposed group
Diseased	500/1200	400/1200
Disease-free	100/1200	200/1200

Table 3. Example. The effect of exposure appears to be limited, as there is little difference in the proportion of diseased individuals between the exposed and unexposed groups.

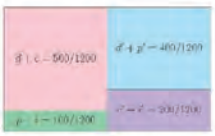

Figure 2. PAR = 0.2; not so high.

In Japanese legal practice, victim A is unlikely to be awarded since PAR is small.

Japanese legal practitioners and scholars often implicitly equate PAR with PN, based on the following assumptions [4]:

1. Individuals of the "doomed" type are equally likely to be exposed or unexposed, i.e., $d/(d+c+p+i) = d'/(d'+p'+c'+i')$.
2. Individuals who are unexposed and diseased would not have been disease-free if they had been exposed — exposure cannot improve health outcomes, i.e., $p' = 0$.

These assumptions imply that the boundary between the "causative" and "doomed" types is represented by a dashed line in Figure 3.

Under those assumptions, we can find c, and this directly indicates the effect of exposure.

So, without those assumptions, how can A demonstrate that PN is large under general conditions?

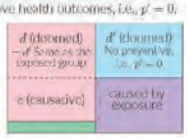

Figure 3. PN = PAR

Proposal: Utilizing Inequality and Additional Information

In general, the following inequality holds [6]:

$$\max\left\{0, \frac{c-p}{d-a}\right\} \le \mathrm{PN} \le \min\left\{1, \frac{c+i}{d+c}\right\} \tag{4}$$

We can estimate the value in (1a) to (1d) from solely observation data.

Furthermore, under certain assumptions, we can calculate the value in (2a) to (2d) [6].

Therefore, we can know the max and min of (4) using the following formula:

$$c - p \quad (d+c) + (d'+p') - (d+d'+p-p')$$
$$c + i \quad (c+c'+i-i') - (c'-i')$$

Assume that we can tell the value of $P(Y_{X=0}=1)$ is 7/15 in the above example.

Since $d - d' - p + p'$ 7/15 and $c + c' + i - i'$ 8/15, the following inequality holds:

$$0.68 \le \mathrm{PN} \le 0.88$$

Although the exact value of PN is unclear, it is evidently larger than PAR.

Moreover, adding individual information allows for more precise estimation [3].

Table 4 shows data on non-smokers.

If $P(Y_{X=0}=1 \mid \text{non smoker}) = 13/24$,

$$0.8 \le \mathrm{PN} \le 1.0.$$

	Exposed group	Unexposed group
Diseased	300/720	240/720
Disease-free	60/720	120/720

Table 4. Subpopulation of Table 3 limited to non-smokers.

Although PAR is also 0.2, A could be awarded since PN is sufficiently large.

Judges can revise their beliefs based on additional information. This proposal refines Ota's theory, a mathematical model of legal reasoning [5]. A more detailed explanation is currently being developed as a part of ongoing joint research [4].

References

[1] Sander Greenland and James M. Robins, "Identifiability, Exchangeability, and Epidemiological Confounding," International Journal of Epidemiology 15 (1986), no. 3, 413–419.
[2] Hisashi Kawano, ed., *Theory and Practice of Pollution and Environmental Dispute Resolution I* (Daiichi Hoki Shuppan Co., Ltd., Tokyo, 1978). (Japanese).
[3] Manabu Iwasaki and Zhi Geng, "Bounds for Probabilities of Causation When Some Confounders Are Unmeasured," Statistics in Medicine 38 (2019), no. 3, 454–472.
[4] Shingo Murakami and Shinto Teramoto, *Causal and Stochastic Tools*, in progress.
[5] Shozo Ota, "Formulation of proof: Theory to date: A Bayesian reconstruction of fact-finding and the system of proof," Hokkaido Law Review 1992 (Japanese).
[6] Judea Pearl, *Causality*, 2nd ed., Cambridge University Press, 2009.

This work was supported by JSPS KAKENHI Grant Number JP25KJ1896.

Non-Brain Memory Mechanism Based on Simplified Reaction–Diffusion System

Kota Nishi

Joint Graduate School of Mathematics for Innovation, Kyushu University, Japan

Human beings possess the capacity for memory, which is governed by brain function. On the other hands, it has been reported that true slime mold, which does not have a brain, possess the ability to memorize repeated stimuli and alter its behavior accordingly. In our study, we developed a mathematical model of slime mold locomotion driven by a chemical reaction–diffusion process. From our analysis of the model, we found that the accumulation of a chemical induced by repeated stimuli stores the stimulus history.

Non-Brain Memory Mechanism Based on Simplified Reaction–Diffusion System

○Kota Nishi[1], Atsushi Tero[2], Yukinori Nishigami[3], Toshiyuki Nakagaki[3]

1. Joint Graduate School of Mathematics for Innovation, Kyushu University. e-mail: nishi.kota.560@s.kyushu-u.ac.jp
2. Institute of Mathematics for Industry, Kyushu University. 3. Research Institute for Electronic Science, Hokkaido University.

1. Background

➢ Key words

- Habituation (non-associative learning)
  → Accustomed to stimulus through repeated application
- True slime mold
  → Single-celled organism (Lacks a brain)
  → Habituation is reported. (Reflects past stimuli in next behavior)

Physarum polycephalum, true slime mold

How slime mold memorizes past stimuli?

➢ Habituation in true slime molds [1]

- Methods

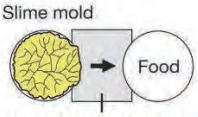

Aversive bridge (b-A)
or
Normal bridge (b-N)

b-A ... Aversive chemical (quinine) is contained

- Results

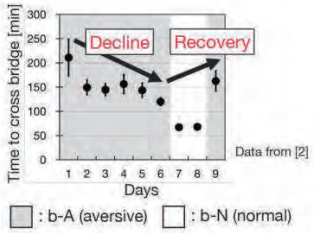

2. Modeling

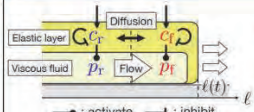

$c_\mathrm{f}, c_\mathrm{r}$: chemical concentration at front / rear

$p_\mathrm{f}, p_\mathrm{r}$: fluid pressure at front / rear

$\ell(t)$: position of slime mold's tip

Identify p_* with c_* $(p_\mathrm{f} = c_\mathrm{f}, p_\mathrm{r} = c_\mathrm{r})$

$$\frac{d}{dt}\ell(t) = \gamma(p_\mathrm{r}(t) - p_\mathrm{f}(t))$$

$$\frac{d}{dt}p_\mathrm{f}(t) = d(p_\mathrm{r} - p_\mathrm{f}) + F_\mathrm{f}(p_\mathrm{f})$$

Diffusion Reaction

$$\frac{d}{dt}p_\mathrm{r}(t) = r_\mathrm{v} d(p_\mathrm{f} - p_\mathrm{r}) + F_\mathrm{r}(p_\mathrm{r})$$

$r_\mathrm{v} = V_\mathrm{f}/V_\mathrm{r}$ (Volume ratio)

$$F_\mathrm{f}(p_\mathrm{f}) = (1-h(t))(-a_\mathrm{de} p_\mathrm{f} + g_\mathrm{f}) + h(t)(-a^s_\mathrm{de} p_\mathrm{f} + g^s_\mathrm{f})$$

$$F_\mathrm{r}(p_\mathrm{r}) = -a_\mathrm{de} p_\mathrm{r} + g_\mathrm{r}$$

$$h(t) = \begin{cases} 1 & \text{(Under stimulation)} \\ 0 & \text{(Under no stimulation)} \end{cases}$$

3. Simulation

➢ Settings

- Case b-A on day n

$$h(t) = \begin{cases} 1 & (t_{n-1} \le t < t_{n-1} + T_\mathrm{s}) \\ 0 & (t_{n-1} + T_\mathrm{s} \le t < t_n) \end{cases}$$

- Case b-N on day n

$h(t) = 0$ $(t_{n-1} \le t < t_n)$, $t_n = 24n$

Ex. day 1: b-A, day 2: b-N

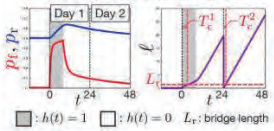

➢ Results

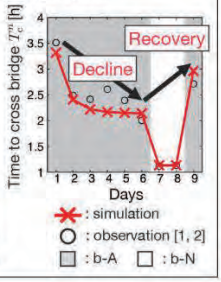

4. Analysis

➢ Change of variables

$$A(t) = p_\mathrm{r} + r_\mathrm{v} p_\mathrm{f} \ (= c_\mathrm{r} + r_\mathrm{v} c_\mathrm{f})$$

Total amount of a chemical

$$R(t) = p_\mathrm{r} - p_\mathrm{f}$$

Response (tip expansion velocity)

Transformed equation (Eq. 1)

$$\frac{d}{dt}A(t) = -(a_\mathrm{de} + r_\mathrm{v}\alpha h(t))A + r_\mathrm{v}\alpha h(t)R + g_\mathrm{r} + r_\mathrm{v} g_\mathrm{f} + r_\mathrm{v}\beta h(t)$$

$$\frac{d}{dt}R(t) = \alpha h(t)A - (a_\mathrm{de} + d + r_\mathrm{v} d + \alpha h(t))R + g_\mathrm{r} - g_\mathrm{f} - \beta h(t)$$

$$\alpha = (a^s_\mathrm{de} - a_\mathrm{de})/(1 + r_\mathrm{v}) > 0, \ \beta = g^s_\mathrm{f} - g_\mathrm{f} > 0$$

➢ Schematics of Eq. 1

$h(t) = 1$ (stimulation)

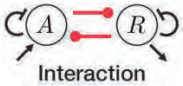

Interaction

$h(t) = 0$ (no stimulation)

Independent

➢ Time course

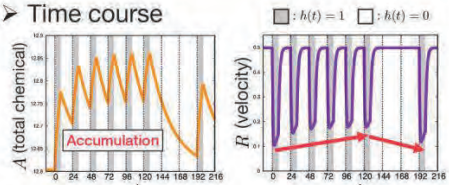

- A stores stimulus history → Deceleration is inhibited.
- R depends on A only under $h(t) = 1$ (stimulation)

A : **Memory function for stimulus history**

5. Discussion

- Difference of decomposition rate between front and rear ($a^s_\mathrm{de} > a_\mathrm{de}$) provides interaction between A and R.
- Accumulation of a specific chemical is reported during habituation in slime mold [3].

Reference list

[1] Boisseau RP et al. Habituation in non-neural organisms: evidence from slime moulds. *Proc. R. Soc. B-Biol. Sci.* 2016; 283(1829).
[2] Boisseau RP et al. Data from: Habituation in non-neural organisms: evidence from slime moulds [Dataset]. *Dryad*. 2016.
[3] Boussard A et al. Memory inception and preservation in slime moulds: the quest for a common mechanism. *Philos. Trans. R. Soc. B-Biol. Sci.* 2019; 374(1774).

Conservative approximation-based feedforward neural network for WENO schemes

Kwanghyuk Park

Graduate school of Artificial Intelligence, POSTECH, Korea

We propose data-driven weighted essentially non-oscillatory (WENO) weighting strategies using a feedforward neural network (FNN) for solving hyperbolic conservation laws. Two nonlinear weights is provided as the output of neural network for a convex combination using point values from a three-point stencil. The supervised learning is adopted using a novel dataset with labels based on conservative approximation to derivative. The symmetric-balancing term is incorporated into the loss function, promoting symmetry properties shared by WENO3-JS and WENO3-Z. The resulting schemes, termed WENO3-CADNNs, show strong generalization ability and robustness across a variety of benchmark cases and grid resolutions — consistently outperforming WENO3-Z and achieving the comparable results to WENO5-JS for some problems.

Conservative approximation-based feedforward neural network for WENO schemes

Kwanghyuk Park [1,3] Jiaxi Gu [2,3] Jae-Hun Jung [1,2,3]

[1]Graduate School of Artificial Intelligence, POSTECH, Korea [2]Department of Mathematics, POSTECH, Korea

[3]POSTECH MINDS (Mathematical Institute for Data Science), POSTECH, Korea

Abstract

We propose data-driven weighted essentially non-oscillatory (WENO) weighting strategies using a feedforward neural network (FNN) for solving hyperbolic conservation laws. Our model predicts two nonlinear weights for a convex combination using point values from a three-point stencil. A supervised training pipeline is developed using a newly constructed labeled dataset based on conservative approximation to derivatives. The symmetric-balancing term is incorporated into the loss function, promoting symmetry properties shared by WENO3-JS and WENO3-Z. The resulting schemes, termed WENO3-CADNNs, exhibit strong generalization ability and robustness across diverse benchmark problems and grid resolutions—consistently outperforming WENO3-Z and achieving the comparable results to WENO5-JS for some problems.

Introduction

- The WENO scheme provides an accurate method that can handle discontinuous solutions without the Gibbs oscillations for the hyperbolic conservation laws for

$$\mathbf{u}_t + \mathbf{div}\mathbf{F}(\mathbf{u}) = 0$$

where $\mathbf{u}$ is the vector of m conserved quantities and $\mathbf{F}:\mathbb{R}^m \to \mathbb{R}^m$ the flux function.
- Since the classical WENO nonlinear weights were defined heuristically and not optimally, recent papers, including [1, 2], applied machine learning to the WENO scheme for optimal weights.
- In [2], we proposed the third-order finite difference WENO nonlinear schemes based on a shallow neural network using the classical WENO3-JS nonlinear weights as labels with the loss function containing the linear term for the accuracy in smooth regions.
- In this work [3], data-driven WENO nonlinear scheme is proposed with the novel dataset derived from the conservation approximation to derivative and new loss function term based on the symmetry which third-order JS and Z weights satisfy.
- The novel dataset with the symmetric-balancing term drives the neural network to learn the WENO properties without any WENO nonlinear weights, while the new term helps to manipulate the numerical dissipation for less dissipative solution without spurious oscillations.

Training Dataset

We construct the dataset derived from the conservative approximation to derivative using the four-point stencils instead of three-point stencils sampled from the smooth and discontinuous functions.

$$v'(x_i) \approx \frac{1}{\Delta x}\left(\hat{v}_{i+1/2} - \hat{v}_{i-1/2}\right)$$

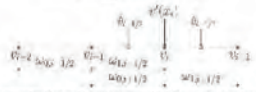

Figure 1. Conservative approximation to the derivative $v'(x_i)$ from a four-point stencil $(v_{i-2}, v_{i-1}, v_i, v_{i+1})$.

For more accurate approximation, the nonlinear weights are required to recover the weights $(1/3, 2/3)$ for smooth stencils and satisfy ENO property for discontinuous stencils, which is consistent to the key properties of WENO nonlinear weights. Therefore by matching the approximation using the nonlinear weights from the neural network and the label, the neural network can be trained without any classical WENO nonlinear weights.

Table 1. Functions for stencils in the dataset

$f(x)=\sin x$	$x_i = \pi(i-1)/N$	100%	Smooth function
$\tanh(5\cos(\pi x))$	$x_i = \pi(i/N)$	100%	Smooth + Periodic
$x \le 0 \to \sin(\pi x)$, $x > 0 \to \cos(\pi x)$	$x_i = -1 + 2(i-1)/N$	100%	Discontinuous + Periodic
$x \le 0 \to 0$, $x > 0 \to 1$	$x_i = -1 + 2(i-1)/N$	100%	Discontinuous + Periodic
$x \le 0 \to 0$, $x > 0 \to 1$	$x_i = -1 + 2(i-1)/N$	100%	Discontinuous + Periodic
$x \le 0 \to 0$, $x > 0 \to 1$	$x_i = -1 + 2(i-1)/N$	100%	Discontinuous + Periodic
$x \le 0 \to 0$, $x > 0 \to 1$	$x_i = -1 + 2(i-1)/N$	100%	Discontinuous + Periodic
$x \le 0 \to 0$, $x > 0 \to 1$	$x_i = -1 + 2(i-1)/N$	100%	Discontinuous + Periodic
$x \le 0 \to 0$, $x > 0 \to 1$	$x_i = -1 + 2(i-1)/N$	100%	Discontinuous + Periodic

The symmetric-balancing term in loss function

In the loss function, we introduced the symmetric-balancing term $C\mathcal{L}_{\mathrm{SYM}}$ with the hyperparameter C to satisfy the symmetry where, given the set of nonlinear weights $\omega = (\omega_0, \omega_1)$ for the stencil $\mathcal{S} = (f_0, f_1, f_2)$, the flipped stencil $\mathcal{S}' = (f_2, f_1, f_0)$ corresponds to the set of nonlinear weights $\tilde{\omega}$.

$$\tilde{\omega} = (\tilde{\omega}_0, \tilde{\omega}_1) = \left(\frac{\omega_1}{4\omega_0 - \omega_1}, \frac{4\omega_0}{4\omega_0 + \omega_1}\right), \tag{1}$$

where the weights ω is used for the linear sum $\hat{v}_{i-1/2} = \omega_0 \hat{v}_{i-1/2,0} + \omega_1 \hat{v}_{i-1/2,1}$. The symmetric-balancing term is defined as, with the batch size N_b,

$$\mathcal{L}_{\mathrm{SYM}} = \frac{1}{2N_b}\sum_{j=1}^{2N_b} |\omega_0 - \tilde{\omega}_1|^2,$$

where the $\tilde{\omega}$ is the nonlinear weights for the flipped stencil and $\hat{v}_i$ is the right-hand side of the $\mathrm{Eq}(\frac{1}{2})$.

- For the $2N_b$-time sum in the balancing term, notice that two pairs of nonlinear weights are given on each four-point stencil.
- In Figure 2, the left panel and middle panel show that the symmetric-balancing term $\mathcal{L}_{\mathrm{SYM}}$ is needed to help the neural network to learn ENO property.
- The middle panel of Figure 2 shows that the hyperparameter C manipulates the numerical dissipation.

Including the symmetric-balancing term $\mathcal{L}_{\mathrm{SYM}}$, the total loss function is designed as

$$\mathcal{L} = \mathcal{L}_{\mathrm{CAD}} + C\cdot\mathcal{L}_{\mathrm{SYM}} + D\cdot\mathcal{L}_{\mathrm{LIN}}. \tag{2}$$

- The error term $\mathcal{L}_{\mathrm{CAD}}$ is utilized to match the approximations using the nonlinear weights from neural network and the labels.
- As in [1, 2], the linear term $\mathcal{L}_{\mathrm{LIN}}$ is included to recover the weights $(1/3, 2/3)$ for smooth stencils.
  - As illustrated in the right panel of Figure 2, the hyperparameter D attached to the linear term $\mathcal{L}_{\mathrm{LIN}}$ (or marks) are the numerical dissipations.

Figure 2. Solution profiles at $T = 0.2$ for the Riemann problem of one-dimensional advection equation, computed by the feedforward neural network with the loss function $\mathcal{L} = \mathcal{L}_{\mathrm{CAD}} + C\mathcal{L}_{\mathrm{SYM}} + D\mathcal{L}_{\mathrm{LIN}}$ and $D = 0$ (left), $C = 500, 5750, 7000$ and $D = 0$ (right). $\mathcal{L}_{\mathrm{LIN}}$ is the term for matching the linear one. $\mathcal{L}_{\mathrm{LIN}}$ is the linear term used in [2, 3].

Results

By training the same form of neural network with the different hyperparameters, we obtain the WENO nonlinear weights strategies WENO3-CADNN1 $(C, D) = (5750, 0)$ and WENO3-CADNN2 $(C, D) = (7000, 500)$. For Sod problem, WENO3-CADNN2 provides the better resolution than the other third-order WENO schemes and comparable result to WENO5-JS.

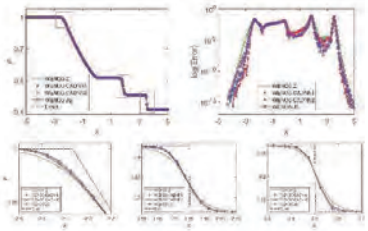

Figure 3. Density profiles for the Sod problem at $T = 2$ (top left), log scale pointwise error (top right) and close-up view of the solutions in the boxes from left to right (bottom left, bottom middle, bottom right) approximated by WENO3-Z (green), WENO3-CADNN1 (blue), WENO3-CADNN2 (red) and WENO5-JS (purple) with $N = 200$. The dashed black line is the exact solution.

In Figure 4, WENO3-CADNNs resolves finer vortical structures of Rayleigh-Taylor instability and finer roll-up structure in the Riemann problem compared to WENO3-Z, while WENO5-JS achieves the best resolution of small scale vortices because of its higher formal order of accuracy.

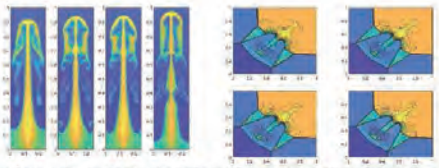

Figure 4. Density in the plot of scale colors for Rayleigh-Taylor instability (left) at the final time $T = 2.95$ and the Riemann problem (right) at the final time $T = 0.25$ by WENO3-Z, WENO3-CADNN1, WENO3-CADNN2 and WENO5-JS from left to right with $N_x = 200$ and $N_y = 800$ in the left panel and from top left to bottom right with $N_x = N_y = 400$ in the right panel.

Discuss and Conclusion

- We propose the data-driven WENO scheme utilizing the novel dataset based on the conservative approximation to derivative and new loss function.
- The consequent neural networks WENO3-CADNNs consistently perform better than WENO3-Z and provide the solution compared to WENO5-JS.

References

[1] S. A. Sirgis, S. J. Sifuentes, and N. A. Adams, WENO-VS: A novel run-over-time point-data-driven weighted essentially non-oscillatory scheme, J. Comput. Phys., 492 (2023), 112420.

[2] K. Park, K. Chen, H. Lee, J. Gu and J. -H. Jung, A third-order finite difference weighted essentially non-oscillatory scheme with shallow neural network, Appl. Numer. Math., 216 (2025), 1–21.

[3] K. Park, J. Gu, and J. -H. Jung, Conservative approximation-based feedforward neural network for WENO schemes, arXiv:2507.09010, 2025.

Intersection Detection in Latent Topic Modeling

Sung-Inn Pyo

Department of Mathematics, Ajou University, Korea

Latent Dirichlet Allocation (LDA) topic modeling does not allow intersections among topics. Constructing strictly disjoint topics can lead to information loss and reduced interpretability, particularly when words are inherently related to multiple clusters. Although previous studies have attempted to consider this limitation through hierarchical or overlapping topic extensions, they have not modeled topic intersections. In this study, we propose a Latent Semantic Algorithm that identifies intersecting topics by leveraging Jensen–Shannon Divergence and margin-based discriminant analysis.

FMII 2025

Intersection Detection in Latent Topic Modeling

Sung-Inn Pyo[1] · Soon-Sun Kwon[2]
[1] M.S Student, Department of Mathematics, Ajou University, [2] Professor, Department of Mathematics, Ajou University

1. Introduction

Traditional topic models such as Latent Dirichlet Allocation (LDA) [1] assume disjoint topic assignments, overlooking words that may inherently belong to multiple semantic contexts. To address this, we propose a hybrid framework that identifies overlapping words using square-root Jensen–Shannon divergence and entropy-penalized distances. Words are embedded in a metric-preserving space, where linear SVMs define soft-margin boundaries, and those within optimal margin bands are labeled as intersections. This approach enables the construction of a refined inclusion matrix, revealing more accurate and interpretable topic structures.

2. Methodology

Jensen–Shannon Divergence (JSD) [2] [3]

JSD is a symmetric divergence that measures similarity between distributions. Here, it represents the distance between a word's topic distribution and a topic centroid.

$$\mathrm{JSD}(P,Q) = \frac{1}{2}\sum_i P(i)\log_2\left(\frac{P(i)}{M(i)}\right) + \frac{1}{2}\sum_i Q(i)\log_2\left(\frac{Q(i)}{M(i)}\right)$$

$\mathrm{JSD}(P,Q)$: Jensen–Shannon divergence between distributions P and Q.
M: weighted distribution.
$P(i), Q(i)$: values of the i-th element in P and Q.

Distance Metric

$$dist\left(P_{w_i}, P_{w_j}\right) = \sqrt{\frac{\ln K}{\mathrm{Var}_{\mathrm{off}}}}\sqrt{\mathrm{JSD}(P_{w_i}, P_{w_j})}$$

$\mathrm{JSD}(P_{w_i}, P_{w_j})$: Jensen–Shannon divergence between the posterior topic distributions of words w_i and w_j
K: number of topics in the LDA model
$\mathrm{Var}_{\mathrm{off}}$: empirical variance of all off-diagonal entries in the $\sqrt{\mathrm{JSD}}$ distance matrix

The hybrid distance used in the algorithm adjusts the Jensen–Shannon divergence with a global scaling factor to preserve its metric properties. This scaling ensures that the distance remains meaningful and comparable across different numbers of topics. Unlike entropy-based normalization, it avoids breaking symmetry and the triangle inequality. As a result, the method offers a stable and principled way to detect overlapping words between topics.

Hybrid Distance satisfies 4 conditions of metric :

Property 1. Non-negativity:

$$dist(P,Q) \geq 0$$

Property 2. Identity of Indiscernibles:

$$dist(P,Q) = 0 \iff P = Q$$

Property 3. Symmetry:

$$dist(P,Q) = dist(Q,P)$$

Property 4. Triangle Inequality:

$$dist(P,R) \leq dist(P,Q) + dist(Q,R), \text{ where } P, Q, R \text{ are distributions}$$

Coherence Score

The coherence score quantifies how semantically related the top words in a topic are. Higher scores indicate more interpretable and coherent topics, computed using NPMI-based measures.

$$\mathrm{Coherence}(w_i, w_j) = \frac{\log\left(\frac{P(w_i,w_j)+\epsilon}{P(w_i)P(w_j)+\epsilon}\right)}{-\log P(w_i,w_j)}$$

3. Algorithm

Step 1. LDA Posterior Estimation

Estimate topic distributions:

$$P(w \mid z_k), \quad P(z_k \mid d_i), \quad P(z_k) = \frac{\sum_{i=1}^{N} P(z_k \mid d_i)\cdot \mathrm{len}(d_i)}{\sum_{i=1}^{N} \mathrm{len}(d_i)}$$

N: number of documents, V: vocabulary size, K: number of topics, $\mathrm{len}(d_i)$: token count in document d_i

Step 2. Word-Level Topic Distribution

For each word w, compute:

$$P(z_k \mid w) = \frac{P(w \mid z_k)\cdot P(z_k)}{\sum_{j=1}^{K} P(w \mid z_j)\cdot P(z_j)}$$

Step 3. Hybrid Distance Matrix

Define safe Jensen-Shannon divergence (JSD), and compute:

$$dist\left(P_{w_i}, P_{w_j}\right) = \sqrt{\frac{\ln K}{\mathrm{Var}_{\mathrm{off}}}}\sqrt{\mathrm{JSD}(P_{w_i}, P_{w_j})}$$

where $\mathrm{Var}_{\mathrm{off}}$ is the variance of all off-diagonal distances.

Step 4. 2D Projection and SVM Margin Learning

Project words into $\mathbb{R}^2$ using classical MDS on hybrid distances. For each topic pair (i, j):

- Train a linear SVM to classify words into z_i vs. z_j
- Compute margin distance $d_{\mathrm{margin}}^{(i,j)}(w)$
- Use silhouette score to find optimal margin width threshold
- Assign words within margin as overlapping in both topics

Step 5. Inclusion Matrix Construction

Construct $M \in \{0,1\}^{V \times K}$:

- If word w is not in any margin: assign topic with $\arg\max_k P(z_k \mid w)$
- If w is in one or more SVM margins: include all relevant topics

4. Application

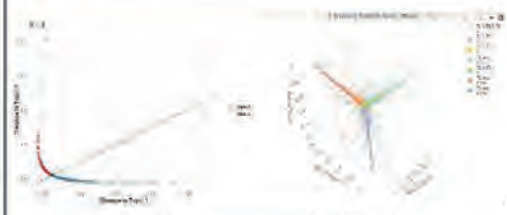

Figure 1. Document embedding with K-2 and K=3 topics
Outliers removed for visualization.

Table 1. Crawled News Data, written in Korean, "Thyroid Cancer", Docs = 80, Words = 2,772

K=2 K=3

Table 2. Coherence scores comparing models across topic settings.

Table 3. Data Text Document Classification from Kaggle, Docs = 300, Words = 18,365

K=2 K=3

Table 4. Coherence scores comparing models across topic settings.

References

[1] Blei, D., Ng, A., & Jordan, M. (2001). Latent dirichlet allocation. Advances in neural information processing systems, 14.
[2] Shannon, C. E. (1948). A mathematical theory of communication. The Bell system technical journal, 27(3), 379-423.
[3] Lin, J. (2002). Divergence measures based on the Shannon entropy. IEEE Transactions on Information theory, 37(1), 145-151.
[4] Cortes, C., & Vapnik, V. (1995). Support-vector networks. Machine learning, 20, 273-297.

Acknowledgment

This research was supported by Basic Science Research Program through the National Research Foundation of Korea(NRF) funded by the Ministry of Education(RS- 2021-NR060141, RS- 2025-00564343)

5. Discussion

- **Identification of the lack of intersection-detecting methodologies within traditional LDA frameworks.**
- **Difficulty in evaluating performance due to the lack of suitable datasets and established benchmarks for intersection detection.**
- **Future work includes improving algorithmic efficiency for the analysis of large-scale datasets.**

Forum “Math for Industry” 2025

- Challenge of Mathematics for Industry in the AI era -

August 18 - 20, 2025, Seoul (POSCO Center), Republic of Korea

Pruning CNN Features by 50 % Without Losing Interpretability: Genetic- Algorithm-Selected EfficientNet Vectors and Grad-CAM on Fluorescence Cells

Panu Sam-Ang

School of Mathematical Sciences and Geoinformatics, Institute of Science, Suranaree University of Technology, Thailand

Deep convolutional networks deliver rich—but often redundant—feature vectors that can overwhelm small biomedical datasets and blur model reasoning. We test whether a genetic algorithm (GA) can prune the 1 280-dimensional EfficientNet-B0 descriptor by roughly 50 % while preserving both performance and Grad-CAM interpretability. After confirming pipeline correctness on two natural-image sanity checks—dog breeds (Golden vs Curly-Coated Retriever) and bird species (Limpkin vs American Coot), each retaining ≥ 99 % accuracy—we turn to the challenging BBBC021 fluorescence-microscopy set (treated vs control HeLa cells). GA (population 50, 30 generations, mutation 5 %) keeps ~650 features; across three seeds test accuracy holds at 81.9 ± 0.4 %, AUC at 0.89 ± 0.01, and recall on the minority treated class rises from 0.71 to 0.74. Grad-CAM heat-maps before and after pruning overlap by > 80 % (SSIM), consistently highlighting nuclei clusters rather than background artefacts. These findings show that evolutionary feature selection can halve dimensionality without sacrificing accuracy—or interpretability—on limited biomedical data. Ongoing work with Dr. Piyamas Petcharoen applies the same pipeline to fluorescence images of forensic evidence (fingerprints, lip-prints, blood, semen, saliva, hair), aiming to build an efficient, explainable tool for crime-lab technicians.

Prunning CNN Features by 50% Without Losing Interpretability:
Genetic-Algorithm-Selected EfficientNet Vectors and Grad-CAM on Fluorescence Cells

Panu Sam-ang, Thanakrit Netchaleerat

School of Mathematical Sciences and Geoinformatics, Institute of Science, Suranaree University of Technology, Thailand

Overview of Problem & Dataset

- Fluorescence-microscopy images are now routine in toxicology and forensic labs, yet automated screening still relies on bulky CNN feature vectors (1,280+ dimensions).
- Most of those activations are redundant; they slow model training and hide biological insight.
- Classical lasso/PCA pruning discards interpretability.
- We propose a Genetic-Algorithm (GA) wrapper that *selects* the most informative EfficientNet-B0 channels while explicitly rewarding AUROC and sparsity.
- Grad-CAM heat-maps on the GA-pruned model remain sharp, enabling expert validation.
- Dataset: BBBC021 — control (DMSO) vs staurosporine-treated HeLa cells.

Methods

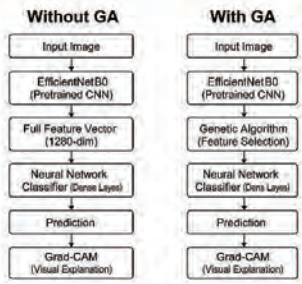

- Feature extractor: EfficientNet-B0 (frozen), 1 280-D vector per image.
- GA hyper-parameters: population 150, 70 generations, mutation 0.5–15 %, crossover 60–98 %.
- Fitness = 0.5 × Accuracy + 0.5 × AUC − sparsity penalty.
- Classifier: 2-layer MLP, label smoothing 0.15, early stopping.
- Evaluation: accuracy, AUC, confusion matrix, Grad-CAM heat-map overlap.

Main Results

- Features: 1280 → 630 (−51 %).
- Accuracy 0.837 → 0.847 (+1 pp).
- Treated recall 0.69 → 0.73 (+4 pp).
- AUC ≈ 0.90 maintained.
- GA converges 11 epochs earlier.

Confusion Matrix: Without GA

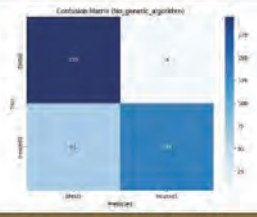

Confusion Matrix: With GA

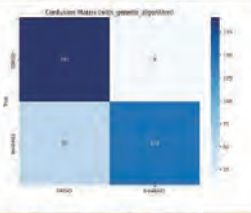

Figures - Grad-CAM Without GA

- Dense: Control

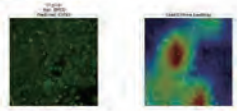

- Sparse: Control

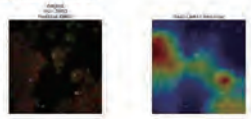

- Dense:Treated

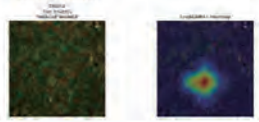

- Sparse:Treated

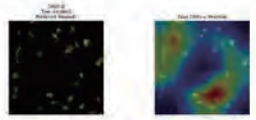

Figures - Grad-CAM With GA

- Dense: Control

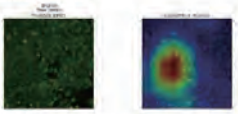

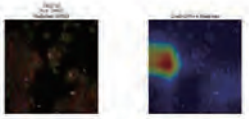

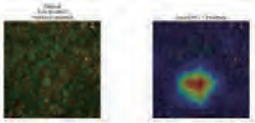

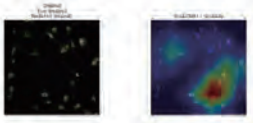

Conclusions and Next Steps

- GA halves feature dimensionality while preserving accuracy and interpretability.
- Improves minority-class sensitivity and reduces training time.
- Ongoing: extend to 5-class forensic fluorescence dataset (fingerprints, lip-prints, blood, semen, saliva, hair).
- Future baselines: PCA, L1-logistic; analyze feature-subset stability.

Acknowledgements

We would like to thank Suranaree University of Technology for the support.

SUT SURANAREE UNIVERSITY OF TECHNOLOGY

Contact Information

Dr. Panu Sam-ang
E-mail: panu.samang@g.sut.ac.th
School of Mathematical Sciences and Geoinformatics
Institute of Science
Suranaree University of Technology
111 Mahawittalai Road, Suranaree, Nakhon Ratchasima 30000
Thailand

Meta-Analysis of Self-Controlled Case Series (SCCS) Studies on VaccineAssociated Stroke

Seol Jang

Department of Mathematics, Ajou university, Korea

Concerns over rare adverse events such as stroke following vaccination have prompted the use of the Self-Controlled Case Series (SCCS) model for postmarketing vaccine safety evaluation. This meta-analysis systematically synthesized evidence from SCCS studies assessing the risk of stroke after vaccination. Relevant studies were identified via PubMed and Embase through March 2025, and study quality was assessed using a modified Newcastle-Ottawa Scale tailored to SCCS designs. Pooled incidence rate ratios (IRRs) were estimated using random-effects meta-analysis, and sources of heterogeneity were examined through meta-regression. A total of 12 eligible studies were included, with a pooled relative risk (RR) of 1.01 (95% CI: 0.93–1.11), indicating no significant association between vaccination and stroke risk. Heterogeneity was low ($I^2 = 28.1\%$), and meta-regression suggested a decreasing trend in RR over time. These findings highlight the robustness of the SCCS method and support its continued use in vaccine safety monitoring.

FMII 2025

Meta-Analysis of Self-Controlled Case Series (SCCS) Studies on Vaccine-Associated Stroke

Seol Jang[1], Soon-Sun Kwon[2]

1) Integrated M.S./Ph.D student, Department of Mathematics, Ajou University, 2) Professor, Department of Mathematics, Ajou University

1. Background

Vaccination is a key public health measure; however, concerns regarding rare adverse events, such as stroke, have prompted rigorous safety evaluations. The Self-Controlled Case Series (SCCS) model is widely applied in vaccine safety research because it controls for fixed individual-level confounders.

However, results may vary across studies due to differences in:

- Risk period definitions
- Adjustments for age and seasonal effects
- Handling of event-dependent exposures

Differences in study populations, vaccine types, and data sources contribute to heterogeneity across SCCS studies.

Careful evaluation of analytical choices—such as risk window length, age or seasonal adjustment, and event-dependent exposure handling—is essential for understanding variability and strengthening methodological transparency and public health recommendations.

2. Objectives

This study presents a systematic review and meta-analysis of SCCS studies on vaccine exposure and stroke.

- Quantifies stroke risk after vaccination
- Assesses methodological differences affecting interpretation
- Examines heterogeneity through meta-regression

3. Methods

1. Search Strategy and Study Selection

- "SCCS" and "Vaccine" were used to search PubMed and Embase (until March 27, 2025)
- Studies included:
  (1) SCCS design (2) vaccine safety (3) adverse (4) IRR of 95% CI

2. Quality Assessment

- The quality of the study was assessed using modified NOS for the SCCS study, which focused on:
- Including SCCS assumptions, risk window definitions, and adjustments for confounders and seasonal variation.

3. Statistical Analysis

- IRRs were pooled using random-effects meta-analysis (DerSimonian-Laird).
- Heterogeneity was assessed using:
- Cochran's Q statistic:

$$Q = \sum_{i=1}^{k} w_i (\theta_i - \bar{\theta})^2$$

- I^2 statistic:

$$I^2 = \frac{Q - (k-1)}{Q} \times 100\%$$

Meta-regression was used to explore heterogeneity in effect size with respect to publication year, vaccine type, and risk window.(e.g., year, vaccine type, risk period).

4. Results

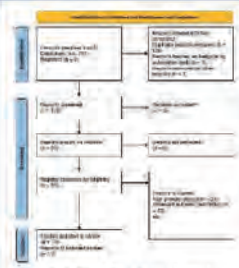

Fig 1. PRISMA Flow diagram for study selection

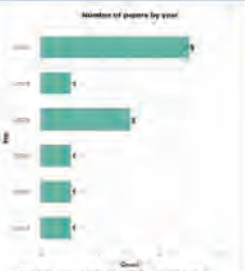

Fig 2. Number of Included Articles by Year

Table 1. Quality assessment based on modified Newcastle-Ottawa Scale (NOS)

Table 2. Univariate Meta-Regression Results

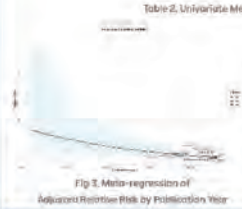

Fig 3. Meta-regression of Adjacent Relative Risk by Publication Year

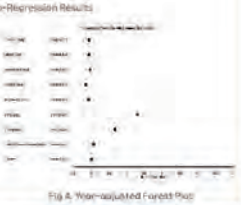

Fig 4. Year-adjusted Forest Plot

5. Conclusion

This meta-analysis of SCCS studies on vaccine safety found little overall relative risk (RR = 1.01, 95% CI: 0.93–1.11) and low heterogeneity (I^2 = 28.1%). Meta-regression revealed a decreasing trend in RR over time, indicating methodological improvements and better bias control in more recent studies. These findings underscore the importance of rigor and temporal factors in interpreting SCCS-based vaccine safety evidence.

Reference

[1] Farrington, C. P. (1995). Relative incidence estimation from case series for vaccine safety evaluation. Biometrics, 51(1), 228–235.
[2] DerSimonian, R., & Laird, N. (1986). Meta-analysis in clinical trials. Controlled Clinical Trials, 7(3), 177–188.

Acknowledgment

This research was supported by Basic Science Research Program through the National Research Foundation of Korea(NRF) funded by the Ministry of Education(RS-2021-NR060141, RS-2025-00564343)

Law of the iterated logarithm for self-similar Gaussian processes

Shuhei Shibata

Joint Graduate School of Mathematics for Innovation, Kyushu University, Japan

Law of the iterated logarithm (LIL) is a fundamental limit theorem in probability theory that describes the precise long-term behavior of random fluctuations. It operates between the Law of Large Numbers and the Central Limit Theorem: they state that the stochastic process scaled by t^{-1} and $t^{-1/2}$ converges to zero almost surely (or in probability) and converges in distribution to a normal distribution, respectively. LIL gives the exact boundary for the size of the largest fluctuations that almost surely occur over time, revealing the sharpest possible growth rate of the stochastic process. In this time, We study the LIL for centered, continuous, self-similar Gaussian processes under a certain decay condition on the covariance kernel.

Law of the iterated logarithm for self-similar Gaussian processes

Shuhei Shibata
Joint Graduate School of Mathematics for Innovation, Kyushu University

Introduction

Law of the iterated logarithm (LIL) is a fundamental limit theorem in probability theory that describes the precise long-term behavior of random fluctuations. It operates between the Law of Large Numbers and the Central Limit Theorem: they state that the stochastic process scaled by t^{-1} and $t^{-1/2}$ converges to zero almost surely (or in probability) and converges in distribution to a normal distribution, respectively. LIL gives the exact boundary for the size of the largest fluctuations that almost surely occur over time, revealing the sharpest possible growth rate of the stochastic process.

Asymptotic evaluation

Let $\{B(t)\}_{t\geq 0}$ be the standard Brownian motion (BM).

- $O(t)$ **(Law of Large Number)**

$$\lim_{t\to\infty} \frac{B(t)}{t} = 0 \quad a.s.$$

- $O(\sqrt{t})$ **(Typical fluctuation)**

$$\left\{\frac{B(t)}{\sqrt{t}}\right\}_{t>0} \overset{d}{=} \{B(1)\}_{t>0} \quad \text{and} \quad B(1) \sim N(0,1).$$

- $O(\sqrt{2t\log\log t})$ **(LIL)** ←**Precise order!**

$$\limsup_{t\to\infty} \pm \frac{B(t)}{\sqrt{2t\log\log t}} = 1 \quad a.s.$$

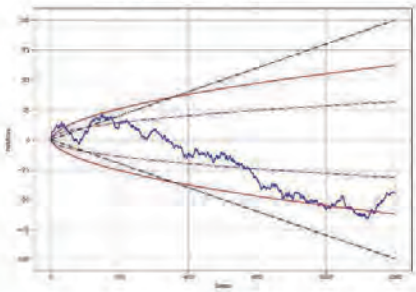

Figure: Conceptual diagram of LIL for Brownian motion

Blue : Numerical realization of sample path of Brownian motion $B(t)$.
Red : The upper and lower curves are $\pm\sqrt{2t\log\log t}$, respectively.
Purple : The upper and lower curves are $\pm\sqrt{t}$, respectively.
Black: The upper and lower lines are $\pm t$, respectively.

Assumptions

Let $\{X(s)\}_{s\geq 0}$ be a centered continuous Gaussian process with covariance kernel $R(s,t) = \mathbb{E}[X(s)X(t)]$.

(A1): **(self-similarity)** There exists $\rho > 0$ such that for any $c > 0$ and $s, t > 0$,

$$R(cs, ct) = c^{2\rho} R(s,t).$$

In other words, we assume

$$\{X(ct)\}_{t\geq 0} \overset{d}{=} \{c^\rho X(t)\}_{t\geq 0} \quad (c > 0).$$

(A2): Under (A1), there exists $\eta > 0$ such that the function $h(x) = x^{-\rho} R(1,x)$ $(x \geq 1)$ satisfies

$$h(x) = O((\log x)^{-\eta}) \quad \text{as } x \to \infty.$$

Main result

Theorem. Let $\{X(s)\}_{s\geq 0}$ be a centered continuous Gaussian process with covariance kernel $R(s,t)$ satisfying (A1) and (A2). Then,

$$\limsup_{s\to\infty} \pm \frac{X(s)}{\sqrt{2s^{2\rho}\log\log s}} = R(1,1)^{\frac{1}{2}} \quad a.s.$$

Examples

(i) X is the fractional Brownian motion (FBM) $\{B_H(t)\}_{t\geq 0}$ for $0 < H < 1$.

- If $H = 1/2$, X is the standard BM.

Then,

$$\rho = H$$
$$R(s,t) = \frac{1}{2}(|t|^{2H} + |s|^{2H} - |t-s|^{2H})$$
$$h(x) = O(x^{-(1-H)}) \quad \text{as } x \to \infty.$$

(ii) X is the generalized Riemann-Liouville FBM, i.e.,

$$X(t) = \int_0^t (t-u)^\beta u^{-\gamma/2} dB(u)$$

for $\beta > -1/2$ and $0 \leq \gamma < 1$.

- If $\beta = \gamma = 0$, X is the standard BM.
- If $\beta = 1, \gamma = 0$, $X(t) = \int_0^t B(u)du$

Then,

$$\rho = \beta - \gamma/2 + 1/2$$
$$R(s,t) = \int_0^{s\wedge t} (s-u)^\beta (t-u)^\beta u^{-\gamma} du$$
$$h(x) = O(x^{-\frac{1}{2}(1-\gamma)}) \quad \text{as } x \to \infty.$$

(iii) If $\{X(t)\}_{t\geq 0}$ satisfies (A1) with $\rho > 0$, there exists a finite measure μ on $\mathbb{R}$ such that

$$h(x) = R(1,1) \int_{\mathbb{R}} e^{i\xi \log x} \mu(d\xi).$$

We consider the symmetric α-stable distribution corresponding to $\mu_\alpha(d\xi) = e^{-|\xi|^\alpha} d\xi$ for $0 < \alpha \leq 2$.

- If $\alpha = 1$, it corresponds to the Cauchy distribution.
- If $\alpha = 2$, it corresponds to the Normal distribution.

For $0 < \alpha < 2$,

$$h(x) = O((\log x)^{-(\alpha+1)}) \quad \text{as } x \to \infty$$

For $\alpha = 2$,

$$h(x) = O(e^{-(\log x)^2/4}) \quad \text{as } x \to \infty$$

The idea of the proof

Lemma. (Erdős-Rényi version of Borel-Cantelli lemma)
Let A_n be a sequence of events such that $\sum_{n=1}^\infty \mathbb{P}(A_n) = \infty$ and

$$\liminf_{n\to\infty} \frac{\sum_{k=1}^n \sum_{l=1}^n (\mathbb{P}(A_k \cap A_l) - \mathbb{P}(A_k)\mathbb{P}(A_l))}{\left(\sum_{k=1}^n \mathbb{P}(A_k)\right)^2} = 0.$$

Then, $\mathbb{P}(A_n \text{ i.o.}) = 1$.

References

[1] S.Shibata and T.Shirai, A remark on elephant random walks via the classical law of the iterated logarithm for self-similar Gaussian processes, to appear in Illinois Journal of Mathematics, 2025.

[2] P.Erdős and A.Rényi, On cantor's series with convergence. Ann. Univ. Sci. Budapest. Eötvös. Sect. Math., 2:93–109, 1959.

Acknowledgement This research was supported by WISE program (MEXT) at Kyushu University, and supported in part JP23K25774 and the Kyushu University Fund "Human Resource Development Initiative in Mathematics for Industry".

Forum “Math for Industry” 2025

- Challenge of Mathematics for Industry in the AI era -

August 18 - 20, 2025, Seoul (POSCO Center), Republic of Korea

HYPERSONIC SIMILARITY LAW FOR STEADY COMPRESSIBLE EULER FLOWS PAST SLENDER BODIES WITHIN THE FRAMEWORK OF RADON MEASURE SOLUTIONS

Shifan Kang

School of Mathematical Sciences, East China Normal University

In this paper, we rigorously establish the mathematical results on statement and validation of the hypersonic similarity law within the framework of Radon measure solutions. We consider two scenarios: (1) two-dimensional steady non-isentropic compressible Euler flows past an infinitely long slender curved wedge; (2) threedimensional steady non-isentropic compressible Euler flows past an infinitely long cylindrically symmetric cone. It turns out that, for the hypersonic flow passing through a slender boundary with tiny slenderness τ, if hypersonic parameter $K=M_\infty \tau$ is fixed, taking the slenderness ratio $\tau\to 0$, the flow structures (after scaling) no longer depend on the obstacle shape and incoming Mach number M_∞ independently, but only on their product K and the gas adiabatic index γ. Mathematically, for non-isentropic flow, we propose a new system of hypersonic small-disturbance equations to describe steady non-isentropic compressible hypersonic flows passing slender bodies. By comparing the Radon measure solutions of the hypersonic flow Euler equations and the corresponding hypersonic small disturbance equations, we demonstrate that when the obstacle slenderness ratio τ is very small, the Radon measure solution of the hypersonic flow problem converges (after dimensionless transformation) to that of the hypersonic small-disturbance equations. The explicit form of the Radon measure solutions effectively simplify the convergence analysis.

HYPERSONIC SIMILARITY LAW FOR STEADY COMPRESSIBLE EULER FLOWS PAST SLENDER BODIES WITHIN THE FRAMEWORK OF RADON MEASURE SOLUTIONS

SHIFAN KANG[1], BINGSONG LONG[1], AND HAIRONG YUAN[1]
1 School of Mathematical Sciences, East China Normal University, Shanghai 200241, China

1.Introduction

In engineering, the flow with Mach number exceeding five is called hypersonic flow. The study of hypersonic flow has attracted considerable scholarly attention owing to its critical importance in aerodynamics. **Physically, the hypersonic similarity law means: for hypersonic flows with different Mach numbers past slender bodies with different slenderness ratios, if the hypersonic similarity parameter $K = M_\infty\tau$ and the adiabatic exponent γ are fixed, then the flow structures are similar under appropriate scaling when M_∞ is sufficiently large.**

2. Mathematical Formulation

- Two-dimensional steady non-isentropic compressible Euler system and hypersonic small- disturbance equations:

$$\begin{cases} \partial_x(\rho u)+\partial_y(\rho v)=0, \\ \partial_x(\rho u^2+p)+\partial_y(\rho uv)=0, \\ \partial_x(\rho uv)+\partial_y(\rho v^2+p), \\ \partial_x(\rho uE)+\partial_y(\rho vE)=0, \end{cases} \tag{1}$$

$$\begin{cases} \partial_{\bar{x}}\bar{\rho}+\partial_{\bar{y}}(\bar{\rho}\bar{v})=0, \\ \partial_{\bar{x}}(\bar{\rho}\bar{u}+\bar{p})+\partial_{\bar{y}}(\bar{\rho}\bar{u}\bar{v})=0, \\ \partial_{\bar{x}}(\bar{\rho}\bar{v})+\partial_{\bar{y}}(\bar{\rho}\bar{v}^2+\bar{p}), \\ \partial_{\bar{x}}(\bar{\rho}\bar{E})+\partial_{\bar{y}}(\bar{\rho}\bar{v}\bar{E})=0. \end{cases} \tag{7}$$

ρ, E and (u,v) are unknowns and represent the density of mass, total enthalpy per unit mass and velocity, respectively; p is the scalar pressure.

- Constitutive relation:

$$p=\frac{\gamma-1}{\gamma}\rho\left(E-\frac{1}{2}(u^2+v^2)\right), \tag{2} \qquad \bar{p}=\frac{\gamma-1}{2\gamma}\bar{\rho}\left(E-2\bar{u}-\bar{v}^2\right). \tag{8}$$

Adiabatic exponent of a polytropic gas $\gamma>1$. Let $c=\sqrt{\gamma p/\rho}$ be the local sound speed of gas, and $M=\sqrt{u^2+v^2}/c$ the Mach number of the fow

- Slip boundary condition:

$$(u,v)\cdot(n_1,n_2)=0 \text{ on } \Gamma, \tag{3} \qquad \bar{v}=b'(\bar{x}) \text{ on } \Gamma. \tag{9}$$

- The oncoming flow of uniform state:

$$U_\infty=(\rho_\infty,u_\infty,0,E_\infty), \tag{4} \qquad \bar{U}_\infty=\left(1,0,0,\bar{E}_\infty\right)^{\top}, \tag{10}$$

$$p_\infty=\frac{\rho_\infty u_\infty^2\tau^2}{\gamma K^2}, \tag{5} \qquad \bar{p}_\infty=\frac{1}{\gamma K^2}, \tag{11}$$

$$E_\infty=\frac{1}{2}u_\infty^2\left(1+\frac{2\tau^2}{(\gamma-1)K^2}\right), \tag{6} \qquad \bar{E}_\infty=\frac{2}{(\gamma-1)K^2}, \tag{12}$$

Problem A: For the oncoming flow U_∞ given by (4)–(6), find a solution to (1)–(2) in the domain Ω with the slip boundary condition (3). After scaling

$$\bar{x}=x,\ \bar{y}=\frac{y}{\tau},\bar{u}=\frac{u-u_\infty}{u_\infty\tau^2},\bar{v}=\frac{v}{u_\infty\tau},\bar{\rho}=\frac{\rho}{\rho_\infty},$$
$$\bar{p}=\frac{p}{\gamma p_\infty M_\infty^2\tau^2},E=\frac{2E-u_\infty^2}{u_\infty^2\tau^2}, \tag{13}$$

We ignore the terms involving τ^2(for $\tau \ll 1$), Problem A turns to B

Problem B: For the oncoming flow U_∞ given by (10)–(13), find a solution to (7)–(8) in the domain Ω with the slip boundary condition (9).

3. Main Theorem

Theorem 1. Suppose that $b(x)\in C^2$ and satisfies

$$\frac{\left(1+\tau^2b'(x)^2\right)^{3/2}}{\gamma K^2}+b''(x)H(x)+b'(x)^2\sqrt{1+\tau^2b'(x)^2}>0,$$
$$b'(x)>0,H(x)=\int_0^x\frac{b'(t)}{\sqrt{1+\tau^2b'(t)^2}}dt. \tag{15}$$

Problem A admits a solution.

Theorem 2. Suppose that $b(\bar{x})\in C^2$ and satisfies

$$b'(\bar{x})>0,\ \bar{p}_\infty+b'(\bar{x})^3+b(\bar{x})b''(\bar{x})>0. \tag{16}$$

Problem B admits a solution.

Theorem 3: Let $\bar{U}^{(\tau)}=(\bar{\rho}^{(\tau)},\bar{u}^{(\tau)},\bar{v}^{(\tau)},\bar{E}^{(\tau)})$ denote the Radon measure solution $U=(\rho,u,v,E)$ of Problem A under scaling (14), **When $\tau\to 0$,** one has $\lim_{\tau\to 0}\bar{U}^{(\tau)}=\bar{U}$, where $\bar{U}$ is the Radon measure solution of Problem B.

4. Radon Measure Solutions

- **To prove the theorems , we constructed the solutions of Problem A and Problem b, then we proved that as $\tau\to 0$, the solutions converge.**
- By employing the Riesz representation theorem for Radon measures, we derive a general form of the system through the nonlinear functional relationships between the Radon-Nikodym derivatives of these measures. Since the Radon-Nikodym derivatives can be defined pointwise, the challenge typically associated with the product of Dirac measures in cases of concentration is avoided. The nonlinearity of the Euler system is subsequently recovered from the algebraic relationships among the Radon-Nikodym derivatives.

Construct solutions of Problem A

By Riesz representation theorem:

$$\langle m,\phi\rangle=\int_{\mathbb{R}^2}\phi(x,y)m(\mathrm{d}x\mathrm{d}y) \qquad \phi\in C_0(\mathbb{R}^2) \tag{17}$$

Definition 1: Let $L=\{(x(t),y(t)):t\in[0,T]$ be a C^2 curve. The weight Dirac measure $w_L\delta_L$ support on $L\subset\mathbb{R}^2$ with a weight $w_L(t)\in L^1_{loc}$ is defined as

$$\langle w_L\delta_L,\phi\rangle=\int_0^l w_L(t)\phi(x(t),y(t))\sqrt{x'(t)^2+y'(t)^2}\,\mathrm{d}t\ \forall\phi\in C_0(\mathbb{R}^2), \tag{18}$$

Definition 2: For a fixed $\gamma>1$, let ϱ, φ be nonnegative Radon measures, m^i, n^i $(i=0,1,2,3)$ be Radon measures on $\bar{\Omega}$, and $w_{ij}(x)\in L^1_{loc}(\mathbb{R}^+\cup\{0\})$ be nonnegative measurable function. We call (ϱ,u,v,E) a Radon measure solution to Problem A.

[linear relaxation] :

$$\langle m^0,\partial_x\phi\rangle+\langle n^0,\partial_y\phi\rangle+\int_0^\infty\rho_\infty u_\infty\phi(0,y)\mathrm{d}y=0, \tag{19}$$

[nonlinear constraints] :

we suppose

$$m^0<<\rho,\ n^0<<\rho, \tag{20}$$

with Radon-Nikodym derivatives

$$u=\frac{\mathrm{d}m^0}{\mathrm{d}\varrho} \quad \text{and} \quad v=\frac{\mathrm{d}n^0}{\mathrm{d}\varrho}. \tag{21}$$

[state equation] :

we suppose

$$p=\frac{\mathrm{d}\varrho}{\mathrm{d}\mathcal{L}^2},\quad p=\frac{\mathrm{d}\varphi}{\mathrm{d}\mathcal{L}^2}=\frac{\gamma-1}{\gamma}\rho(E-\frac{1}{2}(u^2+v^2)). \tag{22}$$

Regular-singular decompositions to Problem A:

$$m^0\doteq\rho_\infty u_\infty\mathcal{L}^2\,\mathrm{mres}\Omega+w_m^0(x)\delta_{y=b(x)},n^0\doteq w_n^0(x)\delta_{y=b(x)}, \tag{23}$$

Radon Measure Solutions to Problem A:

$$u=u_\infty\chi_\Omega+\frac{u_\infty\int_0^x\frac{b'(t)}{\sqrt{1+\tau^2b'(t)^2}}\mathrm{d}t}{b(x)\sqrt{1+\tau^2b'(x)^2}}\chi_{y=b(x)},$$
$$v=\frac{u_\infty\tau b'(x)\int_0^x\frac{b'(t)}{\sqrt{1+\tau^2b'(t)^2}}\mathrm{d}t}{b(x)\sqrt{1+\tau^2b'(x)^2}}\chi_{y=b(x)}, \tag{24}$$
$$\varrho=\rho_\infty\mathcal{L}^2\llcorner\Omega+\frac{\rho_\infty\tau b(x)^2}{\int_0^x\frac{b'(t)}{\sqrt{1-\tau^2b'(t)^2}}\mathrm{d}t}\delta_{y=b(x)},\ E=E_\infty\chi_\Omega+E_\infty\chi_{y=b(x)}.$$

Construct solutions of Problem B

$$\bar{u}=(-b'(\bar{x})^2+\frac{\int_0^{\bar{x}}b(t)b'(t)b''(t)\mathrm{d}t}{b(\bar{x})})\chi_{\bar{y}=b(\bar{x})},$$
$$\bar{\varrho}=\bar{\mathcal{L}}^2\llcorner\Omega'+\frac{b(\bar{x})}{\sqrt{1+b'(\bar{x})^2}}\delta_{\bar{y}=b(\bar{x})}, \tag{25}$$
$$v=b'(x)\chi_{\bar{y}=b(\bar{x})},\bar{E}=\bar{E}_\infty\chi_\Omega+\bar{E}_\infty\chi_{\bar{y}=b(\bar{x})}.$$

The solutions A converge to B

Email address: zhangmingxuan@mail.nwpu.edu.cn.

A proof of existence of Kaleidocycle

Shota Shigetomi

Institute of Mathematics for Industry, Kyushu University, Japan

A Kaleidocycle is a linkage mechanism consisting of k congruent tetrahedra. One of the features of this mechanism is that it deforms like a bubbling ring. It is known that this motion can be described by integrable systems if the motion is regarded as a deformation of discrete curves, but it has not been proven that this mechanism exists in the first place. In this talk, we will show that Kaleidocycle exists if the number of connecting tetrahedra k is greater than or equal to six.

A proof of existence of Kaleidocycle

Shota Shigetomi (Institute of Mathematics for Industry, Kyushu University, Japan)
Collaborators: Kenji Kajiwara (Kyushu Univ.), Shizuo Kaji (Kyoto Univ./Kyushu Univ.)

1.Introduction

- k-Kaleidocycle: A closed linkage mechanism that is composed of k identical tetrahedra jointed by hinges.
  - Everting motion
  - Folding paper
  - Conserved quantities
  - Single degree of freedom (Moblus Kaleidocycle)

- Formulation of Kaleidocycle: Isoperimetric deformation of a closed discrete space curve which is expressed by integrable equations.

Results

- An explicit formula for isoperimetric deformation of discrete space curve with constant torsion angle.
- The motion is expressed by semi-discrete integrable eqns.
- Closure condition→Kaleidocycle
- For any k≥6, k-Kaleidocycle exists

2.Tools: Hirota derivative and τ function

- Hirota derivative

- Elliptic theta function

3.Kaleidocycle and discrete curve

Discrete space curve

- Constructing a discrete curve from binormals

- Discrete Frenet-Serret formula

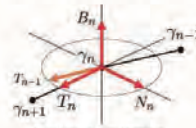

Kaleidocycle as a discrete curve

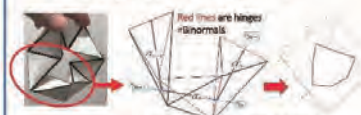

→Kaleidocycle:
Closed discrete curve γ_n with constant torsion angle and segment length

Consider the following deformation: $\left\langle \dot{\gamma}_n, \widetilde{B}_n \right\rangle = 0, \quad \left\langle \dot{\gamma}_n, \dot{\gamma}_n \right\rangle = \rho_\pm^2$

This motion **preserves torsion angle and segment length.**
By introducing the potential function Θ_n, the motion can be expressed by the **semi-discrete sine-Gordon eqn.** or the **semi-discrete potential mKdV eqn.**

$$\frac{\Theta_{n+1} \pm \Theta_n}{2} = (1 \pm \cos\lambda)\,\rho_\pm \sin\left(\frac{\Theta_{n+1} \mp \Theta_n}{2}\right)$$

Signed curvature angle can be written by using potential function: $\kappa_n = \dfrac{\Theta_{n+1} - \Theta_{n-1}}{2}$

4.An explicit formula of the discrete curve

A formula of discrete curve in terms of τ functions

Let $\lambda, \widetilde{G} \in \mathbb{C}$ be solutions to

Then,

satisfy discrete Frenet-Serret formula and

The curvature angle and the torsion angle can be written in terms of τ functions

Signed curvature angle : Torsion angle :

Explicitly construct τ functions with theta function

Main result1: An explicit formula of the curve

Period lattice of theta function:

Choose parameters

are solutions to

is a discrete space curve with **constant torsion angle**:

5.Existence of Kaleidocycle

The curve γ_n should be closed for all $t \in \mathbb{R}$ to form a k-Kaleidocycle
By rewriting closure condition in terms of parameters ν, τ, γ, we get the following:

$$\gamma_{n+k}(t) = \gamma_n(t) \qquad m := k\frac{\nu}{\gamma} \in \mathbb{Z} \setminus \{0\},$$
$$\text{for all } n \in \mathbb{Z}, t \in \mathbb{R} \iff \exp\{\pi i m(4r+1)\}(R_1R_3)^{-k} - 1 = 0,$$
$$(\Delta_3 + \Delta_1)k - 4\pi i m = 0.$$

Main result2

Thm.
For fixed k≥6, let k/2∤m>0. Then, there exist ν,τ,γ s.t. the above conditions are satisfied.

Proof
[1]The third condition can be solved in terms of r:

[2]By substituting r=r(γ;m/k) into the second condition, we see the solution γ exist if m≠3

[3]By considering transformations of m and n:
- m→-m,
- m→ km, n→ kn,

we see that it suffices to consider m in k/2>m>0.

6.Deformation of Kaleidocycle

The deformation equation of the curve changes depending on C, Γ.
By taking special C, Γ, the curve deforms to follow $\left\langle \dot{\gamma}_n, \widetilde{B}_n \right\rangle = 0, \quad \left\langle \dot{\gamma}_n, \dot{\gamma}_n \right\rangle = \rho_\pm^2$

Table 1. Relation between the three deformation equations

Values of C, Γ	Deformation eqn. of the curve	Deformation eqn. of potential function
$C, \Gamma \in \mathbb{R}$	$\dot{\gamma}_n = a_1 T_n - a_3 \tan\frac{\lambda}{2} N_n + a_3 \tan\frac{\lambda}{2} \widetilde{B}_n + \begin{pmatrix} 0 \\ 0 \\ a_4 \end{pmatrix}$	$\dot{\Theta}_n = a_3 \tan\left(\frac{\Theta_{n+1} - \Theta_{n-1}}{4}\right)$
↓ Specialise the deformation equation by choosing rigid transformation parameters C, Γ.		
C_1, Γ_1	$\left\langle \dot{\gamma}_n, \widetilde{B}_n \right\rangle = 0, \quad \left\langle \dot{\gamma}_n, \dot{\gamma}_n \right\rangle = \rho_-^2$	$\frac{\dot{\Theta}_{n+1} + \dot{\Theta}_n}{2} = (1 + \cos\lambda)\rho_- \sin\left(\frac{\Theta_{n+1} - \Theta_n}{2}\right)$
↕ By replacing the parameter m and the variable n of the solution with $m \to k - m, n \to k - n$, these two deformation equations transform to each other.		
C_2, Γ_2	$\left\langle \dot{\gamma}_n, \widetilde{B}_n \right\rangle = 0, \quad \left\langle \dot{\gamma}_n, \dot{\gamma}_n \right\rangle = \rho_+^2$	$\frac{\dot{\Theta}_{n+1} - \dot{\Theta}_n}{2} = (1 - \cos\lambda)\rho_+ \sin\left(\frac{\Theta_{n+1} + \Theta_n}{2}\right)$

7.Summary and future work

Summary
- We constructed an explicit formula for isoperimetric deformation of discrete space curve with constant torsion angle.
- We also checked the relation between signed curvature angle and semi-discrete integrable equations. This relation is consistent with previous research.
- This formula can be regarded as an explicit formula of Kaleidocycle.
- We proved that k-kaleidocycle exists if k≥6.

Future work
- To find conserved quantities of Kaleidocycle by using identities of theta functions.
- Show that Moblus Kaleidocycles has single degree of freedom.

Mathematical Model for Catheter Treatment in case with Multiple Stenoses

Haruka Suga

Joint Graduate School of Mathematics for Innovation, Kyushu University, Japan

There are many types of vascular diseases, some of which can be life-threatening. Catheter-based treatment is one method used to address arterial stenosis. Previous studies have used the Navier–Stokes equations to calculate blood flow in vessels with a single stenosis. However, real blood vessels are long and complex, and applying the Navier–Stokes equations in such cases can be computationally expensive. In this study, we constructed an approximate flow equation by fitting to data provided by our collaborator, Ms. Intan, who simulated the flow in vessels with a single stenosis. Using this fitted model, I determine which of the two stenoses should be treated first in order to complete the treatment in a shorter amount of time.

Mathematical Model for Catheter Treatment in case with Multiple Stenoses

HARUKA SUGA(1) | INTAN DIYANA MUNIR(2) | ATSUSHI TERO(3)

(1)Joint Graduate School of Mathematics for Innovation, Kyushu University (3) Institute of Mathematics for Industry, Kyushu University
(2) Department of Mathematical Science, Faculty of science, University of Technology Malaysia

Introduction

There are many diseases related to blood vessels. Vascular stenosis refers to a narrowing of blood vessels, typically caused by the buildup of plaques due to atherosclerosis. This condition can lead to serious illnesses such as myocardial infarction or stroke. Previous studies have modeled blood flow using the Navier–Stokes equation. However, because blood vessels are complex and long, solving such equation can be time-consuming. Therefore, the aim of this study is to reduce computation time by extracting characteristic parameters of blood vessels . As a first step, this research focuses on the case of a vessel with two stenoses.

Benefits of Catheterization Procedures

1.Improvement of blood flow

2.Allows for localized treatment

3.Less strain on the body

Research Goal

To determine which of the two stenoses should be treated first in order to complete the treatment in a shorter amount of time.

Situation

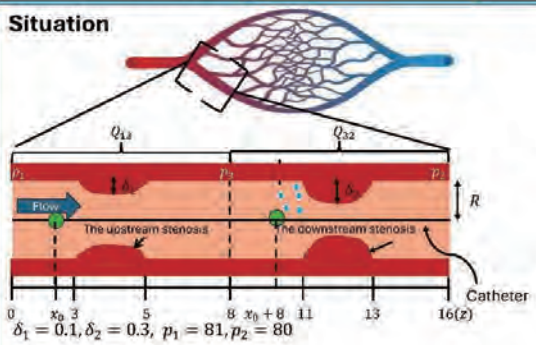

Assumption

- The drug delivered for treating the upstream stenosis does not affect the downstream stenosis.
- The amount of drug administered is constant.

Algorithm

$$Q = a_1\Delta p + a_2(\Delta p)^2 + a_3\delta\Delta p + a_4\delta + a_5\delta^2 + a_6$$

- Using numerical simulations of the Navier–Stokes equations, Ms. Intan analyzed blood flow in a vessel with a single stenosis. ($r \neq z$)
- Presenter fitted Intan's result to this formula.

$$Q = 909\Delta p - 430\delta\Delta p + 41\delta^2 - 12\delta$$

As the stenosis narrows, the amount of drug reaching it decreases.

$$\frac{d\delta}{dt} = -\frac{1}{d(R-\delta)Q} \qquad d : viscosity$$

The calculation is based on flow conservation in the network.

$$Q_{13} = Q_{32}$$

Result

(1) 1st step : Remove the **upstream** stenosis
2nd step : Remove the **downstream** stenosis

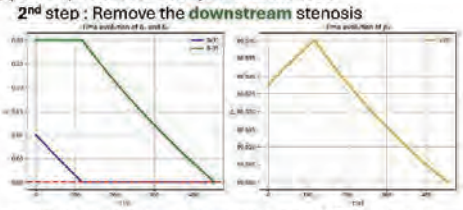

The time to remove **upstream** stenosis : **117.75** second
The time to remove **downstream** stenosis : **334.88** second
Total time : 452.63 second

(2) 1st step : Remove the **downstream** stenosis
2nd step : Remove the **upstream** stenosis

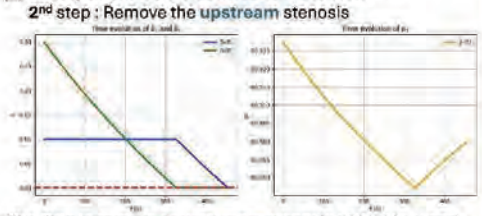

The time to remove **downstream** stenosis : **326.60**second
The time to remove **upstream** stenosis : **128.00** second
Total time : 454.60 second

Conclusion

- It was found that Pattern (1) removes all the stenoses in a shorter time than Pattern (2).
- The time required to remove the upstream stenosis is shorter for Pattern (1) compared Pattern (2)

Future Works

We plan to validate the model using real physiological data and extend this study to a more complex network system that represent realistic vascular system.

Reference

1. Haruka Suga, Construction and Evaluation of a Mathematical Model for Catheter Treatment of Multiple Vascular Stenoses (in progress)
2. Intan Diyana Munir. Flow Rate Analysis in a Catheterized Multi-Stenosed Artery for Optimising Treatment Order (in progress)

Homoclinic tangency of the largest codimension and statistical irregurarity

Kodai Yamamoto

Joint Graduate School of Mathematics for Innovation, Kyushu University, Japan

Given a continuous dynamical systems on a metric space, a point is called statistically irregular if the time average of a continuous function along its orbit does not exist. Takens posed the question of whether there exist persistence classes of smooth dynamical systems for which the set of statistically irregular points has positive Lebesgue measure. In this talk, I present a model of diffeomorphisms with homoclinic tangency of the largest codimension such that every C^r neighborhood of the model contains diffeomorphisms which has a set of statistically irregular points with positive Lebesgue measure.

Homoclinic tangency of the largest codimension and statistical irregularity

Kodai Yamamoto
Joint Graduate School of Mathematics for Innovation, Kyushu University, yamamoto.kodai.508@s.kyushu-u.ac.jp

Introduction

Dynamical systems is a field of mathematics that studies how systems evolve over time according to certain rules. Here, we consider a diffeomorphism f on a closed manifold X. A point $x \in X$ is called **statistically irregular** if the limit of the time average along the forward orbit $\{f^i(x) \mid i \geq 0\}$ does not exist. That is, the time average

$$\frac{1}{n+1}\sum_{i=0}^{n}\delta_{f^i(x)}$$

does not converge as $n \to \infty$ in the weak*-topology, where $\delta_{f^i(x)}$ is the Dirac measure at $f^i(x)$.

Question

- How large is the set of statistically irregular points?

→ Birkhoff's ergodic theorem implies that the set of statistically irregular points has zero measure with respect to any invariant measure.

But, for a general smooth dynamical systems that do not preserve Lebesgue measure, the set of statistically irregular points may have positive Lebesgue measure.

Takens' last problem [5]

Whether there are persistent classes of smooth dynamical systems such that the set of statistically irregular points has positive Lebesgue measure?

This problem has a strong relationship with non-hyperbolic phenomena. We say that a diffeomorphism f has a **homoclinic tangency** of a saddle fixed point p if the stable manifold $W^s(p,f)$ and the unstable manifold $W^u(p,f)$ have a non-empty and non-transverse intersection q. The **codimension of the tangency** $q \in M$ is defined by

$$c_T = \dim\left(T_qW^s(p) \cap T_qW^u(p)\right).$$

Affirmative answers to Takens' last problem have been obtained as a dense subset in the space of $n(\geq 2)$-dimensional diffeomorphisms with homoclinic tangency, beginning with the work of Kiriki and Soma [4]. However, all of these results are in $c_T = 1$, and the problem remains open in $c_T \geq 2$.

Question

Is there a dense set of smooth dynamical systems in the case of higher codimension ($c_T \geq 2$) such that the set of statistically irregular points has positive Lebesgue measure?

The following result provides the first example of a step toward solving Takens' last problem in the case of higher codimension.

Main result

There exists a diffeomorphism f of $\mathbb{R}^1$ and a sequence of diffeomorphisms f_n converging to f such that
(1) f has a homoclinic tangency of the largest codimension $c_T = \dim \mathbb{R}^4/2 = 2$.
(2) for sufficiently large n, f_n has a set of statistically irregular points with positive Lebesgue measure.

Construction

Our main construction generates an orbit exhibiting oscillatory behavior between fixed points p and q of a blender-horseshoe, following the method Colli and Vargas [2] and Kiriki, Nakano and Soma [3], based on the stable intersection of higher-dimensional Cantor sets by Asaoka [1].

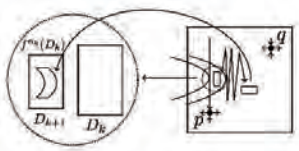

Figure: Construction of statistically irregular orbits.

References

[1] M. Asaoka, Stable intersection of Cantor sets in higher dimension and robust homoclinic tangency of the largest codimension, Trans. Amer. Math. Soc., 375(2):873-908, 2022.
[2] E. Colli and E. Vargas, Non-trivial wandering domains and homoclinic bifurcations, Ergodic Theory Dynam. Systems, 21(6):1657-1681, 2001.
[3] S. Kiriki, Y. Nakano and T. Soma, Historic and physical wandering domains for wild blender-horseshoes, Nonlinearity, 36(8):4007-4033, 2023.
[4] S. Kiriki and T. Soma, Takens' last problem and existence of non-trivial wandering domains, Adv. Math., 306:524-588, 2017.
[5] F. Takens, Orbits with historic behaviour, or non-existence of averages, Nonlinearity, 21(3):T33-T36, 2008.

MI レクチャーノートシリーズ刊行にあたり

本レクチャーノートシリーズは、文部科学省 21 世紀 COE プログラム「機能数理学の構築と展開」（H15-19 年度）において作成した COE Lecture Notes の続刊であり、文部科学省大学院教育改革支援プログラム「産業界が求める数学博士と新修士養成」（H19-21 年度）および、同グローバル COE プログラム「マス・フォア・インダストリ教育研究拠点」（H20-24 年度）において行われた講義の講義録として出版されてきた。平成 23 年 4 月のマス・フォア・インダストリ研究所（IMI）設立と平成 25 年 4 月の IMI の文部科学省共同利用・共同研究拠点として「産業数学の先進的･基礎的共同研究拠点」の認定を受け、今後、レクチャーノートは、マス・フォア・インダストリに関わる国内外の研究者による講義の講義録、会議録等として出版し、マス・フォア・インダストリの本格的な展開に資するものとする。

2022 年 10 月
マス・フォア・インダストリ研究所
所長　梶原 健司

International Project Research-Workshop (I)

Forum “Math for Industry” 2025
- Challenge of Mathematics for Industry in the AI era -

発　行　2026 年 1 月 5 日
編集長　Zaitul Marlizawati Zainuddin, Arifah Bahar
編　集　Shariffah Suhaila Syed Jamaludin, Zaiton Mat Isa, Nur Arina Bazilah Aziz, Taufiq Khairi Ahmad Khairuddin, Shaymaa M.H. Darwish, Ahmad Razin Zainal Abidin, Norhaiza Ahmad, Zainal Abdul Aziz, Hang See Pheng, Mohd Ali Khameini Ahmad
発　行　九州大学マス・フォア・インダストリ研究所
九州大学大学院数理学府
〒819-0395 福岡市西区元岡744
九州大学数理・IMI 事務室
TEL 092-802-4402　FAX 092-802-4405
URL https://www.imi.kyushu-u.ac.jp/

印　刷　城島印刷株式会社
〒810-0012 福岡市中央区白金 2 丁目 9 番 6 号
TEL 092-531-7102　FAX 092-524-4411

シリーズ既刊

Issue	Author／Editor	Title	Published
COE Lecture Note	Mitsuhiro T. NAKAO Kazuhiro YOKOYAMA	Computer Assisted Proofs - Numeric and Symbolic Approaches - 199pages	August 22, 2006
COE Lecture Note	M.J.Shai HARAN	Arithmetical Investigations - Representation theory, Orthogonal polynomials and Quantum interpolations- 174pages	August 22, 2006
COE Lecture Note Vol.3	Michal BENES Masato KIMURA Tatsuyuki NAKAKI	Proceedings of Czech-Japanese Seminar in Applied Mathematics 2005 155pages	October 13, 2006
COE Lecture Note Vol.4	宮田　健治	辺要素有限要素法による磁界解析 - 機能数理学特別講義 21pages	May 15, 2007
COE Lecture Note Vol.5	Francois APERY	Univariate Elimination Subresultants - Bezout formula, Laurent series and vanishing conditions - 89pages	September 25, 2007
COE Lecture Note Vol.6	Michal BENES Masato KIMURA Tatsuyuki NAKAKI	Proceedings of Czech-Japanese Seminar in Applied Mathematics 2006 209pages	October 12, 2007
COE Lecture Note Vol.7	若山　正人 中尾　充宏	九州大学産業技術数理研究センター キックオフミーティング 138pages	October 15, 2007
COE Lecture Note Vol.8	Alberto PARMEGGIANI	Introduction to the Spectral Theory of Non-Commutative Harmonic Oscillators 233pages	January 31, 2008
COE Lecture Note Vol.9	Michael I.TRIBELSKY	Introduction to Mathematical modeling 23pages	February 15, 2008
COE Lecture Note Vol.10	Jacques FARAUT	Infinite Dimensional Spherical Analysis 74pages	March 14, 2008
COE Lecture Note Vol.11	Gerrit van DIJK	Gelfand Pairs And Beyond 60pages	August 25, 2008
COE Lecture Note Vol.12	Faculty of Mathematics, Kyushu University	Consortium “MATH for INDUSTRY” First Forum 87pages	September 16, 2008
COE Lecture Note Vol.13	九州大学大学院 数理学研究院	プロシーディング「損保数理に現れる確率モデル」 ― 日新火災・九州大学 共同研究2008年11月 研究会 ― 82pages	February 6, 2009

シリーズ既刊

Issue	Author／Editor	Title	Published
COE Lecture Note Vol.14	Michal Beneš, Tohru Tsujikawa Shigetoshi Yazaki	Proceedings of Czech-Japanese Seminar in Applied Mathematics 2008 77pages	February 12, 2009
COE Lecture Note Vol.15	Faculty of Mathematics, Kyushu University	International Workshop on Verified Computations and Related Topics 129pages	February 23, 2009
COE Lecture Note Vol.16	Alexander Samokhin	Volume Integral Equation Method in Problems of Mathematical Physics 50pages	February 24, 2009
COE Lecture Note Vol.17	矢嶋　　徹 及川　正行 梶原　健司 辻　　英一 福本　康秀	非線形波動の数理と物理 66pages	February 27, 2009
COE Lecture Note Vol.18	Tim Hoffmann	Discrete Differential Geometry of Curves and Surfaces 75pages	April 21, 2009
COE Lecture Note Vol.19	Ichiro Suzuki	The Pattern Formation Problem for Autonomous Mobile Robots —Special Lecture in Functional Mathematics— 23pages	April 30, 2009
COE Lecture Note Vol.20	Yasuhide Fukumoto Yasunori Maekawa	Math-for-Industry Tutorial: Spectral theories of non-Hermitian operators and their application 184pages	June 19, 2009
COE Lecture Note Vol.21	Faculty of Mathematics, Kyushu University	Forum “Math-for-Industry” Casimir Force, Casimir Operators and the Riemann Hypothesis 95pages	November 9, 2009
COE Lecture Note Vol.22	Masakazu Suzuki Hoon Hong Hirokazu Anai Chee Yap Yousuke Sato Hiroshi Yoshida	The Joint Conference of ASCM 2009 and MACIS 2009: Asian Symposium on Computer Mathematics Mathematical Aspects of Computer and Information Sciences 436pages	December 14, 2009
COE Lecture Note Vol.23	荒川　恒男 金子　昌信	多重ゼータ値入門 111pages	February 15, 2010
COE Lecture Note Vol.24	Fulton B.Gonzalez	Notes on Integral Geometry and Harmonic Analysis 125pages	March 12, 2010
COE Lecture Note Vol.25	Wayne Rossman	Discrete Constant Mean Curvature Surfaces via Conserved Quantities 130pages	May 31, 2010
COE Lecture Note Vol.26	Mihai Ciucu	Perfect Matchings and Applications 66pages	July 2, 2010

シリーズ既刊

Issue	Author／Editor	Title	Published
COE Lecture Note Vol.27	九州大学大学院 数理学研究院	Forum “Math-for-Industry” and Study Group Workshop Information security, visualization, and inverse problems, on the basis of optimization techniques　100pages	October 21, 2010
COE Lecture Note Vol.28	ANDREAS LANGER	MODULAR FORMS, ELLIPTIC AND MODULAR CURVES LECTURES AT KYUSHU UNIVERSITY 2010　62pages	November 26, 2010
COE Lecture Note Vol.29	木田　雅成 原田　昌晃 横山　俊一	Magma で広がる数学の世界　157pages	December 27, 2010
COE Lecture Note Vol.30	原　　隆 松井　　卓 廣島　文生	Mathematical Quantum Field Theory and Renormalization Theory 201pages	January 31, 2011
COE Lecture Note Vol.31	若山　正人 福本　康秀 高木　　剛 山本　昌宏	Study Group Workshop 2010 Lecture & Report　128pages	February 8, 2011
COE Lecture Note Vol.32	Institute of Mathematics for Industry, Kyushu University	Forum “Math-for-Industry” 2011 “TSUNAMI-Mathematical Modelling” Using Mathematics for Natural Disaster Prediction, Recovery and Provision for the Future　90pages	September 30, 2011
COE Lecture Note Vol.33	若山　正人 福本　康秀 高木　　剛 山本　昌宏	Study Group Workshop 2011 Lecture & Report　140pages	October 27, 2011
COE Lecture Note Vol.34	Adrian Muntean Vladimír Chalupecký	Homogenization Method and Multiscale Modeling　72pages	October 28, 2011
COE Lecture Note Vol.35	横山　俊一 夫　　紀恵 林　　卓也	計算機代数システムの進展　210pages	November 30, 2011
COE Lecture Note Vol.36	Michal Beneš Masato Kimura Shigetoshi Yazaki	Proceedings of Czech-Japanese Seminar in Applied Mathematics 2010 107pages	January 27, 2012
COE Lecture Note Vol.37	若山　正人 高木　　剛 Kirill Morozov 平岡　裕章 木村　正人 白井　朋之 西井　龍映 栄　伸一郎 穴井　宏和 福本　康秀	平成23年度 数学・数理科学と諸科学・産業との連携研究ワークショップ　拡がっていく数学　～期待される “見えない力” ～ 154pages	February 20, 2012

シリーズ既刊

Issue	Author／Editor	Title	Published
COE Lecture Note Vol.38	Fumio Hiroshima Itaru Sasaki Herbert Spohn Akito Suzuki	Enhanced Binding in Quantum Field Theory 204pages	March 12, 2012
COE Lecture Note Vol.39	Institute of Mathematics for Industry, Kyushu University	Multiscale Mathematics: Hierarchy of collective phenomena and interrelations between hierarchical structures 180pages	March 13, 2012
COE Lecture Note Vol.40	井ノ口順一 太田　泰広 筧　　三郎 梶原　健司 松浦　　望	離散可積分系・離散微分幾何チュートリアル2012 152pages	March 15, 2012
COE Lecture Note Vol.41	Institute of Mathematics for Industry, Kyushu University	Forum “Math-for-Industry” 2012 “Information Recovery and Discovery” 91pages	October 22, 2012
COE Lecture Note Vol.42	佐伯　　修 若山　正人 山本　昌宏	Study Group Workshop 2012 Abstract, Lecture & Report 178pages	November 19, 2012
COE Lecture Note Vol.43	Institute of Mathematics for Industry, Kyushu University	Combinatorics and Numerical Analysis Joint Workshop 103pages	December 27, 2012
COE Lecture Note Vol.44	萩原　　学	モダン符号理論からポストモダン符号理論への展望 107pages	January 30, 2013
COE Lecture Note Vol.45	金山　　寛	Joint Research Workshop of Institute of Mathematics for Industry (IMI), Kyushu University “Propagation of Ultra-large-scale Computation by the Domain-decomposition-method for Industrial Problems (PUCDIP 2012)” 121pages	February 19, 2013
COE Lecture Note Vol.46	西井　龍映 栄　伸一郎 岡田　勘三 落合　啓之 小磯　深幸 斎藤　新悟 白井　朋之	科学・技術の研究課題への数学アプローチ ―数学モデリングの基礎と展開― 325pages	February 28, 2013
COE Lecture Note Vol.47	SOO TECK LEE	BRANCHING RULES AND BRANCHING ALGEBRAS FOR THE COMPLEX CLASSICAL GROUPS 40pages	March 8, 2013
COE Lecture Note Vol.48	溝口　佳寛 脇　　隼人 平坂　　貢 谷口　哲至 島袋　　修	博多ワークショップ「組み合わせとその応用」 124pages	March 28, 2013

シリーズ既刊

Issue	Author／Editor	Title	Published
COE Lecture Note Vol.49	照井　章 小原　功任 濱田　龍義 横山　俊一 穴井　宏和 横田　博史	マス・フォア・インダストリ研究所　共同利用研究集会 II 数式処理研究と産学連携の新たな発展　137pages	August 9, 2013
MI Lecture Note Vol.50	Ken Anjyo Hiroyuki Ochiai Yoshinori Dobashi Yoshihiro Mizoguchi Shizuo Kaji	Symposium MEIS2013: Mathematical Progress in Expressive Image Synthesis　154pages	October 21, 2013
MI Lecture Note Vol.51	Institute of Mathematics for Industry, Kyushu University	Forum “Math-for-Industry” 2013 “The Impact of Applications on Mathematics”　97pages	October 30, 2013
MI Lecture Note Vol.52	佐伯　修 岡田　勘三 髙木　剛 若山　正人 山本　昌宏	Study Group Workshop 2013 Abstract, Lecture & Report　142pages	November 15, 2013
MI Lecture Note Vol.53	四方　義啓 櫻井　幸一 安田　貴徳 Xavier Dahan	平成25年度　九州大学マス・フォア・インダストリ研究所 共同利用研究集会　安全・安心社会基盤構築のための代数構造 ～サイバー社会の信頼性確保のための数理学～　158pages	December 26, 2013
MI Lecture Note Vol.54	Takashi Takiguchi Hiroshi Fujiwara	Inverse problems for practice, the present and the future　93pages	January 30, 2014
MI Lecture Note Vol.55	栄　伸一郎 溝口　佳寛 脇　隼人 渋田　敬史	Study Group Workshop 2013 数学協働プログラム Lecture & Report 98pages	February 10, 2014
MI Lecture Note Vol.56	Yoshihiro Mizoguchi Hayato Waki Takafumi Shibuta Tetsuji Taniguchi Osamu Shimabukuro Makoto Tagami Hirotake Kurihara Shuya Chiba	Hakata Workshop 2014 ~ Discrete Mathematics and its Applications ~　141pages	March 28, 2014
MI Lecture Note Vol.57	Institute of Mathematics for Industry, Kyushu University	Forum “Math-for-Industry” 2014: “Applications + Practical Conceptualization + Mathematics = fruitful Innovation”　93pages	October 23, 2014
MI Lecture Note Vol.58	安生健一 落合啓之	Symposium MEIS2014: Mathematical Progress in Expressive Image Synthesis　135pages	November 12, 2014

シリーズ既刊

Issue	Author／Editor	Title	Published
MI Lecture Note Vol.59	西井　龍映 岡田　勘三 梶原　健司 髙木　　剛 若山　正人 脇　　隼人 山本　昌宏	Study Group Workshop 2014 数学協働プログラム Abstract, Lecture & Report　196pages	November 14, 2014
MI Lecture Note Vol.60	西浦　　博	平成26年度九州大学 IMI 共同利用研究・研究集会（I） 感染症数理モデルの実用化と産業及び政策での活用のための新たな展開　120pages	November 28, 2014
MI Lecture Note Vol.61	溝口　佳寛 Jacques Garrigue 萩原　　学 Reynald Affeldt	研究集会 高信頼な理論と実装のための定理証明および定理証明器 Theorem proving and provers for reliable theory and implementations (TPP2014)　138pages	February 26, 2015
MI Lecture Note Vol.62	白井　朋之	Workshop on “β-transformation and related topics”　59pages	March 10, 2015
MI Lecture Note Vol.63	白井　朋之	Workshop on “Probabilistic models with determinantal structure” 107pages	August 20, 2015
MI Lecture Note Vol.64	落合　啓之 土橋　宜典	Symposium MEIS2015: Mathematical Progress in Expressive Image Synthesis　124pages	September 18, 2015
MI Lecture Note Vol.65	Institute of Mathematics for Industry, Kyushu University	Forum “Math-for-Industry” 2015 “The Role and Importance of Mathematics in Innovation”　74pages	October 23, 2015
MI Lecture Note Vol.66	岡田　勘三 藤澤　克己 白井　朋之 若山　正人 脇　　隼人 Philip Broadbridge 山本　昌宏	Study Group Workshop 2015 Abstract, Lecture & Report 156pages	November 5, 2015
MI Lecture Note Vol.67	Institute of Mathematics for Industry, Kyushu University	IMI-La Trobe Joint Conference “Mathematics for Materials Science and Processing” 66pages	February 5, 2016
MI Lecture Note Vol.68	古庄　英和 小谷　久寿 新甫　洋史	結び目と Grothendieck-Teichmüller 群 116pages	February 22, 2016
MI Lecture Note Vol.69	土橋　宜典 鍛治　静雄	Symposium MEIS2016: Mathematical Progress in Expressive Image Synthesis　82pages	October 24, 2016
MI Lecture Note Vol.70	Institute of Mathematics for Industry, Kyushu University	Forum “Math-for-Industry” 2016 “Agriculture as a metaphor for creativity in all human endeavors” 98pages	November 2, 2016
MI Lecture Note Vol.71	小磯　深幸 二宮　嘉行 山本　昌宏	Study Group Workshop 2016 Abstract, Lecture & Report　143pages	November 21, 2016

シリーズ既刊

Issue	Author／Editor	Title	Published
MI Lecture Note Vol.72	新井　朝雄 小嶋　　泉 廣島　文生	Mathematical quantum field theory and related topics　133pages	January 27, 2017
MI Lecture Note Vol.73	穴田　啓晃 Kirill Morozov 須賀　祐治 奥村　伸也 櫻井　幸一	Secret Sharing for Dependability, Usability and Security of Network Storage and Its Mathematical Modeling　211pages	March 15, 2017
MI Lecture Note Vol.74	QUISPEL, G. Reinout W. BADER, Philipp MCLAREN, David I. TAGAMI, Daisuke	IMI-La Trobe Joint Conference Geometric Numerical Integration and its Applications　71pages	March 31, 2017
MI Lecture Note Vol.75	手塚　　集 田上　大助 山本　昌宏	Study Group Workshop 2017 Abstract, Lecture & Report　118pages	October 20, 2017
MI Lecture Note Vol.76	宇田川誠一	Tzitzéica 方程式の有限間隙解に付随した極小曲面の構成理論 ―Tzitzéica 方程式の楕円関数解を出発点として―　68pages	August 4, 2017
MI Lecture Note Vol.77	松谷　茂樹 佐伯　　修 中川　淳一 田上　大助 上坂　正晃 Pierluigi Cesana 濵田　裕康	平成29年度　九州大学マス・フォア・インダストリ研究所 共同利用研究集会（I） 結晶の界面，転位，構造の数理　148pages	December 20, 2017
MI Lecture Note Vol.78	瀧澤　重志 小林　和博 佐藤憲一郎 斎藤　　努 清水　正明 間瀬　正啓 藤澤　克樹 神山　直之	平成29年度　九州大学マス・フォア・インダストリ研究所 プロジェクト研究　研究集会（I） 防災・避難計画の数理モデルの高度化と社会実装へ向けて 136pages	February 26, 2018
MI Lecture Note Vol.79	神山　直之 畔上　秀幸	平成29年度　AIMaP チュートリアル 最適化理論の基礎と応用　96pages	February 28, 2018
MI Lecture Note Vol.80	Kirill Morozov Hiroaki Anada Yuji Suga	IMI Workshop of the Joint Research Projects Cryptographic Technologies for Securing Network Storage and Their Mathematical Modeling　116pages	March 30, 2018
MI Lecture Note Vol.81	Tsuyoshi Takagi Masato Wakayama Keisuke Tanaka Noboru Kunihiro Kazufumi Kimoto Yasuhiko Ikematsu	IMI Workshop of the Joint Research Projects International Symposium on Mathematics, Quantum Theory, and Cryptography　246pages	September 25, 2019
MI Lecture Note Vol.82	池森　俊文	令和2年度　AIMaP チュートリアル 新型コロナウイルス感染症にかかわる諸問題の数理 145pages	March 22, 2021

シリーズ既刊

Issue	Author／Editor	Title	Published
MI Lecture Note Vol.83	早川健太郎 軸丸　芳揮 横須賀洋平 可香谷　隆 林　　和希 堺　　雄亮	シェル理論・膜理論への微分幾何学からのアプローチと その建築曲面設計への応用　49pages	July 28, 2021
MI Lecture Note Vol.84	Taketoshi Kawabe Yoshihiro Mizoguchi Junichi Kako Masakazu Mukai Yuji Yasui	SICE-JSAE-AIMaP Tutorial Advanced Automotive Control and Mathematics　110pages	December 27, 2021
MI Lecture Note Vol.85	Hiroaki Anada Yasuhiko Ikematsu Koji Nuida Satsuya Ohata Yuntao Wang	IMI Workshop of the Joint Usage Research Projects Exploring Mathematical and Practical Principles of Secure Computation and Secret Sharing　114pages	February 9, 2022
MI Lecture Note Vol.86	濱田　直希 穴井　宏和 梅田　裕平 千葉　一永 佐藤　寛之 能島　裕介 加葉田雄太朗 一木　俊助 早野　健太 佐伯　　修	2020年度採択分　九州大学マス・フォア・インダストリ研究所 共同利用研究集会 進化計算の数理　135pages	February 22, 2022
MI Lecture Note Vol.87	Osamu Saeki, Ho Tu Bao, Shizuo Kaji, Kenji Kajiwara, Nguyen Ha Nam, Ta Hai Tung, Melanie Roberts, Masato Wakayama, Le Minh Ha, Philip Broadbridge	Proceedings of Forum “Math-for-Industry” 2021 -Mathematics for Digital Economy-　122pages	March 28, 2022
MI Lecture Note Vol.88	Daniel PACKWOOD Pierluigi CESANA, Shigenori FUJIKAWA, Yasuhide FUKUMOTO, Petros SOFRONIS, Alex STAYKOV	Perspectives on Artificial Intelligence and Machine Learning in Materials Science, February 4-6, 2022　74pages	November 8, 2022

シリーズ既刊

Issue	Author／Editor	Title	Published
MI Lecture Note Vol.89	松谷　茂樹 落合　啓之 井上　和俊 小磯　深幸 佐伯　　修 白井　朋之 垂水　竜一 内藤　久資 中川　淳一 濵田　裕康 松江　　要 加葉田雄太朗	2022年度採択分 九州大学マス・フォア・インダストリ研究所 共同利用研究集会 材料科学における幾何と代数 III　356pages	December 7, 2022
MI Lecture Note Vol.90	中山　尚子 谷川　拓司 品野　勇治 近藤　正章 石原　　亨 鍛冶　静雄 藤澤　克樹	2022年度採択分 九州大学マス・フォア・インダストリ研究所 共同利用研究集会 データ格付けサービス実現のための数理基盤の構築　58pages	December 12, 2022
MI Lecture Note Vol.91	Katsuki Fujisawa Shizuo Kaji Toru Ishihara Masaaki Kondo Yuji Shinano Takuji Tanigawa Naoko Nakayama	IMI Workshop of the Joint Usage Research Projects Construction of Mathematical Basis for Realizing Data Rating Service 610pages	December 27, 2022
MI Lecture Note Vol.92	丹田　　聡 三宮　　俊 廣島　文生	2022年度採択分 九州大学マス・フォア・インダストリ研究所 共同利用研究集会 時間・量子測定・準古典近似の理論と実験 ～古典論と量子論の境界～　150pages	Janualy 6, 2023
MI Lecture Note Vol.93	Philip Broadbridge Luke Bennetts Melanie Roberts Kenji Kajiwara	Proceedings of Forum “Math-for-Industry” 2022 -Mathematics of Public Health and Sustainability-　170pages	June 19, 2023
MI Lecture Note Vol.94	國廣　　昇 池松　泰彦 伊豆　哲也 穴田　啓晃 縫田　光司	2023年度採択分 九州大学マス・フォア・インダストリ研究所 共同利用研究集会 現代暗号に対する安全性解析・攻撃の数理　260pages	Janualy 11, 2024
MI Lecture Note Vol.96	澤田　茉伊	2023年度採択分 九州大学マス・フォア・インダストリ研究所 共同利用研究集会 デジタル化時代に求められる斜面防災の思考法　70pages	March 18, 2024

シリーズ既刊

Issue	Author／Editor	Title	Published
MI Lecture Note Vol.97	Shariffah Suhaila Syed Jamaludin Zaiton Mat Isa Nur Arina Bazilah Aziz Taufiq Khairi Ahmad Khairuddin Shaymaa M.H.Darwish Ahmad Razin Zainal Abidin Norhaiza Ahmad Zainal Abdul Aziz Hang See Pheng Mohd Ali Khameini Ahmad	International Project Research-Workshop (I) Proceedings of 4th Malaysia Mathematics in Industry Study Group (MMISG2023)　172pages	March 28, 2024
MI Lecture Note Vol.98	中澤　　嵩	2024 年度採択分 九州大学マス・フォア・インダストリ研究所 共同利用研究集会 自動車性能の飛躍的向上を目指す Data-Driven 設計　92pages	January 30, 2025
MI Lecture Note Vol.99	Jacques Garrigue	2024 年度採択分 九州大学マス・フォア・インダストリ研究所 共同利用研究集会 コンピュータによる定理証明支援とその応用　308pages	March 17, 2025
MI Lecture Note Vol.100	Yutaka Jitsumatsu Masayoshi Ohashi Akio Hasegawa Katsutoshi Shinohara Shintaro Mori	IMI Workshop of the Joint Usage Research Projects Mathematics for Innovation in Information and Communication Technology 274pages	March 19, 2025
MI Lecture Note Vol.101	Makoto Ohsaki Yoshiki Jikumaru	IMI Workshop of the Joint Usage Research Projects Evolving Design and Discrete Differential Geometry:towards Mathematics Aided Geometric Design 528pages	October 1st, 2025
MI Lecture Note Vol.102	Keunsu Kim	Young Researchers and Students-Workshop (I) Topological Data Analysis and Industrial Mathematics 198 pages	December 22, 2025
MI Lecture Note Vol.103	Kulbir Ghuman Pierluigi Cesana, Kenji Kajiwara, Yu Kaneko Linh Thi Hoai Nguyen Daniel Packwood, Yasser Salah Eddine Bouchareb	International Project Research-Workshop (I) Advancing Materials Data, Design and Discovery 102 pages	December 26, 2025

九州大学マス・フォア・インダストリ研究所
九州大学大学院 数理学府
〒819-0395 福岡市西区元岡744　TEL 092-802-4402　FAX 092-802-4405
URL https://www.imi.kyushu-u.ac.jp/